cea DAM

3rd International Workshop

on

THE PHYSICS OF COMPRESSIBLE TURBULENT MIXING

Abbey of Royaumont (France) - JUNE 17 - 19, 1991

FRONT COVER

Colorized version of a black and white Schlieren photograph of a mixing zone between air (top, red color) and sulphur hexafluoride (SF6, bottom, blue) induced by the Richtmyer-Meshkov instability in the Vaujours vertical shock tube (horizontal scale 7.5 cm). The incident shock in SF6 (Mach 1.45) has accelerated upward a 1.7 cm wide molecular diffusion zone with a weak embedded perturbation due to the retraction (from right to left) of a separating blade. The picture shows the amplification of these perturbations, 3.15 ms after the initial interaction, and about the time of passage of the second shock reflected from the end plate of the shock tube (located 54.4 cm above the blade). On the original Schlieren picture (printed upside down on page 25 in CHOCS 2, CEA DAM scientific and technical journal) the fine scales visible on the SF6 side are the signature of turbulent mixing in the boundary layers, but the more puzzling smoothness of the edges of the interpenetrating air bubble (center) and SF6 spikes (on its sides) may be due to an optical effect. These details are somewhat erased by the colorization process which was performed by the laser experiments group at Limeil.

3rd International Workshop

on

THE PHYSICS OF COMPRESSIBLE TURBULENT MIXING

Abbey of Royaumont (France) - JUNE 17 - 19, 1991

Royaumont, France

Edited by D. Besnard, J.-F. Hass, P.-A. Holstein & B. Sitt

Interfaces dynamics is of widening interest. Let us quote for instance the study of targets for fusion by inertial confinement, which leads to necessarily forecast the evolution of two phases regarding thermonuclear and inert medium. The normal process will induce the mixing of these two media, and then the extinction of the wished thermonuclear reactions.

For this seemingly limited problem at first sight, one must use the most sophisticated tools for turbulence, and dynamics systems studies, non linear equations and numerical methods.

The reader will find an up to date report on those subjects in this book.

We are grateful to Mrs WILKE, and her team for the exceptionnally efficient organization. She devoted herself tirelessly and kindly to every step of the intellectual and material event. We owe her a fruitful scientific meeting and thank her warmheartily.

Robert DAUTRAY
Member of Academy of Sciences

SCIENTIFIC COMMITTEE

Robert DAUTRAY	Conference Chairman	Scientific Director of the Commissariat à l'Energie Atomique Member of the Académie des Sciences France
James GLIMM		State University of New York at Stony Brook U.S.A.
Frank HARLOW		Los Alamos National Laboratory U.S.A.
Bernard LARROUTUROU		INRIA-Sophia Antipolis France
Cecil LEITH		Lawrence Livermore National Laboratory U.S.A.
Marcel LESIEUR		Institut de Mécanique de Grenoble France
Evgeny MESHKOV		Experimental Physics Institute, Arzamas Russia
Roland OMNES		Université de Paris XI France
Yves POMEAU		Ecole Normale Supérieure, Paris France
Bradford STURTEVANT		California Institute of Technology U.S.A.
David YOUNGS		Atomic Weapons Establishment, Aldermaston U.K.

ORGANIZING COMMITTEE

Didier BESNARD	CEL-V	Pierre-André HOLSTEIN	CEL-V
Claude CAVAILLER	CEV-M	Jacqueline MONTIGNY	CEL-V
Luc DAGENS	CEL-V	Christiane PARISOT	CEL-V
Paul FIGEAC	CEL-V	Viviane RUPERT	LLNL
Michel de GLINIASTY	CEL-V	Bernard SITT	CEV-M
Jean-François HAAS	CEL-V	Nicole WILKE	CEA

with the participation of : Nicole HUSSON, Edith KURAS, Jacques LAMY, Sylvie LIEGEOIS, Philippe LOREAUX and Florence NICOLAS

FOREWORD

We are happy to finally issue the Proceedings of the Royaumont Workshop on Compressible Turbulent Mixing, the third of a series initiated in Princeton in November 1988 and in Pleasanton in October 1989. The next workshop will be organized at the end of March 1993 in Cambridge (UK) by Paul Linden and David Youngs. For the Royaumont proceedings, we have attempted to be fast and decided to simply duplicate the texts as provided by the authors, almost without any editing or reformatting. We are nevertheless late: the deadline for submitting papers was postponed from July to October but the Organizing Committee takes full responsibility for the subsequent delay, mostly due to the preparation of our reports on the roundtable activities.

The proceedings include the papers of most oral or poster presentations at the workshop (three papers are missing) but we have added nine papers by prospective russian participants who unfortunately could not make it to Royaumont. To the 25 papers and 24 posters, we have added qualitative summaries and overviews of the experimental, numerical and theoretical roundtables, and a somewhat lengthy yet uncomplete compilation of some of the numerical test problems results. Clearly a lot more could be done in terms of precise, quantitative comparisons among models, calculations and experiments. Some progress will certainly made on this account for the next workshop.

The Organizing Committee

COMMUNICATIONS

Page

MONDAY June 17, 1991 :

Royaumont, France *Edited by D. Besnard, J.-F. Hass, P.-A. Holstein & B. Sitt*

TUESDAY June 18, 1991 :

WEDNESDAY June 19, 1991 :

POSTERS

Page

ROUND TABLES

Page

NON - STATIONARY FLOWS IN THE PROXIMITY OF ANGULAR POINTS OF GAS ACCELERATED LIQUID LAYER

V.Rogatchov, I.Zhidov, B.Klopov, E.Meshkov, A.Tolshmyakov
All - Union Experimental Physics Institute, Arzamas-16, USSR

ABSTRACT

Acceleration of a fractured fluid layer by gas is being experimentally (on gel models) and theoretically investigated. In the proximity of angular points the anomalous picture of fluid surface deformation and turbulent mixing layer evolution is observed. Depending on the angle value either fast growing cavern or new angular peculiarity is formed in its vertex.

Investigation of turbulent mixing dynamics is normally conducted according to the classic scheme, i.e. when unstable interface between two different density fluids has a flat form (e.g. [1,2,3]). In this case initial perturbations are insignificant as a rule, and have occasional nature.

To better understand the nature of a mixing process a series of investigations associated with different controlled initial perturbations' spectra has been carried out. The simplest among those is a sinusoidal one, the evolution of which leads to characteristic dynamic structure formation, consisting of "bubbles" and "spikes" (e.g.[4,5,6]). The experimental data helped to understand in more detail the role of individual harmonics in the general turbulent mixing picture and served as a basis for theoretical modeling[7,8] .

We have experimentally investigated[9] the picture of fluid and gas mixing, large initial perturbations at the accelerated surface being present.

The purpose of this report is to investigate evolution of perturbations at the interface between fluid and gas , angular peculiarities being present. Disturbance propagation together with the naturally present occasional disturbances propagation result in the complex mixing picture, characterized by hydrodynamic flow special regular structure springing up.

Typical flows of this kind spring up, for instance, when plates and shells containing surface fractures at the initial stage are accelerated by high explosives. One of the special flows' embodements is a cumulative jet, formed by the oblique plate collision.

EXPERIMENTAL

Specially developed jelly technology[10] have been used in our experimental procedures. Due to its relative strength gel is pretty suitable for complex structures manufacturing. However under the pressure drop of several atmospheres it acts like a fluid, its

strength properties becoming insignificant. It has been experimentally verified (by gel cub squashing) that its characteristic collapsing pressure equals to 0.05 atm. Due to gel transparency photographic techniques for flow registration can be applied.

Figure 1 comprises the experimental device scheme. Flat gel model (1) was disposed between two 20mm thick plates (2), (3), made from plexiglas. The distance between the plates was restricted by 10mm high side walls (4). The gel (6 cm^3 of gelatin, 100 cm^3 of water) at the ambient temperature was poured into the form. The form was kept in the fridge until gel thickening . Experimental device with the upper plate removed served as the form. The inner volume of the model (5) was formed by the contouring foil, fixed inside the experimental device before gel pouring. After gel thickening the foil was removed; the outer model contour was cut out by a scalpel; the excess material was removed. Gel was poured into the device with a small meniscus, overflowing the upper edge of the side walls (4). Thus a reliable contact of gel body with the upper plate (2) was provided when the last was mounted into the model. To avoid significant model deformation paper gaskets (6) adjusting the distance between plates were used. The outer surface of one of the plates was provided with a reference meshwork with 2 cm pitch.

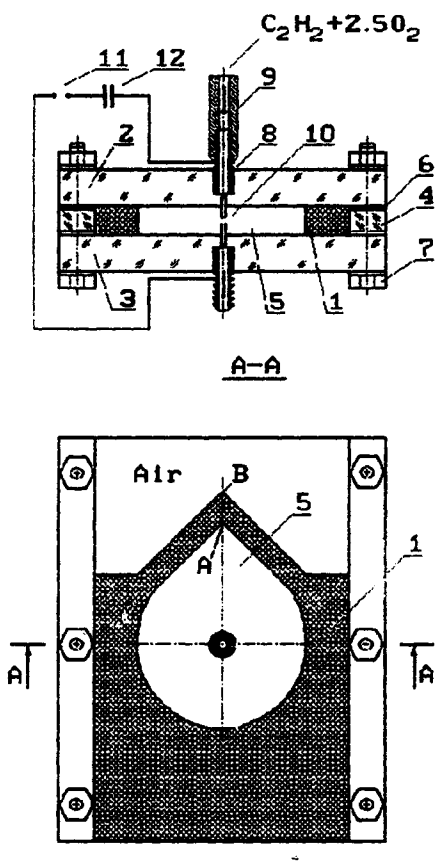

Fig. 1. Experimental device scheme.

The device was bolted (7) and displaced horizontally, in its operating condition.

The volume (5) was filled with gaseous high explosive (C_2H_2+ 2.5 O_2) at the ambient pressure through gas - inlet tube (9) and through the capillaries bored in electrodes (8).

HE purity was guaranteed by the multiple excess of the blown through gas volume over the inner model volume.

HE was detonated by an electrical discharge in a spark gap (10), where high - voltage pulse from condenser (11) was transmitted.

The discharge was initiated by a breakthrough of the controlled discharger (12). Thus, pressure of 15 atm was created in volume (5), which was decreasing further on due to cavity expansion and gas leakage through the capillaries. Model walls' motion was registered with a high-speed camera in transmitted light.

Investigations were conducted on gel models, containing plane 10 mm thick layers with an angle of surface fracture β = 120°, 90°, and 0° (β<5°). Layer motion pictures are shown on fig.2. - fig.4.

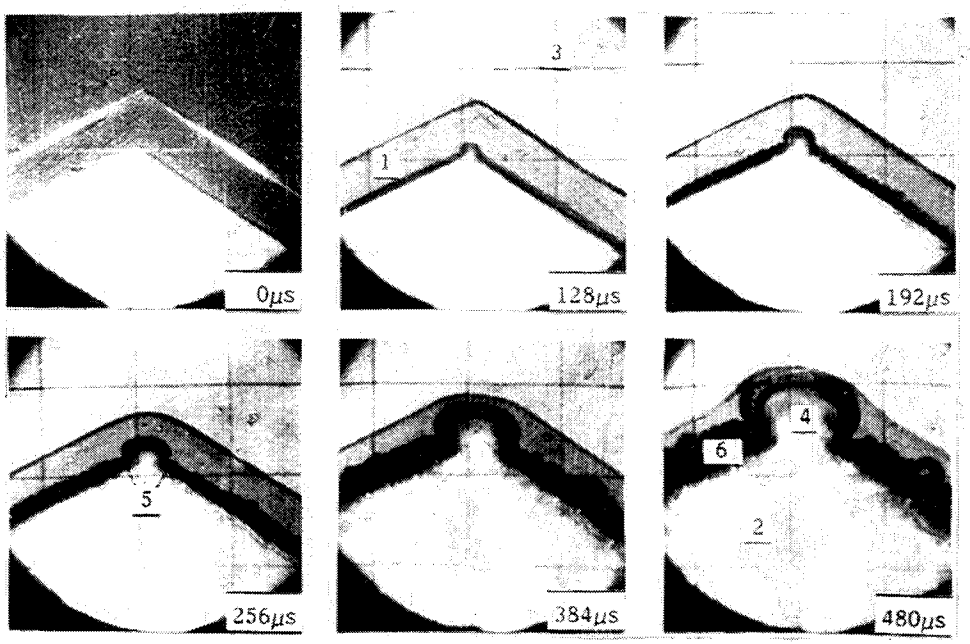

Fig. 2. Experimental photocronogramm, β=120°.
1- accelerated layer, 2- explosion products, 3- air,
4- cavern, 5- new peculiarities, 6- turbulent layer.

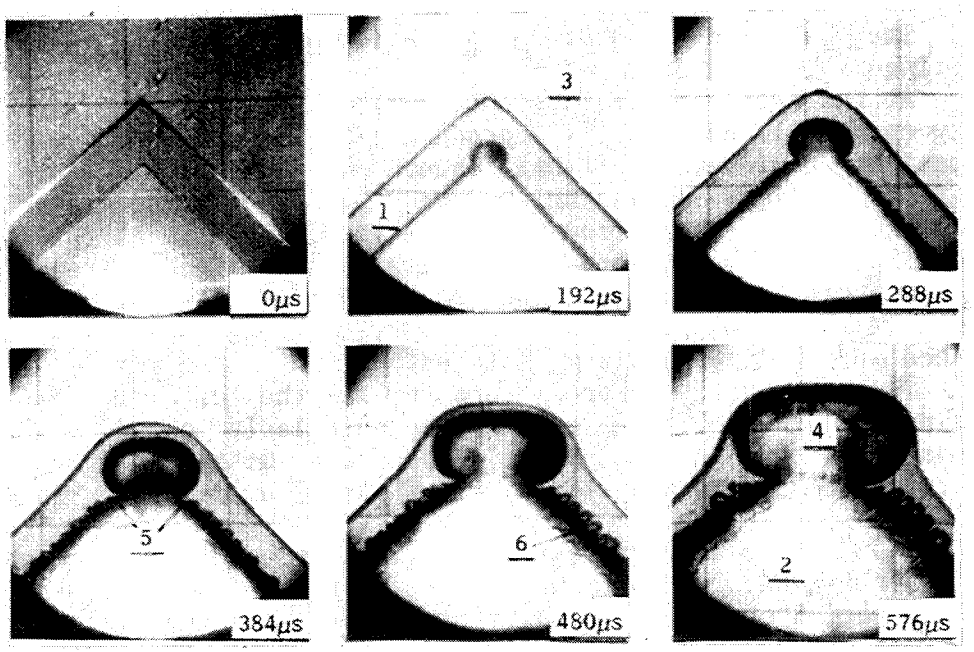

Fig. 3. Experimental photocronogramm, β=90°.
1- accelerated layer, 2- explosion products, 3- air,
4- cavern, 5- new peculiarities, 6- turbulent layer.

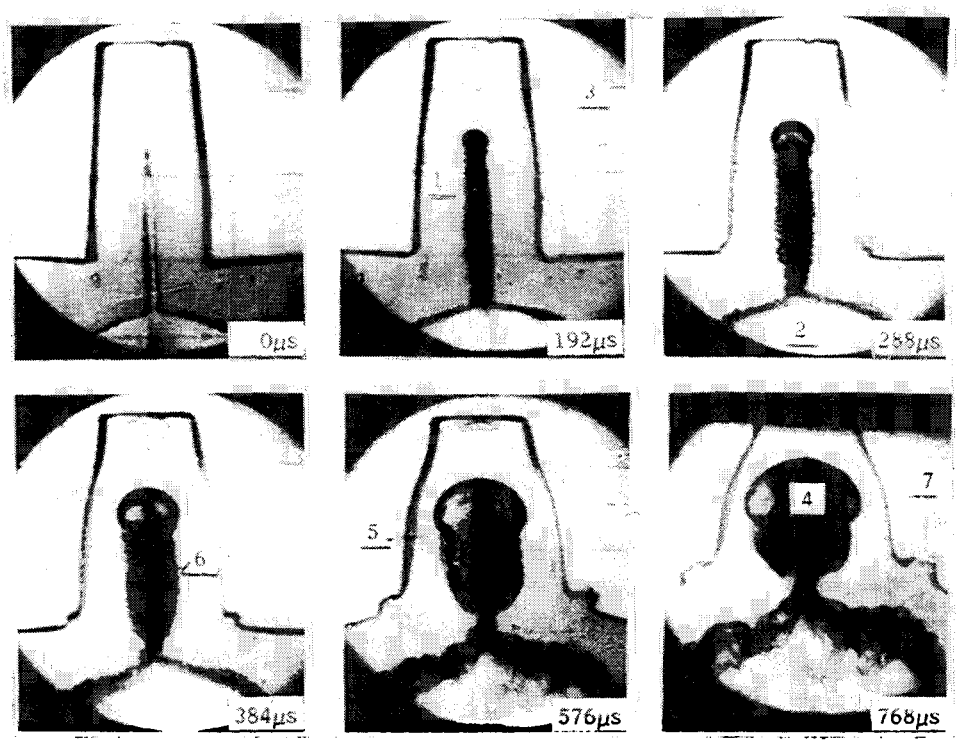

Fig. 4. Experimental photocronogramm, $\beta \cong 0°$.
1- accelerated layer, 2- explosion products, 3- air, 4- cavern, 5- new peculiarities, 6- turbulent layer, 7- cumulative jet embryo.

The observed hydrodynamic flows has the following distinguishing features.

At the proximity of the inner angular point (A) the interface between gel (1) and explosion products (2) is deformed with the anomalous rapidness. At that, cavern (4) formation occurs, the cavern dimensions increasing faster than the plane layer part shifting at the remote from the angle vertex points. At the initial evolution stage the cavern form is that of a cylinder, transforming further into the elliptical one. At the proximity of the newly forming cavern angular points (5) vortex flows springing up is traced at the later evolution stages.

The layer tends to break through in the direction of rays coming from the inner vertex (A) perpendicularly to the inner angle sides. Breakthrough takes place, when the distance, the remote parts of the accelerated layer have shifted to, is lesser than its thickness.

At the proximity of vertex (B) flows of another character can be observed. When $\beta<180°$, angle vertex practically do not shift for a long period of time. The angle grows and at the later stages equals to 180°. Thus, the surface is smoothed. When $\beta>180°$, the character of hydrodynamic flows at its proximity qualitatively changes. Angular peculiarly does not smooth. On the contrary, rapid formation of new flow peculiarity (the embryo of a cumulative jet

(7)) takes place (Fig.4.).

Against the above mentioned background, i.e. regular material motion, turbulent mixing evolution occurs. At the unstable inner interface turbulent mixing between gel and explosion products springs up due to occasional disturbance spreading. As a result of mixing the opaque zone (6) is formed, contours of which are clearly seen on photographs. At the remote from angular points region its form is practically plane. Up to the moment of the layer breakthrough by the explosion products the smaller portion of its thickness turns to be involved into turbulent mixing at the remote from fracture regions. Spreading of a large-scaled structure of turbulent mixing layer can be traced on the photographs. The spatial pulsation scale grows with time. It should further be noted, that unlike the case of infinite layer acceleration, presence of rigid restricting plate surfaces (2),(3) (Fig.1.) in our experiments result in growth rate limitation of the largest turbulent pulsations.

An interesting peculiarity in mixing layer evolution can be observed at the growing cavern surface at the proximity of vertex (A) at $\beta<180^\circ$. This layer thickness is lesser than that of the inner flat layer surface. Note, that characteristic pulsations such as ones at the plane region of accelerated shell, are absent (cavern surface is even). Such a conclusion can be referred from the experimental data, although model walls' distortion hampers precise determination of mixing layer thickness at the cavern surface.

It can be referred from the shots of Fig.2. through Fig.4. that the outer interface of the accelerated layer is even, i.e. no mixing between air (3) and gel (1) is present. This can be accounted for the flow stability (heavier material accelerates the light one).

THEORETICAL

Let us consider gel to be the ideal uncompressible fluid, not taking into account such effects as strength, viscosity and surface tension. Flow of such a fluid can be described by Laplace equation for velocity potential ϕ

$$\Delta\phi = 0 \ . \qquad (1)$$

Velocity vector is determined by $\vec{v} = \vec{\nabla}\phi$ correlation.

Pressure p_1 is given for the inner layer interface, pressure p_2 - for the outer one. Cauchy-Lagrange condition

$$\frac{d\phi}{dt} = \frac{1}{2}(w^2 - u^2) + q \qquad (2)$$

for surface points is the equation, determining surface potential vs time. Here: u, w - tangential and normal components of fluid velocity at its surface; q=0 for the outer layer interface; and

$q=-(p_1-p_2)/\rho$ for the inner layer interface; derivative with respect to time is calculated for the fixed surface point $\vec{r}$, velocity of which is always parallel to its normal $\vec{n}$; ρ - fluid density. The equation for these points motion is as follows

$$\frac{d\vec{r}}{dt} = (\vec{\nabla}\phi\ \vec{n})\vec{n}\ , \qquad (3)$$

When the interface shifting is insignificant if compared to the layer thickness h (which happens only at the early stages) and values u, w are small, equation (2) can be integrated as $\phi=qt$.

In this case surface deformation can be calculated as follows. By setting the initial layer form at t=0 as it is shown on Fig.5. and using boundary values of potential $\phi=qt$, equation (1) can be solved by the conform mapping method (by transforming the region occupied by the fluid to the strip at the complex potential plane). By differentiation of the calculated spatial potential distribution $\phi(\vec{r})$ velocity vector $\vec{v}$ can be determined. To crown it all, by integrating with respect to time equation (3) shifting of the inner and outer layer points of interest can be determined. To be more definite, let us consider that $\beta<180°$.

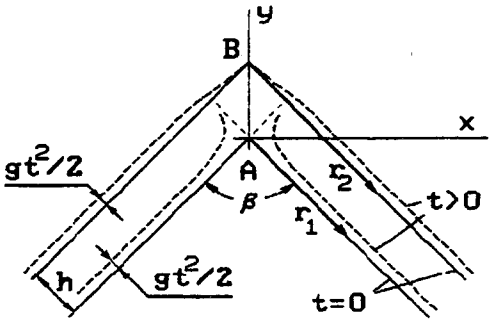

Fig.5. Accelerated fluid layer form.

Boundary points shifting for the outer surface of the accelerated shell can be described as

$$|\Delta\vec{r}_2| = \frac{p_1-p_2}{2\rho h}\, t^2 \left(\frac{\lambda}{1+\lambda}\right)^{(\pi-\beta)/2\pi}\ , \qquad (4)$$

where λ value can be determined by

$$r_2 = \frac{h}{\pi}\, B_\sigma\left(\frac{\beta}{2\pi}\ ,\ 0\right), \qquad \sigma = \frac{\lambda}{1+\lambda}\ ,$$

where $B_\sigma(x,0) = \int_0^\sigma \frac{z^{x-1}}{1-z}\, dz$ - incomplete beta-function; r_2 - the distance between vertex (B) and the designated point at the outer surface. When $r_2 \to \infty$ ($\lambda \to \infty$) then $|\Delta\vec{r}_2| \to (p_1-p_2)t^2/2\rho h$ which, as it has been expected, corresponds to the plane layer motion with acceleration $g=(p_1-p_2)/\rho h$. In the small proximity of

the outer vertex at $r_2 \to 0$ ($\lambda \to 0$) we have the following equation

$$|\Delta\vec{r}_2| \to \frac{p_1-p_2}{2\rho h}\, t^2 \left(\frac{\beta r_2}{2h}\right)^{(\pi-\beta)/\beta} \to 0 .$$

That is, in the observed proximity, the outer angle vertex does not shift, which coordinates with our experimental results.

The inner surface points' shift can be described as follows

$$|\Delta\vec{r}_1| = \frac{p_1-p_2}{2\rho h}\, t^2 \left(\frac{\mu}{1+\mu}\right)^{-(\pi-\beta)/2\pi}, \qquad (5)$$

where μ can be expressed by r_1 - the distance between vertex (A) and the designated surface point from the correlation

$$r_1 = \frac{h}{\pi} B_\sigma\left(1-\frac{\beta}{2\pi}, 0\right), \qquad \sigma = \frac{\mu}{1+\mu} .$$

As is in the above mentioned case, at $\to \infty$ ($\mu \to \infty$), we have $|\Delta\vec{r}_1| \to (p_1-p_2)t^2/2\rho h$. In the small proximity of vertex (A) at $r_1 \to 0$ ($\mu \to 0$) points shifting can be expressed by

$$|\Delta\vec{r}_1| \to \frac{p_1-p_2}{2\rho h}\, t^2 \left(\frac{(2\pi-\beta)r_1}{2h}\right)^{-(\pi-\beta)/(2\pi-\beta)} \to \infty . \qquad (6)$$

Limit infinity in this case signifies that the above mentioned approximations at the inner angle vertex proximity do not work. Such values as u^2 and w^2 mast not be neglected in (2) as well as deformation must not be considered insignificant at any t value. Our experimental results do confirm this.

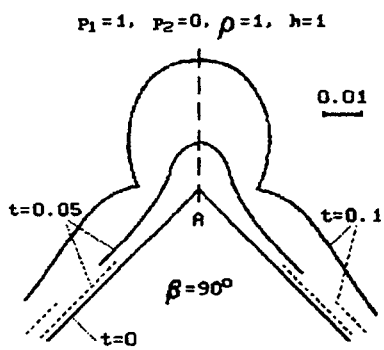

Fig.6. The inner boundary form at the proximity of (A) (calculation).

To more correctly describe hydrodynamic flows, mathematical problem (1), (2), (3) should be solved in full set-up, i.e. in accordance with all conditions, without making simplifying suppositions. Numerical solution of such a problem was conducted in accordance with boundary integral equation method[11] at $\beta=90°$. It was assumed that $p_1=1$, $p_2=0$, $\rho=1$, $h=1$.

Fig.6. comprises the picture of inner surface form evolution, obtained at the initial stages. It can be clearly seen there that at the proximity of vertex (A) (as is in the experiment) a rapidly

growing cavern is formed, assuming cylindrical shape. Two newly formed angular peculiarities spring up at the surface. The distance between the points at the cavern surface grows considerably faster than the distance between the points at the remainder inner surface part. That is, the cavern is "swelling" out the point initially disposed at vertex (A).

Correlation (6), valid at $|\Delta\vec{r}| \ll r_1 \ll h$, points to the existence of intermediate self-similarity asymptotic of two dimensional problem (1), (2), (3). At that, self- similarity index α (in expression $|\vec{r}| = \text{Const}\ t^{\alpha}$) is equal to $2(2\pi-\beta)/(3\pi-2\beta)$. For $\beta=\pi/2$ $\alpha=1.5$, being approximately coordinated with the numerical calculation results.

Of interest are the analytical investigations of the flows in the proximity of newly forming peculiar surface points, hypothesis on self-similarity being taken into account.

We express our gratitude to O.I.Volchenko, who took part in the technology development and in experimental activities.

REFERENCES

1. V. A. Andronov, S. M. Bachrach, E. E. Meshkov, V. N. Mochov, V. V. Nikiforov, A. V. Pevnitsky, A. I. Tolshmyakov, ZhETPh, v.71, N°8, p. 806 (1976).
2. K. I. Read, Physica D12, North Holland, Amsterdam, p. 45 (1984)
3. N. N. Anuchina, Yu. A. Kucherenko, V. E. Neuvazhaev, V. N. Ogibina, L. I. Shibarshov, V. G. Yakovlev, Izv. AN SSSR, MZhG, N°6, p. 157 (1978).
4. D. J. Lewis, Proc.of Royal Soc., London, ser. A 202, p.81, (1950).
5. E. E. Meshkov, Izv. AN SSSR, MZhG N°5, p.151 (1969).
6. H. W.Emmons, G. T.Chang, B. C.Watson, Journ. of Fluid Mech., v.7, p. 177 (1960).
7. J. A. Zufiria, Phys. of Fluids 31(3), p. 440 (1988).
8. J. Glimm, X.L. Li, Phys. of Fluids 31(8), p. 2077 (1988).
9. O. I. Volchenko, I. G. Zhidov, E. E. Meshkov, V. G. Rogatchov, Pisma v ZhTPh, v. 15, p.47 (1989).
10. O. I. Volchenko, I. G. Zhidov, B. A. Klopov, E. E. Meshkov, V. V. Popov, V. G. Rogatchov, A. I. Tolshmyakov, AS. 1026154, Byulleten OIPOTZ, N°24 (1983).
11. I. G. Zhidov, V. G. Rogatchov, ZhVMiMPh, v.3, p.796 (1981).

INTERFACE INSTABILITIES OCCURING DURING AN EXPLOSIVE DRIVEN IMPLOSION

M. LEGRAND , N.TOQUE
Centre d'Etudes de Vaujours - Moronvilliers
B.P. 7, 77181 COURTRY, FRANCE

1) INTRODUCTION

Rayleigh-Taylor[1] and Richtmyer-Meshkov[2] instabilities are of current interest because of their effect on the performance of inertially confined fusion capsules.

In the spherical configuration of an ICF capsule, direct observation of the interfaces is very difficult. On the contrary, an axisymmetric cylindrical geometry can also undergo a concentration phase[3] but allows an easy radiographic observation along the axis of the cylinder. Thus we have developped an experimental device with a cylindrical geometry.

Some of the experiments we have carried out gave us a first insight of the pre-turbulent flow induced by the RM and RT instabilities during a cylindrical implosion.

2) PRINCIPLE OF THE EXPERIMENT.

Implosion is initiated by four cylindrical wave lenses which generate the converging detonation in the cylindrical explosive (fig. 1). The defect is machined on the inner face of the metallic shell (diameter:100 mm,thickness: 2.5/4mm) and is a combination of sinusoidal waves ($R(\theta) = a_0+\Sigma a_n \cos n\theta$). Unless otherwise stated, $a_n = 0.5$ mm (n is the mode order).

We aimed at obtaining a long phase during which the Rayleigh-Taylor instability could develop. This phase, which is correlated to the deceleration of the metallic cylinder, is produced by the rarefaction wave following the detonation and by the counter-pressure coming from the low density inner medium.

These experiments are used to validate the codes which compute the growth of defects respectively in the linear and non linear phases.

3) RESULTS AND INTERPRETATION

3-1 Fit of the implosion parameters

A preliminary experiment carried out with electronic pin diagnostics gave the position of the shock in the inner medium (without defect) as a function of time. This provides the data necessary to adjust the numerical conditions and equations of state of the materials. It is

important to determine by calculation the velocity of the projected cylinder in order to get an accurate evaluation of the Rayleigh-Taylor phase and to make the best choice for the timing of the radiographic observations.

The radiographic facility allows us to make three X-ray snapshots over a fifteen microseconds time period which covers well the implosion phase we want to observe. With a one dimensional hydrodynamic code we thus obtained for the central section of the cylinder the interface velocity history shown on fig. 2.

We can notice that the shell is at first set into motion by a shock. This induces a Richtmyer-Meshkov instability (here with a reversal of the defect as shown on fig. 4).

3-2 Perturbation with single wave number

The experiments performed with a lead cylinder show, as expected, that the growth rate of the perturbation is higher for mode number 16 than for mode number 8 (see for instance 1).

These results are close to numerical evaluations obtained with the two-dimensional eulerian code EAD[4] as shown on fig. 3.

Another experiment carried out with tin and n = 16 leads to similar results.

Our experiment is 3D because of the edge effect. This causes two difficulties:

- The hydrodynamical behaviour of the central section of the cylinder is quite different from the one near the edge. This generates fuzziness around the perturbation on radiographs.

- A 2D code is unable to simulate precisely the behaviour of the cylinder after the maximum density of the inner medium.

Afterwards, we adjusted the thickness of the cylinder in order to obtain a more or less cylindrical geometry during the implosion. However, this does not solve the problem of the lateral rarefaction wave which is the main origin of differences with respect to the ideal case of an infinite cylinder geometry.

We are studying a 2 1/2 D solution to this problem.

3-3 Toward a pre-turbulent stage: wave number combination

After having studied the growth of a single wave number defect, we tried to verify the coupling behaviour as the initial perturbation is no longer a single mode but a combination of several modes. In the case of two modes n_1 and n_2, the spectrum is then widened primarily by the creation of the sum and difference modes $n_1 + n_2$ and $n_1 - n_2$. In the case of a more complicated initial spectrum (3 modes), the flow become very intricate.

3-3-1 Two modes

Numerical simulations were carried out with many pairs of mode numbers, among which we chose for experimentation the pair (13, 29).

The harmonic analysis (Fourier series) of the calculated tin/RTV interface (fig. 4) shows:

- a higher growth rate for the largest wave number,
- the creation of modes sum and difference and of the higher harmonics of the initial modes,
- that the creation of new modes in the non linear phase reduces the growth rate of the mode 29 compared with its behaviour as a pure mode.

The experimental results are very close to numerical evaluations and the last snapshot exhibits a complicated pattern which is very different from a one mode interface.

3-3-2 Three modes

During a two mode implosion, the interface becomes much more complicated than in the case of a one mode implosion. However, the interface region is not exactly a mixing zone. Therefore, our aim will be to generate a pre-turbulent flow by using a more complex initial spectrum of the defect.

It has been shown[5] that for a plane geometry, a real mixing zone is obtained with a 12 modes spectrum, the amplitudes of which have been chosen at random from a gaussian distribution. Unfortunately, this spectrum corresponds to a very complicated initial interface which cannnot be machined at the inner face of the metallic shell.

Therefore, our experiment involves only three modes. We chose for experimentation the combination (13, 21, 29) to evaluate the influence of a third mode on the bimodal flow above mentioned.

The experimental results are very close to numerical evaluations shown on fig. 5. However the interface region is not a mixing zone.

It is the reason why we tried to modify the spectrum of the initial interface.

We were not able to use a greater number of spectral components: We had to lower the corresponding amplitudes to obtain a resulting defect smaller than the shell thickness. With five modes, the flow is not more complex than in the 3-mode case.

We can only modify the amplitude and the order of the modes.

When these parameters increase, the linear phase is shorter and the growth rate of the defect is higher. The vorticity of the flow in the interface region is also higher (pre-turbulent stage).

We have chosen to use a 1 mm amplitude for the three modes. The mode numbers were equal to 26, 42 and 58. Naturally, the meshes used in this computation had to be smaller than in the preceeding one.

Numerical results are shown in fig. 5. The flow becomes very intricate much more rapidly than for the preceeding case

(13, 21,29). For t = 51 μs there is a real mixing zone in the interface region.This experiment will be soon carried out.

4) CONCLUSION

The experimental device we have chosen has shown the development of various initially sinusoidal perturbations in the linear and non linear phases. The growth is well evaluated by 2D eulerian numerical simulation for single and multiple mode numbers.

The very intricate pattern obtained at the end of a 3-mode experiment is very close to numerical evaluations. This leads to the concept of a multimode experiment using higher order modes, in order to reach a final pre-turbulent stage.

As far as these experiments do validate our codes in the linear, non linear and pre-turbulent stage of the flow, they give a sense to a direct simulation of the very intricate flow generated by a randomly defined interface, which is not experimentally accessible for technological reasons.

ACKNOWLEDGEMENTS

We would like to thank all the persons who took part in this study: V. FRACHET, F.GELEZNIKOFF, R.GUIX, A.HAUDUCOEUR, and N. WILKE.

REFERENCES

1 - S. CHANDRASEKHAR, Hydrodynamic and Hydromagnetic Stability
Oxford Univ. Press, Oxford, 1961

2 - R. D. Richtmyer, Taylor Instability in Shock Acceleration of Compressible Fluids
Comm. in Pure and Applied Math. 13 (1960) 297

3 - A. I. TOLSHMIAKOV and E. E. MESHKOV, Development of Perturbations of a Contact Boundary Accelerated by a Convergent Shock Wave in the Cylindrical Case
1989 Plenum Publishing Corporation

4 - C. COSTE and al. Joint CEA - LOS ALAMOS Conference on Hydrodynamic Instabilities (LOS ALAMOS)
in Computing Methods in Applied Science and Engineering
GLOWINSKY and LYONS, North Holland 1982

5 - D. L. YOUNGS, Numerical Simulation of Turbulent Mixing by Rayleigh-Taylor Instability
Physica 12D (1984) 32-44

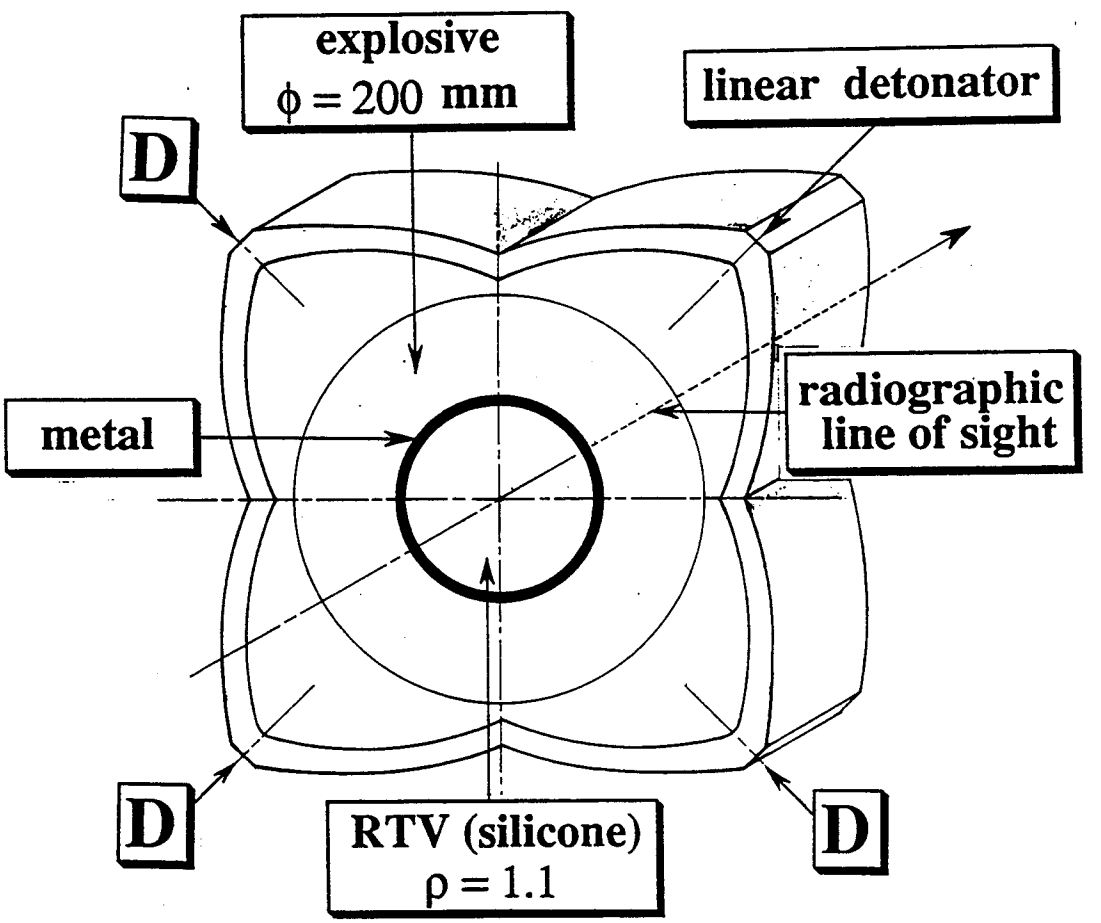
explosive
ϕ = 200 mm
linear detonator
D
radiographic
line of sight
metal
D
RTV (silicone)
ρ = 1.1
D

Fig . 1

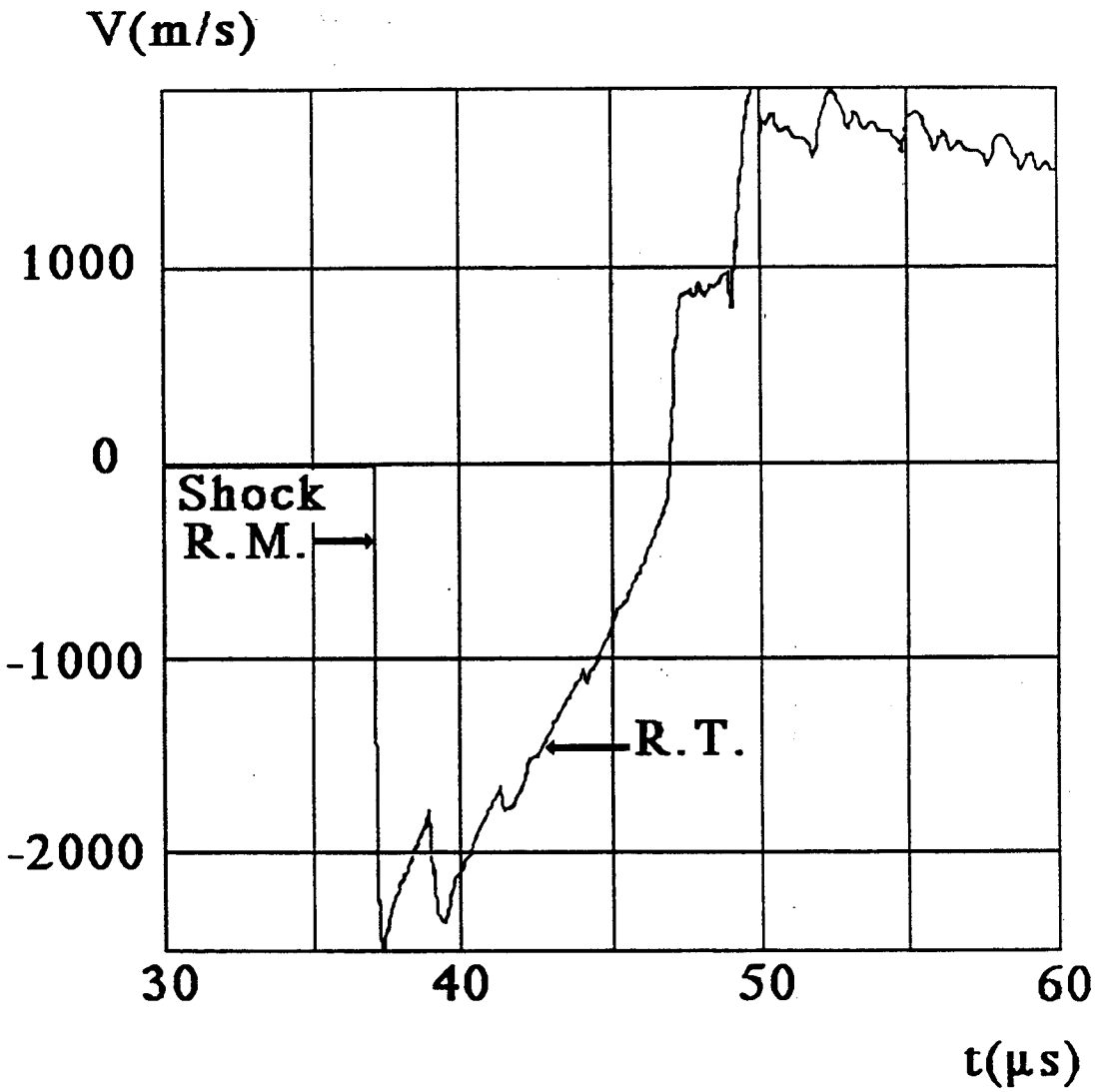

Velocity of the tin/RTV interface

Fig. 2

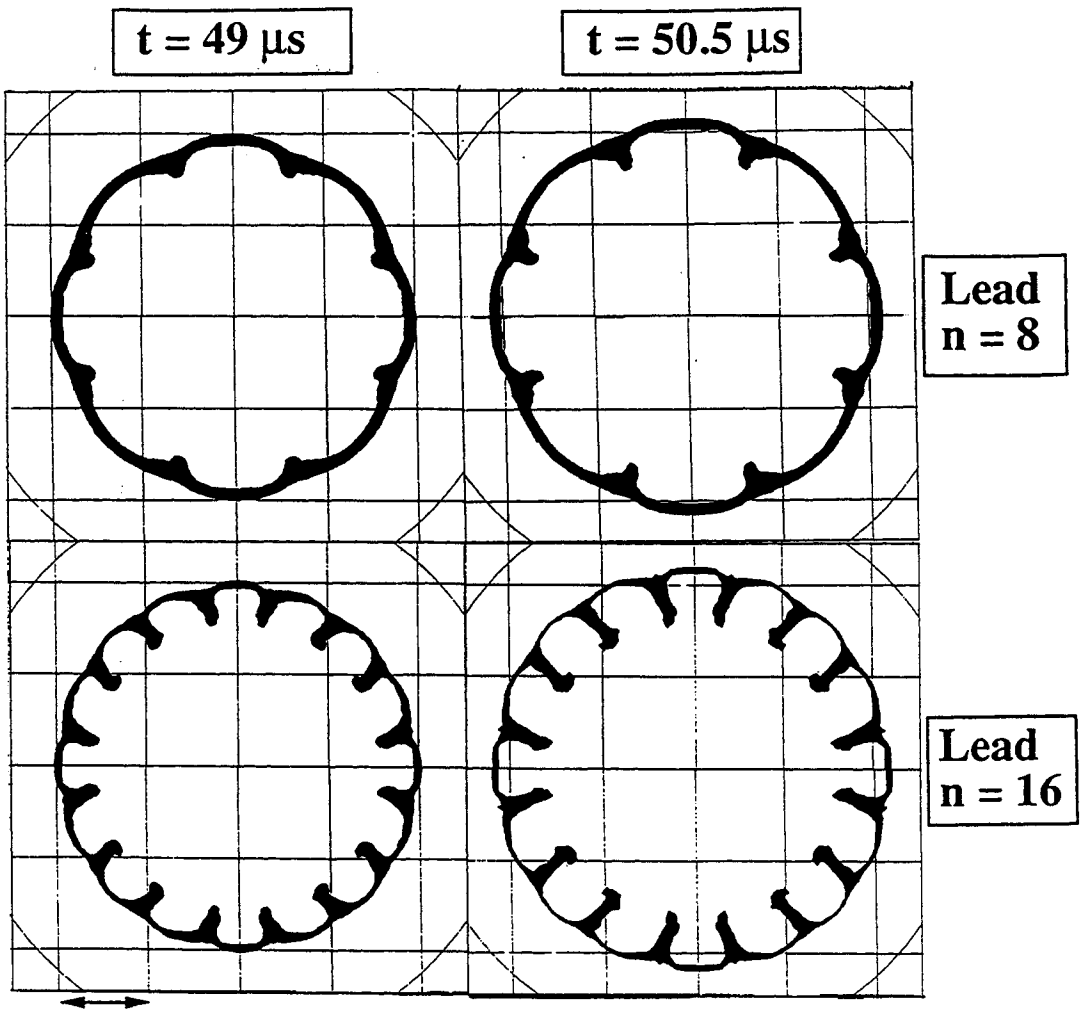

Fig. 3

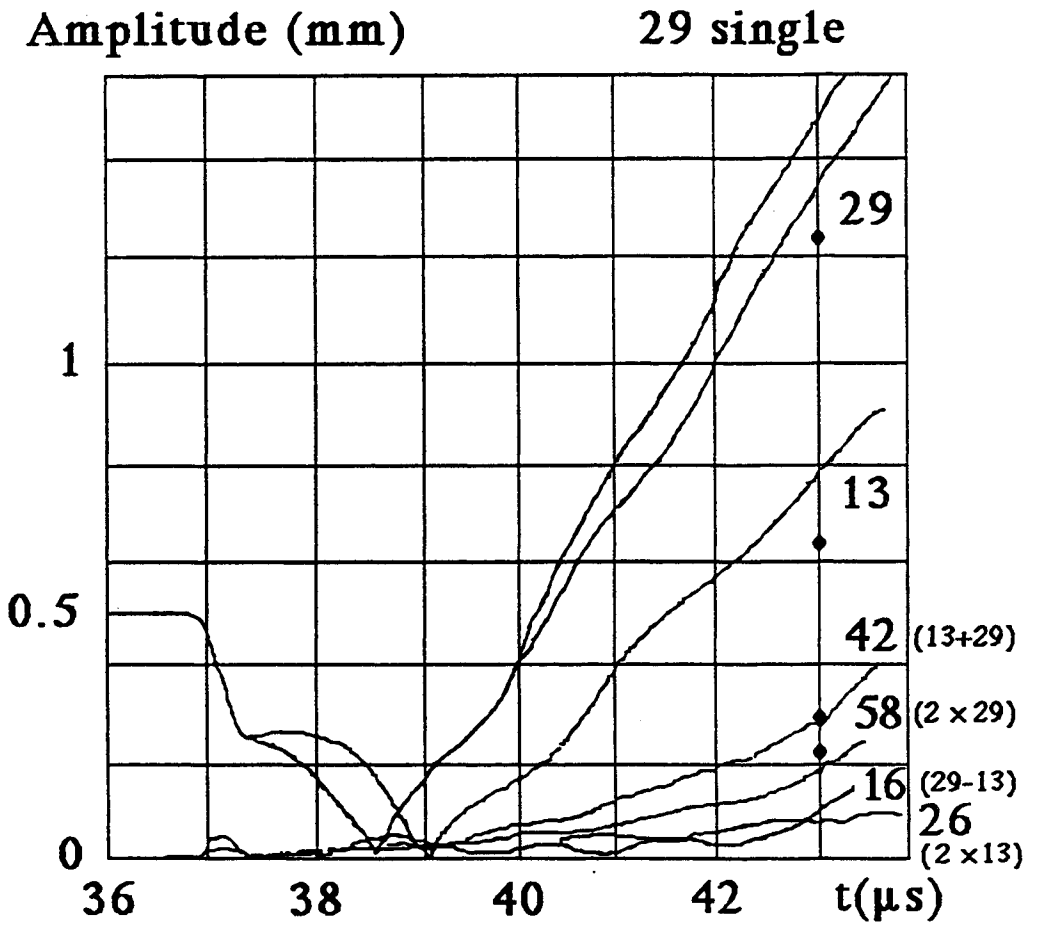

• **Experiment**

Harmonic analysis of the tin/RTV interface

Fig. 4

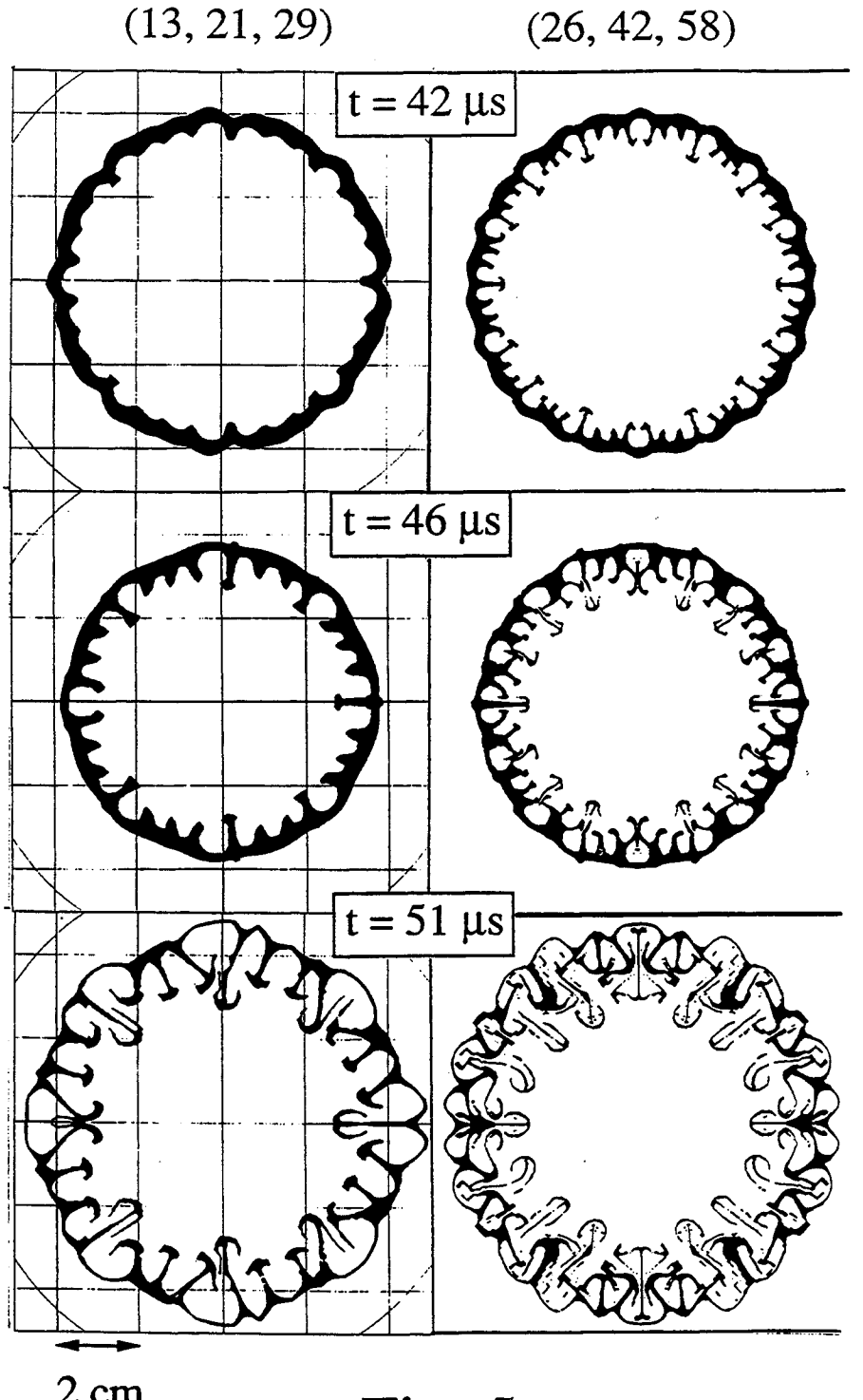

Fig. 5

CHAOTIC MIXING AT UNSTABLE INTERFACES

James Glimm * † ‡
John W. Grove * † §
Yupin Chen ‡
Department of Applied Mathematics and Statistics
University at Stony Brook, Stony Brook, NY 11794

X. L. Li ‡
Department of Mathematics
Indianna University-Purdue University
Indianapolis, ID 46205

ABSTRACT

The computation and analysis of both shock and gravity accelerated interfaces is considered. The chaotic structure produced by the mixing of two fluids can be analyzed using a combination of renormalization analysis and computational simulation. For shock accelerated interfaces the microphysics of the diffraction patterns produced by the shock-fluid interface interaction is of interest. Methods for including an analysis of such diffractions in front tracking simulations are discussed.

INTRODUCTION

Unstable interface problems occur in several areas of mathematical physics. Here we are interested in studying the behavior of the mixing zone between two fluids that is driven either impulsively by a shock wave, or continuously by gravity. In the case of small or vanishing viscosity and surface tension, the mixing state is critical in the sense that there are a large or infinite number of small length scale active unstable modes per unit volume. We see that there are two levels of description of this state: the microphysics of statistical ensembles of mixing modes and the macrophysics of continuum equations satisfied by the state. Effective mixing rates is an example of a quantity successfully predicted by this theory.

Our approach to studying the phenomena is a combination of full scale computational modeling of fluid mixing, together with a statistical analysis of

* Supported in part by the U. S. Army Research Office, grant no. DAAL03-89-K-0017.

† Supported in part by National Science Foundation Grant no. DMS-8901884.

‡ Supported in part by the Applied Mathematical Sciences subprogram of the Office of Energy Research, U. S. Department of Energy, under contract DE-FG02-90ER25084

§ Supported in part by National Science Foundation Grant no. DMS-9057429.

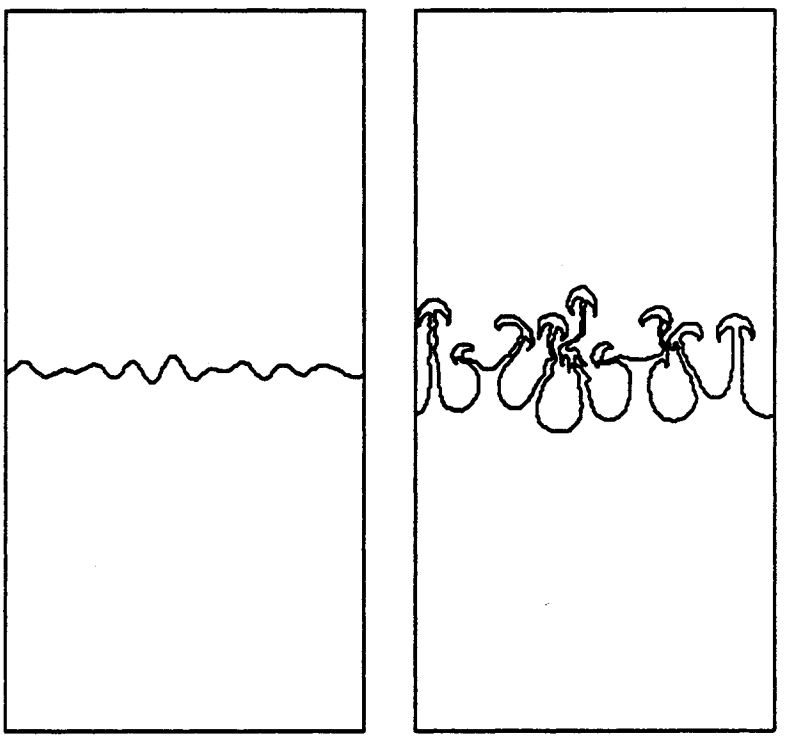

Figure 1: Results from a front tracking simulation of a Rayleigh-Taylor unstable interface. The figures show the intial and later time position of the fluid interface.

the data produced by these simulations. Front tracking has played a crucial role in this process, since it provides the most accurate available description of the interface between the two fluids.

RAYLEIGH-TAYLOR UNSTABLE INTERFACES

In previous work, [1–4] the microphysics of the boundary between the gravitationally accelerated mixing zone and the heavy fluid was studied. The growth rate of this side of the mixing zone is known to be $h(t) = .06Agt^2$, where A is the Atwood ratio and g is the gravity, on the basis of the Read and Youngs experiments. The coefficient, .06, is universal, but does not follow from simple scaling laws such as dimensional analysis. In[3], the same result was obtained for first principles numerical simulation, through the time of bubble merger, for a range of Atwood numbers. In addition, a microphysics model was proposed, as a modification of the Sharp-Wheeler model[5] and shown to have a renormalization group fixed point[1] which also gave the same mixing law, with the same coefficient .06[4].

Here we take the opposite approach and consider the macroscopic equations describing the fluid in the mixing zone. Our approach is to perform exact numerical simulations (i.e. based on the complete two fluid euler equations), as

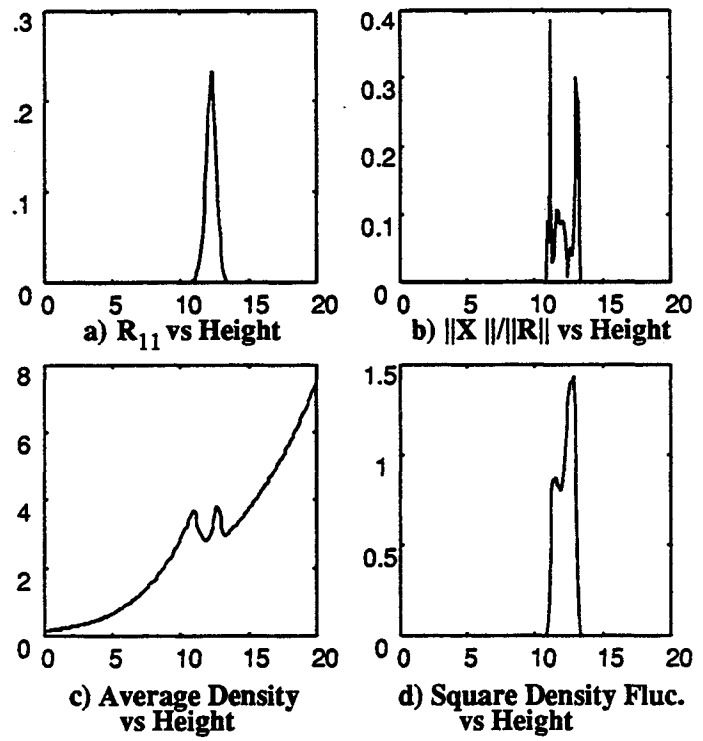

Figure 2: Plots of representative statistics for a Rayleigh-Taylor unstable interface.

illustrated in Fig. 1, and use this computation to generate a data base of statistical measures of the mixing zone. We refer to the approach of Harlow *et al.*[6] for example, in which averaged equations are constructed via closure hypotheses for the averaged fluid quantities and low order moments, such as the Reynolds stress.

We examine our data base from these points of view: Are the closure relations valid as an approximate identity in this data set? Does the data set have any surprising features which are potentially at variance with solutions of the averaged equations? Does the data set display self-similarity which would support the idea that it is described by a renormalization group fixed point? The answers are: tentatively yes, tentatively yes, and at present unknown.

In more detail, we consider the compressible Reynolds stress,

$$R_{i,j} = < \rho v_i v_j > - < \rho v_i >< \rho v_j > / < \rho > , \qquad (1)$$

where the averages are horizontal as well as ensemble average. The dominant component of this tensor is R_{11}, is plotted as a function of height at fixed time in Fig. 2a. Triple correlations, such as

$$X_{ij} = < \delta\rho\delta v_i \delta v_j >, \qquad (2)$$

are suppressed[6]. In Fig. 2b, we plot $||X||/||R||$ as a function of height at fixed time.

These quantities are tentatively reassuring from the point of view of constructing averaged equations. Less reassuring is a blip in the density $< \rho >$ considered as a function of height at fixed time, see Fig. 2c. On Fig. 2d, we plot $< (\delta\rho)^2 >$ vs. height.

RICHTMYER-MESHKOV UNSTABLE INTERFACES

The success in applying front tracking methods to simulations of Rayleigh-Taylor unstable interfaces has been reproduced in shock accelerated, or Richtmyer-Meshkov, unstable problems. However a difficulty presents itself here since the shock wave-fluid interface interaction is complicated and only partially understood. Previous work[7] showed that for highly supersonic (low amplitude) interactions, the combination of front tracking with shock polar analysis provides an accurate method for computing the interaction. Indeed, it was just this idea that was at the basis of Richtmyer's original analysis of this problem[8]. The method consists of using solutions to Riemann problems for the supersonic steady state Euler equations to describe the flow near points of collision between the two waves in reference frames that move with the interactions. For sufficiently supersonic interactions, the solution consists of a self-similar wave pattern containing a transmitted shock wave and a reflected wave that is either a shock or Prandtl-Meyer wave. The complication occurs for transonic flows where the steady flow approximation breaks down. Such interactions are called irregular, as compared to the self-similar regular interaction for supersonic flows.

For Richtmyer-Meshkov problems, we note that since the initial fluid interface is smooth, the refractions produced as the shock first reaches the interface are regular. Indeed the local Mach number is inversely proportional to the sine of the angle between the incident shock and the fluid interface. This means that we need only consider the transition problem of regular to irregular refraction. When such a transition occurs, the point of interaction (or node) scatters into a set of discrete or semidiscrete nodes that propagate away from each other. These scattered nodes[9] are formed by shock-shock interactions (crossings or overtakes), shock refractions at a contact discontinuity (diffraction nodes), or one of three classes of transonic nodes; Mach reflection, shock transmission, or total internal reflection. Semidiscrete interactions like a reflected rarefaction overtaking an incident shock (anomalous reflection) [10] are also possible. Each discrete node can be modeled using a local shock polar analysis, while the semidiscrete interactions are approximated by sets of nearly discrete nodes. Of course subsequent scattering of the individual nodes can also occur. Such transitions include the bifurcation of a cross node into a pair of Mach reflections. However these additional transitions are local to the the affected nodes and can be treated independently, considerably simplfying the scattering problem.

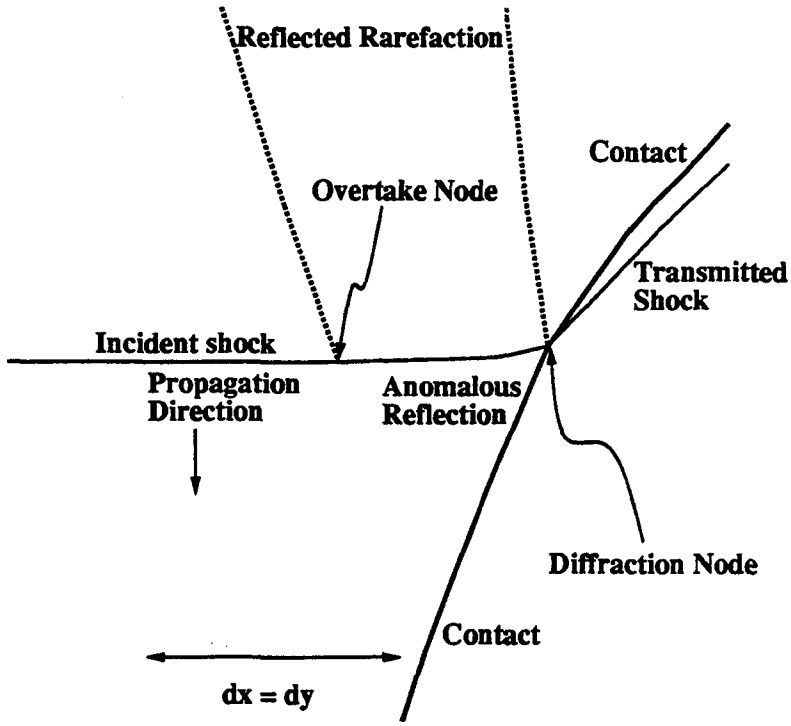

Figure 3: A detail from a full scale Richtmyer-Meshkov simulation showing an anomalous reflection produced by a fast-slow refraction with reflected rarefaction. The wave interaction occurs on the scale of one mesh block as indicated above.

Regular to irregular refraction transitions can be divided into five cases depending on whether the reflected wave is a shock or rarefaction, and on whether the interaction is fast-slow or slow-fast [11, 12]. Fast-slow interactions are characterized by an overtaking of the incident shock by the reflected wave, while slow-fast interactions lead to the precursion of the transmitted wave ahead of the incident shock. The fifth case occurs for refractions with reflected shocks at the mechanical equilibrium point where the reflected, incident, and transmitted shock polars intersect at a common point. This transition leads to the formation of a Mach reflection between the incident and reflected waves, with a shock transmission at the base of the Mach stem on the fluid interface.

Currently two of these five cases has been implemented in our front tracking code. Fig. 3 shows a detail from a simulation with a fast-slow transition with a reflected rarefaction. When the incident shock becomes transonic, the reflected wave overtakes it, forming a two dimensional version of a rarefaction overtaking a shock. The rarefaction expands out onto the incident shock until the flow behind the shock becomes supersonic. This interaction, which we call anomalous reflection, commonly occurs for shocks propagating from a dense nearly incompressible liquid into a gas.

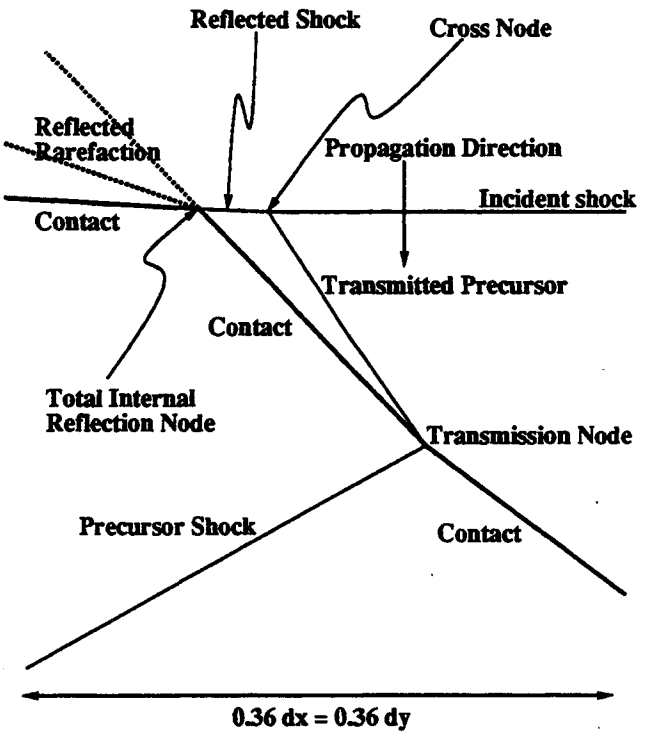

Figure 4: Precursor shock configuration produced by a slow-fast refraction with reflected rarefaction. The figure is taken from a detail of a full scale simulation of a shock colliding with a rippled interface. The scale of the interaction here is about one third of a mesh block. Note that at the cross node, only the reflected shock directed towards the fluid interface is tracked.

Another case is indicated in Fig. 4 for a slow-fast interaction with a reflected rarefaction. The transmitted wave becomes transonic and forms a precursor shock at the interface as it moves ahead of the incident shock. The refraction of the precursor through the interface in turn leads to a cascade of wave interactions.

SURFACE TENSION AND CONVERGENCE OF UNSTABLE INTERFACES

Surface tension on a fluid interface exerts a stabilizing influence on its growth. Without surface tension, the Euler equations are ill-posed for unstable interfaces and numerical simulations converge only for large scaled structures on the interface and exhibit fractal type structures as the computational mesh is refined. Surface tension provides a cut-off length scale that eliminates this fractal structure. Fig. 5, illustrates this by showing the results of two otherwise identical simulations, one with and the other without surface tension.

Neglecting viscosity, the dispersion relation for the Rayleigh-Taylor insta-

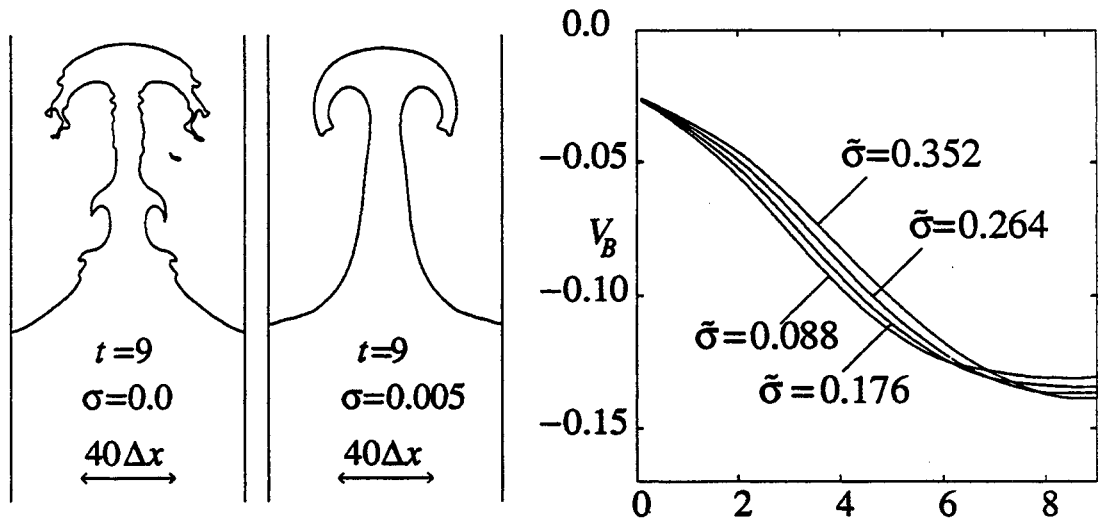

Figure 5 (left): Rayleigh-Taylor simulations illustrating the effect of surface tension on the computation. **Figure 6** (right): Single bubble velocities vs. time for different values of surface tension. As the normalized surface tension $\tilde{\sigma}$ increases, the bubble takes longer to reach terminal velocity. Note that the terminal velocity increases with the surface tension in our range of simulation. The explanation is that surface tension makes the bubble more streamlined, therefore reducing its drag.

bility in the linear regime is given by [13]:

$$\alpha^2(k) = gAk - \frac{2\sigma}{\bar{\rho}}k^3, \tag{3}$$

where α is the growth rate, k the wavenumber, σ the surface tension, and $\bar{\rho}$ the average of the densities of the two fluids. For $\sigma = 0$ this relation diverges for large wave numbers, and hence the Euler equations are considered to be ill-posed. Viscosity decreases the growth rate for large wave numbers, but the net growth rate remains nonzero. For $\sigma \neq 0$, the situation changes qualitatively, with a finite cut-off wave number $k_c^2 = g\Delta\rho/\sigma$ and wavelength $\lambda_c = 2\pi/k_c$, such that modes with wavelength smaller than λ_c are stablized.

In the nonlinear regime, the perturbations grow into bubbles and spikes and the dispersion relation (3) is no longer valid. Further analysis requires the solution of the full Euler equations, and generally involves the use of numerical methods. However the unstable behavior of arbitrarily small modes causes convergence problems for numerical methods under mesh refinement. Although the large scale structure of the interface may remain relatively stable under mesh refinement, the detailed structure does not converge, but rather shows a fractal like behavior as the mesh is refined. Errors in the computation, such as roundoff

and truncation error cause small perturbations in the fluid interface that grow and induce the secondary instabilities. Since these perturbations are randomly distributed, the secondary instabilities are nonunique for different mesh sizes.

Surface tension adds a restoring force to the fluid interface, that is proportional to the local curvature. It can be thought of as a pressure gradient opposite to the direction of curvature at a point. In the small amplitude linear regime this force will stablize modes with wavelength less than λ_c. This effect will continue for large amplitudes as well. It should be noted that for materials, such as gases, whose physical surface tension is small, nonconvergence of the fluid interface represents the fact that mixing occurs at the molecular level. Here only the large scale structures such as the bubble envelope have physical meaning.

Fig. 6 shows that the time needed for the bubble to accelerate from initial velocity to terminal velocity increases from 6.5 to 9 as the surface tension increases from 0.088 to 0.35.

REFERENCES

1. J. Glimm and D. H. Sharp, Physical Review Letters **64**, 2137 (1990).
2. Q. Zhang, "*Validation of the Chaotic Mixing Renormalization Group Fixed Point*," To appear.
3. J. Glimm, X. L. Li, R. Menikoff, D. H. Sharp and Q. Zhang, Phys. Fluids A **2**, 2046 (Nov. 1990).
4. J. Glimm, D. H. Sharp and Q. Zhang, *Phys. Fluids A* (To appear).
5. D. H. Sharp and J. A. Wheeler, *Institute of Defense Analyses. Unpublished Technical Report* (1961).
6. D. Besnard, F. Harlow and R. Rauenzahn, *Conservation and Transport Properties of Turbulence with Large Density Varations*, LANL report LA-10911-MS, 1990).
7. J. W. Grove, Adv. Appl. Math. **10**, 201 (1989).
8. R. D. Richtmyer, Comm. Pure and Appl. Math **13**, 297 (1960).
9. J. Glimm, C. Klingenberg, O. McBryan, B. Plohr, D. Sharp and S. Yaniv, Adv. Appl. Math. **6**, 259 (1985).
10. J. W. Grove and R. Menikoff, J. Fluid Mech. **219**, 313 (1990).
11. A. M. Abd-el-Fattah and L. F. Henderson, J. Fluid Mech. **86**, 15 (1978).
12. A. M. Abd-el-Fattah and L. F. Henderson, J. Fluid Mech. **89**, 79 (1978).
13. D. H. Sharp, Physica D **12**, 3 (1984).

RESULTS FROM THE VAUJOURS VERTICAL SHOCK TUBE

C. Cavailler[a], H. Croso[a], P. Gandeboeuf[a], J.F. Haas[b] and G. Rodriguez[b]
Commissariat à l'Energie Atomique
[a] Centre d'Etudes de Vaujours-Moronvilliers, BP 7, 77181 Courtry, France
[b] Centre d'Etudes de Limeil-Valenton, 94195 Villeneuve St Georges cédex, France

Abstract We describe shock tube experiments on the behavior of gas interfaces submitted to acceleration by a shock wave and deceleration by reflected waves. The gas pairs are either SF6-air or air-helium and their nominally plane interfaces can be discontinuous, i.e. with membrane or diffusive. We extract from the schlieren photographs the position and thickness of the shock-induced turbulent mixing zones and compare them to numerical calculations performed using a k-ε turbulent model embedded in a one dimensional finite differences hydrodynamics code /1/. The limitations of optical diagnostics and 1D calculations are pointed out.

1 Introduction

The observations are performed on an upward firing vertical shock tube /2, 3/ allowing horizontal continuous interfaces with a light gas above a heavier one as well as discontinuous interfaces with a thin membrane initially separating the gases. The continuous interfaces are obtained by molecular diffusion after retraction of a diaphragm. These interfaces are subject to the impulsive Rayleigh-Taylor instability (RTI), or Richtmyer-Meshkov instability (RMI) which arises from the vorticity created by the misalignment of the vertical pressure gradient of the shock and the density gradient of the interface caused by unavoidable three dimensional perturbations on its nominally planar geometry. In the case of discontinuous interfaces, the membrane can be bulged due to a slight pressure unbalance leading to large scale deformations while its fragmentation produces small scale perturbations leading to a thin turbulent mixing zone soon after the incident shock. The molecular diffusion interfaces contain large scale gravity waves due to the retracting blade, which are slowly amplified by shock interaction /4, 5/ but additional initial small scale perturbations, which are possibly present, could not be observed in our experiments. The experimental program carried out so far on our shock tube /2, 3/ with a square 8 by 8 cm section, equipped with schlieren flow visualization and piezoelectric gages, covers the interaction of Mach 1.45 incident shock with sulphur hexafluoride (SF6) - air interfaces (density ratio 5) and Mach 1.3 incident shock with air-helium interfaces (density ratio 7). A movable endplate allows the variation of the length of the downstream gas (up to 50 cm). This program therefore corresponds to the conditions agreed upon at the time of the Princeton symposium for simple, i.e. low Mach number, benchmark experiments.

2 Experiments

In the case of continuous interfaces, the initial diffusion thickness is 1.7 cm for SF6-air and 2.5 cm for air-helium. A slow diaphragm retraction speed (2.5 s) ensures that large scale perturbations are not observable until 1.3 to 2 ms after initial interaction, which is well after the deceleration by the first reflected wave. Shorter retraction times (down to 0.5 s) hasten the apparition

of large structures by about 0.5 ms which prevents us from comparing the corresponding experiments with calculations performed using the turbulence model imbedded in a 1D code.

The thickness of the mixing zone, either initially or just after compression by the incident shock can be measured from the schlieren photographs and compared with a theoretical value. The thickness of a laminar diffusion zone can be calculated with the diffusion equation /6/:

$$\frac{\delta c}{\delta t} = D \frac{\delta^2 c}{\delta x^2} \qquad (1)$$

where c is the mass concentration of one of the components and D the diffusion coefficient of the gas pair. The solution for the concentration on one half ($c < 0.5$) of the diffusion zone is:

$$c(x,t) = \frac{1}{2}\left(1\text{-erf}\,\frac{x}{2(Dt)^{0.5}}\right) \qquad (2)$$

and the total diffusion thickness, defined so that c is equal to $0.5\ 10^{-5}$ at the edge, is $L = 12\ (Dt)^{0.5}$. For the diffusion coefficients of the gas pairs SF6/air (0.097 cm^2/s) and air/helium (0.8 cm^2/s) and a diffusion time of 0.9 s between the end of the blade retraction and the shock wave arrival, this diffusion thickness in both cases is 3.5 cm and 10.2 cm respectively. As we measured from the schlieren photographs initial thicknesses equal to 1.7 cm in the SF6/air case (resp. 2.5 cm in the air/helium case), we find, using equation 2, that the concentration at the observed edges of the mixing zone should be 2% (resp. 15%). This gives an idea on the sensitivity of the schlieren system for diffusive interfaces between different gas pairs.

In the initial experiment (SF6-air) described in /2, 3/ the blade was retracted in a direction perpendicular to the schlieren system optical axis, the initial diffusion zone could be observed and the length of the air was short: 13.2 cm. The mixing zone was observed to be compressed to 1.5 cm by the incident shock and then to widen, because of the RMI, to about 4 cm before large structures eventually appeared (after the second reflected shock). In the experiments described here, the initial interface region is concealed by the metallic structure of the new test section (5 cm wide). The blade is now retracted in the direction of the optical axis, thus the late time waves do not appear in the same way as in the original test section.

A typical schlieren photograph of a continuous air-helium interface shortly after interaction with the reflected wave is shown on figure 1. From top to bottom, one distinguishes pure helium, a dark layer with smooth edges which is the twice shocked diffusion zone, a granular region which is the turbulent mixture of air and helium in the shocked boundary layer, the reflected shock in air and pure air at the bottom. Figure 2 illustrates the apparition of large structures in the diffusion zone after interaction with the second reflected shock. The peculiar circular patterns seen above the dark band are reminiscent of the plumes observed in incompressible simulations of the RMI for a stratified interface /7/. This remark may apply as well to the large structures observed earlier /2, 3/.

3 Calculations

We use a k-ε model imbedded in a 1D Lagrangian code /1, 2, 3, 10/. The results of the model in such an unsteady situation are not only dependent on the adjustment of the coefficients of the Rayleigh-Taylor source term in the k and ε equations, but they are also sensitive to the initialization procedure and, to a lesser extent, to the mesh size.

In order to mimic laminar diffusion in the code, we initialize the turbulence model before the shock induced-acceleration in such a way that the computed turbulent diffusion thickness is equal to the measured laminar one at the time of shock arrival. There is a wide choice in the value of initial turbulence level and time before shock acceleration which achieve that goal, and in the absence of theoretical estimates of the level of shock-induced turbulence in a diffusive interface with random scales, our choice is arbitrary. The results of the code, however, do depend on that initial amount. In earlier calculations /2, 10/, we initialized a triangle of turbulent kinetic energy 10^4 cm^2/s^2 high and 0.8 cm wide about 5.5 ms before shock arrival to obtain the initial diffusion zone thickness. In the present calculations, we used 10^6 erg/cm^2 over 1.3 cm, 0.1 ms before the passage of the incident shock. For most of our calculations, we have used the k-ε model with a concentration threshold of 2% or 5% in the definition of the numerical mixing zone thickness.

In the case of the discontinuous interfaces, the initialization of the initial thickness is given by:

$$L_0 = 2\,\alpha\,(1+\beta)\,A_t\,\Delta Ui\,\delta t \text{ where } \alpha = 0.06 \pm 0.006,\ \beta \approx \left(\frac{\rho_2}{\rho_1}\right)^{0.215},\ A_t = \left(\frac{\rho_2-\rho_1}{\rho_2+\rho_1}\right) \qquad (3)$$

where α and β are obtained from the Foulness rocket rig experiments /8/ dealing with the Rayleigh-Taylor instability of incompressible fluids and transposed to the case of the Richtmyer-Meshkov Instability, A_t is the Atwood number, ΔUi is the velocity jump of the interface and δt is the time interval since the instant of shock-interface interaction.

For the initialization of turbulence intensity, we use the ratio of turbulent kinetic energy to the kinetic energy of the mixing zone given by Mikaelian /9/:

$$k_0 \approx 0.093\,At^2 \qquad (4)$$

A modified expression for k_0, taking in account the asymmetry β of the mixing zone can also be used in the case of the discontinuous interface /10/.

In the SF6-air case (resp. air-helium case), the initial triangle of turbulent kinetic energy, 0.1 ms after shock passage (resp.0.05 ms), was 0.0134 $(\Delta Ui)^2$ wide (resp. 0.01635) and 0.246 cm wide (resp. 0.116).

Most of the constants in the model have been obtained from the literature except for σ_ρ and $c\varepsilon_0$ which appear in the Rayleigh-Taylor source terms in the k and ε equations respectively. These

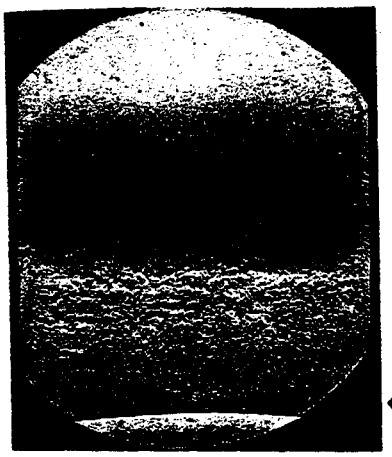

Figure 1 : T=798 μs, Ms=1.3
Continuous interface Air/He L=40 cm

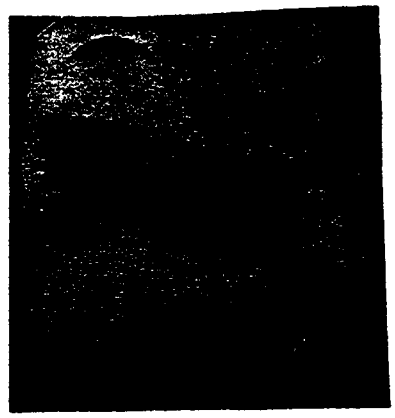

Figure 2 : T=1390 μs, Ms=1.3
Continuous interface Air/He L=40 cm

Figure 3 illustrates the tridimensional mixing zone obtained with a bulged 0.5 μm nitrocellulose membrane separating SF6 and air. The initial upward bulge, created by a slight pressure difference between the gases, has been reversed due the effect of the incident shock RMI. Just after the interaction with the first reflected wave, we distinguish from top to bottom: the pattern of shocks reflected from the bowl shaped interface, the tridimensional interface region with an amplitude of 28 mm and local thickness less than 10 mm, turbulent jets on its square sides and, at the bottom, the reflected shock propagating into the SF6.

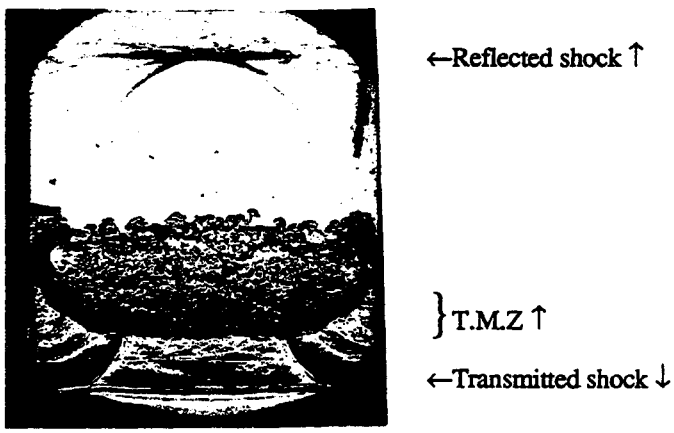

Figure 3 : T=1390 μs, Ms=1.45
Discontinuous interface with initial bulge SF6/Air L=31 cm

The widening of a turbulent mixing zone obtained from experiments performed with planar membranes: SF6-air (31cm) is described on figures 4, 5 and 6. Just before the interaction with the first reflected wave (figure 4) and after (figure 5) the planar mixing zone displays a thin dark layer where the film remnants are located with turbulent structures appearing above and below. While the upper limit of these structures appears clearly, it is very difficult to distinguish the boundary between the turbulence in the interfacial mixing zone from that in the shocked boundary layer. The perturbations seen on the reflected shock system above the interface on figure 5 are due to the corrugations of the interface. At late time, after the interaction with the second reflected wave, figure 6 shows a thick mixing zone with dark patches due to membrane fragments. These 3 photographs show that the average 1D thickness can only be measured with a large error bar.

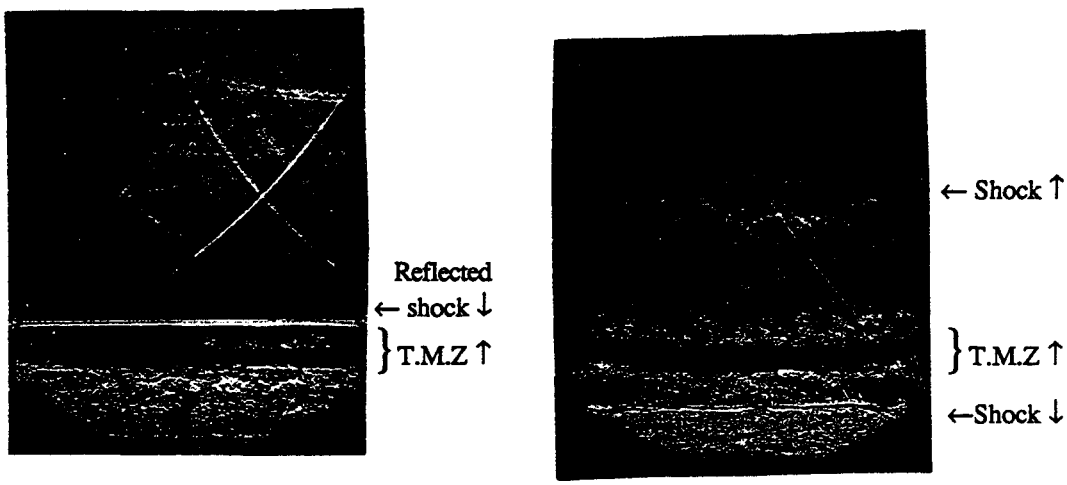

Figures 4 and 5 : Discontinuous interface SF6/Air L=31 cm, Ms=1.45, T=1194 μs and 1292 μs

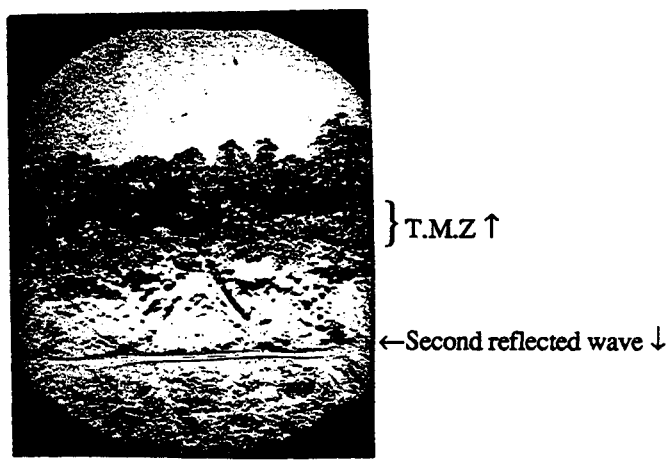

Figure 6 : Discontinuous interface SF6/Air L=31 cm, Ms=1.45, T=2142 μs

Experiments performed with planar air-helium (31cm) interfaces are illustrated by figures 7, 8 and 9. On figure 7 recorded before the return of the reflected shock, one sees that most of the

apparently 1.5 -2 cm wide turbulent layer is in fact associated with a wall structure which appears to entrain the membrane (dark layer). Subsequent pictures (fig. 8, after interaction with the first reflected shock and fig. 9, after interaction with the second reflected shock) again show the difficulties encountered for extracting an unambiguous mixing zone thickness.

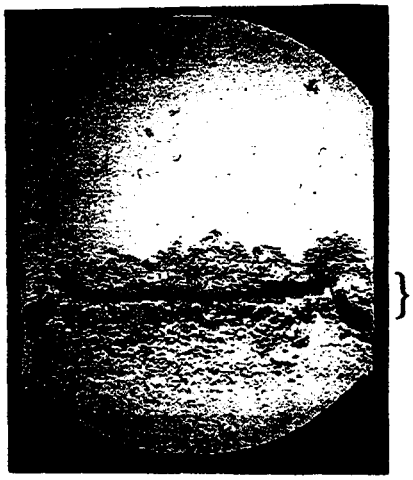

Figure 7 : T=487 µs, Ms=1.3
Discontinuous interface Air/He L=31 cm

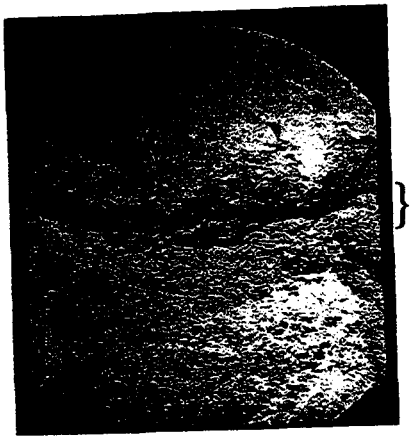

Figure 8 : T=669 µs, Ms=1.3
Discontinuous interface Air/He L=31 cm

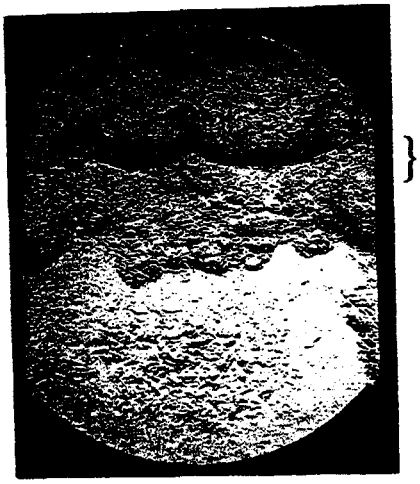

Figure 9 : T=909 µs, Ms=1.3
Discontinuous interface Air/He L=31 cm

two constants, which are interdependent /2, 3, 10/, can be obtained from the calibration of the model in the case of Rayleigh-Taylor experiments /8/ or shock tube experiments such as shown here /3, 4/.

The calculations performed earlier in the diffusive interface case show that the mixing zone thickness for our two SF6-air experiments (13.2 and 31 cm) can be predicted by the k-ε model using the same coefficients for the Rayleigh-Taylor source term as for the discontinuous air-helium (10.5 cm) experiment of Brouillette /4/ but the model overpredicts our continuous air-helium (40 cm) experiment /3/. This was obtained for $\sigma_\rho = 1.625$ and $c\varepsilon_0 = 1 + 0.2\ \sigma_\rho = 1.325$ (our preliminary coupling law /2, 10/).

We present here the results obtained with coefficients $\sigma_\rho = 1.614$ and $c\varepsilon_0 = 0.81$ (from the new coupling law /10/) allowing the restitution of Rayleigh-Taylor experiments /8, 10/. Figures 10 (diffusive SF6-air), 11 (discontinuous SF6-air) and 12 (discontinuous air-helium) are x-t diagrams and thickness plots showing calculated lines and measured points. Figure 10, with a reasonably small scatter of experimental points, indicates an approximate agreement between the continuous SF6-air experiment and its calculation. This agreement was, however, only obtained through our choice of initialization. Data from the two discontinuous interface experiments, with two extreme interpretations of mixing zone edges, are still too few and scattered to allow a meaningful comparison at this time: the most that can be seen on figures 11 and 12 is that the calculation is closer to the lower experimental value, which excludes the wall structures. We will collect more experimental data by carrying more single picture tests under reproducible shock conditions as well by using high speed cinematography.

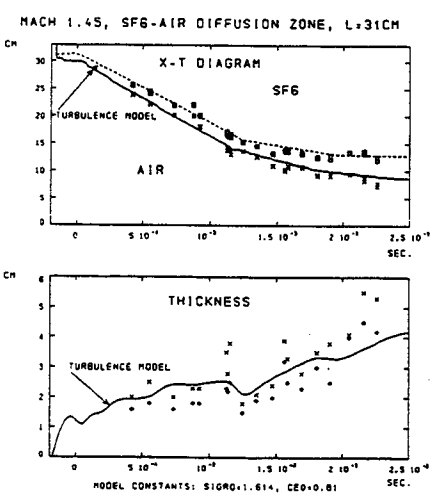

Figure 10 : SF6/Air
continuous interface, Ms=1.45, L=31 cm

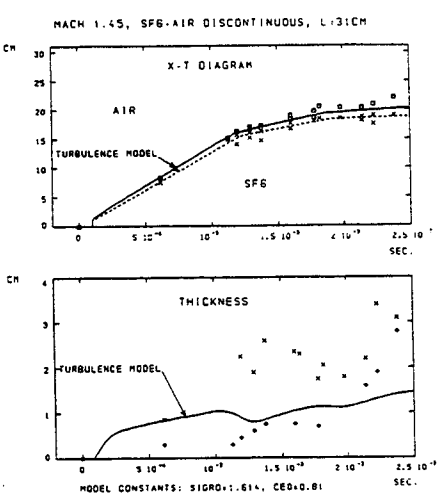

Figure 11 : SF6/Air
discontinuous interface

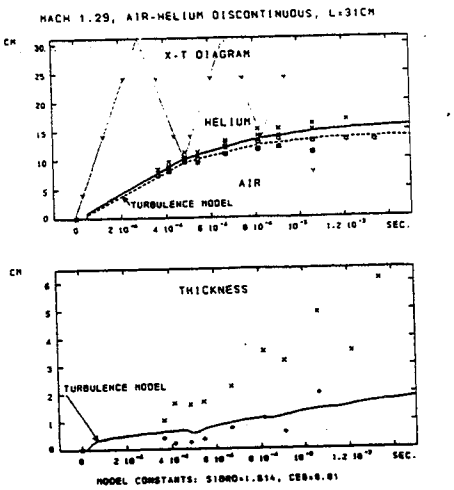

Figure 12 :

Air/Helium discontinuous interface

Ms=1.3, L=31 cm

crosses and lozenges represent upper bound

(wall structures) and lower bound of

measurement of mixing zone thickness

(same for figure 11).

4 Conclusion

This vertical shock tube enables us to carry out a number of experiments with continuous and discontinuous (planar or tridimensional) gas interfaces. In the case of the continuous interfaces, the schlieren system is not equally sensitive for the two gas pairs while turbulent scales cannot be seen. The comparison between predictions by the model and the experiments with discontinuous interfaces is hampered by the lack of discrimination of the schlieren flow visualization between wall and contact surface turbulence and suffers from shot to shot variations. High speed cinematography and X-ray densitometry of air-xenon interfaces are in preparation in order to overcome these deficiencies.

References

1 S. Gauthier and M. Bonnet, "A k-ε model for turbulent mixing in shock-tube flows induced by Rayleigh-Taylor instability", Phys. Fluids A2 (9), September 1990.
2 C. Cavailler, J.-F. Haas, P. Mercier and G. Rodriguez, "A new vertical shock tube built for Rayleigh-Taylor instability measurements", 17th ISSWST, July 1989, in "Current topics in shock waves", Y. Kim ed., A.I.P. Conference Proceedings 208, 1990. Also included in the material distributed after the RT and RM mixing workshop, Pleasanton, November 1989.
3. C. Cavailler, H. Croso, J.-F. Haas and G. Rodriguez, "The DAM vertical shock tube", Chocs 2, June 1991.
4 M. Brouillette and B. Sturtevant, "Richtmyer-Meshkov Instability at a Continuous Interface" 17th ISSWST, July 1989, in "Current topics in shock waves", Y. Kim ed., A.I.P. Conference Proceedings 208, 1990.
5 M. Brouillette and B. Sturtevant, "Growth Induced by Multiple Shock Waves Normally Incident on Plane Gaseous Interfaces", in "Advances in Fluid Turbulence", *Proceedings of the CNLS Annual Conference*, May 16-20, 1988, Physica D37, North Holland, 1989.
6 G. Weber, "Instationäre Strosswellen in Inhomogen Gasen" Engineer's thesis, Rheinish-Westfälische Technische Hochschule Aachen, June 20 1983.
7 Thu Pham, "Numerical studies of incompressible Richtmyer-Meshkov instability in a stratified fluid", Ph-D thesis, Applied Mathematics, California Institute of Technology, October 1990.
8 D. Youngs, "Modelling turbulent mixing by Rayleigh-Taylor Instability" in "Advances in Fluid Turbulence", Physica D 37, North Holland, Amsterdam (July 1989).
9 K. Mikaelian, "Turbulent mixing generated by Rayleigh-Taylor and Richtmyer-Meshkov Instabilities", Physica D 36, North Holland, Amsterdam (1989).
10 P. Spitz and J.-F. Haas, "Numerical calibration of Rayleigh-Taylor induced turbulent flows with a k-ε mix model", Proceedings of the Royaumont workshop, June 17-20 1991.

A TWO-DIMENSIONAL DYNAMIC MIX MODEL IN FREE LAGRANGE HYDRODYNAMICS

Alan K. Harrison and Donald E. Burton
Center for Compressible Turbulence
Lawrence Livermore National Laboratory
L-18, P. O. Box 808
Livermore, California 94551, U. S. A.

ABSTRACT

We are developing a set of dynamic mix algorithms compatible with two-dimensional free Lagrange[1] hydrodynamics. The hydrodynamics algorithms have conservation properties desirable to minimize numerical noise that might otherwise unacceptably degrade the second order moment terms coupling turbulence to the underlying flow. The mix model will consist of a K-ε model[2] of isotropic turbulence, and a set of instability models based on multiphase hydrodynamics. The K-ε model has been tested and has given qualitatively correct results. The instability model is intended to account for subgrid-scale flows which are not yet fully turbulent or well mixed and thus do not conform to the assumptions of the turbulence model. By basing these algorithms on the variables of multiphase hydrodynamics, we will model the *effects* of subgrid-scale interface and mixing layer structure on variables relevant to mixing, without modeling the subgrid-scale structure explicitly.

1. INTRODUCTION

We are developing a set of dynamic mix algorithms for use in two-dimensional free Lagrange[1] hydrodynamics. The completed set will include both a subgrid-scale turbulence model and an instability model based on multiphase hydrodynamics. Both processes will have the capability to mix matter between material regions. The modeled hydrodynamic instabilities will be driven by velocities and accelerations in the underlying flow, and will in turn provide source terms to the turbulence equations.

The turbulence capability has now been tested. Pending completion of the instability model, turbulence is driven by sources taken directly from the underlying velocity and acceleration fields. Early results appear qualitatively correct.

In Section 2 below we introduce the free Lagrange method. In particular, we point out conservation features which we believe make this approach a particularly good environment for a turbulence model. We also recommend data storage features which would allow for the description of a broad variety of mixing events. In Section 3 we define the K-ε turbulence model[2] and its free Lagrange implementation, including results of sample calculations. Finally, in the last section we motivate and explain our use of a multiphase flow model of hydrodynamic instabilities, and relate it to the turbulence model.

2. CODING ENVIRONMENT CONSIDERATIONS

The mix model is being developed in the context of free Lagrange hydrodynamics. The problem mesh, which may contain both quadrilateral and triangular zones, is automatically rezoned as necessary to maintain acceptable zone

shapes and timestep. This approach is more robust than ordinary Lagrange methods and superior in accuracy to Eulerian methods. The hydrodynamic differencing conserves momentum, energy and angular momentum exactly. This method has recently been used to calculate a shock tube test problem with a degree of fidelity comparable to a good Eulerian calculation.[3]

Since the leading terms in a description of turbulent flow are second moments of the basic field variables, that description is more sensitive to calculational inaccuracy than are the field variables themselves (such as the average fluid velocity). It is quite possible that a level of numerical noise and spurious modes that would be tolerable in a simulation of overall fluid velocity would be unacceptably large in a turbulence calculation. We therefore believe that the accuracy and conservation properties described above should be present in any implementation of our mix model in a code.

We recommend designing the database of any mixing code so as not to constrain the physics. For example, one could define *constituents* as material entities sharing a zone which are treated as being distinguishable from each other. They may be distinct materials, or similar materials with different mixing histories, or even identical materials which the user desires to distinguish from each other. Each constituent in a zone may then have its own set of physics variables (e. g., density), so that the corresponding zone variables are sums or averages of the constituent values. This has several advantages, to wit: Different materials coexisting within the same zone can be either well ("atomically") or poorly ("chunk") mixed; any number of constituents may be mixed in the same zone; and mixed material may be treated as a new, separate constituent, so it can be subsequently mixed with something else without requiring the same characteristics of both mixing processes. (For example, it should be possible to mix chunks of one material into a preexisting atomically mixed phase.)

3. MODELING OF TURBULENT MIXING

We depict schematically in Figure 1 the relationship between internal energy and a few of the other physics variables of hydrodynamics. The evolution equation referred to is an equation for internal energy containing a work term. The K-ε equations we use to model turbulence embody analogous relationships for turbulent energy K and turbulent dissipation ε as well as internal energy[2,4]; we diagram those three equations in Figure 2. The turbulence sources in the equations represent Rayleigh-Taylor (RT), Richtmyer-Meshkov (RM) and Kelvin-Helmholtz (KH) instabilities.

The K-ε equations are

$$\begin{aligned}
\rho\frac{D}{Dt}e &= -w_{press} - \rho(s-\varepsilon) + \nabla\cdot\left(\frac{\mu_T}{\sigma_e}\nabla h\right) \\
\rho\frac{D}{Dt}K &= -w_{turb} + \rho(s-\varepsilon) + \nabla\cdot\left(\frac{\mu_T}{\sigma_K}\nabla K\right) \qquad (1) \\
\rho\frac{D}{Dt}\varepsilon &= -C_{1d}\alpha w_{t1} - C_{1s}\alpha w_{t2} + \rho\alpha\left(C_{\varepsilon 1}s - C_{\varepsilon 2}\varepsilon\right) + \nabla\cdot\left(\frac{\mu_T}{\sigma_\varepsilon}\nabla\varepsilon\right)
\end{aligned}$$

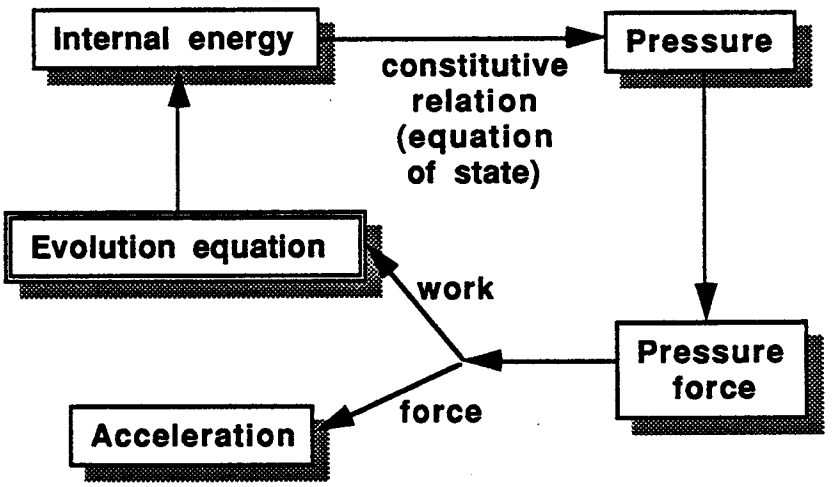

Figure 1. Schematic depiction of relationships among a few of the variables of hydrodynamics.

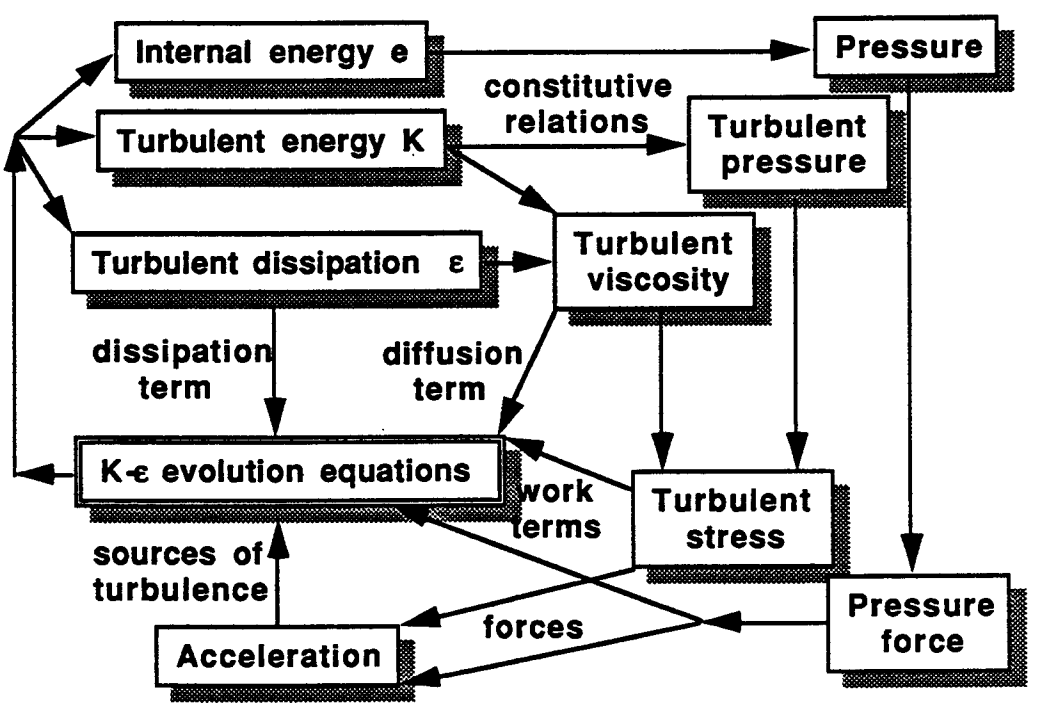

Figure 2. Schematic depiction of relationships among variables in our turbulence model, including all the terms in the K-ε equations.

in which the convective derivative is

$$\frac{D}{Dt} \equiv \frac{\partial}{\partial t} + \boldsymbol{u} \cdot \nabla \tag{2}$$

and the specific enthalpy is

$$h = e + \frac{p}{\rho} \tag{3}$$

In these equations the pressure- and turbulence-based work terms are exactly analogous except for the absence of off-diagonal (viscous) terms in the stress tensor $\boldsymbol{\sigma}$:

$$\begin{aligned} w_{t1} &= p_T \nabla \cdot \boldsymbol{u} & w_{press} &= -\boldsymbol{\sigma} : \mathbf{E} = p \nabla \cdot \boldsymbol{u} \\ w_{t2} &= -\mathbf{R}^* : \mathbf{E} & w_{turb} &= w_{t1} + w_{t2} = -\mathbf{R} : \mathbf{E} \end{aligned} \tag{4}$$

in which the Reynolds stress tensor $\mathbf{R}$, strain rate tensor $\mathbf{E}$ and their deviators $\mathbf{R}^*$ and $\mathbf{E}^*$ are

$$\begin{aligned} \mathbf{R} &= \mathbf{R}^* - p_T \mathbf{1} & \mathbf{E} &= \tfrac{1}{2}\left(\nabla \boldsymbol{u} + \boldsymbol{u} \nabla^\dagger\right) \\ \mathbf{R}^* &= 2\mu_T \mathbf{E}^* & \mathbf{E}^* &= \tfrac{1}{2}\left(\nabla \boldsymbol{u} + \boldsymbol{u} \nabla^\dagger\right) - \tfrac{1}{3}(\nabla \cdot \boldsymbol{u})\mathbf{1} \end{aligned} \tag{5}$$

and the turbulent kinematic viscosity, viscosity, pressure and characteristic dissipation rate are defined as

$$\begin{aligned} \nu_T &= \frac{C_\mu K^2}{\varepsilon} & \mu_T &= \rho \nu_T \\ p_T &= \tfrac{2}{3}\rho K & \alpha &= \frac{\varepsilon}{K} \end{aligned} \tag{6}$$

The work terms (4) are spatially differenced in an energy-conserving way as described in reference 5.

We have defined the RT source term

$$s = \max\left\{ \frac{\nu_T}{\sigma_m} \frac{1}{\rho} \nabla \rho \cdot \left(\frac{D}{Dt} \boldsymbol{u} - \frac{f_{turb}}{\rho} \right), 0 \right\} \tag{7}$$

where f_{turb} is the turbulent force consistent with the Reynolds stress $\mathbf{R}$. We will soon add KH and RM sources as well.

Following Leith's recommendations[2], we use the following values for the dimensionless adjustable parameters in the model:

$$\begin{aligned} C_{1d} &= 2.0 & C_{\varepsilon 2} &= 1.8333 & \sigma_K &= 0.715 \\ C_{1s} &= 1.4 & C_\mu &= 0.09 & \sigma_\varepsilon &= 1.3 \\ C_{\varepsilon 1} &= 0.85 & \sigma_e &= 0.9 & \sigma_m &= 0.7 \end{aligned} \tag{8}$$

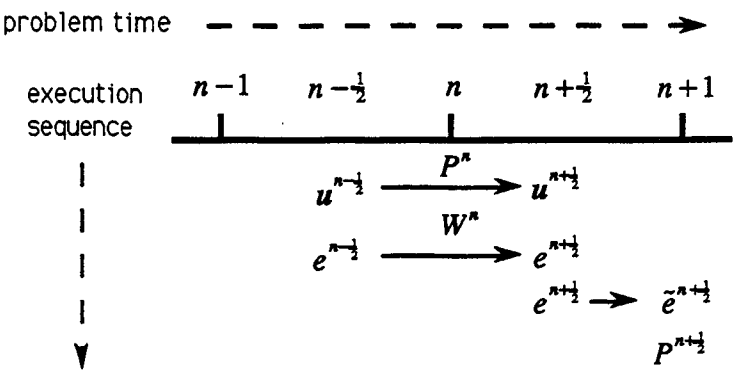

Figure 3. Burton's temporal differencing scheme. We difference K and ε in the same way as internal energy e in the figure; then the turbulent pressure and viscosity play the same role as pressure here.

Based on the obvious analogy among the three quantities, we difference K and ε temporally in the same way as Burton differences energy e in his conservative staggered-grid hydrodynamics.[5] Burton has observed that since the velocities u and hence the kinetic energy of the mesh are known only on the half time step (see Figure 3), the work done W^n is known exactly over the internal from n-1/2 to n+1/2. Therefore the internal energy should also be calculated on the half time step in order to maintain strict energy conservation. Although the internal energy must be extrapolated to the next time step (n+1 in the figure) in order to get a new pressure P^{n+1} from the equation of state, that estimate $\tilde{e}^{n+1}$ should then be discarded. Since we model the exchange of energy between e and K, and the evolution of ε in strict analogy to K, we must difference all three quantities in the same way. Thus we calculate turbulent pressure and the other quantities in (5) and (6) at cycle n (except that $\mathbf{E}^*$ is based on u^{n-1}). We then use (4) to find the forces at n and the work done from n-1/2 to n+1/2. The work, source and estimated dissipation (ε) terms at n are used according to (1) to advance e, K and ε. Subsequently the diffusion terms in (1) are added, by using an advection scheme and the observation that each diffusion term can be written as an advection term; for instance

$$\nabla\cdot\left(\frac{\mu_T}{\sigma_K}\nabla K\right)=-\nabla\cdot\left(\rho K v_K\right) \tag{9}$$

in which the advection velocity is

$$v_K=-\frac{\nu_T}{\sigma_K}\frac{\nabla K}{K} \tag{10}$$

Finally, we estimate new values of K and ε at cycle n+1 based on the work, source and dissipation terms.

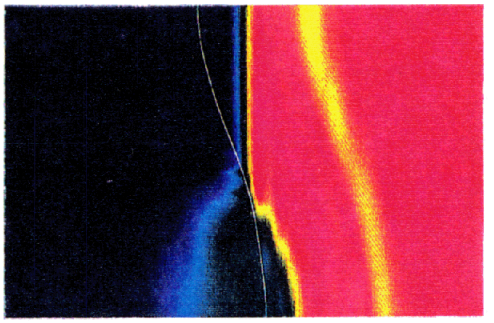

Figure 4. Pressure in shock tube test problem.

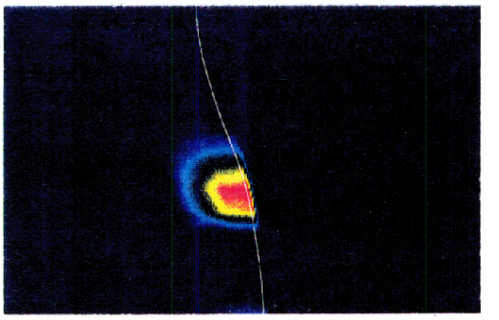

Figure 5. Bouyant source of turbulence in shock tube test problem.

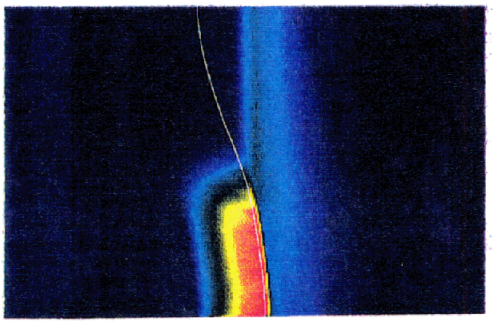

Figure 6. Turbulent energy K in shock tube test problem.

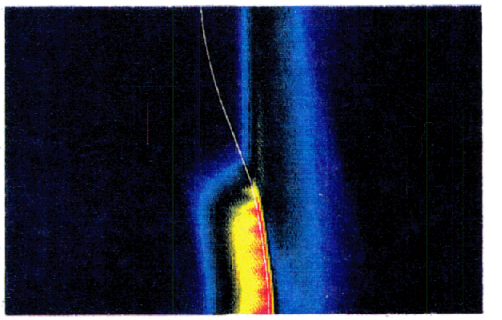

Figure 7. Turbulent dissipation ε in shock tube test problem.

Figures 4 through 7 pertain to a shock tube test problem (test problem 3a of this conference) in which the air-He interface (white curve in the figures) has a pre-emplaced sinusoidal perturbation. The Mach 1.3 shock, proceeding from air into helium (to the left), is crossing the interface at the time shown in the figures. In each figure red corresponds to the largest values and dark blue to the smallest. The incident and refracted shock front are easily identified in Figure 4.

Since the RM source term has not yet been formulated and the given test problem is stable against RT instability, we constructed an artificial bouyant source term for this problem by changing the sign of the expression preceding the comma in (7). The resulting source term is unphysical because it is nonzero for RT stable accelerations and zero for those that are unstable to RT instability, but it is useful for verifying the function of other parts of the model using this test problem. As shown in Figure 5, this bouyant source term is nonzero only near the point where the shock front is crossing the interface. Shortly before the time of the plots, it has been different from zero at points all along the bottom half of the interface (as oriented in the figures); thus turbulent energy and dissipation have been created at those locations, as shown in figures 6 and 7.

Although adjustable model parameters must yet be calibrated, this prototype calculation exhibits qualitatively correct behavior. As the model develops further, we hope to make quantitative comparisons to a variety of experiments and simulations.

4. MODELING OF HYDRODYNAMIC INSTABILITIES

We must recognize that turbulence is only one of several stages in instability-driven mixing. For example, Birkhoff[6] has described the following stages which follow from an infinitesimal sinusoidal perturbation of the interface:

(1) exponential increase in amplitude,
(2) transition to asymmetrical spike-and-bubble configuration,
(3) constant rate of increase of bubble penetration depth,
(4) deformation of shearing interface along bubble sides due to KH instability and the growth of vorticity, and
(5) turbulent motion

We should not expect to model all the physical processes in steps (1)-(4) with a simple model of step (5).

A moderately sophisticated picture of subgrid-scale hydrodynamics ought to describe at least two distinct processes, which we will refer to as instability growth and turbulence. The former refers to structures in the flow which are characterized by a small range of length scales and may be anisotropic. If they occur at an interface between different materials, they do not produce a "well-mixed" phase; in fact, there may be a macroscopic relative velocity between the materials, and what mixing or interpenetration takes place may be at least partly reversible, as shown in the "demixing" observed by Smeeton and Youngs[7]. Turbulence, by contrast, is often modeled as an isotropic superposition of flows on a wide range of length scales. It mixes material well and irreversibly. Our K-ε model of turbulence is consistent with these idealizations.

We believe that a plausible subgrid-scale model of material mix ought to include both processes, because it is not possible to say *a priori* which is more effective at mixing. Although turbulence mixes on many length scales, resulting in a well-mixed system locally, it is modeled as transporting matter in a diffusive way, with displacement increasing asymptotically as the square root of the elapsed time. Instability growth transports matter by convection (streaming), with displacement proportional to time. Therefore we need to add to our turbulence model a model of instability growth with the characteristics listed above.

We intend to model instabilities by multiphase hydrodynamics. By allowing each constituent to have its own velocity field, we hope to model segregation of materials, anisotropy, partial reversibility and mass transport by streaming without explicitly modeling the subgrid-scale structure of the interface and mixing region. The physical quantities which must be tracked in order to model mixing (e. g., rate of growth of the mixed region thickness and measures of its degree of segregation) will be defined as functions of the velocity separations of constituents at the same point in space, and other variables such as Atwood numbers and accelerations.

In a single-phase implementation of the mix model, the hydrodynamics and turbulence packages would have to exchange information on strain rates and turbulent stress, dissipation and diffusion. The hydrodynamic velocities and accelerations must also be used to compute the turbulent source terms. In a multiphase implementation, the turbulence package would have to receive strain rate information from and pass turbulent stress, dissipation and diffusion to the hydrodynamic variables pertinent to each of the constituents. In addition, the hydrodynamics of the constituents should interact with each other via drag forces, and the drag forces can also provide the source

terms to the turbulence package. This last feature is suggested by considerations such as Birkhoff's point (4) above.

It remains for us to define the variables and equations necessary to model the physics of subgrid-scale instabilities and their coupling to turbulence, e. g., the rate of growth of mixing layers, concentration profiles, driving forces and drag forces. This scheme must incorporate the results of experimental and theoretical instability studies implicitly in the form of the equations used. Put another way, we want to model the *effects* of subgrid-scale interface and mixing layer structure on the variables of interest to us, without modeling that structure explicitly. We regard this approach as a promising balance between the need to model complex phenomena and the practical necessity to minimize the memory and processing requirements for a given problem.

Aside from the instability modeling, there are a number of potential improvements which we hope to make to the models, such as theoretical extensions to the K-ε turbulence model and normalization of model adjustable parameters.

ACKNOWLEDGMENTS

We acknowledge helpful discussions with C. E. Leith, E. W. Burke, V. C. Rupert, W. P. Crowley, A. C. Buckingham, W. P. Dannevik and D. E. Nielsen; and programming support from M. T. Uyemura, D. D. Hardin, U. Creach and R. G. Williams. **This work was performed under the auspices of the U.S. Department of Energy by Lawrence Livermore National Laboratory under Contract #W-7405-Eng-48.**

1W. P. Crowley, "FLAG: A Free-Lagrange Method for Numerically Simulating Hydrodynamic Flows in Two Dimensions," Proceedings of the Second International Conference on Numerical Methods in Fluid Dynamics, (Springer-Verlag, New York, 1970), pp. 37-43.

2C. E. Leith, "Development of a Two-equation Turbulent Mix Model," Lawrence Livermore National Laboratory report no. UCRL-96036, Dec. 1986.

3D. E. Burton and A. K. Harrison, "Simulation of Single Mode Richtmyer-Meshkov Instability Using the Adaptive Free Lagrange Method," these proceedings.

4C. E. Leith, private communication.

5D. E. Burton, "Exact Conservation of Energy and Momentum in Staggered-Grid Hydrodynamics with Arbitrary Connectivity," Lawrence Livermore National Laboratory report no. UCRL-JC-104258, June 1990, to appear in the proceedings of The Next Free Lagrange Conference, Jackson Lake Lodge, Wyoming, June 3-7, 1990; D. E. Burton, "Conservation of Energy, Momentum, and Angular Momentum in Lagrangian Staggered-Grid Hydrodynamics," Lawrence Livermore National Laboratory report no. UCRL-JC-105926, November 16, 1990.

6G. Birkhoff, "Taylor Instability and Laminar Mixing," Los Alamos National Laboratory report LA-1862, December 1954.

7V. S. Smeeton and D. L. Youngs, private communication.

PLIF FLOW VISUALIZATION OF SHOCK ACCELERATED LIGHT AND HEAVY GAS CYLINDERS

J. W. Jacobs*
Caltech, Pasadena, CA 91125

ABSTRACT

Experiments have been carried out in which a cylindrical volume of a gas that is either lighter or heavier than its surroundings is impulsively accelerated by a weak shock wave. Laminar jets of helium or sulphur hexafluoride (SF_6) are used to produce the cylinders, and planar laser induced fluorescence is used to visualize the flow. It is found that the vorticity deposited on the boundary of the SF_6 cylinder by the interaction with the shock wave, separates from the heavy gas to form a pair of vortices, which subsequently wrap the SF_6 around them. This process is quite different from what is observed in the light gas experiments, which showed a small amount helium to remain with the vorticity, eventually becoming part of the vortex cores.

INTRODUCTION

When a shock wave passes through a region of gas with density or sound speed that differs from its surroundings, a rich variety of scattered waves are generated at the boundaries of the region. However, the interaction of a shock wave with a density inhomogeneity produces more than an assortment of reflected and refracted waves. The experiments of Haas & Sturtevant[1] and the computational studies of Cowperthwaite[2] and Picone & Boris[3] have yielded remarkable images revealing that this interaction also produces a flow field which subsequently distorts the inhomogeneity, and which persists long after the scattered waves have left the vicinity.

The present investigation focuses on the flow produced by the interaction of a weak shock wave with a cylindrical region of a gas that is either lighter or heavier than its surroundings. Previous experimental investigations[1,4] have utilized shadowgraph visualization, and were limited by the integrating nature of this method to effectively visualize three-dimensional flows. The shortcomings of shadowgraph are overcome in the present study by using planar laser induced fluorescence (PLIF). In the present experiments helium or SF_6 is seeded with a small amount of the

* Present address: Department of Aerospace and Mechanical Engineering, University of Arizona, Tucson, AZ 85721.

biacetyl[5], and then made to fluoresce with a sheet of laser light. Thus, cross-sectional views of the three-dimensional density field are obtained. The visualization of Haas & Sturtevant[1] was further complicated by interference from the nitrocellulose membrane they used to encapsulate their cylinders. In the present experiments, this effect is removed by employing a laminar jet to produce the cylinders, thus eliminating the need for a membrane to contain the light or heavy gas. Not only does this technique improve the quality of visualization, but it also removes the possibility of the membrane affecting the flow on a larger scale.

EXPERIMENTAL APPARATUS

The experiments were performed in a 26.67 cm square test section mounted with a 152 cm long "cookie cutter" to the Galcit 17 inch shock tube. A pair of 15.24 cm diameter round windows provided visual access to the test section, and 0.152 mm thick aluminum diaphragms were used to produce a shock Mach number, M_s = 1.095. A round laminar jet was introduced into the test section through a section of copper tubing that entered the shock tube through the side wall of the test section, and terminated in the central portion of the test section, directly above the lower window. The jet issued from a 0.794 cm diameter opening, oriented vertically upward in the light gas experiments, and vertically downward in the heavy gas experiments. A larger 1.9 cm opening, was situated 8.9 cm directly opposite the jet exit, to collect the light or heavy gas and remove it from the shock tube. Helium and SF_6 were supplied from high pressure bottles and flowed through rotameters and needle valves to monitor and control the flow rate. Portions of these streams were diverted and bubbled through liquid biacetyl, then merged again to seed the flow. A ratio of 10 parts pure helium to 1 part biacetyl laden helium, with a total flow rate of 65.1 cc/s, was used in the light gas experiments, whereas a ratio of 6 parts pure SF_6 to 1 part biacetyl laden SF_6, with a total flow rate of 11.6 cc/s, was used in the heavy gas experiments. The PLIF system utilized a flashlamp pumped dye laser providing 100 mJ 0.7 µs pulses of 430 nm laser light. The 18 mm diameter beam was focused using a set of lenses to provide a sheet of laser light that bisected the biacetyl seeded jet, illuminating a 1 mm thick cross section. The resulting fluorescent image was captured using an intensified solid state video camera, positioned so that it viewed upward through the window in the bottom of the test section. The camera output was sent to a frame grabber housed in a laboratory microcomputer. The laser, camera and frame grabber were triggered by digital delay

generators, which used signals from pressure transducers mounted flush in the test section walls as inputs.

RESULTS AND DISCUSSION

Figures 1 and 2 are series of fluorescent images (each compiled from 7 separate runs) showing the evolution of the helium and SF_6 cylinders after having been traversed by a M_s=1.095 shock wave. Figure 1 illustrates how the initially circular helium cylinder is distorted by the effects of the passing shock wave, eventually becoming a vortex pair. Figure 1b, taken 0.151 ms after the passage of the shock, shows an initial flattening of the cylinder caused by the compression of the shock wave, and the beginning of the formation of two lobes. Figure 1c, taken at t = 0.319 ms, shows further development of these lobes, and the start of their separation. In figure 1d, the thin strand that connects the two halves in 1c is stretched and nearly disappears. In figure 1e, the nearly separated upper and lower halves begin to split into front and back lobes. Figures 1f-h show the disappearance of the rearward portions resulting from that split.

Figure 2 illustrates the evolution process of an cylinder. Figure 2b, taken 0.217 ms after the passage of the shock, again shows an initial flattening of the SF_6 cylinder, along with the beginning of the formation of a crescent shape. The protrusion near the center of the downstream edge of the heavy gas volume in figure 2b and c is caused by a jet of fluid that is produced by the focusing of the transmitted shock wave. Figure 2c, taken at t = 0.374 ms, shows further spreading of the crescent shape. In figure 2d, the vorticity that initially resides on the boundary of the cylinder, appears to be shed from the heavy gas and collect in the wake of the inhomogeneity to form a vortex pair. In figures 2e-h the heavy gas is then wrapped around these vortices by their induced velocity, forming a heavy gas strip. Figure 2e shows the beginning of the formation of waves on this strip. In figure 2f these waves continue to grow as the gas is swept to the rear of the vortices. In figure 2g, similar waves can be observed in the thin filaments of heavy gas that spiral into the vortex cores. Finally, as the heavy gas accumulates at the rearward stagnation point, the waves have grown to a point where they dominate the flow and further help dissipate the gas.

Vorticity is produced in these experiments by the interaction of the pressure gradient from a plane shock wave with the density gradient at the boundary of a circular cylinder. The magnitude of this vorticity is proportional to the product of the density and pressure gradients as well as to the degree of their misalignment. Thus, the vorticity produced is localized at the cylinder

boundary and is distributed with maxima at the top and bottom edges of the cylinder, and is zero at the front and back edges. This distribution is similar to that of two semicircular vortex sheets of opposite sign, with a vortex strength distribution that is maximum at the center of the sheets, and decays towards the ends. Since very little vorticity is produced after the shock wave passes the jet, the evolution of figures 1 and 2 can be described by the dynamics of these two vortex sheets. In the light gas experiments displayed in figure 1, the vortex sheets are observed to roll up onto themselves, slicing through the helium, and chopping the cylinder into first two and then four pieces as the vorticity spirals inward to form a vortex pair.

The initial vorticity distribution for light and heavy gas cylinders is identical, differing only in the sign of the vorticity. Therefore, to first approximation, one might expect the evolution processes for these two cases to be similar, except with reversed flow direction. The images of figures 1 and 2, however, reveal completely different processes. In the later stages of the light gas experiments, a small amount of helium is incorporated with the vorticity, and eventually becomes part of the vortex cores. While, in the heavy gas experiments shown in figure 2, the bulk of the vorticity separates from the heavy gas to form line vortices which are free of SF_6.

In these experiments, circular regions of light or heavy gas have vorticity which is distributed on their boundaries in such a way that it is concentrated on opposite sides of the cylinders. This configuration may be reasonably approximated by the simpler model of a vortex located at the vertex of a wedge shaped region of a gas that is either lighter or heavier than its surroundings. This model is illustrated in figure 3a for a heavy gas wedge, and in figure 3c for a light gas wedge. In this configuration the vortex will induce a circular motion about its center, causing the wedge to wrap around its vertex. The resulting centripetal acceleration, caused by the circular motion of the fluid, will produce a radial pressure gradient ($\partial p/\partial r = \rho v_\theta^2/r$), which will depend on the local gas density, ρ. When the density is larger inside the wedge, the resulting pressure gradient will be larger inside the wedge as well. If pressure is assumed to be uniform at infinity (where there is no motion), then near the vortex, the pressure inside the wedge will be lower than it is outside, resulting in a pressure difference across the interface separating the two gases. This pressure difference will produce a secondary motion causing the interface to move inward, and pinch off the vertex of the wedge as shown in figure 3b. Now, if the wedge shaped region contains gas that is lighter than its

surroundings, the process is reversed. The pressure gradient will be smaller inside the wedge, resulting in higher pressure inside than out. This will produce a secondary flow causing the interface to move outward, and the wedge to swell as shown in figure 3d. Thus with a heavy gas wedge, the vortex is pinched-off from the heavy gas, promoting separation; while with a light gas, the wedge swells, encompassing the vortex.

This process is further enhanced by the difference in the rates of the diffusion of vorticity in the two gases. Suppose that a uniform distribution of vorticity were deposited on the boundary separating two quiescent gases with different kinematic viscosities. Since the rate at which vorticity diffuses in a fluid is governed by its kinematic viscosity, the deposited vorticity will diffuse much more readily into the more viscous gas; and after a period of time, more of the original vorticity will reside in the more viscous gas than in the less viscous one. The kinematic viscosity of a gas is closely linked to its density. Heavy gases usually have lower kinematic viscosities than lighter ones. Thus, in situations where vorticity lies on the boundary separating two gases with different density, it will tend to diffuse into the lighter gas and away from the heavier one.

Therefore, the action of centrifugal forces coupled with the tendency of vorticity to diffuse into regions of higher kinematic viscosity, causes the vorticity deposited on the boundary of a density inhomogeneity to migrate into the lighter of the two gases. As a result, the interaction of a shock wave with a light gas cylinder produces a vortex pair with light gas contained within the cores of the vortices, as shown in figure 1h. Conversely, the shock interaction with a heavy gas cylinder results in a vortex pair which is completely devoid of heavy gas, as shown in figure 2h.

This research was supported by the Air Force Office of Scientific Research.

REFERENCES

1. J.-F. Haas & B. Sturtevant, J. Fluid Mech. 181, 41 (1987).
2. N. Cowperthwaite, Physica D 37, 264 (1989).
3. J.M. Picone & J.P. Boris, J. Fluid Mech. 189, 23 (1988).
4. G. Rudinger & L.M. Somers, J. Fluid Mech. 7, 161 (1960).
5. A.H. Epstein, J. Engineering for Power, Trans. ASME 99, 460 (1977).

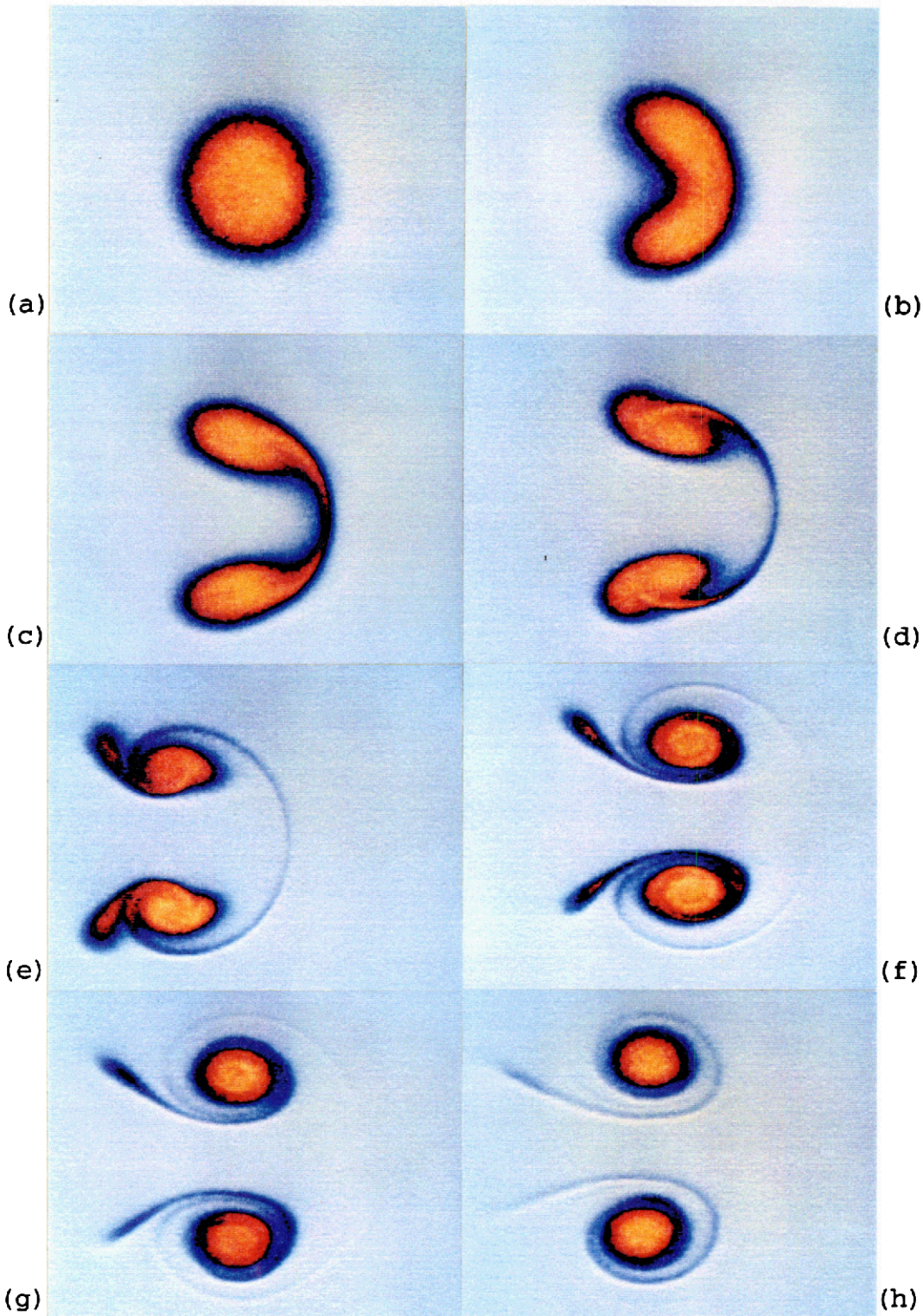

Figure 1. PLIF images of the helium cylinder. a) Initial jet. b) 0.151 ms, c) 0.319 ms, d) 0.417 ms, e) 0.568 ms, f) 0.795 ms, g) 0.982 ms, h) 1.403 ms after the shock passage.

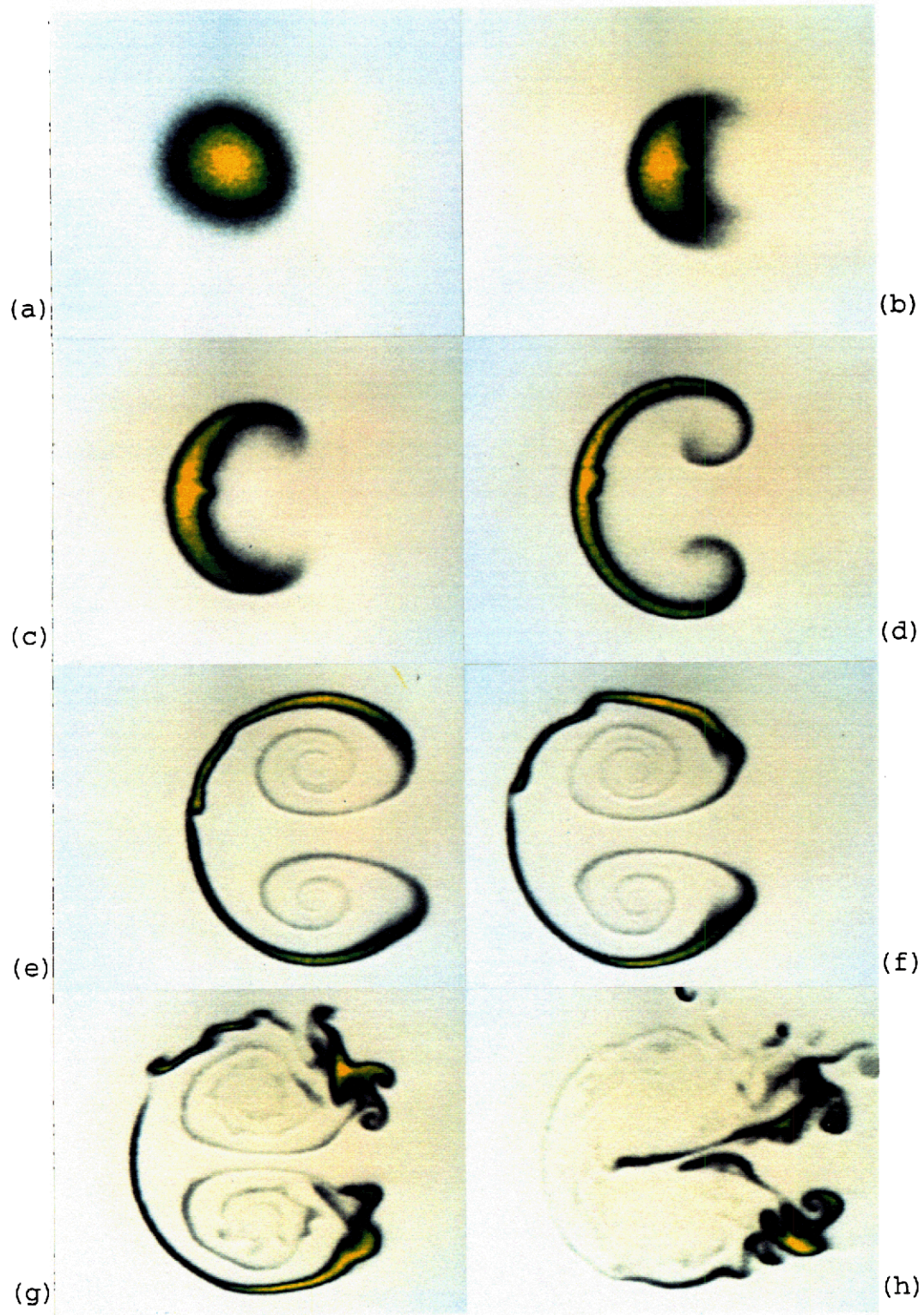

Figure 2. PLIF images of the SF_6 cylinder. a) Initial jet. b) 0.217 ms, c) 0.374 ms, d) 0.588 ms, e) 0.998 ms, f) 1.201 ms, g) 1.403 ms, h) 1.803 ms after the shock passage.

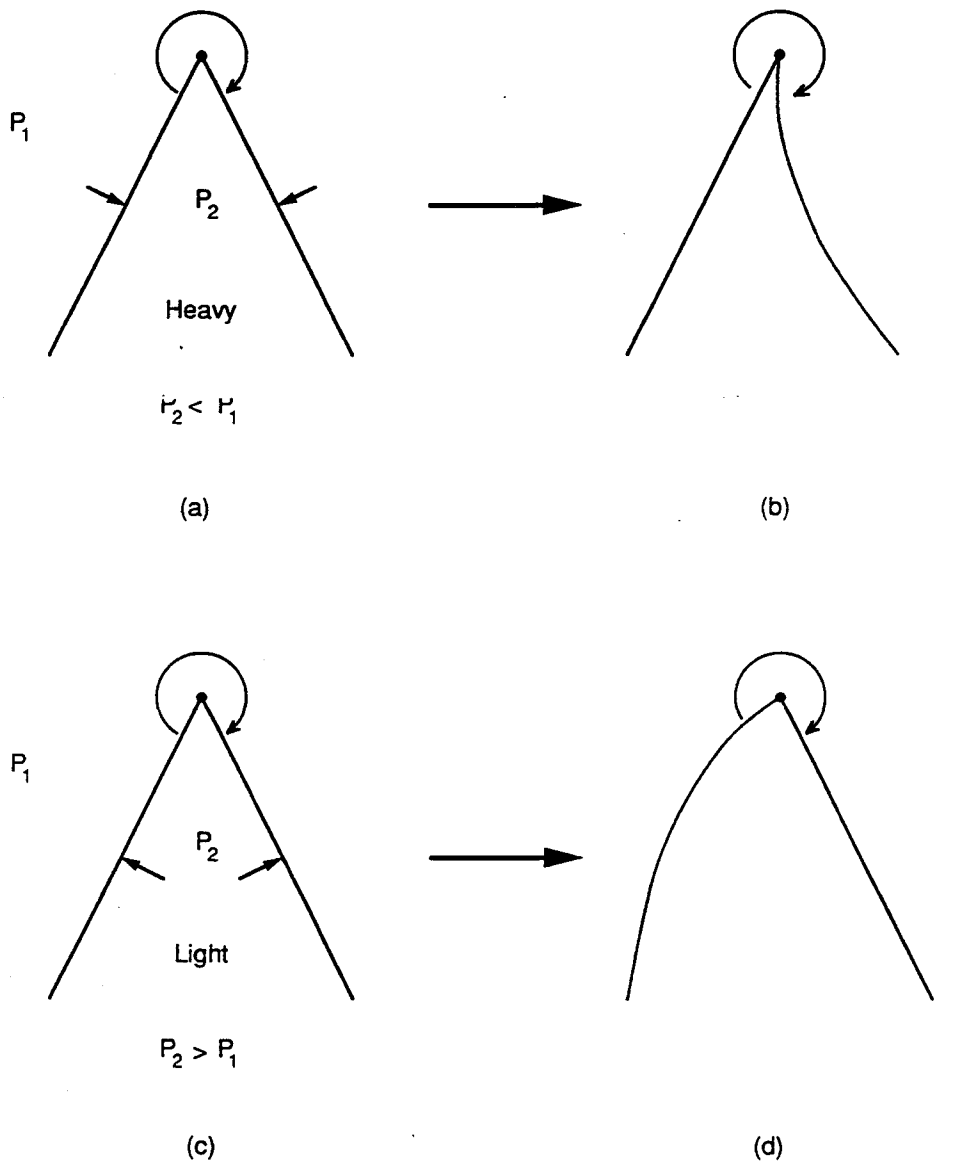

Figure 3. A simple model roughly approximating one side of a shock accelerated light or heavy gas cylinder. a) The heavy gas configuration and b) the resulting motion. c) The light gas configuration and d) the resulting motion.

EXPERIMENTAL INVESTIGATION OF RAYLEIGH-TAYLOR AND RICHTMYER-MESHKOV INSTABILITIES

S. Zaytsev, A. Aleshin, E. Lazareva, S. Titov, E. Chebotareva
The Krzhizhanovsky Power Engineering Institute
(ENIN), Moscow 117071 , Leninsky pr., 19, USSR

V. Rozanov, I. Lebo
P.N. Lebedev Physical Institute of Academy of Sciences
of the USSR, Moscow 117333, Leninsky pr., 53. USSR

V. Demchenko
Moscow Institute of Physics and Technics,
141700 Dolgoprudny of Moscow region, USSR

ABSTRACT

The results of investigations of R-M and R-T instabilities in continuous and discontinuous disturbed interfaces are presented. The experimental investigation of RMI has been carried out on a shock tube. For the investigation of RTI a vertical channel has been used, where a compression wave induces an accelerated motion on a continuous interface. The continuous interface results from the removal of sliding plate that initially separated the gases of different density. The experimental and numerical investigation of the influence of the curvature of the initial disturbed interface on the RMI development has been carried out. The growth rate of RTI for the disturbed continuous interface has been determined.

INTRODUCTION

The recent years have yielded a great number of investigations studying the hydrodynamic instability developed at the interface of different-density media drawn into an accelerated motion. This problem is of paramount importance since it plays a key role in implementation of a number of technical projects, e.g. inertial confinement fusion. With the aim of building adequate models for describing this phenomenon, we have successfully used experiments carried out in shock tubes. These facilities enable us to investigate all the stages of the instability development for a wide range of density ratios and accelerations with a well-developed arsenal of quantitative methods for recording unstable gas dynamic processes (schlieren method, interferometry, etc). In addition to shock waves giving impulsive acceleration to the interface, compression or rarefaction waves may be used in facilities of this type. Application of the latter makes it possible to bring the interface into motion with an acceleration $g(t)$ continuous in time. $g(t)$ obtained by application of unsteady compression waves may reach extreme values such that the position of shock wave formation may be brought closer to the interface.

The experimental investigation of shock wave passage through a curved discontinuous interface with a rather small curvature $a_0 k < 1$ (a_0 amplitude and k wave number of the initial discontinuous interface K_0) was made in ref[1]. The validity of the ratio obtained in ref[2] was confirmed for the variation of interface amplitude $a_k(t)$ after passage of the shock wave from the light gas to the heavy one. It was found that irrespective of direction of shock wave motion, i.e. from the light gas into the heavy one or vice versa, $a_k(t)$ increases: this is specific to the Richtmyer-Meshkov instability (RMI). This paper describes the experimental and numerical investigation of RMI for $a_0 k$ changing from 0.9 to 8.0. It is shown that changes of curvature of the initial interface K_0 alters the quantitative characteristics of RMI.

The second part of the paper is an investigation of the evolution of the interface entrained into the accelerated motion by an unsteady compression wave: thus it deals with the Rayleigh-Taylor instability (RTI). It is shown that the amplitude growth rate for the interface with an initial continuous density variation appears to be less than the one for an interface with a discontinuous density profile, provided the ratios of density and acceleration are the same.

RICHTMYER-MESHKOV INSTABILITY

1. The experiments were carried out in a shock tube. The low-pressure chamber (cross-section 7.2 x 7.2 cm²) is filled with inert gases which are separated by a thin film of preset shape. The gas pressure (0.5 atm) was exactly the same on both sides. The films were made of Lavsan (2 micron thick). The process was recorded by schlieren method. The Mach number M_0 of the incident shock wave S_0 ranged from 2.5 to 3.5 and the Atwood number $A = (\rho_2 - \rho_1) / (\rho_2 + \rho_1)$ ranged from 0.1 to 0.92.
2. Mathematical model. To simulate the passage of a planar shock front though a sinusoidal discontinuous interface, we solved a system of Eulerian equations in two-dimensional space. The numerical scheme was found with the help of one of a version of the mesh-characteristics method[3].
3. Influence of the curvature of initial discontinuous interface K_0 on the RMI. The experimental set-up and the used system of coordinates are given in fig. la. Schlieren pictures of the passage of the incident shock wave S_0 from Ar into Xe ($A = 0.45$) through K_0 for different curvatures (amplitude $a_0 = 1$ cm and wavelengths $\lambda = 7.2, 3.6, 2.4$ and 0.8 cm) are given in fig. 1b which presents all the stages of the evolution of the interface K after diffraction of S_0 on K_0.
i. The linear stage is characterized by similarity of shapes of K and K_0 whereas the change of its amplitude $a_k(t)$ may be satisfactorily described by the Richtmyer relation[2] ($\lambda = 7.2$ cm, fig. 1b)

$$da_k / dt = a_0^* u k A$$

a_0^* - amplitude of K_0 at the moment of the completion of diffraction (for the passage of the shock wave from the light gas to the heavy one); u velocity given to the discontinuous interface by the shock wave.
ii. The non-linear stage is characterized by formation of "spikes" and "bubbles" ($\lambda = 3.6$ cm, fig. 1b).

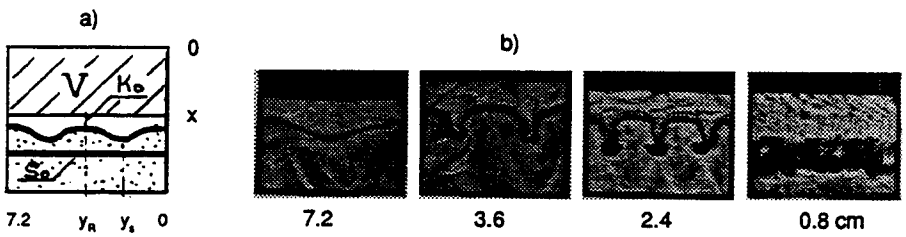

Fig.1 a) Experimental set-up. V: field of view. b) Schlieren pictures. Shock wave passes from Ar (top) into Xe (bottom).

iii. The transitional stage is characterized by the generation of vortex structures at the tip of the spikes which grow in size as time goes on ($\lambda = 2.4$ cm, fig. 1b)
iv. The final turbulent stage results from the interaction of neighboring vortex structures ($\lambda = 0.8$ cm, fig. 1 b).

The speed of penetration of one medium into the other is determined by the value of da_k/dt. The values of da_k/dt for two values of A and ka_0 are presented in fig. 2. In addition to the curvature of K_0, the character of RMI depends upon the Atwood number A of the media in contact and the intensity of the shock wave S_0. The analysis of the schlieren pictures made it possible to reveal the following salient features of the process : for $ka_0 > 0.3$ and $A > 0.5$ one can observe a system of two lines C and Q in the flow between K and S (see fig.3). Lines C travel laterally along the shock compressed gas enclosed between K and S. Lines Q are fixed ("frozen") in respect to this flow. The point of intersection of C with the shock front S (point f, fig.3) is a triple point. This testifies to the fact that C is a secondary shock wave and Q is a slip line. Interaction of C with S reduces the amplitude of the amplitude $a_s(t)$ of S and increases the amplitude $a_k(t)$ of the discontinuous interface K. The described mode is referred to hereinafter as "tough". For these modes "spikes" and "bubbles" start appearing already in the process of diffraction of S_0 on K_0. Therefore, da_k/dt is approximately one half of the value defined by the Richtmyer ratio (ref. lines 2.1 and R2, fig. 2). For small curvatures of K_0 ($ka_0 << 1$) there are no secondary shock waves in the flow structure between S and K and, consequently, no triple point on S. These are called "soft" modes for which the value of da_k/dt remains initially constant and equal to the value given by Richtmyer ratio (line 1.1 and R1, fig. 2).

Fig. 4 presents isobars and a stable concentration line describing the discontinuous interface arrangement. They are the result of a numerical calculation of the shock wave passage from He into Xe through K_0 ($\lambda = 3.6$ cm, $a_0 = 1$ cm) ("tough" mode). As it may be seen, the curved transmitted wave S (along cross-section y_s) and reflected wave R (along cross-section y_R) are followed by high-pressure areas P_S and P_R (fig. 4).

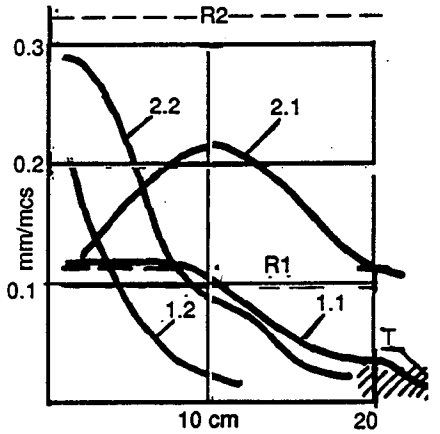

Fig. 2 da_t/dt versus travel path of K. T - dL/dt for turbulent stage, 1.1 and 1.2 : S_o propagates from Ar to Xe (λ = 7.2 cm, 0.8 cm) R1 Richtmyer ratio (λ = 7.2 cm), 2.1 and 2.2 S_o propagates from He to Xe (λ = 7.2 cm, 0.8 cm) R2 Richtmyer ratio (λ = 7.2 cm).

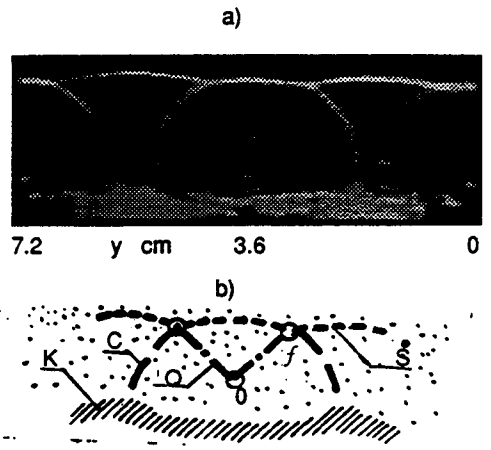

Fig. 3 a) Schlieren picture. So propagates from Xe into He. b) interpretation.

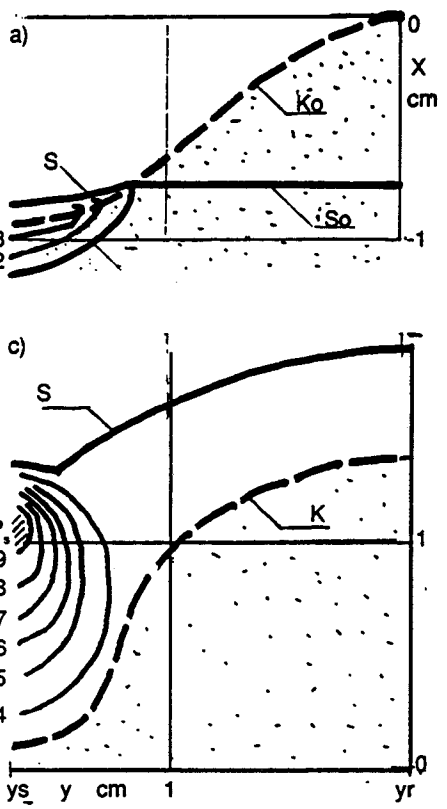

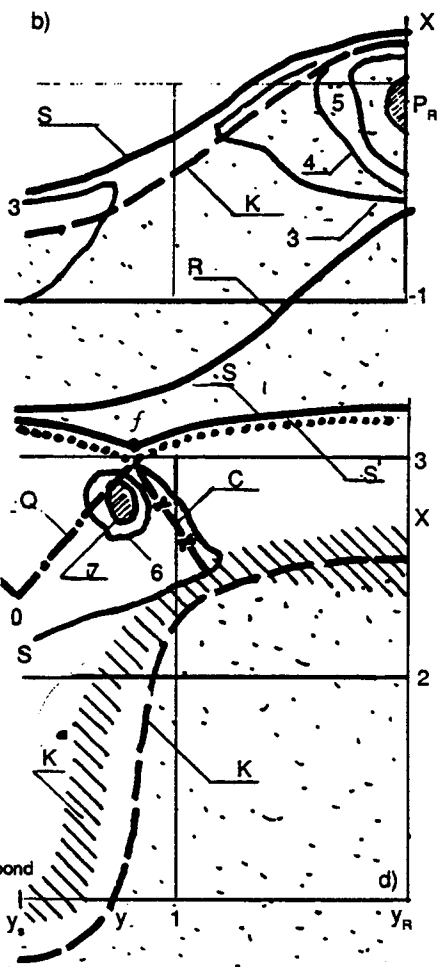

Fig. 4. The calculation map pressure. S_o passes from He to Xe λ = 5.6 cm, M_o = 2.5, p_o = 0.5 atm. a, b, c, d correspond to t = 1,7,30 and 50 µs. Lines 2, 3, 4, 5, 6, 7, 8, 9 correspond to pressures 6, 8, 10, 12, 14, 16, 18 and 19 atm.
S - K: calculated refracted shock wave and interface,
C secondary shock waves and Q slip line. S* experimental refracted shock wave and K* experimental interface.

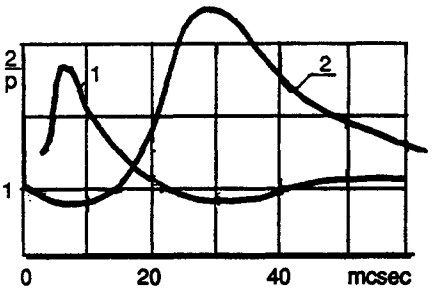

Fig. 5. The maximum pressure behind R (along y_R) - line 1; behind S (along y_S) - line 2; behind R (along y_R)
Location of y_S and y_R is shown in fig. 4.

Fig. 5 gives maximum pressure values behind S and R in cross-sections y_S and y_R : $P_S = P_S(t,y_S)/P^*$ and $P_R = P_R(t,y_R)/P^*$ (Position of y_S and y_R is shown in fig. 4). P^* is pressure obtained by solving one-dimensional conservation equations for interaction of a shock wave with a discontinuous interface. On reaching their maximum value the above localized high-pressure areas start "running". In doing so, secondary shock waves spread along the layer of shock-compressed gas between R and K and S and K (ref. fig. 4c and d). The applied method of calculation "smears" the fronts of these waves. Their interaction with fronts of R and S creates triple point at their front which is rather distinctly registered on isobars (point f, fig. 4c and d).
Fig. 4d gives a comparison of the calculated arrangement of the transmitted shock wave front, compression wave and interface with the results of schlieren pictures processing. As it is seen, the calculation results are in satisfactory agreement with the experimental data. This matching is observed until generation of vortex structures starts in the vicinity of the spike (transitional stage).

RAYLEIGH-TAYLOR INSTABILITY

1. The experimental facilities include a vertical channel with a 7.2 x 7.2 cm² cross-section (fig. 6). The bottom part of the channel accommodates the test section with side walls made of optical glass. A sliding metallic plate 2 is located in the field of view, dividing the channel into two parts. Prior to the experiment both parts of the channel are evacuated and are filled with different gases at the same pressure. The top part is filled with an oxygen-hydrogen mixture (molecular weight: 18.5), the bottom part contains one of the inert gases. The sliding plate is 2 mm thick and is retracted by means of a spring mechanism. The total duration of the plate retraction varies from 40 to 150 ms. The sliding plate retraction leads to the formation of the interface K_0 between the combustible mixture and the inert gas. After retraction of the plate from the channel the combustible mixture is ignited in its upper part and a flame front F spreads downward. A compression wave C is generated in front of F, which imparts an accelerated downward motion to K_0 . The distance between the ignition point and the sliding plate was less than the distance required for formation of shock wave out of the compression wave. In doing so, K_0 was entrained into motion with a monotonously growing velocity: acceleration $g(t) = 10^7$ cm/s². The process was recorded with the help of Mach-Zehnder interferometer. The part of the channel - 5 cm < x < 5 cm is visualized with the exception of a section - 0.15 cm < x < 0.15 cm which accommodates a sealing gasket.
2. Properties of the interface generated after sliding plate retraction. The sliding plate retraction leads to the formation of an interface between "pure" gases in the top and bottom parts of the channel. By changing initial pressure, gas combinations and speed of plate retraction one can alter the properties of the generated interfaces. At Reynolds numbers Re = ud/ν < 40 (u,d are the retraction speed and plate thickness and ν is the kinematic vicosity), the fronts X separating the interface K_0 from "pure" gases are monotonous lines whereas the density distribution along the channel center line depends on molecular diffusion (fig. 7a). At 40 < Re < 100, the interface limiting fronts X feature curved disturbances (fig. 7b). For Re > 100 the interface disturbances have the character of vortex structures (fig. 7c).

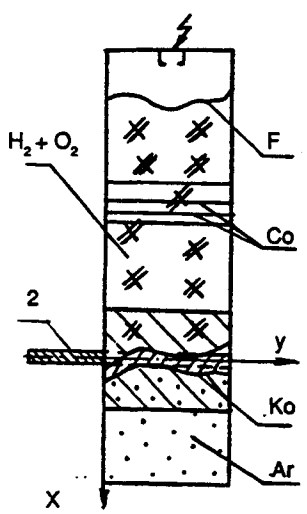

Fig. 6 . Experimental set-up.

3. Experimental results. Fig. 8 presents interferograms of the interface between $H_2 + O_2$ (at the top) and He (at the bottom) recorded 50 ms after completion of the sliding plate retraction. The mixture did not ignite. The observed shape distorsion of the interface is caused by RTI induced by the gravity field. The subsequent ignition of the mixture and entrainment of the interface into accelerated motion in the direction from the heavy gas (H_2 + O_2) to the light gas (He) results in instability stabilization (fig. 8b, c).

RTI was studied with the passage of the compression wave from ($H_2 + O_2$) into Ar or Xe. The sliding plate retraction created a curved front X of the interface. For the combination ($H_2 + O_2$)-(Ar), $\lambda = 1.5 \pm 0.2$ cm. For (H_2 + O_2)-(Xe), $\lambda = 0.9 \pm 0.2$ cm. The disturbance amplitude a_x on the front changes from one disturbance to the other within one experiment and from one experiment to the other, while the wavelength λ is constant for the

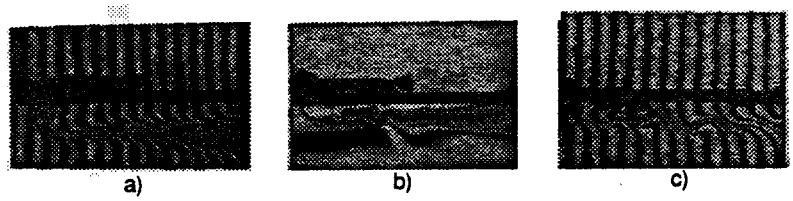

Fig. 7. Different types of continuous interfaces.

selected combination of gases. Depending on the ratio a_x/λ at the arrival of the compression wave, different evolutions of a_x were observed in the course of time.

On fig. 9 are 4 interferograms (taken out of a series of 8 recorded) showing the development of RTI for an interface section containing two disturbances. For the first disturbance, $a_x < \lambda$ (left on fig. 9). At the first four recorded photos this disturbance increases its amplitude with the shape being unchanged (see fig. 9b, x=4.5mm), whereas the fifth and subsequent photos bring forward some change of the front shape and the formation of a mushroom vortex structure on the $H_2 + O_2$ side of the mixture (see figs. 9c and 9d, x= 8 and 24.5mm). Amplitudes a_x of this first disturbance versus travel path x is given in fig. 10 with the 8 measured points. For the initial stage a_x increases exponentially with time. For the second disturbance, $a_x > 0.6\lambda$ already at the arrival of the compression wave, hence the first and most intensive stage of growth is not observed.

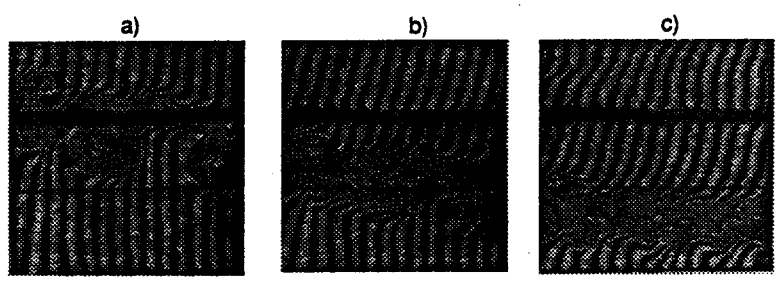

Fig. 8 The evolution of continuous interface with continuous change of density a) in 50 ms after sliding plate retraction from the channel, immediately before beginning of the movement caused by compression wave; b) in 170 μs after beginning of the movement; c) in 273 μs after beginning of the movement.

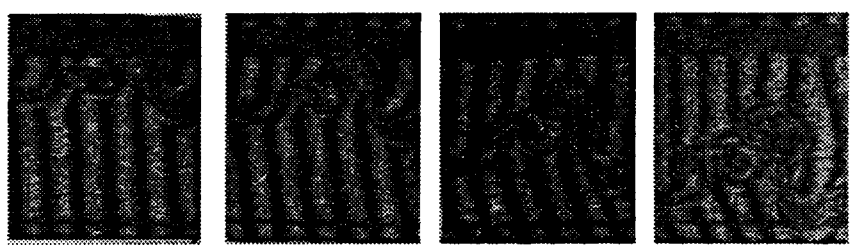

Fig. 9. the evolution of continuous interface, compression wave passes from H2 + O2 into Xe ta = 2.1, tb = 2.2, tc = 2.5 ms. t = 0 moment go out slinding plate from the channel, interface beginning the movement at 1.8 ms.

In this paper an attempt was made to define the influence of the interface thickness Δ on the growth rate of the disturbance amplitude a_x under condition $a_x(t) < 0.6\lambda$ (linear stage). Fig. 11 presents the experimental values of the inverse of the growth rate γ^{**} of $a_x(t)$ normalized by the growth rate for discontinuous interface γ_0 versus interface thickness Δ with the attenuation factor Ψ obtained in ref [5].

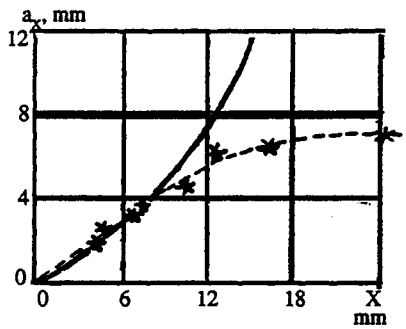

Fig.10. a_x versus t for the first disturbance.

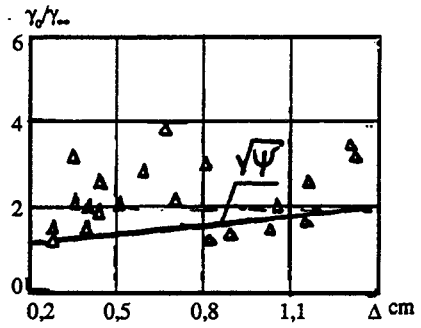

Fig. 11. γ versus continuous interface thickness Δ.

CONCLUSIONS

The diffraction of a shock wave S_0 incident on the initial discontinuous interface K_0 results in the formation of curvilinear transmitted S and reflected R shock waves ($\rho_1 < \rho_2$) or reflected rarefaction wave ($\rho_1 > \rho_2$). The curvature and intensity of the above waves determine the character of subsequent process development. Gas flows behind the refracted shock wave converge toward each other in the vicinity of center line y_R (ref. fig. 1), thus forming a high-pressure area P_R. At comparatively low values of the refracted front curvature arising at $a_0 k < 1$, the relative speed of these flows is small and the expansion ("running") of the generated high pressure area will take place without formation of secondary shock waves. This is the "soft" mode and its initial stage is satisfactorily described by the Richtmyer ratio. At high values of the curvature of S, the expansion of the high-pressure area P_R is accompanied by secondary shock waves formation. This is the "tough" mode. With the passage of the shock wave from the heavy gas into the light one ($\rho_1 > \rho_2$) the discontinuous interface shape at the moment of diffraction completion may have the phase similar or opposite to that of the initial discontinuous interface, or it may be flat. RMI development in this case will be qualitatively similar to the case of shock wave passage from the light gas into the heavy one, since the formation of high-pressure areas is determined by the curvature and amplitude of the refracted and reflected waves. Hence, for a description of the initial stage it is practicable to generalize the Richtmyer ratio by using in place of a^*_0 some function of the transmitted shock wave amplitude a^*_s at the moment of diffraction completion.

Different time evolution of the high-pressure areas in light and heavy gases, caused by differences of sound velocities, results in the asymmetric influence of these areas on the discontinuous interface. As a result, a characteristic form of K_0 is generated which contains "spikes" and "bubbles". The increase of the initial discontinuous interface curvature intensifies the process of RMI development. This is expressed by a decrease of the transition time between stages. In doing so, the rate of penetration of one medium into the other monotonously goes down reaching its minimum value at the final turbulent stage. The comparison of the rates of penetration of one medium into the other found in the experiments with curved discontinuous interfaces K_0 with the data obtained in the experiments where flat films were used (fig. 2) shows some agreement. In the case of flat films the mechanism of generation of interface turbulent stage is evidently different from the one which is involved in the evolution of curved discontinuous interfaces. The above agreement confirms the independence of the process development (at the turbulent stage) from the initial conditions.

The replacement of the discontinuous interface with a layer of finite thickness and a continuously changing density results in the reduction of the RTI growth rate. A numerical solution of equation was obtained in [5] which described RTI in a layer with continuous density change. It was shown that, at the initial stage, the disturbance amplitude grows exponentially with a rate $\gamma = (Agk/\psi)^{0.5}$, where $\psi = \psi(A, \Delta/\lambda)$. Fig. 11 gives the values of γ calculated by extrapolation of ψ for our experimental conditions. The results of this paper reveal that the replacement of the discontinuous density change at the interface of different-density media with a continuous one nearly halves the RTI growth rate. The solutions found in [5] agree qualitatively with the results of this experiment but the experimental values of the growth rate proved to be approximately 30 % lower as compared to the calculated ones.

REFERENCES

1. E.E. Meshkov, collection. The Investigation of Hydrodynamic Instability, Preprint Inst. Appl. Math., the USSR Academy of Sciences (1980).
2. R.D. Richtmyer, Comm. Pure and Appl. Math. 13. 1960 n°2 p. 297 (1960).
3. O.M. Belotserkovsky, V.V. Demchenko, V.I. Kosarev, A.S. Holodov. USSR. Comp. Math. and Math. Phys. v.18, pp.117-137 (Pergamon, 1978), translated from Russian: Zh. vychisl. Mat. mat. Fiz., 18, 2, pp. 420-444, 1978.
4. S.G. Zaytsev, E.V Lazareva, V.V. Chernukha, V.M. Belyaev, Sov. Phys. Dokl. 30 (7) p. 579 (July 1985).
5. R.E. Duff, F.H. Harlow, C.W. Hirt, Phys. Fluids v.5, n°4, p. 417 (1962).

Numerical Simulation of Accelerated Interfaces*

Daniel L. Marcus[§]

Elbridge Gerry Puckett[†]

John B. Bell[§]

Jeffrey Saltzman[‡]

ABSTRACT

We describe two numerical methods that have been designed to model the dynamics of accelerated interfaces. One method is based on the numerical approximation of the incompressible, variable-density Navier-Stokes equations while the other is based on a numerical approximation of the compressible Euler equations. One feature that these methods share is that the numerical approximation to the governing fluid flow equations is accomplished in part by means of a second order extension of Godunov's method. We present the results of computations to model Rayleigh-Taylor instability and Richtmyer-Meshkov instability.

INTRODUCTION

Fluid interfaces that are accelerated by impulsive loading (Richtmyer-Meshkov instability), body forces (Rayleigh-Taylor instability), or an underlying velocity field occur in a wide variety of physics and engineering contexts. Common to all these flows is the baroclinic generation of vorticity along the interface that occurs when density and pressure gradients are non-parallel. Thus, if the dynamics are to be understood, it is essential that the interface be well-resolved. The numerical simulation of such flows poses several challenges. Some of the criteria that the methodology chosen for such a task should satisfy are (LeVeque [14]):

- at least second-order accuracy (without spurious oscillations) in smooth regions

- sharp resolution of discontinuities without smearing

- consistency with the weak form of the conservation laws, along with a discrete form of the entropy condition so that the solution converges to the physically correct one.

It is beyond the scope of this article to present a complete account of numerical methods for the simulation of interfacial flows. (See, for example, Hyman [13], for a survey of such methods.) Rather, we will confine our attention two such approaches, and the description of calculations performed with each. "Front tracking" is a generic description of those methods that, along with the solution of the field equations, explicitly follow a distinguished interface

* The work of the first three authors was performed under the auspices of the U.S. Department of Energy at the Lawrence Livermore National Laboratory under contract number W-7405-ENG-48 and partially supported by the Applied Mathematical Sciences Program of the Office of Energy Research under contract number W-7405-Eng-48 and by the Defense Nuclear Agency under contract number IARCO 90-824.

§ Applied Mathematics Group, Lawrence Livermore National Laboratory, Livermore, CA 94551

† Dept. of Mathematics and Institute of Theoretical Dynamics, U. C. Davis, Davis, CA 95616.

‡ Los Alamos National Laboratory, Los Alamos, NM

(effectively supplementing the solution of the discrete equations with numerical approximations of jump conditions). The difficulty with such an approach is that, particularly in two and three dimensions, the geometry of the interface can become extremely complicated. The goal of "front capturing" methods is to solve the field equations with sufficient accuracy so that discontinuities are resolved "automatically." One major drawback of this approach is that it limits us to single-fluid approximations of multi-fluid systems. In what follows we will describe the application of two methods - one of each of type - to the problem of computing the dynamics of an accelerated interface.

First, we will describe a numerical method for the solution of the variable-density, incompressible Navier-Stokes equations [2], and present calculations of the Rayleigh-Taylor instability, and the collision of a vortex ring with a weak density interface. The methodology uses a second-order upwind differencing procedure for the nonlinear advective terms, first introduced for gas dynamics calculations [7], that captures the interface in the course of solving the mass conservation equations. Next, a multi-fluid algorithm for the compressible Euler equations will be described that uses adaptive mesh refinement [3] together with a volume-of-fluid front-tracking procedure [19] based on a least-squares procedure for reconstructing a piecewise-linear approximation to the interface. Examples of Richtmyer-Meshkov calculations will be presented.

PROJECTION METHODS FOR INCOMPRESSIBLE, STRATIFIED FLOW

The incompressible, variable-density Navier-Stokes equations are:

$$U_t + (U \cdot \nabla)U = -\rho^{-1}\nabla p + \epsilon \Delta U + G(\rho) \tag{1}$$

$$\nabla \cdot U = 0 \tag{2}$$

$$\rho_t + (U \cdot \nabla)\rho = 0 \tag{3}$$

where ϵ is the viscosity and $G(\rho)$ is a gravitational forcing term.

We solve this system of equations by means of a second-order projection method. The method is an extension of Chorin's [4-5] projection algorithm in which advection-diffusion equations are first advanced without enforcing the incompressibility condition, and the resulting intermediate velocity field is projected onto the space of discretely divergence-free vectors. The algorithm is extended to second-order by lagging the pressure from the previous time step and using second-order Godunov methods for the nonlinear advective terms [1]. The generalization to density-stratified flows is made by allowing the density variation to occur in the vector decomposition in a "natural" way; the projection is expressed in a density-weighted inner product space [2].

Two computational examples are presented. The first is a two-dimensional simulation of a Rayleigh-Taylor instability. The conditions are those of test problem 1 in the suite of problems suggested for the Numerical Round Table at the Royaumont. Figure 1 shows vorticity (left) and density contours (right) at 1 ms intervals beginning with t = 1 ms. The growth of the initial perturbation enhances the baroclinic generation of vorticity, which in turn accelerates the deformation of the interface, resulting in the growth of a well-mixed central region. The familiar fingering phenomena and mushroom structures are present. It should be noted that neither the density jump at the interface nor the spatial density variation in the far field pose a problem for the method.

In Figures 2 through 6, we present the diagnostics suggested for the Numerical Round Table. Figures 2 and 3 show, respectively, the growth of the mixed region and the fluctuating kinetic energy averaged over the entire mixed region vs. time. Figures 4, 5, and 6 show the x-averaged

kinetic energy fluctuations, volume fraction, and density as functions of y for $t = 1$, 2, and 3 ms. Of interest are the "blips" in the density and volume fraction, corresponding to spatial inhomogeneities (e.g. mushroom caps) in the mixed region. Both the contour plots and the diagnostics show excellent agreement with the calculations of J. Glimm and D. Youngs which appear in this volume.

The second computational example is a three-dimensional simulation of the interaction of a vortex ring with a weak density interface (Figure 7). This can be seen in the interaction of vorticity with a flame front, the collision of a buoyant thermal with a temperature inversion, or the interaction of a chip or submarine wake with a thermocline of the free surface of the ocean, and has been discussed by Linden [15], Dahm et al. [11], and Bell and Marcus [16]. In this calculation, the Reynolds number is 5000, the Atwood number is 0.05, and the Froude number is 0.5. The ring is canted at an angle of 20 degrees from the vertical and propelled upward from beneath the interface. The ridge of fluid that develops is due to the formation of a secondary, cross-axial pair of vortices that wrap themselves around the primary ring, squeezing a sheet of heavy fluid between them and injecting it into the light fluid above. This is the primary mechanism responsible for the "striations" observed in vortex-surface interactions [20].

A NUMERICAL METHOD FOR COMPRESSIBLE, MULTI-FLUID FLOW

We model the Euler equations for two dimensional, compressible fluid flow

$$U_t + \nabla \cdot \mathbf{F}(U) = 0 \tag{4}$$

where

$$U = (\rho, \rho u, \rho v, \rho E)^T ,$$

ρ is the density, (u, v) is the velocity, E the total energy per unit mass, and $\mathbf{F} = (F, G)^T$ with

$$F = (\rho u, \rho u^2 + p, \rho uv, \rho uE + up)^T ,$$

$$G = (\rho v, \rho uv, \rho v^2 + p, \rho vE + vp)^T .$$

We assume a gamma-law equation of state. We solve these equations on a rectangular mesh with grid spacing Δx and Δy imposing Dirichlet boundary conditions on the right hand wall of the computational domain and reflecting boundary conditions on the other three walls.

Our numerical method incorporates four features which are important to the accurate computation of the shock refraction problem. First, we approximate equations (4) with a second order Godunov method of the type described in Colella [6] and Colella & Glaz [8]. Second, we employ a local, adaptive gridding strategy as described in Berger and Colella [3]. Third, we use a volume-of-fluid approach (e.g. see Noh and Woodward [17]) to track the fluid interface. At each time step we reconstruct a piecewise linear representation of the interface from the volume fraction information using an algorithm due to Puckett [19]. Similar ideas have been used by Puckett and Saltzman [18] and Youngs [21-22]. Finally, our numerical method incorporates an algorithm for accurately modeling the disparate thermodynamic properties of the two gases on a subgrid scale due to Colella, Ferguson, and Glaz [9]. Since in the work presented here $\gamma \approx 1.67$ for both gases this poses no particular difficulty for mixed fluid cells. However, in general the numerical method has been designed so that we may use a different γ for each each gas - even on a subgrid scale.

We used the numerical method just described to model test problems 8-11. In all four computations the shock tube was 80 cm long and 8 cm high. The shock started at 50 cm from

the left end wall and traveled from right to left. The gas interface was initially positioned at 37 cm and the time was arranged so that the incident shock reaches the position 37 cm at time $t = 0$. In each computation we used an initial coarse grid of $\Delta x = \Delta y = 0.4$ cm. In addition, we employed one finer level of grid with $\Delta x = \Delta y = 0.1$ cm in important regions - notably about the fluid interface and the incident shock. This is a relatively coarse gridding scheme which took a very modest amount of computer time. The computations for test problems 8 & 9 took less than 43 minutes of CPU time each while those for test problems 10 & 11 took less than 80 CPU minutes each. All runs were made on a CRAY 2.

For the purposes of displaying our results we plotted contours of volume fractions at each of three times. We find that this is the best method for observing the dynamics of the interface before substantial mixing has occurred. (Once the gases are well mixed in some region - say once most cells in that region contain fractions of both gases - it is probably desirable to plot color graphics of volume fraction instead.) In Figure 8 we display the interface between argon and helium after it has been struck by a Mach 3.45 shock from the argon side. The interface shown in the left hand column had an initial perturbation which consisted of one cosine mode with wave length 8 cm and amplitude 0.24 cm while the interface shown in the right hand column had an initial perturbation which consisted of five cosine modes with varying wave lengths and amplitudes. In Figure 9 we display an interface between helium and argon after it has been struck by a Mach 2.77 shock from the helium side. As in Figure 8 the interface shown in the left hand column had an initial perturbation of one cosine mode with wave length 8 cm and amplitude 0.24 cm while the interface shown in the right hand column had an initial perturbation consisting of five cosine modes with varying wave lengths and amplitudes.

It is apparent from both Figures 8 & 9 that the dynamics of the interface depend substantially on the initial perturbation. It appears from Figure 8 that in the single mode computation the helium has been entrained by the argon more effectively than in the multi-mode computation. However it is difficult to draw any definite conclusions from these pictures with regards to the rate or efficiency of mixing.

In Figures 10 & 11 we display graphs of the fluctuating kinetic energy (FKE) (averaged over the mixing region) versus time for test problems 8 & 9 and 10 & 11. In both graphs there appear two sharp spikes. Each spike is caused by the passing of a shock through the mixing layer. The first spike occurs when the incident shock first strikes the interface while the second spike occurs when this shock has reflected off the left end wall and once again passes through the interface. For the times considered here there appears to be little difference in the FKE between the single and multi-mode problems. The only apparent difference is that in test problems 8 & 9 the multi-mode FKE is less than the single mode FKE *after the reshock*. We don't see this when we compare the results of test problems 10 & 11. We have no explanation for this phenomenon and are of the opinion that further study is required before any definite conclusions can be drawn.

CONCLUSION

We have presented two methods for the numerical simulation of flows with accelerated interfaces. Between them, the methods can accommodate a broad range of flow conditions, from high Mach number regimes with strong shocks to the $M \rightarrow 0$ limit. The compressible methodology uses a second-order Godunov scheme and a sophisticated front-tracking procedure embedded within an adaptive mesh refinement shell to achieve high resolution at a minimal cost. The incompressible methodology is considerably younger; while it uses Godunov methodology for the nonlinear advective terms, the variable density formulation has not yet been implemented in an adaptive context, or with true multi-fluid capability. Nevertheless, it represents an important step in the development of a high-resolution capability for incompressible flows. Future work in

this area includes high-resolution three-dimensional Richtmyer-Meshkov calculations and merger of the front-tracking procedure described above and the variable-density projection method into a true incompressible multi-fluid algorithm.

REFERENCES

[1] J. B. Bell, P. Colella, and H. M. Glaz, A Second-Order Projection Method for the Incompressible Navier-Stokes Equations, *J. Comput. Phys.* **85**, 257-283 (1989).
[2] J. B. Bell and D. L. Marcus, A Second-Order Projection Method for Variable-Density Flows, *submitted to J. Comput. Phys.*, LLNL Report no. **JC-104132**, (1990).
[3] M. J. Berger and P. Colella, Local Adaptive Mesh Refinement for Shock Hydrodynamics, *J. Comput. Phys.* **82**, 64-84 (1989).
[4] A. J. Chorin, Numerical Solution of the Navier-Stokes Equations, *Math. Comput.* **22**, 745-762 (1968).
[5] A. J. Chorin, On the Convergence of Discrete Approximations to the Navier-Stokes Equations, *Math. Comput.* **23**, 341-353 (1969).
[6] P. Colella, A Direct Eulerian MUSCL Scheme for Gas Dynamics, *SIAM J. Sci. Stat. Comput.* **6**, 104-117 (1985).
[7] P. Colella, Multidimensional Upwind Methods for Hyperbolic Conservation Laws, J. Comput. Phys. **87**, 171-200 (1990).
[8] P. Colella and H. M. Glaz, Efficient Solution Algorithms for the Riemann Problem for Real Gases, *J. Comput. Phys.* **59**, 264-289 (1985).
[9] P. Colella, R. Ferguson, and H. M. Glaz, A Single Step Eulerian Algorithm for Multi-material Compressible Flow Calculation, manuscript, (1991).
[10] P. Colella, L. F. Henderson, and E. G. Puckett, A Numerical Study of Shock Wave Refraction at a Gas Interface, *Proceedings of the AIAA 9th Computational Fluid Dynamics Conference*, Buffalo, New York, 426-439 (1989).
[11] W. J. A. Dahm, C. M. Scheil, G. Tryggvason, Dynamics of Vortex Interaction with a Density Interface, *J. Fluid Mech.* **205**, 1-43 (1989).
[12] L. F. Henderson, P. Colella, and E. G. Puckett, On the Refraction of Shock Waves at a Slow-Fast Gas Interface, *J. Fluid Mech.* **224**, 1-27 (1991).
[13] J. M. Hyman, Numerical Methods for Tracking Interfaces, *Physica* **12D**, 396-407 (1984).
[14] R. J. LeVeque, Numerical Methods for Conservation Laws, Birkhauser, Basel, (1990).
[15] P. F. Linden, The Interaction of a Vortex Ring with a Sharp Density Interface: A Model for Turbulent Entrainment, *J. Fluid Mech.* **60**, 467-480 (1973).
[16] D. L. Marcus and J. B. Bell, Numerical Simulation of a Viscous Vortex Ring Interaction with a Density Interface, AIAA 22nd Fluid Dynamics, Plasma Dynamics, and Lasers Conference, June 24-26, 1991, Honolulu, HI
[17] W. F. Noh and P. R. Woodward, SLIC (Simple Line Interface Method), in *Lecture Notes in Physics* **59**, A. I. van de Vooren and P. J. Zandbergen (ed.), Springer Verlag, Berlin (1976).
[18] E. G. Puckett, and J. S. Saltzman, A 3-D Adaptive Mesh Refinement Algorithm for Multimaterial Gas Dynamics Mixing, *Proceedings of the Conference on Experimental Mathematics: Computational Issues in Non-Linear Science*, Center for Non-Linear Studies, Los Alamos National Laboratory, May 20-24, 1991.
[19] E. G. Puckett, A Volume-of-Fluid Interface Tracking Algorithm with Applications to Computing Shock Wave Refraction, in *Proceedings of the 4th International Symposium on Computational Fluid Dynamics*, U. C. Davis, September 9-12, 1991.
[20] T. Sarpkaya, J. Elnitsky II, and R. E. Leeker Jr., The Wake of a Vortex Pair on a Free Surface, *Proceedings of the 17th Symposium on Naval Hydrodynamics*, The Hague, The Netherlands, August 29 - September 2, 1988.
[21] D. L. Youngs, Numerical Simulation of Turbulent Mixing by Rayleigh-Taylor Instability, *Physica* **12D**, 32-44 (1984).

[22] D. L. Youngs, Time-Dependent Multi-Material Flow with Large Fluid Distortion, in "Numerical Methods for Fluid Dynamics", K. W. Morton and M. J. Baines (eds.), Academic Press, London, 273-285 (1982).

List of Figures

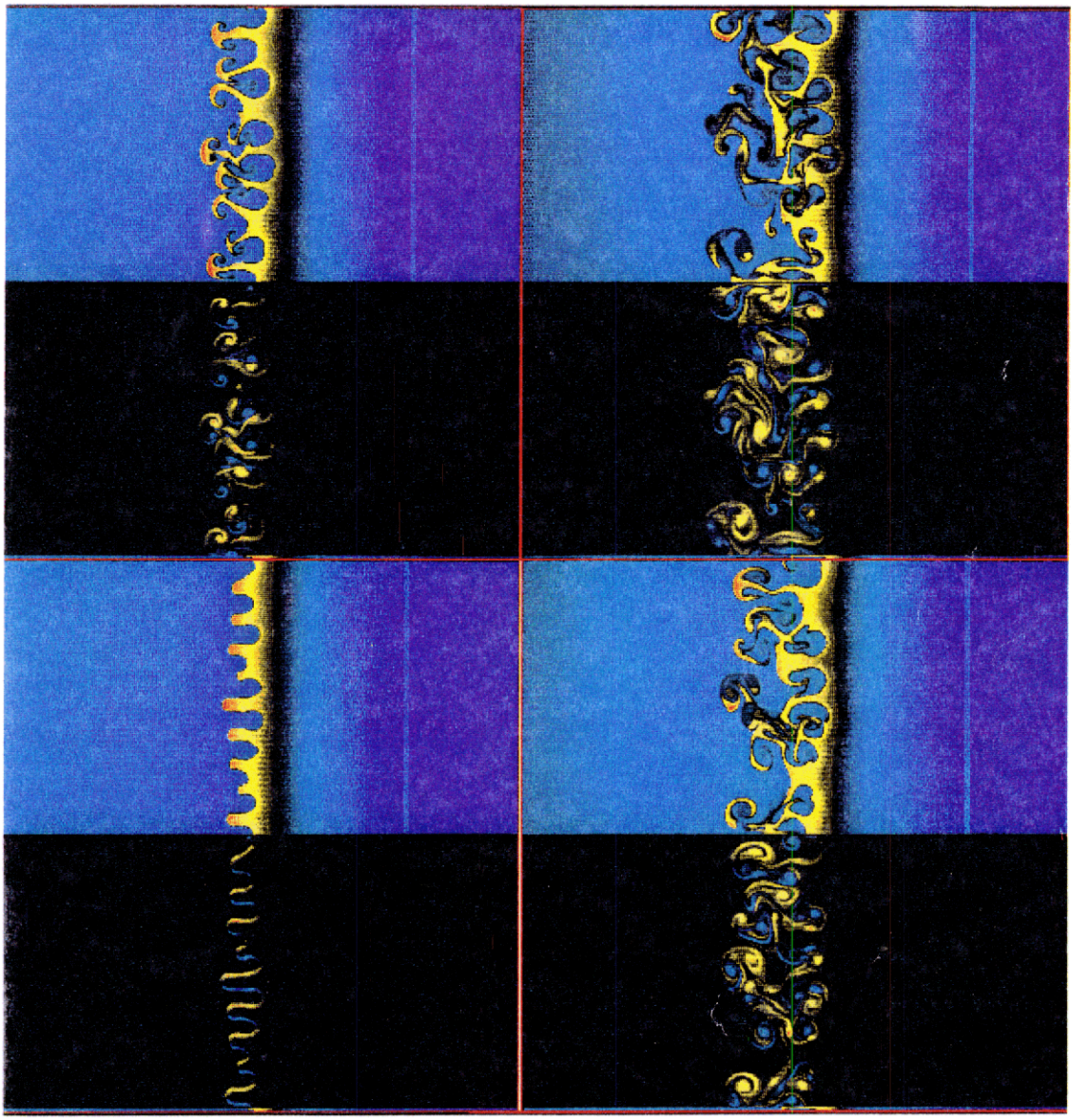

Figure 1

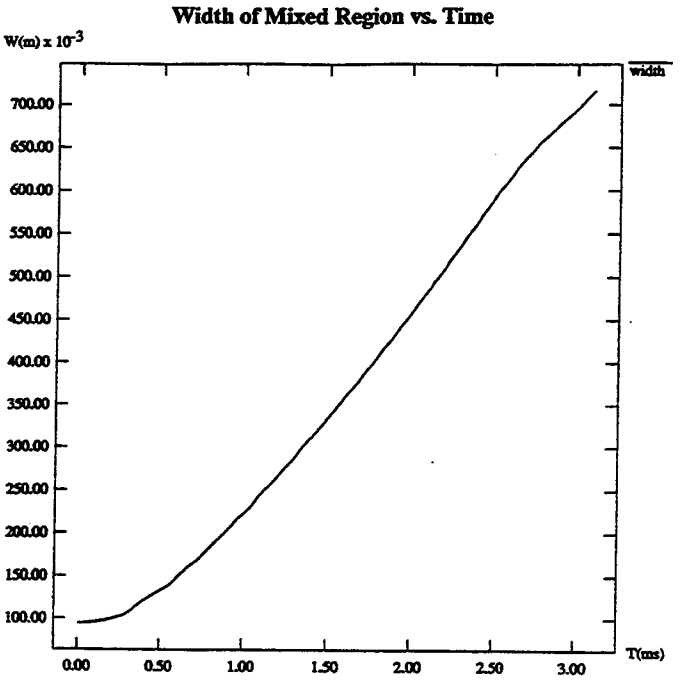

Figure 2

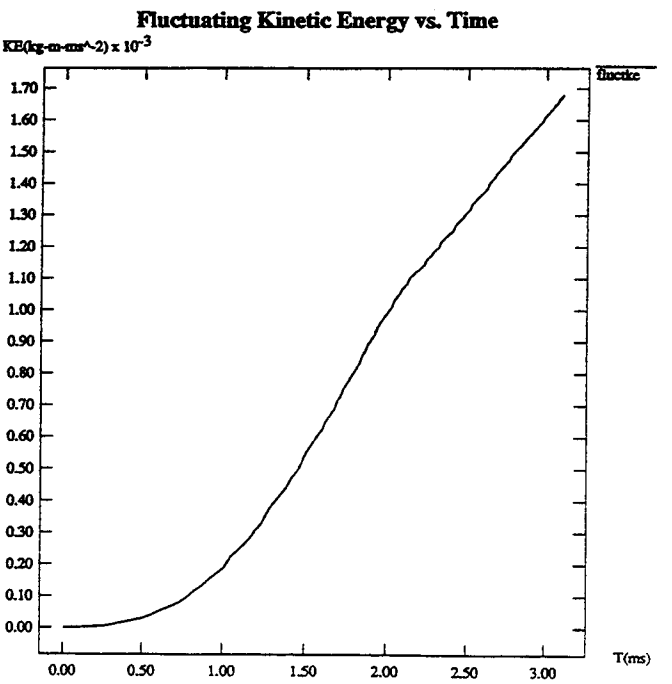

Figure 3

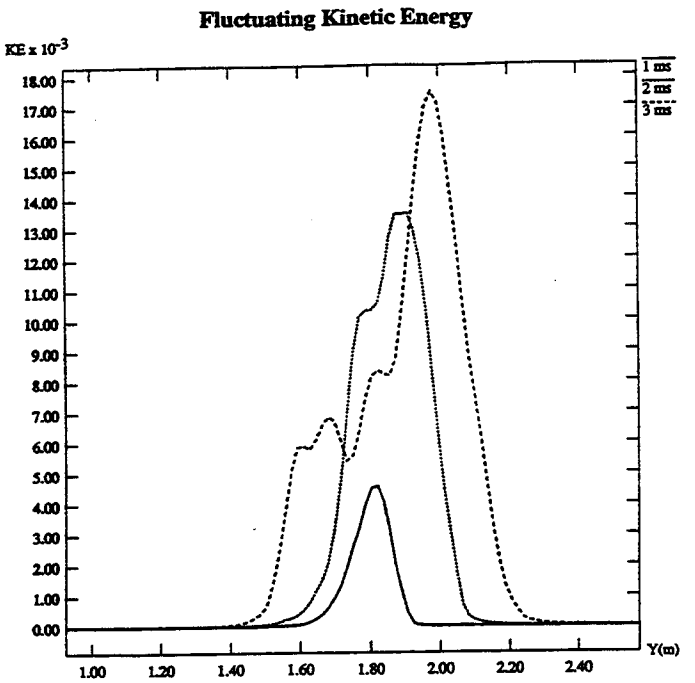

Figure 4

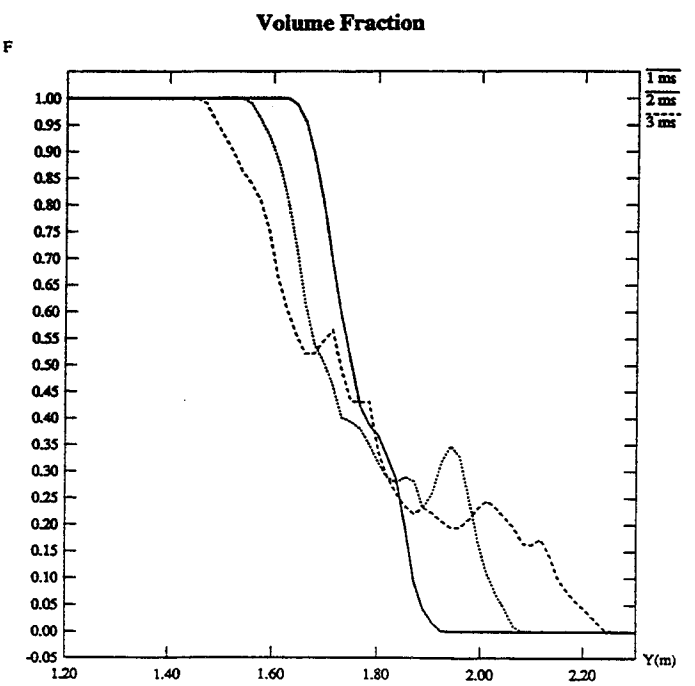

Figure 5

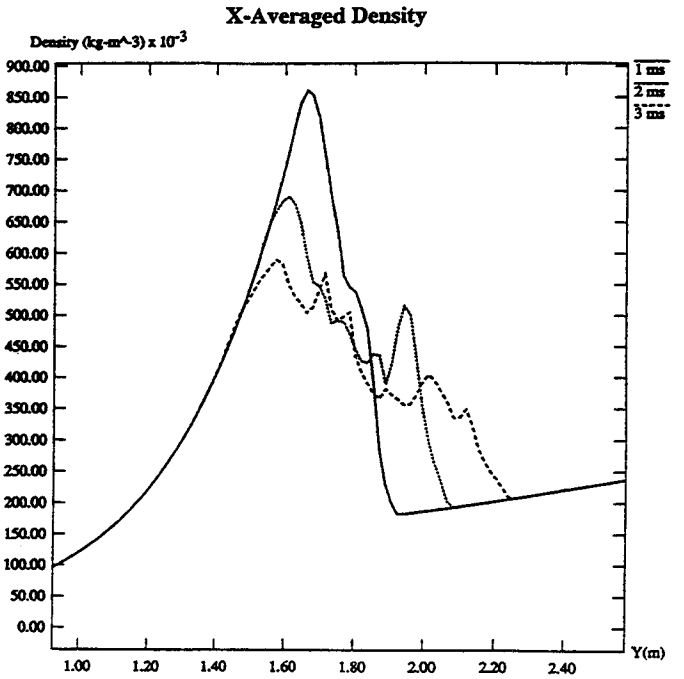
X-Averaged Density
Density (kg-m^-3) x 10^-3
900.00
850.00
800.00
750.00
700.00
650.00
600.00
550.00
500.00
450.00
400.00
350.00
300.00
250.00
200.00
150.00
100.00
50.00
0.00
1.00
1.20
1.40
1.60
1.80
2.00
2.20
2.40
Y(m)
1 ms
2 ms
3 ms

Figure 6

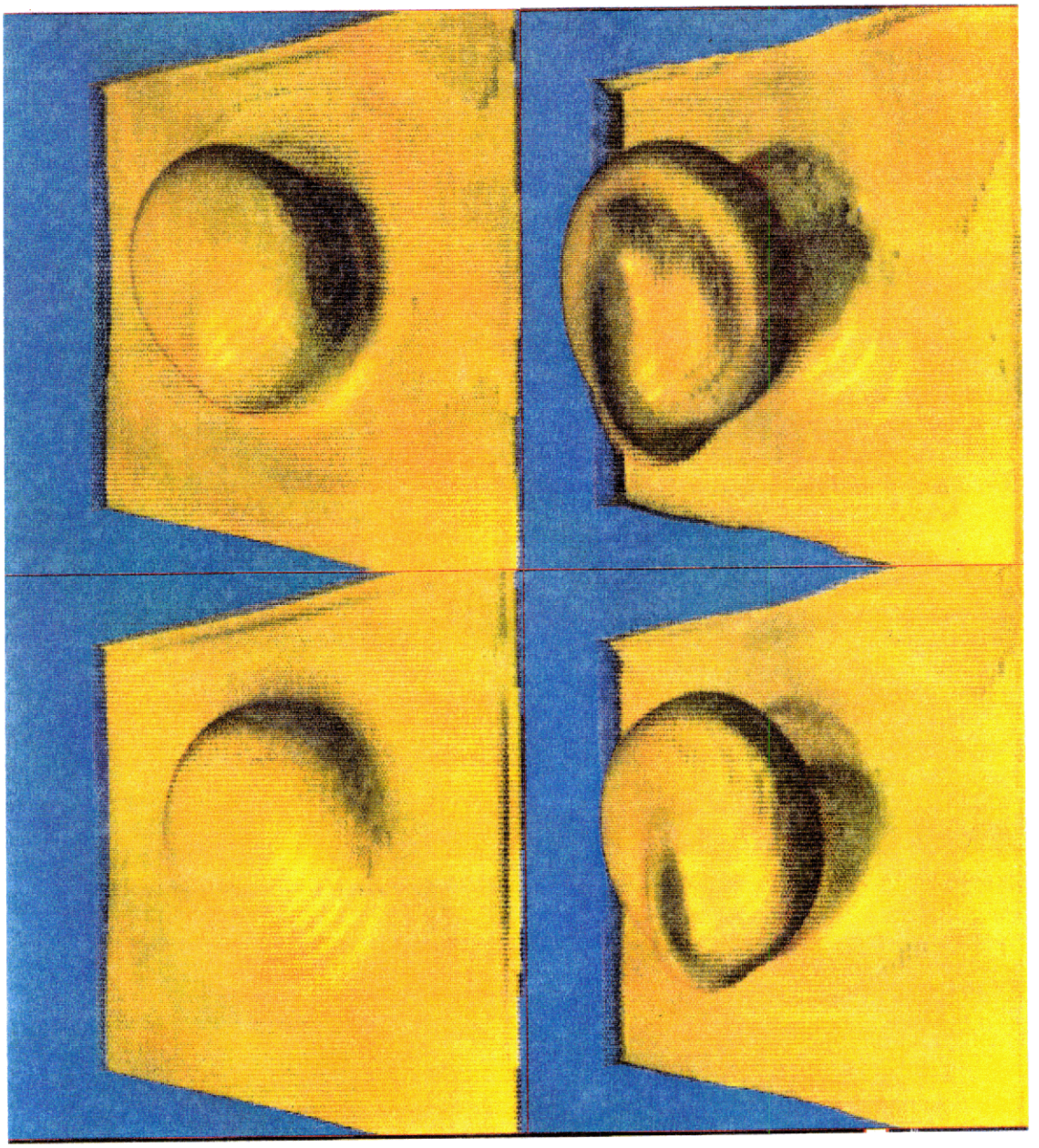

Figure 7

Test Problems 8 and 9

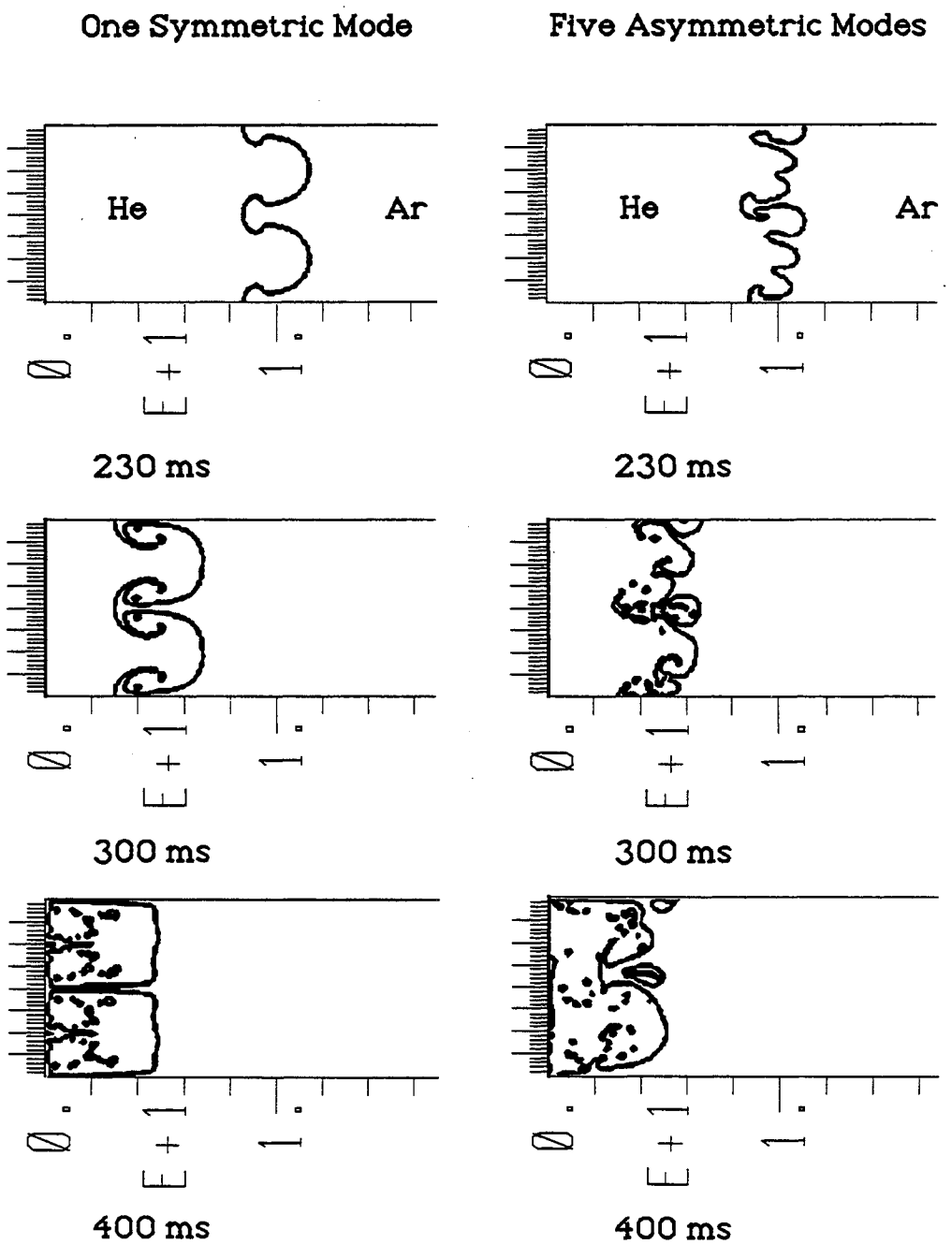

Figure 8

Test Problems 10 and 11

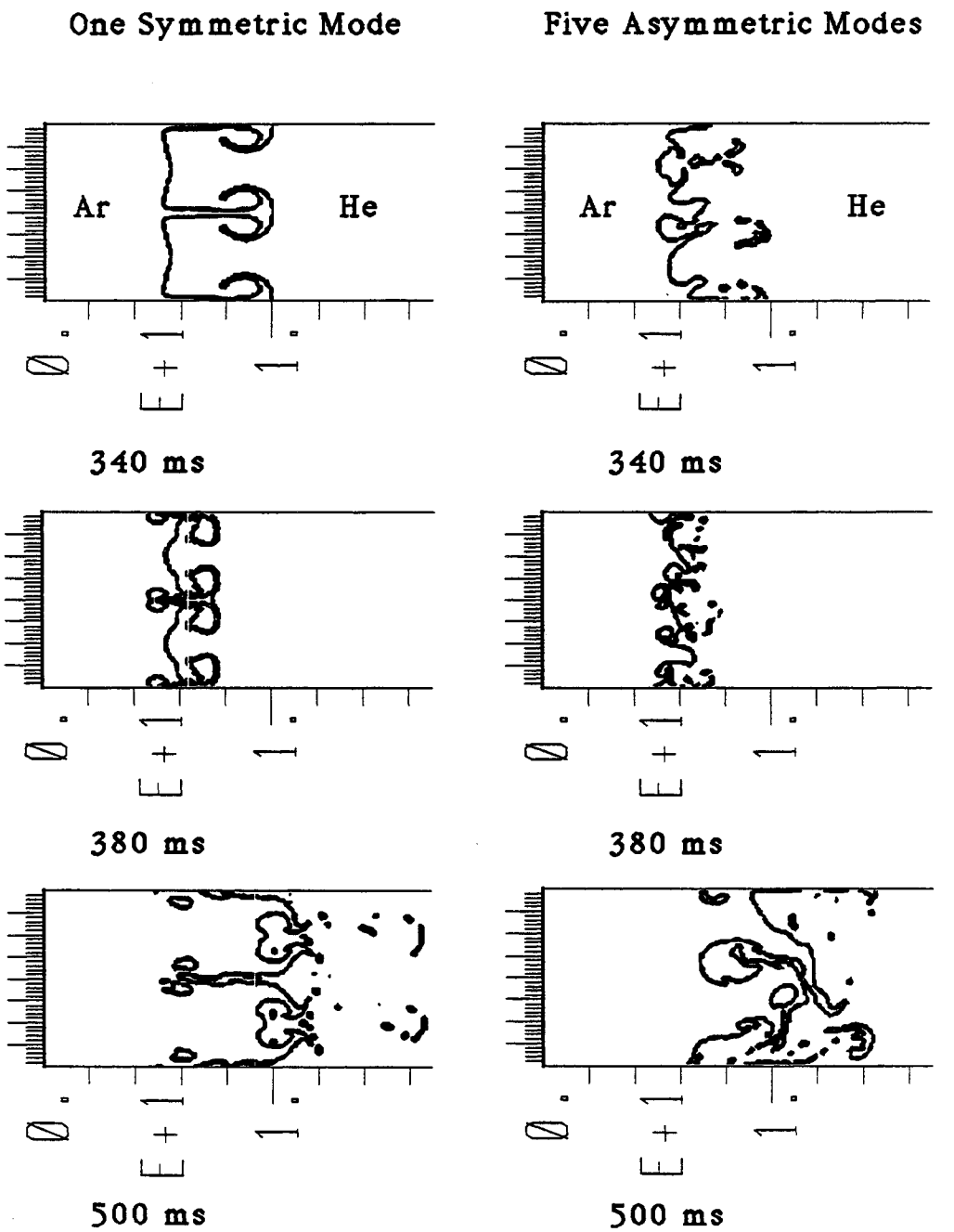

Figure 9

Fluctuating Kinetic Energy

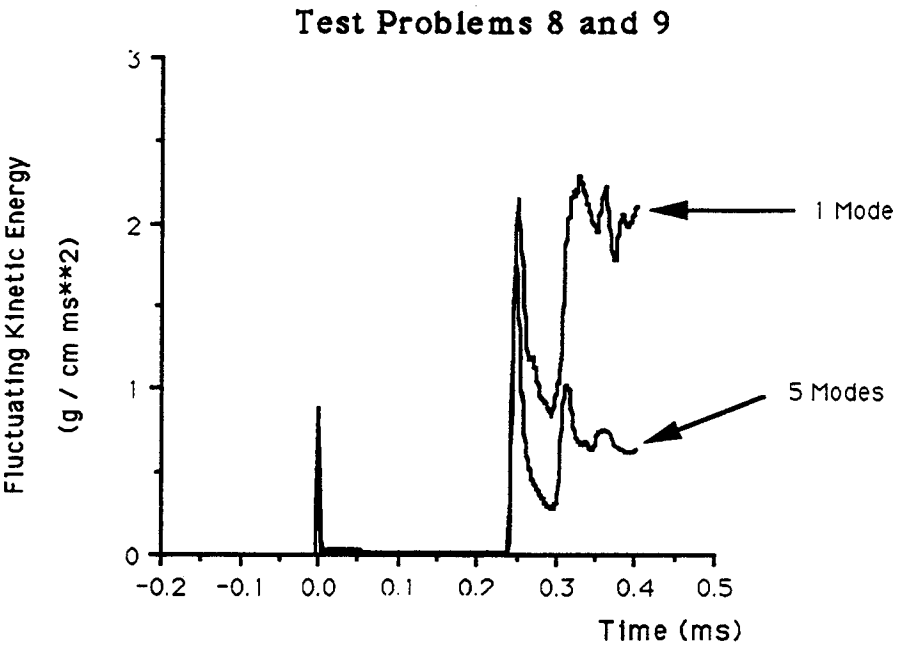

Figure 10

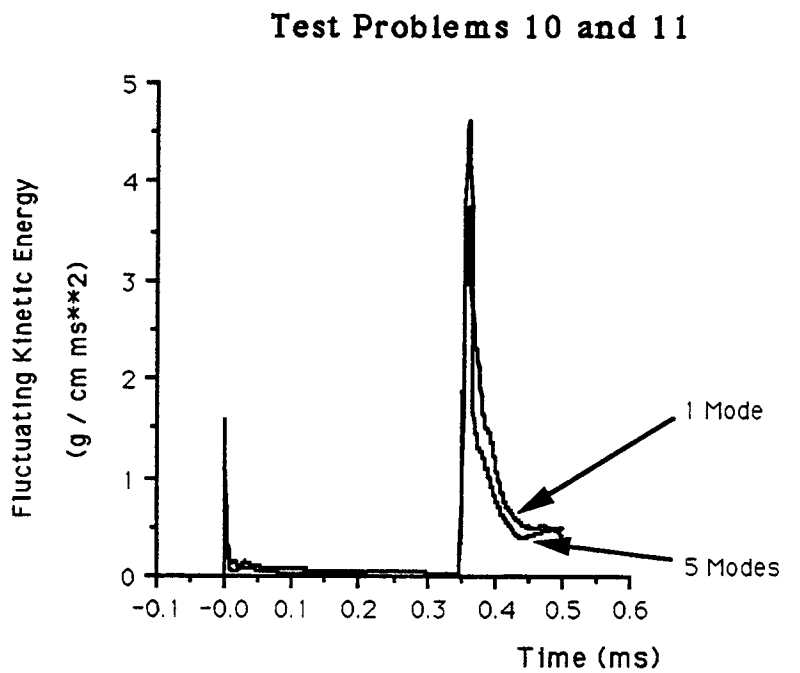

Figure 11

NUMERICAL SIMULATION OF 2D SHOCK-TUBE MULTIMATERIAL FLOW
A REVIEW OF THE NUMERICAL ROUNDTABLE, "RT AND RM MIXING" WORKSHOP, PLEASANTON, 1989.

D. Besnard *, J. Glimm **, J.F. Haas*,
R. M. Rauenzahn,*** V. Rupert****, D. Youngs*****

*Centre d'Etudes de Limeil-Valenton, 941915 Villeneuve-St-Georges CEDEX, France
**Dept. of Appl. Math., State University of New York at Stony Brook, New York 11794-3600, USA
***Los Alamos National laboratory, Group T-3, MS-B216, Los Alamos, NM 87545, USA
****Lawrence Livermore National Laboratory, P.O. Box 808, Livermore, Ca 94550, USA
*****Atomic Weapons Establishment, Aldermaston Reading RG7 4PR, England

Abstract: We present here a short review of some of the results presented during numerical roundtable held during the "RT and RM mixing" workshop, Pleasanton, November 1989.

1-INTRODUCTION

Understanding instability induced turbulent mixtures is at the heart of the series of workshops, of which this one is the third. To support theoretical and experimental efforts, codes must have a predictive capability. Apart from determining what kind of physics must be used for a given application, a basic question is up to what point can we trust our numerical results, even under such simple circumstances as the interpenetration of two inviscid immiscible fluids, especially for the late time stage of well developed instabilities. This implies that codes must be calibrated against realistic flow configurations. As a first step, a collaborative testing of 2D codes having a multimaterial capability (without turbulence model) was thus proposed.

In the second workshop on Rayleigh-Taylor and Richtmyer-Meshkov instability induced mixing, test cases for 2D simulations were proposed, coming from current experiments, and provided stimulating discussions with experimentalists.

One of the goal of this workshop was to compare several hydrodynamic codes on realistic 2D multimaterial flow test cases. This idea was to go beyond well-known 1D test cases, very useful for testing numerical schemes, but of little interest for multifluid cases. Because experimental results of mixing in shock tubes are available, it makes such flows good candidates for numerical simulations.

Test cases were based on experiments of contact surface instabilities in shock-tubes. A planar shock wave accelerates a contact surface and later brings it to rest because of its reflection(s) on the shock-tube end wall. Two types of experimental results are available:

-the membrane is shaped as a single sinusoidal wave; the corresponding test problems are TP1 (air/helium, Mach 1.24) and TP3 (air/SF6, Mach 1.32). They are roughly based on experiments by Benjamin /1/ and Brouillette and Sturtevant /3,4/;

-the membrane is nominally flat. Because of the acceleration, the nominally flat interface (usually a membrane thinner than 1μm) breaks in an uncontrollable fashion, thus imposing on the gaseous interface some random scales which are then amplified due to the shock-induced Richtmyer-Meshkov instability /2,3/. It was not attempted to simulate

the details of the rupture of the membrane; what was rather treated was the shock-induced deformation of a contact surface defined by five modes, in order to test mode coupling. The corresponding test problems are TP2 and 4, respectively identical to 1 and 3.

These finely meshed experimental simulations were performed in order to obtain quantities such as the fluctuations kinetic energy (FKE) of the mixing process, which are difficult to get from laboratory experiments. One-dimensional profiles of pressure, density, concentration, and components of velocity fluctuations stress tensor are obtained through a strip averaging in the direction transverse to the mean flow. More precisely, we concentrate on the local velocity fluctuations kinetic energy defined as

$$\overline{\rho}\ k = \left(\overline{\rho u_k u_k} - \overline{\rho}\ \hat{u}_k \hat{u}_k \right) , \qquad (1)$$

where

$$\overline{\rho}\ \hat{u}_k = \overline{\rho u_k} \quad .$$

We then integrate $\frac{1}{2}\ \overline{\rho}\ k$ along the mean flow direction, over the extent of the mixing zone, to obtain the kinetic energy (per unit area) of the fluctuating velocity field. Its time evolution, as well as of the mixing zone thickness (MZT) are obtained and the latter can be compared with experimental results (most experiments report only the mixing zone thickness; more recently, concentration and density profiles were obtained /2,3/. However, no experimental result was obtained regarding the mixing zone energetics.

2-TEST PROBLEMS

The test cases describe the interaction of a Mach 1.24 (resp. 1.32) shock with a single mode air/helium (resp. air/SF6) interface. In the air/SF6 case, the physical quantities are based on recent Caltech shock-tube experiments /4/ with 10 cm of SF6 between the interface and the end plate and a channel height of 11.3 cm; in the air/helium case, they are based on LANL experiments, with 8.5 cm of helium and a channel heigth of 7.5 cm. The details of the simulations are given below.

-Test Problem 1

x=0, mean position of the interface; W, square shock tube width

region 1: Helium at rest (8.5 cm), left of interface, density = 0.0001694 g/cm3, pressure = 1.013 10^6 baries, $\gamma = 1.67$;

region 2 : air at rest, density = 0.001225 g/cm3, pressure = 1.013 10^6 baries, $\gamma = 1.4$;

region 3 : shocked air, velocity = 12.29 cm/ms, Mach = 1.24, density = 0.0017285 g/cm3, pressure = 1.6482, $\gamma = 1.4$.

Initial interface: single wavelength perturbation $x = 0.24 \cos 2\pi\ 2y/W$, where W =7.5 cm.

For comparison use t=0 when the incident shock reaches x=0; Outputs close to 0.12, 0.22, 0.32 ms; Boundary conditions: at Xmax, applied pressure = 1.6482 bar, at Xmin, Ymin, Ymax rigid wall (zero normal velocity); Suggested initial mesh: square cells, size 0.25 mm in the mixing zone.

-Test Problem 2

same as for TP1, except for initial interface perturbation.

initial interface perturbation at x=0: multiple wavelength perturbation $x = \sum a_n \cos 2\pi\, ny/W$, (n,a_n) = (0.5,0.05), (1.5,0.10), (2.,0.07), (3.5,0.11), (5.5,0.09).

-Test Problem 3

region 1: SF6 at rest (10 cm), density = 0.006187 g/cm3, pressure = 1.013 10^6 baries, $\gamma = 1.06$;

region 2 : air at rest, density = 0.001225 g/cm3, pressure = 1.013 bar, $\gamma = 1.4$;

region 3 : shocked air, velocity = 15.95 cm/ms, Mach = 1.32, density = 0.001900 g/cm^3, pressure = 1.8993 10^6 baries, $\gamma = 1.4$.

Initial interface perturbation at x=0: single wavelength perturbation $x = 0.24 \cos 2\pi\, 2y/W$, W=11.3 cm.

For comparison use t=0 when the incident shock reaches x=0; Outputs close to 0.70, 1.10, 1.65 ms; Boundary conditions: at Xmax, applied pressure = 1.8993 bar, at Xmin, Ymin, Ymax rigid wall (zero normal velocity); Suggested initial mesh: square cells, size 0.25 mm in the mixing zone.

-Test Problem 4

same as for TP3, except for initial conditions.

initial interface perturbation at x=0: multiple wavelength perturbation $x = \sum a_n \cos 2\pi\, ny/W$, (n,a_n) = (0.5,0.05), (1.5,0.10), (2.,0.07), (3.5,0.11), (5.5,0.09).

The numerical diagnostics that were asked to participants were 2D maps, 1D profiles (through strip averaging in the direction orthogonal to the mean flow), and time history of fluctuations energy and mixing zone thickness. More precisely, the following figures were asked for:

-a plot of the y averaged density versus x, for each time (indicated in the initial problem definition);
-same for the volume fraction of He (or SF6);
-a plot of the mixed layer width versus time, where the layer is defined as the distance over which the y averaged volume fraction varies from 5% to 95%;
-the value of the fluctuating part of the kinetic energy defined as $\overline{\rho u^2} - \left(\overline{\rho u}\right)^2 / \overline{\rho}$, where the bar indicates an average over y, then integrated over x, and and ρ is the density, and u is the x directed velocity, calculated over the mixed region (defined above); this expression is equivalent to equation (1);
-a plot of the fluctuating energy, where the average is taken over y only, as a function of x, for each time;
-a 2D plot of density for each time;
-a 2D plot of vorticity for each time;
-a 2D plot of the divergence of velocity for each time;
-a 2D plot of pressure for each time.

One of the difficulties in the comparison between codes is that all these codes solve Euler equations and not Navier-Stokes equations. This means that, in the case of

numerical simulations of instability development, there is no physical upper bound for wavenumbers above which energy dissipates directly into heat; only cell size acts as such a bound. The more the mesh is refined, the more scales appear. One should not expect convergence with mesh size, apart from large structures in the flow. This implies that a precise comparison of patterns at cell size is not relevant (Note here that Kolmogorov scale, in air/helium test problems, is 0.008 cm for helium, and 0.01 for air). Even if mesh size is chosen to be of the order of Kolmogorov length scale, small scales are not dissipated through numerical schemes as they would be through physical viscosity. This shows the advantages of a Navier-Stokes solver over an Euler solver. However, the problem of multi-material flow in the context of Navier-Stokes equations is much more difficult to address.

3-CODES

Most of the codes used to simulate the experiments described in the previous Section are second-order in space, and have a multimaterial capability. Results reported at the numerical roundtable involved the following codes:

-AMR, which is based on the work by Collela /5/. It is 2D, eulerian, second order, and has a multifluid capability. The early version considered here uses SLIC for treating mixed cells, generalized to the case of oblique interfaces. It also allows for mesh refinement;

-EAD, developed at CEL-V /6/. It uses SLIC, and a FCT-like algorithm;

-PETRA, developed by D. Youngs at AWE /7/. It uses a Van Leer method for the projection phase, and the lagrangian phase can be divided in several sub-time steps. The mixed cell algorithm is close to SLIC;

-CAVEAT, developed by T-3 Group at LANL /8/. It is an ALE code, used here in its eulerian version. The mixed cell treatment is SLIC, and its scheme is based on an approximate Riemann solver;

-The code developed by J. Glimm et al /9/ at SUNY. It is based on a front-tracking algorithm and a Riemann solver. It is denoted here as FTM.

Other results are available in the Pleasanton proceedings. However, only those results of the actual participants to the roundtable are compiled here.

4-RESULTS

Table 1 shows the number of square cells used in TP3. Note that in the case of AMR, the number shown is the number of cells (on a heigth of 11.3 cm) at output time (the initial number is given in brackets); this code having a capability of mesh refinement, more cells are created along the simulation to account for small scale deformations.

TABLE 1: Mesh size, TP3-4

	AMR	EAD	PETRA	CAVEAT	FTM
number of cells	226 (160)	200	100	100	200
cell size, cm	0.0441 (.07065)	.0565	.113	.113	.0565

The most appropriate diagnostic, that can be compared with experimental results is the interpenetration zone thickness. It is defined as the limits (5% to 95%) of the helium volumetric fraction (in the case of EAD code, mass fraction is used). Here again, mesh size can change the results /11/, and more so if the Atwood number is close to 1. (its value here is .75). Figure 1 gives the Mixing Zone Thickness (MZT) as a function of time for test problems 1 (codes AMR, CAVEAT, EAD) and 2 (AMR, PETRA, CAVEAT, EAD), which confirms the generally good agreement obtained in these calculations. The differences are more important in the case of test problems 3 and 4 (Figure 2). Compared to a turnover time of the eddies created by shock-interface interaction, these simulations (air/SF6) are longer. Angular conservation momentum conservation is a difficult problem for eulerian codes, and shows differently depending of the codes (which include various levels of numerical dissipation). The impact is a spreading of the results. A more precise comparison is made here for TP4 (air/SF6, 5 modes simulation), at two times: first, when the initial shock has reflected onto the end wall, and second, well in the nonlinear regime of the interface development. Results are given in Table 2; note that FTM results are only preliminary, the code being still under development for shock-interface interaction.

TABLE 2: Mixing Zone Thickness (cm), air/SF6, 5 modes (TP4)

	AMR	EAD	PETRA	CAVEAT	FTM
First return shock (700 μs)	2.4	2.4	2.4	2.4	1.7
nonlinear regime (1500 μs)	5.3	4.8	5.	4.7	4.4

It is interesting to note both the excellent agreement of the measures at first return shock time and their spreading (about 15%) at late time. This is signature of the level of numerical dissipation of the codes (once mesh size effects have been taken into account). The shock that passes through the interface generates eddies that induce in turn interpenetration of the two fluids. Numerical dissipation impedes eddy rotation, and can be interpreted as drag of one material acting on the other one. The level of numerical dissipation determines the departure of MZT from its exact value. At 700 μs (which corresponds to a fraction of an eddy rotation time) dissipation did not have time to act; at 1500 μs, it definitely did.

This shows also on the energies. The only available data are those of CAVEAT and EAD; there is a good agreement for the fluctuations energies created by the initial shocking of the interface and the first return shock; however, a much lower value is attained at third shocking time by CAVEAT code. The above explanation holds here: CAVEAT mesh is coarser by a factor of 2, and therefore the small scales dissipate faster in CAVEAT simulation; these small scales do not exist at earlier time (the initial interface shape is composed of only five modes), and therefore results diverge only at late time (with respect to an eddy turn-over time). This is examplified in Figure 3.

Regarding Mixing Zone Thickness growth rate, experiments by R. Benjamin /1/ indicate a value of about 40 m/s. This measure is far below simultation results (see Table 3). During experimental roundtable, this point was discussed, but no strong conclusion was obtained. However, strong evidence of membrane effect were shown in other experiments /10/, indicating that differences observed between experiments and

simulations were due in part to the mechanics of the membrane rupture (which is of course not taken into account in the simulations).

TABLE 3:Mixing Zone Thickness initial growth rate (TP1; air/helium, single mode)

	Experiment	AMR	EAD	FTM
growth rate, m/s	37.8	76.	74.	62.

1D profiles were also compared, but only two codes could offer figures, namely EAD and AMR,. For reasons of availability, we compared the quantity $T_{kk} = \overline{\rho u^2} - \overline{\rho}\,\overline{u}^2$, which is sligthly different from the velocity fluctuations kinetic energy, as defined in Introduction. In particular, this quantity is not always positive definite, which shows in rare cases. This is examplified in Figure (6a), in test problem 1 (air/helium), rather different from Figure (6d), because the time difference between the numerical diagnostics involves the passage of the first return shock in the interface region. As shown in Figures 4 and 6, there is otherwise a good agreement between AMR and EAD regarding 1D turbulent kinetic energy profiles. This shows in the shape of the profiles, as well as in their extensions, and the peaks. Let us emphasize this trough an example: Table 4 gives, for test problem 4 (air/SF6, 5 modes), the extension of the Mixing Zone, and the peak of energy in the zone. However, some differences appear between CAVEAT and EAD, which are probably related to the differences in numerical dissipation discussed above.

TABLE 4: Mixing Zone extension and peak energy, air/SF6, 5 modes (TP4)

	1100 ms		1700 ms	
	extension	peak	extension	peak
AMR	-5,-9 cm	$3.10^5 erg/cm^2$	-9,-2.3 cm	$9.10^4 erg/cm^2$
EAD	-5,-9 cm	$2.9.10^5 erg/cm^2$	-9,-2.3 cm	$9.10^4 erg/cm^2$

5-CONCLUSION

This comparison between codes somewhat similar, on complex multimaterial flows, seemed extremely useful, even if incomplete, and not formalized enough. It was detailed enough to suggest a few interrogations:

-What is the degree of confidence we can have regarding our codes? This question is extremely important, not so much for code developers, than for users, applying them to engineering problems.

For a given code, this is of course intimately related to quality of the numerical scheme, and the mesh size. However, this comparison shows that, in this particular case (multifluid Euler equations), one obtains differences in MZT of about 10-15%; this number is in fact a function of the turnover time of the energy containing eddies existing in the flow. It seems therefore crucial to try, as much as possible, to estimate error bars in numerical experiments, as well as in physical experiments.

-Should additional physical processes added to Euler equations? One of the main question is to know if much effort should be put in dealing with Navier-Stokes equations instead of Euler equations. One answer is that numerical viscosity acts as a sort of physical

viscosity, though totally uncontrolled. It is not necessarily isotropic, and depends on mesh size; however, to introduce a Navier-Stokes solver is an additional complexity, especially regarding mixed cells treatment. Moreover, in flows driven by strong accelerations and shocks, it is not clear that it is a crucial piece of physics, at least regarding the simulation of energy containing eddies. This problems pertains to smaller scales, which emphasizes the above comments regarding mixed cells; one must even envision additional phenomena, such as surface tension, or diffusivity, that might have a more important impact on the results, such as those obtained experimentally by A. Roshko in shear layers (private communication), with slightly miscible fluids.
-Do we learn anything about initialization of turbulence models in non-stationnary circumstances with these simulations? A large fraction of the velocity fluctuations kinetic energy is transferred to turbulence if transition takes place, i.e. if the flow Reynolds number is large enough. For now, calculations described above give a very rough estimate of the amount of large scale energy that might feed turbulence; however, an approach might be to include in these code either a sub-grid scale model (or even a transport model, such as the model already implemented in CAVEAT, which deals with a larger part of the turbulence spectrum than the sub-grid scale model). A crucial point in this respect is the modeling of source terms for turbulence. In this respect, the models discussed during the Pleasanton workshop are an interesting step in this direction.

References

1-A preliminary account of the Los Alamos observations appeared as R.F. Benjamin, Proceedings of the "International Workshop on the Physics of Compressible Turbulent Mixing", Princeton 1988, Eds. W.P. Dannevik, A. Buckingham, C.E. Leith, Springer-Verlag, N.Y., to be published 1991.
2-L. Houas, J. Fortes, and R. Brun, in "Shock Tubes and Shock Waves", H. Grönig Ed., Proceedings of the 16th ISSWST, Aachen 1987, VCH 1988;
3-B. Sturtevant, R. Bonazza, M. Brouillette, "Richtmyer-Meshkov Instability at a continuous interface", "International Workshop on RT and RM Mixing", Pleasanton, November 1989;
4-Experiments with a nominally planar interface: for example
i/with membrane:
M. Brouillette and B. Sturtevant, Physica D37 (1989) 248-263; S.G. Zaitsev et al., Tep. Vys. Temp., 23, 3, (1985) 535-541;
ii/without membrane: M. Brouillette and B. Sturtevant, Physica D37 (1989) 248-263; C. Cavailler et al., AIP Conference Proceedings 208, (1990) 564;
5-J.B. Bell, P. Collela, and J.A. Trangenstein, "Higher-order Godunov Method for General Systems of Hyperbolic Conservation Laws", J. Comp. Phys. 82, (1989) 362-397;
6-C. Coste et al, in Computing Methods in Applied science and Engineering", Glowinski and Lions Eds., North Holland, Amsterdam, 1982;
7-D.L. Youngs, "Time-Dependent Multi-Material Flow with Large Fluid Distortion", in "Numerical Methods for Fluid dynamics", K.W. Morton and M.J. Baines, Eds., Academic Press, New York, 1982;
8-F.L. Addessio et al., "CAVEAT: A Computer Code for Fluid Dynamics Problems with Large Distortion and Internal Slip", Los Alamos National Laboratory Report LA-10613-MS-REVISED, 1991;
9-I.L. Chern, J. Glimm, O. McBryan, B. Plohr, and S. Yaniv, "Front Tracking for Gas Dynamics", J. Comp. Phys., 62, 1986, pp 83-110;
10-A. Smith, "Turbulent Mixing in Shock Tube experiments with a High Initial Perturbation","International Workshop on RT and RM Mixing", Pleasanton, November 1989;
11-D.C. Besnard, J.F. Haas, and R.M. Rauenzahn, in Proceeding of the "International Workshop on the Physics on Compressible Mixing", Princeton, 1988, Eds. W.P. Dannevik, A. Buckingham, C.E. Leith, Springer-Verlag, N.Y., to be published 1991.

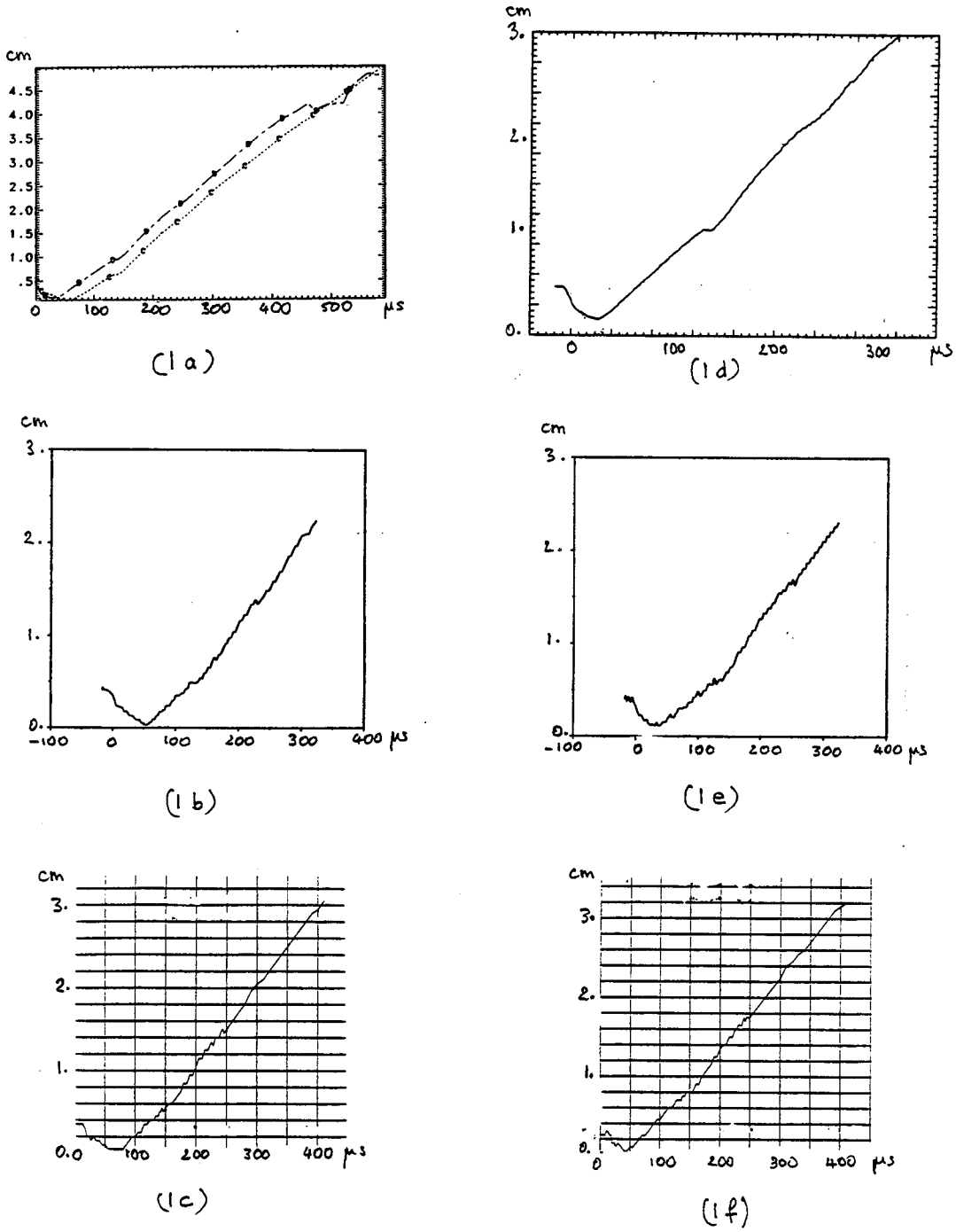

Figure 1: Mix width (in cm) versus time (in μs) for test problems 1 and 2 (air/helium)

-single mode interface: (1a, line B) AMR; (1b) CAVEAT; (1c) EAD.

-multimode interface: (1a, line C) AMR; (1d) PETRA; (1e) CAVEAT; (1f) EAD.

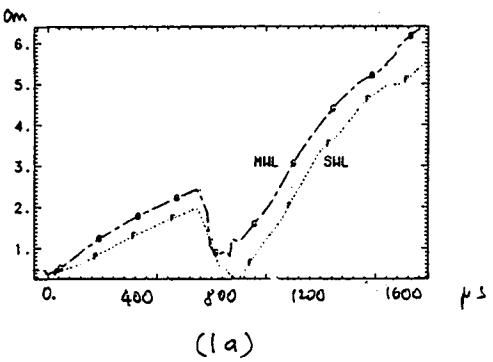

(1a)

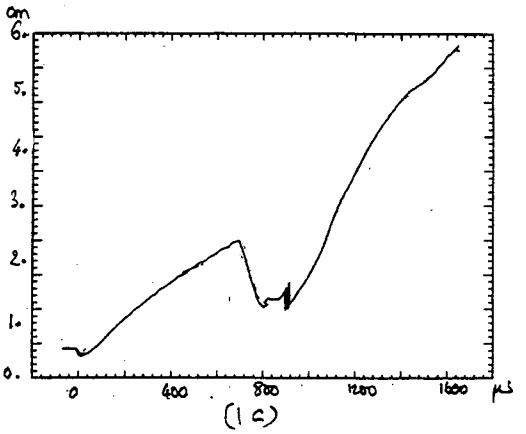

(1c)

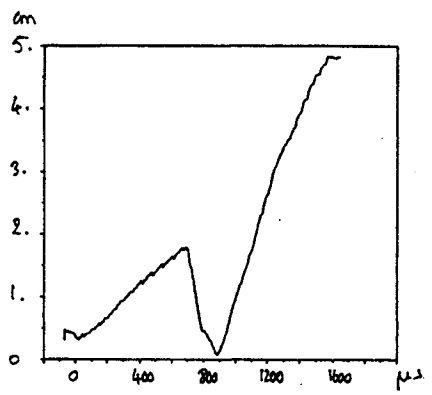

(1b)

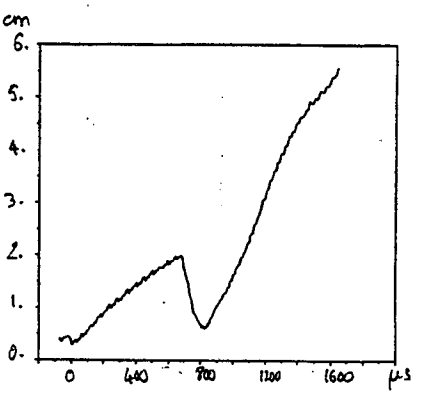

(1d)

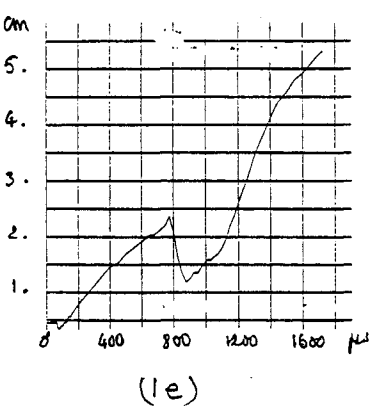

(1e)

Figure 2:
Mix width (in cm) versus time (in μs) for test problems 3 and 4 (air/SF6)

-single mode interface:
(1a, line SWL) AMR; (1b) CAVEAT.

-multimode interface:
(1c) PETRA; (1d) CAVEAT; (1e) EAD.

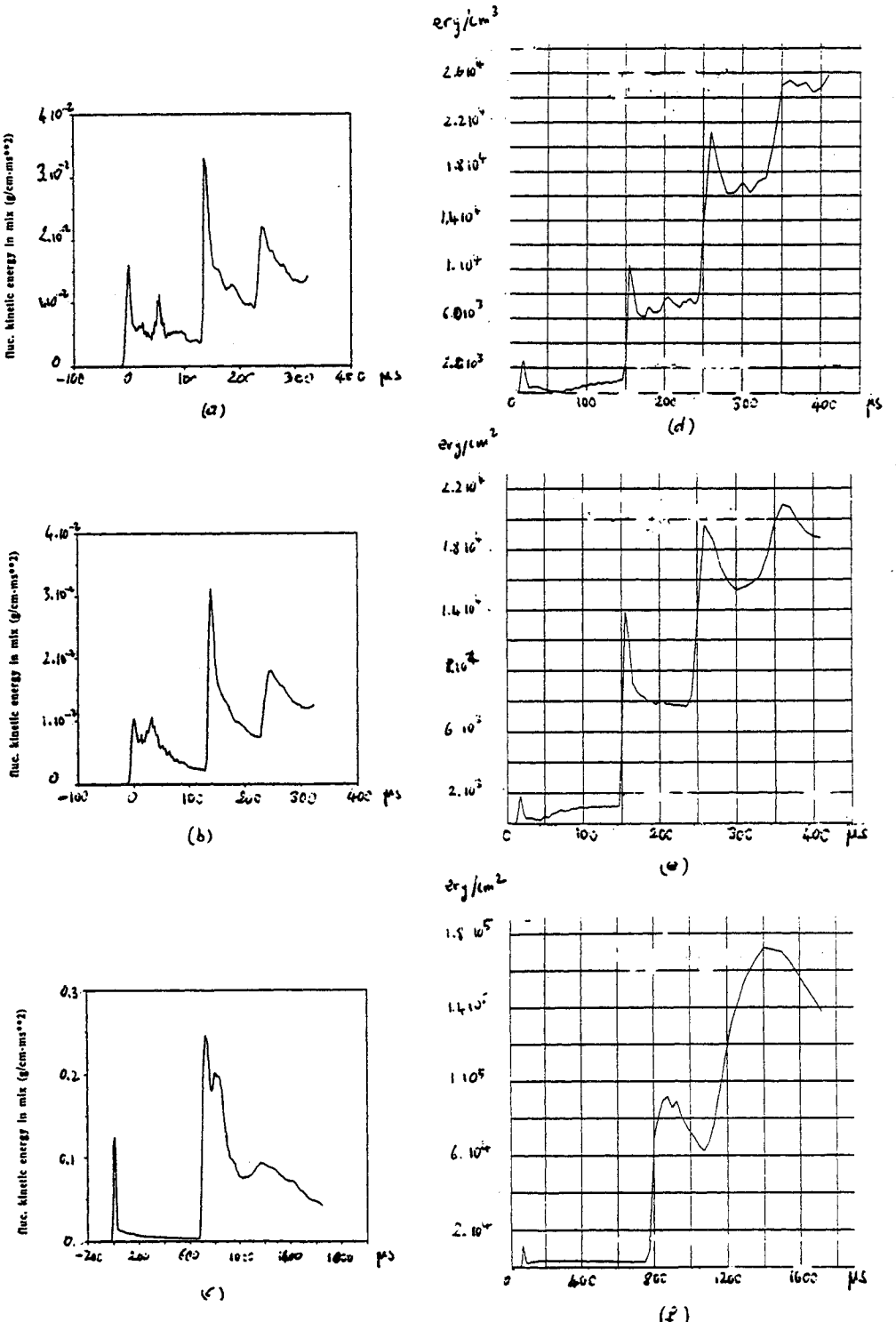

Figure 3: Velocity fluctuations kinetic energy versus time (in μs)
-single mode interface, test problem 1 (air/helium): (3a) CAVEAT (energy in g/cm-ms**2), (3d) EAD (energy in erg/cm2);
-mutimode interface, test problem 2 (air/helium): (3b) CAVEAT, (3e) EAD;
-multimode interface, test problem 4 (air/SF6): (3c) CAVEAT, (3f) EAD.

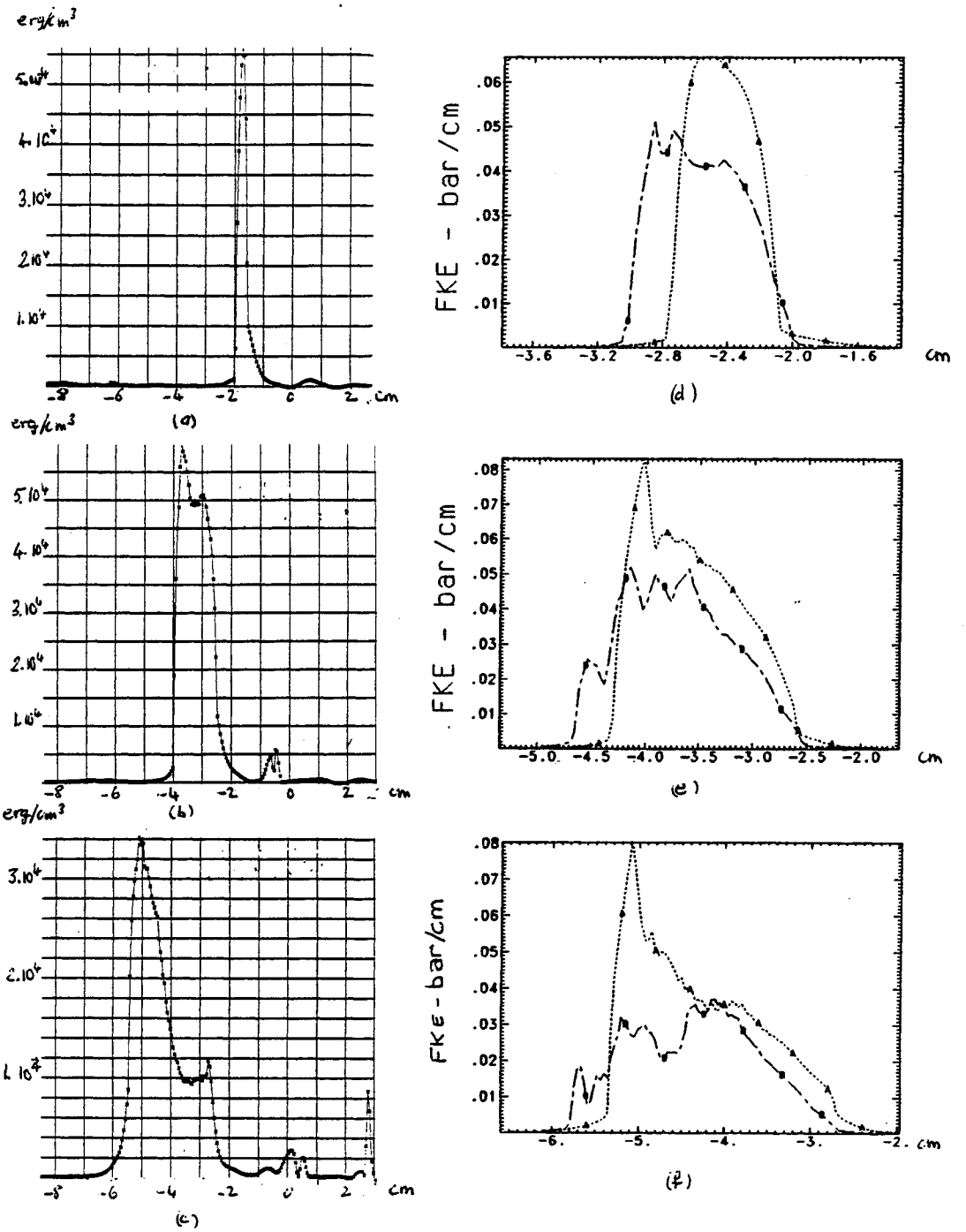

Figure 4: Velocity fluctuations kinetic energy 1D profile versus space ($\overline{\rho u^2} - \overline{\rho}\ \overline{u}^2$)
-single mode interface (air/helium): (4a) EAD t = 115 µs, (4b) EAD t = 230 µs, (4c) EAD t = 360 µs, (4d, curve A) AMR t = 120 µs, (4e, curve A) AMR t = 220 µs, (4f, curve A) AMR t = 330 µs;
-multimode interface (air/helium): (4d, curve B)) AMR t = 120 µs, (4e, curve B) AMR t = 220 µs, (4f, curve B) AMR t = 330 µs;

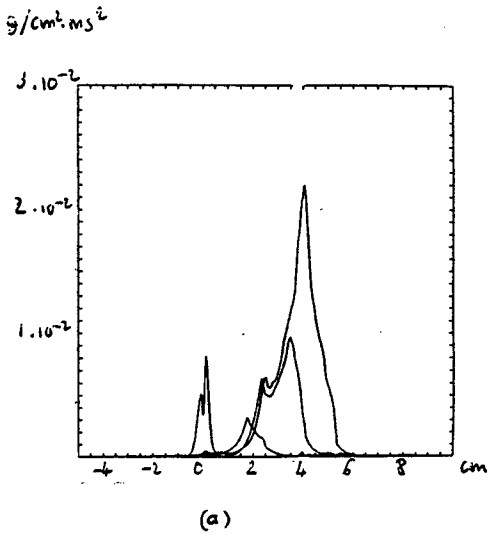

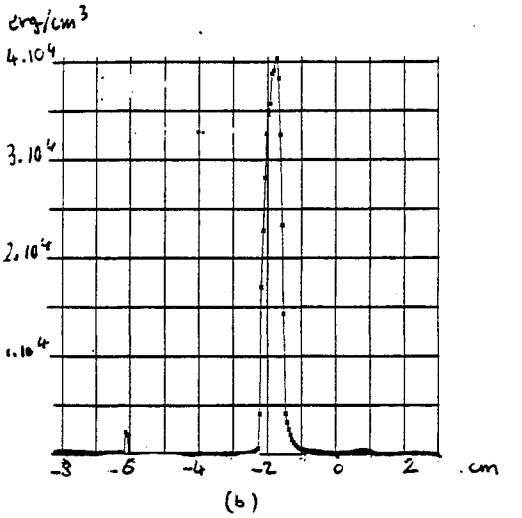

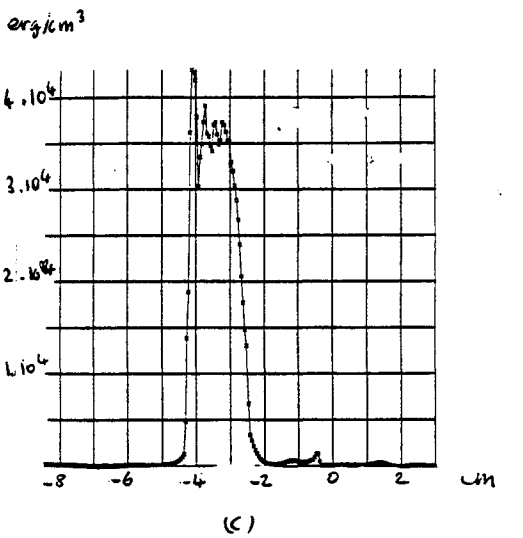

Figure 5: Velocity fluctuations kinetic energy 1D profile versus space ($\overline{\rho u^2} - \overline{\rho}\,\overline{u}^2$)
-multimode interface (air/helium):
(5a) CAVEAT, (5b) EAD t = 115 µs,
(5c) EAD t = 230 µs
-multimode interface (air/SF6):
(5d) CAVEAT

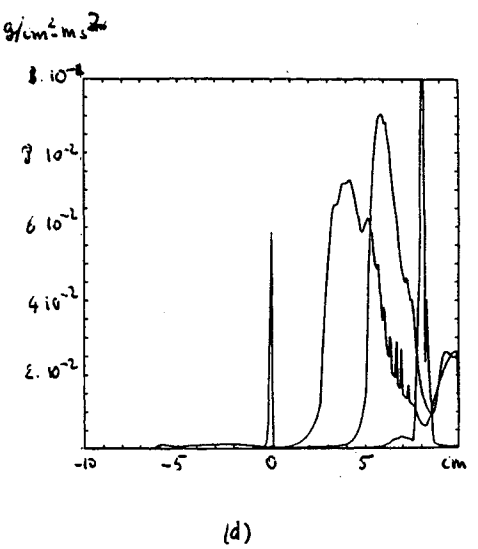

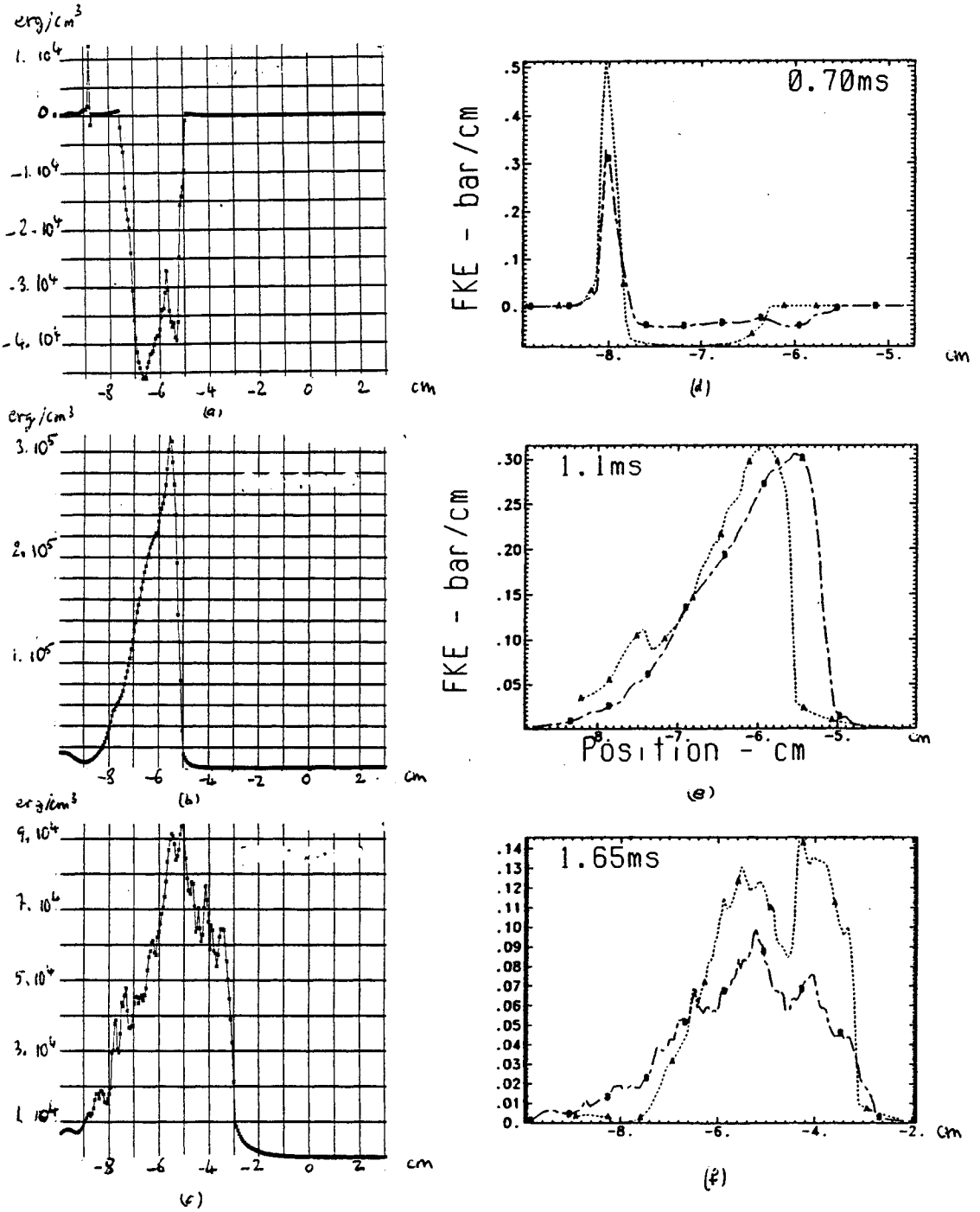

Figure 6: Velocity fluctuations kinetic energy 1D profile versus space ($\overline{\rho u^2} - \overline{\rho}\ \overline{u}^2$)
-single mode interface (air/SF6): (6a) EAD t = 630 µs, (6b) EAD t = 1100 µs, (4c) EAD t = 1650 µs, (6d, curve A) AMR t = 700 µs, (6e, curve A) AMR t = 1100 µs, (6f, curve A) AMR t = 1650 µs;
-multimode interface (air/helium): (6d, curve B)) AMR t = 700 µs, (6e, curve B) AMR t = 1100 µs, (6f, curve B) AMR t = 1650 µs;

Double Shock-Induced Turbulence

Jeff D. Colvin
Los Alamos National Laboratory
&
U.S. Department of Energy

ABSTRACT

Following an analytical treatment by Mikaelian (1985) I derive the Richtmyer-Meshkov turbulence energy density at an interface transited by two shocks in succession, and show that, for a given final velocity of the interface, when the two shocks are approximately of equal strength only about half the turbulent energy is generated than when one shock is much stronger than the other.

INTRODUCTION

When the interface between two fluids is impulsively accelerated by the passage of a shock, perturbations on the interface become unstable, grow with time, and a turbulent mixing layer develops. Richtmyer[1] developed an analytical description of the instability growth by treating the shock as an instantaneous acceleration. Subsequent experiments by Meshkov[2] support Richtmyer's treatment. For Richtmyer-Meshkov (RM) instabilities the fundamental questions are how the mix layer evolves in time, how much turbulent energy is generated, and how large the turbulent eddies are at the shocked interface.

There is also interest in these same questions for the situation where several shocks in succession pass through the same interface, i.e., how the turbulent energy grows when a shock passes through a region of pre-existing turbulence. This question is of particular interest in inertial confinement fusion (ICF) because an ICF capsule requires a shaped driving pressure in order to compress it efficiently to the conditions required for fusion ignition. Thus, an ICF capsule must first be compressed by a relatively weak shock so as to keep the shell on a near-degenerate adiabat (to minimize the energy required to compress the shell), and then hit with a much stronger

shock to bring the shell up to the minimum velocity required for ignition. A minimum velocity is required because the compressional heating rate of the fuel, which is velocity dependent, must exceed the energy loss rates by radiation and conduction, which are velocity independent, for ignition to occur. The minimum energy required for ignition is a strong function of the shell velocity.[3] Thus, RM turbulence will develop at the shell/fuel interface and possibly inhibit ignition by redirecting kinetic energy of the shell into turbulence energy instead of into internal energy of the fuel.

Unfortunately, the amount of turbulent energy generated by two shocks in succession, as shown in this paper, is about twice as great when one shock is much stronger than the other -- which is the desired situation for efficient fusion ignition -- than when the shocks are about of equal strength. In this paper I first discuss the previous work on which the present work is based, then derive the double shock-induced turbulence energy, and finally draw conclusions about the turbulence energy for various relative strengths of the two shocks.

BACKGROUND

Mikaelian[4,5] developed a simple analytical model for turbulence generated by Richtmyer-Meshkov (RM) instabilities, based on the rocket-rig experiments of Read and Youngs.[6] In those experiments Read and Youngs discovered that, for the case of a constant acceleration, the height of the turbulent mixing layer at a Rayleigh-Taylor unstable interface is given by

$$h = 0.07Agt^2 , \qquad (1)$$

where $A=(\rho_2-\rho_1)/(\rho_2+\rho_1)$ is the Atwood number of the two fluids, g is the constant acceleration of the interface, and t is the time. Comparable experimental data on RM turbulence was not available at the time of Mikaelian's work in 1985; in the absence of such

experimental data Mikaelian treated the shock as an impulsive acceleration of the interface, i.e.,

$$\frac{d^2h}{dt^2} = 0.14A\Delta v\delta(t) , \tag{2}$$

where Δv is the jump velocity of the interface caused by the shock and $\delta(t)$ is the Dirac delta function. Thus, for RM turbulence equation (1) becomes

$$h = 0.14A\Delta vt . \tag{3}$$

Mikaelian then infers the amount of turbulent energy per unit area as the potential energy lost during the mixing process. Assuming a linear density profile in the mixing region he finds for RM turbulence

$$\frac{d^2}{dt^2}\left(\frac{E_{TURB}}{\text{unit area}}\right) = \frac{g}{3}(\rho_2-\rho_1)\left[\left(\frac{dh}{dt}\right)^2 + h\left(\frac{d^2h}{dt^2}\right)\right] . \tag{4}$$

Then, for the single-shock case we substitute equation (3) into equation (4), integrate once over time, and obtain

$$\frac{d}{dt}\left(\frac{E_{TURB}}{\text{unit area}}\right) = \frac{(\rho_2-\rho_1)}{3}(0.14)^2A^2(\Delta v)^3 . \tag{5}$$

DERIVATION OF THE DOUBLE SHOCK-INDUCED TURBULENCE ENERGY

Let us assume that two shocks pass in succession through the same interface at times 0 and $t_2 > 0$, so that

$$g = \Delta v_1\delta(0) + \Delta v_2\delta(t_2) , \tag{6}$$

and further assume that $\Delta v_1 + \Delta v_2 = v_s$ = constant. For the two-shock case equation (3) becomes

$$h = \begin{cases} 0.14 \Delta v_1 A t , & 0 \leq t \leq t_2 \\ 0.14 \Delta v_1 A t_2 + 0.14(\Delta v_1 + \Delta v_2)(t - t_2), & t \geq t_2 \end{cases} \tag{7}$$

If we substitute equations (6) and (7) into equation(4) and integrate once over time we obtain

$$\frac{d}{dt}\left(\frac{E_{TURB}}{\text{unit area}}\right) = \frac{(\rho_2 - \rho_1)}{3} (0.14)^2 A^2 \left\{ (\Delta v_1)^3 + \Delta v_2 (\Delta v_1 + \Delta v_2)^2 \right\} . \tag{8}$$

Now let us compare the turbulence energy densities for this case with the case of a single shock with velocity jump equal to v_s. The ratio of the turbulence energy densities at any time for these two cases is

$$R = \frac{\Delta v_1^3 + \Delta v_2 v_s^2}{v_s^3} . \tag{9}$$

When one shock is much stronger than the other, i.e., when either $\Delta v_2 >> \Delta v_1$ or $\Delta v_1 >> \Delta v_2$, then R ~ 1. On the other hand, when the two shocks are of comparable strength, i.e., when $\Delta v_1 \sim \Delta v_2 \sim v_s/2$, then

$$R \simeq \frac{(v_s/2)^3 + (v_s/2) v_s^2}{v_s^3} = \frac{5}{8} . \tag{10}$$

Thus, when two shocks pass in succession through the same interface, accelerating it to a final constant velocity, only about half the turbulent energy is generated when the two shocks are about of equal strength than when one of the shocks is much stronger than the other. Indeed, as is clear from equations (5) and (8), the RM turbulence energy is a strong function of the velocity jump, so when there is a substantial advantage to be gained in minimizing turbulence, as there is in ICF, then a sequence of several relatively weak shocks generates less turbulence than does one or two strong shocks.

Furthermore, it is seen from equation (8) that for the two-shock case the turbulence energy for a given v_s is a minimum when $\Delta v_1 = v_s/\sqrt{3}$; at this first-shock velocity the ratio of turbulence energies (two-shock to one-shock) is

$$R_{min} = 1 - \frac{2}{3\sqrt{3}} \quad , \tag{11}$$

which is a little less than 5/8.

REFERENCES

1. R.D. Richtmyer, Comm. Pure Appl. Math. 13, 297 (1960).

2. E.E. Meshkov, Izv. Akad. Nauk SSSR, Mekh. Zhidk. Gaza 5, 151 (1969).

3. S.A. Colgate and A.G. Petschek, "Minimum Conditions for the Ignition of Fusion," Los Alamos National Laboratory Report LA-UR-88-1268, 1988.

4. K.O. Mikaelian, "Turbulent Mixing Generated by Rayleigh-Taylor and Richtmyer-Meshkov Instabilities," Lawrence Livermore National Laboratory Report UCRL-93499, Sept. 20, 1985.

5. K.O. Mikaelian, "Turbulent Energy at Accelerating and Shocked Interfaces," Lawrence Livermore National Laboratory Report UCRL-93977, Jan. 10, 1986.

6. D.L. Youngs, Physica 12D, 32 (1984); K.I. Read, Physica 12D, 45 (1984).

Measurements by X-Ray Densitometry of Shock-Excited Turbulent Mixing at an Air-Xenon Interface

Riccardo Bonazza
Bradford Sturtevant
California Institute of Technology
Pasadena CA 91125, USA

1. Introduction

The interaction of a shock wave with a non-planar interface between fluids of different densities leads to distortion of the interface shape and mixing of the fluids. The interface distorts due to the baroclinic generation of vorticity resulting from misalignment of the pressure gradient perpendicular to the shock and the density gradient perpendicular to the interface. This is a shock-induced Rayleigh-Taylor instability, and is known as the Richtmyer-Meshkov instability. The equations describing the dynamics of the motion can be linearized as long as $\eta << \lambda$, where η and λ are the amplitude and wavelength of the perturbation, respectively. In most applications there naturally occurs a broad spatial spectrum of perturbations, and the largest wave-number components of the spectrum almost immediately grow into the nonlinear regime and, by nonlinear interaction, effect the smaller wave-number contributions. By this route the Kelvin-Helmoltz instability develops and induces mixing of the two gases, growth of the interface thickness, and the generation of turbulence. Reverberating waves in the region between the interface and the end of the shock tube enhance turbulent mixing by depositing new turbulent energy with every interaction.

Different types of interfaces have been studied both experimentally and numerically: Discontinuous interfaces (see *e.g.* Meshkov (1969), Andronov *et al.* (1976), Brouillette & Sturtevant (1989)) and continuous interfaces, consisting of diffuse layers between two gases (see *e.g.* Duff *et al.* (1962), Brouillette & Sturtevant, Mikaelian (1982, 1989, 1990)). The investigations have been concerned with the growth of the perturbations of 'quasi sinusoidal' (or 'single scale') interfaces, and the growth of the thickness of nominally flat (or randomly perturbed) interfaces. No study has been conducted so far on the growth of the thickness of a single scale interface.

We report here the results of a new densitometry technique, based on the differential X-ray absorption by the two gases at the interface. The interface is imaged on X-ray negative plates, which are subsequently digitized and analyzed with a newly developed self-calibrating procedure. From the distribution of film density, the density field of the heavy gas (*viz.* xenon) throughout the test section is reconstructed. The shape of the interface, average density profiles, and density contours are extracted from such density distribution. To our knowledge these are the first measurements of this kind. The technique is demonstrated in a vertical shock tube set up so that a shock of strength $M_s = 1.3$ interacts with an initially thick ($\sim$1 cm) air/xenon interface with a quasi-sinusoidal shape.

2. Theory

The time-evolution of the interface between two fluids of different densities, featuring two-dimensional perturbations and subjected to a constant acceleration g in a direction perpendicular

to itself, was first studied by Lord Rayleigh (1900) and Taylor (1950). Taylor's linear theory referred to a pair of incompressible, inviscid fluids. Linearization was based on the assumption of small-amplitude perturbations ($\eta/\lambda << 1$, in figure 1). The amplitude η is governed by the differential equation:

$$\frac{\partial^2 \eta}{\partial t^2} = kgA\eta \tag{1}$$

where

$$A = \frac{(\rho_1 - \rho_2)}{(\rho_1 + \rho_2)} \tag{2}$$

is the Atwood number for the fluid combination and k is the wave number of the perturbation on the interface. If $A < 0$ (the heavy fluid is accelerated into the light one) the solution to the differential equation is a trigonometric function: the amplitude of the perturbations oscillates between two finite limits, and the interface is termed 'stable'. When $A > 0$ (the light fluid accelerated against the heavy one), the solution is an exponential and the amplitude grows unbounded; thus the interface is 'unstable'. The quantity

$$n = \sqrt{kgA}, \tag{3}$$

is the growth rate of the perturbations. The linear theory is only valid in the first stage of the process: As η grows and becomes of the same order of λ, the linear theory no longer applies.

In the case of impulsive acceleration (as that produced by a shock wave hitting the interface) the first theory was developed by Richtmyer (1960) who studied shocks weak enough that the speed of the fluids behind them be subsonic, and compressibility effects could be neglected: Taylor's linear theory would then apply with the constant acceleration g replaced by

$$g \rightarrow [u]\delta(t), \tag{4}$$

where $\delta(t)$ is Dirac's delta-function and $[u]$ is the velocity jump induced on the two fluids by the shock wave. Eq. 1 can thus be integrated once with respect to time to yield

$$\frac{\partial \eta}{\partial t} = k[u]A\eta_0 \tag{5}$$

where η_0 is the initial amplitude of the perturbations. The solution to this equation is always a linear function, irrespective of the sign of A. This means that all interfaces are unstable under impulsive acceleration: the amplitude of the perturbations on those with $A < 0$ initially decreases in time leading to the flattening of the interface, its phase reversal, and the subsequent unbounded growth. For $A > 0$ the amplitude of the perturbations starts to grow immediately after the passage of the shock wave. Use of A' and η_0' (the postshock values) in Eq. 5 was suggested by Richtmyer, in order for his numerical calculations to agree within 5% with the model.

The case of interfaces of finite thickness (*i.e.* interfaces across which the density changes from one uniform value to another with a finite density gradient, see figure 2) under constant acceleration g has been examined by Duff *et al.* (1962). Duff proposed that the linear-theory growth rate be given by the expression

$$n^2 = \frac{kgA}{\psi}. \tag{6}$$

The differential equation for the amplitude of the perturbations on the interface then becomes

$$\frac{\partial^2 \eta}{\partial t^2} = \frac{kgA}{\psi}\eta, \tag{7}$$

showing that the physical significance of ψ is that of a growth rate reduction factor for interfaces with finite density gradients. For a discontinuous interface $\psi = 1$ (so as to recover Taylor's formula). For a finite density gradient across the interface $\psi = \psi(\Delta/\lambda, A)$, where Δ is the interface thickness and λ the wavelength of the perturbation.

Mikaelian (1982, 1983) studied an interface of finite thickness under both continuous and impulsive acceleration, by modeling the interface as a series of M fluid layers, stacked in the direction of the acceleration. More recently (1989a), he investigated the same problems using continuous density profiles of different types. He found that finite density gradients reduce the growth rates in both Rayleigh-Taylor and Richtmyer-Meshkov configurations, and that the reduction is greater for the case of impulsive acceleration.

For a shocked, continuous interface, following the proposal of Richtmyer (1960), Eq. 7 can be used with g replaced by $[u]\delta(t)$.

The other important interface feature is its thickness, Δ: the non-linear stages of the Richtmyer-Meshkov instability, and the Kelvin-Helmoltz instability (also a non linear process) cause the formation of large-scale structures from the small-scales associated with fluid motion, entrainment and mixing of the two gases, and growth of the interface thickness. The analyses by Barenblatt (1983) and Leith (1985) describe the mixing in two stages: A first, linear stage, during which viscosity effects are neglected, and the thickness growth is given by:

$$\Delta = [u]tf(\frac{\rho_1'}{\rho_2'}) \tag{8}$$

with the indices referring to the gas on each side of the interface. A nonlinear stage, characterized by the decay of the turbulent intensity: in this case

$$\Delta \propto t^{\alpha} \tag{9}$$

with $\alpha < 2/3$.

Mikaelian (1989b, 1990) has studied the evolution of the mixing layer looking at the ratio E_{turb}/E_{dir} of turbulent to directional kinetic energy within the layer. He has used different approaches to estimate the turbulent kinetic energy in the layer, including the Canuto-Goldman analytical model for large scale turbulence, and a model of turbulent diffusion proposed by Belenkii and Fradkin. The interfaces studied so far were both of the discontinuous and the continuous types, initially nominally flat, with only small amplitude, small wavelength, random perturbations. The evolution of the thickness of an interface initially featuring some large wavelength perturbations has not been studied so far.

3. Experimental Apparatus and Procedure

The experiments are performed in a vertical, square shock tube designed and fabricated specially for the study of the Richtmyer-Meshkov instability. The tube is vertical to make use of the earth's gravity to separate two fluids of different density to prepare a continuous interface. The cross section is square to provide the parallel walls necessary for any imaging technique to be used in the study of the flow. In the present experiments a shock wave is launched from the top of the shock tube towards its bottom where a gas interface has been prepared, and the interface is imaged with an X-ray source and medical X-ray film.

The driver section is round, of inner diameter 16.5 cm and 1.83 m length; the driven section is square, of side 11.4 cm and 4.91 m length; the test section has a length of 38.7 cm and its side matches that of the driven section. The driver gas is room-temperature nitrogen in all the present experiments. At the beginning of each run the driver section is pressurized to about 0.3 atm below the bursting pressure of the diaphragm in use. To fire the shock tube a high-pressure (40.0 - 67.0 atm) boost-tank is discharged into the driver section: this ensures the release of the shock wave within 500 ms from the opening of the boost-tank. A schematic of the shock tube is presented in figure 3. The test section is equipped with two square windows 11.4 cm on the side to image the full width of the flow inside the tube. Since the present imaging technique is based on X-ray absorption by one of the gases in the test section, it is necessary to minimize X-ray absorption by the windows: thus conventional glass windows are replaced by a pair of Narmco Rigidite 5208/T300 carbon-fiber plates, 1 mm thick; each plate is supported against the internal pressure of the shock-compressed gases by an egg-crate aluminum structure.

A flash X-ray source (Hewlett-Packard Flash X-Ray Electron Beam System Model 43731A) is mounted 1.83 m away from the rear window of the test section, with its axis perpendicular to the planes of the windows. The source generates a 50 ns long X-ray flash. During each run one 20 x 25 cm 3M-XM X-ray negative (a type used for medical imaging), sandwiched between two 3M-T12 fluorescent screens (also used in medical diagnostics) in a film-holder mounted on the outside of the rear window, is exposed.

A system for sliding a thin (1.2 mm), horizontal, stainless steel plate in and out of the test section (used to prepare a continuous gas interface) is mounted on one of the test section's outside walls (see figure 4). The plate travels in a direction perpendicular to the axis of the X-ray beam. To prepare a continuous interface, the test gas is introduced from the bottom of the shock tube, with the plate fully inserted in the test section, and air is pushed out through a valve located just below the plate. Prior to releasing the shock from the driver section, the plate is extracted from the test section: air and the test gas come into intimate contact and start to diffuse into each other. Furthermore, during its withdrawal, the plate drags along a volume of fluid, due to the no-slip boundary condition on its surface. Once the plate completes its motion out of the test section, this volume of fluid propagates back towards the opposite wall as a surface gravity-wave. Thus, depending on the amount of time elapsed between the end of the plate retraction and the shock arrival at the interface, this latter will feature different initial conditions: for a time interval not larger than 0.5 seconds the interface has a 'bump' perturbation at the side where the plate exited and is flat and diffused (with random, small scale perturbations) at the opposite side. If about 1.2 seconds elapse prior to shock arrival the interface is "quasi sinusoidal" all across its span. This is the configuration studied in the present experiments. On the other hand, if the two gases are exposed to each other for a period of the order of 4.0 - 6.0 seconds, the interface is fully diffused, free of surface waves, and thicker than in the first case, but presumably containing random perturbations of small amplitude.

In the present experiments the test section is located at the bottom of the driven section and the end wall of the shock tube is 1.9 cm below the lower edge of the test section windows. The interface is initially located 11.3 cm above the end wall of the shock tube. The test gas is always xenon, chosen because of its high atomic number.

An 8085 microprocessor board controls the experimental sequence which consists in: retracting the plate from the test section; let the desired time interval elapse (so as to prepare the interface

of interest); discharge the high-pressure boost-tank into the already pressurized driver section to release the shock wave. As it travels towards the interface, the shock passes in front of two piezoelectric pressure transducers: the signal from the uppermost transducers triggers the digital delay box that fires the X-ray flash at the desired time.

The film holder is mounted with its left, short side aligned with the left, vertical side of the windows and it protrudes 3.4 cm to the right side of the test section. A pair of aluminum step-wedges (of thickness ranging from 0.3 to 14.4 mm) are placed on the front of the film holder, in the area not covered by the test section. Thus, when the X-ray flash is fired, the images of the gases inside the test section and of the aluminum step wedges on its side are recorded on the negative; the aluminum step wedges are used for calibration, as described in the next section. A schematic of the X-ray source, shock tube and film holder is presented in figure 5. The portion of the negatives corresponding to the side wall of the test section is removed after developing; the remaining parts (corresponding to the test section and aluminum wedges) are joined together and digitized.

4. Image Analysis

4.1 Calibration

After the negatives are developed they are illuminated by a Truelite DC Backlight Illumination System, imaged with a Sony AVC-D1 CCD camera and digitized with an Epix Inc. Silicon Video Frame Grabber (installed on an IBM AT microcomputer), yielding a field of 376 × 480 8-bit pixel values. In processing the images it is necessary to account and correct for the items listed below:

1. Temporal fluctuations of the CCD output
2. Calibration of the CCD response
3. Spatial nonuniformity of the illuminating box
4. CCD "pixel noise" (spatial fluctuations)
5. Film response
6. Spatial nonuniformity of the X-ray beam
7. Temporal (shot-to-shot) variations of the X-ray beam
8. Calibration of aluminum thickness *vs.* xenon density

To reduce the noise due to fluctuations in the CCD response (item 1.), 25 digitizations of the image I_v are averaged into one final record. The intensity distribution I_{v0} of the backlight illumination system without any negative is also recorded. The optical density, D, of the negative is defined as

$$D = \log \frac{I_v}{I_{v0}} . \tag{10}$$

The response $V(x,y)$ of the CCD camera to light intensity $I_v(x,y)$ is determined using a series of commercially available neutral density filters illuminated by the backlight source. The quantity I_v/I_{v0} is known for each filter. Measurements of both neutral density filters and X-ray negatives with our system must be corrected for spatial nonuniformity of the CCD response and of the backlight source. This is accomplished by correcting the response $V(x,y)$ of the CCD camera recorded by the frame grabber with the signal $V_0(x,y)$ recorded without any filter or negative,

$$V_{corr}(x,y) = \frac{V(x,y)}{V_0(x,y)/\overline{V}_0} , \tag{11}$$

where $\overline{V_0}$ is the average reference signal over the entire backlight source. To obtain the CCD response the corrected values are averaged over the area of each filter to determine $V_{corr}(I_v/I_{v0})$. A linear fit

$$V_{corr} = a_1 \frac{I_v}{I_{v0}} + a_2 \tag{12}$$

is shown in figure 6, where $a_1 = 399.4$ and $a_2 = 28.4$ are the slope and the vertical intercept, respectively. This result is applicable to the processing of X-ray negatives if the viewing region of the CCD camera on the backlight source is always maintained the same. The optical density of a digitized negative follows from Eqs. 10 and 12

$$D(x,y) = \log\left(\frac{a_1}{V_{corr}(x,y) - a_2}\right). \tag{13}$$

This procedure corrects for items 1, 2, 3, and 4 above.

Experience has shown that it is nesessary to further correct the optical density field of each negative for nonuniformity of the spatial distribution of the X-ray source and for shot to shot variation of the intensity and the spectral content of the X-ray. For this purpose it is necessary to convert from film optical density D to exposure E. A portion in the range $0.22 < D < 2.2$ of the relation between D and E obtained in plotted form from 3M was fitted with the function

$$\frac{D - D_{min}}{D_{max} - D_{min}} = \frac{\tanh(c_1 \log E - \log E_0) + 1}{2} \tag{14}$$

and is shown in figure 7. Here c_1 is a scaling factor.

The correction procedure is based on the observation that for the source tube presently in use most of the spatial variation is in the horizontal direction. The optical density distribution $D_{ref}(x)$ in a 25 pixel high reference strip at the top of each negative is evaluated. The strip is chosen to be entirely in a region about 230 pixels wide occupied by air, both in the test section and above the aluminum wedges, where X-ray absorption by xenon is always zero. The optical density is averaged at each value of x over the height of the strip. The distribution of exposure across the strip $E_{ref}(x)$, is then evaluated from the film response. Next, the 'normalized' correction factor $\Delta E(x) = E_{max} - E_{ref}(x)$ is evaluated, where E_{max} is the exposure corresponding to the maximum optical density D_{max} in the reference strip.. At every point in the image the measured exposure $E(x,y)$ (evaluated from $D(x,y)$) is corrected by $\Delta E(x)$, $E_{corr}(x,y) = E(x,y) + \Delta E(x)$. Then a corresponding corrected film density $D_{corr}(x,y)$ is evaluated from the film response curve. This procedure corrects for items 5, 6 and 7 in the list above.

Next, a relation between ρ_{Xe} and D_{corr} (henceforth we drop the subscript) is derived from

1. the dependence $D(t_{Al})$ of the optical density on the thickness of aluminum in each negative, and
2. the relationship $\rho_{Xe}(t_{Al})$ between xenon density and aluminum thickness obtained once from X-ray photographs of calibration cells.

The average optical density of each aluminum step in the negative from each experiment is evaluated, and a function of the same form used for the film response curve (figure 7, Eq. 14) is used to determine $D(t_{Al})$, namely

$$\frac{D - c_3}{c_2 - c_3} = \frac{\tanh(c_0 - c_1 t_{Al}) + 1}{2} \tag{15}$$

where c_0 is a shift in the horizontal direction, c_1 is the scaling factor, c_3 is an asymptote, and where we take $c_2 \equiv D_{max}$ evaluated from the procedure that leads to Eq. 14. The coefficients c_0, c_1 and c_2 are determined by a nonlinear least squares fitting algorithm.

If the X-ray beam were monochromatic it would be possible to determine $\rho_{Xe}(t_{Al})$ simply from absorption coefficients available in the literature. However, our X-ray source emits with an unknown spectral distribution, so it is necessary to determine $\rho_{Xe}(t_{Al})$ by calibration. X-ray images of a calibration cell 12.5 mm in diameter and 11.5 cm long fitted with with carbon fiber windows and filled with known pressures of xenon were exposed and processed by the procedure described above. A fit to $D(t_{Al})$ (Eq. 15) is made to each calibration negative and is used to interpolate between the discrete values of aluminum thickness. A straight-line fit to the result yields the calibration curve shown in figure 8. The result of this procedure is a curve $\rho_{Xe}(D)$ for each experiment whose form is

$$\frac{D - c_3}{c_2 - c_3} = \frac{\tanh(c_0 - c_1'\rho_{Xe}) + 1}{2} \tag{16}$$

where c_1' is the c_1 of equation 15 multiplied by the relation $\rho_{Xe}(t_{Al})$. Figure 9 is a collection of all the calibrations from a series of 11 experiments, and figure 10 shows all of the same data normalized with respect to the fitting parameters c_i. The good collapse (6%) of all of the data demonstrates that the hyperbolic functions chosen to represent the data are appropriate and further that the behavior of the X-ray source is sufficiently universal that it can be characterized in terms of three empirical constants. In fact, the constants can be interpreted in terms of physical parameters, namely the X-ray source intensity, the spectral content of the X-ray beam and the parameters of the film developing procedure. Assume that the exposure E is proportional to the X-ray intensity (I_x),

$$E = AI_x \ , \tag{17}$$

use Lambert's law,

$$\frac{I_x}{I_{x0}} = e^{-k\rho_{Xe}t_{Xe}} \ , \tag{18}$$

where I_{x0} is the intensity of the incident X-ray beam, k is the absorption coefficient, and t_{Xe} is the thickness of xenon. With Eqq. 17 and 18, the terms

$$\log E - \log E_0 = \log \frac{E}{E_0} \tag{19}$$

of Eq. 14 can be replaced by

$$\log \frac{AI_{x0}}{E_0} - \frac{1}{\ln 10} k\rho_{Xe}t_{Xe} \tag{20}$$

Thus the coefficient c_0 in Eq. 16 can be interpreted as a measure of the shot-to-shot variation of I_{x0}, the X-ray source intensity and c_1' as a measure of k, *i.e.* of variations in the spectral content of the X-ray beam. c_3 corresponds to D_{min}, which depends on the parameters of film developing.

4.2 Density Profiles, Contour Plots and Interface Distortion

For each negative a xenon density profile $\rho_{Xe}(y)$ is constructed for each vertical column of pixels in the test section region from $D(x, y)$ and the calibration curve for that negative (Eq. 16). See figure 11 for an example. Each density profile exhibits three horizontal spikes corresponding to the horizontal elements of the window stiffeners; these are eliminated by linear interpolation if they fall within an undisturbed field (like the top two in figure 11) or by a least squares fit of a polynomial of fifth degree if they fall in the interface region.

In order to describe the thickening and distortion of the interface region due to the Richtmyer-Meshkov instability in simple and quantitative terms, a mean density profile and interface shape are defined. The centroid of each local density profile is calculated from (see figure 12)

$$y_c(x) = \frac{\int_0^Y \rho(x,y)dy}{\rho_{Xemax}}, \tag{21}$$

where Y is the height of the field of view in the test section. We call the locus of these centroids the 'shape' $S(x)$ of the interface. The shape constructed by Eq. 21 is interrupted in three places by the vertical elements of the stiffening grid. These gaps are filled by linear interpolation (figure 13). The spatial spectrum of the result is constructed by FFT and the behavior of the lower order modes (low wave numbers) is studied. Figure 14 is a plot of the inverse transform of the first six modes of the interface shape, obtained from the data of figure 13 without windowing.

A mean density profile $\overline{\rho_{Xe}}(y)$ free of any thickening introduced by averaging over a distorted interface is constructed by shifting the centroids of the density profiles to the same point before averaging. A typical result is shown in figure 15. Then the interface thicknes Δ is constructed from the line of minimum slope through the profile as shown in the figure.

Contour plots are made of the density field smoothed with a two-dimensional ideal low-pass filter with cut off at the 20th mode. To accomplish this the density $\rho_{Xe}(x,y)$ must be interpolated across the vertical gaps caused by the window stiffener. An example of a contour plot at late times is shown in figure 16. In the figure the dashed lines show the boundaries of regions where data are lacking due to the presence of the stiffeners. Artifacts introduced by the treatment of the data at the stiffeners are evident in the figure, especially at the bottom.

5. Results and Discussion

Figure 17 shows false color images of three of a series of eleven X-ray negatives of air/xenon interfaces from which the results reported in this paper are taken. The interfaces are accelerated by a M =1.32 shock wave, and the negatives are obtained at increasing times after shock interaction with the interface. At the top of each photograph is a color bar representing the scale of optical density from $D = 0$ (small exposure) on the left (white) to $D = 2.55$ (large exposure) on the right (yellow). The contrast of the images has been enhanced by stretching the density scale to represent the minimum value measured in the xenon region on any negative $D = 0.45$ by $D = 0$ and the maximum measured value $D = 1.75$ by $D = 2.55$. The shock wave moves from top to bottom. The interface is initially located just below the top edge of the pictures and moves downwards as the xenon is compressed by the shock wave. The grid pattern is the image of the aluminum support structure. To the side of the test section is the image of the aluminum step wedges. In figure 17a (taken 0.26 ms after shock-interface interaction) the yellow-red region is shocked air, the light blue region is shocked xenon, and the dark blue region is unshocked xenon. The interface lies between the yellow and light blue regions. The transmitted shock wave is located at the light blue-dark blue boundary. In figures 17b and 17c (taken 2.54 ms and 3.56 ms after shock arrival at the interface, respectively) the reflected shock wave has propagated out of the viewing region.

In figure 17a the perturbations on the interface are imperceptible. From figure 19 below, however, it is seen that the fourth mode dominates somewhat over the others. This is consistent with figures 17b and 17c, when it is clear that 3–4 crests develop. At $t = 2.54$ ms (figure 17b) the interface has interacted with the rarefaction wave generated during the first reverberation of

the reflected wave, which seems to induce a larger growth rate than the incident and reflected shocks, and a compression during the second reverberation. See figure 18 for a depiction of the wave trajectories in one dimensional space and time ($y - t$). At $t = 3.56$ ms (figure 17c) several reverberations have processed the interface. In figure 17c the amplitude of the perturbations is of the same order of their wavelength, indicating that the distortion process has entered its non-linear stage.

In figure 17b and c can be seen low density (dark blue) protrusions into the xenon near the shock tube walls. The schlieren photographs of Brouillette & Sturtevant (1989) show clearly that these structures are vortices. These last authors propose that they are vortices which form from the interaction of the reflected shock wave with the boundary layer on the sidewalls of the shock tube. The interface distortion induced by the no-slip condition at the walls is amplified by the reflected shock. Though the image of similar vortices on the shock tube front and back windows, with horizontal axes extending transversely across the image, were visible in the schlieren images of Brouillette, they are not easily distinguishable in the X-ray images. However, their cross sections are visible at the side walls and can be measured. Measured concentration distributions across the vortex cross section can provide the basis of a correction for the effect of the vortices on the front and back windows on the interface measurements at the center of the image.

The time evolution of the amplitude of each of the first six modes of the interface shape is shown in figure 19. Only modes 1 – 4 grow by an appreciable amount during the duration of the experiments. Modes 5 and higher are either strongly damped or saturate early in the development. As the X-ray densitometry technique is developed further, the decomposition of the interface shape into short-wave and long-wave components may provide a useful tool for studying linear and nonlinear growth, saturation and modal interactions.

Figure 20 shows the time evolution of the interface thickness $\Delta(t)$ (the two vertical lines correspond to the arrival at the interface of the first reflected shock and first reflected expansion, respectively). The decrease at early times is due to compression by the reflected shock. As already stated, the subsequent growth is thought to be initialized by reverberations of the reflected wave fields between the interface and the shock tube end wall, and, in addition, by the resulting acoustic field. A tentative linear least squares fit through the data at later times yields a growth rate of 1.47 m/s. Future work will be directed at filling in and extending the data set to distinguish whether there is any decrease of growth rate with time, as suggested by figure 19.

6. Conclusions

A new technique for the measurement of gas density, based on X-ray absorption, has been developed. The technique has been successfully applied to the study of shocked interfaces, allowing for the first time the quantitative determination of density fields and density profiles. From the density data the interface thickness and the modal decomposition of the interface shape have been deduced. The time evolution of the mode amplitude suggests that, for the conditions of these experiments, the first four modes are at all times the dominant ones in the distorted shape of the interface. The interface thickness grows linearly at a rate of 1.47 m/s, with an apparent reduction of the growth rate at late times. The objective of future work will be to obtain more data for interfaces of the same type as those treated in this paper and new data for a thicker, randomly perturbed type.

7. References

Andronov, V.A., Bakhrakh S.M., Meshkov, E.E., Mokhov, V.N., Nikiforov, V.V., Pevnitskii, A.V. & Tolshmyakov, A.I. 1976 Turbulent Mixing at Contact Surface Accelerated by Shock Waves, *Sov. Phys. JETP* **44**, 424.

Barenblatt, G.I. 1983 Self-Similar Turbulence Propagation from an Instantaneous Plane Source, In: *Non-Linear Dynamics and Turbulence*, edited by G.I. Barenblatt, G. Ioos and D.D. Joseph, Pitman, Boston, 48.

Brouillette M., Sturtevant B. 1989 Growth Induced by Multiple Shock Waves Normally Incident on Plane Gaseous Interfaces, *Physica D* **37**, 247

Duff, R.E., Harlow, F.H. & Hirt, C.W. 1962 Effects of Diffusion on Interface Instability Betwen Gases, *Phys. Fluids* **5**, 417.

Leith C.E. 1985 Acceleration-Induced Turbulent Mixing: Model One, Unpublished Report, Lawrence Livermore National Laboratory.

Lord Rayleigh 1900 Investigation of the Character of the Equilibrium of an Incompressible Heavy Fluid of Variable Density, In: *Scientific Papers*, Vol. 2, Dover, New York, 200.

Meshkov,E.E. 1969 Instability of the Interface of Two Gases Accelerated by a Shock-Wave, *Sov. Fluid Dynamics* **4**, 101.

Mikaelian, K.O. 1982 Rayleigh-Taylor Instabilities in Stratified Fluids, *Phys. Rev. A* **26**, 2140.

Mikaelian, K.O. 1983 Time Evolution of Density Perturbations in Accelerating Stratified Fluids, *Phys. Rev. A* **28**, 1637

Mikaelian, K.O. 1989a Explicit Growth Rates for the Rayleigh-Taylor Instability in Exponential Density Profiles, *Phys. Rev. A* **40**, 4801.

Mikaelian, K.O. 1989b Turbulent Mixing Generated by Rayleigh-Taylor and Richtmyer-Meshkov Instabilities, *Physica D* **36**, 343.

Mikaelian, K.O. 1990 Turbulent Energy at Accelerating and Shocked Interfaces, *Phys. Fluids A* **2**, 592.

Richtmyer, R.D. 1960 Taylor Instability in Shock Acceleration of Compressible Fluids, *Comm. Pure Appl. Math.* **8**, 297.

Taylor, G.I. 1950 The Instability of Liquid Surfaces when Accelerated in a Direction Perpendicular to their Planes. I, *Proc. Roy. Soc. A* **201**, 192.

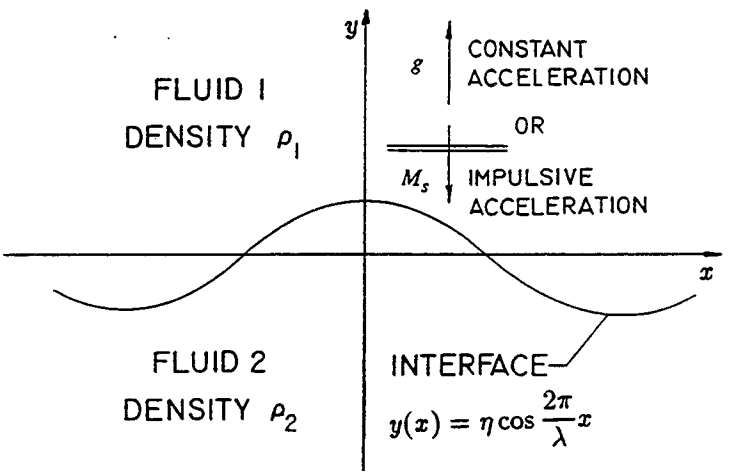

Fig. 1 Discontinuous Interface

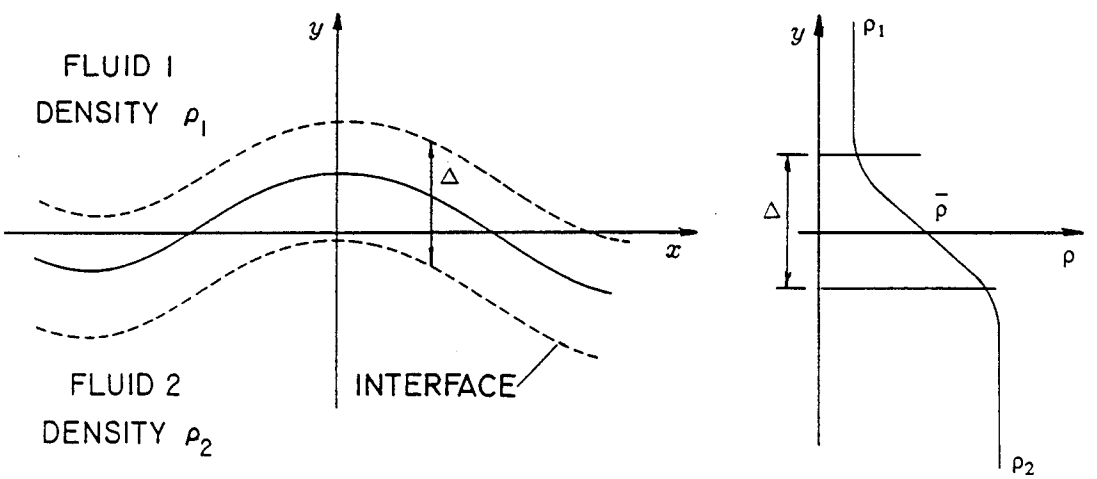

Fig. 2 Continuous Interface

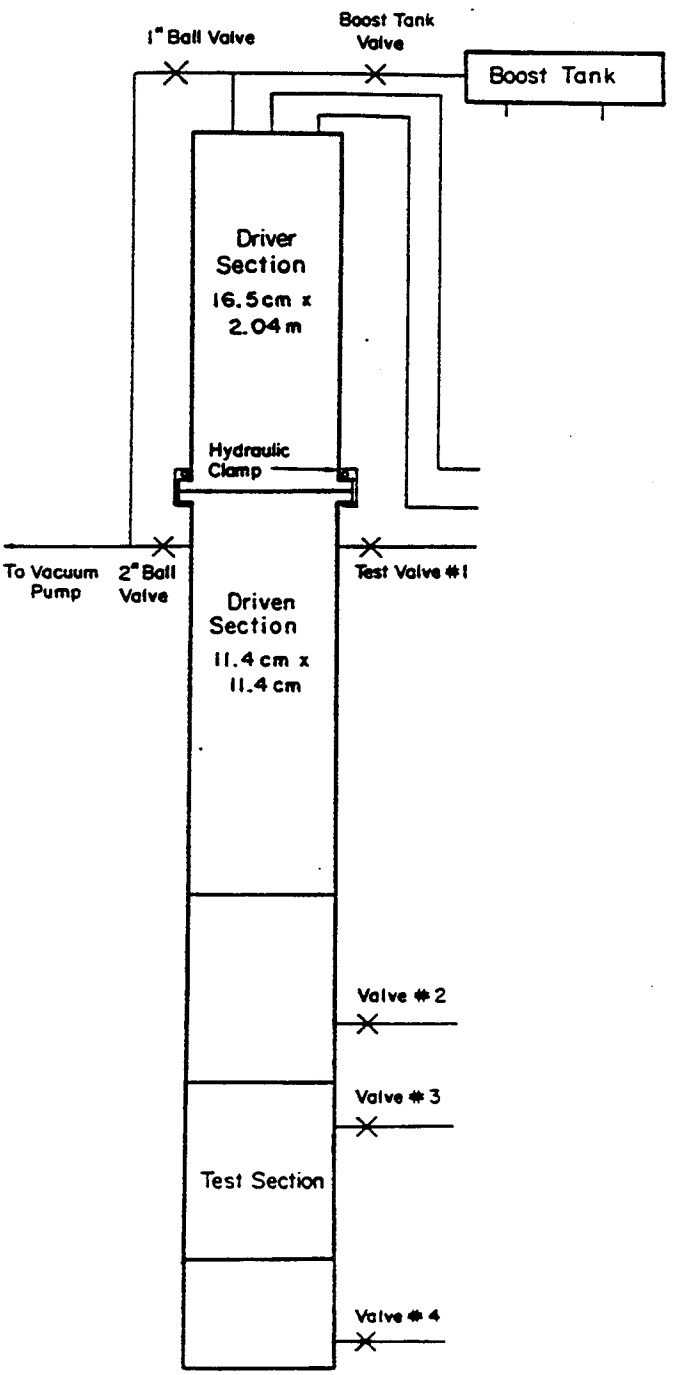

Fig. 3 Schematic of GALCIT Vertical, Square Shock Tube

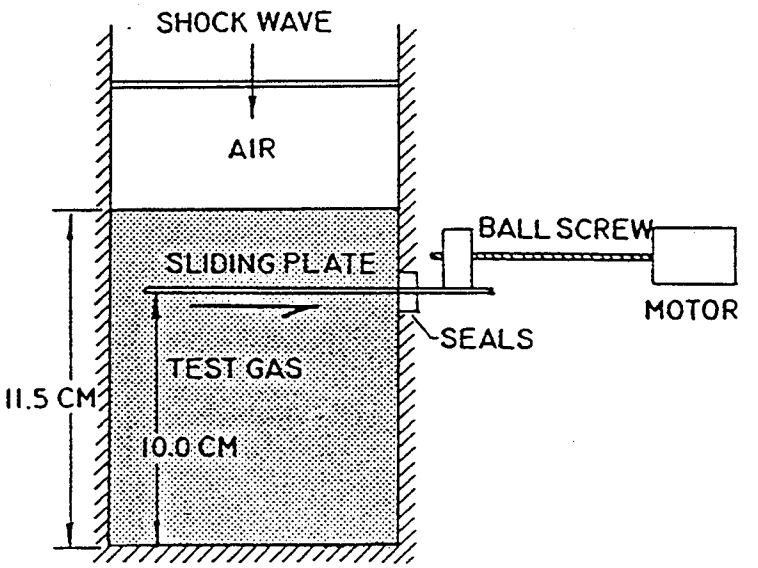

Fig. 4 Sliding Plate Mechanism

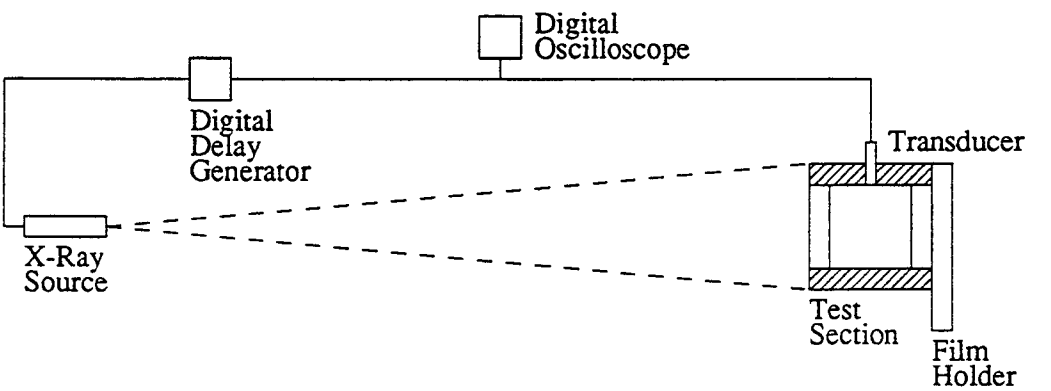

Fig. 5 Schematic of Experimental Apparatus Layout

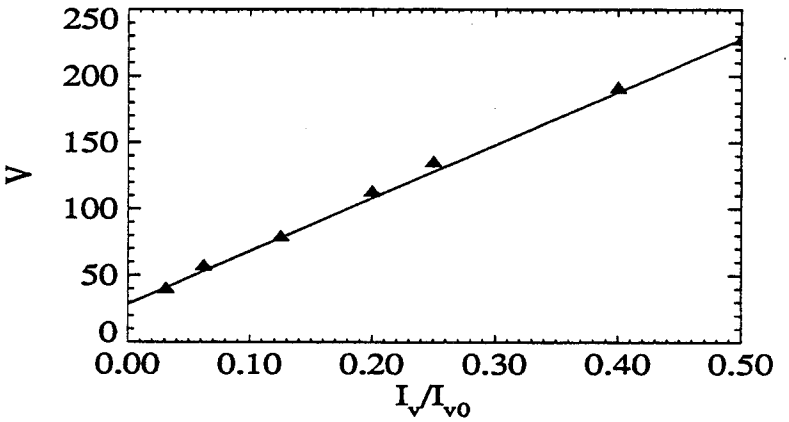

Fig. 6 Calibration of CCD Response to Light Intensity

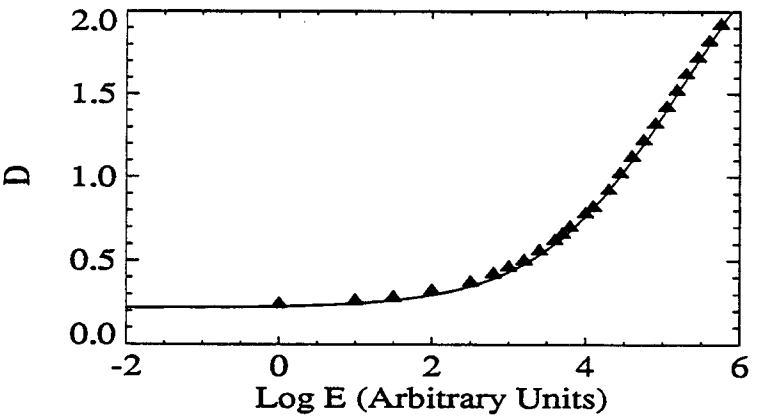

Fig. 7 Film Response Curve

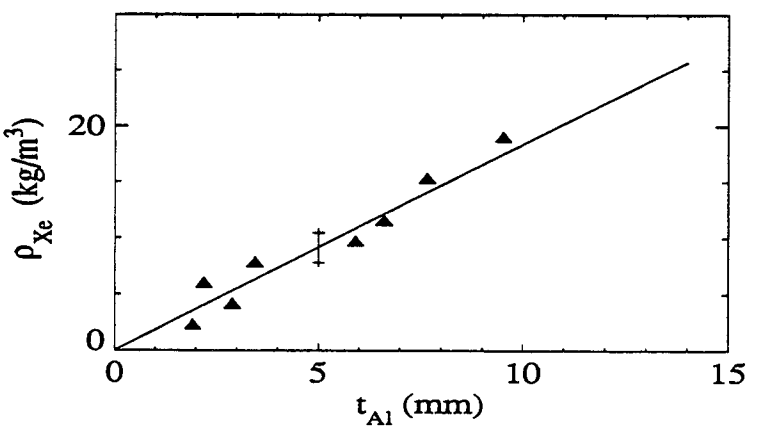

Fig. 8 Calibration Between Xenon Density and Aluminum Thickness

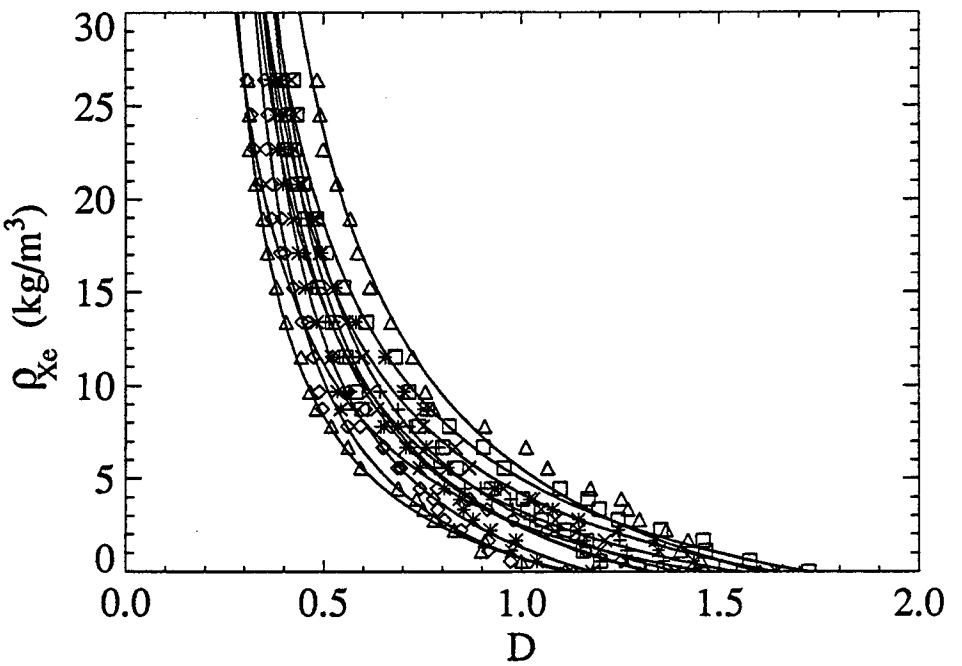

Fig. 9 Calibration Curves from 11 Experiments

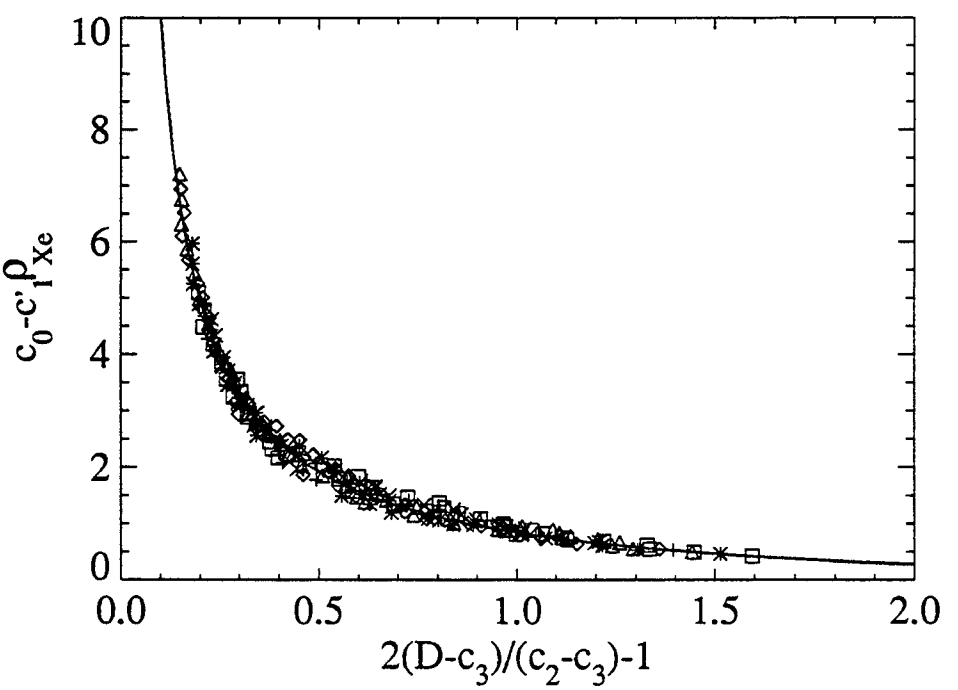

Fig. 10 Calibration Curves Normalized with Respect to the Fitting Parameters

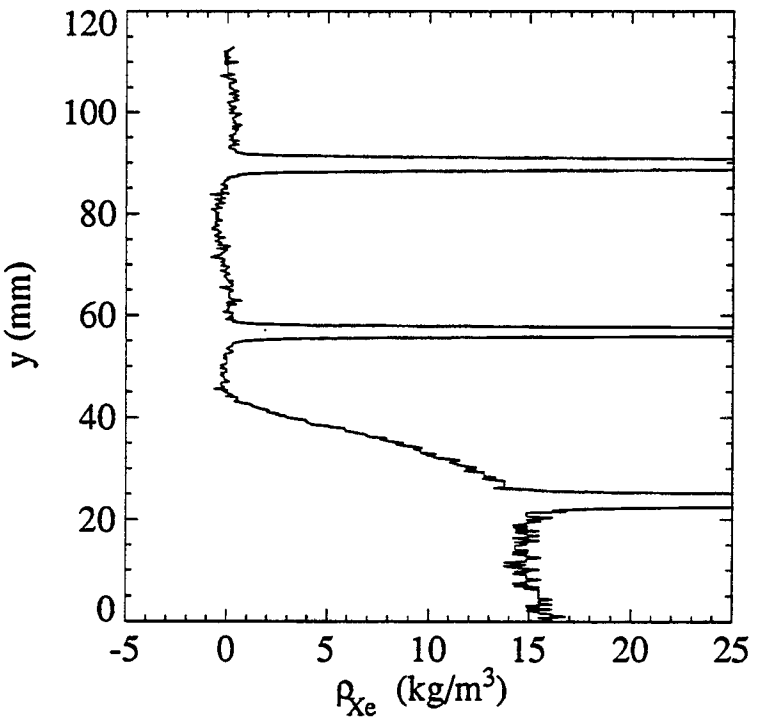

Fig. 11 Uncorrected Density Profile at Typical x Station; $t = 2.54$ ms

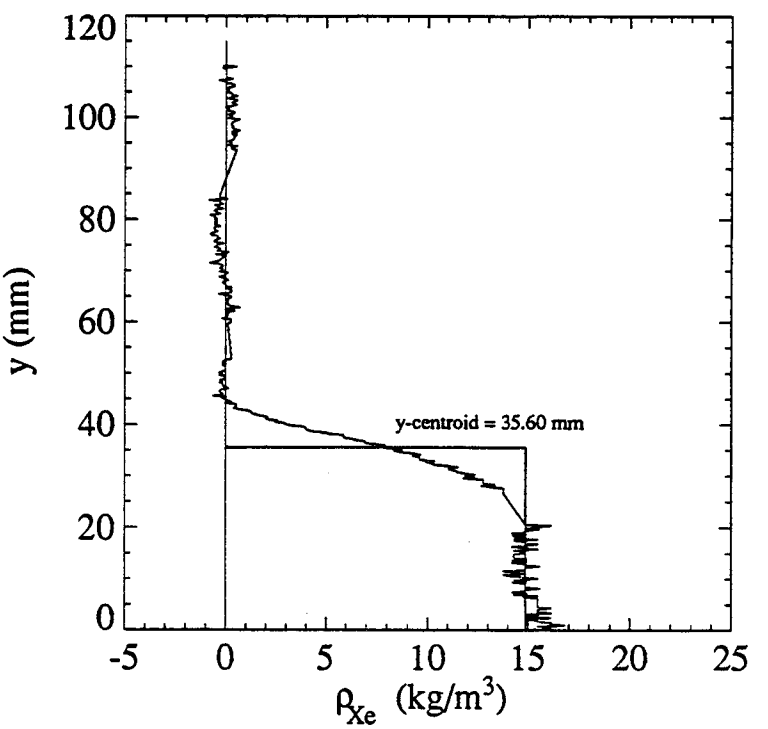

Fig. 12 Location of Centroid of Typical Density Profile; $t = 2.54$ ms

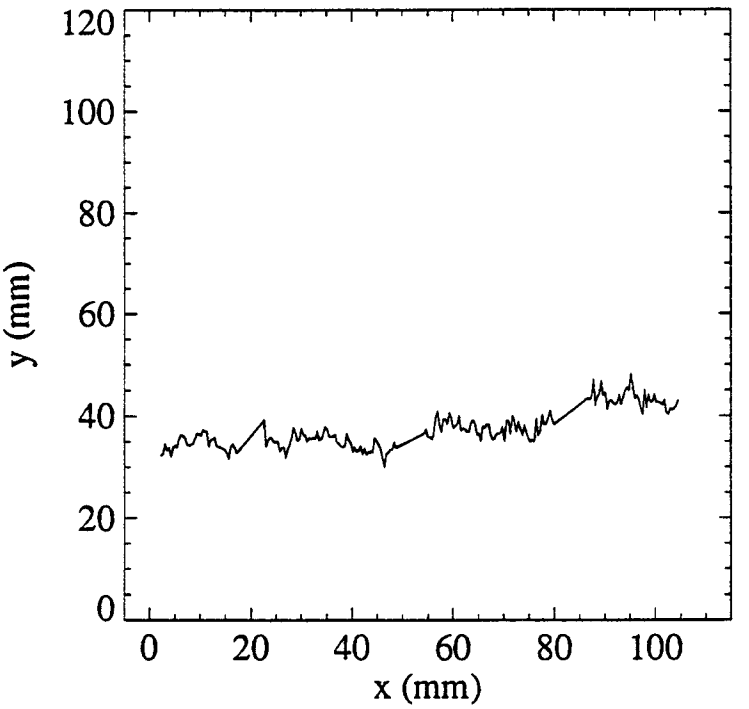

Fig. 13 Interface Shape; $t = 2.54$ ms

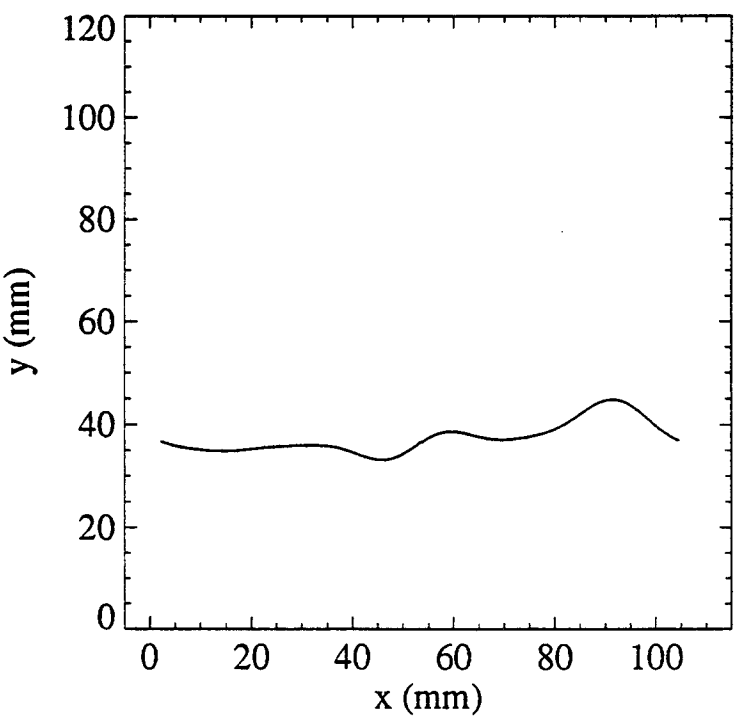

Fig. 14 Filtered Interface Shape; $t = 2.54$ ms

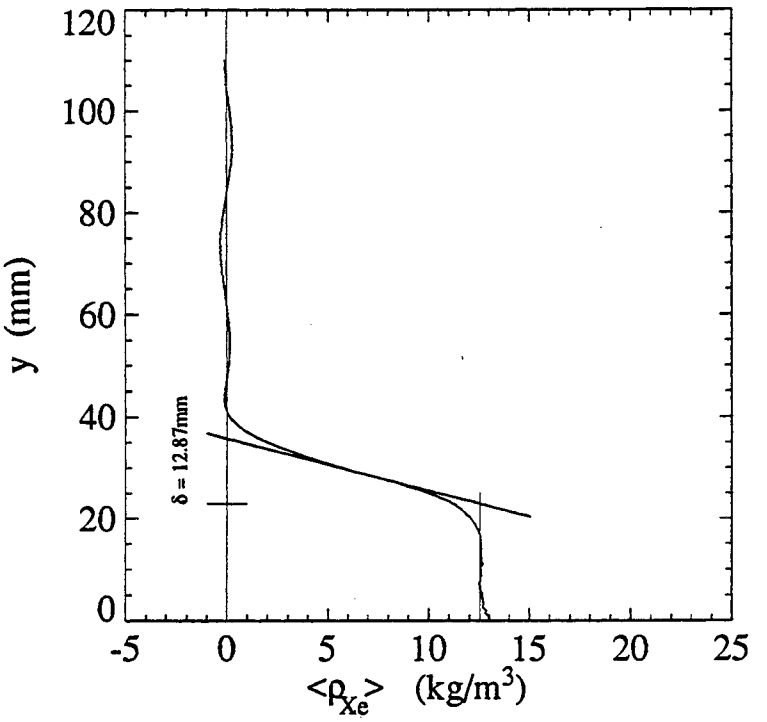

Fig. 15 Typical Mean Density Profile; t = 2.54 ms

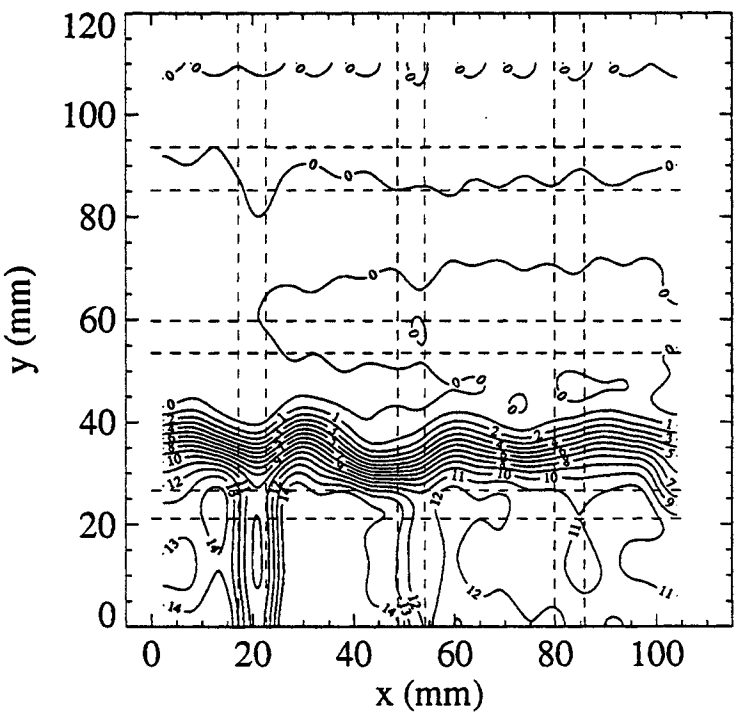

Fig. 16 Density Contours; t = 2.54 ms

a. $t = 0.26$ ms.

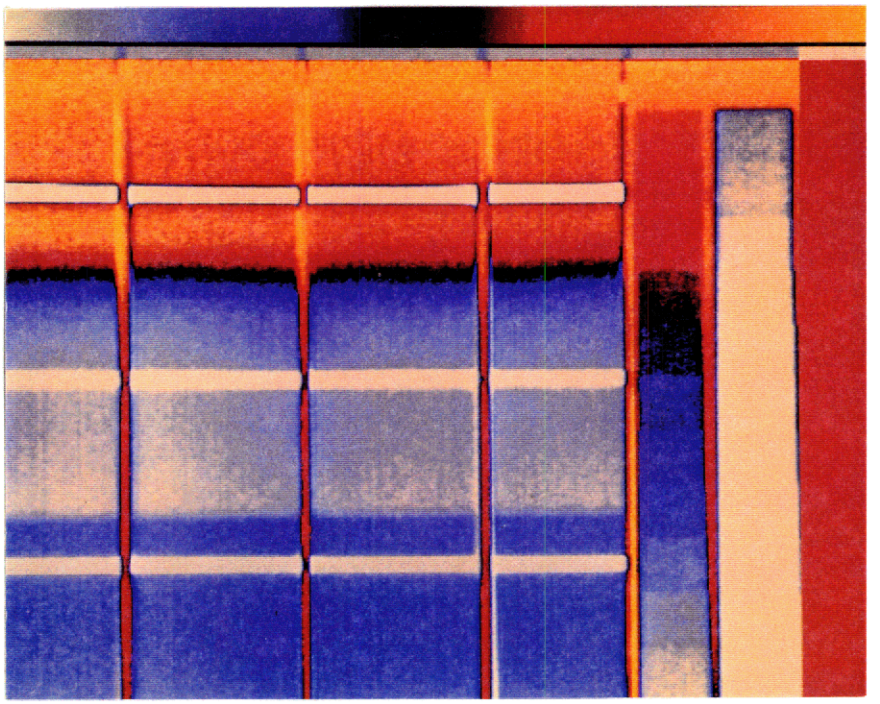

b. $t = 2.54$ ms.

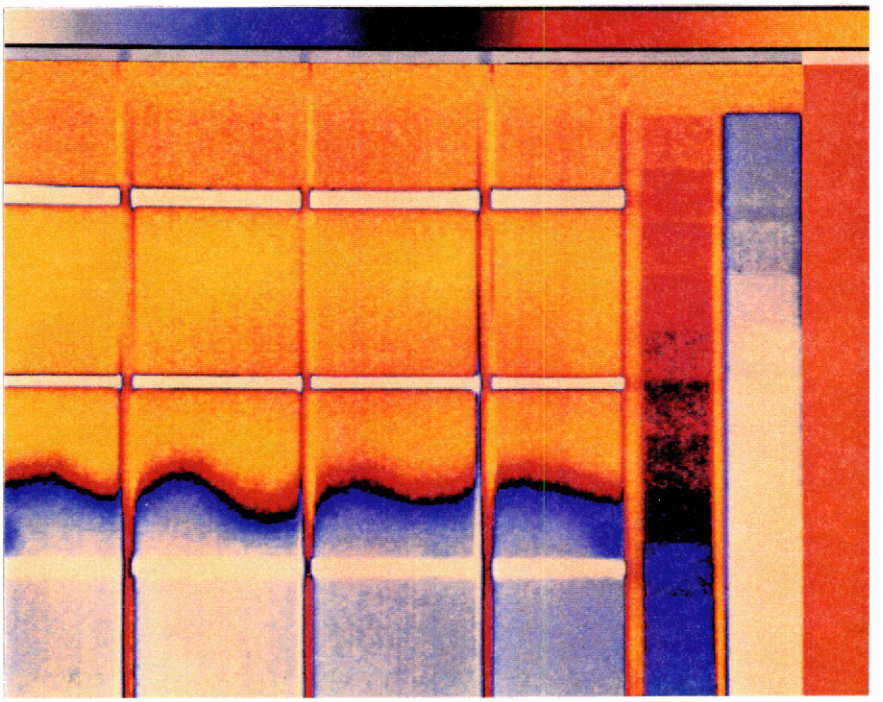

Fig. 17 Time Sequence

c. $t = 3.56$ ms.

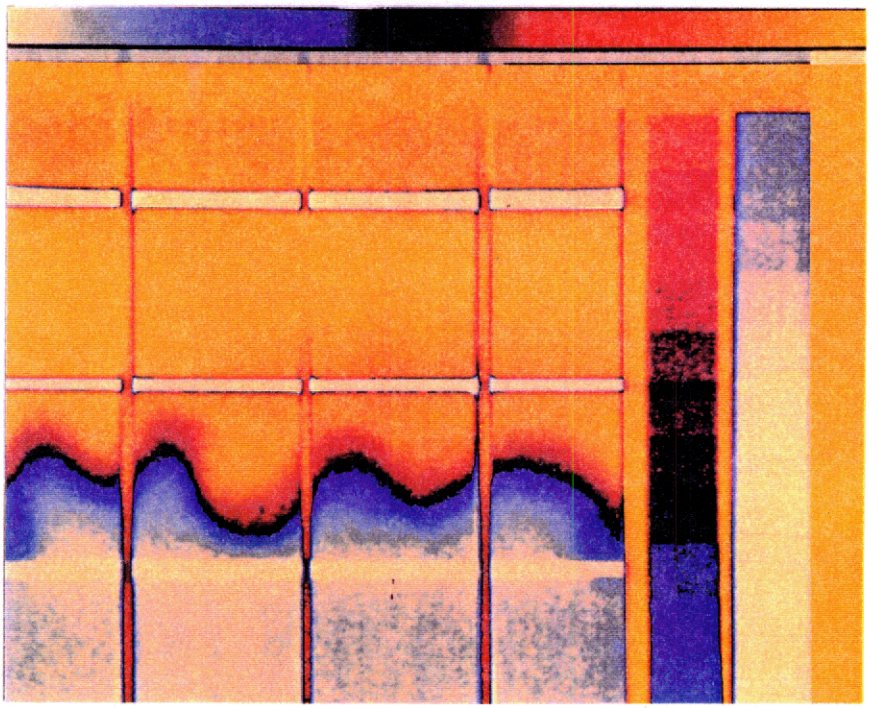

Fig. 17 (continued)

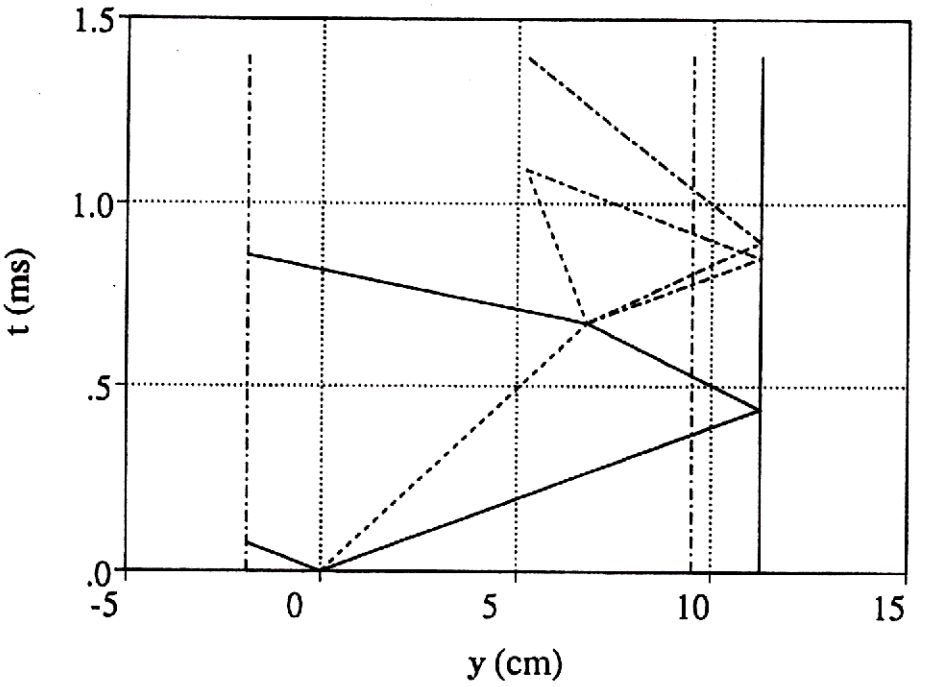

Fig. 18 $y - t$ diagram

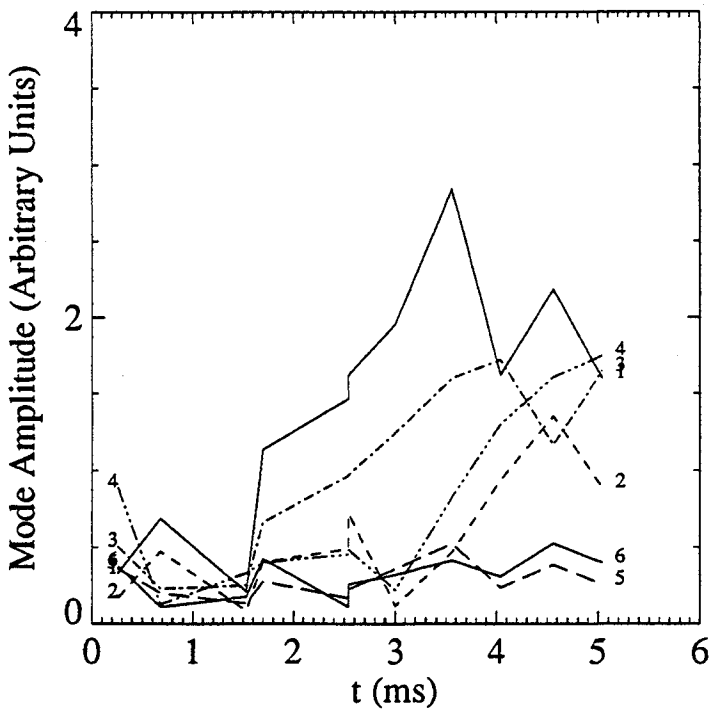

Fig. 19 Time Evolution of the Amplitude of the First Six Modes

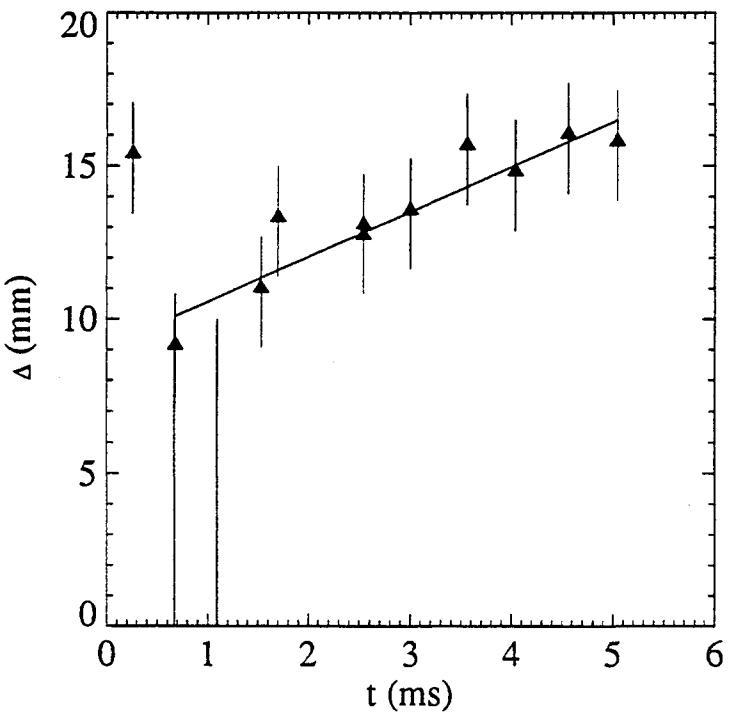

Fig. 20 Time Evolution of the Interface Thickness

EXPERIMENTAL INVESTIGATION OF RICHTMYER-MESHKOV INDUCED TURBULENT MIXING OVER LONG DISTANCES

L. Houas, I. Chemouni, A. Touat and R. Brun

Université de Provence, C.N.R.S. URA 1168, Laboratoire S.E.T.T., Milieux Hors d'Equilibre, Faculté Saint Jérôme, 13397 Marseille cedex 13, France.

ABSTRACT

Thickness measurements, by Schlieren visualizations, of initially plane interfaces between two gases of different densities submitted to shock acceleration and deceleration allow to obtain the thickness evolution of the turbulent mixing zone hence created. The effects of viscous boundary layer which stretch out and slow down the mixing region on the shock tube walls and consequently modify its thickening is pointed out. It is also shown that the rupture mode of the membrane, which initially separates the two gases, is more important than its effective thickness on the development of the mixing zone. It seems that the initial membrane has no more influence on the turbulent mixing zone development after deceleration by the first reflected shock.

INTRODUCTION

The elaboration of turbulent mixing codes able to describe correctly Rayleigh-Taylor or Richtmyer-Meshkov instability phenomena needs accurate experiments to determine and verify constants and other hypotheses made for their conception. These instabilities occur for example in laser implosion of deuterium-tritium fusion targets and the turbulent mixing which may occur is quite undesirable. In these experiments, even for initially small-scale perturbations of the interface (between deuterium-tritium and the shell material), the instability induces a rapid small scale turbulence behavior caused by the development of vorticity induced by the micro misalignment of pressure and density gradients.

For a better understanding of this, an important parameter to be determined is the thickness of the mixing region originated from the interaction of a shock and an interface initially separating two gases having different densities in the shock tube environment. As the turbulent energy developed in this phenomenon is strongly dependent on the Turbulent Mixing Zone (TMZ) thickness, the knowledge of the evolution of this parameter is of primordial importance.

In this experimental work, we try first to confirm if, as said by most scientists working on the subject, the evolution of the thickness of the TMZ obeys a power law, and secondly to determine if this power law evolution is not typical of experiments in shock tubes always influenced by viscous boundary layer effects. Furthermore, some Schlieren photograph thickness measurements have been performed with the same initial conditions than other experimental works[1,2] and comparisons on thickness growth are made.

EXPERIMENTAL APPARATUS

Experiments are carried out in a double diaphragm shock tube, 8.5 x 8.5 cm square cross section and about 9 m total length. The test section length is variable from 70 to 140 cm long. This allows to obtain the TMZ passage corresponding with the different possible positions of the Schlieren visualization windows (field of view is 75 mm diameter for figures 1, 3 and 7b and 85 mm square for figure 2) disposed on the shock tube lateral sides. To obtain very low Mach numbers, the driver gas is nitrogen and the pressure ratio is small. The other gases are air upstream, and helium, argon or carbon dioxyde downstream, which enables us to test three different mixing zones corresponding to three different Atwood number values. These gases are initially separated from air by one, two or four layers of a thin nitrocellulose membrane of about 0.5 µm thick which constitutes the initial interface. In all the experiments presented in this paper pressure on both sides of the membrane is the same and equal to 1 atmosphere. This is to eliminate initial perturbations of the interface which amplify considerably boundary layer effects and have the

consequence that the TMZ incident front is never planar[3]. Before introducing the test gases, a 10^{-2} torr vacuum is made on both sides of the membrane. Pumping and gas introduction without breaking the membrane are the tedious part of the experimental procedure.

When the shock wave breaks the membrane and accelerates the interface, a mixing zone between the two gases is rapidly created and thickens with time. Then, after a certain time, this shock reflects at the end of the shock tube and decelerates the mixing zone which, after a relatively short compression phase, thickens again with time. The study of this phenomenon is the aim of the present work.

The initial conditions of experiments presented in this work are sumarized in Table 1 where TSL represents the test section length, $Ms_{,i}$ and $Ms_{,t}$ the incident and transmitted shocks in Air and He, Ar or CO_2 respectively, At is Atwood number calculated just after the shock passage, the subscripts 1 and 2 corresponding to the first and the second shock interface interactions respectively and ΔU is the interface velocity jump.

RESULTS AND DISCUSSION

Schlieren Visualizations

Figure 1 shows several photos, stages of the Air/Ar TMZ, each one taken at different run. If we look at the good planarity of the TMZ presented on photo 1, we can say that the nitrocellulose membrane was initially planar. However, when the TMZ is considerably deformed by a complexe membrane rupture (see photos 2 and 3), this effect is easily observable and the TMZ thickness value can be estimated at the thinner part. The cylindrical waves observed on photo 5, just after the TMZ compression by the reflected shock , seem to result from the interaction of this shock with the TMZ wall toe shape, consequence of the viscous boundary layer in the case of a negatively bulged TMZ front. They are very well visible perhaps because we are close to the tailorised interface conditions with similar sound velocity on both sides of the TMZ. At last, we can notice that the double layer membrane is not completely destroyed by the reflected shock.

Figure 2 presents the difference between the shape of the TMZ as a function of the nature of the test gases at nearly the same abscissa and for a view including all the shock tube section. We observe the negatively bulged Air/He interface and the weak viscous boundary layer effects in the Air/Ar case. But the most important information that we can take out from these photos is the complex shape of the Air/CO_2 TMZ comparatively with the Air/Ar one in spite of the lower Air/CO_2 Atwood number value. This is perhaps due to the effect of the non monoatomicity of CO_2 and its influence on the viscous boundary layer development.

Figure 3a illustrates the difference on the structure of the TMZ just before and after its compression by the shock and figure 3b shows the undertailorised interface, going to the left, and the detachment of the membrane pieces which seem to continue in the same direction, to the right, because of their different inertia.

Turbulent Mixing Zone Thickness and Membrane Influence

Experimental results obtained for Air/He, Air/Ar and Air/CO_2 TMZ are presented on figures 4, 5 and 6 respectively. First, we can say that the TMZ thickness seems to grow quite linearly with t during a long time following its acceleration, even if, taking into account our error bars, one can fit the three accelerated TMZ thickness curves by a $t^{0.7}$ to $t^{0.9}$ power law. But in the deceleration phase (see fig. 4b and 6b) the TMZ thickness power law is more clearly observed. We can also see on figure 4 that it seems that, as previously observed by Brouillette et al.[2], Andronov measurements have been affected by wall effects. Unfortunately, it has not been possible to obtain more information on the Air/CO_2 TMZ evolution after interaction with the reflected shock (see figure 5) because of the complex three dimensional interaction occuring between this TMZ, the reflected shock and the boundary layer which is important in this case. Comparatively, the change in the TMZ thickening rate only appears for the decelerated Air/Ar TMZ (figure 6) in spite of very similar Atwood numbers. Thus, the Air/Ar couple of gases seems to be more interesting for the TMZ thickness study than the Air/CO_2 one for almost the same Atwood number.

To study the influence of the membrane, two other experiments have been undertaken :

- first, an Air/Air test which is presented in figure 7. We can observe on the (x,t) diagram that the "interface" is well tailorised as expected. The aspect of the nitrocellulose membrane illustrated on figure 7b, shows that our membrane rupture mode is not as clear as Brouillette[4]'s one because at x=298 mm the perturbation of the membrane is about 3.5 mm (2.5 mm for Brouillette) which is still not negligible.
- second, we have tested again Air/Ar TMZ but with two and four nitrocellulose film layers. Results are presented on figure 8 showing no significant difference in the thickness. We than believe that the membrane rupture mode has more influence on the TMZ thickening than its effective initial thickness (one layer membrane is less flat than two or four). Furthermore, after deceleration by the reflected shock, we see that there is no more influence of the initial membrane in spite of the presence of membrane pieces still visible on the photographs. So, it seems that for the second impact of the shock, the development of the TMZ becomes independent of the initial conditions of the membrane. However, as we can see on figure 3, we are in this case close to the tailorisation phase and the membrane particules, due to their different inertia, are separated from the TMZ which changes its direction of propagation.

Previous experiments made with higher Mach numbers and lower initial pressures[5], that corresponds to the presence of an important viscous boundary layer, have shown that the evolution of the TMZ thickness can be fitted by a t^{α} ($0.1 \leq \alpha \leq 1$) power law. Furthermore, it is known[6,7] that in the absence of viscosity, the TMZ thickness evolution is proportional to $t^{2/3}$. In the low Mach numbers experiments presented in this paper, the evolution of the accelerated TMZ thickness is more rapid than a $t^{2/3}$ law. This may indicate that viscous boundary layer effects are still important for these both high pressure and low Mach number experiments.

Turbulent Mixing Zone Thickness Growth Rates

Table 2 presents a comparison between TMZ thickness growth rates of present work and Andronov, Zaitsev[8] (from empirical formulae) and Brouillette results. We observe that if the TMZ thickness growth rate is calculated with average values for long time observations, our results are in good agreement with Brouillette's ones. Furthermore, if we have the opportunity to observe the TMZ development just after its compression by the reflected shock, and calculate its thickness growth rate for a short time afterwards (less than one hundred microseconds), we measure a very important TMZ thickness growth rate about 12 instead of 1.6. But these observations have to be confirmed by future work.

CONCLUSION

Shock tube experiments on Richtmyer-Meshkov mixing over long distances with low Mach number and high initial pressure, performed in order to decrease boundary layer effects, have been undertaken. They have indicated that the evolution of the thickness of a turbulent mixing region, originated from the shock-interaction interface between two gases having different densities, seems to be quite linear with time during an important phase after the passage of the incident shock and than obeys a power law. However viscous boundary layer effects can slow down the thicknening of the TMZ as observed, earlier, in high Mach number and low pressure experiments. One of the reasons of this growth rate thickness decrease is that viscous boundary layer, always present in shock tube experiments, contributes to stretch out the TMZ and thus its thickening increases less rapidly. But this explanation is not avalaible when the flow velocity is too small. About the membrane, we have shown that its effect seems to become negligible after the first reflected shock TMZ deceleration and that the same behaviour can be obtained for several layers.

AKNOWLEDGMENTS

This work is supported by the C.E.A. Centre d'Etudes de Limeil-Valenton on Contract N° 1253/S 766 II Y.

REFERENCES

1. V. A. Andronov, S. M. Bakhrakh, E. E. Meshkov, V. V. Nikiforov, A. V. Pevnitskii and A. I. Tolshmyakov, Sov. Phys. JETP 44:424, (1976).
2. M. Brouillette and B. Sturtevant, Physica D37, (1989).
3. L. Houas, A. Farhat and R. Brun, Phys. Fluids 31: 807, (1988).
4. M. Brouillette, P. H. D. thesis, California Institute of Technology, (1989).
5. L. Houas, I. Chemouni and A. Touat, to be published in the Proceedings of the 18th I.S.S.W. by Springer Verlag, K. Takayama Editor, Sendai, Japan, (1991).
6. G. I. Barenblatt, Non-Linear Dynamics and Turbulence, G. I. Barenblatt, G. Ioos and D. D. Joseph Editors, Pitman, Boston, (1983).
7. C. E. Leith, Report UCRL-96036, Lawrence Livermore National Laboratory, (1986).
8. S. G. Zaitsev, E. V. Lazareva, V. V. Chernukha and V. M. Belyaev, Sov. Phys. Dokl. 30: 579, (1985).

Table 1 : Initial conditions of present experiments

Test Gas	Air/He	Air/Ar	Air/CO_2
TSL (mm)	1238	955	955
Pressure (Atm)	1	1	1
$M_{S,i}$	1.28	1.30	1.30
$M_{S,t}$	1.08	1.31	1.31
At1	-0.76	0.13	0.17
At2	0.77	-0.10	-0.14
$\Delta U1$ (m/s)	177	129	134
$\Delta U2$ (m/s)	69	135.7	124

Table 2 : Turbulent Mixing Zone Growth Rate

Interface	Experiments	$M_{S,i}$	At1	At2	dL1/dt(m/s)	dL2/dt(m/s)	TSL(mm)
Air/He	Present Study	1.28	-0.76	0.77	4.5	10	1238
	Brouillette	1.32	-0.76	0.77	3.3	9.2	1090
	Zaitsev		-0.76	0.77	12.9	64.5	370
	Andronov	1.30	-0.76	0.77	11.4	77.0	169
Air/Ar	Present work	1.30	0.13	-0.1	3.6	1.6< <12	955
	Zaitsev		0.13	-0.1	25.7	3.7	370
Air/CO_2	Present work	1.30	0.17	-0.14	8.6	?	955
	Brouillette	1.32	0.17	-0.14	6.5		169
	Zaitsev		0.17	-0.14	32.9	3.7	370

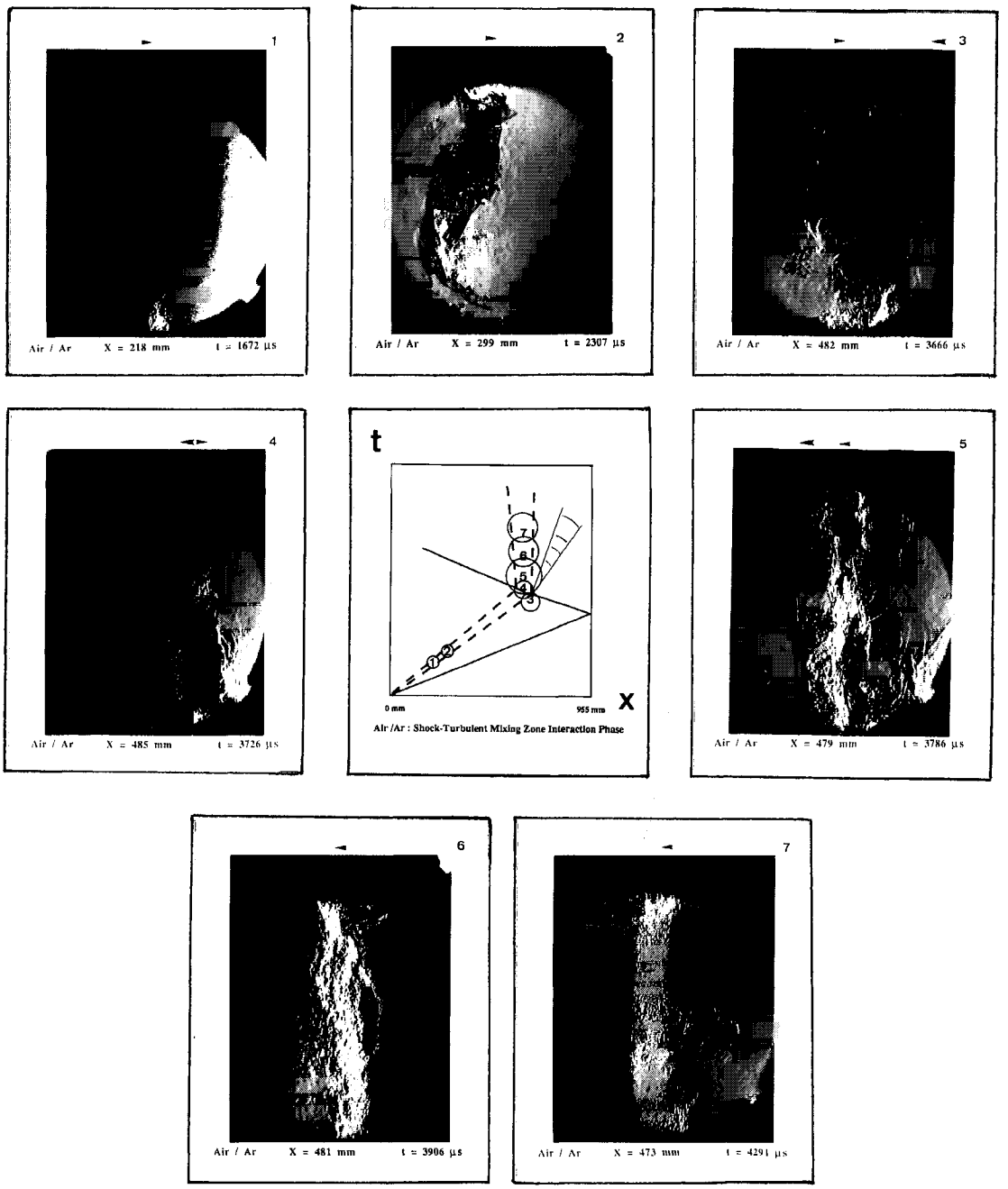

Figure 1 : The Air/Ar Turbulent Mixing Zone interaction with the reflected shock (membrane 2 x 0.5 µm)

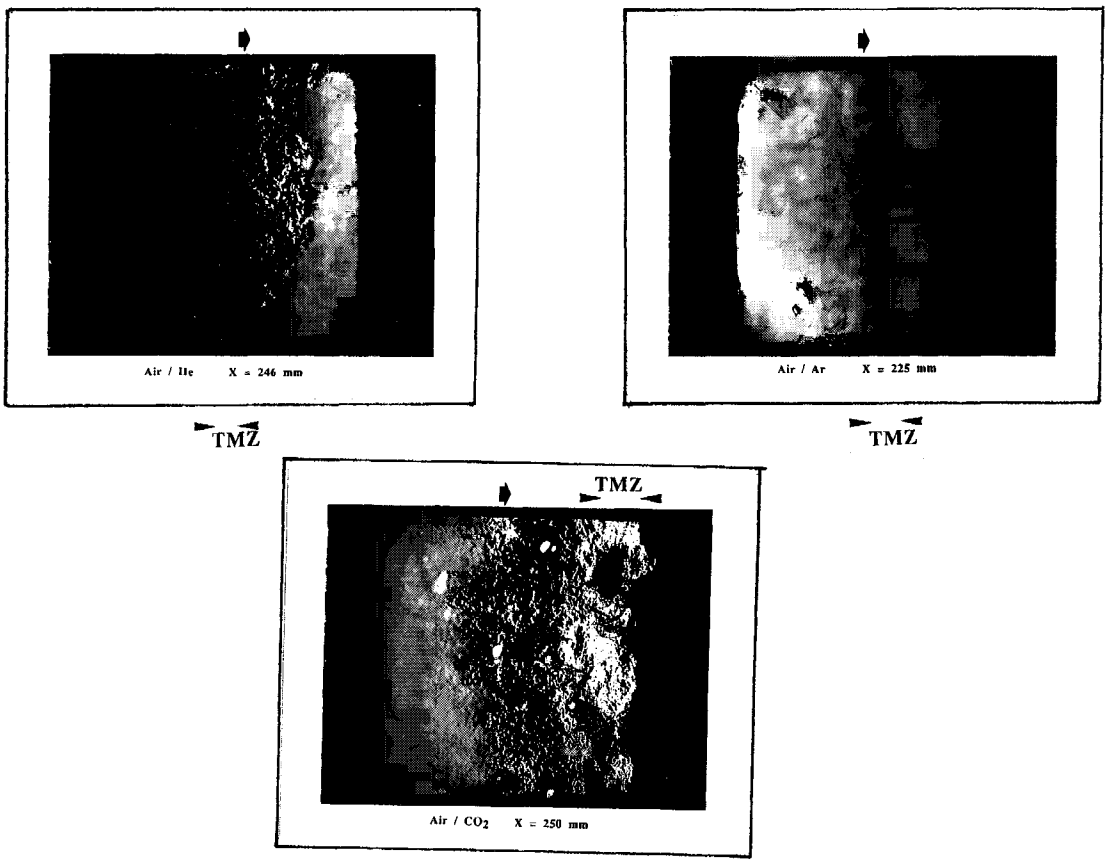

Figure 2 : Comparison of Air/He, Air/CO_2 and Air/Ar Turbulent Mixing Zones (membrane 0.5 µm)

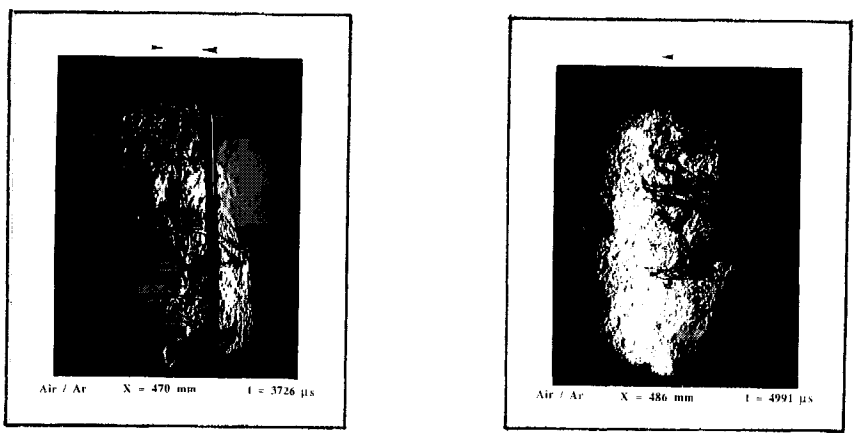

Figure 3 : Air/Ar Turbulent Mixing Zone during and after interaction with the reflected shock (membrane 0.5 µm)

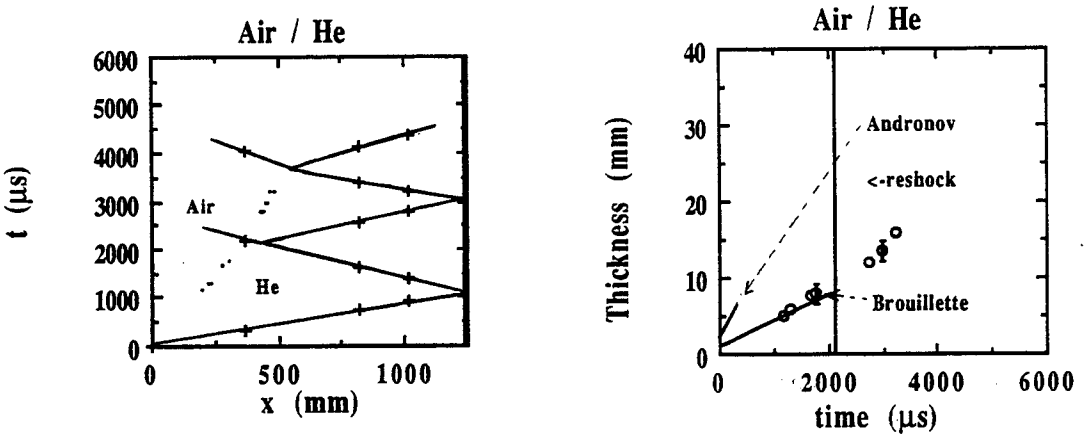

Figure 4 : Air/He (x-t) diagram and Turbulent Mixing Zone thickness evolution (membrane 0.5 µm)

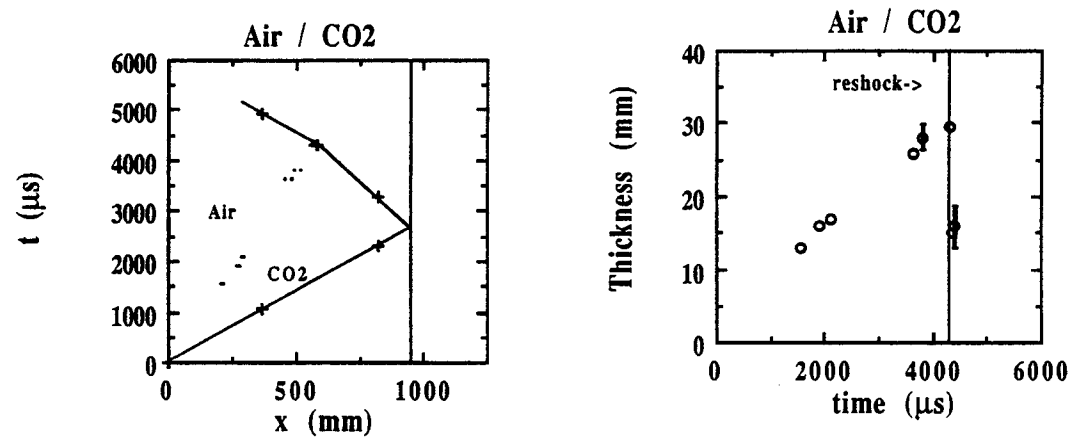

Figure 5 : Air/CO_2 (x-t) diagram and Turbulent Mixing Zone thickness evolution (membrane 0.5 µm)

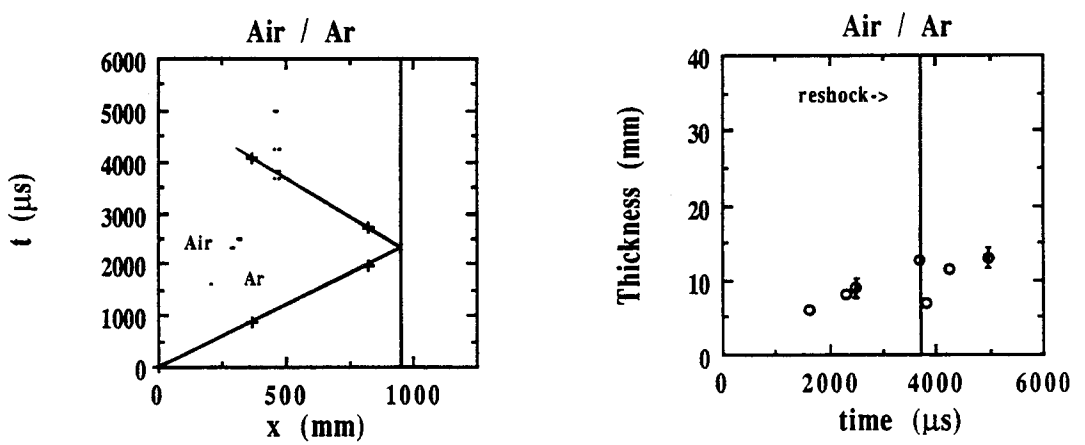

Figure 6 : Air/Ar (x-t) diagram and Turbulent Mixing Zone thickness evolution (membrane 0.5 µm)

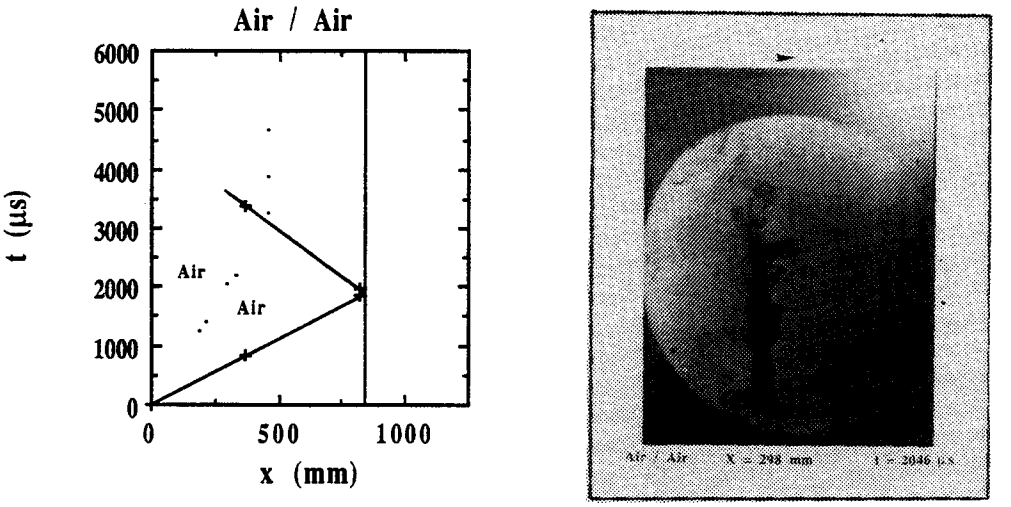

Figure 7 : Air/Air (x-t) diagram and Schlieren photograph of the membrane (Msi = 1.30; membrane 0.5 µm)

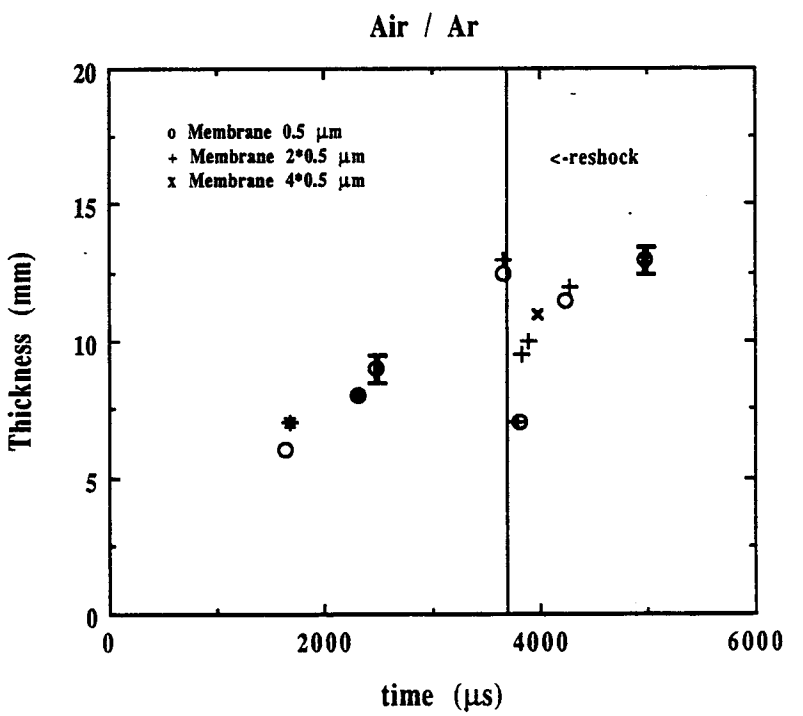

Figure 8 : Air/Ar Turbulent Mixing Zone thickness evolution for different membranes : 0.5; 2 x 0.5 and 4 x 0.5 µm

DESIGN CALCULATIONS FOR A NOVA MIX EXPERIMENT*

Karnig O. Mikaelian
Lawrence Livermore National Laboratory
Livermore, California

This is a summary of code calculations we carried out to design a mix experiment with a radiatively driven target on Livermore's NOVA laser. The target is a double layer pill about 1 mm in diameter and 300 μm thick: 100 μm of Be on 200 μm of SiO_2 aerogel. The drive generates a Mach 25 shock in the Be ablator whose initial density is about 2 g/cc. The shock reaches the Be/SiO_2 interface in about 4 ns and compresses the low density (ρ=0.2 g/cc) aerogel by a factor of about 6. This 1D motion, calculated with a Lagrangian code, is shown in Fig. 1a as position vs. time. The density profile is sketched in Fig. 1b where we see the ablation surface, the rarefaction moving back into Be, the shocked Be/SiO_2 interface, and the shock itself proceeding thru the aerogel. It breaks thru the backside of aerogel in 6 ns, so that the total time for the laser drive is about 10 ns.

2D calculations with the same Lagrangian code are shown in Fig. 2 where we plot $|\eta|/\sqrt{2}$ or the rms deviation from a planar interface for perturbations of wavelength λ=50 μm at the Be/SiO_2 interface (η denotes the amplitude of the cosine wave perturbations). The three curves correspond to η_0=1, 4 and 8 μm. They are compressed as the shock crosses the interface, they change phase and grow. The growth will be measured by "face-on" X-ray radiography with a backlighter as a source and a 22× microscope focusing the transmitted X-rays onto a streak camera. We also expect to field a "side-on" diagnostic to measure the bulk motion of the target and perhaps the extent of the perturbations (or, more ambitiously, the width of the mixing layer) across the Be/SiO_2 interface.

The Lagrangian code bowties when the perturbations grow too large and therefore we switched to the Lagrangian/Eulerian hydrocode we have used in the past to simulate CalTech shock tube experiments. For the present NOVA experiment we have considered a variety of initial perturbations; examples are shown in Fig. 3. The vertical scale in Figures 3-6 is 100 μm; the horizontal scale changes depending on the type of the perturbation.

---

*Work performed under the auspices of the U.S. Department of Energy by Lawrence Livermore National Laboratory under contract W-7405-Eng-48.

We expect our 2D code to be adequate for relatively large scale perturbations like the first five examples shown in Fig. 3. The last one showing very small random perturbations at the interface cannot possibly remain 2D, although we have carried out several such simulations to test their sensitivity to zoning, to initial conditions, etc. We found a very weak dependence on initial conditions. These results were presented at the Workshop along with isodensity contours showing the feed-thru of long wavelength perturbations from the interface to the ablation surface. For lack of space here we will show only the λ=50 μm, η_0=8 μm case (Fig. 4); the λ=50 μm, η_0=7 μm next to λ=100 μm, η_0=14 μm case (Fig. 5); and the case of a λ=50 μm, η_0=7 μm perturbation separated by a flat region from a two-wavelength composite perturbation of λ=50 μm, η_0=7 μm plus λ=20 μm, η_0=-7 μm (Fig. 6).

The times indicated above each frame in Figs. 4-6 refer to the times in nanoseconds after the shock hits the interface. In Fig. 4 the extra line (initially at 5.01 cm) is an imaginary tracer interface in the middle of the aerogel. The backside of the aerogel, on the other hand, comes into view in the last snapshop (t=6 ns) in all cases. In Fig. 5 note that the backside under the λ=50 μm section of the interface is smooth while the backside under the λ=100 μm perturbation is itself perturbed, revealing how long wavelength perturbations feed thru from the interface in both directions: towards the ablation surface as well as towards the backside.

Another effect seen in Fig. 5 is the saturation of the 50 μm wavelengths. The linear growth depends only on η/λ which is the same left and right: 7μm/50μm=14μm/100μm. Note that the perturbations are about the same at t=2, 3 and 4 ns but subsequently the λ=50 μm perturbations on the left side saturate while the λ=100 μm perturbations on the right side keep growing. There is some "nearest neighbor" interaction in the middle section of the target where the λ=50 μm and the λ=100 μm components meet. The flat middle section in Fig. 6 is intended to suppress such nearest neighbor interactions: compare the evolution of single wavelength perturbations on the lhs of Fig. 6 with that of a two-wavelength (50 μm+20 μm) perturbation on the rhs.

Assuming that the backlighter is uniform across the whole 1 mm diameter of the target we believe that such "left-right" comparisons in each shot are most promising. We hope that the experimental data will be available by the 4th Workshop in 1993.

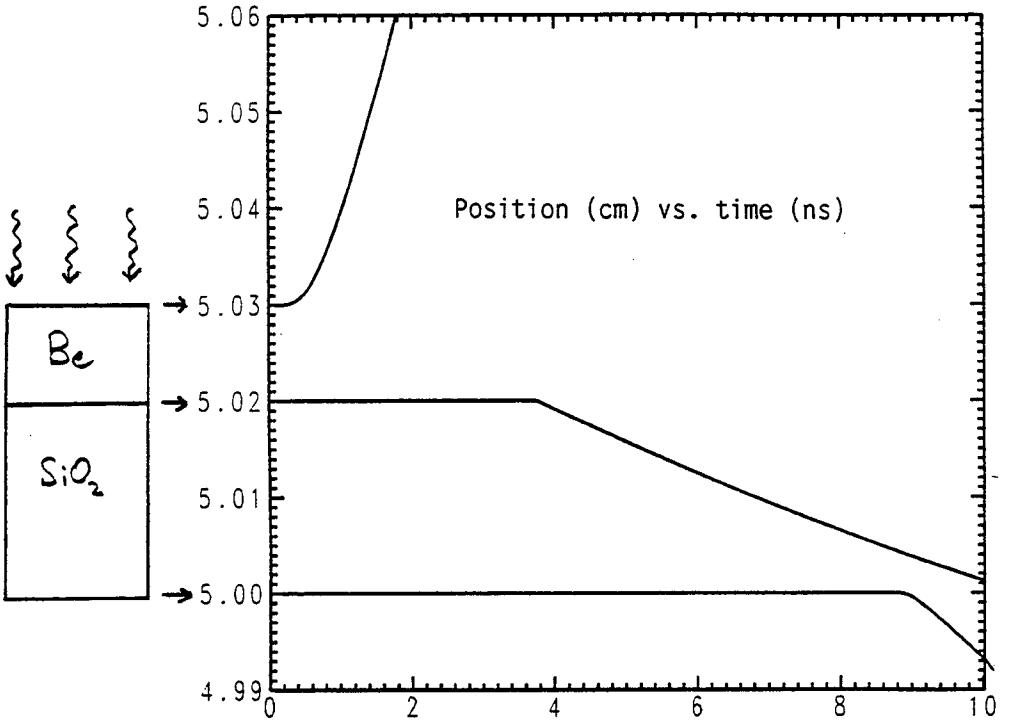
Position (cm) vs. time (ns)
Be
SiO2
5.06
5.05
5.04
5.03
5.02
5.01
5.00
4.99
0
2
4
6
8
10

Fig. 1a

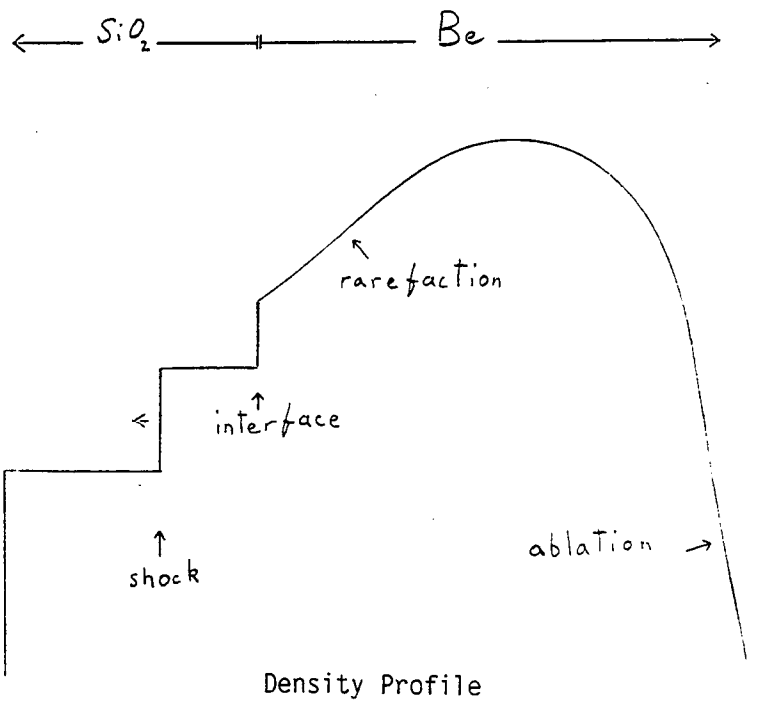
SiO2
Be
rarefaction
interface
shock
ablation
Density Profile

Fig. 1b

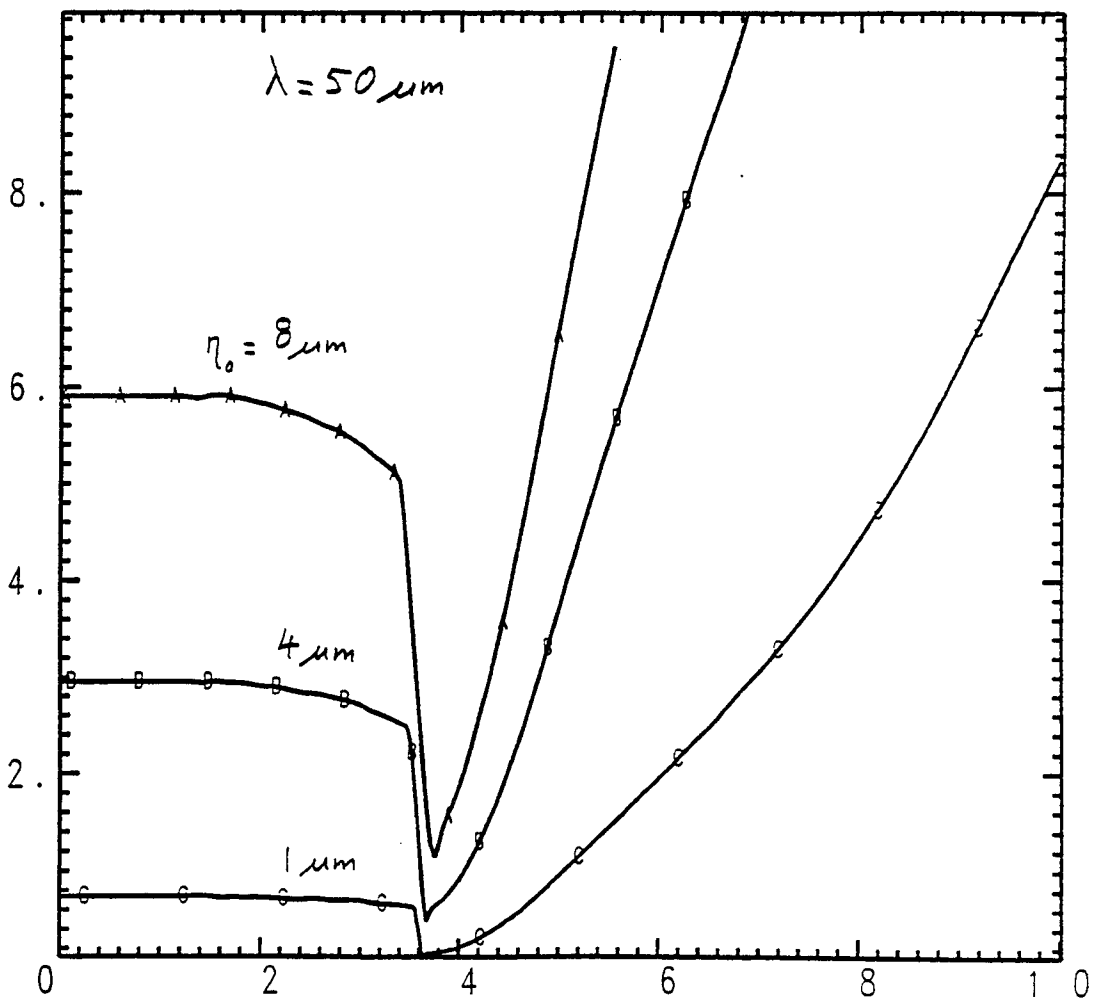
λ = 50 μm
η₀ = 8 μm
4 μm
1 μm
8.
6.
4.
2.
0
2
4
6
8
10
RMS Position (microns) vs. time (ns)

Fig. 2

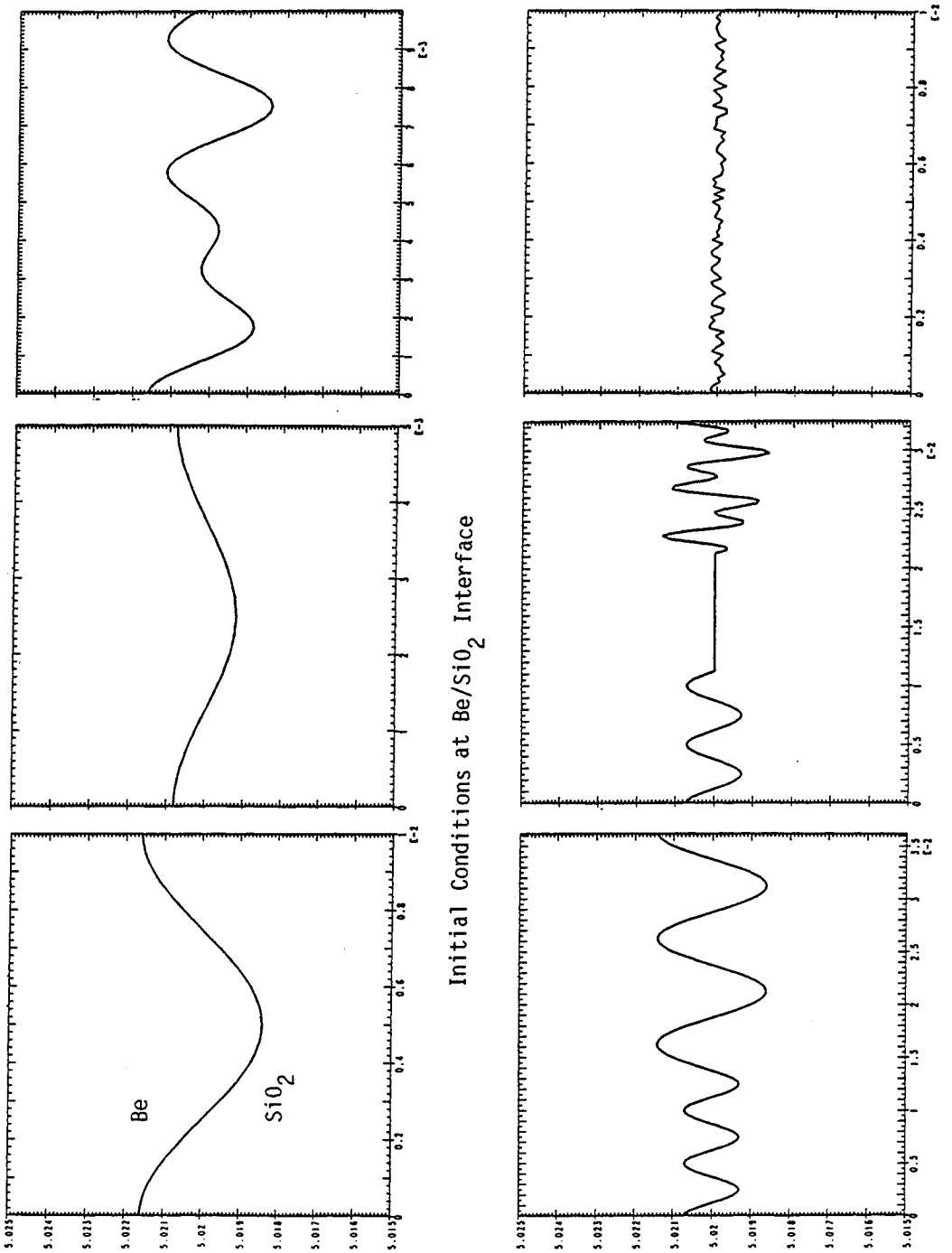

Fig. 3

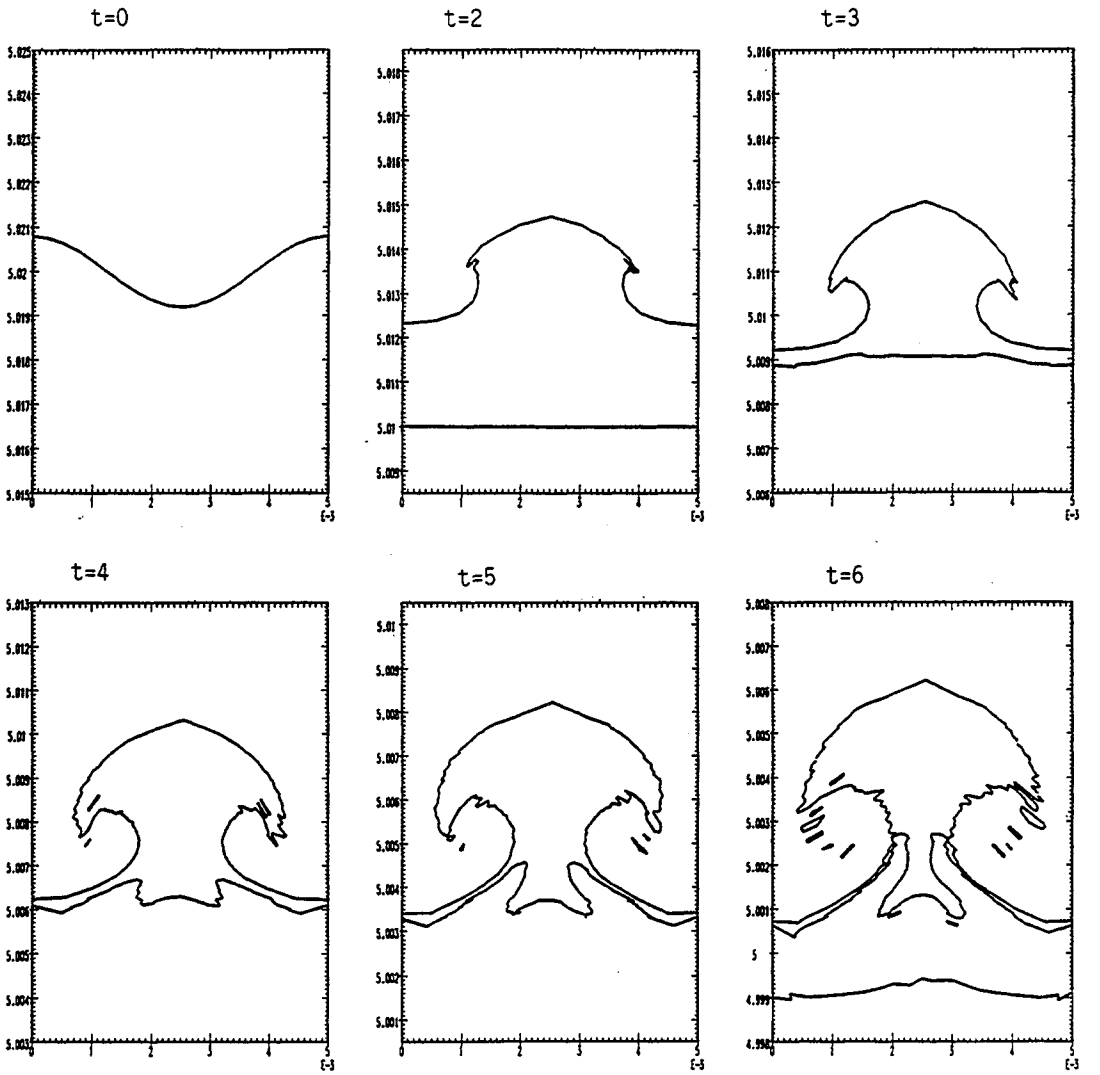

Fig. 4

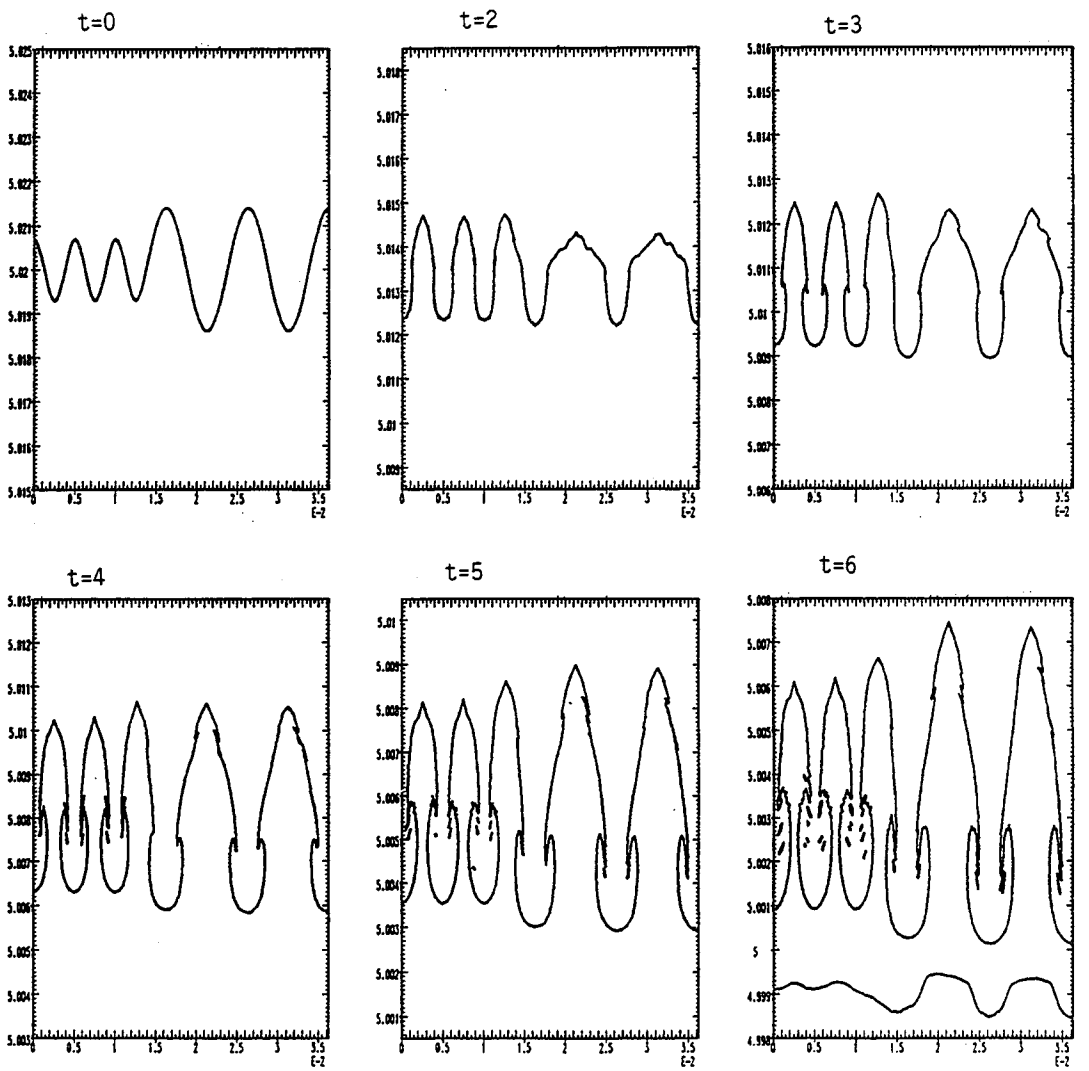

Fig. 5

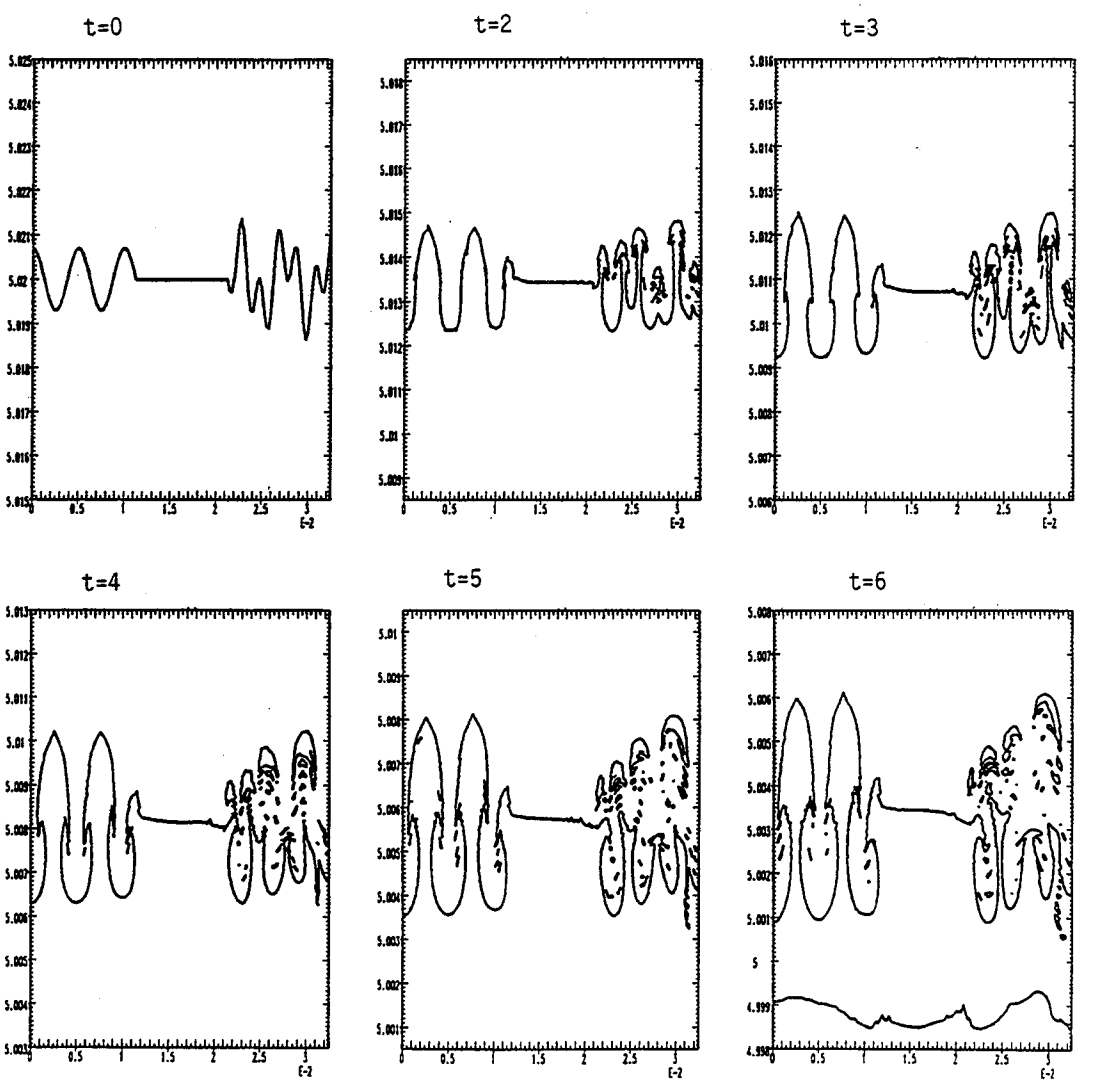

Fig. 6

A NUMERICAL STUDY OF RICHTMYER-MESHKOV INSTABILITY IN CONTINUOUSLY STRATIFIED FLUIDS

Thu Pham and Dan Meiron
Applied Mathematics
California Institute of Technology, Pasadena, CA 91125

ABSTRACT

Theory and calculations are presented for the evolution of Richtmyer-Meshkov instability in continuously stratified fluid layers. The initial acceleration and subsequent instability of the fluid layer are induced by means of an impulsive pressure distribution. We calculate the subsequent dynamics of the fluid layer numerically using the incompressible equations of motion. Both initial conditions having single scale perturbations and multiple scale random perturbations are considered. It is found that the growth rates for Richtmyer-Meshkov instability of stratified fluid layers are substantially lower than those predicted by Richtmyer for a sharp fluid interface with an equivalent jump in density. The initial behavior is linear over a time equivalent to the traversal of several layer thicknesses. It is observed that the nonlinear development of the instability results in the formation of plumes of penetrating fluid. Late in the process, the initial momentum deposited by the incoming shock is primarily used in the internal mixing of the layer rather than in the overall growth of the stratified layer. At intermediate time, there is some evidence for scaling behavior in the width of the mixing layer for the multiple scale random perturbations, but not for the single scale perturbations. The time variation of the layer thickness differs from a scaling hypothesis based on the self-similarity ideas of Barenblatt even at low Atwood ratio, presumably because of the inhomogeneity and anisotropy due to the excitation of vortical plumes.

THEORETICAL CONSIDERATIONS

In this study, we hope to gain some insights into the long time behavior as well as the effect of the density gradient on the growth rate of Richtmyer[1]-Meshkov[2] instability in stratified fluids. Our approach is to carry out a full 2-D numerical simulation of the time dependent incompressible equations. We model the initial effect of compressibility by approximating the action of an incoming shock as an impulsive pressure using an incompressible impulsive theory. This idea was used by Saffman and Meiron[3] to study the kinetic energy deposited by an impulse at a layer of stratified fluid with a weak density perturbation in the transverse direction to the flow. This incompressible approximation is a reasonable one for an impulsive acceleration induced by a weak shock, since the induced velocity is subsonic. Moreover, one expects that for such weak shocks, the effect of the compressibility is limited to some initial modification of the density distribution, since the residence time of the shock in the nonuniform region is very small compared to the characteristic time for the evolution of the instability. A justification for the use of the incompressible impulsive approximation as well as an assessment of its range of validity is made by examining the solution of a planar shock passing a region of non-uniform density distribution using one-dimensional gas dynamics. Details of this study are presented in the thesis of Pham[4]. In this section, we will only summarize the relevant theory governing the instability.

Saffman and Meiron[3] modeled the motion of a perturbed planar interface undergoing a shock-induced acceleration as one generated by the impulsive motion of the fluid with a velocity V directed parallel to the undisturbed density gradient. Since the fluid is incompressible, this motion induces instantaneously a pressure field $P(x,y)\delta(t)$, where $\delta(t)$ is the delta function, and there exists a balance between only the pressure gradient and the acceleration (viscous and inertial terms are negligible). Note that the function $P(x,y)$ has units of pressure times time.

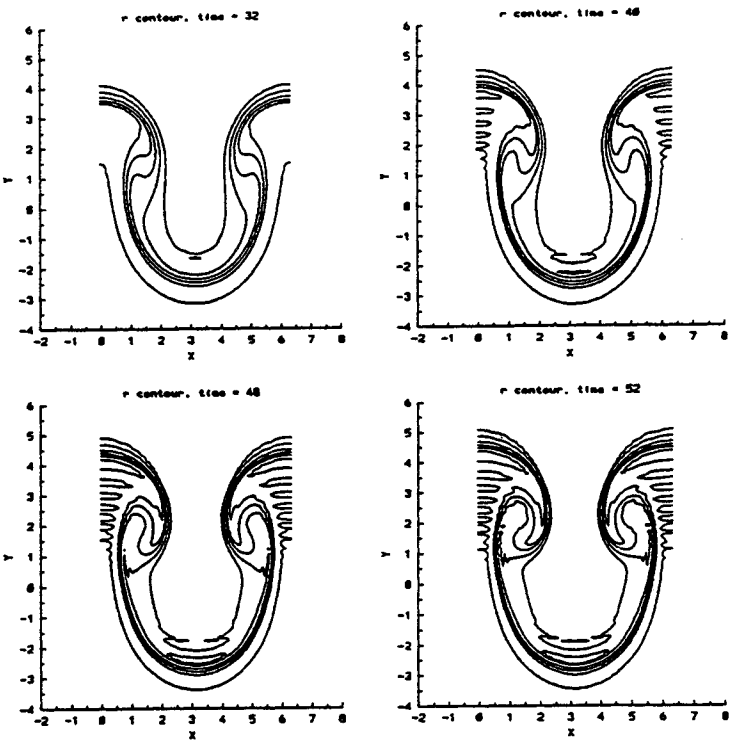

Figure 1. Time evolution of the density contours for the single scale profile with $L = 1.0$, $A = -0.5$, $\epsilon = 0.5$. Shown here are times $t = 32, 40, 48, 52$. The contours are at $\rho = 0.26$, 0.3, 0.4, 0.5, 0.6, 0.74 in that order from top to bottom of each figure.

Let y be the vertical axis parallel to the undisturbed density gradient, and x be the horizontal axis. The upper fluid has density ρ_+, and the lower fluid has density ρ_- as $y \to \pm\infty$ respectively. Integrating the momentum equations, one obtains the equations for the induced initial velocities,

$$u = -\frac{1}{\rho_0}\frac{\partial P}{\partial x}H(t),$$
$$v = -\frac{1}{\rho_0}\frac{\partial P}{\partial y}H(t), \tag{1}$$

where $H(t)$ is the Heaviside function, and ρ_0 is the density distribution at the time $t = 0^-$. Using the continuity equation, the impulsive pressure is determined by

$$\frac{\partial}{\partial x}\left(\frac{1}{\rho_0}\frac{\partial P}{\partial x}\right) + \frac{\partial}{\partial y}\left(\frac{1}{\rho_0}\frac{\partial P}{\partial y}\right) = 0. \tag{2}$$

The boundary conditions are

$$\frac{\partial P}{\partial y} \to -\rho_+ V, \quad as \quad y \to +\infty,$$
$$\frac{\partial P}{\partial y} \to -\rho_- V, \quad as \quad y \to -\infty. \tag{3}$$

Table 1

Ratio of the initial Richtmyer growth rate over that of numerical simulation.

A	$\epsilon \Downarrow$ L $\Rightarrow$	10.0	1.0	0.1	0.01	0.001
± 0.2	0.01	15.026	2.1280	1.1023	1.0283	1.0187
	0.1	15.027	2.1304	1.1052	1.0163	1.0125
	1.0	15.118	2.3657	1.3626	1.1503	1.0971
	10.0	19.359	10.519	7.5656	7.5863	7.6016
± 0.5	0.01	14.363	2.0371	1.0886	1.0266	1.0187
	0.1	14.364	2.0365	1.0915	1.0147	1.0127
	1.0	15.066	2.2155	1.3451	1.3329	1.3326
	10.0	18.505	9.9856	6.9315	6.9807	6.9815
± 0.8	0.01	12.776	1.8298	1.0580	1.0228	1.0187
	0.1	12.776	1.8294	1.0608	1.0153	1.0590
	1.0	12.842	2.0520	1.3040	1.2310	1.1956
	10.0	16.554	8.8304	5.6359	6.0836	6.0445

In this study, the solution of the incompressible impulsive model is used as the initial condition for a fully nonlinear simulation of the finite-amplitude stage of the instability. In the subsequent motion, the flow is governed by the two dimensional unsteady Navier-Stokes equations,

$$\frac{\partial \rho}{\partial t} + \mathbf{u} \cdot \nabla \rho = 0, \tag{4}$$

$$\rho \frac{\partial \mathbf{u}}{\partial t} + \rho \mathbf{u} \cdot \nabla \mathbf{u} = -\nabla P + \mu \nabla^2 \mathbf{u}, \tag{5}$$

$$\nabla \cdot \mathbf{u} = 0, \tag{6}$$

where μ is the viscosity of the fluid. The above equations are solved subject to the boundary conditions,

$$\mathbf{u} \rightarrow (0, V) \quad as \quad y \rightarrow \pm\infty, \tag{7}$$

$$\rho \rightarrow \rho_{\pm} \quad as \quad y \rightarrow \pm\infty, \tag{8}$$

and $\mathbf{u}$, and ρ are periodic in x, with period $2\pi/k$. Since we are interested in the inviscid regime, the magnitude of the viscosity used is very small. We scale the above equations using the following characteristic quantities

$$u_c = |V|, \quad l_c = L, \quad p_c = \rho_c u_c^2,$$

$$\rho_c = \rho_+ + \rho_-, \quad \text{and} \quad t_c = \frac{L}{u_c}. \tag{9}$$

Here L is a characteristic layer thickness. In both cases, the equations have the same forms as shown in equations (4)-(6), except that in the non-dimensional momentum equation the viscosity μ in equation (5) is replaced by the factor Re^{-1}, where $Re = \rho_c u_c l_c / \mu$ is the Reynolds number. In the actual simulations, we choose $V = -1$, $k = 1$, and $\mu = 10^{-6}$.

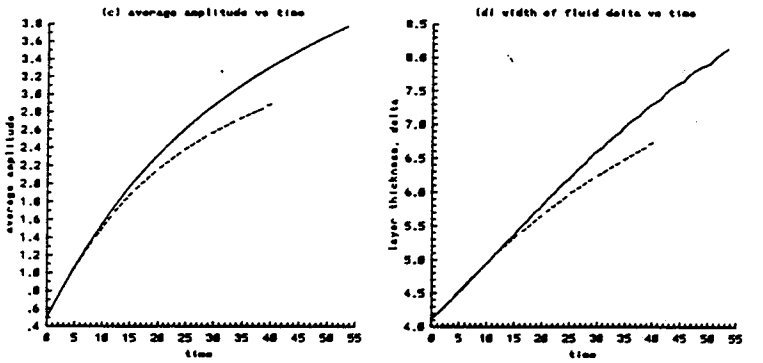

Figure 2. Time evolution of the average quantities for the single scale profile with $L = 1$, $A = -0.5$, $\epsilon = 0.5$, $0, t < 40$. The solid lines correspond to the numerical computation; the dashed lines correspond to the prediction of linear theory. Shown here are the average amplitude, and the width of the density layer vs t.

NUMERICAL ALGORITHM

Due to the sharp gradient of the initial density profile in some parts of the flow domain, we use a non-uniform grid in a moving frame in order to resolve this region. We use a finite difference discretization with a staggered grid and with the primitive variables as the unknowns. The system of equations is discretized in time with an implicit Crank-Nicolson scheme applied to all terms. Central differencing is used to compute spatial derivatives. The resulting nonlinear set of equations is solved by an iterative technique known as the artificial compressibility method. To solve the resulting nonlinear equations we use an iterative scheme proposed by Soh and Goodrich[5] with a modification to include the density equation.

RESULTS FOR SINGLE SCALE PERTURBATIONS

In order to characterize our results, we consider two kinds of density averages quantities for the density, one in the y-direction, and the other in the x-direction. The average in the y-direction is defined as follows,

$$\bar{\rho}_y(x) \equiv \frac{2Y\rho_+ - \int_{-Y}^{Y} \rho(x,y)dy}{\rho_+ - \rho_-} - Y, \tag{10}$$

where Y is the maximum value of y used in the calculation, and ρ_+, ρ_- are the uniform densities as $y \longrightarrow \pm\infty$ respectively.

Equation (10) is a kind of area average of the density. The expression (10) for $\bar{\rho}_y(x)$ defines an average interface for the stratified layer. It gives the exact functional form of a sharp interface $y = f(x)$ which separates two regions of uniform density ρ_+, and ρ_-. Hence, this definition is convenient for the comparison of the numerical results to those predicted by the Richtmyer theory[1], since an average amplitude based on $\bar{\rho}_y(x)$ can be defined as,

$$a \equiv \frac{\max(\bar{\rho}_y(x)) - \min(\bar{\rho}_y(x))}{2}. \tag{11}$$

The growth of the instability is characterized by the time derivative of a.

The second density average is defined as follows,

$$\bar{\rho}_x(y) \equiv \frac{1}{2\pi}\int_0^{2\pi} \rho(x,y)dx, \tag{12}$$

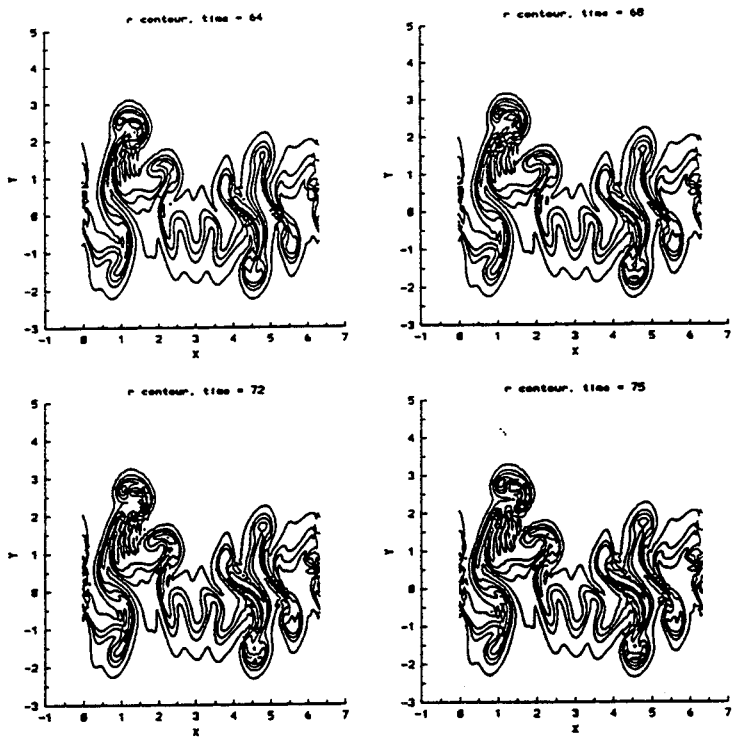

Figure 3. Time evolution of the density contours for a random initial condition with $A = -0.2$. Shown here are $t = 64, 68, 72, 75$. The contours are at $\rho = 0.41, 0.45, 0.50, 0.55, 0.59$.

which is the standard area average. From $\bar{\rho}_x(y)$, we can define a width δ of the stratified layer. Let y_+ be the position of $\bar{\rho}_x(y)$ such that,

$$y_+ \equiv \min\left(\|\bar{\rho}_x(y) - \rho_+\| \leq d\|\rho_+ - \rho_-\|\right),$$

where d is some specified percentage. Similarly, let y_- be such that,

$$y_- \equiv \max\left(\|\bar{\rho}_x(y) - \rho_-\| \leq d\|\rho_+ - \rho_-\|\right).$$

Then the width of the density layer is defined as,

$$\delta \equiv y_+ - y_-. \tag{13}$$

In order to understand the growth of the instability, we consider two different kinds of initial density distributions. The first one which we term the single scale perturbation is given by

$$\rho(x, y) = \frac{1}{2}\left[1 + A\tanh\left(\frac{1}{L}(y - \epsilon\cos x)\right)\right], \tag{14}$$

where A is the Atwood number, and L is the characteristic thickness of the density layer. For $L > 0$, equation (14) describes a continuously stratified interface. As L approaches zero, the layer reduces to a sharp interface with ϵ as the amplitude of the perturbation. Richtmyer[1] considered the instability of a sharp interface with an infinitesimal perturbation subject to an impulsive acceleration. With the density profile (14), we can justify our numerical results when L, and ϵ are taken to zero, in that order, for a sharp interface with infinitesimal

perturbations. Besides this consistency check, this profile is convenient for the study of the nonlinear effects in the growth of the instability of a highly perturbed interface.

In view of a more realistic perturbation which occurs in experimental studies, we would like to have some randomness as well as a range of wave numbers present in our initial distribution. To accomplish this, we replace $\cos(x)$ in equation (14) by the sum,

$$\sum_{k=1}^{N} e^{-\varsigma(k-1)^2} \left(\frac{1}{2} - r_{k1}\right) \cos(kx), \tag{15}$$

or

$$\sum_{k=1}^{N} e^{-\varsigma(k-1)^2} \left\{ \left(\frac{1}{2} - r_{k1}\right) \cos(kx) + \left(\frac{1}{2} - r_{k2}\right) \sin(kx) \right\}, \tag{16}$$

where k is the wave number, r_{k1}, r_{k2} are random numbers with $0 \leq r_{k1}, r_{k2} \leq 1$, and ς is a controlling parameter for the spread of the wave number distribution.

Shown in Figure 1 are the density contours for a typical single scale run. Depictions of the relevant average quantities may be found in the thesis of Pham[4]. Our results are qualitatively similar to those seen in numerical simulation by Mikaelian[6] and Youngs[7] which include effects of compressibility. In general, for small A, and ϵ, the speeds of the bubble and the spike are equal and opposite. The light fluid penetrates the heavier fluid at the same speed as the heavy fluid falls into the lighter one. As time increases, the speeds decrease at roughly the same rate. For higher A, and ϵ, initially, the spikes and the bubbles have approximately the same speeds. The nonlinearity, however, causes the bubbles to decelerate much faster than the spikes. For small ϵ, the roll-up is delayed in time. For larger ϵ, the nonlinearity sets in faster, and the rolling up of the heavy fluid causes the pocket of the light fluid to widen horizontally.

In Table 1 we compare the Richtmyer expression for the growth rate of a discrete interface with the growth rate obtained from our simulation at various values of A, ϵ, and L. We tabulate the ratio of the Richtmyer result to the observed growth rate. In general, since less kinetic energy is generated when the layer is thick the ratios have a lower bound of one[3]. In calculating the equivalent Richtmyer growth rate for a continuous interface,

$$a = a_0, \quad \frac{da}{dt} = k v_0 a_0 A, \tag{17}$$

we use the initial average amplitude defined in equation (2) as a_0, the velocity V of the flow at infinity as the jump velocity v_0 of the interface after the impulsive acceleration, and $k = 1$.

For a given Atwood ratio, A, as L approaches zero, *i.e.*, a sharp interface, the ratios approach the lower bound of 1 except for the cases with $A = -0.8$, and $\epsilon = 10.0$, in which there is a minimum around $L = 0.1$. This latter case is, of course a large deformation. For small perturbation amplitude ϵ, the limit approaches 1.0 from above as $L \to 0$. For $L < 0.1$, the ratios of the growth rate do not vary significantly. A more significant increase is seen for $L > 0.1$ For a thicker interface $L = 1.0$ to $L = 10.0$, the ratios continue to grow to $O(10)$. Thus our numerical results are consistent with the predictions of the Richtmyer theory for a sharp interface. They also confirm the fact that by decreasing the density gradient, one can reduce the growth of the Richtmyer-Meshkov instability as predicted by the linear theory of Saffman and Meiron[3]. The results also agree qualitatively with the experiments of Brouillette[8] in which he observes a tenfold reduction in the growth rate for a ratio of wavelength to thickness of roughly 3. Thus, for a continuous interface, the Richtmyer formula (17) overpredicts the growth rate.

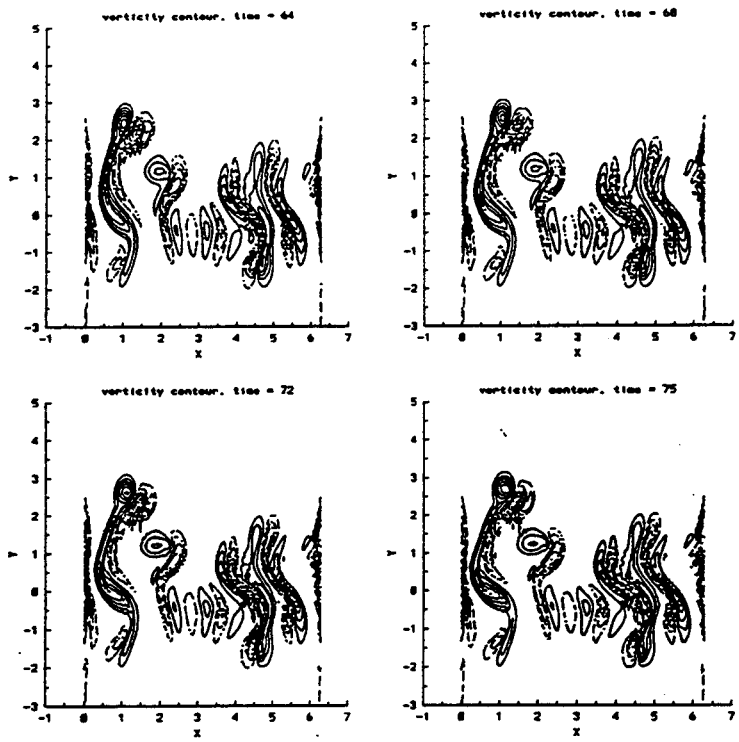

Figure 4. Time evolution of the vorticity contours for a random initial condition with $A = -0.2$. Shown here are $t = 64, 68, 72, 75$. The minimum and maximum vorticities are respectively: $(t = 64)$ -0.6 to 0.3, $(t = 68)$ -0.65 to 0.4,$(t = 72)$ -0.6 to 0.6,$(t = 64)$ -0.6 to 0.7. Negative values are indicated by dashed lines.

The only source of energy for the flow is due to the initial impulsive acceleration, and since we have a small kinematic viscosity $\mu = 10^{-6}$ in the simulation, energy is approximately conserved. Due to this constancy of the total kinetic energy, and its dependence on the initial wavelength in the case of a sharp interface, it has been argued by Brouillette and Sturtevant[9] that the Richtmyer-Meshkov instability will not approach a self-similar asymptotic limit. Indeed, we see no evidence for any universality in the behavior of various quantities such the layer width at late times. The time asymptotic limits of a and δ depend on both A and ϵ in some complicated way.

Since the instability is weak, it can be modeled by fixing the initial flow field after the impulsive acceleration, and then using this flow field to evolve the density. This essentially corresponds to the use of linear theory. A comparison of the full simulation with the predictions of linear theory are shown in Figure 2. Linear theory accurately describes the growth of the layer at early times For example, up to time $t = 15$ for the case shown, the differences in the predicted average amplitude a, and the layer width δ relative to the actual calculation are small, 4.43%, and 0.62% respectively. This agreement holds over a time interval which is equivalent to travel of the layer over a distance comparable to $2\frac{1}{2}$ to 3 layer widths. At lower Atwood ratio, this agreement extends for even longer times. The roll-up is more compact and symmetric for the linear case. This results in a more symmetric form for the average quantities $\bar{\rho}_x(y)$. The widening of the light fluid globule is not seen and thus a sharper lower peak of $\bar{\rho}_y(x)$ is observed.

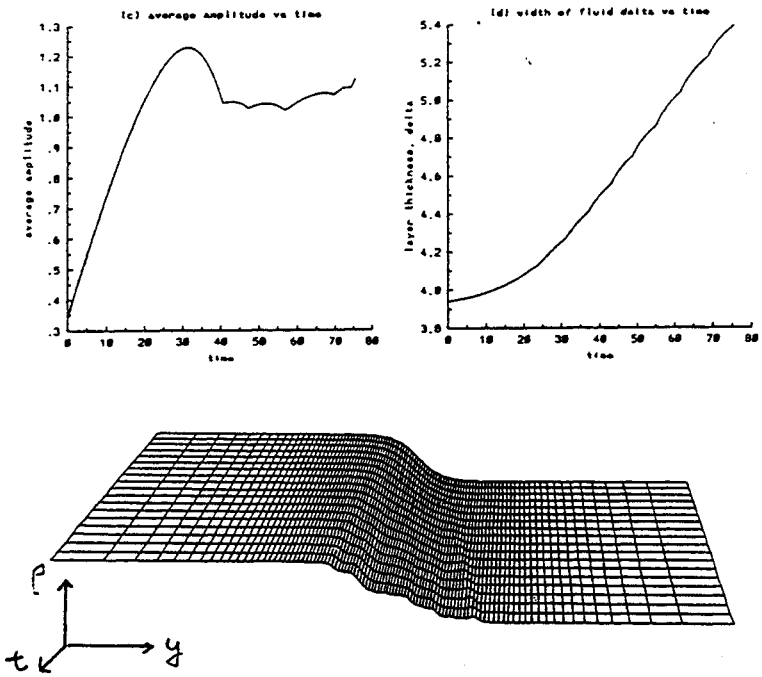

Figure 5 (a) Average amplitude and width of fluid layer vs. time for the initial condition described in Figure 3. (b) Surface plot of $\bar{\rho}_x(y,t)$.

RESULTS FOR MULTIPLE SCALE PERTURBATIONBS

In most experimental studies, and realistic applications, the interface is composed of many random modes of perturbation. In this section, we study the instability of a continuous interface having a random initial density distribution as given in equations (16) with $L = 1.0$, and $\epsilon = 0.2$.

In Figure 3 we display density contours at late times for a simulation with a random disturbance of the type given by equation (16). We note the emergence of vortical plumes which at late times dominate the dynamics of the layer. This is more clearly seen in Figure 4 which displays the associated vorticity at each time. The plumes correspond to dipolar vortex structures. As in the case of a single scale perturbation, there exist dipolar regions of vorticity consisting of elongated vortices of equal and opposite strength. Until the emergence of the globules, the growth is in the linear regime. Hence it is proportional to the initial strength of circulation, which is in turn proportional to the density gradient. The average densities for the run depicted in Figure 4 are shown in Figure 5. Note that the average amplitude which is an average of the density in the y-direction eventually stalls while the layer thickness continues to increase. This is a reflection of the fact that internal mixing dominates the fluid motion at late times.

An important issue in this study is the development of a self-similar asymptotic behavior independent of the initial random distribution. Barenblatt[10] proposed that the evolution of a uniform turbulent layer initially deposited in an inviscid homogeneous fluid is self-similar in time. From a dimensional argument, he found a time exponent of around 2/3 for the thickness of the layer. Due to the presence of large structures in our problem, there may not exist a scaling behavior governing late time growth. Even if there exists a limit, the value of 2/3 for the time exponent is questionable. In an attempt to answer this issue, we plot in

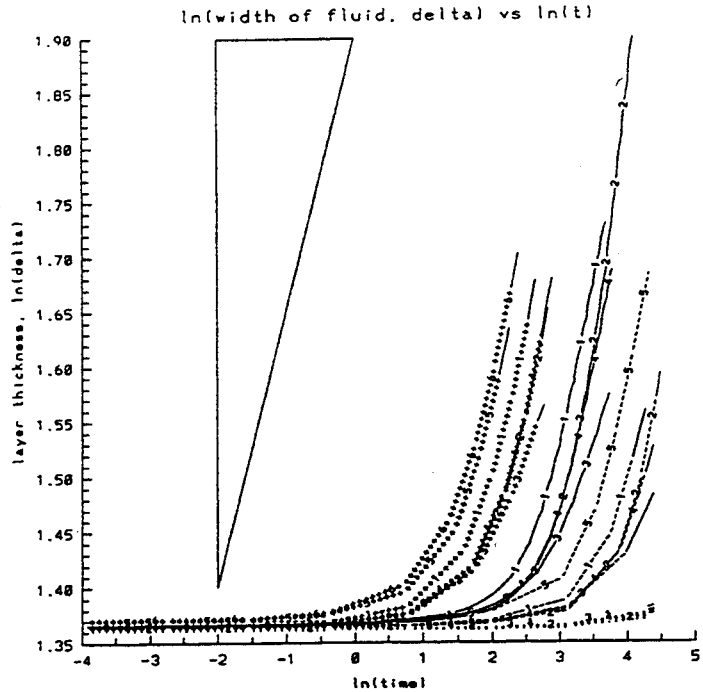

Figure 6. Combined results of $\log \delta$ vs. $\log t$ for six different initial random profiles: dotted line $A = -0.05$, medium dash $A = -0.2$, long dash $A = -0.5$, plus $A = -0.8$. A slope of 1/4 is shown for reference.

Figure 6 the time evolution of the width δ of the stratified layer. The late time behavior of δ seems to follow a power law in time with an exponent close to 1/4 but which varies slightly with the Atwood ratio. Longer simulations with enhanced resolution should provide more definitive information regarding this scaling behavior.

REFERENCES

[1] Richtmyer, R.D., *Comm. Pure Appl. Math.*, **8**, 297, (1960).

[2] Meshkov, E.E. *Sov. Fluid Dynamics*, **4**, 101, (1969).

[3] Saffman, P.G. & Meiron, D.I. *Phys. Fluids*, **A1**(11), 1767, (1989).

[4] Pham, T. Ph.D. Thesis, California Institute of Technology, (1990).

[5] Soh, W.Y. & Goodrich, J. *J. Comput. Phys.*, **79**, 113, (1988).

[6] Mikaelian, K.O. Unpublished Report, Lawrence Livermore National Laboratory, (1988).

[7] Youngs, D.L.,*Physica*, **D12**, 32, (1984).

[8] Brouillette, M., Ph. D. Thesis, California Institute of Technology, (1989).

[9] Brouillette, M. & Sturtevant, B., *Physica* ,**D37**, 248, (1989).

[10] Barenblatt, G.I. in *Non-Linear Dynamics and Turbulence*, G.I. Barenblatt, G. Ioos, and D.D. Joseph editors, (Pitman, Boston), 48, (1983).

Shockwave Considerations for Sub-grid Closure Modeling in Turbulent Large Eddy Simulations

Alfred C. Buckingham

Center for Compressible Turbulence
University of California, Lawrence Livermore National Laboratory
Livermore, California 94550

SUMMARY

This work continues the development of sub-grid closure procedures tailored specifically for large eddy simulations (LES) in strongly compressible turbulent flow. A time-explicit finite difference calculation is used to simulate the resolvable large scale features. The influence of the non-resolvable sub-grid scales on the large, computable scale range are modeled through application of a grid scale dependent, nonlinear eddy viscosity of the classical Smagorinsky form, $\nu_t^v = (C_S\lambda)^2\underline{S}$, but modified for dynamic viscoelasticity. Here $\underline{S}$ is the locally evaluated resolvable scale magnitude of the mean strain rate tensor, λ is a grid related length scale, and C_S is the appropriate Smagorinsky constant. Extended for simulating dynamic viscoelasticity, the sub-grid model mimics the well-established (and physically substantial) viscoelastic response of a turbulent field to the influence of an imbedded, interacting shock wave. The model viscoelastic parameters are developed separately from statistical realizations obtained independently from stochastic numerical simulations of shock-turbulence interactions.

1. INTRODUCTION

Physically, when a shock interacts with an upstream turbulent field, a substantial enhancement of the turbulent intensity and a simultaneous distortion and realignment of the turbulent strain field and resulting turbulent stress field occurs. Associated turbulent transport and mixing of phase components and species constituents are similarly amplified. Our ability to predict, to measure and to model a diversity of significant flow processes is severely inhibited by lack of understanding about shock/turbulence interactions. Discomforting levels of uncertainty develop concerning predictions of supersonic heat and mass transfer mixing leading to supersonic combustion, initiation of detonation and subsequent product evolution, and associated energy transport processes such as those dominating hypersonic thermal and electromagnetic radiation.

To compound the difficulty, developing information on the crucial details of shock-turbulence interaction presents a daunting experimental and theoretical problem. For example, experimental separation, isolation, and evaluation of the concomitant influences of entropy, velocity, and temperature fluctuations is forbiddingly difficult. This is particularly evident in the presence of strong shocks. Here the classical analytical procedures for linearized isolation and superposition of these influences is invalid, except for very weak shocks and often produce misleading experimental interpretations.

Theoretical analysis, assisted by computer model studies and numerical simulations have provided assistance and guidance, in design of experiments, refinement of diagnostics and in experimental interpretation. However, even with the enhanced resolution obtained by use of adaptive grid techniques, multigrid procedures and/or spectral methods (where the shock discontinuity can be isolated by analytical shock fitting schemes), the results are usually severely under resolved for all but the lowest Reynolds Number scale flow situations.[1]

Large eddy simulation (LES) procedures which explicitly follow the largest scale motions while providing, at their best, a carefull partition from direct influence while incorporating the ensemble averaged influence of the non-resolvable scales; appear to be an intermediate (and perhaps long term) answer to this dilemma.

This paper presents a report on progress in developing a successful LES technique. Particular attention has been given to computational test applications where the presence and interaction of strong shocks with compressible turbulent fields is of paramount importance. A specific focus, at this stage, is on the sub-grid problem. As concisely stated in a recent study by Leith: in sub-grid scale considerations, the turbulence problem is reduced to treating, as well as one can, the effect of the unresolved subgrid scales on those which are explicitly computed.[2] This also serves to place in proper perspective, the subgrid problem in relation to the encompassing probem of LES development.

2. TECHNICAL DEVELOPMENT

As demonstrated in the recent work by Leith[2] the unresolvable sub-grid scales have at least two distinct influences on the resolvable grid scale motions. One is the well known influence on dissipation of the energy in the computable scales. The other, lesser recognized, is the spectral range stochastic influence of non-linear interactions between the small scales which feed back into the large scale motions. While less recognized, this other influence has been well established for two decades or more. For example, in a 1976 paper, Kraichnan identifies other work on this phenomena from the previous decade and develops a firm theoretical spectral analysis basis for it as well as for the characteristic viscoelastic response of a turbulent field to an imposition of variations in mean strain.[4]

For the present we impose an initial stochastic seed on the development of the turbulent field, prior to shock arrival. We elect to avoid continuing the stochastic backscatter influence of the seed throughout the calculation. A partial argument for this apparent neglect has been supplied by Leith. He observes that within his own LES examination of a developing free shear layer, approximately 25 explicit cycles of the stochastic seed potential influence on the velocity field are sufficient to both initiate grid scale turbulence and to impart about 95% of the fluctuating energy into the resolvable scales.[2] Hence the seed can, in effect, be turned off after initiation without significantly altering the evolution or statistical structural content of the turbulent field.

For compactness, we will here reserve our outline as a focus on the sub-grid scale development. The process is illustrated with the help of some sample results from numerical tests.

In the basic Smagorinsky model[3] a non-linear coupling relates the eddy viscosity, ν_t^v, to the mean local strain rate magnitude, $\underline{S}$.

$$\nu_t^v = (C_S\lambda)^2\underline{S} \qquad (1)$$

The symbols have been identified previously. The mean strain is developed from the deviatoric strain rate tensor, S_{ik},

$$\underline{S} = [\, S_{ik}u_{i,k} \,]^{1/2} \qquad (2)$$

$$S_{ik} = u_{i,k} + u_{k,i} - (2/3)(u_{j,j})\delta_{ij} \qquad (3)$$

In eqns. 2 & 3 repeating subscripted tensor indices are used with cartesian, x_i, spatial derivative components of the resolved scale velocity vector components, u_i, while δ_{ij} is the Kronecker delta.

The viscoelastic property is defined as that rheological non-Newtonian transient state of the stress modulus, ν_t, which may either decrease (thixotropic) or increase (rheopectric) with applied shear stress, T_{ik}, and then partially return (relax) to a former state.

In our work a simple, linear viscoelastic form is assumed,

$$\nu_t = \nu_t^v \pm \left| \nu_t^p(M, i_u) - \nu_t^v \right| \exp-(t/\tau^*) \qquad (4)$$

Here the excursion metastable state, ν_t^p, has been determined, from numerical experiments, to be a function of both interactive shock Mach No, M, and relative intensity of the fluctuating velocity in the resolved scales, i_u. The symbol, t, represents the real time of application and τ^* is the transient relaxation parameter. Both ν_t^p and τ^* are developed from independent, stochastic shock turbulence interaction simulations, previously described and discussed later on with respect to their application here.[8,9]

Neglecting body force, the flow relations for conservation of mass, momentum and energy in a non-viscous, turbulent, calorically perfect ($\gamma = 7/5$) fluid may be written as follows. The framework is a two dimensional cartesian frame of reference, with coordinates, x_i, $i = 1, 2$. The flow field solution describes the unsteady evolution of density, $\rho(x_i, t)$, velocity, $u_i(x_i, t)$, pressure, $p(x_i,t)$, and internal energy, $e(x_i, t)$.

Convolution averaging over the non-resolvable motions below the scale of the grid produces an effective sub-grid turbulent shear stress, T_{ij}, which must be modeled with the viscoelastic procedure introduced in Eqns. (1) through (4).

Conservation equations for mass momentum and energy are written in this system as follows.

$$\rho_{,t} + (\rho u_j \delta_{ij})_{,i} = 0, \tag{5}$$

$$(\rho u_i)_{,t} + (\rho u_i u_j + p\delta_{ij} - T_{ij})_{,j} = 0, \tag{6}$$

$$(\rho e)_{,t} + (\rho e u_j \delta_{ij} + p u_j \delta_{ij})_{,i} - \Phi = 0, \tag{7}$$

$$(p/\rho\gamma)_{,i} = 0. \tag{8}$$

The sub-grid influence on the turbulent shear stress, T_{ij}, and the dissipation associated with that turbulent shear stress, Φ, are written in transport gradient form,

$$Tij = \rho \nu_t^{\nu}(u_{i,j} + u_{j,i}) - 2/3 u_{i,j}\delta_{ij}, \tag{9}$$

$$\Phi = (T_{ij} u_j \delta_{ij})_{,i}. \tag{10}$$

As in Rotman's simulations[6] an initial specification of space-time white noise velocity potential as a seed, generates a homogeneous isotropic turbulent field throughout the computational domain following about 100 computational cycles. Flow through boundary conditions are applied at the horizontal extrema while slip flow conditions apply at top and bottom of the two dimensional rectangular domain. Following the transient turbulence developmental period, a plane shock wave of specified strength is introduced at the right boundary and propagates through the grid-generated turbulence. The shock interacts with the turbulence during passage. Analysis is made of the flow field immediately ahead of and throughout the region behind the advancing shock.

3. RESULTS

A major concern here is the development of an LES procedure for flows in which both shockwaves and turbulence must be simulated with consistent accuracy and compatibility. The sub-grid prescription ideally must be, to all intents and purposes, nearly universal and general enough to properly define the energy redistribution between the dynamically interactive shock wave and the three collective modes of turbulent fluctuations in a compressible field.

A weak planar shock, however, does not remain planar. It distorts and oscillates when exposed to a sufficiently strong turbulent field. The shock tube experiments of Hesselink in which weak shocks were propagated into a test chamber filled with a random turbulent density distribution of two gases vividly illustrated these effects.[5]

These experimental results illustrated the diffraction and breakup of very weak shocks and the distortion of slightly stronger shocks, respectively, as they move into an intensely fluctuating density field. They also illustrate the intensification of the turbulence by the shockwave as indicated by the increase in population of fine scale random disturbances in the density and density gradients observed in the flow visualization behind the advancing shock.

Our present initial LES trials are inviscid and two dimensional with the indicated sub-grid viscoelastic response closure model. Rotman's earlier work made use of a two-dimensional, explicit second-order Godunov method originated by Colella and Woodward and extended by Colella and Glaz and by Rotman[6] to simulate the Hesselink experiments. These earlier calculations were solutions of Euler's equations. There was no sub-grid model. The extension of this work to develop and include an effective sub-grid model is the principle contribution of the present effort.

The current test computations make use of an explicit, two-dimensional ALE (arbitrary eulerian lagrangian) computer procedure. For the present tests this is run in the strictly eulerian mode.[10] A specific version of this code is used which includes tensor viscoelasticity convenient for our work here.[11]

Review of the difficulty in simulating and resolving the influence of the statistically random shock distortions during interactions suggested the necessity of obtaining results of some stochastic shock turbulence interaction simulations on which to base further development of the sub-grid procedure. Attention was given to some compelling theoretical studies on the necessary imposition of two dimensional non-steady boundary conditions for properly imposition of the shockwave evolution process in realistically inhomogeneous flow.[7]

The two-dimensional Monte-Carlo shock interaction simulations and the statistical results which form a basis for the present analysis have been described elsewhere.[8,9] Here the description is focused on how use is made of this information in developing and testing the sub-grid model.

Figs. 1 and 2 show statistical realizations of the random velocity field during shock interaction and probability density distributions of random internal energy, velocity and density.

The results of the shock-turbulence stochastic interaction simulations include the important predicted amplification of the initial turbulence energy and the associated enhancement of mixing as a function of Mach Number and low initial turbulence intensity (< 1.0%). The earlier Rotman computational results, with a variable, but larger initial turbulence intensity are shown together with a collection of experimental results in Fig. 3.

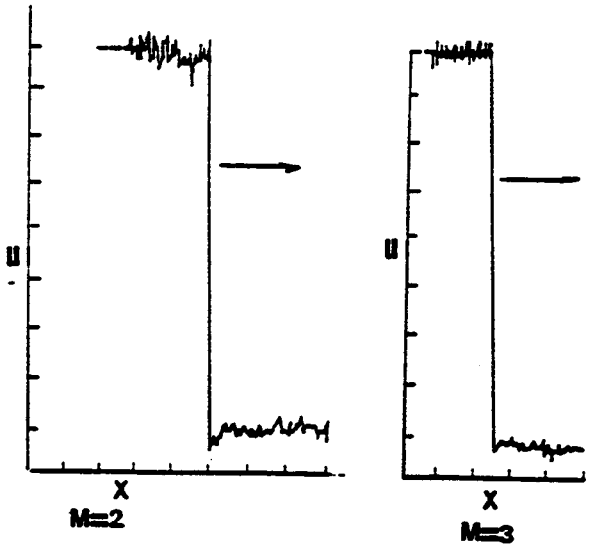

Fig. 1 Individual realizations of random velocities at discrete (η) levels from Monte-Carlo shock interaction simulations at indicated Mach No.s.

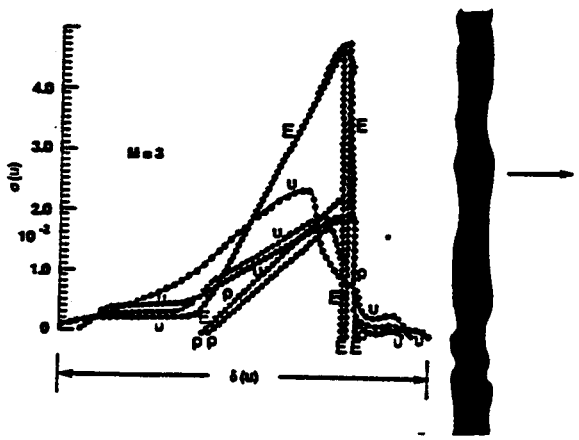

Fig. 2 Ensemble Averaged pdf's of individual realizations for internal energy (E), velocity (U), and density (ρ) fluctuations from a M = 3 stochastic simulation of shock-turbulence interactions.

The predicted stochastic variation of the apparent shock front distortions or random motions during shock front turbulence interaction are illustrated in Fig. 4. The zone of interaction is seen to contract significantly as shock Mach No. increases, and the shock steepens non-linearly with the added compression. The predicted contraction in nominal fluctuational length scale (integral) correlation is also quite evident in the data graphed in Fig. 4. These two scales are used in the present analysis to develop the viscoelastic relaxation parameters of Eqns. (1) through (4).

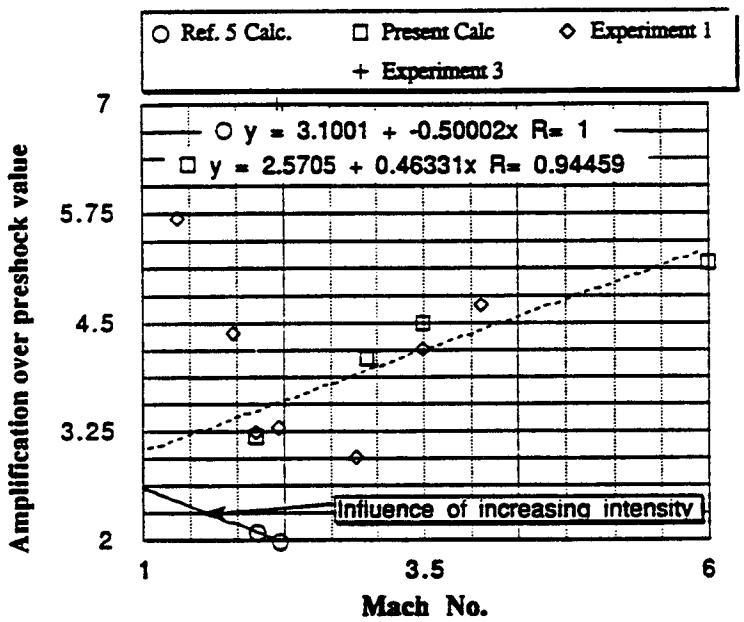

Fig. 3 Amplification of intitial turbulence kinetic energy by passage of an interactive shock front as a function of Mach No. Shown are experimental and numerically predicted values.

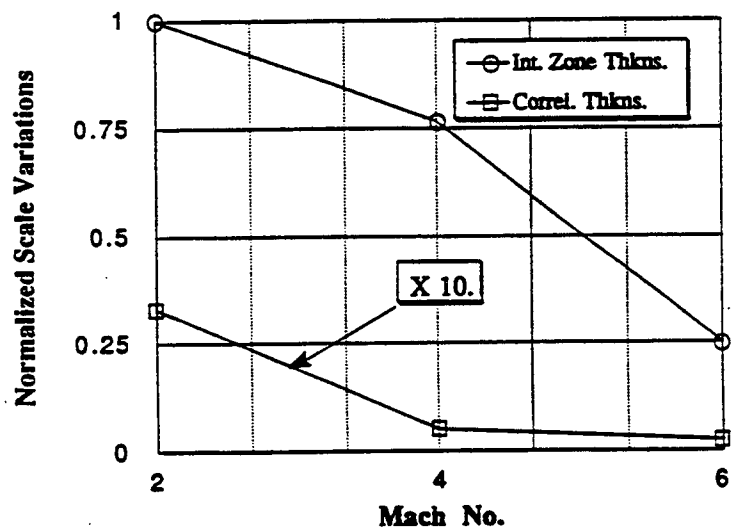

Fig. 4 Variation in stochastic model predictions of apparent shock interaction zone thickness and vorticity correlation length scales as a function of shock Mach No. All values are ratioed to interaction zone thickness at M = 2.

Fig. 5 illustrates the predicted dominance of the velocity (u') and density (ρ') fluctuations on developing grid scale motion in comparison to the near-negligible influences of the acoustic (p') fluctuations. This is somewhat misleading however since the mean and low frequency acoustic disturbances are very significant in modulating the pressure distributions of the background flow during both incident and reflected phases of their radiation from the source. This subtle influence can be traced in the computation. However, the rapid propagation to the boundaries is evidently imperfectly resolved in the explicit grid scale results.

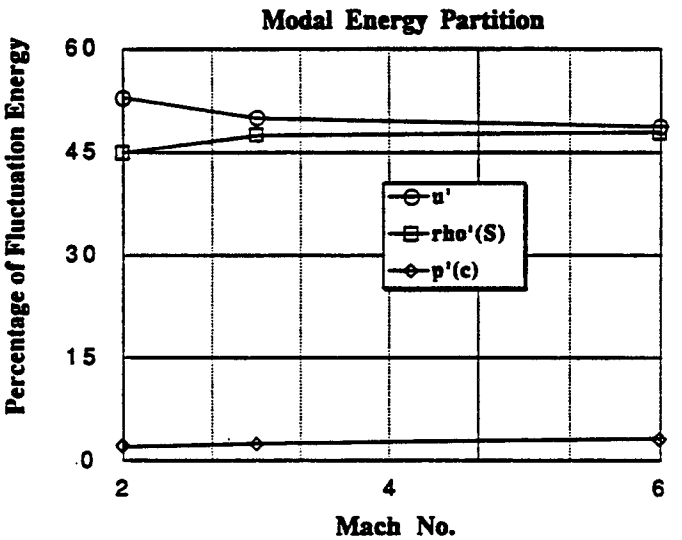

Fig. 5 Velocity (u'), density (entropy, ρ') and acoustic (p') modal fluctuationalenergy partition predicted by stochastic numerical simulations as a function of Mach No.

Leith[2] has observed that a randomly deforming, unsteady shock interaction may produce an imperfection in obtaining all of the content of the predicted stationary Hugoniot limits on shock transition variables. The suggestion is that this is particularly true for weak shocks which may distort or move randomly when subjected to the influence of an intense turbulent field. This imperfection may be expressed as the degree of adiabatic energy change that is encountered in comparison to the diabatic ideal Hugoniot change predicted for the stationary limit.

The ratio of adiabatic to diabatic energy change through the shock interaction is illustrated in Fig. 6. A limited number of experimental results are also shown. These experiments were run at relatively low Mach No. ($2 \leq M \leq 2.2$) where the influence could be expected to be more noticeable.[12]

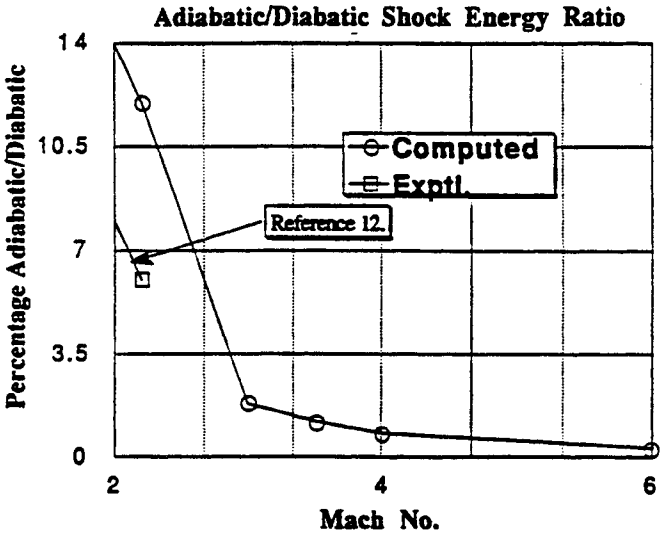

Fig. 6 Ratio of adiabatic to diabatic shock transitional energy imperfection predicted by stochastic numerical simulation and oscillating shock wave experiments.

In some cases (for low shock Mach Number and strong turbulence) this transitional energy deficit may be responsible for a small part of the enhanced turbulent field energy developed during shock interaction. This remains to be proved however, since the energy transferred during such interactions is much more substantial than what would be predicted by this kind of balance. The stochastic simulations, at least qualitatively, predict the appropriate trends.

Figures 7 and 8 show the distribution behind the advancing shock of the ratio of shock-wave enhanced to free stream turbulent kinetic energy, κ/κ_o. The results of the basic Smagorinsky closure model are compared with the viscoelastic response model up to the point of asymptotic matching (identified by the limit designation on the figures). The distributions are given as a function of units of true molecular shock thickness at these flow conditions. Also plotted, for reference is the width of the artificial viscosity interaction zone used for computations without a sub-grid model. This is inactive in these calculations since the sub-grid scale diffusive effects on grid scale motions dominate.

4. CONCLUSIONS

A sub-grid scale model has been tested for consistency in application to shock turbulence interaction flow situations at modest Mach No. (<6.0). Based on a limited number of experimental results and some previous computational tests, the results of the present tests show promise in qualitatively modeling the sub-grid scale influences.

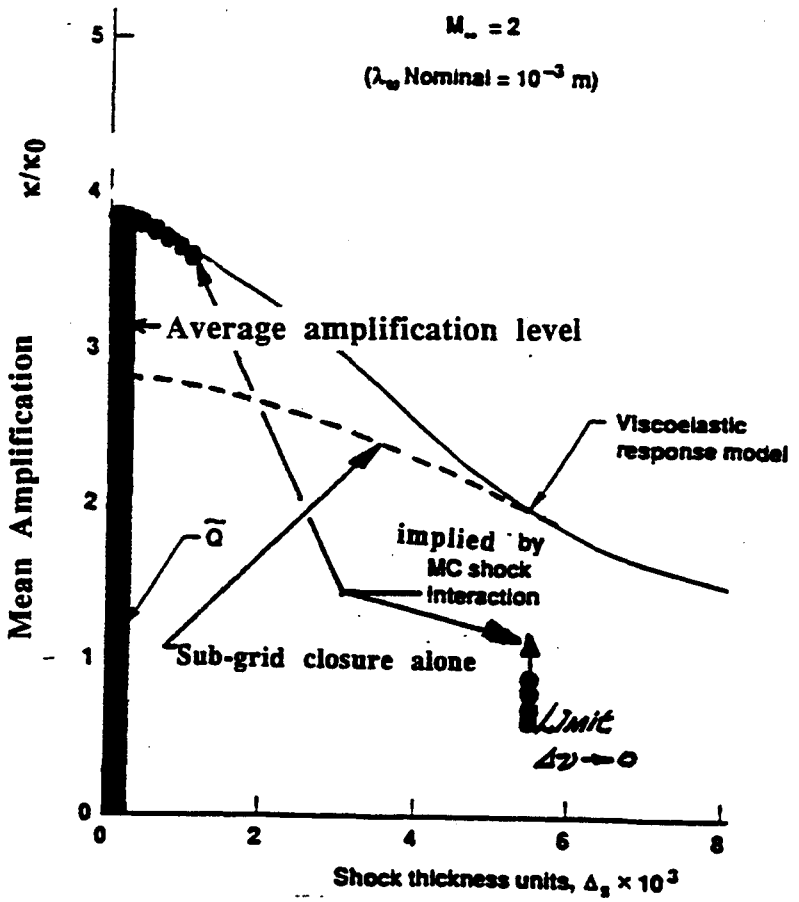

Fig. 7 Predicted intensification and relaxation of average turbulence kinetic energy, κ, relative to that upstream of an interacting shock front, κ_0, at M = 2.

Contraction of length and time scales with increases in interactive shock Mach Number are developed in separate stochastic caluculations of the shock interaction dynamics. These results were used to help establish some test metastable shear modulus and temporal relaxation parameters for the sub-scale viscoelastic model.

Test results from the demonstration calculations have been obtained which provide support for continuing the viscoelastic closure model efforts in simulation of two-dimensional shock turbulence interaction influences. The present results are limited to two spatial dimensions and to relatively low Mach Number. Hence, it needs to be stated that these results represent only an initial phase of a much more extensive study and development of useful LES procedures for compressible high Reynolds number turbulent flow simulation applications.

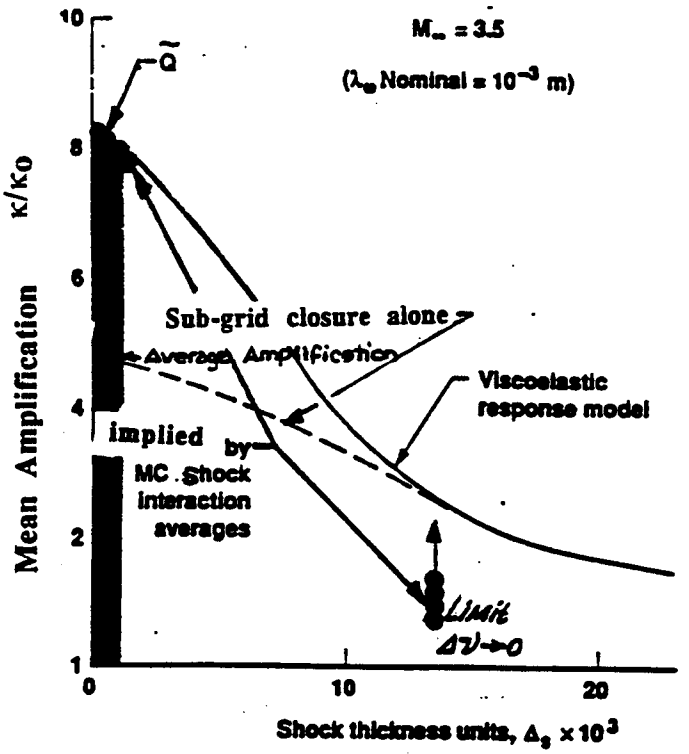

Fig. 8 Predicted intensification and relaxation of average turbulence kinetic energy, κ, relative to that upstream of interacting shock front, κ_0, at M = 3.5.

5. ACKNOWLEDGEMENT

This work was supported and performed under the auspices of the U.S. Department of Energy by the Lawrence Livermore National Laboratory under Contract No. W-7405-Eng-48.

6. REFERENCES

1. Buckingham, A. C., Numerical Methods in Laminar and Turbulent Flow, V, ed. C. Taylor, Pineridge Press, Swansea, UK, 1987, p. 963.
2. Leith, C. E., Phys. Fluids A, 2, p. 297, (1990).
3. Smagorinsky, J., Mon. Weather Rev., 91, p. 99, (1963).
4. Kraichnan, R. H., J. Atmos. Sci., 33, p. 1521, (1976).
5. Hesselink,L., "An Experimental Investigation of Propagation of Weak Shock Waves in Random Medium", Calif. Inst. of Technology, Pasadena, CA, Ph.D. Thesis ,(1977).

6. Rotman, D., "Shock Wave Influences on a Turbulent Flow", Phys. Fluids A , **3**, (7), (1991).

7. Emanuel,G. and Liu, M.-S., Phys. Fluids, **31**, p. 3625, (1988).

8. Buckingham, A. C., Numerical Methods in Laminar and Turbulent Flow, VI, eds. C. Taylor, P. Gresho, R. Sani, J. Hauser, Pineridge Press, Swansea, UK, 1989, p. 805.

9. Buckingham, A. C. , "Interactive Shock Structure Response to Passage through Turbulence", AIAA Paper 90-1642, AIAA 21st Fluid and Plasma Dynamics Conf. Seattle, WA (June 18-20, 1990) revision in review for AIAA JOURN. (1991).

10. Hirt, C. W. , Amsden, A. A. and Cook, J. L., J. Comp. Phys., **14**, p. 227, (1974).

11. Demuth,R. B., Margolin,L. G., Nichols, B. D., Adams, T. F. and Smith, B. W., "SHALE: A Computer Program for Solid Dynamics", Los Alamos National Laboratory, Los Alamos, NM, LA-10236 (1985).

12. Shigemi, M., Koyama, H., and Alhara, Y., "A Note on the Oscillating Shock Wave - Some Experiments", Trans. Japan Soc. Aero. and Space Sciences, **19**, (44), 1976, pp. 68-81.

*LARGE EDDY SIMULATION AND COHERENT STRUCTURES DOWN A BACKWARD FACING STEP FLOW

A. Silveira Neto and D. Grand
C.E.A./Departement de Thermohydraulique et Physique
85 X - 38041 GRENOBLE CEDEX

ABSTRACT

A statistical and topological study of a complex turbulent flow over a backward-facing step is realized by means of large-eddy simulations. The subgrid-scale model is a local adaptation to the physical space of the spectral eddy-viscosity concept introduced by Kraichnan and implemented for isotropic turbulence by Chollet and Lesieur. The statistics of turbulence are in good agreement with the experimental data, corresponding to an aspect ratio of 2.5 (small step). Furthermore, calculations at a lower aspect ratio of 1.25 (higher step) show the the eddy structure of the flow presents striking analogies with the plane shear layers, with large billows shed behing the step, and longitudinal vortices strained between these billows.

INTRODUCTION

For many years, the only practical approach to the computation of industrial flows was through the time-averaged equations in one point and the use of semi empirical turbulence models.

An alternative approach is the development of large-eddy simulation[1,2], in which the temporal evolution of the large-scale structures is obtained directly from the numerical simulation. The motions of wavelengths smaller than the computational grid (subgrid-scales) have to be represented by a proper statistical model.

These large scale structures play an important role in the physical characteristics of technological problems : thermo-hydraulics in nuclear reactors, environmental studies, acoustics, vibrations, aerodynamics, combustion, etc... Comprehension of the dynamics of this organized large-scale movement is necessary for the mechanical control of their production.

We report on the results of a three-dimensional (3*D*) large-eddy simulation of a complex inhomogeneous shear flow : the flow downstream of a backward-facing step in a plane channel (Figure 1). The results of the

numerical simulation are compared to the experiment of Eaton and Johnston[3]. In this experiment, the aspect ratio defined as the height W of the channel downstream of the step over the height of the step H is 2.5. The Reynolds number based upon the upstream bulk velocity U_0 and H is 38 000. These are the velocity and length scales used afterwards in the presentation of the results.

GOVERNING EQUATIONS

We solve the Navier-Stokes equations for an incompressible fluid, relating the filtered velocity vector u_i and pressure p :

$$\partial_i u_i = 0 \tag{1}$$

$$\partial_t u_i + \partial_j(u_i u_j) = -\frac{1}{\rho}\partial_i p + \nu\partial^2 u_i + \partial_j \tau_{ij} \tag{2}$$

Here, τ_{ij} is the subgrid-stress tensor. The boundary conditions are : at the inlet, $u_1 = U_0+\xi$, where U_0 is the bulk velocity and ξ a white noise of amplitude $10^{-4}\ U_0$, modeling the residual turbulence within the upstream flow.

The subgrid model is based on the gradient transport hypothesis :

$$\tau_{ij} = \nu_t S_{ij} - \frac{2}{3}k_s\delta_{ij} \tag{3}$$

where $S_{ij}=(1/2)(\partial_i u_j+\partial_j u_i)$ is the local strain, δ_{ij} the unit tensor and K_s the subgrid turbulent kinetic energy. The eddy-viscosity ν_t is borrowed from Kraichnan's spectral eddy-viscosity[4], developed by Chollet and Lesieur[5] for isotropic turbulence and generalized to highly-intermittent and non-homogeneous situations in physical space by Métais and Lesieur[6]. The eddy diffusivity is obtained under the assumption that the energy spectrum follows Kolmogorov's law above the cutoff. It is found :

$$\nu_t(\vec{x},\Delta,t) = 0.104\ C_K^{-\frac{3}{2}}\ \sqrt{\overline{F}_2(\vec{x},\Delta,t)}, \tag{4}$$

where Δx is the mesh size uniform in the three spatial directions. The quantity F_2 is the second order velocity structure function deduced from the filtered velocity field and defined by :

$$F_2(\vec{r},t) = <||\vec{u}(\vec{x}+\vec{r},t)-\vec{u}(\vec{x},t)||^2> \tag{5}$$

where $<\cdot>$ is the spatial average over the shell of radius $\|\vec{r}\|$. The development of this model is presented by Lesieur[7].

The transport equation, completed by the subgrid model, are solved numerically with the aid of a software used for 3D computations of industrial flows : the *TRIO* code, developed at Commissariat à l'Energie Atomique. The finite-volume version of the code derived from *SOLA* method[8] is used hereafter, with a third-order discretization scheme for the convective terms (SMART scheme)[9].

RESULTS OF LARGE-EDDY SIMULATION

The first calculations correspond to an aspect ratio W/H = 2.5, on a grid with, respectively, 200, 30 and 30 grid points in the longitudinal, transverse and spanwise directions.

Figures 2 (a) and (b) show the transverse profiles of the mean longitudinal velocity and of the turbulent kinetic energy. The profiles are located in the reattachment region (x/H=8) in the middle of the channel. The turbulent kinetic energy, evaluated at each point by an integration over a time interval 400 H/U_o, consists of two parts : a contribution $u_i u_i/2$ corresponding to the fluctuactions u_i with respect to the time average u_i of the instantaneous filtered field ui on the one hand, and a subgrid energy K_s, on the other hand. The latter is estimated by a proper extrapolation of the local kinetic energy spectrum, derived from the local structure function. Results are compared with a laboratory experiment[3]. The agreement between numerical and experimental results is satisfactory, the maximum discrepancy beeing less than 10 %.

On Figure 2 (a) and (b), are also shown the resultats given by the standard K-ϵ statistical model implemented in the *TRIO* code : the position of the peak of K is not well predicted, neither is the mean velocity profile.

The large-eddy simulation improves also the prediction of the reattachment distance x_R/H, as shown by the following results :

Experiment[3]	x_R/H=7.8
Large-eddy simulation (fine grid)	x_R/H=8.1
K - ϵ model (grid independent result)	x_R/H=6.2

A visualization of the instantaneous flow field at time $t = 90\ H/U_o$ is now presented. Figure 3 displays the vortex structure : a plane sheet appears just down-stream of the step (left-hand side of the figure). It oscillates, giving rise to large billows of spanwise vorticity. Streamwise vortices are streched between the primary billows. Near the reattachment region, the presence of the wall introduces an extra source of streching, leading to a high three-dimensionalization of the structures.

In the above case of a low step, the vortex structures forming downstream are strongly influenced by the lower wall. On the other hand laboratory experiments and numerical simulations are available which free mixing layers (that is, a step of infinite height). We considere then another configuration with a higher step (W/H=1.25), and compare the resulting structures with those obtained in free shear flows. The number of grid points is now 130 x 40 x 25. Figure 4 shows the vorticity field at $t = 138\ H/U_o$. Five primary rollers are present in the channel. As compared with Figure 3, they are much less three-dimensional, but exhibit spanwise oscillations, as other plots show. The strain field induced by two consecutive Kelvin-Helmholtz vortices leads to the formation of streamwise vortices stretched along the braids. The ratio between their spanwise spacing and the local vorticity thickness is in good agreement with laboratory observation[10] (0.7 against 0.8).

Additionnal informations on these results is presented by Silveira et al.[11]

CONCLUSIONS

These new results concerning an inhomogeneous turbulent shear flow demonstrate the potentialities of a large-eddy simulation carried out with a finite-volume method (TRIO code) and a recently proposed subgrid model. In the two different geometries considered, the numerical simulations compare favourably with experiments, even for the detailed topology of the flow.

This study shows also the similarity of the flow downstream of a backward-facing step with the free mixing layer.

REFERENCES

1. P. Moin and J. Kim. J. Fluid Mech., 118, pp.341-377 (1982)

2. H. Schmidt and U. Schumann, J. Fluid Mech., 200, pp. 511-562 (1989)

3. J.K. Eaton, and J.P. Johnston, Stanford, Report MD.39 (1980)

4. R.H. Kraichnan, J. Atmos, Sci., 33, pp. 1521-1536 (1976)

5. J.P. Chollet and M. Lesieur, J. Atmos, Sci., 38, pp.2747-2757 (1981)

6. O. Métais and M. Lesieur, "Spectral large-eddy simulation of isotropic and stable-stratified turbulence", submitted to J. Fluid Mech., (1990)

7. M. Lesieur, Communication at the 3rd International workshop on the Physics of Compressible Turbulent Mixing (1991)

8. F.W. Harlow and A.A. Amsden, J. Comp. Phys., 8, pp. 197-213 (1971)

9. P.H. Gaskell and A.K.C. Lau, Int. J. for Num. Meth. in Fluids, 8, pp. 617-641 (1988)

10. L.P. Bernal and A. Roshko, J. Fluid Mech., 170, pp.499-525 (1986)

11. A. Silveira, D. Grand, O. Metais and M. Lesieur, Phys. Review Letters, 66, pp.2320-2323 (1991)

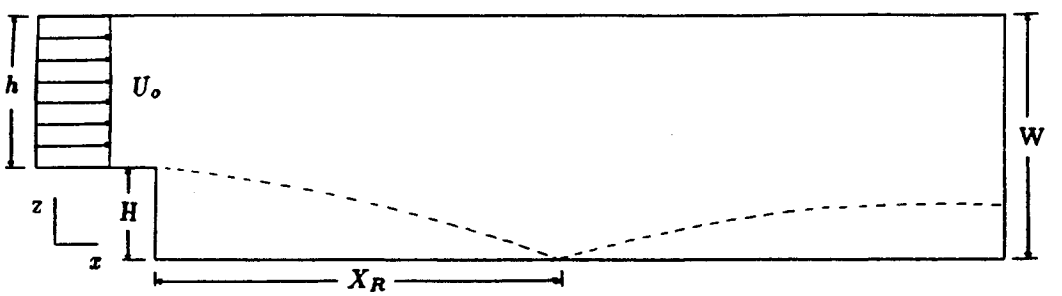

Fig. 1 Flow domain

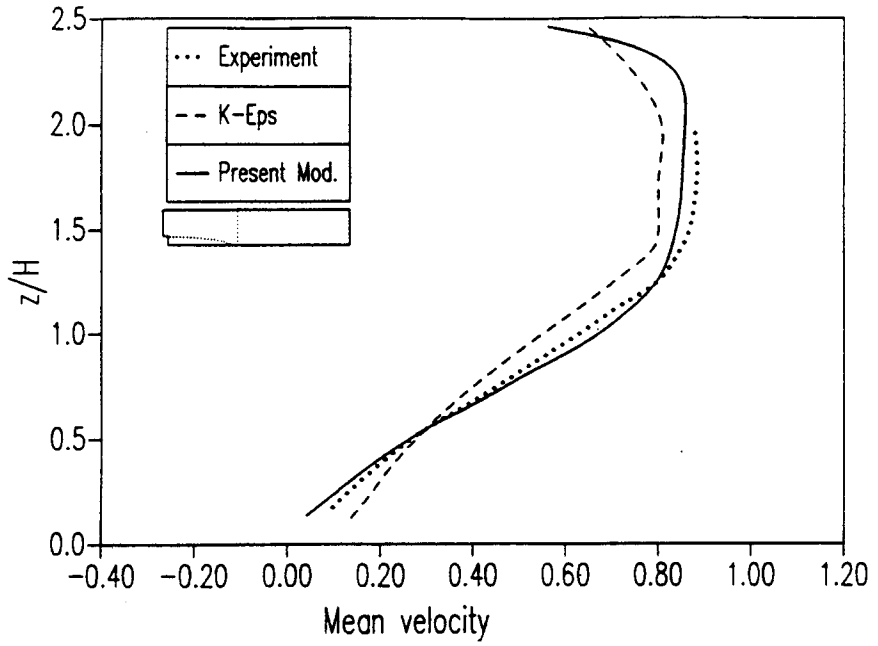

(a)

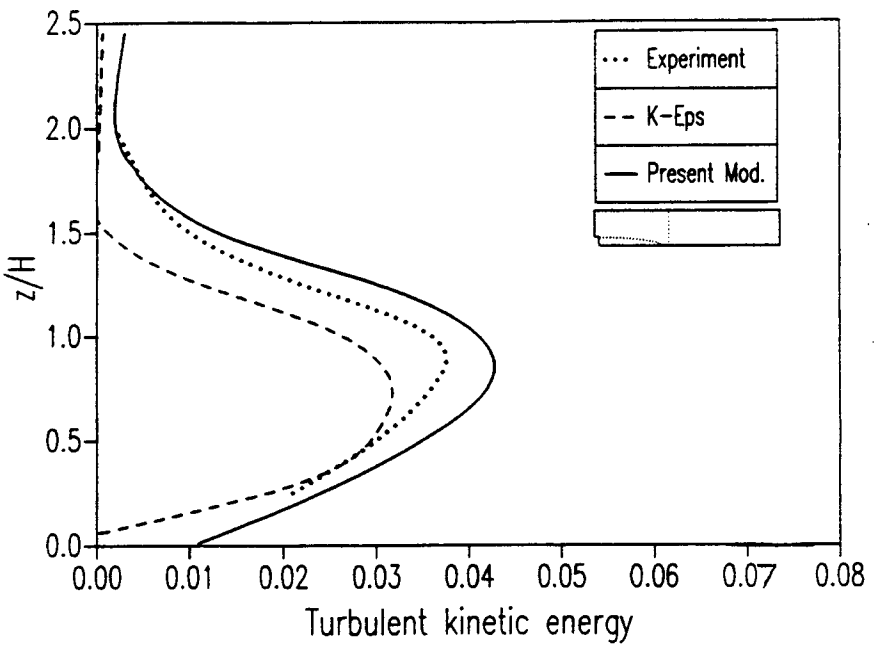

(b)

Fig. 2 Statistical quantities at $x/H = 8$;

(a) transverse profile of the longitudinal component of mean velocity ;

(b) transverse profile of the turbulent kinetic energy.

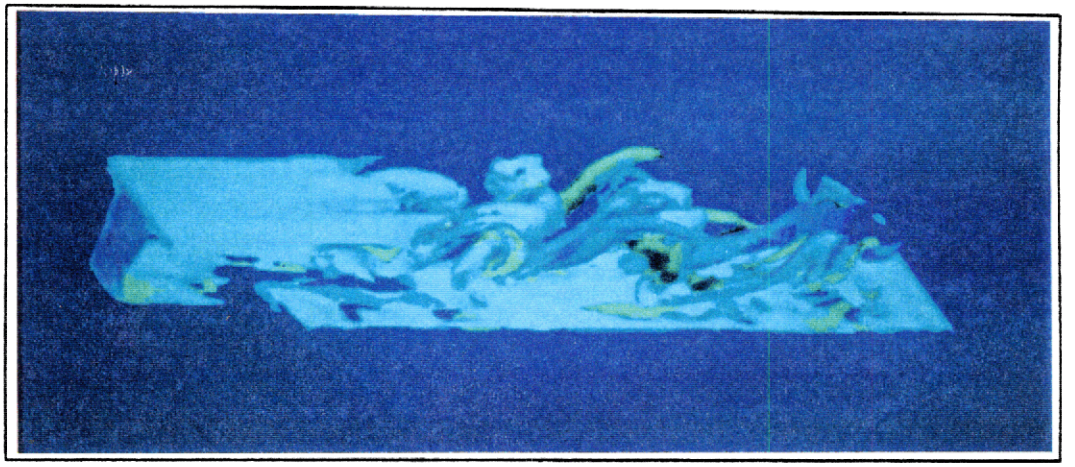

Figure 3 : Vorticity contours at time t = 90 H/U_o
light blue : vorticity modulus $\|\vec{w}\|$ = 3.5 U_o/H
dark blue and green : streamwise vorticity w_x = 2.5 U_o/H
(aspect ratio W/H = 2.5)

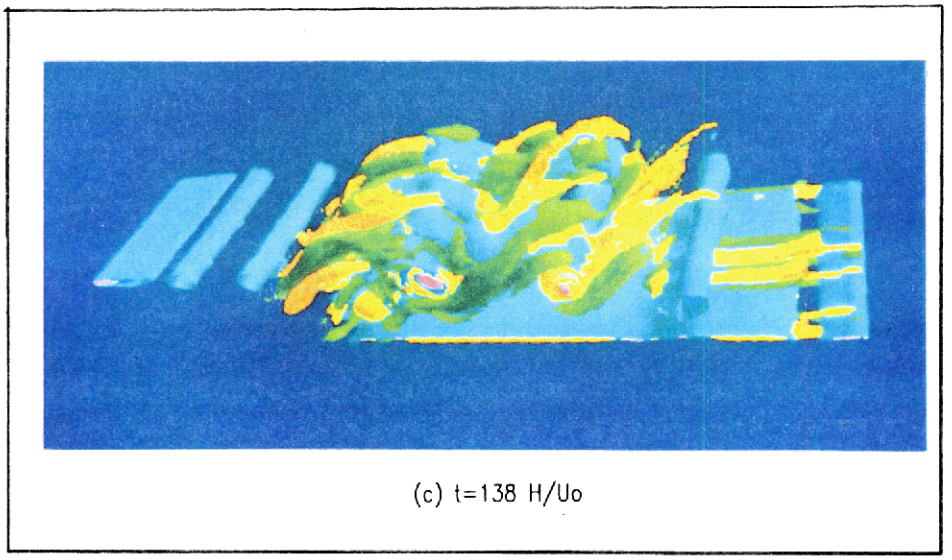

(c) t=138 H/Uo

Figure 4 : Vorticity contours at time t = 138 H/U_o
light blue : vorticity modulus $\|\vec{w}\|$ = 1.8 U_o/H
green and yellow : streamwise vorticity w_x = 0.8 U_o/H
(aspect ratio W/H = 1.25)

SHOCK ACCELERATION WITH TURBULENCE MINIMIZATION*

Nelson Hoffman
Los Alamos National Laboratory
P. O. Box 1663, Los Alamos, New Mexico 87545 , USA

*Work supported under USDOE contract W-7405-ENG-36.

I. INTRODUCTION

Suppose we desire to use a series of shock waves to bring a fluid interface, initially at rest, to a final velocity V after the interface has traveled a distance x (Fig. 1). The interface is initially "nominally smooth", meaning it is discontinuous and has a full spectrum of small perturbations. The problem is to bring the interface to the desired final state with as little turbulence generation as possible. The present work is an attempt to find a prescription for doing this, in the framework of a simplified version of a one-point turbulence transport model developed by Besnard, Harlow, and Rauenzahn[1].

The model equations are transport equations for the turbulent statistical quantities E (the turbulent kinetic energy density) and a (the correlation of density and velocity fluctuations), with a prescription for b (the self-correlation of density fluctuations) based on the local concentrations c_1, c_2 of fluids 1 and 2, initially on either side of the interface. The concentrations obey a diffusion equation. Thus the equations are similar to those implemented by Rauenzahn in the CAVEAT code, although we include a diffusion term in the a equation. The configurational prescription for b is the same as that used by Besnard, Haas, and Rauenzahn in Ref. 2.

II. SIMPLIFYING ASSUMPTIONS

A. *Simplification of model equations.* We simplify this model still further by transforming to a frame in which the shocked interface is at rest, so that the mean flow velocity u_i vanishes. We assume dissipation is unimportant. We consider one-dimensional situations, so that all quantities vary only in one coordinate. Finally, we assume isotropic turbulence, so that the Reynolds tensor $R_{xx} = (2/3)\bar{\rho}E$. With these approximations, the model equations take the form

$$\frac{\partial \bar{\rho}E}{\partial t} = a\frac{\partial \bar{p}}{\partial x} + \frac{\partial}{\partial x}\left(\bar{\rho}\nu_t \frac{\partial E}{\partial x}\right), \tag{1}$$

$$\frac{\partial \bar{\rho}a}{\partial t} = \frac{b}{\bar{\rho}}\frac{\partial \bar{p}}{\partial x} - \frac{2}{3}E\frac{\partial \bar{\rho}}{\partial x} + \frac{\partial}{\partial x}\left(\bar{\rho}\frac{\nu_t}{\sigma_a}\frac{\partial a}{\partial x}\right), \tag{2}$$

$$\frac{\partial \bar{\rho} c_k}{\partial t} = \frac{\partial}{\partial x}\left(\bar{\rho}\frac{\nu_t}{\sigma_c}\frac{\partial c_k}{\partial x}\right), k = 1, 2, \tag{3}$$

$$b = \alpha_1 \alpha_2 \frac{(\rho_1 - \rho_2)^2}{\bar{\rho}}. \tag{4}$$

Here $\bar{\rho}$ is the mean flow density, u is the mean flow velocity, $\bar{p}$ is the mean flow pressure,and ν_t is the turbulence diffusivity. The models mentioned above include a transport equation for dissipation ε, but we omit it and set ε to zero in the following analysis. The constants σ_a and σ_c are of order unity. The volume fractions α_1 and α_2 are related to the concentrations c_1 and c_2 by $\alpha_1\rho_1 = c_1\bar{\rho}$ and $\alpha_2\rho_2 = c_2\bar{\rho}$. Of course $\alpha_1 + \alpha_2 = 1$ and $c_1 + c_2 = 1$.

B. *Additional simplifying approximations.* To make the problem analytically tractable, we introduce some additional simplifying assumptions which we do not expect to alter the qualitative significance of the conclusions reached. These include *(i)* assuming the density to be nearly uniform, in the sense that density gradients are insignificant to the dynamics of turbulence transport, yet large enough to give finite density self-correlation. This is equivalent to dropping the density-gradient term in Eq. (2), while retaining $\rho_1 - \rho_2$ as non-zero in Eq. (4). Another assumption is *(ii)* the impulsive-pressure approximation of Saffman and Meiron[3], in which the turbulent velocities after shock passage are taken to be much smaller than the sound speed. This is strictly true only for weak shocks.We have already mentioned the assumptions of *(iii)* no dissipation and *(iv)* isotropic turbulence.

III. ANALYSIS OF THE PROBLEM.

We treat the given problem in three phases. The first phase is the initialization of turbulence at the discontinuous interface by the first shock wave, seeded by a spectrum of perturbations at the interface. This sets the initial conditions for the second phase, which is the transport of turbulence and growth of the interface's thickness during the period between shocks. The third phase is the arrival at the interface of the next shock wave, generating turbulence from finite density self-correlation b and density-velocity correlation a . We restrict attention to the case of two shock waves for now.

A. *Phase I: Turbulence generation by first shock wave.* For the first phase, we use the results of Saffman and Meiron[3] to initialize the turbulent kinetic energy and the density-velocity correlation at the discontinuous interface. They give, for a discontinuous interface with a small perturbation of wavenumber k, the following expression for the total turbulence energy per unit cross-sectional area generated by a weak shock wave which accelerates the interface to a velocity V_1:

$$[\rho]_E E_{Tot} = \frac{1}{2}\langle\rho\rangle A^2 V_1^2 k\eta^2 \tag{5}$$

where $\langle\rho\rangle$ is the mean of the postshock densities on either side of the interface:$\langle\rho\rangle = (\rho_1 + \rho_2)/2$, A is the postshock Atwood number $(\rho_1 - \rho_2)/(\rho_1 + \rho_2)$, $[\rho]_E$ is an E-weighted mean density, and η is the postshock amplitude of the perturbation. From Saffman and Meiron's results, we evaluate the total density-velocity correlation (units

are momentum per unit cross-sectional area) as

$$[\rho]_a a_{Tot} = \langle\rho\rangle A^2 V_1 k\eta^2. \tag{6}$$

where $[\rho]_a$ is an a-weighted mean density. For a full spectrum of linear, non-interacting perturbations at the interface, we sum over all wavenumbers to obtain

$$[\rho]_E E_{Tot,0} = \frac{1}{2}\langle\rho\rangle A^2 V_1^2 S \quad \text{and} \quad [\rho]_a a_{Tot,0} = \langle\rho\rangle A^2 V_1 S, \tag{7}$$

where S is an initial scale defined as

$$S = \sum_k k\eta_k^2 = \sum_k \frac{(k\eta_k)^2}{k}. \tag{8}$$

Consistent with these values of $E_{Tot,0}$ and $a_{Tot,0}$ we define a quantity which plays the role of total density self-correlation, with units density × length:

$$b_{Tot,0} = \langle\rho\rangle A^2 S. \tag{9}$$

B. *Phase II: Transport of turbulence and growth of interface's thickness.* In this phase, the turbulence quantities generated by the passage of the first shock wave disperse through space in accordance with the transport terms in the governing equations (1) - (4). In this study we have modeled the transport terms as diffusive. Using the impulsive pressure approximation, we treat the pressure gradient terms in Eqs. (1) and (2) as delta functions in time, acting only at the instant of passage of the first shock, so that they vanish during Phase II. We also assume that the density gradient is dynamically negligible during Phase II, so that density-gradient creation of a vanishes in Eq. (2). This is not really a good approximation, since the density-gradient term is of comparable or greater magnitude than the diffusion term. However, the density-gradient term has the same time dependence as the diffusion term, and so the two may be combined, if we are not interested in the detailed spatial distribution of a. We do so for now, in order to employ Barenblatt's[4] similarity solution technique. Then the governing equations (1) and (2) become

$$\frac{\partial\bar{\rho}E}{\partial t} = \frac{\partial}{\partial x}\left(\bar{\rho}\nu_t\frac{\partial E}{\partial x}\right), \tag{10}$$

and

$$\frac{\partial\bar{\rho}a}{\partial t} = \frac{\partial}{\partial x}\left(\bar{\rho}\frac{\nu_t}{\sigma_a}\frac{\partial a}{\partial x}\right), \tag{11}$$

while the concentration equation is the same as before.

An exact solution to the turbulence energy equation (10) is given by Barenblatt[4], who writes the turbulence diffusivity ν_t as the product of a turbulence length scale l and a turbulence velocity $\sqrt{E}$. He models the turbulence length scale l as a definite fixed part α of the actual thickness of the turbulent layer, denoted $h(t)$. That is, $l = \alpha h(t)$ and $\nu_t = \alpha h(t)\sqrt{E}$, so that Eq. (10) becomes

$$\frac{\partial \bar{\rho} E}{\partial t} = \frac{\partial}{\partial x}\left(\bar{\rho}\alpha h(t)\sqrt{E}\frac{\partial E}{\partial x}\right). \tag{12}$$

Barenblatt considers only uniform density, so that $\bar{\rho}$ cancels across the equation; having assumed the dynamical negligibility of the density gradient, we do the same thing. Using dimensional analysis, Barenblatt writes

$$h(t) = \xi_0(\alpha) E_{Tot,0}^{1/3} t^{2/3} \tag{12a}$$

and

$$E(x,t) = \xi_0^2 E_{Tot,0}^{2/3} t^{-2/3} \Phi\left(\frac{x}{h(t)}\right) = \frac{h^2(t)}{t^2}\Phi\left(\frac{x}{h(t)}\right), \tag{13}$$

where ξ_0 is a positive constant. The form of $\Phi(\zeta)$ need not concern us now. The constant ξ_0 is found to equal $(135\,\alpha^2/4)^{1/3}$. The Prandtl number α must be determined experimentally since it cannot be evaluated within the framework of this model. Typically it is about 0.1.

Using a similar dimensional analysis, we find a solution to the a equation Eq. (11) by writing

$$a(x,t) = \frac{h(t)}{t}\Gamma\left(\frac{x}{h(t)}\right) + \frac{a_{Tot,0}}{2h(t)} \tag{14}$$

since a has units of velocity, i.e., length / time. The form of the dimensionless function Γ need not concern us here, especially since our neglect of the density-gradient term probably gives us an incorrect idea of the true distribution of a. We have added a contribution due to $a_{Tot,0}$, by assuming that the initial a is spread out uniformly over the turbulent layer of thickness $2h(t)$. The similarity solution is valid only when $h\Gamma/t >> a_{Tot,0}/2h$.

In a similar way, the composition gradient must have units 1 / length, so

$$\frac{\partial c_1}{\partial x} = \frac{1}{h(t)}\tilde{\Lambda}\left(\frac{x}{h(t)}\right).$$

Integrating, with the boundary condition that $c_1(-h,t) = 0$ and $c_1(h,t) = 1$, gives

$$c_1(x,t) = \frac{1}{2} + \frac{x}{h(t)}\Lambda\left(\frac{x}{h(t)}\right), \text{where} \quad \tilde{\Lambda}(\zeta) = \frac{\partial}{\partial\zeta}(\zeta\Lambda) \tag{15}$$

and we have the boundary condition $\Lambda(-1) = \Lambda(1) = 1/2$. Again, the detailed form of Λ need not concern us.

With this representation for c_1, we now use Eq. (4), the configurational prescription for the density self-correlation, to evaluate b. Since $\alpha_1 = c_1\bar{\rho}/\rho_1$ and $\alpha_2 = c_2\bar{\rho}/\rho_2 = (1 - c_1)\bar{\rho}/\rho_2$, we find from Eq. (4) that

$$b(x,t) = \alpha_1\alpha_2\frac{(\rho_1 - \rho_2)^2}{\bar{\rho}} = \bar{\rho}(x,t)\frac{A^2}{1-A^2}\left[1 - \frac{4x^2}{h^2(t)}\Lambda^2\left(\frac{x}{h(t)}\right)\right].$$

We need to add to this shock-generated density self-correlation a term representing the pre-existing density self-correlation $b_{Tot,0}$. As with a, we assume this contribution to b is uniformly distributed over the layer, so that the expression for b becomes

$$b(x,t) = \bar{\rho}(x,t)\frac{A^2}{1-A^2}\left[1-\frac{4x^2}{h^2(t)}\Lambda^2\left(\frac{x}{h(t)}\right)\right]+\frac{b_{Tot,0}}{2h(t)}. \qquad (16)$$

We evaluate the total magnitude of the turbulence quantities, integrated over the turbulent layer, from Eqs. (13) - (16). For example,

$$a_{Tot}(t) \equiv \frac{h(t)}{t}\left(\int_{-1}^{1}\Gamma(\zeta)\,d\zeta\right)h(t) + a_{Tot,0} = \xi_0^2 E_{Tot,0}^{2/3} t^{1/3}\Gamma_0 + a_{Tot,0} \qquad (17)$$

where the constant Γ_0 denotes the integral in parentheses and $\zeta = x/h(t)$. Thus the total quantity of a increases with time as $t^{1/3}$, for times such that the first term dominates the second. Likewise

$$b_{Tot}(t) \equiv \int_{-h}^{h} b(x,t)\,dx = \xi_0\Lambda_0\left(\frac{A^2}{1-A^2}\right)\hat{\rho}(t)\,E_{Tot,0}^{1/3}t^{2/3} + b_{Tot,0},$$

where

$$\hat{\rho}(t)\,\Lambda_0 \equiv \int_{-1}^{1}\bar{\rho}[\zeta h(t),t]\,(1-4\zeta^2\Lambda^2(\zeta))\,d\zeta$$

defines a weighted mean density $\hat{\rho}(t)$, which we expect to be a slowly varying function of time, being of order $\langle\rho\rangle = (\rho_1 + \rho_2)/2$. Thus the total quantity of b increases with time approximately as $t^{2/3}$, for times such that the shock-generated part of b, which grows during the inter-shock period, dominates the pre-existing b.

C. *Phase III: Arrival of second shock wave.* We treat the second shock wave in the impulsive -pressure approximation, so that pressure gradients are modeled by delta functions in time. All other processes like turbulent diffusion are imagined to occur on a much longer time scale. The insignificance of the density gradient term in the a equation may be argued validly for this phase. Thus the model equations take the form

$$\frac{\partial\bar{\rho}E}{\partial t} = a\frac{\partial\bar{p}}{\partial x}, \qquad \frac{\partial\bar{\rho}a}{\partial t} = \frac{b}{\bar{\rho}}\frac{\partial\bar{p}}{\partial x}, \qquad (18)$$

while the concentrations remain constant. Solving the a equation for $\partial\bar{p}/\partial x$ and substituting in the E equation gives

$$\frac{\partial\bar{\rho}E}{\partial t} = a\frac{\bar{\rho}}{b}\frac{\partial\bar{\rho}a}{\partial t} = \frac{1}{2b}\frac{\partial(\bar{\rho}a)^2}{\partial t}.$$

Since the concentrations do not vary during the instant of shock passage, b remains fixed at the value $b_2 = b(t_2)$ and we integrate to obtain

$$\bar{\rho}E_{2+} = \frac{(\bar{\rho}a_{2+})^2}{2b_2} - \frac{(\bar{\rho}a_{2-})^2}{2b_2} + \bar{\rho}E_{2-}\,. \qquad (19)$$

Here the second shock arrives at time t_2, and E_{2-} is the turbulence energy immediately prior to shock passage. (We are suppressing the explicit x-dependence for now.)

To evaluate a, we use Eq. (18) with the pressure gradient replaced by $(\partial\overline{P}/\partial x)\,\delta(t)$, following Saffman and Meiron[3], where $\overline{P}$ is the shock impulse with units of pressure × time and $\delta(t)$ has units of 1 / time as usual. The shock impulse is related to the

interface velocity V_2 after shock passage (in a reference frame traveling at velocity V_1 relative to the lab frame) by $\partial \bar{P}/\partial x = \bar{\rho} V_2$, as shown by Saffman and Meiron. So, integrating the a equation, we obtain

$$\bar{\rho} a_{2+} = \frac{b \partial \bar{P}}{\bar{\rho} \partial x} + \bar{\rho} a_{2-} = b_2 V_2 + \bar{\rho} a_{2-} . \qquad (20)$$

Use Eq. (20) in Eq. (19):

$$\bar{\rho} E_{2+} = \frac{b_2 V_2^2}{2} + V_2 \bar{\rho} a_{2-} + \bar{\rho} E_{2-}, \qquad (21)$$

which shows clearly the seeding of turbulence by b_2, the density self-correlation at time t_2, and by a_{2-}, the density-velocity correlation immediately prior to shock passage.

From Eq. (21) we evaluate the total turbulence kinetic energy after the second shock by integrating over the turbulent layer:

$$E_{Tot,2+} = \frac{V_2^2}{2} \int_{-h}^{h} \frac{b_2}{\bar{\rho}} dx + V_2 \int_{-h}^{h} a_{2-} \, dx + \int_{-h}^{h} E_{2-} \, dx$$

$$= I_\Lambda \left(\frac{A^2}{1-A^2} \right) h_2 \frac{V_2^2}{2} + I_{b0} \frac{b_{Tot,0}}{\langle \rho \rangle} \frac{V_2^2}{2} + V_2 a_{Tot,2-} + E_{Tot,0} \qquad (22)$$

where $h_2 = h(t_2)$, $I_\Lambda = \int_{-1}^{1} [1 - 4\zeta^2 \Lambda^2(\zeta)] \, d\zeta$, and $I_{b0} = \frac{\langle \rho \rangle}{2} \int_{-1}^{1} \frac{d\zeta}{\bar{\rho}(\zeta h_2, t_2)}$.

Substituting for $a_{Tot,2-}$ from Eq. (16a), inserting the expressions for $a_{Tot,0}$, $b_{Tot,0}$, and $E_{Tot,0}$, from Eqs. (7) and (9), defining $w_a = (\langle \rho \rangle / 2[\rho]_a)^{1/3}$, $w_E = (\langle \rho \rangle / 2[\rho]_E)^{1/3}$, and substituting

$$h_2 = \xi_0 E_{Tot,0}^{1/3} t_2^{2/3} = \xi_0 w_E A^{2/3} V_1^{2/3} S^{1/3} t_2^{2/3};$$

$$L = V t_2; V_1 = zV; \text{ and } V_2 = (1-z) V$$

leads to

$$\frac{E_{Tot,2+}}{V^2 S} = \gamma_1 \frac{A^{8/3}}{1-A^2} \left(\frac{L}{S} \right)^{2/3} z^{2/3} (1-z)^2 + \gamma_2 A^{4/3} \left(\frac{L}{S} \right)^{1/3} z^{4/3} (1-z)$$

$$+ A^2 \left[\frac{I_{b0}}{2} (1-z)^2 + w_a^3 z (1-z) + w_E^3 z^2 \right] \qquad (23)$$

where $\gamma_1 \equiv \frac{\xi_0}{2} w_E I_\Lambda$ and $\gamma_2 \equiv \xi_0^2 w_E^2 \Gamma_0$. The terms in powers of L/S in this equation represent the b and a seeds that grow during the inter-shock period, while the terms in the square bracket represent pre-existing b, and a and E created immediately by the first shock.

IV. EVALUATION OF TURBULENCE ENERGY

We consider two limiting cases of Eq. (23) to simplify some coefficients. These are the cases for $z = 0$ and $z = 1$, which are equivalent since they correspond to a situation in which there is only one shock wave accelerating the interface. For $z = 0$, we find

$$E_{\mathrm{Tot},2+} = \frac{I_{b0}}{2} A^2 V^2 S$$

while for $z = 1$ we find

$$E_{\mathrm{Tot},2+} = w_E^3 A^2 V^2 S.$$

Requiring these cases to be equivalent means $w^3_E = I_{b0}/2$, which we take as a definition of $[\rho]_E$.

We proceed now to evaluate the function $E_{Tot,2+}(A,S;L,z) / V^2S$ for several cases. In so doing, we explicitly set the coefficients γ_1, γ_1, w_E^3, and w_a^3 to unity. These coefficients are products of other constants near unity, so for illustrative purposes in evaluating Eq. (23) it is adequate to do this.

Figures 2 and3 show $E_{Tot,2+}/ V^2S$ as a function of $z = V_1/ V$ for L/S fixed at a value of 100 and Atwood number $A = 0.99$ and 0.50. The dotted line shows the contribution from the seeds that grow during the inter-shock period (i.e., the first two terms in Eq. (23)) while the dashed line shows the contribution from the remaining terms, which describe the pre-existing or immediately created seeds. For $A = 0.99$ and $L/S = 100$ (Fig. 2), the first term in Eq. (23) dominates, by virtue of the denominator $1- A^2$ and the 2/3 power of L/S. Thus the dependence of $E_{Tot,2+}$ on z is almost entirely given by the function $z^{2/3}(1-z)^2$. This function peaks at $z = 1/4$. We see that in this high-Atwood-number, small-perturbation limit, the turbulence energy is maximized if the first shock is somewhat weaker than the second. For accelerations in which 60% or more of the maximum velocity is acquired in the first shock, the turbulence energy may be less than half what it is when only 25% of the maximum velocity is acquired in the first shock. Of course, the absolute minimum values of turbulence are obtained for $z = 1$ or $z = 0$, but typically other constraints, such as entropy generation, require intermediate values of z.

As the Atwood number decreases (Fig. 3) , the other terms in Eq. (23) become relatively more important, although the absolute amount of turbulence energy drops.

V. ACKNOWLEDGEMENTS

The author wishes to thank Frank Harlow, Charles Cranfill, Rick Rauenzahn, Tim Clark, Charles Zemach, and Bill Varnum for valuable suggestions and useful discussions.

REFERENCES

1. D.C. Besnard, F. H. Harlow, and R. M. Rauenzahn, "Conservation and Transport Properties of Turbulence with Large Density Variations," Los Alamos National Laboratory report LA-10911-MS, February 1987.

2. D. C. Besnard, J. F. Haas, and R. M. Rauenzahn, "Statistical Modeling of Shock-Interface Interaction," Physica D **37** (1989) , pp. 227 - 247.

3. P. G. Saffman and D. I. Meiron, "Kinetic energy generated by the incompressible Richtmeyer-Meshkov instability in a continuously stratified fluid," Phys. Fluids A **1** (11), November 1989, pp. 1767 - 1771.

4. G. I. Barenblatt, "Selfsimilar Turbulence Propagation from an Instantaneous Plane Source", In: *Non-Linear Dynamics and Turbulence,* edited by G. I. Barenblatt, G. Ioos, and D. D. Joseph, Pitman, Boston (1983), pp. 48 - 60.

FIGURE CAPTIONS

1.Possible interface trajectories for the case of two shocks, such that the interface is brought to velocity V at position x, no later than time t. There is a doubly infinite family of such trajectories, characterized by the parameters V_1 (the interface velocity after the first shock)and t_2 (the arrival time of the second shock).

2. Scaled total turbulence energy ($E_{Tot,2+}/ V^2S$) after second shock, as a function of first shock strength, for Atwood number $A = 0.99$ and scale-ratio parameter $L/S = 100$. Peak value occurs at $V_1/ V = 1/4$.

3. Similar to Fig. 2, but for $A = 0.50$, $L/S = 100$. Peak value occurs at $V_1/ V \sim 0.3$. Dotted line shows contribution from seeds grown during Phase II, while dashed line shows contributions from seeds pre-existing or created at Phase I.

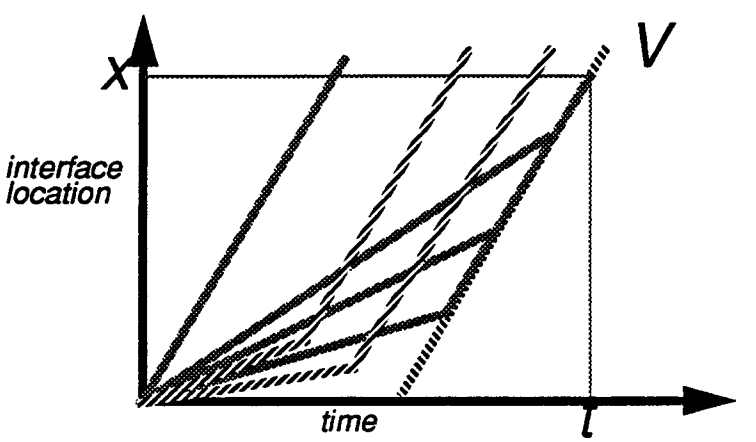

Fig.1

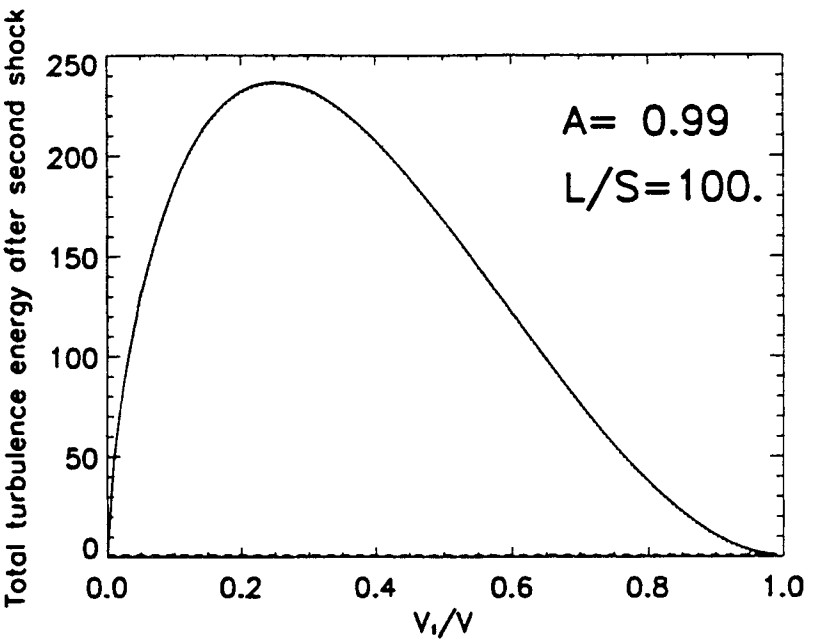
Total turbulence energy after second shock
250
200
150
100
50
0
0.0
0.2
0.4
0.6
0.8
1.0
V_t/V
A= 0.99
L/S=100.

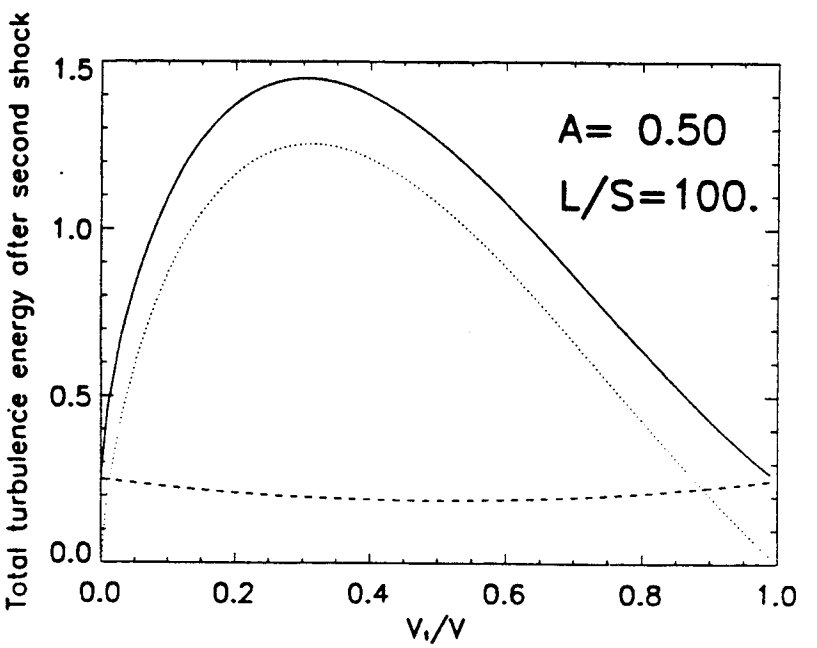
Total turbulence energy after second shock
1.5
1.0
0.5
0.0
0.0
0.2
0.4
0.6
0.8
1.0
V_t/V
A= 0.50
L/S=100.

SPECTRAL TRANSPORT MODEL FOR VARIABLE DENSITY TURBULENT FLOW

D. Besnard
Centre d'Etudes de Limeil-Valenton, 94195 Villeneuve-St-Georges CEDEX France
F.H. Harlow, R.M. Rauenzahn, C. Zemach
Los Alamos National Laboratory, Group T-3, MS B216, Los Alamos NM 87545 USA

Abstract: The spectrum of inhomogeneous turbulence is modeled by an approach that is not limited to regimes of Large Reynolds numbers or small mean-flow strain rates. In its simplest form and applied to incompressible flow, this one-equation model depends on five phenomenological constants defining the strength of turbulence coupling to mean-flow, turbulence transport in physical and wave-number space, and mixing of stress-tensor components. When applied to variable density flow, it includes two additional equations, that increase greatly its complexity. The implications for homogeneous incompressible turbulence, isotropic or anisotropic,were found to correspond well to the conclusions from more fundamental theories. It was shown in this case that a turbulent system described by the model relaxes over time into a state of spectral equilibrium, permitting a reduction to a one-point model very close from the familiar "K-ε" model. We address here the problem of deriving the equations generalizing the model to variable density flow, and present some results for homogeneous turbulence.

1-INTRODUCTION

The theoretical modeling of complex turbulent flows, after decades of efforts, is still far from adequate. Only the relatively simple one-point transport models /1/ come close to being useful for simulating flows of practical interest to the engineering community. Among these,models of the "K-ε" family /2,3/ are simple and robust, and have enjoyed the favor of many researchers; however, there are limitations in what such models can describe. K-ε models and their extensions /4/ can deal with flow close from equilibrium, in a sense that was defined more precisely elsewhere /5, 6/. Starting from Navier-Stokes equations, velocity and pressure fields are then divided in mean and fluctuating parts. The most general second order correlation that can be considered here involves velocities at two different points and two different times; to deal with flow far equilibrium, one has to keep some information on fluctuations both in physical space and in wave number space. If $C(x_1,x_2)$ denotes such a correlation, the above constraint means that we must know the dependance of C both with regard to $(x_1+x_2)/2$, and (x_1-x_2). An evolution equation is therefore derived /5/ for a generalized Reynolds tensor defined as $R_{ij}(x_1,x_2) = \overline{u'_i(x_1)u'_j(x_2)}$. These correlations vanish at finite distance, of the order of the characteristic scale of turbulence, and a Fourier transform of the equation obtained for R_{ij} is used to obtain a spectral model. For the sake of simplicity, the resulting equation is averaged over wavevector angles, and the model describes therefore the evolution of the turbulent kinetic energy density in physical space and wavenumber space, defined as

$$E_{ij}(x,k,t) = \frac{1}{2} \int R_{ij}(x,k,t)\, k^2 \frac{d\Omega_k}{(2\pi)^3} \quad .$$

Integrating the trace of this tensor over wavenumber, one obtains the density of turbulent kinetic energy at point x. The usual Reynolds tensor is therefore

$$R_{ij}(x,x,t) = 2 \int_0^\infty E_{ij}(x,k)\, dk$$

Obtaining an evolution equation for E_{ij} relies on the formal expansion of the initial equation in a series of differential operators, for which it is very difficult to prove convergence. However, it is intuitively plausible that the terms of order n are proportional to the ratio $(L_T/L_u)^n$, where L_T is the characteristic scale of turbulence and L_u is the gradient length of the flow velocity. The ration of these two quantities may be assume to be small, meaning that fluctuations vary at a smaller scale than those of the mean flow. This hypothesis suggests to keep only low order terms in the above mentioned expansion. Reference /5/ retains first order terms. At this point, there are still some unknown correlations in the equation that have to be modeled. This is done using known variables, and the criteria is to take the simplest formulations, namely linear or quadratic, that are dimensionally correct and have the required invariance properties (for example, translational invariance), and the specific properties of the original correlations. One obtains an equation which, in its simplest form /5/, writes

$$\frac{\partial E_{ij}}{\partial t} = -(1 - c_B)\left(E_{in} \frac{\partial u_j}{\partial x_n} + E_{nj} \frac{\partial u_i}{\partial x_n}\right) - \frac{2}{3} c_B\, \delta_{ij}\, E_{mn} \frac{\partial u_m}{\partial x_n} - E_{nj} \frac{\partial u_i}{\partial x_n} + \frac{1}{2} \nu \nabla^2 E_{ij}$$

$$- 2\nu k^2 E_{ij} + c_M k\sqrt{kE}\left(E\frac{\delta_{ij}}{3} - E_{ij}\right) + c_D \frac{\partial}{\partial x_n}\left(\nu_t \frac{\partial E_{ij}}{\partial x_n}\right) - c_1 \frac{\partial}{\partial k}\left(k^2 \sqrt{kE}\, E_{ij} \right)$$

$$+ c_2 \frac{\partial}{\partial k}\left(k^3 \sqrt{kE} \frac{\partial E_{ij}}{\partial k}\right)$$

where u_i is the mass averaged velocity, E is the trace of E_{ij}, and the turbulent viscosity ν_t is defined as

$$\nu_t = \int_0^\infty \frac{\sqrt{kE(x,k)}}{k^2} dk \quad .$$

There are five phenomenological constants in this model, c_B, c_D, c_1, c_2, and c_M.For this model to have a reasonable degree of universality, these coefficients have to stay constant for all the flows we are interested in. They are obtained through theoretical reasoning and comparisons with experiments. It is shown in /5/ that c_1 and c_2 are related to the Kolmogorov constant C_K through the relationship $c_1 + \frac{5}{3} c_2 = C_K^{-3/2}$. Moreover, the ratio c_1/c_2 may be taken to be equal to 2 if one uses the so-called equirepartition of energy property of triple correlations /6/. Analysis of the model in the circumstances of turbulence undergoing homogeneous irrotational strains suggests also /6/

$c_1 = \frac{6}{11} C_K^{-3/2}$, $c_2 = \frac{3}{11} C_K^{-3/2}$, and $c_M = \frac{26}{33} C_K^{-3/2}$. Each of the terms in Equation (1) can be associated with a well defined physical process which affects the evolution of the turbulence spectral density. Turbulence is transported by mean-flow, including shears $\left(E_{in} \frac{\partial u_j}{\partial x_n} + E_{nj} \frac{\partial u_i}{\partial x_n}\right)$ However, these terms are separated from the total derivative of E along the mean flow to be interpreted as a source of energy to the mean flow. If the flow is incompressible, it is possible to show that the correlation relating pressure and velocity do not furnish any energy to the system; rather, they induce a relaxation of the flow into an isotropic state. They are usually modeled through two terms; the first one is independent of the mean flow, persisting in homogeneous circumstances; the second one includes mean flow shear effects. In Equation (1), they are the terms respectively

proportional to c_M and c_B. Viscous effects appear in the terms proportional to ν; one notices direct dissipation into heat and diffusion in physical space. Triple correlations arise in the derivation of Equation (1), demonstrating non-linear, non-local of the turbulence on itself. They are modeled as diffusion in physical space $\left(\text{i.e. } c_D \frac{\partial}{\partial x_n}\left(\nu_t \frac{\partial E_{ij}}{\partial x_n}\right)\right)$. The last terms that are not yet commented in Equation (1) do not involve mean variables; they correspond therefore to a physical process which is characteristic of homogenous turbulence. It is the well-known nonlinear coupling between modes in the spectrum of turbulence. Even though it is widely recognized that this transfer is non-local, it was chosen in /5/ an approximation based on and its two first derivatives, $- c_1 \frac{\partial}{\partial k}\left(k^2\sqrt{kE}\, E_{ij}\right)+c_2\frac{\partial}{\partial k}\left(k^3 \sqrt{kE} \frac{\partial E_{ij}}{\partial k}\right)$. It was demonstrated that this approximation gives excellent results /5/.

It was demonstrated /5/ that, in the constant density case, our model allows for self-similar regimes of homogeneous isotropic turbulence, as well as free shear layer turbulence. However, it was shown recently /7/ that such self-similar rgimes exist for other flows, in particular for Rayleigh-Taylor instability induced turbulence. We want to describe in Section 2 a generalization of the model derived in /5/ that can be applied to this other family of flows. This step toward non-constant density flow is not straightforward. In effect, previous theories and experiments furnish information about the spectrum of homogeneous isotropic turbulence, which helps support our modeling. For variable density flows, very little is known, and what we propose here is by no means cast into concrete. As a guidance, we can use the fact that we should find a self-similar solution for the model when applied to such circumstances as Rayleigh-Taylor instability induced turbulence. Also, by taking moments of the model, we should obtain equations similar to second order models as described, for example, in /4/ and /8/. A third constraint is that the limiting case of buoyancy driven turbulence must be recovered.

2-VARIABLE DENSITY CASE

2.1-Basic notations

Compared to the constant density case, the new ingredient is the mass conservation equation. Even though we still assume that the divergence of the velocity vanishes, density can vary throughout the flow. This allows us to deal with such circumstances of the mixing of two incompressible fluids, as studied by Read and Youngs /9/. We start from the continuity equation, which reads

$$\frac{\partial \rho}{\partial t} + (\rho u_n),_n = 0, \qquad (2)$$

and Navier-Stokes equation,

$$\frac{\partial \rho u_i}{\partial t} + (\rho u_i u_n),_n = -p,_i + \nu\,(\rho u_i,_n),_n \ , \qquad (3)$$

together with the incompressibility condition

$$u_n,_n = 0 \ . \qquad (4)$$

We also define the quantities $B(x_1,x_2) = \overline{\rho'(x_1)\rho'(x_2)}$,

$A_j(x_1,x_2) = \overline{\rho'(x_1)u'_j(x_2)}$, $T_{ij}(x_1,x_2) = \overline{u'_i(x_1)u'_j(x_2)}$.

After a spherically averaged Fourier Transform, these correlations are denoted by $B(x,k)$, $A_j(x,k)$, and $T_{ij}(x,k)$, and have dimensions of respectively M^2L, ML^2T^{-1}, and L^3T^{-2}. Triple correlations will also be considered. Among those, let us define

$X^{\rho u_i - u_n}(x_1,x_2) = \overline{\rho'(x_1)u'_i(x_1)u'_n(x_2)}$.

In terms of energy balance, Equations (2-3) imply that

$$\frac{d}{dt}\left(\frac{1}{2}\,\overline{\rho}\,\overline{u_i}\,\overline{u_i}\right)+\frac{\partial}{\partial t}\int dk\left(\overline{\rho}\,(x)\,T_{ii}(x,k) + \overline{u_i}\,(x)A_i(x,k) + \frac{1}{2}\Sigma_i\, X^{\rho u_i - u_i}(x,k)\right)$$

should be conservative.

2.2-Generic approach for second order correlations

We have to derive evolution equations for second order correlations that involve the fluctuations of two different variables. We therefore develop here a generic approach to this problem. Let a(x), b(x) be field variables subject to evolution equations with advection by the velocity field u(x). We have

$\frac{\partial a}{\partial t} + u_n\, a_{,n} = S_a$,

$\frac{\partial b}{\partial t} + u_n\, b_{,n} = S_b$,

where S_a and S_b may include pressure and viscosity terms.

Separating a and b into mean and fluctuating parts, we derive an evolution equation for the cross-correlation $\overline{a'b'}$ which writes

$$\frac{\partial}{\partial t}\,\overline{a'(x_1)b'(x_2)} = -\,\overline{u_n}\,(x_1)\frac{\partial}{\partial x_{1n}}\left(\overline{a'(x_1)b'(x_2)}\right) - \overline{u_n}\,(x_2)\frac{\partial}{\partial x_{2n}}\left(\overline{a'(x_1)b'(x_2)}\right) \qquad (5)$$

$$-\frac{\partial\,\overline{a}\,(x_1)}{\partial x_{1n}}\,\overline{u'_n(x_1)b'(x_2)} - \frac{\partial\,\overline{b}\,(x_2)}{\partial x_{2n}}\,\overline{a'(x_1)u'_n(x_2)}$$

$$-\frac{\partial}{\partial x_{1n}}\left(\overline{a'(x_1)u'_n(x_1)b'(x_2)}\right)$$

$$-\frac{\partial}{\partial x_{2n}}\left(\overline{a'(x_1)u'_n(x_2)b'(x_2)}\right) + \overline{S_a(x_1)b'(x_2)} + \overline{a'(x_1)S_b(x_2)}$$

The rigth hand side of Equation (5) has four different types of terms:
(1) advections terms, (2) mean gradient coupling to $\overline{a}$ and $\overline{b}$, (3) divergences of triple correlations of type $X^{a u_n - b}$, $X^{a - u_n b}$, (4) S_a and S_b terms. Note that in the limit of $x_1 \to x$ and $x_2 \to x$, terms (1) take the conservative form $-\frac{\partial}{\partial x_n}\left(\overline{u_n}\,(x)\,\overline{a'b'}\right)$, term (2) is a coupling term $-\frac{\partial\,\overline{a}}{\partial x_n}\,\overline{u'_n b'} - \frac{\partial\,\overline{b}}{\partial x_n}\,\overline{a'u'_n}$,
and terms (3) take the conservative form $\frac{\partial}{\partial x_n}\left(\overline{a'u'_n b'}\right)$.

2.3-Fourier Transform

Consider now the Fourier Transform to (x,k) space. It is defined as
$FT\,\{\phi(x_1,x_2)\} = \phi(x,k)$,

$$\phi(x,k) = \int e^{-ik.(x_1-x_2)}\, f(x_1,x_2)\, d(x_1-x_2) .$$

Inversely,

$$f(x_1,x_2) = \int e^{ik.(x1-x2)}\, \phi(x,k)\, \frac{dk}{(2\pi)^3}\,.$$

The spherical average in k-space is defined as

$$\phi(x,k) = \int \phi(x,\mathbf{k})\, k^2\, \frac{d\Omega_k}{(2\pi)^3}\,.$$

Then

$$\int \phi(x,k)\, dk = \phi(x,x).$$

We apply a Fourier Transform to Equation (5), and consider first the advection terms (1). Their Fourier Transform involves formal expansion in differential operators, of which we keep only the lowest order terms (i.e. first order), as in reference /5/. We obtain that they become

$$-\overline{u_n}\,\frac{\partial}{\partial x_n}\left(\overline{a'b'}\right) - \frac{\partial\,\overline{u_n}}{\partial x_n}\,\frac{\partial}{\partial k_m}\left(k_n\,\overline{a'b'}\right)\,. \qquad (6)$$

Similarly, mean-flow coupling terms (2) become

$$-\frac{\partial\,\overline{a}}{\partial x_m}\left(\overline{u'_n b'}\right) - \frac{\partial\,\overline{b}}{\partial x_m}\left(\overline{u'_n a'}\right)\,. \qquad (7)$$

Third order correlation terms (3) can be rewritten as

$$T3 = -\frac{1}{2}\left(\frac{\partial}{\partial x_{1n}} + \frac{\partial}{\partial x_{2n}}\right)\left(\overline{a'(x_1)\{u'_n(x_1)+u'_n(x_2)\}b'(x_2)}\right)$$

$$-\frac{1}{2}\left(\frac{\partial}{\partial x_{1n}} - \frac{\partial}{\partial x_{2n}}\right)\left(\overline{a'(x_1)\{u'_n(x_1)-u'_n(x_2)\}b'(x_2)}\right)\,. \qquad (8)$$

The first line in Equation (8), after Fourier Transform, becomes a term explicitely conservative in physical space, namely

$$-\frac{1}{2}\,\frac{\partial}{\partial x_n}\left(X^{a\text{-}un\,b}(x,\mathbf{k}) + X^{au\,n\text{-}b}(x,\mathbf{k})\right)\,.$$

Both terms in the second line vanish when x_1 goes to x_2, so their transforms vanish when integrated over **k**. Using our modeling strategy to approximate terms with the simplest possible expression, we propose the first line to be the sum of an advection and a diffusion term in physical space, namely

$$T3 = C_{D2}^{(a,b)}\,\frac{\partial}{\partial x_n}\left(\nu_t(x)\frac{\partial}{\partial x_n}\left(\overline{a'b'}\right)\right) - C_{D1}^{(a,b)}\,\frac{\partial}{\partial x_n}(w_t(x))_n\left(\overline{a'b'}\right)\,,$$

where $w_t(x)$ is a turbulent velocity. For example, we might chose $A_n(x,x)/\overline{\rho}$.

The second line in Equation (8) vanishes when integrated over k, and is therefore modeled as a transfer term in wavenumber space (after spherical average). As in reference /5/, we propose advection and diffusion to be only operative in this approximation.

To compute spherical averages in wavenumber space of $\frac{\partial}{\partial k_m} Q_m(\mathbf{k})$, we integrate over a sphere of radius k, to obtain

$$\int_0^k k'^2\, dk' \int d\Omega_{k'} \left(\frac{\partial}{\partial k'_m} Q_m(\mathbf{k}')\right) = \int Q_m(\mathbf{k}).dS_m) \,, \qquad (9)$$

after use of Gauss's theorem. For a shell of radius k, $dS_m = \frac{k_m}{k} k^2\, d\Omega_k$. We then differentiate Equation (9) with respect to k, to obtain that

$$\int \frac{\partial}{\partial k_m} Q_m(\mathbf{k})\, k^2\, d\Omega_k = \frac{\partial}{\partial k} \int Q_m(\mathbf{k}) \frac{k_m}{k} k^2\, d\Omega_k \,. \qquad (10)$$

2.4-Evolution equation for correlation B

We now specialize Equation (5) to the case of the correlation B, and use Equations (6-10). We obtain

$$\frac{\partial B}{\partial t} = - \overline{u_n} \frac{\partial B}{\partial x_n} - 2 \frac{\partial \overline{\rho}}{\partial x_n} A_n - C_{D1}^{(B)} \frac{\partial}{\partial x_n}\left((w_t(x))_n B\right) + C_{D2}^{(B)} \frac{\partial}{\partial x_n}\left(\nu_t(x) \frac{\partial B}{\partial x_n}\right)$$

$$- C_{1T}^{(B)} \frac{\partial}{\partial k}\left(k^{5/2} \sqrt{T}\, B\right) + C_{2T}^{(B)} \frac{\partial}{\partial k}\left(k^{7/2} \sqrt{T} \frac{\partial B}{\partial k}\right) \qquad (11)$$

$$- C_{1A}^{(B)} \frac{\partial}{\partial k}\left(k^3\, a\, B\right) + C_{2A}^{(B)} \frac{\partial}{\partial k}\left(k^4\, a \frac{\partial B}{\partial k}\right),$$

where $T = T_{mm}$, and $a = (A_m A_m)^{1/2} / \overline{\rho}$.

2.5-Evolution equation for the correlation A_i

Similarly, we obtain an evolution equation for A_i. In this case, there is a spherical averaging to perform, which writes

$$N_j^{nm} = \frac{\partial \overline{u_n}}{\partial x_m} \frac{\partial}{\partial k}\left(\frac{1}{4\pi} \int A_j(x,\mathbf{k}) \frac{k_m k_n}{k} d\Omega_k\right).$$

We then assume that this integral can be expressed as a linear combination of the available vector A_i and tensor δ_{ij}. We have

$$N_j^{nm} = \frac{\partial \overline{u_n}}{\partial x_m} \left(q_1\, \delta_{nm}\, A_j(x,k) + q_2\, (\delta_{mj} A_n + \delta_{nj} A_m)\right) . \qquad (12)$$

Two additional constraints apply to Equation (12). It must contract into A_j itself, and the incompressibility condition, to lowest order, implies that N_l^{nl} vanishes. We thus obtain $q_1 = \frac{4}{10}$ and $q_2 = \frac{1}{10}$. The evolution equation for A therefore reads

$$\frac{\partial A_j}{\partial t} = - \overline{u_n} \frac{\partial A_j}{\partial x_n} - \frac{\partial \overline{\rho}}{\partial x_n} T_{nj} - \frac{\partial \overline{u_j}}{\partial x_n} A_n - \frac{1}{10}\left(\frac{\partial \overline{u_n}}{\partial x_j} + \frac{\partial \overline{u_j}}{\partial x_n}\right) \frac{\partial}{\partial k}(k A_n)$$

$$- C_{D1}^{(A)} \frac{\partial}{\partial x_n}\left((w_t(x))_n A_j\right) + C_{D2}^{(A)} \frac{\partial}{\partial x_n}\left(\nu_t(x) \frac{\partial A_j}{\partial x_n}\right)$$

$$- C_{1T}^{(A)} \frac{\partial}{\partial k}\left(k^{5/2} \sqrt{T} A_j\right) + C_{2T}^{(A)} \frac{\partial}{\partial k}\left(k^{7/2} \sqrt{T} \frac{\partial A_j}{\partial k}\right) \qquad (13)$$

$$- C_{1A}^{(A)} \frac{\partial}{\partial k}\left(k^3 a A_j\right) + C_{2A}^{(A)} \frac{\partial}{\partial k}\left(k^4 a \frac{\partial A_j}{\partial k}\right) - \overline{\rho' \left(\frac{p,i}{\rho}\right)} ,$$

where the last term is modeled as the sum of a decay term and a coupling to mean-flow pressure gradient, that is

$$- \overline{\rho' \left(\frac{p,i}{\rho}\right)} = - C_a k^2 a A_j + \frac{B}{\rho} \frac{\partial P}{\partial x_j} ,$$

where $P = \overline{p}$.

2.6-Evolution equation for the correlation T_{ij}

The same procedure is applied to T_{ij}, to obtain

$$\frac{\partial T_{ij}}{\partial t} = - \overline{u_n} \frac{\partial T_{ij}}{\partial x_n} - SAT_{ij} - T_{nj} \frac{\partial \overline{u_i}}{\partial x_n} - T_{in} \frac{\partial \overline{u_j}}{\partial x_n}$$

$$- C_{D1}^{(T)} \frac{\partial}{\partial x_n}\left((w_t(x))_n T_{ij}\right) + C_{D2}^{(T)} \frac{\partial}{\partial x_n}\left(\nu_t(x) \frac{\partial T_{ij}}{\partial x_n}\right) \qquad (14)$$

$$- C_{1T}^{(T)} \frac{\partial}{\partial k}\left(k^{5/2} \sqrt{T} T_{ij}\right) + C_{2T}^{(T)} \frac{\partial}{\partial k}\left(k^{7/2} \sqrt{T} \frac{\partial T_{ij}}{\partial k}\right)$$

$$- C_{1A}^{(T)} \frac{\partial}{\partial k}\left(k^3 a T_{ij}\right) + C_{2A}^{(T)} \frac{\partial}{\partial k}\left(k^4 a \frac{\partial T_{ij}}{\partial k}\right) - \frac{1}{2} \overline{u'i \left(\frac{p,j}{\rho}\right)} - \frac{1}{2} \overline{u'j \left(\frac{p,i}{\rho}\right)} ,$$

where

$$SAT_{ij} = - \frac{\partial}{\partial k} k \left(q1 \left(\frac{\partial \overline{u_i}}{\partial x_m} T_{mj} + \frac{\partial \overline{u_j}}{\partial x_m} T_{im} \right.\right.$$

$$\left.\left. + \frac{\partial \overline{u_j}}{\partial x_m} T_{im} + \frac{\partial \overline{u_j}}{\partial x_m} T_{im} \right) + q3 \, \delta_{ij} \frac{\partial \overline{u_n}}{\partial x_m} T_{nm} + q5 \left(\frac{\partial \overline{u_i}}{\partial x_j} + \frac{\partial \overline{u_j}}{\partial x_i} \right) T \right) ,$$

where $q1 = -3 C_B + 2$, $q3 = 4 C_B - 2$, and $q5 = 2 C_B - \frac{7}{5}$.

The two last terms in Equation (14) are modeled as

$$PV_{ij} = \frac{1}{2} \left(\frac{A_i}{\rho} \frac{\partial P}{\partial x_j} + \frac{A_j}{\rho} \frac{\partial P}{\partial x_i} \right) . \qquad (15)$$

2.7-Viscosity terms

It is very easy to take viscosity into account. One obtains additional terms in Equations (13) and (14). They respectively write

$$-\nu\left(k^2 + \frac{1}{2}\nabla_x{}^2\right)A_j \text{ and } -\nu\left(2k^2 + \frac{1}{2}\nabla_x{}^2\right)T_{ij}\,.$$

3-INERTIAL RANGES

To address this problem, we consider the simpler case of homogeneous turbulence, first without density gradient, then in the presence of a gradient. Even though, our model equations present a formidable complexity defying any analytical treatment. To exhibit trends, we further simplify Equations (12-14) and neglect diffusion in wavenumber space in both equations (13) and (14), on the basis this terms are only a correction to the first-order derivatives in wavenumber space. Furthermore, for the sake of simplicity, we discard both advection and diffusion in k-space that are driven by the turbulent mass flux density a.

3.1-Inertial ranges of homogeneous two-phase turbulence under acceleration

In this case, the turbulence is assumed to be driven by a constant pressure gradient. Neglecting viscosity terms, and assuming isotropy, we obtain in this case

$$\frac{\partial E}{\partial t} = -c_1\frac{\partial}{\partial k}\left(k^{5/2}\sqrt{E}\,E\right) + c_2\frac{\partial}{\partial k}\left(k^{7/2}\sqrt{E}\frac{\partial E}{\partial k}\right) + a\,g_0\,, \tag{16}$$

$$\frac{\partial a}{\partial t} = c_{ae}\frac{\partial}{\partial k}\left(k^{5/2}\sqrt{E}\,a\right) + c_{aa}\frac{\partial}{\partial k}\left(k^3\,a^2\right) + b\,g_0 - c_a\,k^2\,a^2\,, \tag{17}$$

$$\frac{\partial b}{\partial t} = +c_{be}\frac{\partial}{\partial k}\left(k^{5/2}\sqrt{E}\,b\right) + c_{ba}\frac{\partial}{\partial k}\left(k^3\,a\,b\right)\,, \tag{18}$$

where b is non-dimensionalized using the density ρ, and g_0 is the constant acceleration acting on the flow.

We then look for inertial ranges, and assume that

$$E = \gamma(t)\,k^p,\ a = \alpha(t)\,k^m,\ \text{and } b = \beta(t)\,k^r. \tag{19}$$

Equations (16-18) then become

$$\frac{d\gamma}{dt} = \frac{3}{2}\,\gamma^{3/2}\,c_2\left(p + \frac{5}{3}\right)\left(p - \frac{c_1}{c_2}\right)k^{(p+3)/2} - \alpha\,g_0\,k^{m-p}\,, \tag{20}$$

$$\frac{d\alpha}{dt} = \alpha^2\,\gamma^{1/2}\,c_{aa}\,(3+2m)\,k^{2+m} + \alpha^2\,c_{ae}\left(\frac{5}{2} + \frac{p}{2} + m\right)k^{3/2+p/2} - c_a\,\alpha^2\,k^{2+m}$$
$$+ \beta\,g_0\,k^{r-m}\,, \tag{21}$$

$$\frac{d\beta}{dt} = \alpha\beta\,c_{ba}\,(3+m+r)\,k^{2+m} + \beta\,\gamma^{1/2}\,c_{be}\left(\frac{5}{2} + \frac{p}{2} + r\right)k^{3/2+p/2}\,. \tag{22}$$

We want values of p, m, and r such that the time dependent functions g, a, b are independent of k. If m is positive, the only possible case is that the pressure gradient $-g_0$ is zero. If m is negative, from equation (20), one obtains that p=-5/3, $p=c_1/c_2$, and p=-3. The first case corresponds to free decay, the second one to equipartitioning of energy between smaller and larger modes, and the third one, although apparently in agreement with so-called 2D turbulence, remains to be explained. From equations (21-22), we see that the value -5/3 for m and r is also possible, this value putting c_{ae} and c_{be} terms to zero, and negating exponents of k in the other terms. This particular triplet of values is the one observed in early results by Rudman /10/. Other possible values for m are -3/2 (putting the first term in equation (21) to zero), and m=-1, with p still equal to -5/3 or -3. The exponent r can take any of the values m, p, -(m+3).

As for the existence of such inertial ranges, equations (20-22) show that the triplet (-5/3, -5/3, -5/3) exists, provided $c=c_1/c_2$ is larger than -5/3. The k^{-1} inertial range for a may exist (as well as for b, in fact) and implies a t^{-1} behavior for α at large t. Integrated over k, equation (20) expresses the constraint that turbulence energy is finite, therefore that $\int a\,dk$ must be convergent, which in turn shows that such an inertial range would exist only for smaller k's than in the Kolmogorov inertial range. The same comment can be made for the possible $k^{-3/2}$ inertial range for a (and for b).

3.2-Self-similar solutions

We consider here a sligthly different system of equations, considered elsewhere /10/. It was obtained by balancing source and decay in equation (21), and introducing the obtained expression for a in equation (20) (let us emphasize that the analysis in § 3.1 is still valid here). This particular modeling of acceleration driven source term for turbulence is very close in spirit to what is obtained through a two-field approach. For example, one can refer to the one-point closure model derived by Youngs /9/ or Besnard et al /12/. Equation (20) thus becomes

$$\frac{\partial E}{\partial t} = - c_1 \frac{\partial}{\partial k}\left(k^{5/2} \sqrt{E}\, E\right) + c_2 \frac{\partial}{\partial k}\left(k^{7/2} \sqrt{E} \frac{\partial E}{\partial k}\right) + 2\, c_D\, k^3\, a^3 . \qquad (23)$$

Looking for self-similar solutions, we assume that

$$\begin{aligned} E &= K(t)\, L(t)\, f(kL(t)) , \\ a &= w(t)\, L(t)\, g(kL(t)) , \\ b &= Z(t)\, L(t)\, h(kL(t)) , \end{aligned} \qquad (24)$$

where $\xi = k\,L(t)$, $\int f(\xi)d\xi = \int g(\xi)d\xi = \int h(\xi)d\xi = 1$.

We also define $\xi_{max} = 1$, such that $k_{max}(t) = L^{-1}(t)$. In equation (24), K is an energy, W a velocity, and Z is dimensionless. Equations (21-22) and (23) then become

$$K^{-3/2} \frac{dK}{dt} L\, f + K^{-1/2} \frac{dL}{dt} \frac{d}{d\xi}(\xi f) = - c_1 \frac{d}{d\xi}(\xi^{5/2} f^{3/2}) + c_2 \frac{d}{d\xi}(\xi^{7/2} f^{1/2} \frac{df}{d\xi})$$
$$+ 2\, c_D\, K^{-3/2}\, w^3\, \xi^3 g^3 , \qquad (25)$$

$$w^{-2} \frac{dw}{dt} L\, g + w^{-1} \frac{dL}{dt} \frac{d}{d\xi}(\xi g) = c_{aa} \frac{d}{d\xi}(\xi^3 g^2) + c_{ae} \frac{K^{1/2}}{w} \frac{d}{d\xi}(\xi^{5/2} f^{1/2} g) - c_D\, \xi^2 g^2$$
$$+ \frac{ZL}{w^2} g_0\, h , \qquad (26)$$

$$\frac{1}{wZ}\frac{dZ}{dt} L\, h + w^{-1}\frac{dL}{dt}\frac{d}{d\xi}(\xi h) = c_{ba}\frac{d}{d\xi}(\xi^3 g h) + c_{be}\frac{K^{1/2}}{w}\frac{d}{d\xi}(\xi^{5/2} f^{1/2} h)\ . \quad (27)$$

From Equations (25-27), we can obatin the time evolution of K, w, and Z, enforcing time independence of the coefficients in these equations. From Equations (25-27), we have

$K^{-3/2}\frac{dK}{dt} L = -\alpha$, $K^{-1/2}\frac{dL}{dt} = \beta$, and $K^{-3/2} w^3 = \gamma$, α, β, and γ being constants.

The other constraints relating K, L, w, and Z can be expressed as functions of these three relationships. This yields

$$K = K_0\left(1 + \frac{t}{t_0}\right)^{-\alpha/(\alpha/2+\beta)},$$

$$L = L_0\left(1 + \frac{t}{t_0}\right)^{\beta/(\alpha/2+\beta)},$$

$$w = w_0\left(1 + \frac{t}{t_0}\right)^{-\alpha/(\alpha+2\beta)}, \quad (28)$$

and

$$Z = Z_0\left(1 + \frac{t}{t_0}\right)^{-(\alpha+\beta)/(\alpha/2+\beta)}.$$

Initial values are related through the constraints

$$w_0 = \gamma^{1/3} K_0^{1/2},$$

$$L_0 = (\alpha/2 + \beta)\, t_0\, K_0^{1/2}, \quad (29)$$

$$t_0 = \frac{\gamma^{1/3}}{\alpha/2 + \beta}\frac{L_0}{w_0}\ .$$

(note that Z_0 is not related to other initial values because equation (22) is linear in b).

Inserting Equations (28-29) in Equations (25-27) leads to

$$\alpha f - \beta\frac{d}{d\xi}(\xi f) - c_1\frac{d}{d\xi}(\xi^{5/2} f^{3/2}) + c_2\frac{d}{d\xi}(\xi^{7/2} f^{1/2}\frac{df}{d\xi}) + 2\, c_D\, \gamma\, \xi^3 g^3 = 0, \quad (30)$$

$$\frac{\alpha}{2} g - \beta\frac{d}{d\xi}(\xi g) + c_{aa}\gamma^{1/3}\frac{d}{d\xi}(\xi^3 g^2) + c_{ae}\frac{d}{d\xi}(\xi^{5/2} f^{1/2} g) - c_D\, \gamma^{1/3}\, \xi^2 g^2 + P\, h = 0, \quad (31)$$

$$(\beta+\alpha)\, h - \beta\frac{d}{d\xi}(\xi h) + c_{ba}\gamma^{1/3}\frac{d}{d\xi}(\xi^3 g h) + c_{be}\frac{d}{d\xi}(\xi^{5/2} f^{1/2} h) = 0, \quad (32)$$

where $P = \left(\frac{L_0}{w_0^2}\right) g_0$.

Integrating Equation (30) over ξ, we obtain that

$$\alpha + 2\, c_D\, \gamma \int \xi^3 g^3\, d\xi = \lim_{\xi\to\infty}\left(c_1\, \xi^{5/2} f^{3/2} - c_2\, \xi^{7/2} f^{1/2}\frac{df}{d\xi}\right). \quad (33)$$

In the Kolmogorov inertial range, i.e. for large k's, we have $f \equiv f_\infty \xi^{-5/3}$, and we therefore obtain the following relationship between c_1 and c_2, generalizing the results presented in /5/

$$\alpha + 2\, c_D\, \gamma \int \xi^3 g^3\, d\xi = (f_\infty)^{3/2} \left(c_1 + \frac{5}{3} c_2\right) . \qquad (34)$$

Two similar relationships can be obtained from equations (31-32). Note also that the integration of Equation (32) over ξ leads to an inertial range in -5/3 for h, confirming the results of §3.1. When the transfer terms in Equation (32) are negligible, we obtain that $\alpha+\beta=0$. This in turns implies $K=K_0\left(1 + \frac{t}{t_0}\right)^2$, $L = L_0\left(1 + \frac{t}{t_0}\right)^2$, $w = w_0\left(1 + \frac{t}{t_0}\right)$, and $Z = Z_0$. This corresponds to the case of differential acceleration induced turbulence, applied to the case of an infinite medium. An example is given by a particulate gas (as in a fluidized bed); one observes particle clamping at larger and larger scales. Indeed, the condition $\alpha+\beta=0$, for small ξ's, implies that h behaves as ξ^{-1}(note that the rhs of Equation (32) is indeed negligible for small ξ's). This result has to be analyzed in more detail regarding its relationship to spectra of passive scalars in a turbulent field. The fact that this solution diverges when ξ goes to zero should not be troublesome. In efect, there is no damping mechanism on the production of turbulence, only a mere stabilization of turbulence growth rate. Note that the time evolutions obtained above are physically significant. In fact, in this problem, the acceleration is the only given parameter; one can therefore build only one length scale and one velocity scale from it, respectively proportional to $t^2$and t.

3.3-Similarity analysis

Defining the flux F_f as

$$F_f = \left(c_1\, \xi^{5/2} f^{3/2} - c_2\, \xi^{7/2} f^{1/2} \frac{df}{d\xi} \right), \qquad (35)$$

we note that Equations (30-32) are invariant under the change of variables $\xi \to \lambda\xi$, $f \to \lambda^{-3} f$, $F_f \to \lambda^{-2} F_f$, $g \to \lambda^{-2} g$, and $h \to \lambda^{-2} h$. Let us define $s=(c_2/\beta)^2 \xi^3 f$, $\phi=\beta^{-1}(c_2/\beta)^2 \xi^2 F_f$, $G=\beta^{1/3}(c_2/\beta)^{2/3} \xi^2 g$, and $H= \beta^{-1/3}(c_2/\beta) \xi^2 h$. We also define $b=\gamma/\beta$, $d_{aa}=c_{aa}/c_2$, $d_{ae}=c_{ae}/c_2$, $d_{ba}=c_{ba}/c_2$, $d_{be}=c_{be}/c_2$, $m=2bd_D$. From Equations (30) and (35), we deduce equations for s, ϕ, G, and H. They write

$$\xi \frac{ds}{d\xi} = (3+c)\, s - \frac{\phi}{s^{1/2}} , \qquad (36)$$

$$\xi \frac{d\phi}{d\xi} = 2\phi + (a-1-c)\, s + \frac{\phi}{s^{1/2}} + m\, G^3 , \qquad (37)$$

$$\xi \frac{dG}{d\xi} (1 - 2\, b^{1/3} d_{aa}\, G - d_{ae}\, s^{1/2}) =$$

$$\left(\frac{a}{2} + 1 + d_{ae} \frac{d\xi s^{1/2}}{d\xi} - 2\, d_{ae}\, s^{1/2}\right) G + \frac{\phi}{s^{1/2}} + b^{1/3} (d_{aa}+d_D)\, G^2 + P\, b^{1/3}\, H, \qquad (38)$$

$$\xi \frac{dH}{d\xi} (1 - 2\, b^{1/3} d_{ba}\, G - d_{be}\, s^{1/2}) =$$

$$\left(a + 2 + b^{1/3} d_{ba}\, \xi \frac{dG}{d\xi} - b^{1/3} d_{ba}\, G + d_{be} \frac{d\xi s^{1/2}}{d\xi} - 2\, d_{be}\, s^{1/2}\right) H . \qquad (39)$$

We already know the large wavenumber behavior of f, g, and h. Let us now consider the limit of small ξ's. To do so, let us consider the behavior of $\phi(s)$ and $s(\xi)$ near s=0. Equations (36-37) combine to give

$$\frac{d\phi}{ds} = \left(\frac{2\frac{\phi}{s} + (a-1-c) + \frac{\phi}{s^{1/2}} + m\,\frac{G^3}{s}}{(3+c)\,s - \frac{\phi}{s^{3/2}}} \right). \qquad (40)$$

From equation (40), one can have two possible cases when $s \to 0$. Either $\frac{\phi}{s^{3/2}} \to A$=constant, and $\phi(s)=(1+c-a)\ s^{3/2} + o(s^2)$; we thus deduce that s behaves as ξ^{a+2}. Similar reasoning leads to the conclusion that G behaves as $\xi^{a/2+1}$ and H as ξ^{a+2}. We therefore deduce that f, g, and h respectively behave as ξ^{a-1}, $\xi^{a/2-1}$, and ξ^{a} for ξ near 0. The other case is when $\frac{\phi}{s^{3/2}} \to \infty$, and $\frac{G^3}{s} \to 0$; we obtain that $\phi(s)=-\phi_0 - s + o(s^{3/2})$, and that s, therefore G and H vanish at $\xi=\xi_0$. Near $\xi=\xi_0$, they behave respectively as $(\xi-\xi_0)^2/4\xi_0^2$, $(\xi-\xi_0/2\xi_0)^{2(a/2+1+dae/2)}$, and $(\xi-\xi_0/2\xi_0)^{2(a+2+dbe/2)}$.

4- CONCLUSION

We extended in this paper a model derived /5/ for incompressible turbulence, extending it to the case of variable density turbulence. This version includes equations for the turbulent mass flux, as well as the density self-correlation.

As a first step, we explored the case of pressure gradient induced turbulence. As a conclusion all three spectra f, g and h (of respectively E, a and b) offer an $\xi^{-5/3}$ inertial range for large ξ's, and a small wavenumber behavior with an exponent depending of a, when extending clear to zero; the turbulence energy spectrum keeps in fact the same features than in the incompressible case. More analysis and numerical simulations are necessary to demonstrate that we recover the same spectra than those observed in /5/. Early results obtained by Rudman /10/ suggest this such a conclusion.

The next step is to study homogeneous circumstances in presence of a constant density gradient, then eventually consider the case of Rayleigh-Taylor instability induced turbulence, the main problem of interest to us.

References

1-B.E. Launder and D.B. Spalding, "Mathematical Models of Turbulence", Academic Press, New York, 1972.
2-B.E. Launder and D.B.Spalding, "The Numerical Computation of Turbulent Flows", Computer Methods in App. Mech. and Eng. 3, 269-289 (1974).
3-B.E. Launder, A.Morse, W. Rodi, and D.B. Spalding, "The Prediction of Free Shear Flows- A Comparison of Performance of Six Turbulence Models", Proceedings of the NASA Conference on Free Shear Flows, Langley Press, 1972.
4-D.C.Besnard, J.F. Haas, and R.M. Rauenzahn, Physica 37 D, 229-249 (1989).

5-D.C. Besnard, F.H. Harlow, R.M. Rauenzahn, and C. Zemach, "Spectral Transport Model for Turbulence", Los Alamos National Laboratory Report LA-11821-MS, submitted.
6-T. Clark, PhD Thesis, in preparation.
7-K.I. Read, Physica 12 D, 45-58 (1984).
8-J.L. Lumley, Advances in App. Mech. 18, 123-177 (1978).
9-D.L. Youngs, Physica 37D, 270-287 (1989).
10-M. Rudman, private communication. Rudman solved numerically a system of equations very close to equations (20-22), looked for self-similar solutions, and observed inertial ranges defined by the triplet (-5/3, -5/3, -5/3).
11-M. Lesieur, Turbulence in Fluids; Stochastic and Numerical Modeling, Martinus Nijhoff Publishers, (1987).
12-D.C Besnard, I. Kataoka, and A. Serizawa, submitted.

TRANSITION TO TURBULENCE IN COMPRESSIBLE SHEAR FLOWS

M. Lesieur
Institut de Mécanique de Grenoble
B.P. 53 X, 38041 Grenoble-Cedex, France

ABSTRACT

We study, with the aid of 2D and 3D direct-numerical or large-eddy simulations, the effect of compressibility on the dynamics of coherent vortices in shear layers (mixing layer and boundary-layer on a flat plate). We develop in particular a new subgrid model, the *structure-function model*, which allows to take into account the effects of intermittency and inhomogeneity of turbulence. This model permits us to perform a *forced-transition numerical experiment* in a boundary-layer at Mach 5: a staggered mode of large breaking-down Λ-shaped vortices is found.

INTRODUCTION

One of the most spectacular advances of Computational Fluid Dynamics is the possibility of visualizing the coherent structures and their interactions within flows which, for a long time, seemed to escape to any deterministic study. The Direct-Numerical Simulations (DNS) or Large-Eddy Simulations (LES) allow both to understand the fundamental physical mechanisms which control transition to developed turbulence, and can also serve as a reference for the modelling of industrial flows.

This DNS or LES-based approach is of interest, in particular, to study the influence of strong density differences or compressibility on transition in shear flows. These effects are not taken into account by classical modelling approaches such as the $K - \epsilon$ model, and may have drastic effects on turbulence, such as the inhibition of the spreading of a mixing layer, or the enhancement of three-dimensional instabilities growth when some convective Mach number is increased. These effects are of course of prior importance in order to understand mixing in compressible turbulence.

In this paper, one will study successively 2D and 3D mixing layers, both in the incompressible and compressible cases. The case of strong density differences (even in a quasi-incompressible fluid) will be in particular looked at. Afterwards, we will examine the effects of compressibility on the dynamics of 3D hairpin coherent vortices in a boundary layer close to a flat plate. This study will

require at high Mach number the use of a subgrid-model, the structure-function model, which will be briefly described.

THE TWO-DIMENSIONAL MIXING LAYER

The 2D dynamics of incompressible mixing layers between two parallel flows of different velocity is presently well understood, following numerous numerical simulations (see [1]). This is true both in the temporal (periodicity in the mean-flow direction) and spatially-growing cases. These calculations show in particular how coherent structures form by roll up of the initial vortex sheet, after the development of Kelvin-Helmholtz instability, and undergo successive pairings. Plate 1, taken from [2], shows the vorticity and passive temperature fields in the DNS of a 2D incompressible spatially-growing mixing layer between two streams of velocity U_1 and U_2, at a Prandtl number of 1: here, the flow is forced upstream by a basic velocity

$$\frac{U_1 + U_2}{2} + \frac{U_1 - U_2}{2} \tanh \frac{2y}{\delta_i} \quad ,$$

and a random perturbation (white noise) of low amplitude. The upstream temperature profile is identical to the basic velocity, so that the temperature plays the role of a numerical dye which is wrapped around the coherent concentrations of vorticity. Although this is a 2D calculation, we have checked, by varying the relative velocity ratio $\lambda = (U_1 - U_2)/(U_1 + U_2)$ that the computed spreading rate of the layer satisfies the universal law

$$\frac{d\delta}{dx} = 0.17\ \lambda \quad , \tag{1}$$

in good agreement with the laboratory experiments of [3]. Such a law (but not the value of the constant), may be recovered for instance by a self-similar study of the Reynolds equations (using Prandtl's mixing-length theory).

In order to study compressible flows, we have developed a finite-difference code based on a predictor-corrector method, solving Navier-Stokes equations for an ideal gas (see [2] for details). This code will here be called SHEARCOMP, and will be used either in the DNS version (SHEARCOMP-DNS), or with a subgridscale model which will be described below (SHEARCOMP-LES). Boundary conditions are (for the open boundaries) of the non-reflexive type.

Let us start with a 2D compressible mixing layer between two flows of same density upstream. The relevant Mach number is here the convective Mach number M_c, with respect to a frame following the coherent vortices. The calculations (temporal or spatial) confirm (for a given relative velocity ratio), a tendency for the Kelvin-Helmholtz instability to saturate when M_c is increased. This is due to the approximate conservation of the potential vorticity ω/ρ following the motion, valid as far as the flow remains barotropic: indeed, the fluid in one of

the layers will be compressed from the coherent vortices (where the pressure is minimum) to the stagnation points, and the density and vorticity will therefore increase (since p/ρ^γ and ω/ρ are conserved following the motion). This source of vorticity in the stagnation region goes against Kelvin-Helmholtz's instability. Plate 2 shows a spatial mixing layer at $M_c = 0.4$, and confirms this convergence effect in the stagnation region, although the layer is still essentially incompressible.

When the convective Mach number is increased up to about 0.7, the flow is accelerated around the Kelvin-Helmholtz vortices, and the situation is close to transsonic, with the formations of shocklets: this is visible on plate 3, showing the pressure jumps. One can check that these shocks do satisfy the mass, momentum and generalized enthalpy conservation. However, this situation does not persist very much if M_c is further increased: above 0.8, the Kelvin-Helmholtz vortices do not roll up, and become very elongated and flatened. Therefore, the flow is not accelerated any more, and shocklets disappear. In fact, this situation does not seem to be very realistic, since it is well known from various linear-stability studies or numerical simulations (see [4] and [5]) that 3D oblique waves are more amplified than 2D waves above $M_c = 0.6$.

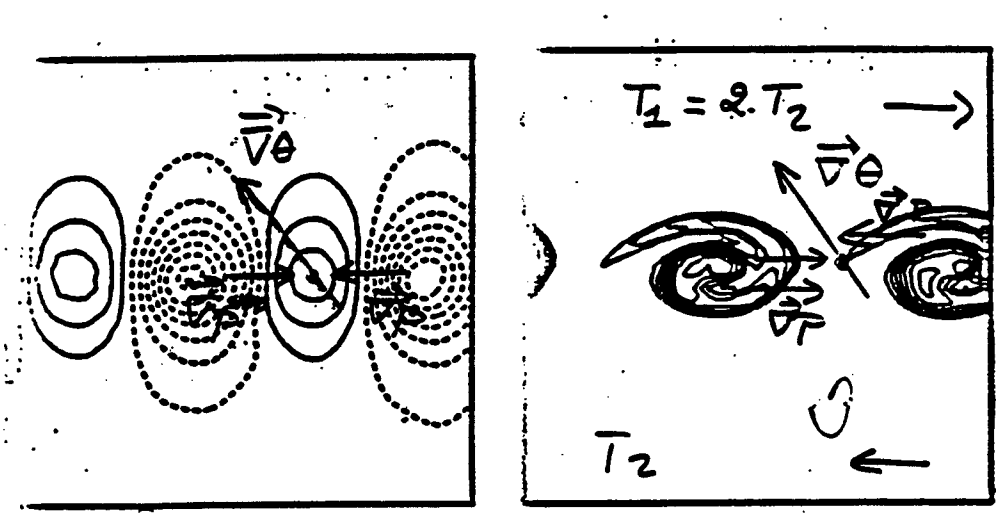

Figure 1: pressure and vorticity in a 2D compressible mixing layer, $M_c = 0.3, T_2 = 2\,T_1$ (from [4], courtesy Y. Fouillet).

Still in two dimensions, and at a weaker convective Mach number ($M_c = 0.3$), we

have examined the effects of strong density differences between the two flows in the mixing layer. Figure 1 corresponds to a temperature ratio of 2 between the two layers, and shows the pressure and vorticity fields at the end of the roll up of Kelvin-Helmholtz vortices. Comparing with the uniform temperature case, one observes the cancellation of vorticity in the cold part of the braids, while it is reinforced in the warm part. The result is a "cornue-shaped" vortex, which may be explained by considering the 2D potential vorticity equation which, for an ideal gas, writes (in the Euler case)

$$\frac{D}{Dt}(\frac{\vec{\omega}}{\rho}) = (\frac{\vec{\omega}}{\rho}).\vec{\nabla}\vec{u} + \frac{A}{\rho^2\Theta}\vec{\nabla}p \times \vec{\nabla}\Theta \quad , \tag{2}$$

where Θ is the potential temperature, conserved following the motion:

$$\frac{D\Theta}{Dt} = 0 \quad . \tag{3}$$

A is a constant. Therefore, the baroclinic torque is proportional to $\vec{\nabla}p \times \vec{\nabla}\Theta$. Since the braid may be considered as following the interface between the two layers, it is normal to the potential-temperature gradient, which keeps a constant direction all along the braid. On the other hand, the pressure gradient changes sign across the stagnation point (where the pressure is maximal, while it is minimal in the vortex core). Thus, the baroclinic torque changes sign on the braid across the stagnation point. This explains the reinforcement of vorticity on the lightest side.

THE THREE-DIMENSIONAL MIXING LAYER

Here, we just summarize some direct-numerical simulation results described in [6] and concerning the 3D temporal incompressible mixing layer forced initially by a hyperbolic-tangent velocity profile to which is superposed a random perturbation of low amplitude: if the perturbation is quasi two-dimensional, quasi 2D Kelvin-Helmholtz vortices will develop, which strain longitudinal hairpin vortex filaments between them. If the initial perturbation is three-dimensionally isotropic, a staggered mode of Kelvin-Helmholtz vortices will appear, corresponding to a helical-pairing instability (see plate 4):

These various topologies of the coherent-vortex field influence the large-scale mixing efficiency of the flow, the helical-pairing configuration being more diffusive (since more three-dimensional) than the quasi-2D one. We have not checked yet whether the mixing in the small scales (and the corresponding Kolmogorov $k^{-5/3}$ kinetic energy cascade) is influenced by the type of organization of the large scales.

We have also looked at the influence of compressibility on the 3D mixing layer (temporal or spatial) using the SHEARCOMP-DNS code, in the case of natural transition (see [4]): at low Mach numbers ($M_c = 0.3$), the helical-pairing

instability is still active. At $M_c = 0.8$ on the contrary, the most amplified mode predicted by the linear-stability theory (oblique mode) emerges, and the flow is highly three-dimensional.

THE STRUCTURE-FUNCTION SUBGRIDSCALE MODEL

It is well known that high-Reynolds number flows cannot be simulated at all the scales of motion, from the largest to the dissipative ones. In the large-eddy simulations, a space-filtered field is computed, the filter being of width Δx, the mesh size of the computational lattice.

If homogeneous isotropic turbulence is considered, the filter consists in retaining all the Fourier wavevectors such that $|\vec{k}| < k_c$, where $k_c = \pi/\Delta x$ is the cutoff wavenumber. We assume here that k_c lies in a $k^{-5/3}$ Kolmogorov range. For $k << k_c$, the subgridscale transfer across k_c commes from nonlocal triadic interactions such that $\vec{k} = \vec{p} + \vec{q}$, with $p, q >\sim k_c$. These transfers can be calculated analytically (at the level of the kinetic energy) using the EDQNM two-point closure (see [1]): it is found, by expansions with respect to the small parameter k/k_c, that the subgridscales play the role of an eddy-viscosity independant of k and equal to

$$\nu_t(k_c) = 0.44\ {C_K}^{-3/2}\ [\frac{E(k_c)}{k_c}]^{1/2} \quad , \tag{4}$$

where C_K is the Kolmogorov constant (which will be taken equal to 1.4). In fact, the exact EDQNM calculation (without small-parameter expansions) shows (see [1]) that the eddy-viscosity becomes k-dependant for k close to k_c, with a sharp cusp due to both local transfers in the neighbourhood of $k_c (k \sim p \sim k_c \sim q)$ and to large-scale velocity shears acting at $q << k \sim k_c \sim p$. In this spectral region (close to k_c), the eddy-viscosity concept is anyhow not very meaningful, since the subgridscales have an action both on the amplitude and the phase of the complex velocity. Since our aim is to come back to the physical space, where the spectral-cusp behaviour has no evident counterpart in terms of dissipative operator, we will approximate the action of the subgridscales on the spectral range $[0, k_c]$ by a constant eddy-viscosity of the same form as (4), but with a different constant given by the energy-conservation principle. This leads to

$$\nu_t(k_c) = \frac{2}{3}\ {C_K}^{-3/2}\ [\frac{E(k_c)}{k_c}]^{1/2} \quad . \tag{5}$$

Up to now, this is valid for homogeneous isotropic turbulence. However, if we come back to physical space (for any kind of turbulence, isotropic or not), it is well known that the flow presents a high degree of intermittency, with quiet quasi-irrotational regions surrounding intense-vorticity regions. In the calm regions, there is no need for any subgridscale dissipation. The latter is needed in the active regions: thus, we are lead to introduce the concept of local kinetic energy spectrum $E_{\bar{x}}(k_c)$, characterizing the local turbulence activity in

a neighbourhood Δx of $\vec{x}$. This spectrum may be calculated with the aid of the 2nd order velocity structure function, assuming that the subgridscale turbulence follows a Kolmogorov cascade. Introducing a correction due to the fact that the large-eddy simulation gives only access to the structure-function of the filtered field, it is found (see [7]):

$$\nu_t(\vec{x}|\Delta x) = 0.104\ {C_K}^{-3/2}\ \Delta x\ [\bar{F}_2(\vec{x}|\Delta x)]^{1/2}] \quad , \tag{6}$$

where $\bar{F}_2$ is the square velocity difference between the point $\vec{x}$ and any point a distance Δx apart, averaged upon the six grid points surrounding $\vec{x}$.

This *structure-function model* has been used satisfactorily in [7] for isotropic turbulence and homogeneous stratified turbulence, and in [8] for the backward-facing step flow (see also the presentation by Grand and Silveira in the same volume). Here, we apply the model to the compressible boundary-layer above an insulated flat plate.

THE COMPRESSIBLE BOUNDARY LAYER

This section summarizes a work published in [9] and concerning a boundary layer over an insulated flat wall. We will consider successively the low ($M_\infty = 0.5$) and high ($M_\infty = 5$) Mach number cases. At low Mach number, we assume periodicity in the streamwise direction. We have used the code SHEARCOMP-DNS in this case, and checked that it predicts satisfactorily the transition to small-scale developed turbulence, starting initially with a set of Tollmien-Schlichting (T.S.) waves perturbed by a 3D white noise of low amplitude. These calculations show the straining by the mean shear of vortex filaments organized in phase in the spanwise direction. These hairpin (or Λ-shaped) filaments, which correspond to Klebanoff's peak-valley structure, are submitted to self-induction effects, and rise about 45^0 from the boundary. Plate 5 shows these hairpin vortices before the transition: between the legs of the Λ (peak plane), the induced velocity corresponds to an upward flux of fluid which is closer to the wall, and hence of slower longitudinal velocity. In the valley planes, on the contrary, exists a downward flux of faster fluid. Therefore, the longitudinal velocity in a horizontal cross section of the hairpin vortices is alternatively rapid (valley) and slow (peak), and corresponds to longitudinal alternate streaks observed in many laboratory experiments. The longitudinal velocity profile becomes locally inflexional in the peak planes, and Kelvin-Helmholtz vortices are shed. These local mixing layers are well described by our calculation, as shown on figure 2 (taken from [9]). Afterwards, the boundary layer degenerates catastrophically to turbulence, with a logarithmic mean velocity profile and a friction coefficient in excellent agreement with the experimental results. Notice that a large-eddy simulation done with the code SHEARCOMP-LES in this case gives comparable results, and predicts the same transition time (determined by the abrupt rise of the friction coefficient). These calculations are done at a moderate resolution ($30 \times 25 \times 20$), and take about 10 hours on an ALLIANT VFX40 machine.

One must emphasize the fact that these transitional processes are highly three-dimensional, and that our code used in 2D simulations (with a sufficient extent of the domain in the transverse direction) does not show any two-dimensional roll up of the T.S. waves, which saturate[1].

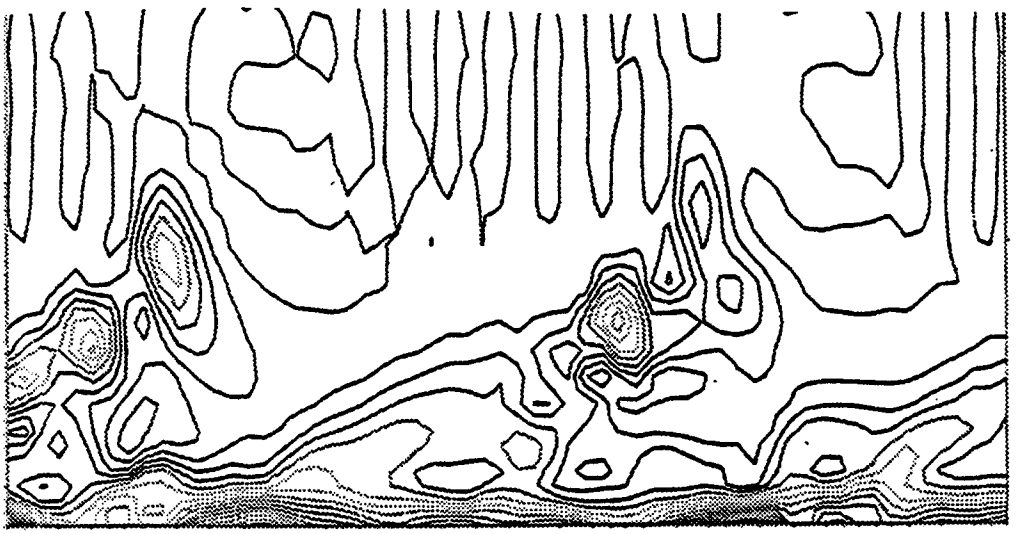

Figure 2: periodic weakly-compressible boundary layer, spanwise vorticity in a peak plane (courtesy X. Normand).

In the high supersonic regime (Mach 5), we have carried out a 3D simulation in the spatially growing case. At this Mach number, the critical Reynolds number for the development of linear instabilities is too high to allow for a direct-numerical simulation. We work at an upstream Reynolds number (based on the displacement thickness) of 10 000, and have implemented successfully the structure-function model in a large-eddy simulation. The resolution of the calculation is $400 \times 40 \times 20$ grid points in, respectively, the streamwise, transverse and spanwise direction. The flow is forced upstream by a set of 2D waves[2] to which is superposed a white noise of small amplitude. This is again a numerical experiment of forced transition. Plate 6 (taken from [9]) shows a horizontal section of the longitudinal velocity at the top of the boundary layer. It clearly indicates how upstream 2D waves evolve towards longitudinal filaments. The corresponding vortex structure in the transitional region is presented on plate 7 (taken from [9]). It indicates the presence of large Λ vortices staggered in the spanwise direction, looking like breaking-up waves. This topology resembles the

[1] contrary to the 2D Poiseuille flow, where the boundary layers on both walls detach, leading to two rows of vortices in phase opposition

[2] The second mode, corresponding to an inviscid linear instability, and calculated with the same code in a 2D calculation.

secondary staggered mode found by Herbert [10] in the incompressible boundary layer undergoing natural transition. The typical computational times are of 20 CRAY 2 hours. It seems then that the effect of compressibility is to favour the emergence of the staggered pattern.

CONCLUSION

We have demonstrated the immense possibilities of direct or large-eddy simulations, when applied to the study of 2D and 3D turbulence. In the case of the 2D compressible mixing layer, we have shown that Kelvin-Helmholtz instability is inhibitted above a convective Mach number of 0.6, with formation of shocklets at the edge of the coherent vortices. In the low Mach number case, but with strong temperature differences between the two layers, we have shown that the baroclinic torque cancels the vorticity in the cold side of the braid, and reinforces it in the warm side. For the 3D incompressible mixing layer, we have shown how a weak 3D residual turbulence may trigger a helical pairing between the K.H. vortices. On the contrary, a quasi 2D perturbation produces intense longitudinal hairpin vortices strained between the KH vortices. In the compressible case, linear effects (corresponding to 3D oblique waves) determine the naturally-transitioning 3D mixing layer when the convective Mach number exceeds 0.6. Finally, the direct-numerical simulation has allowed us to study the hairpin vortex dynamics during the transition in a weakly-compressible boundary layer.

We have also used a new subgridscale model, the structure-function model, for large-eddy simulations of turbulence. This model allows to simulate the transition in a Mach 5 boundary-layer at a Reynolds number of 10 000: in the forced-transition case, one obtains Λ-shaped vortices staggered in the spanwise direction.

AKNOWLEDGEMENTS

This study was sponsored by CCVR (Centre de Calcul Vectoriel pour la Recherche), CGCV-CEA (Centre Grenoblois de Calcul Vectoriel), and the HERMES programme.

REFERENCES

[1] Lesieur, M., 1990, *Turbulence in Fluids* (2nd revised edition), Kluwer Publishers.

[2] Normand, X., 1990, PhD dissertation, Institut National Polytechnique de Grenoble.

[3] Brown, G.L. and Roshko, A., 1974, "On density effects and large structure in turbulent mixing layers", J. Fluid Mech., **64**, pp 775-816.

[4] Fouillet, Y., 1991, PhD dissertation, Institut National Polytechnique de

Grenoble (in preparation).

[5] Sandham, N.D. and Reynolds, W.C., 1991, "Three-dimensional simulation of large eddies in the compressible mixing layer", J. Fluid Mech., **224**, pp 133-158.

[6] Comte, P. et Lesieur, M., 1990, "Large and small-scale stirring of vorticity and a passive scalar in a 3D temporal mixing layer", submitted to Phys. Fluids.

[7] Metais, O. and Lesieur, M., 1990, "Spectral large-eddy simulations of isotropic and stably-stratified turbulence", submitted to J. Fluid Mech.

[8] Silveira Neto, A., Grand, D. Métais, O. and Lesieur, M., 1991, "Large-eddy simulation of the turbulent flow in the downstream region of a backward-facing step", Phys. Rev. Letters, in press.

[9] Normand, X. et Lesieur, M., 1991, "Numerical experiments on transition in the compressible boundary layer over an insulated flat plate", Theor. and Comp. Fluid Dynamics, in press.

[10] Herbert, T., 1988, "Secondary instability of boundary layers", Ann. Rev. Fluid Mech., **20**, pp 487-526.

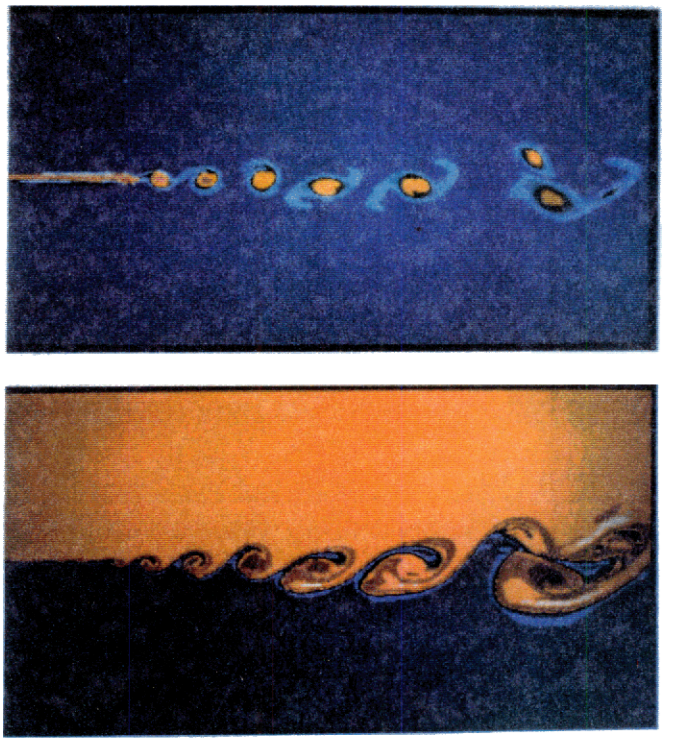

Plate 1: 2D direct-numerical simulation of an incompressible spatially-growing mixing layer, vorticity and passive temperature (from [2], courtesy X. Normand).

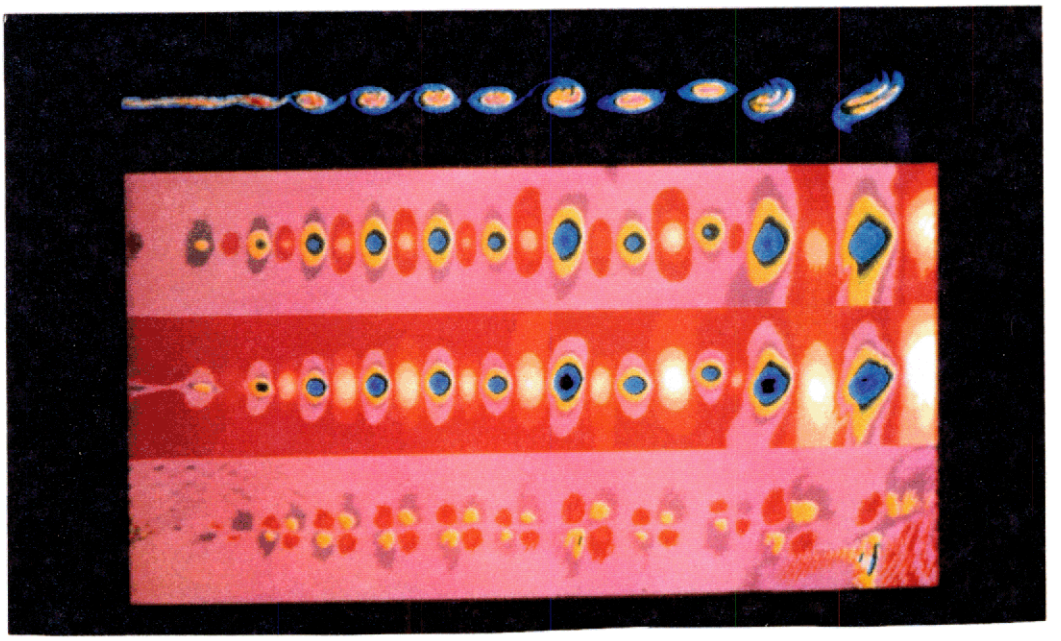

Plate 2: 2D compressible spatially-growing mixing layer, $M_c = 0.4$; from top to bottom, vorticity, pressure, density, divergence (from [4], courtesy Y. Fouillet).

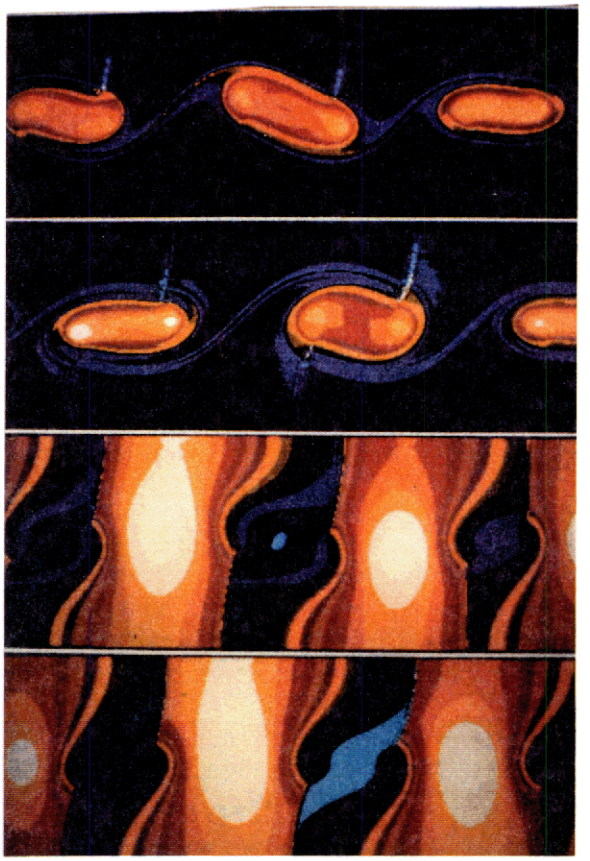

Plate 3: 2D compressible temporal mixing layer, $M_c = 0.7$; vorticity and pressure field (from [2], courtesy X. Normand).

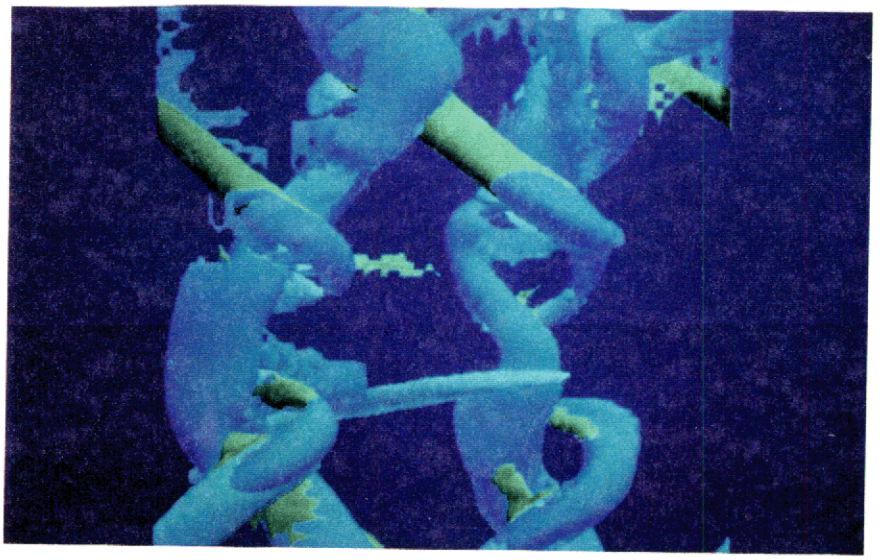

Plate 4: helical-pairing mode in an incompressible temporal mixing layer undergoing natural transition; top view of the vortex tubes (courtesy P. Comte).

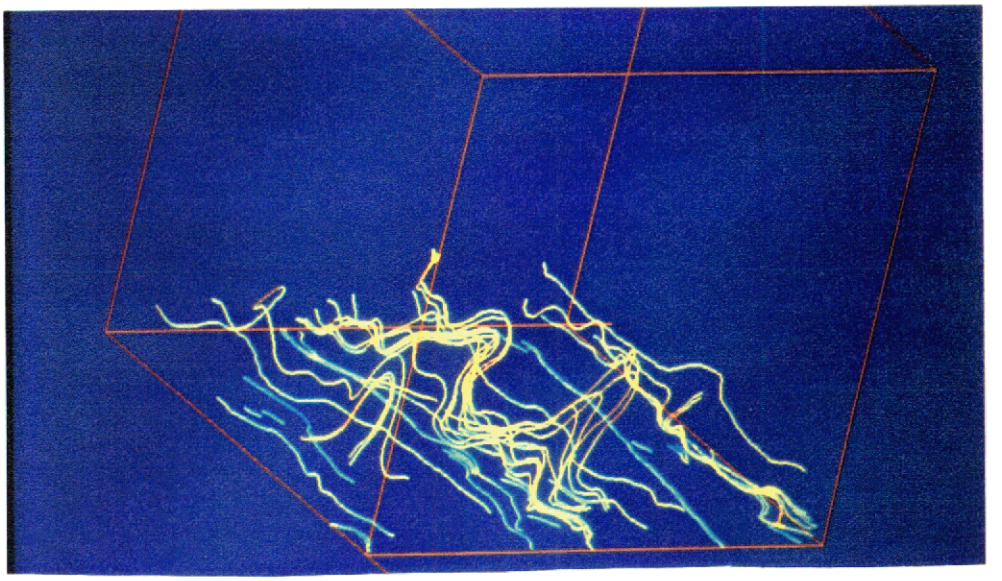

Plate 5: hairpin vortices in a periodic weakly-compressible boundary layer (courtesy X. Normand).

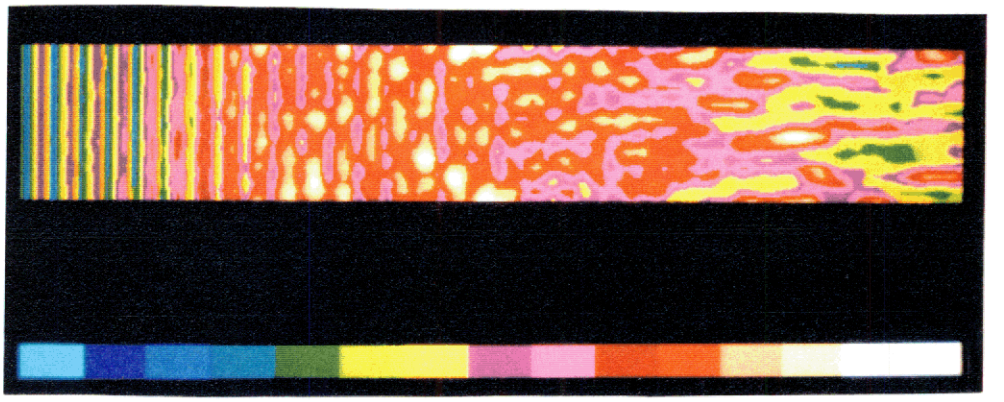

Plate 6: spatially-growing boundary layer at Mach 5, horizontal cross-section of the longitudinal velocity (courtesy X. Normand).

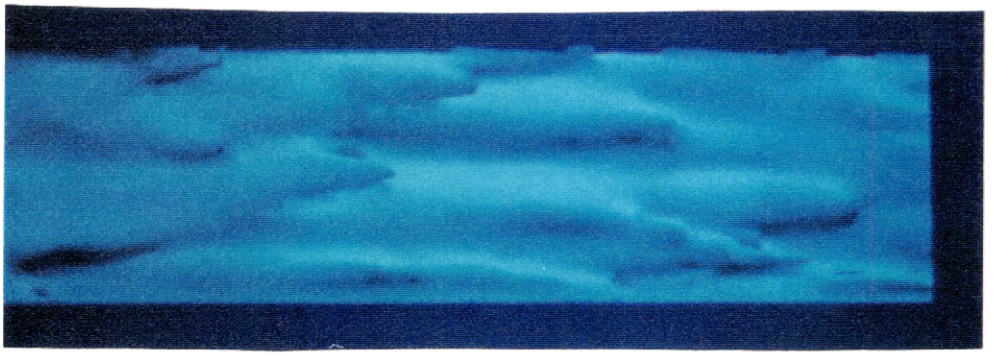

Plate 7: same calculation as in plate 6, enlarged 3D perspective of the vorticity modulus (courtesy X. Normand).

EMERGENCE OF SPATIO-TEMPORAL STRUCTURES IN TRANSITIONAL AND TURBULENT FLOWS

N. Aubry
Benjamin Levich Institute and Department of Mechanical Engineering
City College of the City University of New York
New York, NY 10031

ABSTRACT

A space-time deterministic decomposition has been proposed by Aubry *et al.*[1] for the treatment of spatially and temporally evolving flows. The method consists in expanding the flow into orthogonal spatial modes (in a Hilbert space H(X), where X is the spatial domain) and orthogonal temporal modes (in a Hilbert space H(T), where T is the temporal domain) with a well-defined dispersion relation, so that each spatial function is associated with a temporal one, and vice versa. This is a way to follow the evolution of the spatial configuration of the flow structures and their temporal behavior as the Reynolds number increases and the various instabilities take place. Moreover, if the flow is self-similar, the spectrum provided by such a decomposition follows an exponentially decreasing law[2] and all spatio-temporal structures can be deduced from one only. This implies that, even if the number of degrees of freedom of the flow is infinite, a simple model using only *one* structure should be possible.

THE BI-ORTHOGONAL DECOMPOSITION

We call here 'bi-orthogonal decomposition' any expansion of a function u(x,t) into orthogonal modes $\varphi_k(x)$ in a Hilbert space H(X) ($x \in X$) and orthogonal modes $\psi_k(t)$ in a Hilbert space H(T) ($t \in T$) which defines a one-to-one correspondence between both sets of modes. When the two variables x, t represent space and time (which is assumed in the following), this correspondence has the physical meaning of a dispersion relation. Two particular examples of such a decomposition are the two-dimensional Fourier decomposition for plane waves and the probability theory tool called the proper orthogonal decomposition, Karhunen-Loève expansion or principal component analysis (which uses $L^2(X)$) when the statistical average is chosen to be the time average. The application of the latter to turbulence was first proposed by Lumley[3, 4, 5] and the technique was applied to a certain number of flows[6-21]. The power of the bi-orthogonal decomposition results from the consideration of two Hilbert spaces (which are not necessarily $L^2(X)$ and $L^2(T)$) that permits the introduction of two characteristic (phase) spaces (spanned by the temporal and spatial modes) linked to each other by an isomorphism. This isomorphism precisely constitutes the dispersion relation.

The theory has been developed[1] for a complex valued function u(x, t) (called signal) defined on X×T where X and T are the spatial and temporal domains. Each signal defines a linear operator from a Hilbert space H(X) to a Hilbert space H(T):

$$U: H(X) \rightarrow H(T)$$

such that

$$\forall \varphi \in H(X), \quad (U\varphi)(t) = \int_X u(x,t)\varphi(x)d\mu(x), \tag{1}$$

the adjoint operator being

$$U^*: H(T) \rightarrow H(X)$$

such that

$$\forall \psi \in H(T), \quad (U^*\psi)(x) = \int_T \overline{u(x,t)}\psi(t)d\tilde{\mu}(t) \tag{2}$$

where the bar represents the complex conjugate and $d\mu(x)$, $d\tilde{\mu}(t)$ denote the measures in H(X) and H(T). If the operator U is compact, there exists a decomposition of the signal u which corresponds to the spectral analysis of the operator U and can be written in the following way:

$$u(x,t) = \sum_k A_k \overline{\varphi_k(x)}\psi_k(t) \; . \tag{3}$$

$$\text{with} \quad A_1 \geq A_2 \geq \ldots > 0,$$

$$\lim_{N\to\infty} A_N = 0$$

$$\text{and} \quad (\varphi_k, \varphi_l) = (\psi_k, \psi_l) = \delta_{k,l}$$

where parentheses denote the scalar products in H(X) and H(T). The functions $\varphi_k(x)$ are the eigenfunctions of the operator U^*U associated with the eigenvalues α_k^2 and similarly the functions $\psi_k(t)$ are the eigenfunctions of the operator UU^* also associated with the eigenvalues α_k^2. In other words, $\varphi_k(x)$ satisfies the integral equation

$$\int R^*(x,x')\varphi_k(x')d\mu(x') = A_k^2 \varphi_k(x) \tag{4}$$

whose kernel is the spatial correlation function:

$$R^*(x,x') = \int_X u(x,t)\,\overline{u(x',t)}d\tilde{\mu}(t) \tag{5}$$

and $\psi_k(t)$ satisfies the equation

$$\int R^{**}(t,t')\psi_k(t')d\tilde{\mu}(t') = A_k^2 \psi_k(t) \tag{6}$$

whose kernel is the temporal correlation function:

$$R^{**}(t,t') = \int_X u(x,t)\,\overline{u(x,t')}d\mu(x). \tag{7}$$

Although, given the Hilbert spaces H(X) and H(T), the decomposition (3) is not unique (if the eigenspaces have a multiplicity greater than 1), the subspace associated with each eigenvalue is unique and has finite dimension. It is interesting to note that there is a one-to-one correspondence (i.e. a dispersion relation) between spatial and temporal orthogonal modes, namely

$$U\varphi_k = \alpha_k \psi_k, \tag{8}$$

which is still valid in the case of degenerate eigenspaces. This is due to the fact that the ψ_k's (resp. φ_k's) are both Fourier coefficients and orthogonal modes. This remarkable feature is a characteristic of the above decomposition and it is satisfied by the space-time Fourier expansion for plane waves (in this case, the two decompositions coincide). Now, let us rewrite the signal as a function of H(X) for each t, i.e.

$$\forall x \in X, \xi_t(x) = u(x,t) \tag{9}$$

or as a function of H(T) for each x, i.e.

$$\forall t \in T, \eta_x(t) = u(x,t). \quad (10)$$

Then, the minimal (euclidean) subspace which contains all the vectors $\{\xi_t(x)\}$ (resp. $\{\eta_x(t)\}$) is the subspace $\chi(X)$ of H(X) (resp. $\chi(T)$ of H(T)) spanned by the φ_k's (resp. ψ_k's). The series defined by (3) converges optimally fast in this sense. Then, one may define a dimension of the signal as the common dimension of $\chi(T)$ and $\chi(X)$. An spatio-temporal entropy has also been introduced[1].

Although a natural choice for H(X) and H(T) are $L^2(X)$ and $L^2(T)$, under certain circumstances, it may be more advantageous to choose other Hilbert spaces[2]. Moreover, it may happen that these choices are not possible if the integrals in (1) and (2) do not converge with $d\mu(x) = dx$, $d\tilde{\mu}(t) = dt$ (then it is possible that the operator U may be neither compact nor bounded). Even in this case, bi-orthogonal decompositions (whose form is different from (3)) can be derived by the introduction of other Hilbert spaces[22]. These cases are important in hydrodynamics where the spectrum of U has often a continuous component or where u may have singularities (as in three dimensional turbulence).

APPLICATIONS TO TRANSITIONAL AND TURBULENT FLOWS

First, let us notice that bi-orthgonal decompositions can be extended in a straightforward manner to the case where the signal u and the variable x are vectors. Then, u(x, t) can be chosen as the velocity field $u_1\vec{x}_1 + u_2\vec{x}_2 + u_3\vec{x}_3$ for incompressible flows and the velocity/density field $u_1\vec{x}_1 + u_2\vec{x}_2 + u_3\vec{x}_3 + \rho\vec{x}_4$ for compressible flows, although in the latter case, it is also possible to consider the velocity and the density independently. It is well-known that in open systems, the flow becomes time and space dependent from the first instabilities, so that one point measurements and theories are inadequate. This is the reason why the utility of dynamical systems theory, which deals only with temporal systems, has been severely criticized. The bi-orthogonal decomposition allows this space-time approach of dynamical systems by the introduction of the two minimal configuration (phase) spaces $\chi(T)$ and $\chi(X)$ as defined above. It then offers a way to treat bifurcations or instabilities of the flow in each of these subspaces[1, 2, 23]. From a purely physical point of view, it introduces the notion of spatial and temporal structures in the flow. Until recently, researchers have concentrated in the spatial configuration of turbulent flows, searching for 'coherent structures', organized patterns which could be responsible for turbulence production, drag, mixing, etc. However, as pointed out by many authors, it is as important to determine the temporal evolution of these structures. In this regard, we should mention that experimental techniques used for simultaneous measurements at multiple locations have recently experienced tremendous progress such as those using a rake of probes, laser scanning techniques[24], image processing of visualizations and particle image velocimetry (PIV)[25, 26]. The bi-orthogonal decomposition is a way to analyze these enormous amounts of experimental -or numerical- data, extracting structures, as well as a technique to compact them.

The bi-orthogonal decomposition is built on both the spatial and temporal correlation functions of the signal u(x, t). The spatial correlation $R^*(x, x')$ as defined in (5) is of common utilization in turbulence (with (1/T) dt as the measure) when the

flow is stationary. However, we use it independently of the flow stationarity. Although the temporal correlation function $R^{**}(t, t')$ as defined in (7) is not a traditional concept in turbulence or fluid mechanics, its importance should be recognized in terms of 'temporal structures' of the flow. It is worth noting that two (spatial) point measurements using two probes have been extensively used in the past to determine $R^{*}(x, x')$ in stationary turbulence. Similarly, one spatial point measurements can be used to determine $R^{**}(t, t')$ in homogeneous turbulence. One of the most difficult problems in physics is the closure problem of turbulence, due to the fact that the equations for the spatial moments of various orders are not closed. A way to avoid this problem is to consider the two second order statistics R^{*} and R^{**}, i.e. the two-spatial point correlation and the two-temporal point correlation. Note that this is valid even if the flow has singularities since a bi-orthogonal decomposition can still be found in this case[22]. It should, however, be pointed out that there is still a slight indeterminacy in R^{*} and R^{**} if one wants to recover u(x, t) which we now describe. It is certainly true that R^{*} and R^{**} give all the temporal and spatial orthogonal modes φ_k and ψ_k. However, the extra information needed to reconstruct u is the dispersion relation, which is determined only if the eigenvalues have a multiplicity 1.

Finally, we should mention that the bi-orthogonal decomposition can be applied to laminar, transitional and turbulent flows. In particular, turbulent flows do not need to be statistically stationary. It introduces deterministic spatial and temporal structures in turbulence and statistics in transitional flows, thus providing a uniform way to treat the flow as it evolves towards the fully developed turbulent stage (i.e. when the Reynolds number tends to infinity).

THE BI-ORTHOGONAL DECOMPOSITION AND THE REYNOLDS AVERAGING

In particular when the bi-orthogonal decomposition is applied to turbulence, we may ask whether a Reynolds decomposition separating the mean from the fluctuation should be applied first. In the context of the bi-orthogonal decomposition, it should be pointed out that there are two possible means: the spatial and the temporal one. A decomposition of the temporally centered signal is given by the decomposition of the original signal with temporally centered ψ_k's suitably renormalized. Similarly, a decomposition of the spatially centered signal is given by the decomposition of the original signal with spatially centered φ_k's also suitably renormalized. More precisely, if averages are defined as:

$$\forall \psi \in H(T), E_t(\psi) = \int_T \psi(t) d\tilde{\mu}(t). \tag{11}$$

$$\forall \varphi \in H(X), E_x(\varphi) = \int_X \varphi(x) d\mu(x), \tag{12}$$

$$< u >_t (x) = \int_T u(x,t) d\tilde{\mu}(t), \tag{13}$$

$$< u >_x (t) = \int_X u(x,t) d\mu(x), \tag{14}$$

then the fluctuating signals can be decomposed in the following manner:

$$u(x,t) - < u(x,t) >_t = \sum_{k=1}^{\infty} \alpha_k \overline{\varphi_k(x)} (\psi_k(t) - E_t(\psi(t))) \tag{15}$$

$$u(x,t) - < u(x,t) >_x = \sum_{k=1}^{\infty} \alpha_k \overline{\varphi_k(x) - E_x(\varphi_k(x))}\ \psi_k(t). \qquad (16)$$

We now assume that the temporal and spatial means of the signal are not the zero functions and we discuss equation (15) (discussion of (16) is analogous). It is interesting to note that:

(a) centered temporal functions are not normalized: their norm is $(1\text{-}E_t(\psi_k)^2)^{1/2}$, which implies that normalization changes the eigenvalues as well as their order (in general).

(b) centered temporal functions are not orthogonal in H(T): The difference between the scalar product of two centered functions and that of the original functions is equal to $r_{kl} = -E_t(\psi_k)E_t(\psi_l)$. Centering the temporal functions is thus equivalent to introducing an extra correlation which is non zero when these functions have their own mean. In this case, decomposition (15) is not bi-orthogonal. In other words, the bi-orthogonal decomposition of the centered signal and decomposition (15) do not coincide in general. If, however, in the decomposition of the original signal, the (temporal) mean of the ψ_k's is zero for all k except for one, then the previous correlation r_{kl} is zero for all k, l; in this case, the temporal mean of the signal is a φ_k (up to a normalization factor) and temporally centering the signal does not make any difference, except that the number of non zero eigenvalues is different (by 1), the eigenvalue corresponding to the temporal mean vanishing through the centering process. All this, of course, is true for spatial functions when the signal is spatially centered (see equation (16)). This leads to the conclusion that the temporal or spatial mean of the signal is not necessarily an eigenfunction and thus a first extraction of the mean may not be advantageous in the sense that one loses the property of optimal convergence (as defined above) for the full signal. Note, however, that there are cases where both decompositions indeed coincide of which we can give two examples: the first one can occur in the instability of a steady solution (or a uniform solution) through which newborn ψ_k's (or φ_k's) have zero mean, the second one occurs when $R^{**}(t, t')$ (or $R^{*}(x, x')$) is only a function of t-t' (or x-x'). A particular example of the former case occurs when the instability is linear and newborn temporal modes are Fourier modes, as it is often the case for hydrodynamic instabilities. This suggests that although the Reynolds average is a natural operation in homogeneous and stationary turbulence, and perhaps in the first stage of a hydrodynamic instability, it may not be the case otherwise.

THE BI-ORTHOGONAL DECOMPOSITION AND SYMMETRIES

It is interesting to investigate the influence of the flow symmetries onto the elements of the bi-orthogonal decomposition. Spatio-temporal *symmetries* and *quasi-symmetries* have been introduced[2] as pairs of operators $(S,\tilde{S})$, S being defined in H(X) and $\tilde{S}$ in H(T) such that

$$US = \gamma \tilde{S} U \text{ and } US^{*} = \gamma^{-1} \tilde{S}^{*} U. \qquad (17)$$

If γ equals 1, the pair $(S,\tilde{S})$ defines a spatio-temporal *symmetry*, otherwise it defines a spatio-temporal *quasi-symmetry*. The presence of symmetries implies that each temporal eigenspace of decomposition (3) is invariant under the temporal symmetry $\tilde{S}$ and each spatial eigenspace is invariant under the spatial symmetry S. This may result into the multiplicity of the eigenvalues of the bi-orthogonal decomposition.

Perhaps more importantly, under the condition that the kernel of the operator S equals that of U, the presence of quasi-symmetries as defined in (17), is equivalent to an exponentially decaying law for the spectrum:

$$A_{k+1}^2 = \gamma^2 A_k^2, k \in N. \tag{18}$$

Moreover, in this case, all orthogonal spatial (temporal) modes can be deduced from a basic one via the symmetry S (resp. $\tilde{S}$):

$$S\varphi_k = \sqrt{\gamma}\varphi_{k+1}, k \in N \tag{19}$$

and

$$\tilde{S}\psi_k = \sqrt{\gamma}\psi_{k+1}, k \in N. \tag{20}$$

An example of such a quasi-symmetry is given when the signal is globally self similar, namely there exist α, β, γ such that

$$u(x, \gamma t) = \beta u(\alpha x, t). \tag{21}$$

Then the condition under which the spectrum is exponentially decreasing is automatically satisfied. Note that equation (21) is satisfied in hydrodynamics with $\gamma = \lambda^{1-h}$, $\beta = \lambda^h$ and $\alpha = \lambda^{-1}$ if the fully developed turbulent flow is itself invariant under the scaling invariance of the Navier-Stokes equations in the limit of zero viscosity (infinite Reynolds number)[22]. The latter states that under the spatial and temporal transformations:

$$\begin{aligned} x &\to \lambda x \\ t &\to \lambda^{1-h} t \end{aligned} \tag{22}$$

the solution u becomes $\lambda^h u$:

$$u \to \lambda^h u. \tag{23}$$

We should mention, however, that this scaling should be approximately valid for turbulent solutions only in the inertial range, the symmetry being broken for the energy containing eddies and in the dissipation tail of the spectrum. Note that even if the symmetry is only valid in a statistical sense[27] as assumed in kolmogorov's theory of homogeneous turbulence (K41)[28], namely the spatial two-point correlation is invariant under the spatial symmetry S, the fact that the operator U realizes an isomorphism between the two characteristic spaces $\chi(X)$ and $\chi(T)$ implies that there exists a temporal symmetry $\tilde{S}$ such that (17) is true. Exponential convergence of the spectrum has been indeed observed in several turbulent flows[29, 30] and in spatio-temporal complex solutions of the Kuramoto-Sivashinsky equation[23]. Finally, the existence and knowledge of the 2 symmetry operators S and $\tilde{S}$ should have tremendous consequences on turbulence simulations and modeling since equations (19) and (20) then imply that a dynamical equation is needed only for the first spatio-temporal structure $\psi_1(t)\ \varphi_1(x)$ (in the inertial range).

CONCLUDING REMARKS

The bi-orthogonal decomposition has been proposed to study temporally and spatially evolving flows. It can also be applied to other physical phenomena displaying space-time complexity. It has been derived by the introduction of two Hilbert spaces, one defined on a temporal domain, the other one on a spatial domain. The advantage of such a decomposition is that it decomposes the flow into orthogonal spatial modes and orthogonal temporal modes, so that temporal and spatial phase spaces are disjoint. Disjointedness, however, does not imply independence: there is a one-to-one correspondence, namely a dispersion relation, between both spaces. This leads to a spatio-temporal theory of nonlinear dynamics particularly adapted for studies of spatio-temporal bifurcations.

For fluid mechanics studies, this approach allows one to follow transition to turbulence from the first hydrodynamic instability to fully developed turbulence from a bifurcation viewpoint via the various spatio-temporal instabilities of the flow. This is valid for both compressible and incompressible flows. Absolute and convective instabilities, for instance, can be treated in this manner as well as their further evolution.

In fully developed turbulence where instabilities are probably not as clear and the dimension is much higher, considerations such as the detection of quasi-symmetries (in the sense defined above) may be of great help to deduce an exponentially decaying spectrum and spatio-temporal structures which can all be deduced from one only. This should have tremendous consequences on turbulence modeling. Preliminary results such as those presented by other authors[31] make us anticipate that symmetries of this type may be present in mixing zones between two fluids such as those generated by gravity or by a shock wave.

REFERENCES

1. N. Aubry, R. Guyonnet and R. Lima, *J. Stat. Phys.*, vol. 64, issue 3/4 (1991).
2. N. Aubry, R.Guyonnet and R. Lima, The bi-orthogonal decomposition for analysis of spatio-temporal symmetries and bifurcations, *Journal of Nonlinear Science* (submitted) (1991).
3. J. L. Lumley, in atmospheric turbulence and radio wave propagation, A.M. Yaglom and V.I. Tatarski:, eds.: 166-178. Moscow: Nauka (1967).
4. J. L. Lumley, *Stochastic Tools in Turbulence.* Academic (1970).
5. J. L. Lumley, in Transition and Turbulence (ed. R.E. Meyer), pp. 215-242. Academic (1981).
6. H. P. Bakewell, Ph.D. thesis, Pennsylvania State University (1966).
7. H. P. Bakewell and J. L. Lumley, *Phys. Fluids* **10**, 1880-89 (1967).
8. F. R. Payne, Large eddy structure of a turbulent wake. Ph.D. thesis, Pennsylvania State University (1966).
9. F. R. Payne and J. L. Lumley, *Phys. Fluids*, S194-6 (1967).
10. P. Moin, in: AIAA 22nd Aerospace Sciences Meeting (1984).
11. S. Herzog, The large scale structure in the near-wall region of turbulent pipe flow. Ph.D. thesis. Ithaca, NY: Cornell (1986).
12. S. K. Hong and F. R. Payne, in: AIAA 19th Fluid Dynamics, Plasma Dynamics and Lasers Conference (1987).
13. M. N. Glauser, S. J. Leib and W. K. George, in: Turbulent Shear Flow 5, Springer Verlag (1987).
14. L. Sirovich, M. Maxey and H. Tarman, in Turbulent Shear Flows 6 (ed. F. Durst et al.). Springer (1987).
15. N. Aubry, P. Holmes, J. L. Lumley and E. Stone, *J. Fluid Mech.* **192**, 115-173 (1988).

16. D. H. Chambers, R. J. Adrian, P. Moin, D. S. Stewart and H. J. Sung. *Phys. Fluids* **31** (9), pp. 2573-82 (1988).
17. P. Moin and R. D. Moser, *J. Fluid Mech.* **200**, 471-509 (1989).
18. N. Aubry and S. Sanghi, in: Turbulence and coherent structures, ed. M. Lesieur. Netherland: Kluger (1990).
19. L. Sirovich, M. Kirby and M. Winter, *Phys. Fluids A* 2(2), pp.127-136 (1990)
20. L. Sirovich, L. and H. Park, *Phys. Fluids A*, to appear (1991).
21. A. Deane, I. G. Kevrekidis, G. E. Karniadakis and S. A. Orszag 1990 Low dimensional models for complex geometry flows: Application to grooved channels and circular cylinders. *Phys. Fluids A.* (to appear).
22. N. Aubry and R. Lima, On the turbulence spectra, Levich Institute (preprint) (1991).
23. N. Aubry and W. Y. Lian, Spatio-temporal bifurcations in the Kuramoto-Sivashinsky equation, Levich Institute (preprint).
24. S. Ciliberto, F. Francini and F. Simonelli. 1985 Real time measurements of optical disuniformity fields. *Optics Commun.* 54, pp. 251-256.
25. R. J. Adrian, *Appl. Opt.* **23**, pp. 1690-1 (1984).
26. S. Dalziel and J. Redondo, Rayleigh-Taylor instability: recent particle tracking experiments, in: this volume (1991).
27 A. N. Kolmogorov: Dokl. Akad. Nauk SSSR, 30, p. 301 (1941)
28. U. Frisch. From Global (Kolmogorov 1941) scaling to local (multifractal) scaling in fully developed turbulence. To appear in the special 1991 issue on Kolmogorov of *Proc. Roy. Soc. A.* (1991).
29. N. Aubry, M. P. Chauve and R. Guyonnet, Transition to turbulence on a rotating flat disk. *Phys. Fluids*, submitted (1991).
30. S. Sanghi and N. Aubry, An interaction mode model in near wall turbulence. Levich Institute, preprint (1991).
31 P. F. Linden, J. M. Redondo and D. L. Youngs, Mixing in Rayleigh-Taylor instability: a comparison between experiment and calculations. This volume (1991).

Planar Rayleigh-Taylor Experiments on NOVA

B.A. Remington, S.W. Haan, S.G. Glendinning,
J.D. Kilkenny, and R.J. Wallace
Lawrence Livermore National Laboratory
Livermore, CA 94550

ABSTRACT

We have performed experiments at the Nova Laser Facility to study surface perturbation growth on planar foils accelerated radiatively by a shaped x-ray drive. The experiments are designed to address in two dimensions the extent to which single-mode perturbations grow and multiple-mode perturbations couple to one another. Using a 22× magnification x-ray microscope in combination with a large area backlighter as our primary detector system, we have accelerated planar fluorosilicone (FS) foils and plastic foils doped with bromine (CH(Br)). Using face-on radiography, we have measured the growth of single-mode sinusoidal surface perturbations in an amplitude-scaling series with FS foils and in a wavelength-scaling series with CH(Br) foils. We have also measured the growth of a perturbation consisting of the superposition of two modes. Measurements in side-on geometry give the foil trajectory. Comparisons with 2-D computer simulations show generally good agreement, though results depend on the choice of opacity model.

I. INTRODUCTION

Hydrodynamic instabilities[1] play a key role in the performance of laser driven, inertial confinement fusion implosions.[2] The ablation front is Rayleigh-Taylor (RT) unstable,[3,4] with low density plasma blowoff accelerating inwards the higher density pusher. Capsule surface imperfections will grow at the ablation front, possibly leading to shell breakup. Amplified external perturbations can feed through to seed perturbations on the inner surface of the shell which grow during the deceleration phase, perhaps leading to mix at the pusher-fuel interface and degrading capsule performance. High gain capsule designs call for shaped drive pulses[2] and large aspect ratios[5] (radius/wall-thickness) to maximize the implosion hydrodynamic efficiency. Computer simulations suggest that these high-gain designs can be particularly susceptible to failure from hydrodynamic instabilities,[5,6] due to the steep density gradient, large in-flight aspect ratios, and extended acceleration phase. High quality experimental results capable of stringently testing these predictions, unfortunately, are extremely sparse.

Experiments to date have measured RT growth on planar foils accelerated by direct laser illumination,[7] by illumination with smoothed laser pulses,[8] with square pulses of x-rays,[9] and in direct-drive implosion geometry.[10] Though the amount of growth typically observed was limited and the drive pulse shapes rather arbitrary, the measured RT growth rates were somewhat reduced from classical. We report here on an extensive set of recent planar experiments[11] designed to examine in detail (1) the RT instability over an extended exponential growth phase using a shaped x-ray drive, (2) the transition from the linear to the nonlinear RT regime, (3) the effect of foil material on RT growth, and (4) the effect of mode coupling on subsequent growth when more than one initial mode is present on the foil.

We discuss the experimental setup in Sec. II, and in Sec. III present the results of our single-mode amplitude-scaling series using fluorosilicone (FS) foils. In Sec. IV, we discuss our more recent results from a λ-scaling series using CH(Br) foils. Initial results from our 2-λ mode-coupling experiments and our foil trajectory experiments are contained in Sections V and VI, and a summary of our effort to date is given in Sec. VII.

II. EXPERIMENTAL SETUP

The experimental setup for face-on geometry is illustrated in Fig. 1. A sinusoidal surface perturbation typically is imposed on one side of a 750 μm diameter FS ($SiOC_4H_7F_3$) or CH(Br) foil (specifically, $C_{50}H_{50}Br_3$). These materials were chosen for their admixture of opacities, which allow an extended acceleration period without early foil burn through. The uncertainties in foil thickness, perturbation wavelength and amplitude are estimated to be ±2%, ±2%, and ±10%, respectively. The foil is accelerated as shown schematically in the figure for face-on geometry. The growing modulations in the foil areal density translate to modulations in transmitted backlighter x-rays, which are recorded as a function of time with the streaked Wölter x-ray microscope (the "22×".[12] The streaked images begin promptly when the backlighter beam turns on, and the relative timing between the backlighter beam and the drive beams is measured on an optical[13] and on a soft UV[14] streak camera on each shot, thus establishing t=0. The spatial and temporal resolution of the 22× and Kentech x-ray streak camera are approximately 7 μm and 140 ps in these experiments. A more relevant form for specifying the detector spatial resolution is given by the ratio of measured to actual foil optical depth modulation, namely, the modulation transfer function (MTF). For perturbation wavelengths of 100 μm, 70 μm, 50 μm, and 30 μm, the MTF for the 22× is measured to be 0.71, 0.66, 0.62, and 0.55, respectively, for the sector of the Wölter optic used in these experiments.

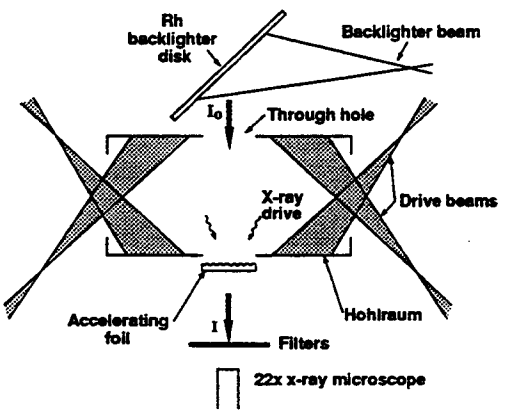

Figure 1. Schematic of the experimental setup (not to scale). The foil is mounted on the front wall of a cylindrical gold hohlraum with surface perturbation facing inwards, and drive beams entering the ends of the hohlraum generate a thermal x-ray drive. As the foil accelerates by x-ray ablation towards the 22×-magnification x-ray microscope, a backlighter beam striking a Rh disk generates a back illumination of x-rays which travel through the hole on the back wall of the hohlraum, and subsequently through the accelerating foil. Modulations in foil areal density translate to modulations in exposure at the x-ray camera.

The x-ray drive was generated by eight 0.35 μm, 2.1 kJ, 3.2 ns Nova[15] beams. The laser pulse shape is shown in Fig. 2 (the x-ray drive has a similar shape in flux vs time) and is designed to keep the foil on a low P-ρ trajectory, as in high gain implosion designs.[2,5] The foil was backlit with a 750 μm diameter spot of x-rays created by irradiating a rhodium disk with a ninth Nova beam of wavelength, shape, and energy of 0.53 μm, 5 ns square, and 2.4 kJ, respectively. After including the 22× response, the dominant feature in the backlighter is a band of x-rays at 2.7–3.2 keV, corresponding to Rh L-band emission.

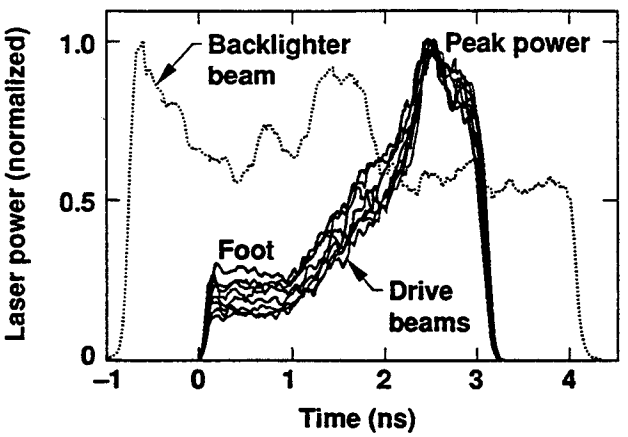

Figure 2. Relative laser power versus time for the nine Nova beams used on a typical shot. The eight solid curves correspond to the 0.35 μm wavelength drive beams, and the dotted curve represents the 0.53 μm wavelength backlighter beam (prior to frequency doubling).

III. AMPLITUDE-SCALING SERIES

A. The Data

Using FS foils with perturbation initial amplitudes, a_o, of 4.5 μm, 0.8 μm, and 0.16 μm, the growth in optical depth modulation, namely "contrast," was measured as a function of time. For a qualitative overview of this series, the contrast (averaged over 35 pixels, i.e., 480 ps), at peak perturbation growth for each foil is shown in Fig. 3. For the large a_o foil, the shape of the modulation at peak growth is no longer sinusoidal, but rather has evolved into the bubble-and-spike shape characteristic of the nonlinear RT regime. Since the foil has formed thin regions due to substantial bubble growth, the resulting large backlighter x-ray transmission leads to the high statistical quality of the data. The intermediate a_o foil is also starting to enter the nonlinear phase of RT growth, and again the statistical quality of the data is quite good. For the very small a_o foil, however, even at peak perturbation growth only limited foil thinning has occurred and the statistical quality of the data is somewhat poorer than for the larger a_o foils. Hence, it is difficult to determine from the shape of the profile alone whether bubble-and-spike formation has commenced. For comparison, we show a late-time profile ($t \approx 3$ ns) from an accelerated blank foil, that is, a FS foil with no initial surface perturbation. Other than statistical fluctuations, we see no growth in optical depth modulation for this accelerated blank foil at any time. The smooth curves on the left side of the figure represent the corresponding calculated results and will be discussed below.

To illustrate the full time dependence of the perturbation growth, we present in Fig. 4 the Fourier transform coefficient of the fundamental mode for each foil as a function of time. Error bars are estimated by taking the transform of each individual period. The standard deviation of the resulting ensemble of Fourier coefficients for each harmonic at each time step is equated with the uncertainty, with representative error bars shown in the figure. For the foils with large a_o and with intermediate a_o, contrast was observable throughout the experiment, including at $t = 0$, when the drive beams just turn on. The contrast for the large a_o foil appears to be increasing nearly linearly between 0.5 ns and 3.0 ns with a slope of about 0.23 ns^{-1}, after which the contrast starts to decrease. The growth in contrast for the intermediate a_o foil appears to be nearly exponential [$a(t) \approx a_o e^{\gamma t}$] until about 3.3 ns, with a growth rate of $\gamma \approx 1.0$ ns^{-1}, after which time the contrast levels off and eventually starts to decrease. For the very small a_o foil, however, contrast

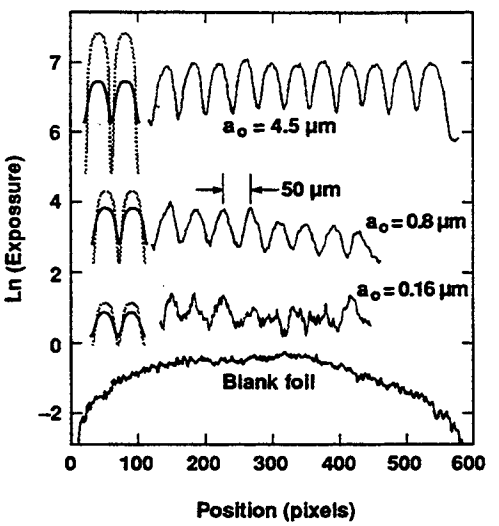

Figure 3. *Ln(Exposure)* profiles ("contrast") at peak growth for the large (a_o = 4.5 μm), intermediate (a_o = 0.8 μm), and very small (a_o = 0.16 μm) initial amplitude fluorosilicone foils. Each curve represents the experimental contrast averaged over 35 pixels (480 ps). The vertical offsets are arbitrary. The small a_o and intermediate a_o foils had only eight 50 μm wavelength periods, whereas the large a_o foil had initial modulations across the full field of view (~700 μm) of the x-ray microscope. Also shown at the bottom is a late-time (t ≈ 3 ns) optical depth profile for an accelerated blank fluorosilicone foil (no initial perturbation). The smooth curves shown at the left of the data for the top three profiles show the calculated contrast at peak growth prior to (gray) and after (solid black) folding with the instrumental resolution function. Relative to the start of the drive, the calculations correspond to the instantaneous contrast at t = 2.5 ns (top), 3.3 ns (middle), and 4.5 ns (bottom).

was not observable until t ≈ 2.0 ns, after substantial growth had occurred. After the drive beams turn off at t = 3.2 ns, the contrast appears to be increasing nearly linearly during this "drift" phase, with a slope of about 0.24 ns^{-1}.

B. The Simulations

The smooth curves shown in Fig. 4 represent the results of two-dimensional computer simulations using the code LASNEX.[16] The essential features of LASNEX have been compared extensively with theory[17] and with results of experiments on Nova. The foil acceleration phase of the calculation uses an x-ray drive spectrum which was measured on separate drive characterization shots. The output from the perturbation growth calculation was post-processed by transporting the measured backlighter x-ray spectrum through the calculated foil opacity zone by zone at each time step and folding in the measured instrumental response. In addition to the approximately constant x-ray spectrum resulting from the 5 ns square laser pulse incident on the Rh backlighter disk, there is additional backlighting due to "self-emission" from within the hohlraum. This latter component exists only as a short burst, peaking about 300–400 ps after peak power of the drive lasers, and was measured on separate shots. (A detailed discussion of this component is given elsewhere.[11])

Results of the calculated contrast, both with and without self emission in the backlighter spectrum, are shown in the figure. The effect of including self emission is most evident for the intermediate a_o foil, where perturbation and self-emission both reach their maxima at approximately the same time. The self-emission backlighting results in slightly more contrast because the spectrum is somewhat softer than that of the Rh backlighter. The interpretation of our data, however, is largely unaffected by this short burst of additional backlighting. The agreement between simulation and experiment is quite good. For the large a_o foil the calculated perturbation growth appears roughly linear, whereas the intermediate and small a_o foils appear to have exponential growth. For the large and intermediate a_o foils, the calculated contrast peaks just prior to "burn through," the time at which the perturbation bubbles break out of the back side of the foil. For the small a_o foil, the perturbations never grow sufficiently large for the foil to burn through. We note that the calculated growth appears to peak slightly earlier in time than

was observed for the large a_o foil, and to a lesser extent for the intermediate a_o foil. This may result from inadequate treatment of the detailed shape of the strongly nonlinear spikes and bubbles. (The calculated shapes of the modulations at peak growth, given on the left side of Fig. 3, show a rather extreme bubble-and-spike shape.) Another likely possibility is the uncertainty in the opacity calculation; the sensitivity to opacity is examined next.

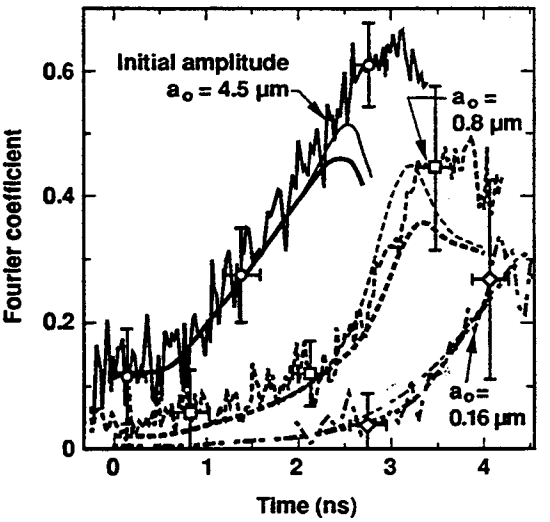

Figure 4. Coefficient of the fundamental mode from a Fourier transform of *ln(Exposure)* for accelerated fluorosilicone foils with large (solid, a_o = 4.5 μm), intermediate (dashed, a_o = 0.8 μm), and small (dot-dashed, a_o = 0.16 μm) initial amplitude perturbations. The smooth curves are the results of 2-dimensional computer simulations. The thick curves assume constant back-illumination from the rhodium backlighter disk only; the thin curves include the additional transitory contribution from self emission (see text). All curves are timed relative to the start of the drive lasers at t = 0.

Our calculated results depend on details of the modeling of sub-keV opacity in the hot ablated material, because this determines the amount of drive reaching the ablation front. In the previous RT experiments, done with simple 1 ns square pulse shapes,[9] initial LASNEX calculations predicted too slow a growth rate and foil burn-through times that were too late compared to observation. One interpretation of this discrepancy was that the default average-atom XSN opacity package[18] in LASNEX overestimates the line widths in the hot ablated material. Hence, too much x-ray drive gets absorbed before reaching the ablation front. A proposed improvement is a model in which the line widths are set to be very narrow, and the continuum lowering is also adjusted slightly.[19] Better agreement with observation in the previous RT experiments[9] was achieved using this opacity modification. We will show next that this conclusion extends to the current experiments with FS foils as well.

In Fig. 5, we show the effect of this opacity modification on our experiment with the intermediate a_o foil. Figure 5(a) shows the temporal evolution of the calculated contrast for the two opacity models (the solid curve is the same as in Figure 4). The default XSN opacity results in slower growth, since x-ray drive is absorbed in the hot blow-off plasma prior to reaching the ablation front. Hence, the foil never burns through in this calculation, which is in clear disagreement with the data (see Fig. 4). The calculations presented in Figs. 3 and 4 were all done with the modified opacity model.

We can see the overall effect of these two models more clearly in Figs. 5b and c. Due to the different mass ablation rates, these two opacity models predict different acceleration trajectories for the unstable ablation front, shown in Fig. 5b. The calculated RT growth, however, is primarily a function of the foil acceleration, or equivalently, the distance moved by the ablation front in the two cases, as illustrated in Fig. 5c. Prior to foil burn through, growth versus distance moved is nearly the same for both calculations. The different opacity models do not result in significantly different ablative stabilization of the instability growth, but do generate different

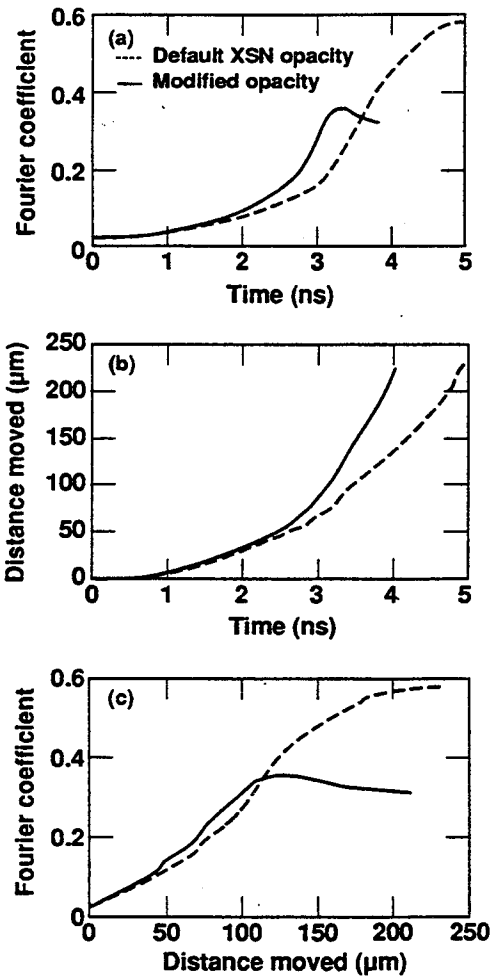

Figure 5. Illustration of the sensitivity of the calculated contrast to opacity modeling for the fluorosilicone foil with intermediate initial amplitude (a_o = 0.8 μm). In (a) the calculated contrast is shown as a function of time using the default average atom opacity model XSN (dashed curve) and using a modification where the opacity lines are artificially narrowed (solid curve). In (b) the resulting trajectories of the ablation front are shown for each opacity model, and in (c) the calculated contrast versus distance moved is plotted. Making the opacity lines narrower increases the amount of x-ray drive that reaches the ablation front, hence increasing the ablation velocity, acceleration, and rate at which the foil burns through.

foil trajectories. At this point, the opacity modification must be regarded as an uncertainty in the modeling; experiments are in progress to test the effect directly.[20]

To allow ready comparison with other work, we compare our measurements with classical growth,[1] $a(t) = a_o e^{\gamma_{Cl} t}$, where $\gamma_{Cl} = (ka)^{1/2}$, $k = 2\pi/\lambda_{perturbation}$, and a is the foil acceleration. Due to the shaped drive pulse, the calculated foil acceleration and γ_{Cl} change with time. Typical values during the foot are a = 6 μm/ns^2 and γ_{Cl} = 0.9 ns^{-1}, and at peak power a = 75 μm/ns^2 and γ_{Cl} = 3.1 ns^{-1}. Integrating the growth rate over time using the time-dependent acceleration from the simulation, we have calculated the number of classical e-foldings, $\int \gamma_{Cl} dt$, for the small a_o foil.[11] The observed (and simulated) e-foldings is about 60% of that predicted for classical growth, namely, $\gamma \approx 0.6\gamma_{Cl}$. We have also compared our measurements with a simple expression for ablative flow across a density gradient,[21]

$$\gamma = \alpha(ka)^{1/2} - \beta k v_a , \qquad (1)$$

where $\alpha = (1+kL)^{-1/2}$, L is the density gradient scale length ($L = \rho/\nabla\rho$), v_a is the ablation velocity [$v_a = \dot{m}/(\rho A)$], and β is a multiplier thought to be between 1 and 3. Due to the shaped drive, typical gradient scale lengths at the ablation front are calculated to be short, L = 1–3 μm, giving α = 0.94 – 0.85, which suggests that the effect of gradient scale length stabilization is relatively small. The data and simulation[11] fall in between the e-folding curves for β = 1 and β = 2.

IV. λ-SCALING SERIES

A. The Data

We have recently done a series of experiments accelerating CH(Br) foils with sinusoidal perturbations of wavelength λ = 30, 50, 70, and 100 μm at a variety of initial amplitudes. A qualitative overview of a subset of this series is given in Fig. 6, where contrast at peak growth is shown for each λ. The foil thicknesses, drive, and filtering were all held fixed for the series represented in the figure, and most of the perturbations had the same initial amplitude (a_o = 2.5 μm) as well.

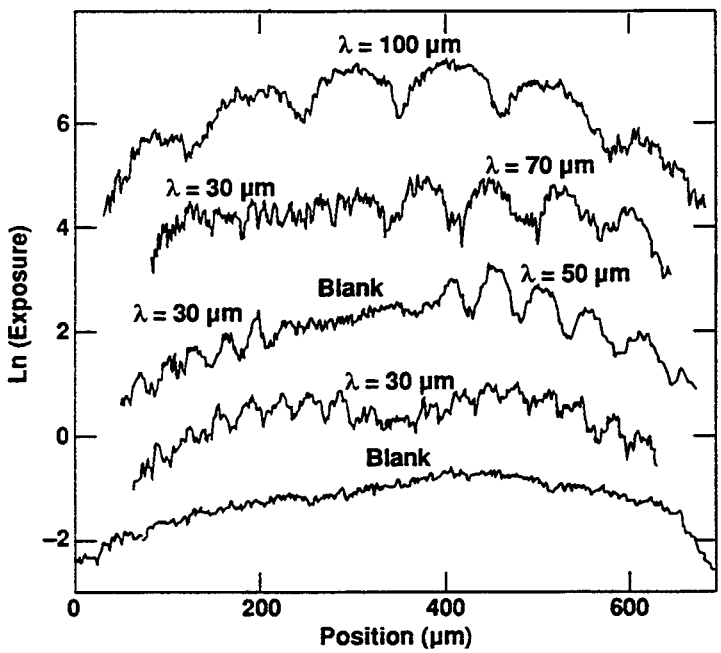

Figure 6. Contrast at peak growth for the λ-scaling series with CH(Br) foils. The vertical offsets are artificial. Starting with the top curve, the foils had perturbation wavelengths (λ) and initial amplitude (a_o) of λ = 100 μm, a_o = 2.5 μm; λ = 70 μm, a_o = 2.5 μm (side-by-side with λ = 30 μm, a_o = 1.0 μm); λ = 50 μm, a_o = 2.5 μm (side-by-side with λ = 30 μm, a_o = 1.5 μm); and λ = 30 μm, a_o = 2.5 μm. The bottom curve corresponds to a late-time profile from a blank CH(Br) foil (no initial perturbation).

We present in Fig. 7 the full time dependence of the Fourier coefficients of the data shown in Fig. 6. The error bars are determined as discussed above in Sec. III.A. The strong wavelength dependence of the RT instability is readily apparent in the data in Fig. 6. The λ = 70 μm perturbation clearly grows to the largest peak contrast. For example, comparing peak contrast for the 70 and 30 μm perturbations, after correction for the instrument MTF, we find that the λ = 70 μm perturbation grows to be about a factor of (0.54/0.66)/(0.29/0.55) = 1.6 larger. The reduced growth for the λ = 30 μm perturbation occurs both because the perturbation more quickly enters the nonlinear RT regime and because the instability is more strongly stabilized by ablation. Future analysis and experiments will try to isolate these two effects.

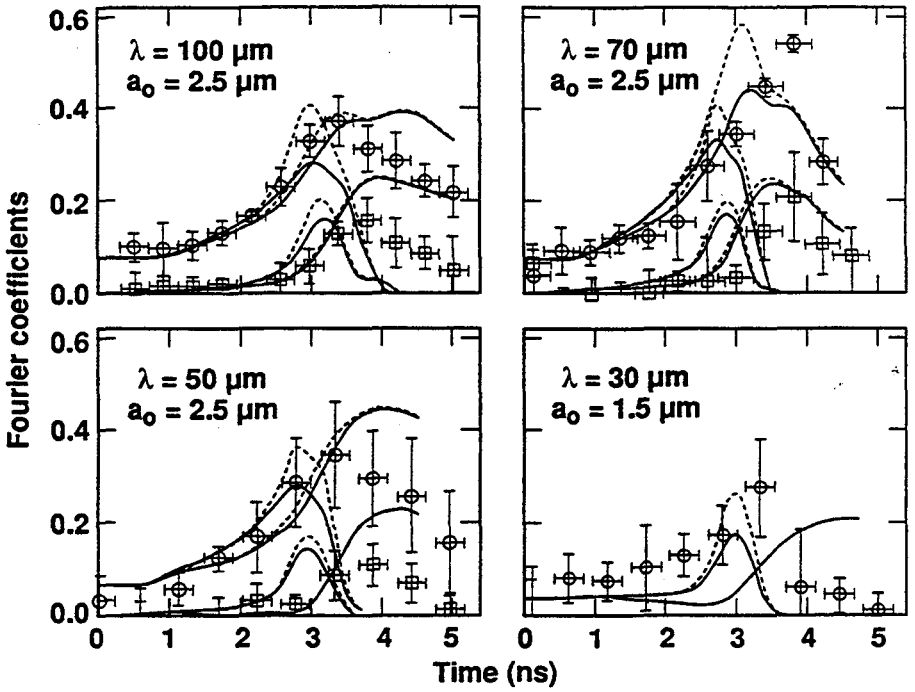

Figure 7. Fourier analysis of the data shown in Fig. 6. The λ = 30 μm data is taken from the foil with side-by-side perturbation with λ = 50 μm. The circles represent the coefficient for the first harmonic (fundamental mode), and the squares the second harmonic. From top to bottom, left to right, the wavelengths and amplitudes of the perturbations were λ =100 μm, a_o = 2.5 μm; λ = 70 μm, a_o = 2.5 μm; λ = 50 μm, a_o = 2.5 μm; and λ = 30 μm, a_o = 1.5 μm. The smooth solid curves represent the corresponding LASNEX calculations, assuming only the constant Rh backlighter x-rays. The dashed curves include the additional transitory burst of backlighter x-rays from self emission. The curves that peak later use the default XSN average-atom opacity model; the modified opacity model was used in the calculations shown by the rest of the curves.

B. The Simulations

Overlaid on the data are the results of LASNEX simulations, both with default XSN opacities and with the opacity modification setting the lines to be narrow, and also with and without including self emission (see Sec. III.B.). The opacity modification appears to be an over correction for CH(Br) foils. The modification (narrow lines) allows too much x-ray drive to traverse the plasma blow-off region to reach the ablation front, leading to early foil burn-through times. Using default XSN opacities, however, still results in too much opacity in the blow-off, hence too slow a foil burn-through time. It would appear that an intermediate opacity correction, say, a line-width multiplier of ~0.25, is required to more closely reproduce the observed perturbation growth and burn-through times for CH(Br) foils.

V. 2-MODE EXPERIMENTS

In Fig. 8 we show initial results from our mode-coupling experiments. The data shown at the top of the figure represent a CH(Br) foil with perturbation consisting of the superposition of $\lambda_{1,2} = 50, 75$ μm and $a_o = 2$ μm. The mold is also schematically illustrated at the top of the figure. The results of the time-dependent Fourier analysis are shown at the bottom of Fig. 8. The contrast from the two pure modes (corresponding to $\lambda_{1,2} = 50, 75$ μm) is observed at t = 0, and grows to peak values at about 3 ns. Contrast from the $k_1 \pm k_2$ modes (corresponding to wavelengths of 30 and 150 μm) is observed only after about 2.6 ns, when the RT instability has

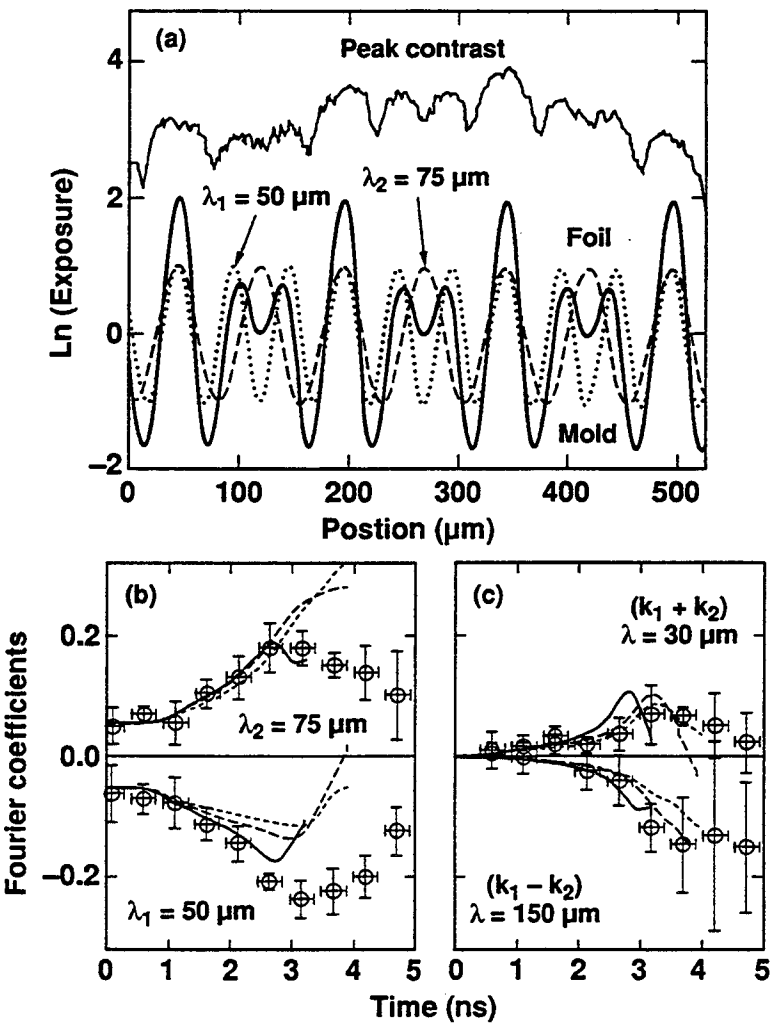

Figure 8. (a) The design of a mold corresponding to the superposition of two wavelengths, λ_1 = 50 μm (dotted curve) and λ_2 = 75 μm (dashed curve). The resultant superposition is shown by the smooth solid curve. A late time contrast profile of an accelerated CH(Br) foil made with an initial perturbation from this mold is shown by the curve at the top. The full time-dependent Fourier analysis is shown in (b) and (c). (b) The upper data is the fundamental Fourier coefficient for λ = 75 μm, and the lower data the fundamental mode for λ = 50 μm. (c) The upper data is the $k_1 + k_2$ mode (λ = 30 μm) and the lower data the $k_1 - k_2$ mode (λ = 150 μm). The smooth curves represent the corresponding LASNEX calculations. The dotted curves use the default XSN opacity model, the solid curves the modified opacities with very narrow lines. The dashed curves use an intermediate opacity model with a line-width multiplier set to 0.25.

entered the nonlinear regime. The $\lambda = 30$ μm coupled mode does not grow much, probably due to ablative stabilization. An additional concern for the $k_1 - k_2$ mode ($\lambda = 150$ μm) is the contribution from the structure in the backlighter. An initial estimate suggests that the additional uncertainty introduced at $\lambda = 150$ μm is non-negligible, but quite small at the shorter wavelengths. This point is currently under further investigation. All modes diminish late in time, $t > 3.5$ ns, as the foil starts to decompress after the drive turns off. The simulations give a reasonably good description of the growth phase of the experiment. Again, results are sensitive to opacity, and an intermediate opacity model seems to be preferred. The late-time, decompression stage, however, appears to be more difficult to calculate. Though the calculated results are qualitatively in agreement, a full quantitative description will require more detailed input into the calculation, such as the late-time drive conditions and shot-to-shot variation in the precise shape of the drive.

VI. FOIL TRAJECTORY EXPERIMENTS

Initial foil trajectory experiments have been performed where we observe the foil edge-on, as it accelerates across (and progressively occludes) the backlighter spot. By thus measuring the gross hydrodynamics of the foil, we hope to have more direct experimental input to the opacity modeling uncertainties. These experiments are more difficult to perform and interpret, and analysis is still in progress. We show in Fig. 9a our initial results for optical depth as a function of time. The backlighter spatial structure and the 22× resolution have both been removed (deconvolved) from the data. The region of low optical depth results from directly viewing the backighter spot. The transition to large optical depth marks the transition across the back edge of the foil. This back edge does not begin to move until the shock breaks out the back side of the foil at about 2 ns. The back edge of the foil then starts to accelerate and to flatten out.

Defining an edge as the point where the optical depth has increased by 1 from the baseline, we show in Fig. 9b the experimental trajectory, and the results predicted by LASNEX for the three opacity models discussed above. Our initial conclusions are that the foil is accelerating more slowly than predicted when the modified opacity model is used, consistent with the tentative conclusion from the face-on results above. Both the default and the intermediate opacity model lead to edge trajectories which are consistent with the data. The simulations also suggest that after about 1.5 ns, we should "see" behind the foil, since the low density ablated foil material should have very low optical depth to the backlighter x-rays. We never do see behind the foil in the data, which suggests that there is gold plasma blowing out with the foil as it accelerates away from the hohlraum wall. Future experiments should help to make our data analysis less ambiguous, especially as regards seeing behind the foil and, hence, edge determination.

VII. CONCLUSION AND SUMMARY

In conclusion, we have done experiments accelerating FS foils and CH(Br) foils by x-ray ablation. In face-on geometry, we have accelerated foils with initial sinusoidal surface perturbations over a range of amplitudes and wavelengths. For foils with large wavelength or small initial amplitude, the perturbations initially grow exponentially, though at a rate reduced somewhat from classical. When the perturbation growth exceeds ~0.1λ, bubble-and-spike formation is observed, and the growth slows down substantially, becoming approximately linear. Shaping the drive to lower the adiabat makes the ablation front more RT unstable, due to the steep density gradient. Under similar conditions, we observe less RT growth in CH(Br) foils than with

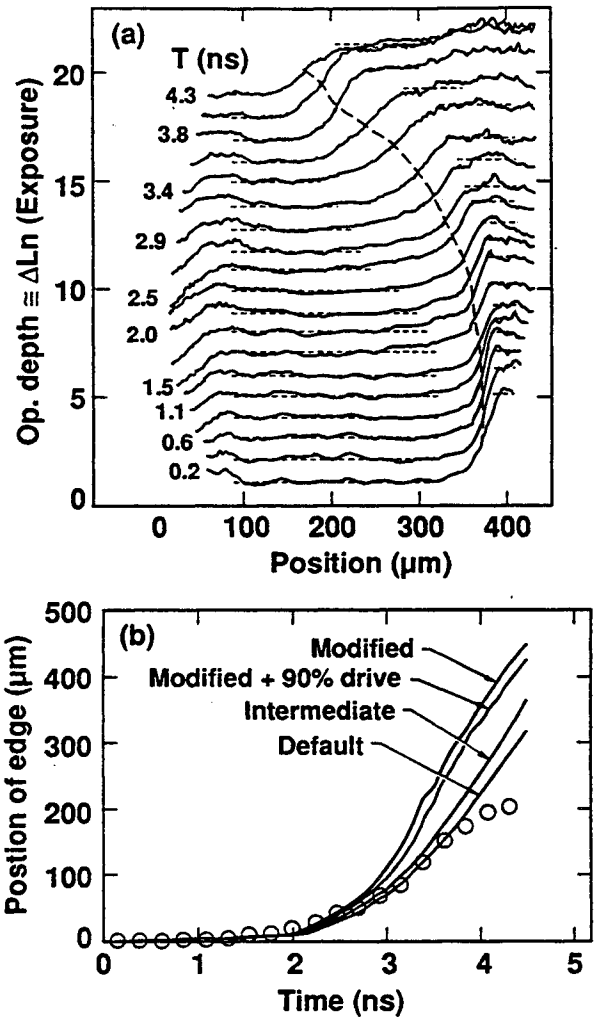

Figure 9. (a) Optical depth profiles viewing the backlighter spot across the foil edge-on. The curves are artificially offset from bottom to top in order of increasing time, with the time for every other curve indicated. The transition from low optical depth (direct view of the backlighter) to high optical depth marks the back edge of the foil. The horizontal dashed curves mark the estimated baseline and peak optical depth (OD) at each time step. The curved vertical dashed line illustrates the trajectory of the $0.5(OD_{max})$ point of the edge. (b) Alternatively, an "edge" can be defined as the point where the optical depth increases from 0 to, say, 1. The experimental trajectory of an edge so defined is shown compared with LASNEX simulations. The lowest curve uses the default XSN average atom opacity model, and the top curve uses the modified opacities with narrow lines. The two intermediate curves use the modified opacities with 10% lower drive (upper) and an intermediate opacity model with line-width multiplier of 0.25 (lower).

fluorosilicone foils, presumably due to preheat slightly decompressing the plastic, leading to a larger density gradient at the ablation front. When two modes are superposed on the same foil, the individual pure modes grow independently until late in time, when mode coupling causes the $k_1 \pm k_2$ modes to appear. Our observations are in reasonably good agreement with simulations, though our calculations are quite sensitive to opacity modeling. Initial results from foil trajectory experiments give us a measurement of the foil gross hydrodynamics, and may offer a more direct measure of foil opacities at and near the ablation front.

We wish to acknowledge the dedicated staff and support personnel at Nova; S. Davidson, T. Perry, H. Kornblum, R. Kauffman, and D.W. Phillion for spectral and timing measurements; and D. Munro for many illuminating discussions and assistance with analysis software. This work was performed under the auspices of the U.S. DOE by the Lawrence Livermore National Laboratory under contract number W-7405-ENG-48.

REFERENCES

1. S. Chandrasekhar, *Hydrodynamic and Hydromagnetic Stability* (Oxford U.P., London, 1968), Chap. 10.
2. J. Nuckolls, L. Wood, A. Thiessen, and G. Zimmerman, Nature **239**, 139 (1972).
3. S. E. Bodner, Phys. Rev. Lett. **33**, 761 (1974); K. A. Brueckner, S. Jorna, and R. Janda, Phys. Fluids **17**, 1554 (1974); D. B. Henderson, R. L. McCrory, and R. L. Morse, Phys. Rev. Lett. **33**, 205 (1974); J. N. Shiau, E. B. Goldman, and C. I. Weng, Phys. Rev. Lett. **32**, 352 (1974); J. D. Lindl and W. C. Mead, Phys. Rev. Lett. **34**, 1273 (1975).
4. R. L. McCrory, L. Montierth, R. L. Morse, and C. P. Verdon, Phys. Rev. Lett. **46**, 336 (1981); C. P. Verdon, R. L. McCrory, R. L. Morse, G. R. Baker, D. I. Meiron, and S. A. Orszag, Phys. Fluids **25**, 1653 (1982); D. H. Sharp, Physica 12D, 3 (1984); M. J. De C. Henshaw, G. J. Pert, and D. L. Youngs, Plasma Physics and Controlled Fusion **29**, 405 (1987); S. E. Bodner, M. H. Emery, and J. H. Gardner, Plasma Physics and Controlled Fusion **29**, 1333 (1987).
5. S. E. Bodner, J. Fusion Energy, **1**, 221 (1981); S. M. Pollaine and J. D. Lindl, Nucl. Fusion **26**, 1719 (1986).
6. M. Tabak, D. H. Munro, and J. D. Lindl, Phys. Fluids B **2**, 1007 (1990).
7. A. J. Cole, J. D. Kilkenny, R. T. Rumsby, R. G. Evans, C. J. Hooker, and M. H. Key, Nature **299**, 329 (1982); R. R. Whitlock, M. H. Emery, J. A. Stamper, E. A. McLean, S. P. Obenshain, and M. C. Peckerar, Phys. Rev. Lett. **52**, 819 (1984).
8. J. Grun, M. E. Emery, C. K. Manka, T. N. Lee, E. A. McLean, A. Mostovych, J. Stamper, S. Bodner, S. P. Obenshain, and B. H. Ripin, Phys. Rev. Lett. **58**, 2672 (1987); M. Desselberger, O. Willi, M. Savage, and M. Lamb, Phys. Rev. Lett. **65**, 2997 (1990).
9. J. D. Kilkenny, Phys. Fluids B **2**, 1400 (1990); LLNL Laser Program 1987 Annual Report (1989), p. 3–163.
10. J. S. Wark, J. D. Kilkenny, A. J. Cole, M. H. Key, and P. T. Rumsby, Appl. Phys. Lett. **48**, 969 (1986); H. Nishimura, H. Takabe, K, Mima, F. Hattori, H. Hasegawa, H. Azechi, M. Nakai, K. Kondo, T. Norimatsu, Y. Izawa, C. Yamanaka, and S. Nakai, Phys. Fluids **31**, 2875 (1988).
11. B. A. Remington, S. W. Haan, S. G. Glendinning, J. D. Kilkenny, D. H. Munro, and R. Wallace, Bull. Am. Phys. Soc. **35**, 1970 (1990); ibid, submitted to Phys. Rev. A (1991); ibid, submitted to Phys. Fluids B (1991); ibid, LLNL Laser Program Winter Quarterly Report (1991), in press.
12. R. J. Ellis, J. E. Trebes, D. W. Phillion, J. D. Kilkenny, S. G. Glendinning, J. D. Wiedwald, and R. A. Levesque, Rev. Sci. Instrum. **61**, 2759 (1990), and references therein; S. G. Glendinning, UCRL-50021-87, LLNL Laser Program 1987 Annual Report (1989), p. 3–201.
13. J. B. Richards, D. M. Pennington, C. E. Thompson, and P. J. Wegner, UCRL-50021-86, LLNL Laser Program 1986 Annual Report (1987), p. 3–129.
14. D. W. Phillion, K. G. Estabrook, R. P. Drake, and R. E. Turner, UCRL-50021-84, LLNL Laser Program 1984 Annual Report (1985), p. 5–22.
15. E. M. Campbell, J. T. Hunt, E. S. Bliss, D. R. Speck, and R. P. Drake, Rev. Sci. Instrum. **57**, 2101 (1986).

16. G. B. Zimmerman and W. L. Kruer, Comments Plasma Phys. Controlled Fusion **2**, 51 (1975).
17. David H. Munro, Phys. Fluids B **1**, 134 (1989); M. Tabak, D. H. Munro, and J. D. Lindl, Phys. Fluids B **2**, 1007 (1990); K. O. Mikaelian, Phys. Rev. A **42**, 4944 (1990); C. E. Max, C. F. McKee, and W. C. Mead, Phys. Fluids **23**, 1620 (1980).
18. W. A. Locke and W. H. Grasberger, LLNL report UCRL-52276 (1977).
19. S. Hatchett, D. Munro, private communication (1990).
20. O. Landen and S. Hatchett, private communication.
21. H. Takabe, L. Montierth, and R. L. Morse, Phys. Fluids **26**, 2299 (1983); H. Takabe, K. Mima, L. Montierth, and R. L. Morse, Phys. Fluids **28**, 3676 (1985); David H. Munro, Phys. Rev. A **38**, 1433 (1988).

FIRST MIX EXPERIMENTS AT NOVA
THE LoRo SERIES

V. C. Rupert
Lawrence Livermore National Laboratory, Livermore, Ca. 94550

ABSTRACT

The first series of experiments using the Nova laser to investigate mix at an interface between different materials has been completed. Mix was induced by a shock crossing the interface and initiating a Richtmyer-Meshkov instability. Both low and high Atwood number targets were used and the results compare favorably with simulations using a kε mix model. These experiments pave the way for new designs which should provide data needed to develop mix models with predictive capabilities.

INTRODUCTION

In 1988, preliminary results of the Nova LoRo Experiments were reported at the International Workshop on the Physics of Compressible Turbulent Mixing[1]. Since then this series of experiments has been completed, and has provided us with the information needed to design a comprehensive series of laser driven mix experiments. The principal objective of all these experiments is to generate a data base against which various mix models can be tested, and with which the models' adjustable parameters can be determined.

In all these experiments, the laser provides the source used to drive a shock through a material interface thus initiating mix due to the Richtmyer-Meshkov instability[2,3], coupled in some circumstances with a Rayleigh-Taylor instability[4]. Very high Mach numbers (~50) can be attained. In contrast to shock tube experiments high temperatures and well defined discontinuous interfaces without membranes can be investigated. Low Atwood number samples were used to minimize the impact of mix , and allow us to better understand the physics which describe the basic evolution of such targets. High Atwood number samples then provide data against which mix models can be tested.

Simulation of the targets behavior has been performed primarily with a 1D code which incorporates a kε mix model[5]. Comparison of simulations and experiments provide calibration data for the model's adjustable parameters. 2D calculations were performed to assess the relationship between the axial distribution of materials simulated in 1D and the measured data influenced by the lateral expansion of the target. A few 2D calculations of perturbation growth provided additional insight into the interface evolution.

THE LoRo EXPERIMENTS

The LoRo series of experiments used simple targets consisting in a low density plastic ablator seeded with sulphur and a "payload" of either high density Mo or nearly matched density chlorine seeded plastic (Fig.1).

Since sulphur, molybdenum and chlorine all have characteristic spectroscopic features in the 2 to 3.2 keV range, the spatial location of the different materials could be determined by using Point Projection Spectroscopy[1,6]. A laser irradiated backlighter provided a fairly uniform spectrum in that range. In the most recent series of experiments no tamper was used whereas the preliminary experiments discussed in 1988 comprised a spectroscopically neutral plastic tamper.

PPS [Poly(p-phenylene sulfide)], with an average density of 1.36, and containing 29.6% per weight of sulphur was used as the ablator. It was coupled with a molybdenum payload to give a high Atwood number (initially 0.77) target for which significant mix was expected. In these preliminary experiments the emphasis was on the development of an experimental capability, so that a Rayleigh-Taylor unstable interface was selected to maximize the mix and it's detection. Comparison of the mix mass distribution in such targets with the result of simulations provides a more stringent test of the mix models incorporated in the calculations, than the simple determination of a mix width.

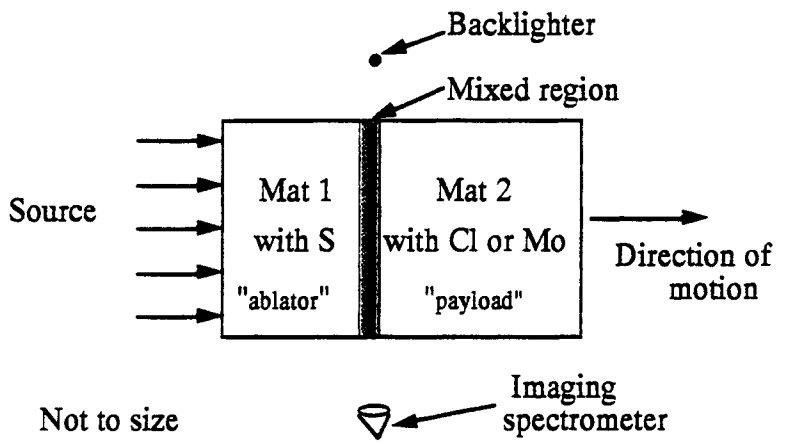

Fig. 1 Nominal LoRo target - The payload thickness is 1/30th (Mo) or 1/3 (PyC) that of the ablator.

In parallel to the high Atwood number targets, low Atwood number targets were also irradiated. In these targets the payload consisted in PyC [Poly(chloro-p-xylylene)] with 25.6% per weight of chlorine, and a nominal density of 1.29. Thus these targets had not only a low Atwood number (~ 0.03), but were also Rayleigh-Taylor stable. Under these circumstances very little mix was expected. Any apparent mix resulted primarily from a convolution of motion blurring and instrumental resolution. It was then possible to determine directly the effect of these parameters on the data, and take them into account in the experiment/simulation comparisons for the high Atwood number targets. In addition the density distribution of the two materials as a function of time provided information on the source and characteristics of the target materials such as equation of state and opacities.

Details of the experiments and the unfolding of the experimental data are discussed by J. Molitoris[6] and T. Goldsack[7] in companion papers presented at this workshop.

The nominal hydrodynamic evolution of all targets resulted from the ablation of the PPS . As a result a shock propagated towards the interface, was transmitted into material 2 (fig. 1) and broke out of the rear surface sending a rarefaction wave back towards the interface. This rarefaction wave further accelerated the interface in the direction of propagation of the initial shock. Because in these experiments material 2 was very thin (2μm in the case of Mo), the time between acceleration of the interface due to the shock and the rarefaction wave was negligible, and the total duration of the acceleration phase was quite short. The interface then continued to coast while the whole target expanded under the influence of the rarefaction wave. Other multiple reflected waves had minimal influence on the system within the observation time.

The width of the mixed region across the interface increased significantly because of the strong decompression of the target so that it was detectable with the current diagnostics.

LOW ATWOOD NUMBER TARGETS

Since the low Atwood number targets are Rayleigh-Taylor stable, the interface perturbations are expected to change phase at shock passage. Two dimensional calculations confirm this behavior and indicate that at 5.5ns, when an experimental snapshot is possible, the perturbation has grown by a factor of roughly 100, but remains in the near linear regime, as shown in figure 2. Since surface finishes on these targets are of the order of a nanometer, mix widths should remain below 1μm which is not resolvable with the current diagnostics. The behavior of these low Atwood number targets can be simulated without concerns about the influence of mix.

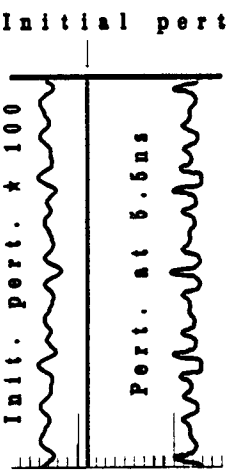

Fig. 2 2D calculations of perturbation growth for a low At# sample

The experimental data show however an overlap between the ablator and the payload. This is due to both motion blurring and diagnostic resolution. While the instrument resolution will affect equally all parts of the image, within the linear response of the detector, motion blurring will result in varying amount of uncertainty in the measurement as different parts of the sample move at different speeds. Numerical simulations show that motion blurring corresponds to no more than 8μm uncertainty in the mix region as shown in figure 3.

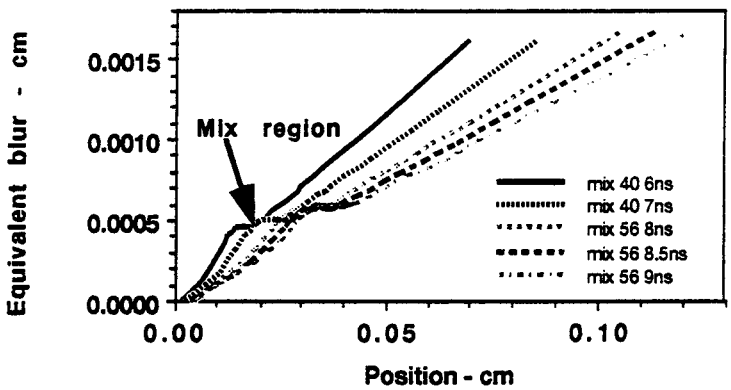

Fig. 3 Calculated motion blurring for two low At# experiments, at snapshot times .

The total blurring, including diagnostic resolution, can actually be backed out of the calculations by comparing the calculated density distributions convolved with a given blurring width to the measured distributions. Matching the apparent mix width gives an effective blurring distance of approximately 24μm, which corresponds to an instrumental resolution of the order of 23μm, and is comparable to the resolution measured in dedicated experiments[5].

Figure 4 shows the agreement between calculated and measured density distributions for one of the low Atwood number experiments. Note that the motion blurring (24μm) included in the calculations simulates ~ 50μm overlap between the materials. Similar agreement is obtained for the other snapshot for this experiment (at 7ns) and for other experiments. This give us confidence that we can properly calculate the behavior of the LoRo targets in the absence of mix. Factors influencing the calculated results include :

the EOS : for the PPS and PyC we used a calculated EOS, without the benefit of experimental check points.

opacities : no experimental data are available in the regime where these targets operate (from solid to partially ionized and highly decompressed). Results are sensitive to the lines in the hot ablator.

the drive : while the incident laser energy is measured, these targets are indirectly driven and no independent measurement of the drive has been possible in the experimental configuration used for the LoRo targets. Calculations show that mix data are not sensitive to laser energy variations of 1/2kJ. However changes in the drive duration affect the density distribution in the ablator which can be measured with low At# targets.

the radiation transport model : here we use multigroup diffusion normalized to a spherical harmonic photon transport calculation.

the target preheat : experiments were conducted with 1/3μm laser irradiation to minimize any preheat which could result in a change of the material densities prior to shock arrival.

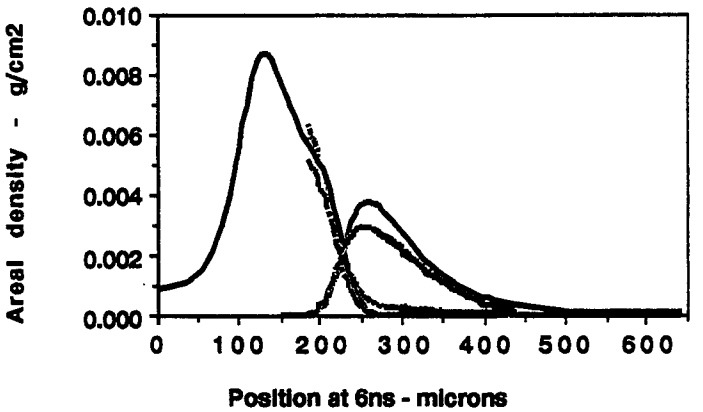

Fig. 4 Comparison of calculated (solid) and experimental density distributions for a low At# LoRo target. Results for two options of data reduction are shown. The 1D calculation was transformed to areal density assuming an average 200μm chord length (initial target diameter : 192μm). Motion blurring is included in the calculated data.

HIGH ATWOOD NUMBER TARGETS

With the source defined through the low At# shots, high At# experiments can be simulated to study the mix region.

One of the concerns in comparing the experimental data which reflect an areal density, with data calculated with a one dimensional mix model which provides density distributions along the target axis, is the effect of lateral expansion. To study this question experiments were run with a rotated spectrometer[6] : alignment problems were very severe so that a simultaneous measurement of the lateral extent of both materials was not obtained. Two dimensional simulations of the target behavior in the absence of mix were performed prior to these experiments (fig. 5). These simulations clearly show a large "halo" of ablator expanding from the target and partially enveloping the payload. This would tend to mimic mix, as a measurement of the areal density would show both materials collocated at a given axial position. In fact the two dimensional calculations show that the areal densities of the materials in the overlap region are barely if at all resolvable with the current diagnostics, and would therefore not affect the mix measurement. The same calculations also provide a justification for some of the assumptions made in the experimental data reduction[7] such as the near gaussian lateral distribution of the densities and the small variation of the opacities near the interface region.

Simulations of the mix region, similar to those discussed in the context of low At# targets, were also performed with the CALE[8] code for a typical high At# target (figure 6). Perturbations applied to the interface for the low and high At# targets (fig. 2 and 6) and the source driving them were identical. As expected, the growth of the perturbation is far greater for the high At# case. By 5.5ns, the perturbation has increased by about 50 times more than for the low At# target. Moreover the perturbation is clearly out

of the linear range, and the interface can be qualified as "fully turbulent". We note however that the symmetry of the initial perturbation with respect to the target axis has been maintained[9].

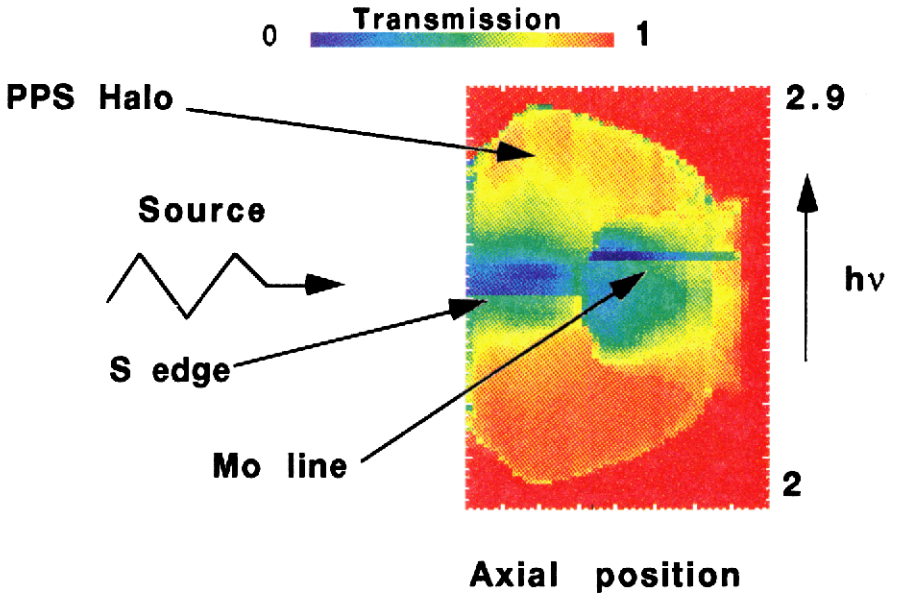

Fig. 5 Simulated dispersed radiograph from a 2D calculation of a high At# LoRo target with no mix. When the sample moves out of it's holder, the PPS expands outwards and a tenous halo envelops the bulk of the target. If the spectral range had not been correctly centered, the S edge axial extent could have partially overlapped the axial extent of the Mo line.

In the calculations, the RMS amplitude of the initial perturbation was of the order of 5/100μm, which is commensurate with the measured surface finish of the LoRo targets, while it's spectrum includes ninteen wavelengths from 1 to 20μm. In this case vortices developing on the spikes of heavy fluid were closely spaced and interacted strongly with each other, resulting in a rapid transition through the nonlinear growth regime into the "turbulent" regime. Another initial perturbation was used, with an RMS amplitude of the order of 1/10μm, and only five wavelengths, from 4 to 40μm. The calculated growth rate was a factor of two higher in the latter case, and reflects the persistence of the large scale features associated with the initial perturbation. It should not therefore be characteristic of the LoRo targets growth rates.

While the LoRo series was designed to demonstrate the feasibility of such experiments at Nova, the main object of the mix experiments is ultimately to provide a data base against which lower order mix models can verified and calibrated. Most of the measured mix width for the LoRo targets is due to the overall decompression of the samples which is the reason why these targets are not ideally suited to our final goal. Nonetheless, mix is generated by the Richtmyer-Meshkov and Rayleigh-Taylor instabilities, and if our codes correctly calculate the hydrodynamic expansion, mix models should apply in this case as well.

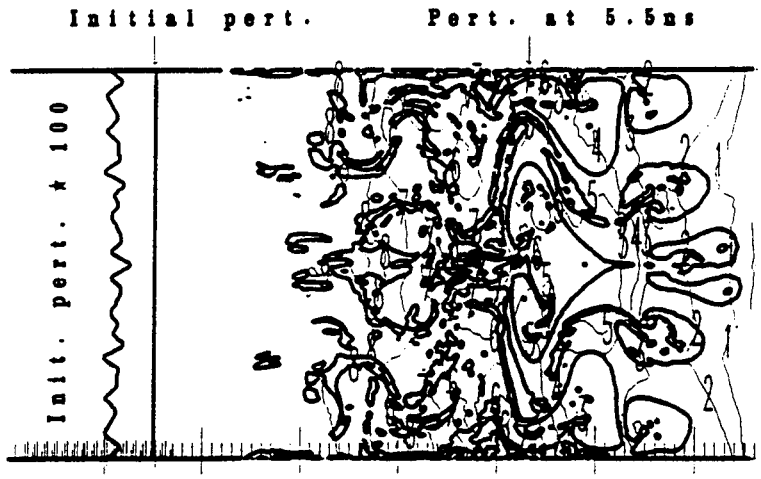

Fig. 6 2D calculations of perturbation growth for a high At# sample

Our kε model was applied to the high At# targets, and compared with both our two dimensional calculations and the experiments. With parameters optimized to match one experiment at a given time, the comparison between the model and the two dimensional calculation with the small random initial perturbation is excellent. Comparison with a measured density distribution is shown on figure 7.

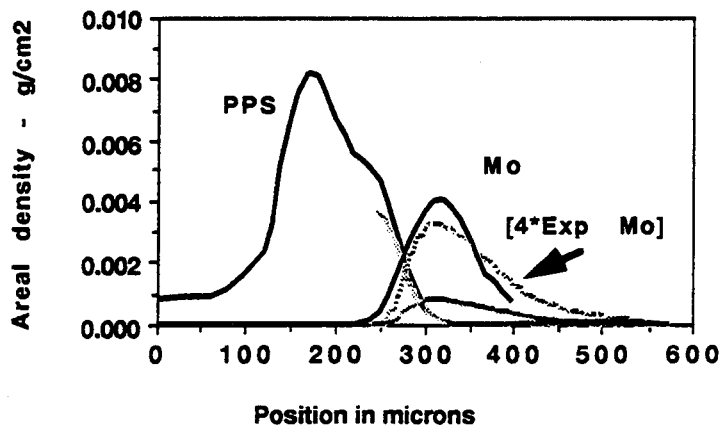

Fig. 7 Areal densities for mix 47 at 5.5ns. Solid lines from a 1D calculation, transformed to areal density assuming an average 200μm chord length . Dotted lines, reduced experimental data. The experimental Mo distribution multiplied by four is also shown. Motion blurring is included in the calculated data.

Figure 7 shows the molybdenum density distribution as extracted from the experimental data, and multiplied by a factor of four. Indeed, when the experimental areal density is integrated, the recovered mass is

considerably lower than the nominal initial mass even though all of the molybdenum is in the diagnostic line of sight[7]. The origin of this discrepancy has not yet been determined, but an error of this magnitude in the initial mass is unlikely, both from a target fabrication standpoint, and by comparison of the mass distributions at snapshot times between experiments and calculation using a smaller molybdenum mass. With this factor of four included, figure 7 shows that our kε model simulates the data quite well.

Comparisons such as those shown on figure 7 are more reliable than comparisons based on mix widths, since the definition of the mix width is not unique. In most of our work, we have used as mix width the distance between points where the payload mass fraction (payload density/total density) varies from 5 to 95%. In the experiments these points are not always accessible, and some extrapolation of the data is required, or an alternate definition of the mass fraction is used. A rough idea of the match between experiments and a calculation based on a given set of parameters can however be obtained on the basis of mix widths. Since the experiments provide at most two snapshots, a complete set of mix widths require using results from different experiments. Because of shot to shot variations in laser irradiation, time is not an appropriate normalization variable between experiments. It is preferable to plot the mix widths as a function of the target displacement[6], as calculations have shown that such a plot collapses all the data from the different experiments close to a single curve. Figure 8 shows a comparison between the calculated and measured mix widths for a number of experiments (Note that the outlying experimental point with a mix width of 110μm is still being investigated). This figure also shows that an appropriate choice of model parameters will match the data very well. However, the mix widths for these high Atwood number targets are uncomfortably close to the ~ 50μm obtained for nominally unmixed targets (fig. 4).

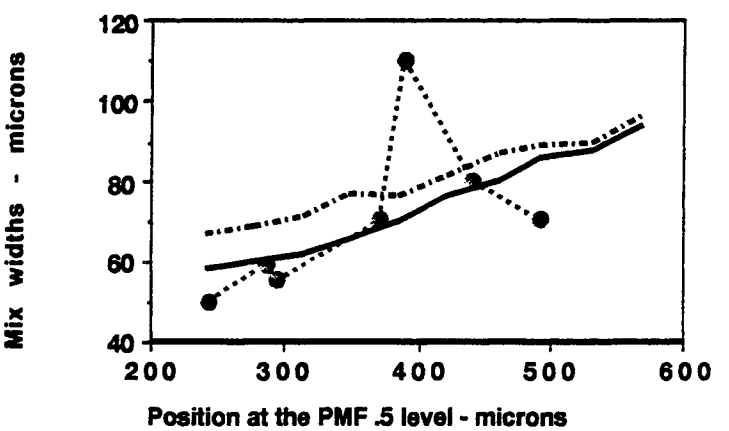

Fig. 8 Comparison of experimental (large dots), and calculated mix widths for a number of LoRo experiments. Two curves are shown for the calculations, corresponding to two possible definitions of the mix width.

CONCLUSION

We have conducted a set of experiments using the Nova laser and LoRo mix targets. Comparisons of calculations and experiments using the low Atwood number version of these targets have helped us verify the ability of our codes to properly model the basic target behavior.

The high Atwood number targets have shown evidence of mix. Their data were used to determine a set of parameters for our kε model with which a good match of the calculated and experimental mix region was possible. But because the LoRo targets decompress severely, and because the resolution of the experiments was not sufficiently high, these experiments are not well suited to pin point the mix model.

The principal value of the LoRo experiments has been to show clear and direct evidence of Richtmyer-Meshkov induced mix in a configuration very different from the usual shock tube experiments. They have provided us with an approximate mix model which can be used to design targets better suited to normalize and verify mix models.

ACKNOWLEDGEMENTS

Many people both at AWE and LLNL have been involved in the design, fabrication, diagnosis, implementation and analysis of the Nova LoRo Mix Experiments, and without each of them the work could not have reached it's fruition.

The contributions of Tim Goldsack, Jonathan Hansom, Leslie Pearson, Paula Rosen, Doug Sutton and Brian Thomas of AWE , John Molitoris, Gail Glendinning and Russell Wallace are specifically acknowledged.

This work was performed under the auspices of the U.S. Department of Energy by Lawrence Livermore National Laboratory under contract #W-7405-Eng-48.

REFERENCES

1. A. Buckingham Ed., Proc. Int'l Work. Phys. Comp. Turb. Mix., (1988), (Springer Verlag, N. Y.)
2. R. D. Richtmyer, Comm. Pure Appl. Math. 13, 297 (1960)
3. Ye. Ye. Meshkov, NASA Tech. Trans. NASA TT F-13, 074 (1970)
4. G. I. Taylor, Proc. Roy. Soc. A 201,191 (1950)
5. W.P. Crowley, Proc. Int'l Work. Phys. Comp. Turb. Mix., (1988), (Springer Verlag, N. Y.)
6. J. D. Molitoris, Proc. 3rd Int'l Work. Phys. Comp. Turb. Mix., (1991), (AIP, N. Y.).
7. T. J. Goldsack, Proc. 3rd Int'l Work. Phys. Comp. Turb. Mix., (1991), (AIP, N. Y.).
8. R. E. Tipton, Private communication
9. Results from such calculations must only be considered qualitative and the significance of small features should not be emphasized. Indeed in these simulations, the ablated part of the target was ignored, and a pressure drive was applied on the resulting boundary. The heating of the target was therefore not correctly simulated. The existence of "computational viscosity", and the lack of real viscosity affect the cascade of scales towards smaller wavelengths.

Study of a mix in directly or indirectly driven planar targets

P.A.Holstein, D.Galmiche, F.Mucchielli, P.Schneider.

Commissariat à l'Energie Atomique,
Centre d'Etudes de Limeil-Valenton
94195 Villeneuve-Saint-Georges Cedex

ABSTRACT

Mixing experiments have been performed using Si/Al/Au trilayer targets accelerated directly or indirectly with laser beams smoothed by Random Phase Plates. Al-Au mix is detected by heating the rear of the target with a probe beam and by observing the Al line emissions. A null-mix experiment has been performed with Si/Al/Si, stable according to Rayleigh-Taylor in order to check that the probe beam does not induce a specific mixing. We made hydro-simulations to characterize the main features of the target when the instabilities occur. In the case of Si/Al/Au targets directly driven, Al emission points out that a mix is observed for driver irradiance as low as 10^{13} W/cm^2 and that most of the gold is mixed with aluminum. We compare the effect of the instabilities for similar targets directly and indirectly accelerated.

1. Introduction

In a laser-driven implosion of a fuel-filled microballoon two stages are unstable according to Rayleigh-Taylor (RT): during the acceleration of the microballoon, the ablation front is unstable and then during the slowing-down stage, the microballoon-fuel interface is unstable. The perturbations may be due to the target imperfections (small scale) or due to the non-uniformities of the laser irradiation amplified in the first stage (large scale). These instabilities can lead to the penetration of pusher spikes into the fuel and/or finally to the mixing between the pusher and the fuel. This mixing lowers implosion performances very much.

This paper is devoted to the experimental study of heavy-light interface instabilities of the same kind as the pusher-fuel interface ones. In this experiment our goal is to estimate the mix thickness in order to compare it to the turbulence code results. Indeed, another experiment made in Limeil pointed out that the mix does not have large structures (see Poster session).

The principle of our experiment is the following [1,2]: a laser beam accelerates a Si/Al/Au foil (Fig 1); at the front, the Si/Al interface is stable according to RT because the densities are very similar. At the rear interface (Al/Au) the density jump can induce RT and Richtmyer-Meshkov instabilities and can generate a mix between aluminum and gold. This mix is detected with a second laser beam, the probe beam, which is focused on the rear of the foil (gold side) and ablates it. The probe beam is delayed with respect to the driver beam in order to permit the mixing to occur. Only the center of the accelerated foil is probed. The gold thickness is chosen larger than the ablation depth measured for a foil at rest; if aluminum x-ray lines are detected it means that some aluminum is mixed with the gold. If the laser ablates directly the foil (direct drive), the silicon layer at the front prevents the

heating of the aluminum with the driver beam and the production of an aluminum emission which could be observed by the spectrograph. If the laser creates a x-ray source which accelerates the foil (indirect drive), we use Al/Au foils.

There are three important results in the experiment presented here:

1) We made a null-mix experiment in order to check the principle of the diagnostic with a probe beam. By using stable targets Si/Al/Si we check that we do not observe a mixing for direct and indirect drives.

2) We have fitted the hydrocode simulations to the experiment by comparing target velocities against those ones deduced from a x-ray streak camera. So we have informations on the "zero-order" fluid state, that is to say, on the state that governs the start of the instabilities.

3) We observed the aluminum line emission which is the signature of the mixing with a temporal resolution: as the line appears simultaneously with the probe pulse we infer that the gold at the rear is totally mixed with the aluminum for a large range of driver energy.

2 Experimental features

The important and new features of this experiment are the followings:

-The large scale non-uniformities of the laser beams (d>30μm) are smoothed out by Random Phase Plates (RPP) for the driver and the probe. The light wavelengths are both 0.35μm and the pulse durations are 0.9ns. The FWHM of the driver focal spot is 200μm and the irradiance is in the range 10^{13}-2.10^{14} W/cm^2 for direct drive. For the indirect drive the target scheme is drawn in Fig 2. The probe FWHM is 120μm and the average irradiance is 10^{14} W/cm^2 within ±10%.

- An alumina layer reduces the migration of the gold into the aluminum during the target fabrication (it was not the case for the previous experiments [1,2]). In

Fig 3 we can see that the region where Al and Au coexist is reduced from 0.12μm to 0.06μm and half of it is probably due to the rugosity of aluminum.

-The target velocity is deduced either from a x-ray backlighting technique using a streak camera or from both plasma emissions due to the driver beam and due to the probe beam recorded on the same camera (Fig 4 for direct drive and Fig 5 for indirect drive). It allows us to fit the hydrocode with the experiment.

-The temporal evolution of the Al Heα line emission coming from the mixing is given by a spectrograph coupled to a streak camera; this evolution can provide detailed informations about the mixing. The time integrated emission is given by a second spectrograph.

3 Experimental results

The exact composition of our standard trilayer is Si(5μm)/Al(2μm)/Au(0.3μm) for direct drive and Al(2μm)/Au(0.2μm) for indirect drive. Indeed, we measured the gold depth ablated by the probe beam in our conditions and for a Al/Au target at rest: x=0.2±0.02μm which is in good agreement with the known values for 10^{14} W/cm^2. In table I we sum up the experimental conditions for a typical shot.

Table I

drive	Energy / focal spot	Irradiance W/cm^2	press Mbar	probe delay	equiv foil	velocity cm/s
Direct	50J /ø200μ	10^{14}	12	1ns	7μm Al	8.10^6
Indirect	2J /ø120μ	510^{12}	4	2ns	3.3μm Al	4.10^6

Let us notice that the pressure is much lower for indirect drive, that is why the targets are less expanded than for direct drive.

The second stage of this experiment deals with accelerated "stable trilayers", Si/Al/Si; in the previous targets we replace the rear gold by 1.5μm of Si. As there is almost no density jump between Al and Si, we do not expect any mixing induced by RT instability. But the use of a probe beam comes up against two difficulties. Firstly it can generate ablation-front instabilities at the rear of the target. Secondly, because of the radiative preheating or because of the shock wave, the target is expanded when the probe beam is on: a part of gold at the rear is undercritical for the probe beam ($n < 9.10^{21}$ $e.cm^{-3}$) and the aluminum line emission could be no longer the signature of a mixing.

In Fig 6 we can see the temporal profiles of Al Heα and Si Heα lines on stable targets for direct drive and indirect drive. The delay of 0.88ns between Al and Si emissions corresponds to the ablation duration of 1.5μm of silicon by the probe beam. This delay is in good agreement with the value deduced from the hydrocode or given by the usual scaling laws. But for direct drive the probe delay is 1ns and for indirect drive, it is 2ns; to some extent, we can say that, for direct drive, the target expansion at 1ns is equivalent to the expansion at 2ns for indirect drive. Finally, we have given evidence of no mixing for stable trilayer Si/Al/Si.

The third stage of this experiment deals with unstable Si/Al/Au trilayers. In Fig 7 the temporal profiles of Al Heα line and of Au M-band have been drawn: by superimposing the probe laser pulse we checked that both emissions have almost the same duration as the pulse. By comparison to the previous profiles for stable trilayers we see that the instabilities generated a mixing region. The fact that the aluminum emission starts simultaneously with the gold emission is an important feature of this graph. It means that the aluminum penetrated the major part of the gold. A more important point is that this simultaneity occurs for driver intensities from 10^{13} to 3.10^{14} W/cm^2. We discuss this point later.

The Al Heα energy measured with the time-integrating spectrograph increases with increasing driver irradiance (Fig 8). Indeed we expect that the mixing is more important when the acceleration increases. This energy increases more slowly for the higher intensities. By numerically-integrating the time-resolved emission we found a good agreement with this direct measurement, except for small driver irradiance because of the low Al signal/noise ratio.

In order to compare trilayers of different masses and accelerated in different conditions we choose to use the relevant parameter, $X \approx 1/2gt^2$ which is the target recoil, instead of the driver irradiance I. Indeed in linear and nonlinear regimes, the amplitude of the perturbations can be expressed with X. The resolution of the streak camera is not good enough to measure the small values of X, but we deduced it from the code which has been fitted to the experiment. In Fig 9 we notice that the Al emission is smaller for indirect drive than for direct drive. Even if the error bars of the recoil are important we think that the difference is meaningful.

4. Results of the hydrocode

The code used for this study is an two-dimensional lagrangian code. Its features are standard for laser-matter interaction: limited heat flux conduction with f=0.1, diffusion multigroup radiation, non-LTE package for gold[4]. The x-ray streaked camera allows us to characterize the motion of the target and to compare it with pure hydro-simulations, i.e. without any treatment of the instabilities.

In Fig 10 we can compare the Al-Au interface velocity for both drives: for these particular cases the shocks break out at the same time (0.7ns). For direct drive and during a period of 0.9ns the acceleration is almost constant (so the displacement can be approximated by $1/2gt^2$). For indirect drive the behaviour is qualitatively the

same up to 3.10^6 cm/s, but there is a second acceleration of the target after t=1.6ns, this is due to the laser intensity transmitted through the gold foil which converts laser light into x-rays. There is no experimental measurement of this transmission, moreover the measured target velocity is 4.10^6 cm/s in average which is closer to the pure indirect velocity than the velocity after the second acceleration.

In Fig 11 we can compare the Atwood number near the interface : during the unstable stage it is 0.7 for direct drive and 0.5 for indirect drive: indeed, for indirect drive the shock is less intense but the preheating of the gold by the x-rays is more important, so the gold density is closer to the aluminum density. But it is not sure that the instabilities keep developping during all the accelerating stage.

In Fig 12 we have schemed the state of the foil and the mixing region due to the instabilities: a mix front propagates through the gold but it meets decreasing gold density so the instability source decreases (the whole Atwood number decreasing and/or the density profile softening) even if the target acceleration is maintained. Moreover, when the probe pulse is switched on the critical density must be somewhere at the rear inside the mixing region if we believe the experimental result; indeed, the aluminum emission starts at the same time as the probe pulse.

In table II we compare the mix thicknesses for both drives by using Youngs's formula [5]: the bubble amplitude is $A_B = 0{,}06\alpha g t^2$ (the spike amplitude is $A_S \approx 1.4A_B$), α is the Atwood number, g is the acceleration and t is the unstable stage duration, all given by the code. We add an estimation of the mix thickness using Leith's formula relevant to Richtmyer-Meshkov instabilities ($A_B = 0.14\alpha\delta v t$).

Table II

drive	instab	t	g cm/s^2	Atw	Al bubble	dense Au
Direct: code 2D	RT	0.9ns	10^{16}	0,7	4μ	0,2μ
Direct: code 2D	RM	0.9ns	$\delta v \approx 2.10^6$	0,7	1.8μ	0,2μ
Indir R X: code2D	RT	0.5ns	5.10^{15}	0,5	0,2μ	0,2μ

The depth of dense gold is the thickness of gold with a density larger than the critical density, refered to its initial density and taken at the beginning of the probe pulse (t=1ns). We took for "t" the acceleration duration which is also the delay of the probe beam: the bubble amplitude is larger than the gold depth for direct drive. This conclusion holds for small driver energy giving an acceleration stage of 0.4ns and an acceleration of the same order of magnitude. Indeed, even if the unstable stage is three times shorter, the table II shows that the bubble is still larger than the gold depth. For Richtmyer-Meshkov instabilities the same conclusion can be drawn. So, the Al emission is going to appear simultaneously with the probe pulse as observed in the experiment.

On the contrary, for the indirect drive the probe pulse begins at t=2ns; if the unstable stage lasts only 0.5ns the mix thickness is of the same order of magnitude as the gold depth. So the result is uncertain; for the time being the time-resolved measurement of the line has not been done.

5 Conclusion

We succeeded in making a "null-mix" experiment with accelerated Si/Al/Si targets. It proves that the targets without density jump are quasi-stable during the acceleration stage. Moreover we checked that the probe beam does not induce RT instabilities at the ablation front in our conditions so it validates the diagnostic of the mix region with a probe beam. With unstable trilayer Si/Al/Au directly driven we observed a mixing Al-Au for a driver irradiance as small as 10^{13} W/cm^2. The time-resolved spectrum showed that the aluminum penetrates very far into the gold even for a small driver energy, that is, for a short RT unstable stage. It is consistent with a rough estimate using Youngs's formula.

For indirect drive the mixing is much less important for an equivalent target recoil, but these results are going to be completed in the near future. However, by comparing the results obtained with direct drive we can infer that the laser non-uniformities seem to play an important part in the direct-drive experiment. These non-uniformities have probably small size because we did not see large scale structure in targets diagnosed with selfbacklighting.

We thank the people working at the target laboratory, the team which is in charge of the experimental facility, "Heliotrope" for their participation to this work. We are very grateful to J.F.Haas for several helpful discussions.

References

1. A.Raven, H.Azechi, T.Yamanaka and C.Yamanaka, Phys. Rev. Lett. 47 (1981) 1049

2. P.A.Holstein, B.Meyer, M. Rostaing, D.Galmiche and N. Wilke, Cr. Acad. Sci Paris 307 (1988) 211

3. C.C.Chang,T.A.Callcott, E.T.Arakawa, Phys. Rev. B 32 (1985) 6138

4. M.Busquet, Phys Rev A 25 (1982) 2302

5. D.Youngs, Physica 12D (1984) 32

   K.I.Read, Physica 12D (1984) 45

Figure captions

Fig 1 : Principle of a mixing experiment: the probe beam heats up the rear of the target so the Al mixed with the gold emits x-ray lines detected with a spectrograph.

Fig2 : Scheme of a target for indirect drive acceleration of a bilayer target.

Fig 3 : Gold concentration in a bilayer Al/Au given by an ion probe: an alumina barrier reduces the migration of the metals through each other.

Fig 4 : Picture given by a x-ray streak camera for direct drive: the front emission is due to the driver beam, the rear emission is due to the probe beam.

Fig 5 : Picture given by a x-ray streak camera for indirect drive: in this case we do not see the emission on the gold foil which converts laser light into x-ray. The spatial reference allows us to draw the time axis.

Fig 6 : For stable target Al/Si we observe a delay between Si and Al emission. This 0.88ns delay correspond to the ablation of the Si and is almost the same for both drives.

Fig 7 : For unstable target and direct drive we do not observe any delay between gold and Al emissions (for indirect drive the measurement has not been done).

Fig 8 : Al line emission for direct drive as a function of incident laser energy.

Fig 9 : Al line emission for both drives as a function of target recoil.

Fig 10 : Al/Au Interface velocity given by the 2D Hydrocode. The second acceleration in the indirect drive case is due to the laser transmitted through the gold foil.

Fig 11 : Atwoood number given by the 2D Hydrocode .

Fig 12 : Density profile scheme at the beginning of the probe pulse: the critical density where probe energy is deposited is inside the mix region.

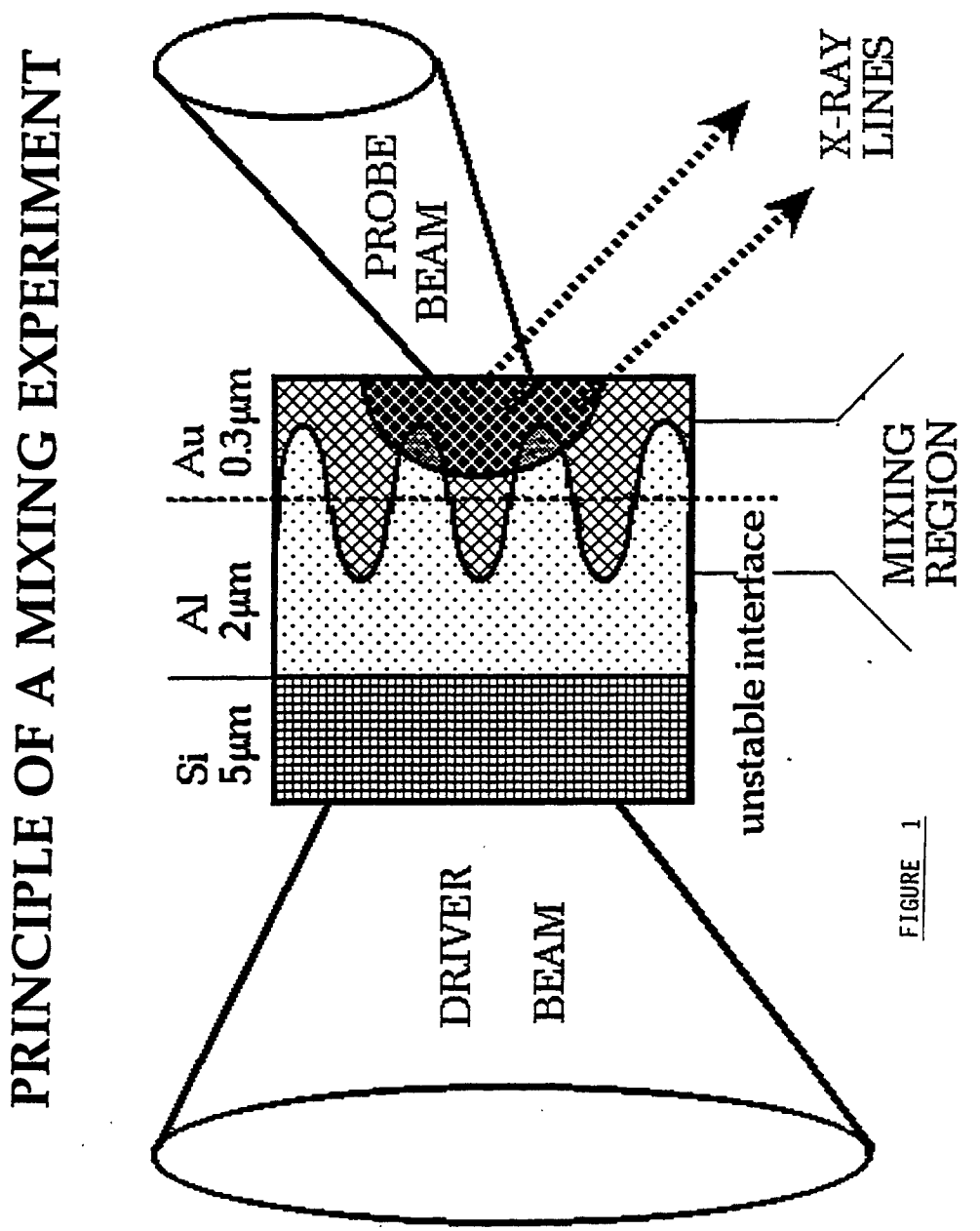
PRINCIPLE OF A MIXING EXPERIMENT
PROBE BEAM
X-RAY LINES
Au 0.3µm
Al 2µm
Si 5µm
unstable interface
MIXING REGION
DRIVER BEAM

FIGURE 1

Target for the indirect drive

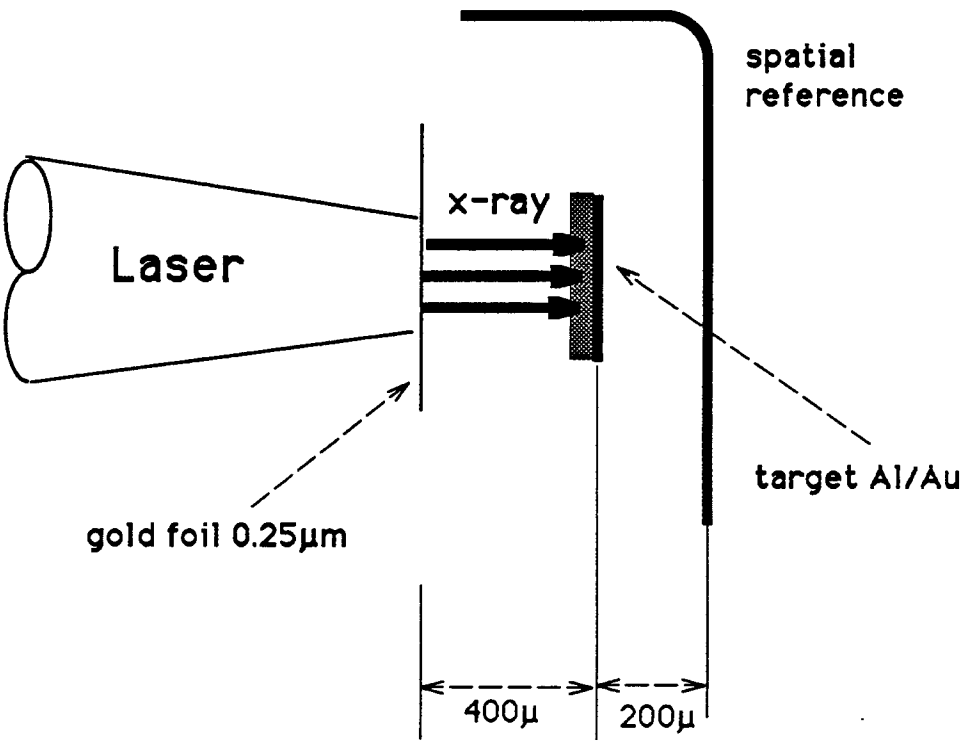

FIGURE 2

cone-i

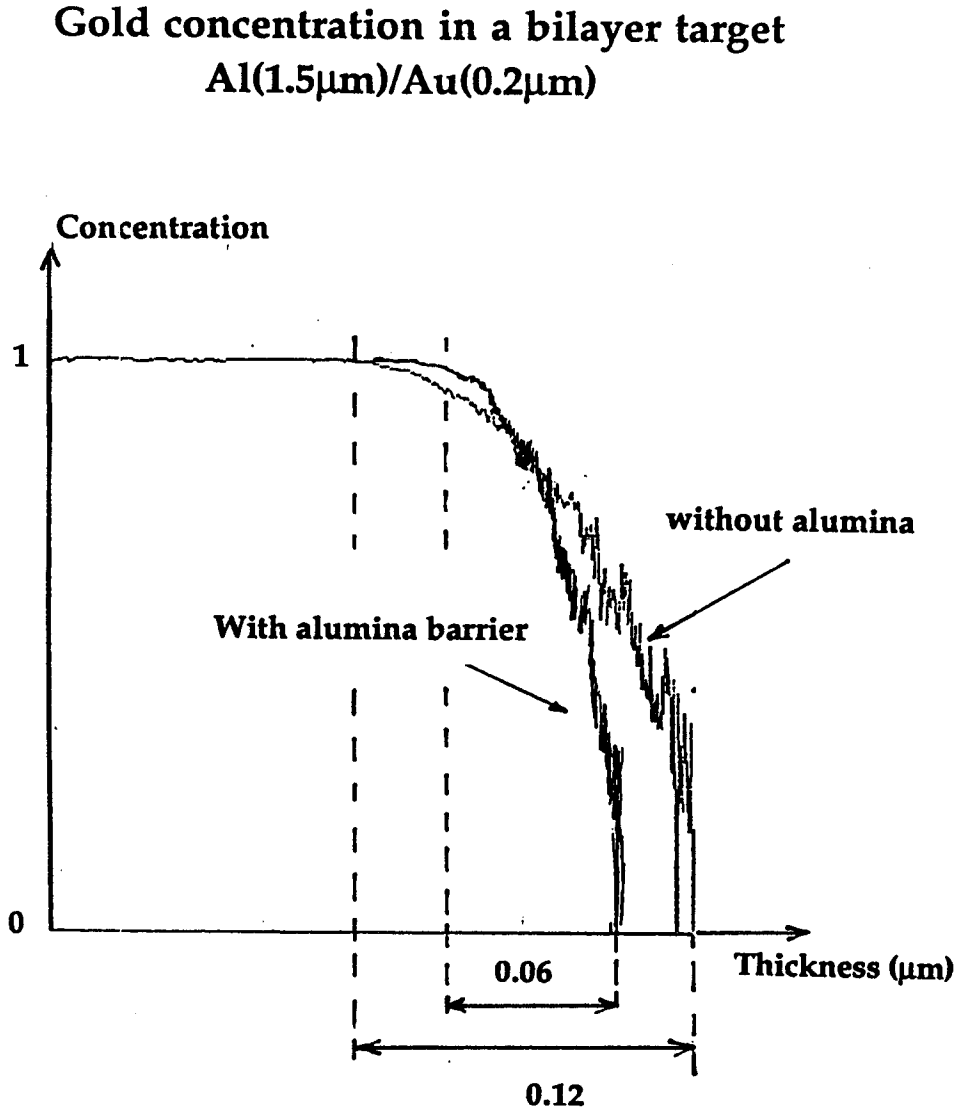
Gold concentration in a bilayer target
Al(1.5μm)/Au(0.2μm)
Concentration
1
0
without alumina
With alumina barrier
0.06
Thickness (μm)
0.12

FIGURE 3

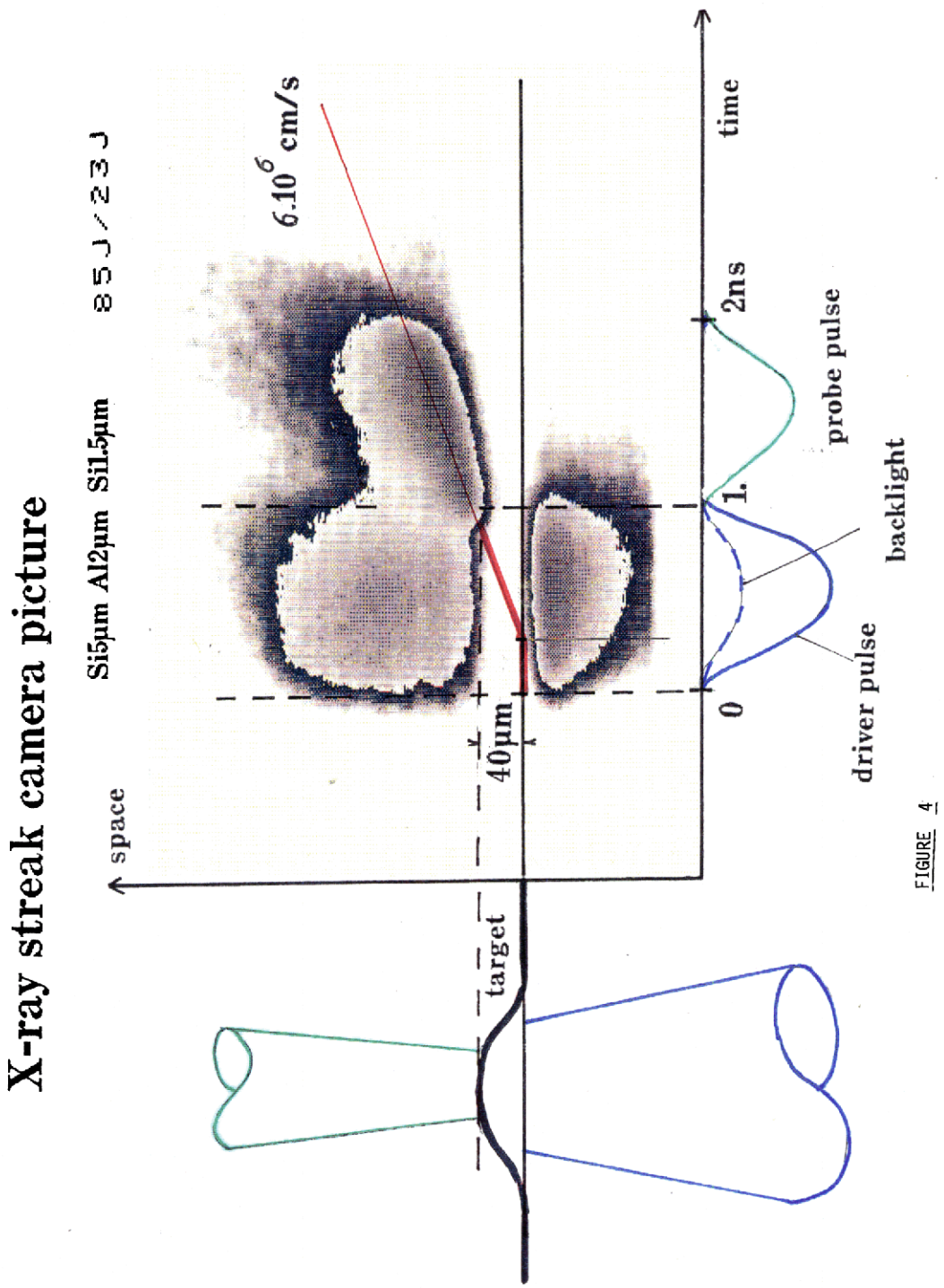
X-ray streak camera picture
Si5µm Al2µm Si1.5µm
85J/23J
6.10^6 cm/s
space
40µm
target
time
2ns
1.
0
probe pulse
backlight
driver pulse

FIGURE 4

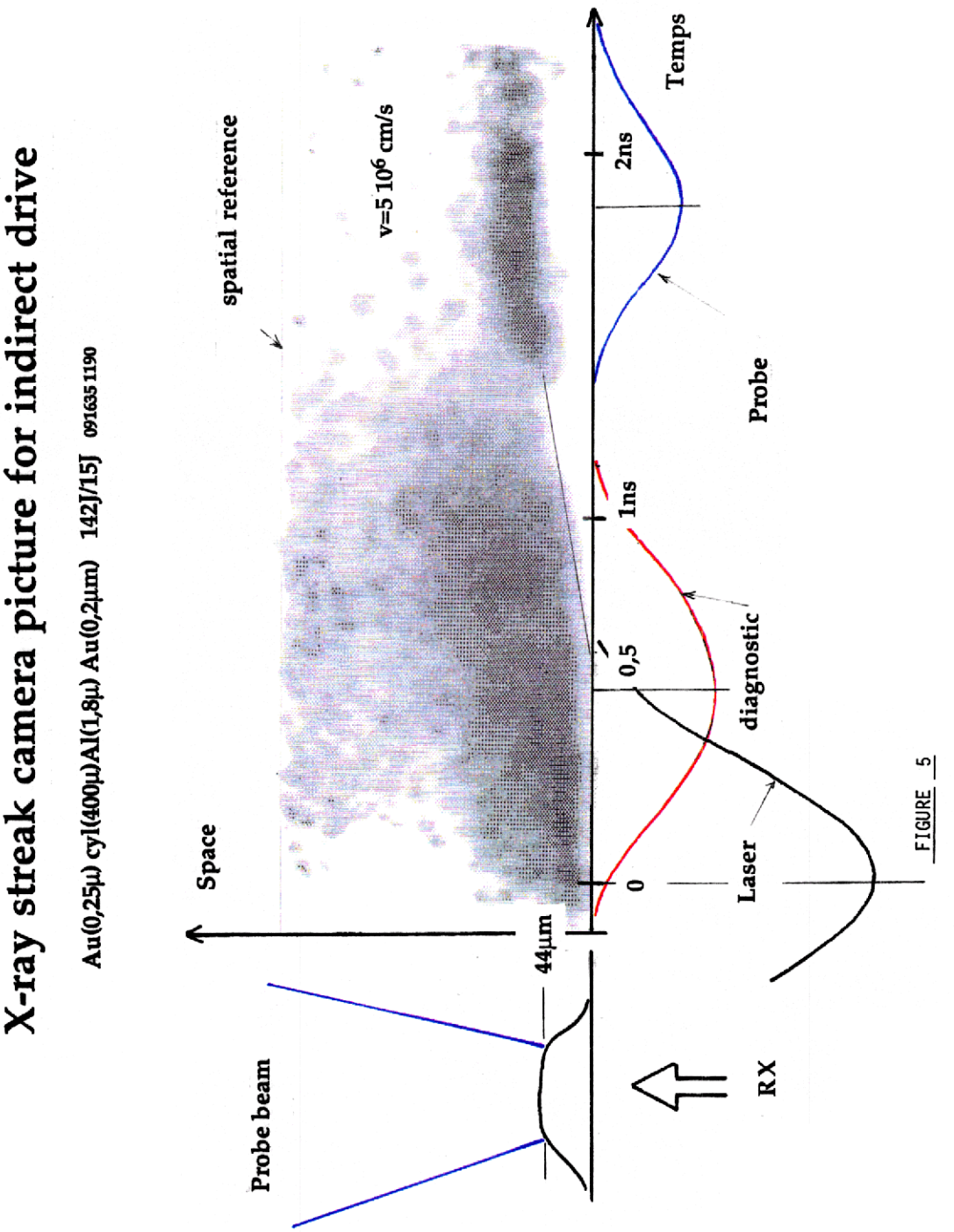
X-ray streak camera picture for indirect drive
Au(0,25µ) cyl(400µ)Al(1,8µ) Au(0,2µm) 142J/15J 091635 1190
spatial reference
v=5 10⁶ cm/s
Space
Temps
2ns
1ns
0,5
0
Probe
diagnostic
Laser
RX
Probe beam
44µm

FIGURE 5

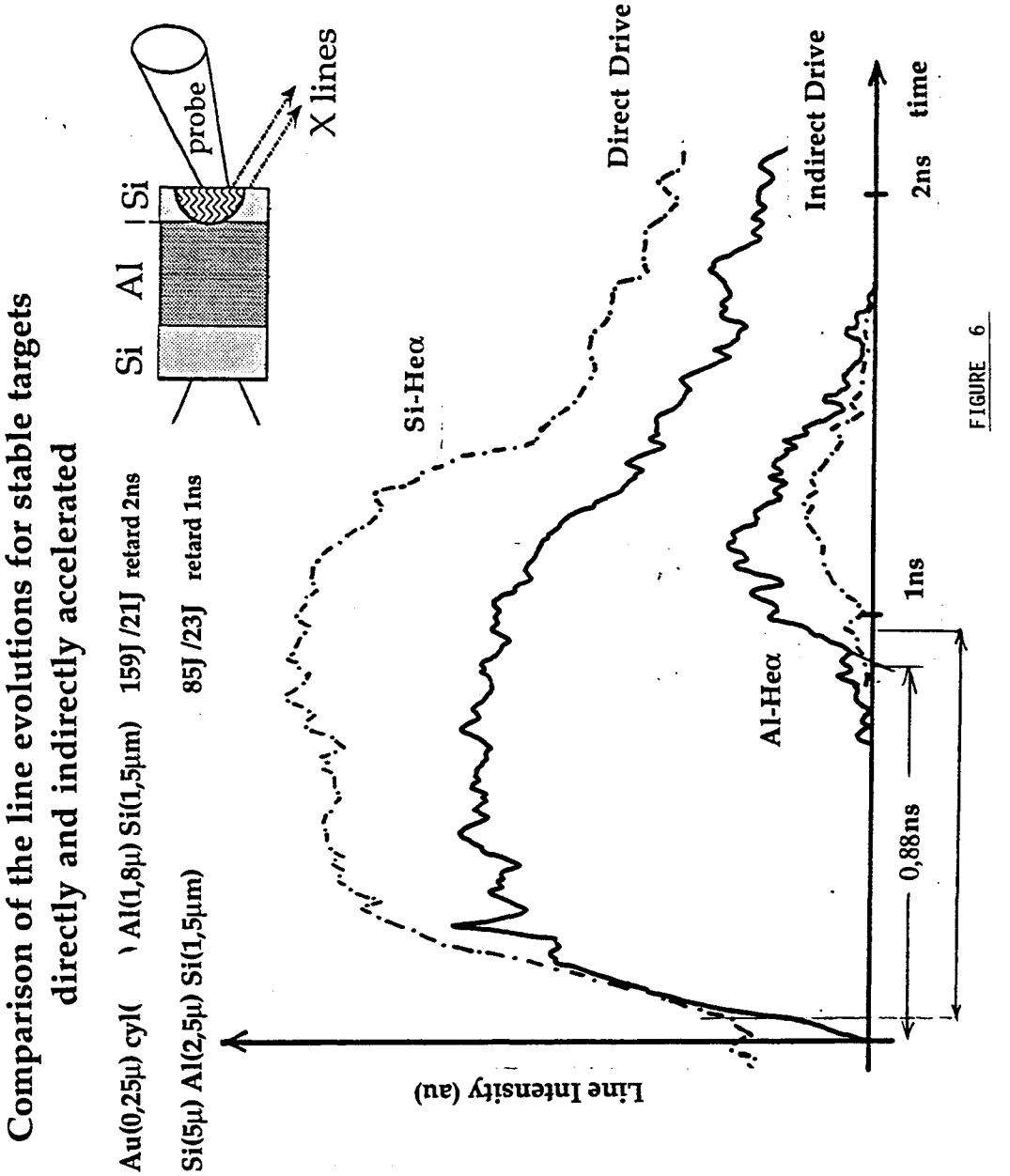
Comparison of the line evolutions for stable targets
directly and indirectly accelerated
Au(0,25µ) cyl(' Al(1,8µ) Si(1,5µm) 159J /21J retard 2ns
Si(5µ) Al(2,5µ) Si(1,5µm) 85J /23J retard 1ns
Si Al Si
probe
X lines
Si-Heα
Direct Drive
Al-Heα
Indirect Drive
Line Intensity (au)
0,88ns
1ns
2ns time

FIGURE 6

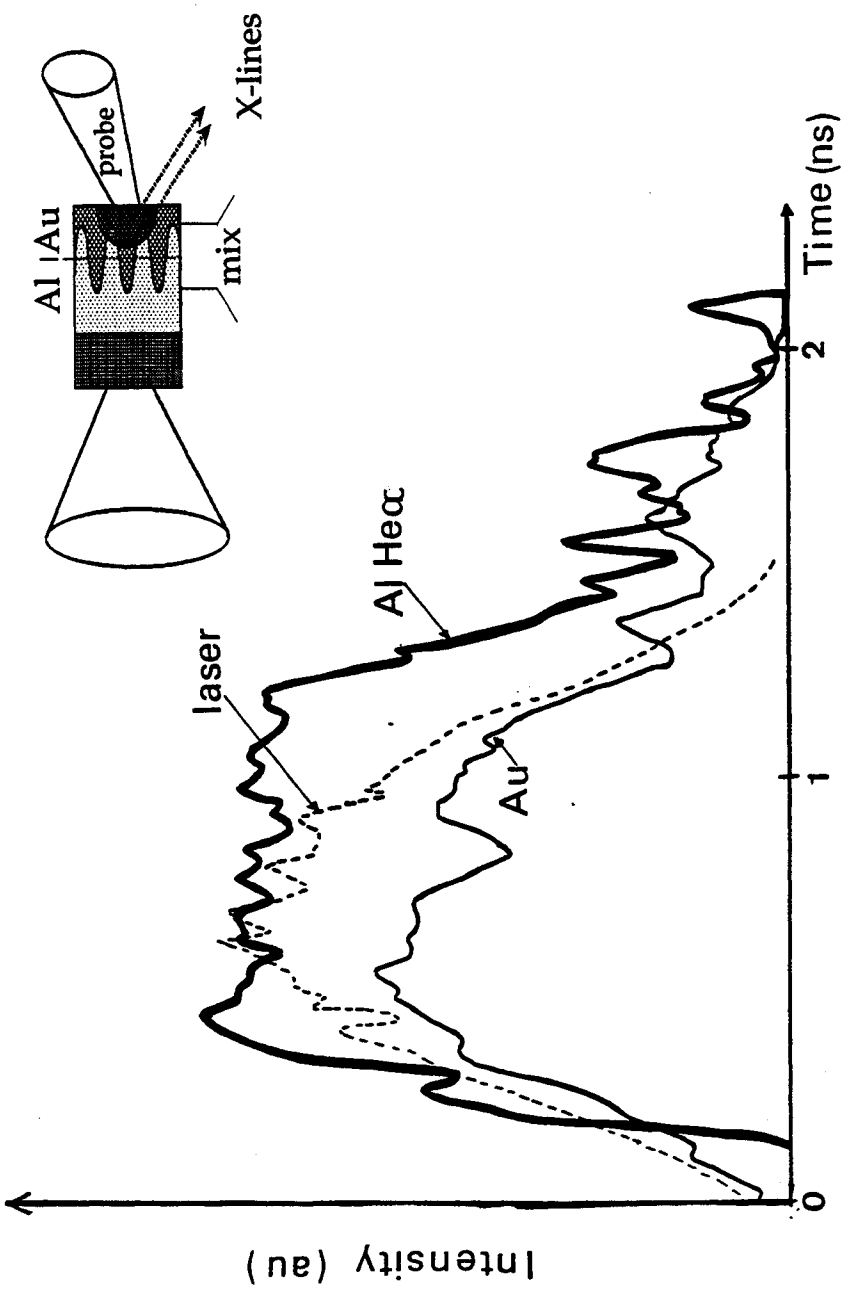
Temporal evolution of the lines for an unstable target accelerated with direct drive.
probe
X-lines
Al
Au
mix
laser
Al Heα
Au
Intensity (au)
0
1
2
Time (ns)

FIGURE 7

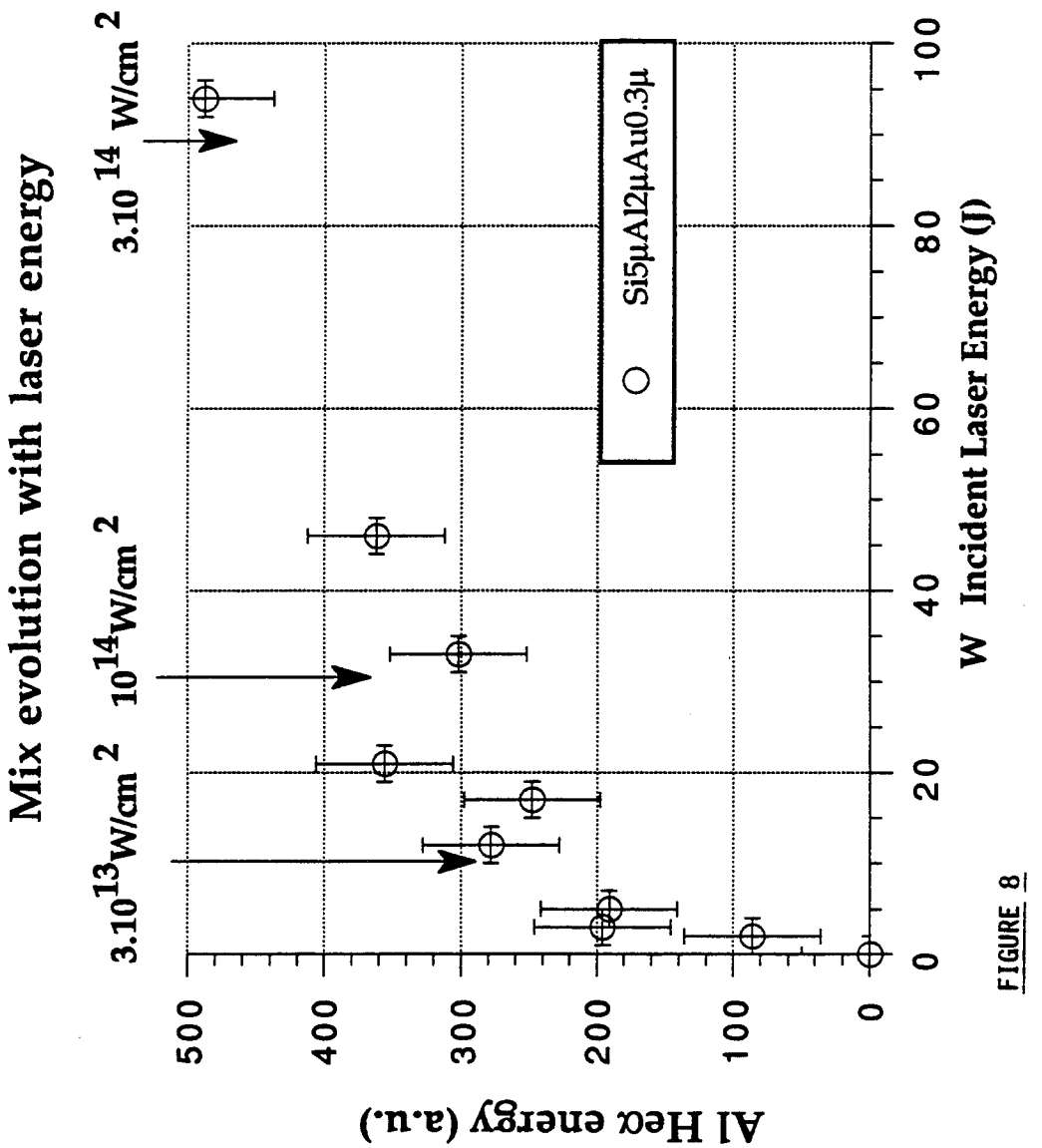
Mix evolution with laser energy
3.10^13 W/cm^2
10^14 W/cm^2
3.10^14 W/cm^2
Si5µAl2µAu0.3µ
Al Hea energy (a.u.)
W Incident Laser Energy (J)
0
100
200
300
400
500
0
20
40
60
80
100

FIGURE 8

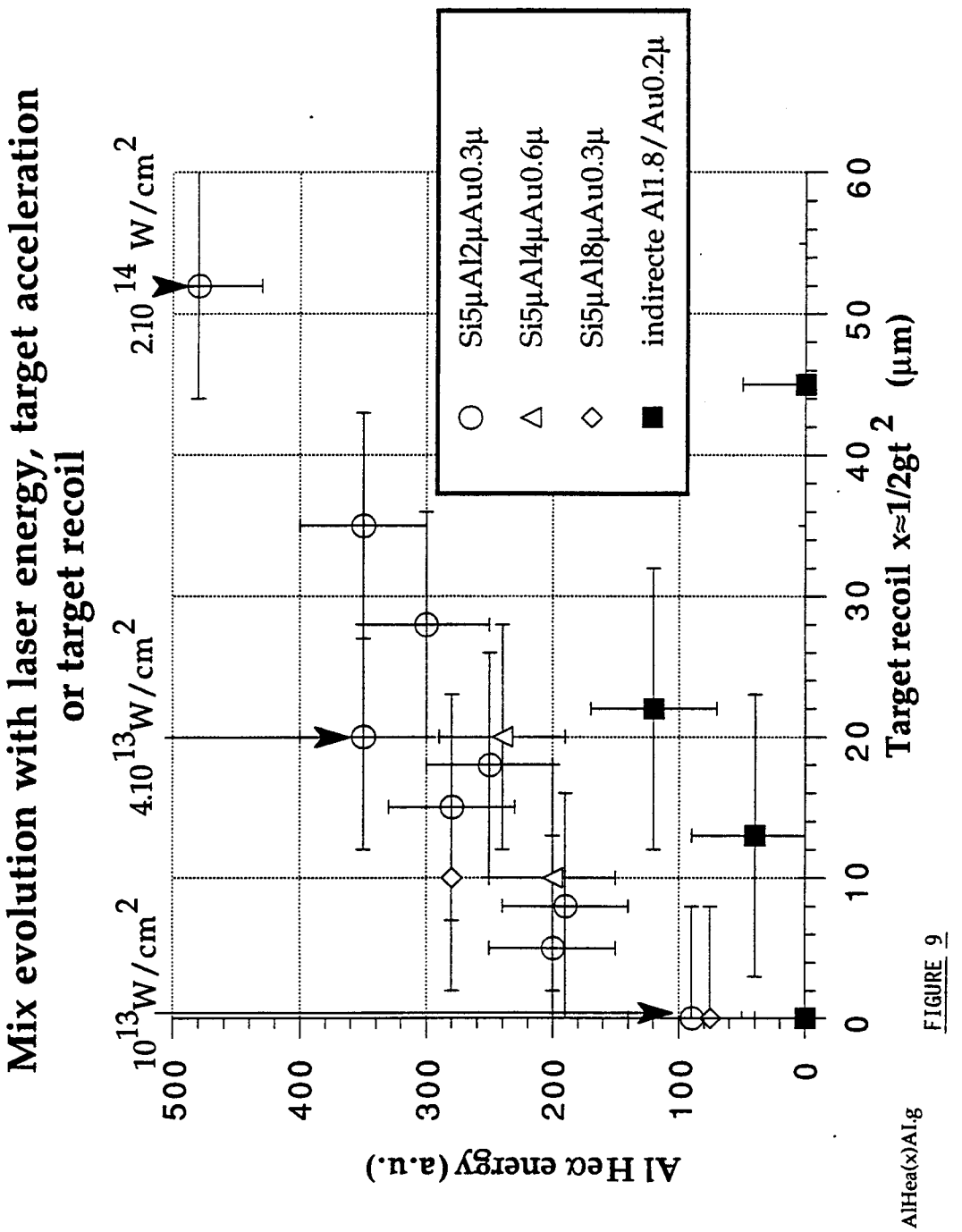
Mix evolution with laser energy, target acceleration or target recoil
10^{13}W/cm^2
4.10^{13}W/cm^2
2.10^{14} W/cm^2
Si5µAl2µAu0.3µ
Si5µAl4µAu0.6µ
Si5µAl8µAu0.3µ
indirecte Al1.8/Au0.2µ
Al Hea energy (a.u.)
Target recoil x≈1/2gt^2 (µm)
AlHea(x)Al.g

FIGURE 9

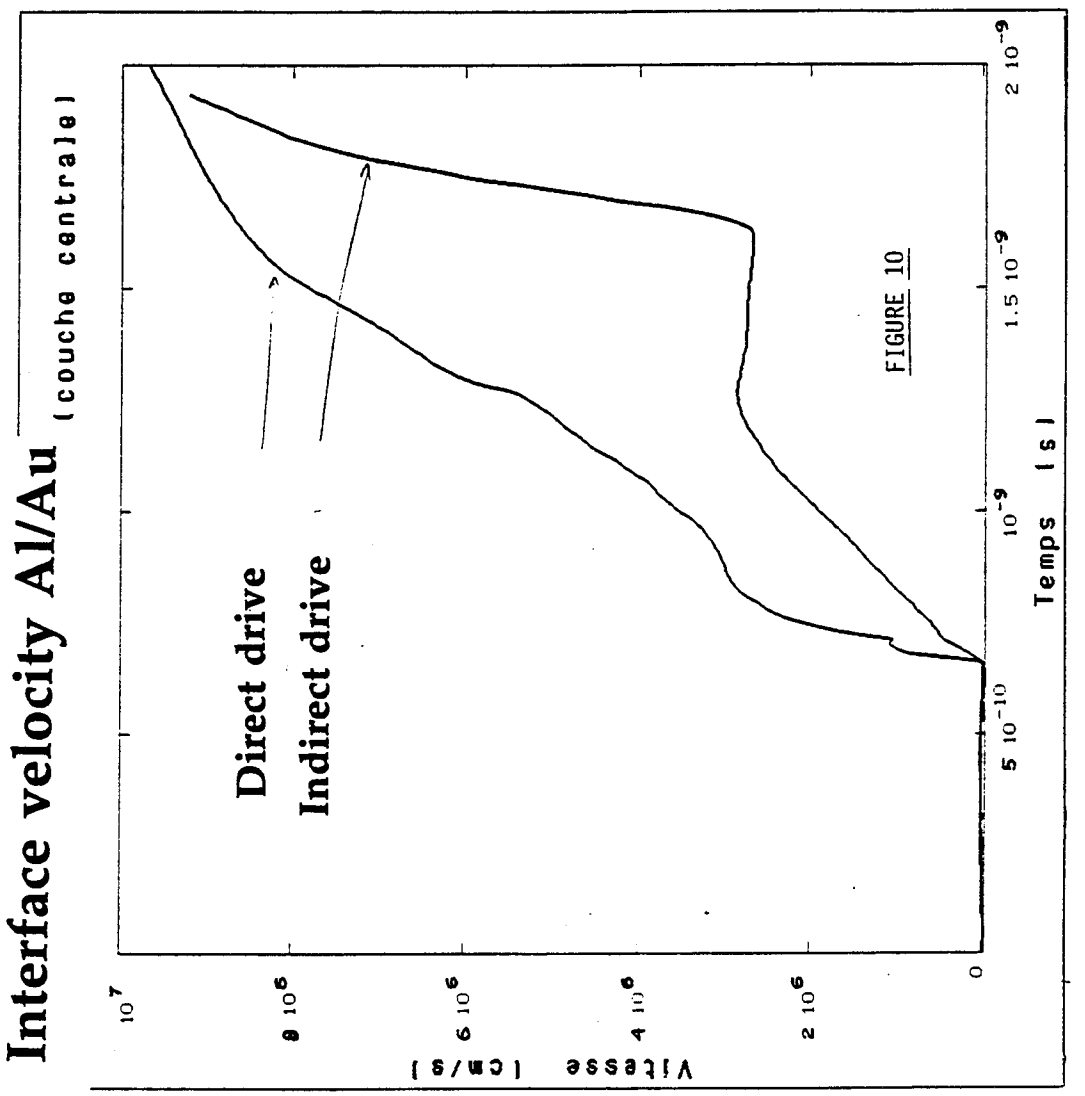
Interface velocity Al/Au (couche centrale)
Direct drive
Indirect drive
Vitesse (cm/s)
Temps (s)
FIGURE 10

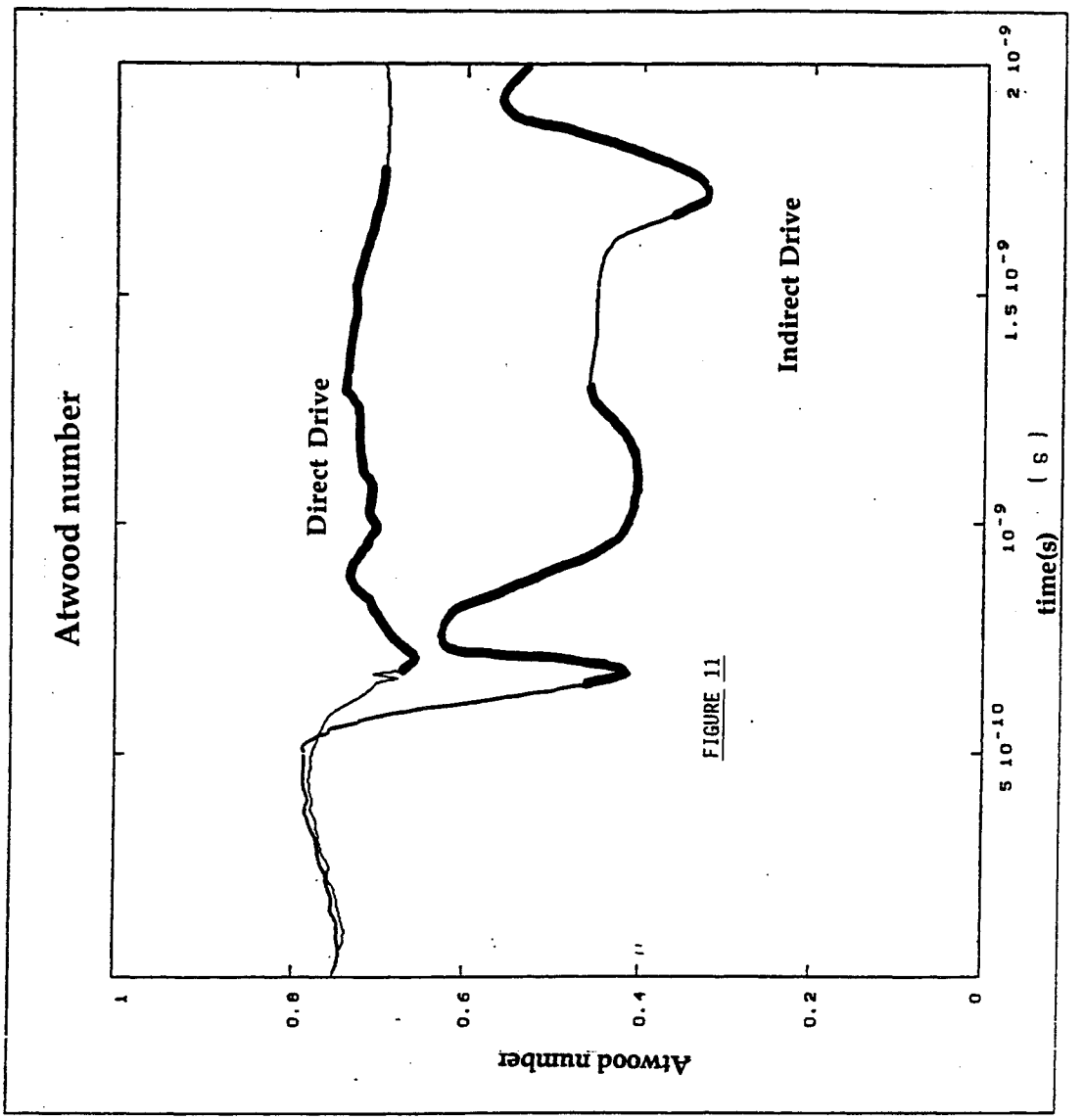
Atwood number
Direct Drive
Indirect Drive
Atwood number
1
0.8
0.6
0.4
0.2
0
5 10-10
10-9
1.5 10-9
2 10-9
time(s)
(s)

FIGURE 11

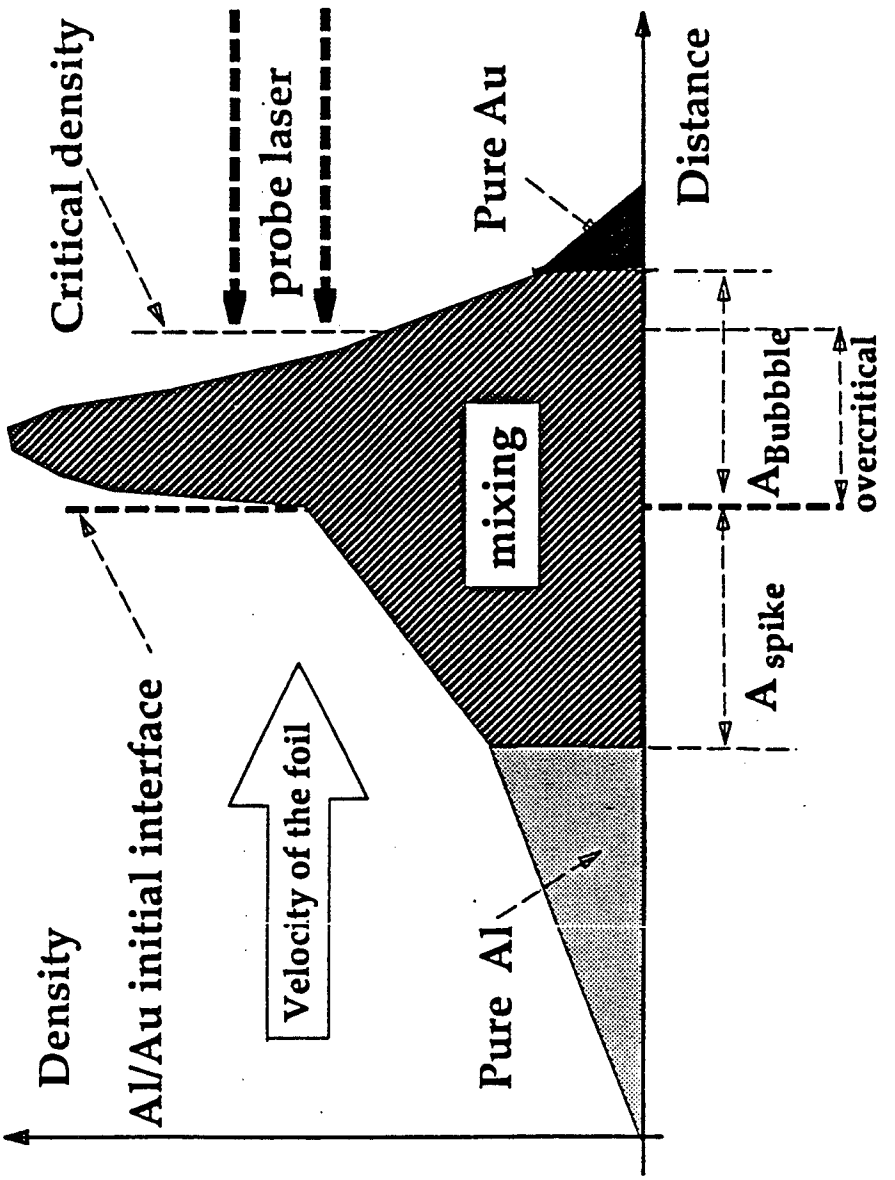
Critical density
probe laser
Pure Au
Distance
mixing
A_{Bubble}
overcritical
A_{spike}
Velocity of the foil
Al/Au initial interface
Density
Pure Al

FIGURE 12

The AWE/LLNL Planar Foil Mix Experiment

T.J.Goldsack, J.C.V.Hansom, N.Cowperthwaite
AWE Aldermaston, Reading, Berks., UK;

J.D.Molitoris
Lawrence Livermore National Laboratory, Livermore, CA.

Abstract

The AWE/LLNL planar foil mix experiment, in which point-projection spectroscopy is used to diagnose hydrodynamic mixing between the ablator and payload in a radiatively-accelerated package, has been described previously. In this paper we present a detailed analysis of the data, using a new, two-dimensional unfold technique which allows chord-length effects to be taken into account. We find that with the new technique the derived mix distributions are less subject to errors caused by chord-length effects, leading to much less scatter in the calculated mix widths. We find that high Atwood-number packages mix more than do low Atwood-number packages. Comparisons with two-dimensional calculations and a one-dimensional model are made.

Introduction

In the AWE/LLNL planar foil mix experiment,[1] point-projection spectroscopy is used to diagnose hydrodynamic mixing between a low-density ablator and a high-density payload in a radiatively-accelerated package. The package consists of a 60 μm poly-phenylene sulphide ablator ("PPS", 29% sulphur by weight, density = 1.36 g cm^{-3}) and a molybdenum payload (density = 10.22 g cm^{-3}); with these materials the nominal Atwood number is 0.8 and so Richtmyer-Meshkov[2] and Rayleigh-Taylor[3] instability growth is expected at the interface. The experimental arrangement for diagnosing this instability growth is shown in Fig. 1. Approximately 6 kJ of 0.53 μm laser light in a 1ns-long square pulse is used. The package is backlit at between 4 and 10 ns after the start of the laser pulse. The backlighter X-rays are generated by focusing one of the Nova beams (pulse length = 200 ps FWHM) onto a subsidiary target - in this case 20 μm-diameter copper wires coated with an approximately equimolar mixture of Bi, Au, and Pt to give an X-ray emission band in the 2-to-3 keV range. There are two such lines-of-sight (denoted by "Sim 1" and "Sim 2") on each shot. A typical image recorded in this way is shown in Fig. 2(a). Figure 2(b) shows the image after conversion to transmission, a process which has been described elsewhere.[4] The foil is the central blob; below it can be seen the shadow of a displacement fiducial. This frame is well aligned in that the sulphur K edge at 2.47 keV and the Mo L_{III} edge at 2.52 keV both pass close to the centre of the foil.

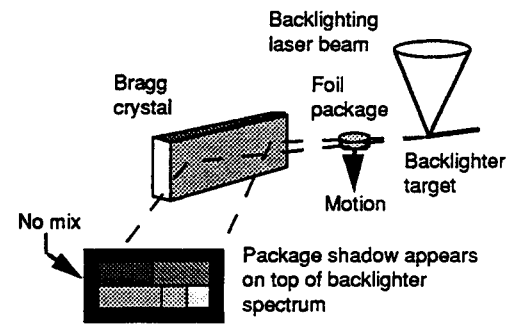

Figure 1: The experimental arrangement.

Determination of mix

Previous experiments, reported elsewhere, have shown that the observed overlap between the ablator and payload absorption edges is not caused by effects such as blow-by.[1,4] Other experiments, including some point-projection shots using packages where the molybdenum was replaced by chloro-polystyrene (29% Cl by weight, density = 1.24 g cm^{-3}) to give a nominal Atwood number of 0.05 and hence, according to classical theory, very little

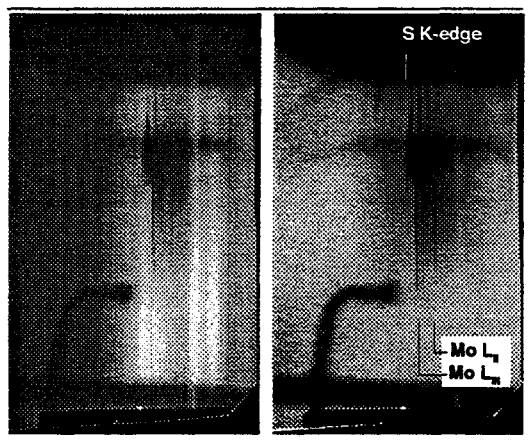

Figure 2:
a (left): the raw image (film density) from shot 19122104 (Mix 47 Sim 2)
b (right): the same image after conversion to a map of transmission.

The previous (line-out) method for determining mix from the spectral overlap is sensitive to chord-length effects.

Until recently, mix widths were obtained by taking line-outs above and below the sulphur K and Mo L_{III} edges:

$$T_a = \exp(\kappa_{1a}\int\rho_{1a}(l_{1a})dl_{1a}) \times \exp(\kappa_{2a}\int\rho_{2a}(l_{2a})dl_{2a})$$

$$T_b = \exp(\kappa_{1b}\int\rho_{1b}(l)_{1b}dl_{1b})\times\exp(\kappa_{2b}\int\rho_{2b}(l_{2b})dl_{2b})$$

where T is the transmission, κ is the opacity ($cm^2\ g^{-1}$), ρ is the density, and dl is an elemental distance along the line-of-sight. Subscripts 1 and 2 refer to materials 1 (PPS ablator) and 2 (Mo foil) respectively, and subscripts a and b refer to quantities defined above or below the absorption edges.

Consider the case where the line-outs have been taken above and below the sulphur absorption edge. In this case material 2 is the "contaminant" and it is possible to combine the above two equations to give the areal density of material 1 if the following assumptions are made:

(i) the opacity of material 2 is constant across the absorption edge of material 1;

$$\kappa_{2a} = \kappa_{2b}$$

(ii) the areal density of material 1 is the same above the absorption edge as below it;

$$\int\rho_{1b}(l_{1b})dl_{1b} = \int\rho_{1a}(l_{1a})dl_{1a}$$

(iii) the areal density of material 2 is the same above the absorption edge as below it.

$$\int\rho_{2b}(l_{2b})dl_{2b} = \int\rho_{2a}(l_{2a})dl_{2a}$$

With these assumptions the areal density of material 1 becomes:

$$\int\rho_1(l_1)dl_1 = \frac{\log_e(T_b/T_a)}{\Delta\kappa}$$

where $\Delta\kappa = \kappa_{1a} - \kappa_{1b}$ is the jump in opacity at the edge.

instability growth, have shown that the overall system resolution is around 40 μm.[1] The amount of mix between the ablator and the payload can therefore be determined from the overlap between the sulphur K edge and the Mo L_{III} and L_{II} edges in the case of the high Atwood-number targets, and the overlap between the sulphur K edge and the chlorine K edge in the case of the low Atwood-number targets. In the past this has been performed by taking line-outs above and below each absorption edge and then calculating the areal density in the line of sight, as shown in Box 1. A problem with this approach is that errors can be introduced if the amount of material in the line-of-sight at a given displacement varies between the "above-edge" line-out and the "below-edge" line-out. If the frame is well-aligned (Fig. 2) this variation is small, but if the frame is not well aligned the calculated areal density may be seriously in error. We have therefore developed a "2-dimensional" analysis method which makes use of as much of the information in the image as possible.

The 2-D analysis method.

At the heart of the 2-D analysis lies an attempt to characterise the radial distribution of the foil material - i.e. chord-length effects are taken into account implicitly. The procedure may be summarised as follows. The lateral shape (i.e. perpendicular to the direction of motion) of the material distribution is measured outside the mix region by fitting a given function to the observed transmission data above the mix region (i.e. in the ablator) and below the mix region (i.e. in the payload). The shape within the mix region is then obtained by interpolation across the gap. Finally, an iterative procedure calculates the amounts of ablator and payload which, given the shape of the foil within the mix region, best fit the experimental data. A detailed description of this process now follows.

The image is split into three areas (see Fig. 3) - a region of pure ablator, a region of pure payload, and a region between them, larger than the mix width, containing the mix layer. In each of the two pure-material regions a weighted, non-linear least-squares error-minimisation algorithm is used

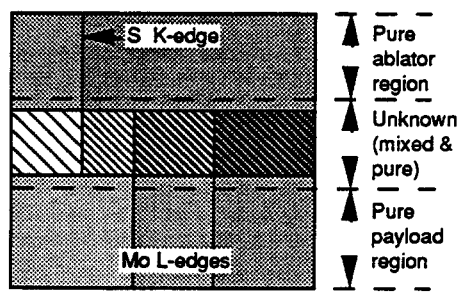

Figure 3. The image of the foil is split into three areas.

to fit a function to the material distribution for each record (horizontal row) within the image. We fit to optical depth [$\tau = -\log_e(I/I_0)$] rather than transmission, since by so doing we can more easily take into account uncertainties in the image processing. The function used is the sum of a Gaussian plus a quadratic:

$$\tau = \kappa a_0 \exp(-z^2/2) + a_3 + a_4 x + a_5 x^2 \qquad (1)$$

$$\text{where } z = (x-a_1)/a_2 \qquad (2)$$

The opacity is included in the Gaussian term but not in the quadratic, since the assumption is that the quadratic term describes an optical density background (Fig. 4). The use of a Gaussian function to describe the shape of the foil's areal density distribution is justified largely by examination of line-outs through foil absorption images recorded with a rotated spectrograph. [1] In such images, where the spectral dispersion is parallel to the direction of motion, rather than

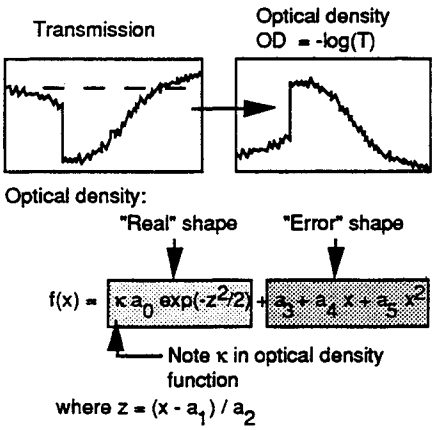

Figure 4. The shape of the optical density surface is fitted by the sum of a Gaussian term (which describes the foil material distribution) and a polynomial of degree ≤2.

perpendicular to it as in the data presented here, the material distribution does appear to be very nearly Gaussian. The assumption of a Gaussian distribution is, however, only an assumption and care is taken in every analysis to check that it is appropriate.

To ensure that regions in the image which are unduly influenced by uncertainties in image processing (principally areas where the transmission is close to zero) do not adversely affect the analysis, a weighting scheme is used which selectively reduces their contribution to the fitting procedure as their transmission tends to zero. In addition, absorption lines (which are observed close to the absorption edges) are also ignored, since their opacities are high and uncertain and they are instrumentally blurred.

In some frames it is found that a better fit can be obtained by fitting a function with fewer free parameters - e.g. a linear background:

$$\tau = \kappa a_0 \exp(-z^2/2) + a_3 + a_4 x \qquad (3)$$

or even a constant background:

$$\tau = \kappa a_0 \exp(-z^2/2) + a_3 \qquad (4)$$

Sometimes a super-Gaussian gives a better fit, with either a constant or a linear background:

$$\tau = \kappa a_0 \exp(-z^{a_6}/2) + a_3 \; [+ a_4 x] \qquad (5)$$

where a_6 is the power of the super-Gaussian term. In such cases a quadratic background cannot be used because there are too many free parameters. Care is taken to choose an appropriate fitting function, and a number of different functions are tried in repeated analyses of the same frame to test the sensitivity to the fitting function of the derived result. The lowest-order polynomial possible is used.

The result of this fitting is up to 6 vectors (a_0 through a_5 or a_6) which contain elements derived in the two pure material regions only. The values within the mix region are obtained by fitting an appropriate function to the known values and interpolating across the gap (Fig. 5). In doing so, the coefficient a_0 - the amplitude of the Gaussian - is ignored, since to interpolate its value would be to impose a solution.

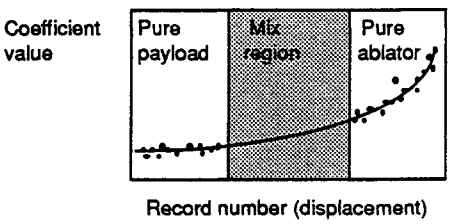

Figure 5: The values within the mix region of each coefficient are derived by interpolation after fitting an appropriate function to the values outside the mix region.

A number of implicit assumptions are made in performing this analysis. First, the assumption that the coefficients can be interpolated across the mix region is equivalent to assuming that the radial expansions of the ablator and the payload are the same. We believe that any errors arising from this assumption are much less than those arising from chord-length effects. Secondly, in assuming a Gaussian areal density distribution it is assumed that there is no annulus of PPS which has blown past the payload. Previous experiments have shown that this is a good assumption. [1] Finally, it is assumed that the amount of mix is independent of radial position. This too is likely to be a good assumption.

The next stage in the analysis is to perform an iterative search to find the amounts of ablator and payload which best fit the observed transmission data. (In the remainder of this note it is assumed that the fitted function is Gaussian foil + quadratic background.) An initial guess is made of the amount of ablator and payload present - say A_{PPS} and A_{Mo} - (actually, the guess is that it is the same as the previous record) and the optical depth is calculated:

$$\tau = (A_{PPS}\kappa_{PPS} + A_{Mo}\kappa_{Mo}) \times \exp(-z^2/2) + a_3 + a_4 x + a_5 x^2 \qquad (6)$$

Note that the optical depth due to background or error has been included. The amounts of ablator and payload (A_{PPS} and A_{Mo}) are then varied iteratively until changes to either A_{PPS} or A_{Mo} of less than 1% from one iteration to the next result in a worse match to the experimentally-measured transmission (Fig. 6).

The horizontal variation in the areal densities ξ of the ablator and payload are calculated:

$$\xi_{ablator} = A_{PPS}\exp(-z^2/2) \qquad (7)$$

$$\xi_{payload} = A_{Mo}\exp(-z^2/2) \qquad (8)$$

and from these the payload mass fraction (pmf):

$$pmf = \xi_{payload}/(\xi_{payload}+\xi_{ablator}) \qquad (9)$$

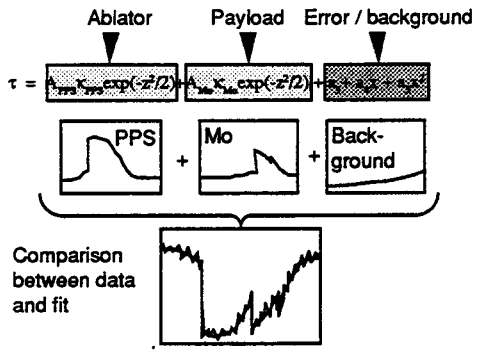

Figure 6: The amounts of ablator and payload are varied iteratively until changes to either of less than 1% from one iteration to the next result in a worse match to the experimentally-measured transmission.

Figure 7 shows the areal densities calculated in this way for shot MIX 36, Sim 1, together with the areal densities calculated in the old "1-D line-out" way. The 2-D unfold shows distributions which - ignoring noise - roll over monotonically, in contrast to the 1-D unfolds which show a spurious bump on the Mo and a low-level foot on the ablator - both due, in the main, to chord-length effects.

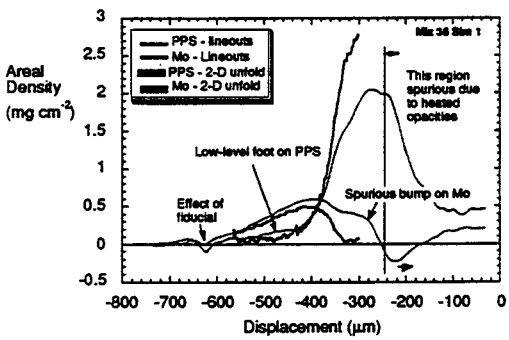

Figure 7: The areal densities calculated from a 2-D unfold of shot MIX 36, Sim 1, together with the areal densities calculated in the old "1-D line-out" way. The 2-D unfold shows distributions which - ignoring noise - roll over monotonically, in contrast to the 1-D unfolds which show a spurious bump on the Mo and a low-level foot on the ablator - both due to chord-length effects.

To enable us to compare measured mix with mix calculated in simulations, we define a quantity we call the "mix width". In reality, of course, the mix is described by a distribution, not a single quantity, but a mix *width* is a useful way to parametrise different shots. The importance of determining whether the foot and bump are real may be seen from Figure 8 where the payload mass fraction from each analysis is plotted. In the old 1-D analysis the payload mass fraction rolls over at values of just under 0.25 and just under

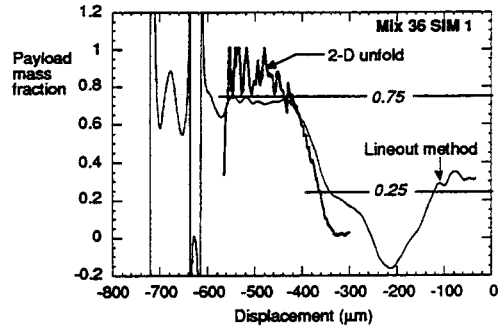

Figure 8: The payload mass fraction curve derived from 2-D analysis of MIX 36, Sim 1, is compared with the payload mass fraction derived from a 1-D line-out analysis of the same data. The sensitivity of the deduced mix width to the effects of roll-over caused by chord-length-induced feet and bumps is apparent. In this data the deduced mix width is 120 μm.

0.75. Clearly, the derived mix width is extremely sensitive to this roll-over. If, for example, the mix width were to be defined as twice the separation between the 0.25 and 0.75 values on the payload mass fraction curve, the 1-D analysis would give around 300 μm whereas the 2-D analysis gives a more reasonable 120 μm.

We define a normalised mix width w_{norm} such that:

$$w_{norm} = (x_{1-v} - x_v) / (1 - 2v) \qquad (10)$$

where $x_{1-v} - x_v$ is the distance between the values v and $1-v$ on the payload mass fraction curve. (If the payload mass fraction curve is linear - i.e. fitted by $y = mx + c$ - and of total width w (i.e. the distance between 0 and 1.0 on the payload mass fraction curve is w), then $w_{norm} = w$.) Figure 9 shows the results of applying this to the 2-D unfold data in Fig 8. We then look to see how constant the normalised mix width is over the range ~0.25 - 0.45 in limit values (i.e. v, above), and quote this range as the mix width for this particular analysis. In Fig. 9 we quote 100-120 μm. We then re-analyse the frame with different fits to the coefficients (a_0 through a_5 or a_6), with different backgrounds (i.e. constant, or linear, or quadratic), and with a super-Gaussian foil profile, if appropriate. Finally, we choose limits to the deduced mix width by examination of all of the results from the above analyses, bearing in mind how well each analysis fits the observed data and replicates the observed image. This is then our final value.

It can be seen from the above description that the mix width is a somewhat fuzzy number; this is, as was stated earlier, primarily because we are attempting to quantify a distribution with a single number. *We therefore highlight the observation that, for comparison with hydrocode simulations, it is far better to use the individual material distributions from each frame rather than match to the mix width.* The mix width does, however, fulfil a useful role in that all data can be plotted on a single graph to look at trends and identify outliers.

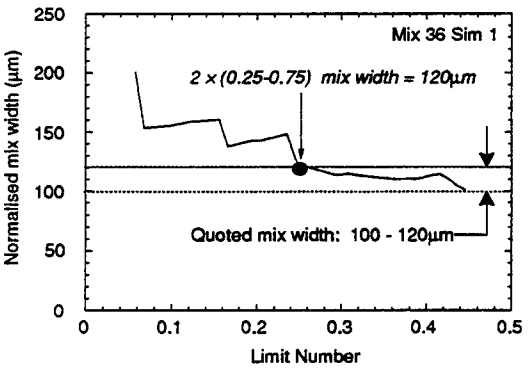

Figure 9: The normalised mix width from Mix 36, Sim 1, is roughly constant (~100 - ~120 μm) over the range ~0.25 - 0.45 in limit values.

Results of the Analysis

We are in the process of analysing all possible data in this way. Figure 10 shows our results so far. In this figure are plotted the mix widths (defined from the normalised mix width curves, as described above) against displacement. We have taken the 50% point on the payload mass fraction curve to be the "displacement" and it is with respect to the initial (i.e. at time = zero) position of the outer surface of the payload. There are two different data sets. The filled circles (•) show results from high-Atwood-number (PPS/Mo) packages; the open circles (o) show results from low-Atwood-number (PPS/PCS) packages. The horizontal error bars reflect uncertainty in the measurement of displacement. The vertical error bars, however, include only the uncertainty in the 2-D unfold and do not include the uncertainties caused by the earlier processing (i.e. film density to package transmission). Efforts are underway to quantify this.

A number of points can be made. First, although in Fig 10 it seems that low Atwood-number packages (PPS/PCS, A~0.05) seem to exhibit around 50 μm mix, it must be remembered that the overall system resolution is around 40 μm. When this is taken into account, the low Atwood-number packages show between no and ~20 μm mix. (The small- but finite - Atwood number means that some instability growth is possible. Simulations predict a few tens of microns of mix, depending upon conditions.[5]) Secondly, the high-Atwood-number packages show around 50 μm mix at small displacement, and around 100 μm mix at the largest displacements measured. Since the displacement is essentially proportional to time (simulations show that the pack-

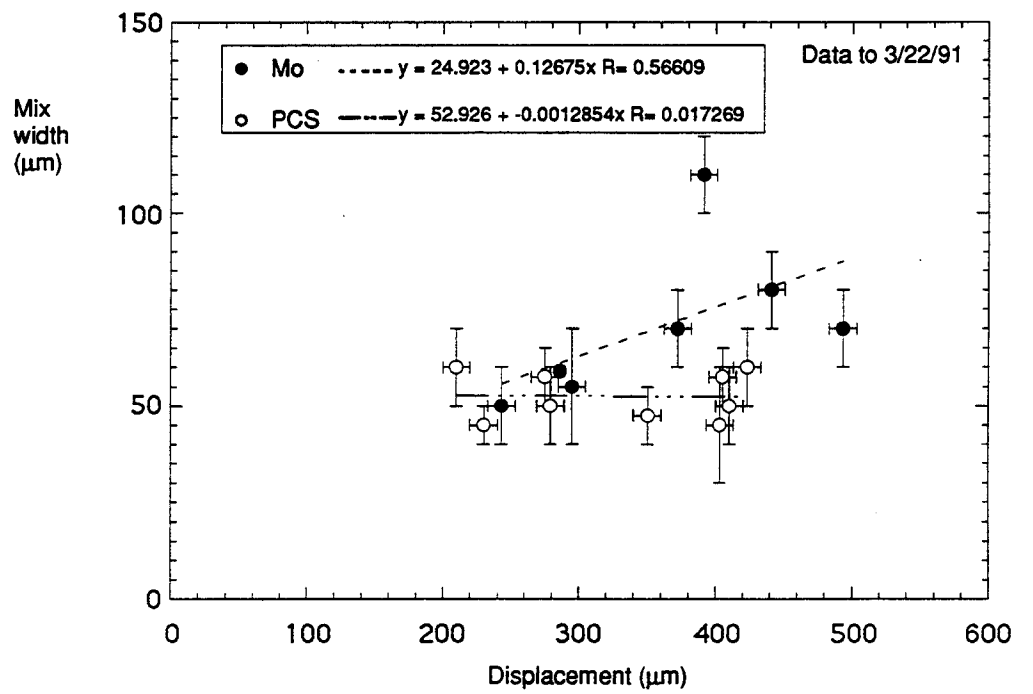

Figure 10: The results so far. In this figure are plotted the mix widths (defined from the normalised mix width curves, as described above) against displacement (the 50% point on the payload mass fraction curve). The filled circles (¥) show results from high-Atwood-number (PPS/Mo) packages; the open circles (o) show results from low-Atwood-number (PPS/PCS) packages . The horizontal error bars reflect uncertainty in the measurement of displacement. The vertical error bars, however, include only the uncertainty in the 2-D unfold and do not include the uncertainties caused by the earlier processing (i.e. film density to package transmission).

age stays still for the first nanosecond or so until the shock breaks out from its rear surface and then coasts with only a small amount of further acceleration), the small values at small displacement correspond to early time. In other words, the increase in mix width with displacement is caused almost entirely by the package -and hence also the mix region - expanding with time. Since little or no such increase in mix width with displacement is observed for the low-Atwood number packages, we conclude that the high-Atwood-number packages are indeed mixing more than the low-Atwood number packages.

Comparisons with calculation.

The experimental data have been compared with two different calculations - a two-dimensional explicit hydro-code calculation and a one-dimensional mix model. These calculations are part of a on-going programme of work and future calculations will address some of the shortcomings noted here.

Comparison with a 2-D hydro calculation

The two-dimensional "PETRA" code was used to calculate the mix resulting from the unstable growth of an initially-perturbed interface. PETRA [6] is a Eulerian code which explicitly follows the motion of the fluids as they move under the imposed pressure gradients. A representation of the initial geometry is shown in Figure 11.

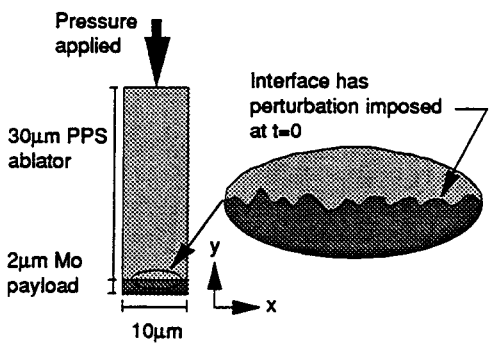

Figure 11: The 2-D Petra calculations were of a 10 μm-wide sample of the foil. It was assumed that half of the PPS had been ablated. A pressure pulse was applied at the rear of the ablator.

Small zones were used in order to resolve the interface with sufficient accuracy to follow the evolution of the mix. However, computer memory limitations restricted the amount of the foil that could be considered to a 10μm-wide subsection of the 200μm-wide foil. The foil was thus considered to be infinite in the x direction and edge effects were ignored. The pressure was applied in the y direction and was uniform across the sample (the x direction in Fig. 11) but varied appropriately in time.

The perturbation applied to the interface was derived from the interferometrically-measured profile [7] of a typical sample shown in Figure 12. Note that only a part (~80 μm) of the foil is measured on any one scan. The device had a vertical resolution of ~1 nm and a horizontal resolution of ~0.3 μm.

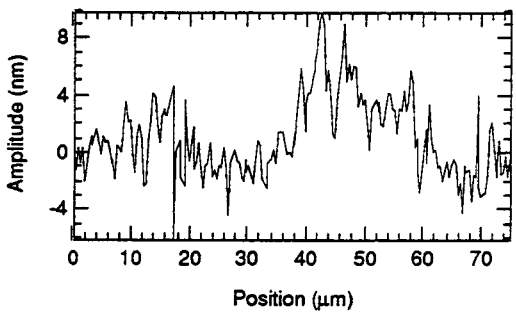

Figure 12: A lineout taken though the 2-D interferometically-measured surface profile of sample 38-30 shows that the surface finish is better than 15 nm peak-to-peak, with a dominant wavelength of ~30 μm.

Its mode spectrum (Fig. 13) shows that the dominant wavelength is around 30μm, with wavelengths down to a micron or less also present. The amplitudes of the individual modes are less than 2.5nm (0.0025μm, 25Å).

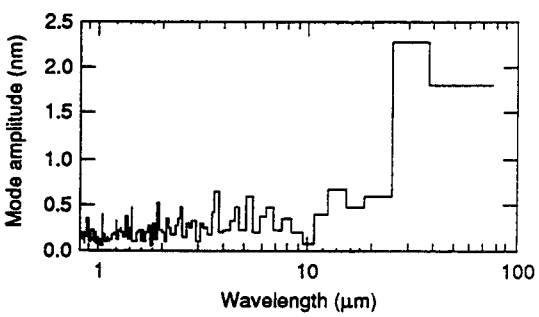

Figure 13: The mode spectrum from Figure 12 (i.e. the magnitude of the Fourier transform) shows that apart from a wavelength of ~30 μm the spectrum is fairly flat.

This was smaller than could be resolved computionally, so a larger amplitude was used. The perturbation applied was a random superposition of 20 cosine waves of individual amplitude 0.01μm given by:

$$h_j = \sum_{j=1}^{n} \sigma_j \cos(\pi j y_j)$$

and normalised so that the standard deviation was 0.01μm. An example is shown in Fig. 14, together with a sub-section of the measured profile.

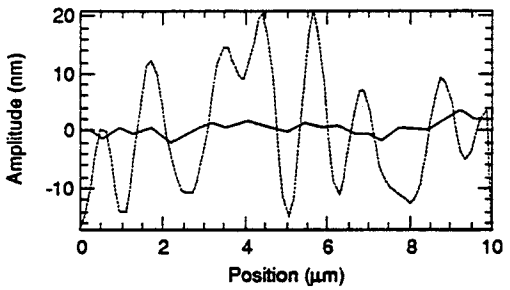

Figure 14: Solid line: part of the experimentally-measured surface profile for sample 38-30 (from Fig. 12). Broken line: Perturbation applied to interface in 2-D Petra calculations.

Figure 15 shows the measured profile together with eight applied perturbations joined end-to-end for comparison. The applied perturbation is clearly of greater amplitude than seen experimentally, a point which will be mentioned again later.

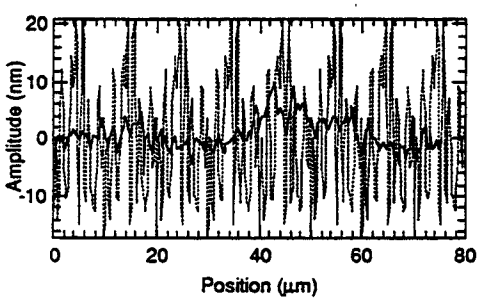

Figure 15: Solid line: part of the experimentally-measured surface profile for sample 38-30 (from Fig. 12). Broken line: Perturbation applied to interface in 2-D Petra calculations.

The calculation was run to 5 ns, the observation time of the experiment. The material densities were then averaged across the 10 μm sample and are shown in Figure 16. Some noise is apparent due to the relatively large scale of the mixed "chunks".

To take into account motion blurring and other instrumental effects, the density profiles were blurred by convolution with a 40μm FWHM Gaussian, as shown in Figure16. This, we now believe, is an underestimate of the system resolution - it is probably nearer 30μm [9].

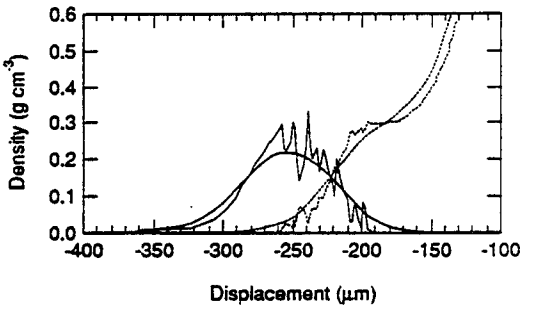

Figure 16: Jagged lines: the averaged material densities from the 2-D Petra calculation. Smooth lines: the densities convolved with a 40 μm FWHM Gaussian to take into account the limited diagnostic resolution. The foil package is travelling from right to left and so the ablator, shown by broken lines, is on the right and the payload (solid lines) is on the left.

In order to compare these calculational results with experiment, the density has to be integrated along the line-of-sight to give the areal density ξ:

$$\xi = \int \rho(l)dl$$

We have approximated the integral by a product:

$$\xi = \rho \times 100\mu m$$

Figure 17 shows the resulting comparison for Mix 42, Sim 1 at 5 ns.

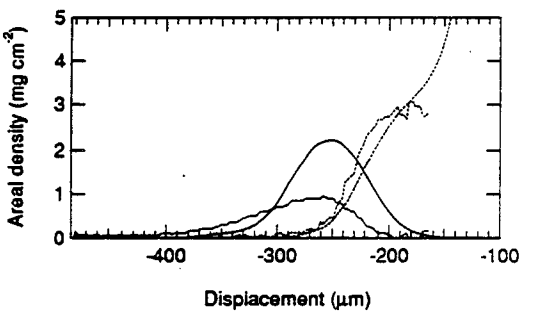

Figure 17: Comparison between experimental results from Mix 42, Sim 1 at 5 ns (jagged lines) and smoothed 2-D Petra results (smooth lines).

Agreement is reasonable, but the simulation underestimates the foil displacement slightly and overestimates the amplitude of the Mo payload.

Figure 18 shows the comparison for the same shot, but for the other channel (Sim 2) at 8.5 ns. Here we were obliged to compare with a calculation at 8 ns since that was the latest time available. Agreement is less good than in the earlier frame, for similar reasons - the simulation underestimates the foil displacement slightly and overestimates the amplitude of the Mo payload.

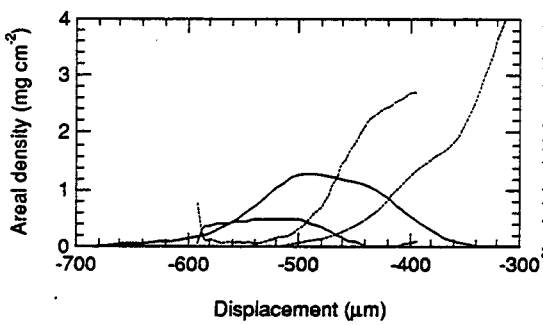

Figure 18: Comparison between experimental results from Mix 42, Sim 2 at 8.5 ns (jagged lines) and smoothed 2-D Petra results at 8.0 ns (smooth lines).

Figure 19 shows a comparison between the payload mass fractions from experimental data at 5 ns and 8.5 ns (solid curve) and the calculation (dot-dash curve) at 5 ns and 8 ns.

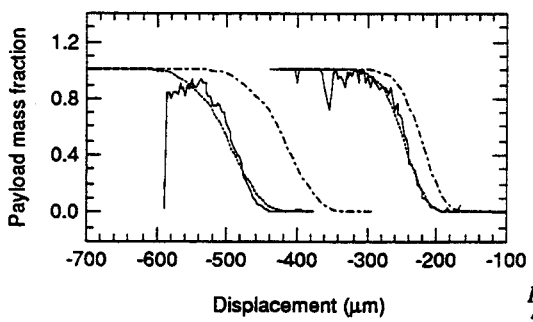

Figure 19: The payload mass fraction - experimental data at 5 ns and 8.5ns.(solid curve) ; calculation (dot-dash curve) at 5 ns and 8 ns. The broken curve shows the calculation shifted by an arbitrary amount to make it lie roughly on top of the experimental data for shape comparison.

The calculation quite severely underestimates the displacement, as mentioned above. The broken curve shows the calculated payload mass fractions shifted by *arbitrary* amounts to superimpose them roughly upon the experimental results; by doing so it is clear that the *shape* of the payload mass fraction curve is reasonably well predicted. The magnitude of its gradient is, however, slightly underestimated in both frames, leading to an overestimate of the mix. Indeed, if the calculated foil displacement were to be increased in a future calculation by increasing the imposed pressure, then, if the mix width does grow as $\sim gt^2$ (where g is the acceleration and t is the time) - and hence distance at a given time, the mix may be significantly overestimated. On the other hand, if the blurring used (40μm FWHM Gaussian) is too much, the mix width will be reduced. Work is in hand to look at these issues.

Comparison with a 1-D hydro model

A 1-D Lagrangian hydrocode, incorporating a version of Young's mix model [9] in which the mix affects the hydrodynamic behaviour of the package (the "dynamic" model), was used to estimate the mix. In this calculation the instability growth at early time was modelled by the so-called "passive model" [9] in which the mix does not affect the hydro behaviour. At later time - when the perturbation amplitude has become comparable to or greater than the minimum wavelength - the "dynamic" model was used. The initial amplitude and wavelength were assumed to be 0.01μm and 1μm respectively.

Figure 20 shows the density distributions of each material in the direction of motion at 5 ns. The noise seen in the 2-D calculation shown in Fig. 16 is absent, of course, because this calculation employs a 1-D model. Motion blurring and other instrumental effects were taken into account by blurring these distributions by convolution with a 40μm FWHM Gaussian, as in the 2-D calculation.

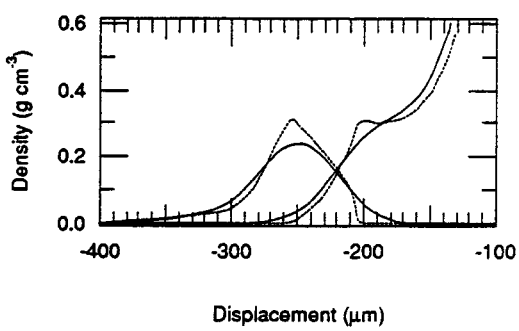

Figure 20: Broken lines: material densities from the "dynamic" mix model. Solid lines: densities after convolvolution with a 40 μm FWHM Gaussian. The foil package is travelling from right to left.

Figure 21 shows the comparison with Mix 42, Sim 1 at 5 ns, where again we have approximated the line-of-sight integral by assuming a path-length of 100μm. Again, agreement is reasonable, but again the simulation underestimates the foil displacement slightly and overestimates the amplitude of the Mo payload.

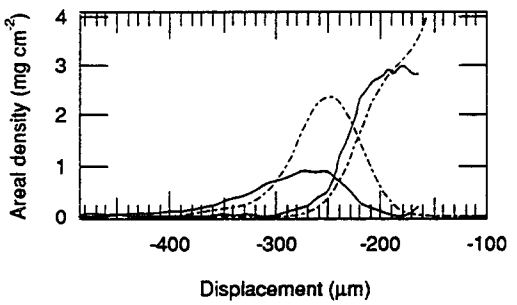

Figure 21: Comparison between experimental results from Mix 42, Sim 1 at 5 ns (solid lines) and blurred mix-model results (dot-dash lines).

Figure 22 shows the comparison for the same shot, but for the other channel (Sim 2) at 8.5 ns. Here we were obliged to compare with a calculation at 8 ns since that was the latest time available. Again, agreement is less good than in the earlier frame, for similar reasons.

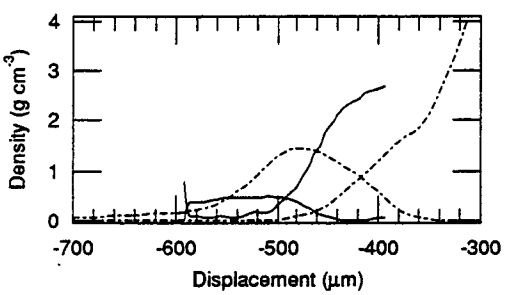

Figure 22: Comparison between experimental results from Mix 42, Sim 2 at 8.5 ns (solid lines) and blurred mix-model results at 8 ns (dot-dash lines).

Figure 23 shows a comparison between the experimental data at 5 ns and 8.5 ns (solid curve) and the calculated payload mass fractions at 5 ns and 8 ns (dot-dash curve). Again, the calculation quite severely underestimates the displacement, as mentioned above, but the shifted curve shows that the *shape* of the payload mass fraction curve is reasonably well predicted. The same comments apply as were made in the case of the 2-D calculation - if the calculated foil displacement were to be increased in a future calculation by increasing the imposed pressure the mix may be significantly overestimated.

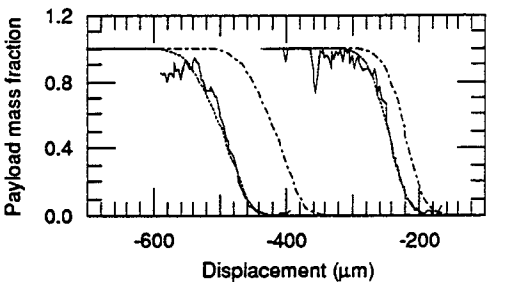

Figure 23: The payload mass fraction - experimental data at 5 ns and 8.5 ns (solid curve); calculation (dot-dash curve), at 5 ns and 8 ns. The broken curve shows the calculation shifted by an arbitrary amount to make it lie roughly on top of the experimental data for shape comparison.

In order to compare the mix widths predicted by the simulations we have analysed them in the same way as in the experiment. That is, the mix width has been defined as twice the distance between the 0.25 and 0.75 points on the payload mass fraction curve after the respective density distributions have been blurred by the 40μm Gaussian. We repeat the observation made earlier that *it is better to use the individual material distributions from each frame rather than match to the mix width.* However, figure 24 shows the results. The data shown in Fig. 10 are replotted together with the results from the 2-D calculation (cross-in-square) and from the 1-D simulation (hour-glass shape). Both sets of calculations significantly overestimate the amount of mix.

Three possible sources of error are present, however, as has been mentioned. First, in both sets of simulations the package was not driven as far as was seen experimentally. This is because there is always a small uncertainty in the actual pressures generated experimentally and the pressure applied in the simulation was too low. The foil would have been driven further if this pressure had been increased. However, if the mix width does grow as $\sim gt^2$ (where g is the acceleration and t is the time) - and hence distance at a given time, then even more mix would have been calculated at the observation times. Secondly, if the instrumental resolution is such that a blurring of *less* than 40μm FWHM should be used to compare simulation with experiment, then less mix would be predicted. Thirdly, because of computer limitations on the number of cells that could be used, the surface profile imposed in the calculations was rougher than that seen experimentally. Less mix would have been seen if a smoother interface had been calculated. Work is in hand to examine these issues.

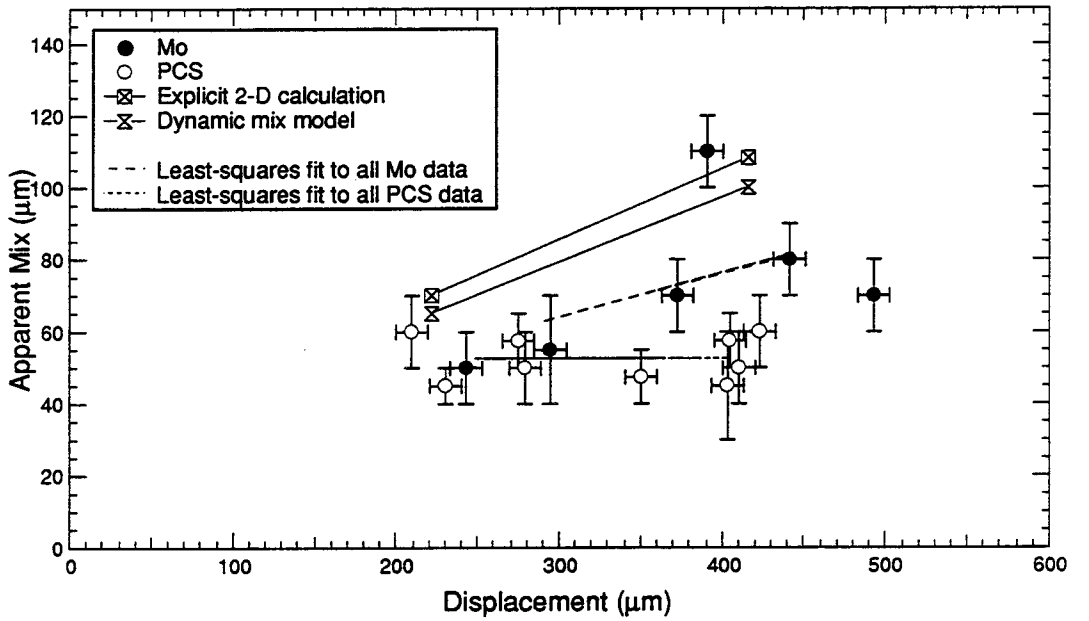

Figure 24: The data shown in Fig. 10 are replotted together with the results from the 2-D calculation (cross-in-square) and from the 1-D simulation (hour-glass shape). Both sets of calculations significantly overestimate the amount of mix. Note caveats in text, however.

Conclusions

A detailed analysis of the data from the AWE/LLNL planar-foil mix experiment has been performed, using a new, two-dimensional unfold technique which allows chord-length effects to be taken into account. We have found that with the new technique the derived mix distributions are less subject to errors caused by chord-length effects, leading to much less scatter in the calculated mix widths. We find that high-Atwood-number packages mix more than do low-Atwood-number packages, but that experimental resolution is a limitation. Comparison with two-dimensional calculations and one-dimensional modelling shows that in both cases somewhat too much mix is predicted. However, some of this over-estimation may arise from known shortcomings in the calculations performed so far. Further work is under way to look at these points.

Acknowledgements

We are grateful to the large number of people at LLNL and AWE without whose help these experiments could not have taken place. In particular we should like to thank Russell Wallace of the LLNL target fabrication section and Tony Tyrrell of the AWE target fabrication section for their help in assembling and characterising the packages used.

References

1 J.D.Kilkenny, D.Bach, R.J.Wallace, Lawrence Livermore National Laboratory, T.J.Goldsack, J.C.V.Hansom, K.Oades, P.Fieldhouse, Atomic Weapons Establishment, "Measurement of the Turbulent Mix of Hydrodynamically Unstable Packages"; Bulletin of the American Physical Society, **33**, 9, 1988.

2 E.E.Meshkov, "Instability of a Shock Wave Accelerated Interface Between Two Gases" (NASA, Washington, DC), N70-30945 (translated from the Russian).

3 G.I.Taylor, Proc. Roy. Soc. (A), **201A**, 192 (1950)

4 J.C.V.Hansom, P.A.Rosen, T.J.Goldsack, K.Oades, P.Fieldhouse, N.Cowperthwaite, D.L.Youngs, N.Mawhinney, and A.J.Baxter, "Radiation Driven Planar Foil Instability and Mix Experiments at the AWE Helen Laser", *Laser and Particle Beams*, **8**, 1-2, 1990.

5 Other simulations performed at AWE, and V.C.Rupert, private communication.

6 D.L.Youngs, "Time Dependent Multimaterial Flow with Large Fluid Distortion", *Numerical Methods for Fluid Dynamics*, K.W.Morton & M.J.Baines (Eds); Academic Press, New York, 1982.

7 The packages were examined on a laser interferometric microscope, model Maxim 3-D 5700, from the Zygo Corp.

8 S.Rothman, private communication.

9 D.L.Youngs, "Modelling Turbulent Mixing by Rayleigh-Taylor Instability", Physica D 37, (1989), 270-287.

EFFECTS OF PREHEAT ON MIX IN LASER ACCELERATED PLANAR FOILS

J. D. Molitoris, D. W. Phillion, M. M. Morin*
Lawrence Livermore National Laboratory Livermore, California U.S.A.

T. J. Goldsack, S. D. Rothman, J. C. V. Hansom
Atomic Weapons Establishment, Aldermaston, United Kingdom

ABSTRACT

We have investigated the effect of x-ray preheat on the development of mix. In these experiments a planar foil package consisting of two materials separated by a smooth interface was ablatively accelerated using a laser produced x-ray drive source. In the normally preheated case the drive had a component which coupled to the interface, while in the low preheat case that component was absent. The measured mix widths and hydrodynamics are compared for both situations.

INTRODUCTION

Mix is the interpenetration of two materials arising from instability growth due to perturbations in an accelerated interface. Instabilities can develop from interfaces between gases, liquids, solids, or plasmas. In the experiments discussed below, we study mix in accelerated planar foils which evolve from a solid into a plasma. The interface is ablatively accelerated by a laser generated radiation source providing both a continuous acceleration and acceleration due to the passage of a shock. Hence, the resultant mix is due to a combination of Rayleigh-Taylor[1] and Richtmyer-Meshkov[2,3] instabilities. Both the radiative drive and an intense shock of about 60 Mbar in amplitude and 50 ps in rise time form the plasma. However, the drive affects the interface prior to the shock via x-rays which penetrate the ablator foil and couple with the interface. As this process heats the interface prior to instability growth, it is known as preheat. The primary purpose of these experiments is to determine how preheat affects mix development. Preheat is one of the principal differences between mix in laser driven experiments and those driven by rocket rigs or explosives. Furthermore, as lasers are presently the drivers of choice in inertial confinement fusion studies, the effect of preheat on mix is of great interest.

In this investigation we measure the width, which is taken to be the most fundamental property of the mixing layer, for two similar experiments under different degrees of preheat. In the normally preheated case, x-rays from the drive strongly coupled to the interface, while in the low preheat case, the drive spectrum was altered so there was no such coupling. We also examine apparent hydrodynamic differences in the two experiments.

CALCULATIONAL OVERVIEW

The mix package is a set of circular foils consisting of a thick plastic ablator separated from a thinner molybdenum payload by a nominally smooth interface (surface imperfections are typically less than 0.01 μm). The drive acts on the package as a function of time as illustrated by Figure 1, which is a one dimensional position / time calculation[4] of the experiment showing possible effects of x-ray preheat. This simulation included a plastic (PyN) coating over the outer surface of the molybdenum

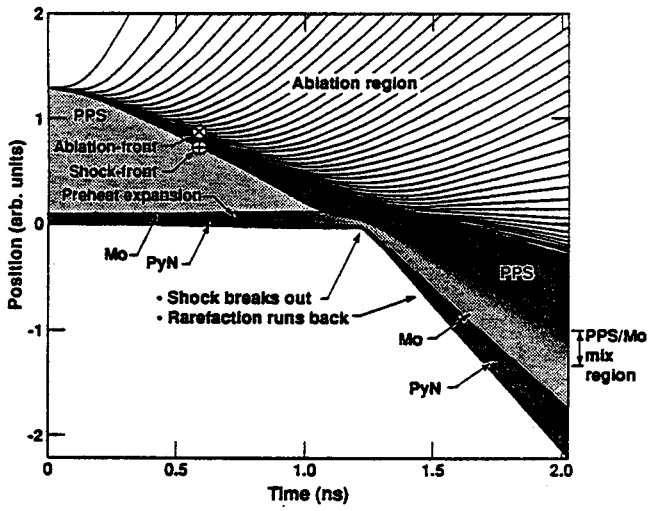

Fig.1. Simulation (ref 4) of a normally preheated experiment. The calculation shows the effect of the preheat on the Mo and polyphenylene sulfide (pps)/Mo interface prior to the shock break-out (about 1.2 ns). At break-out, instabilities induce material interpenetration and a mix region develops. The mix region and package then decompress. The calculation does not account for any mixing of the PyN tamper with the rest of the package.

payload which was not included in the actual experiments. The coating does not alter the effects of preheat in the calculation. At time t=0 the drive is turned on and the plastic begins to ablate sending a shock front toward the interface. At the same time x-rays from the drive penetrate the package and couple to the molybdenum. The molybdenum heats up and expands. As the plastic ablator is impregnated with sulfur, there is also some expansion in the ablator due to preheat, but it is negligible. The interface continues to change until the shock front passes through it at about 1.2 ns, driving instabilities which develop into a mixed region. After this the package begins decompressing. If we neglect any further net accelerations, the shock induced mix region just expands with the rest of the planar foil package to a point where it is large enough to measure with our diagnostics (roughly 50 to 150 μm after delay times of 5 to 9 ns).

Our primary interest is the effect of a reduction in preheat on the mix width. As preheat changes the density of the molybdenum, it also changes the Atwood number.

For this experiment, calculations[5] show that both the Atwood number and the molybdenum density decrease as the preheat is increased. The reduction in preheat between the experiments leads to a 13% increase in the Atwood number and a 26% increase in the molybdenum density prior to shock breakout as illustrated in Figures 2a and 2b. The differences in payload density and Atwood number for the normal and reduced preheat situations will change how the mix width develops in each case.

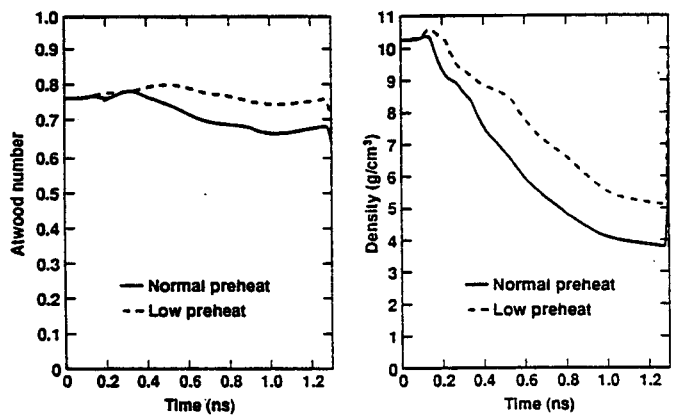

Fig.2. Calculations (ref 5) showing the change of Atwood number and Mo density prior to shock breakout for the low and normally preheated situations. For the low preheat mix width calculations, the drive spectrum was set to zero flux for transition energies of lower order than the gold N-band, which mimicked the experimental situation.

Prior to performing the experiment, calculations of the mix width (shown in Figure 3) were done by two different laboratories[6,7] for normal and reduced preheat. For the low preheat mix width predictions, the drive spectrum was set to zero flux for transition energies of lower order than the gold N-band, which mimicked the experimental situation. Both calculations predict that the mix width increases for a low preheat scenario, but one shows a 27% increase in the width while the other shows only a marginal increase of 6%. The increase in mix width for the lower preheat case is due mainly to the increased Atwood number prior to shock breakout (recall Figure 2). However, as the molybdenum payload is cooler with lower preheat, it also decompresses less which reduces the apparent mix width. It is clear that each code handles these competing effects differently, leading to a disagreement in the predictions.

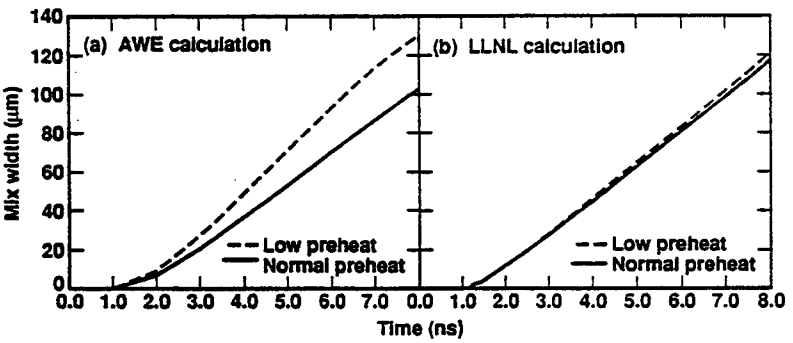

Fig.3. Comparision of predicted mix widths for low and normally preheated conditions done prior to the experiment from a) the Atomic Weapons Establishment (ref 6) and b) Lawrence Livermore National Laboratory (ref 7).

This calculational disagreement gave us a greater impetus to perform an experiment investigating the effects of preheat on mix. Finally, as the lower preheat scenario had higher payload densities, we were curious to see whether the hydrodynamics would change. A denser payload could alter the character of the image data, making the molybdenum more visible and distinct from the ablator. Furthermore, the normally preheated experiment had already been performed so the data was available for comparison[8].

EXPERIMENT

The most crucial part of these experiments is the planar foil mix package. The ablator is a layer of plastic, polyphenylene sulfide (C_6H_4S), which is 30% sulfur by weight and 9% by atomic make up. The surface of the plastic ablator, which is to be the interface, is formed by pressing it while in a molten state against an optical quality flat. The plastic reproduces this smooth surface and is then coated with Mo. This is the interface which mixes during the experiment. The layered package is cradled in a gold washer as shown in Figure 4.

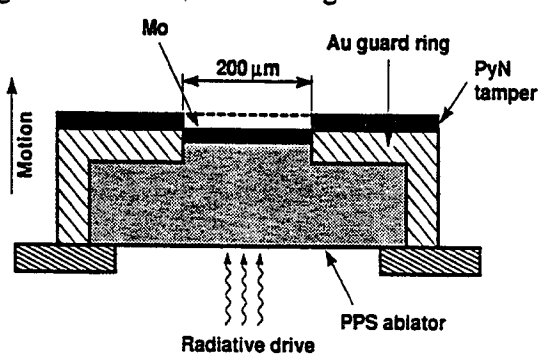

Fig.4. Cross section of the cylindrically symmetric final mix package design for these experiments.

The x-ray drive acts on the ablator and the mix package is accelerated, eventually being ejected from the assembly. The surface of the washer is coated with another plastic (PyN, polyxylyene) which prevents gold plasma from sheathing the mix package. We have found that this design tends to be ejected smoothly and evenly.

These experiments use the method of point projection spectroscopy (PPS) which was developed by Kilkenny[9] and applied extensively by Foster *et al.*[10] Figure 5 schematically outlines PPS as applied to these planar foil mix experiments.

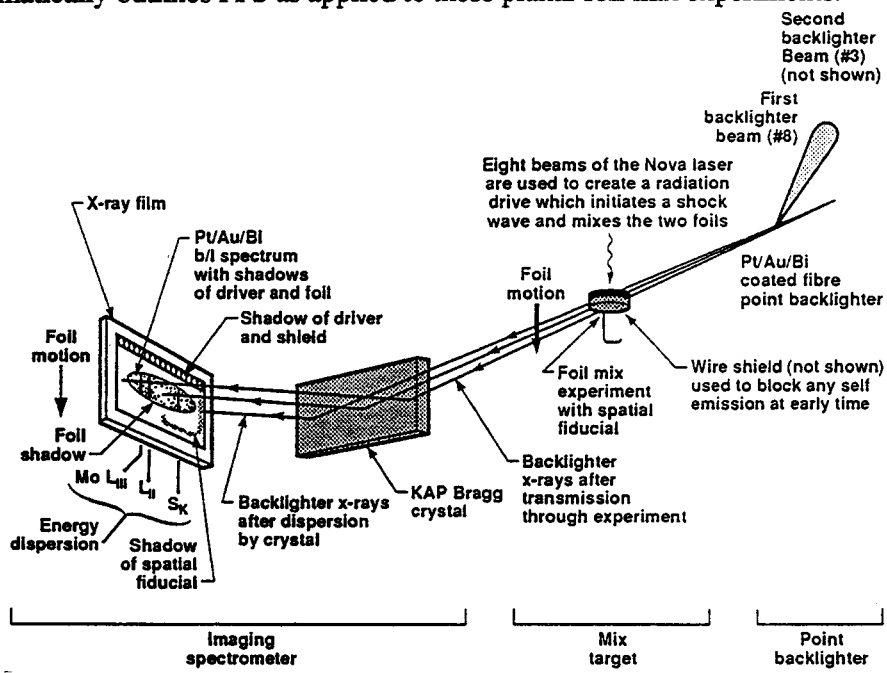

Fig.5. Schematic of NOVA planar foil mix experiment. The actual experiment uses two of these diagnostic arms during each laser shot.

Here, eight drive beams of the Nova laser produce a 1.0 ns square pulse of 3ω light which is converted to x-rays initiating the acceleration of the mix package. After a suitable delay time (5.0 to about 9.0 ns), two other laser beams strike small diameter (25 μm) fibers to create point x-ray sources backlighting the mix. The backlighter laser is typically a 200 ps FWHM Gaussian pulse of 3ω light which impinges upon a copper pin co-sputtered with Bi, Pt and Au. X-rays from the resulting point-like plasma form a continuous spectrum in the 1.7 keV to 3.5 keV range. The ejected mix package is imaged by this emission, with the transmitted x-rays being dispersed in energy by a Bragg crystal and reflected to a piece of film set normally to the central ray. The Bragg crystal also acts as a mirror in PPS, reflecting a two-dimensional snapshot of the object being imaged. Thus one axis contains both spectral and spatial information, while the other is purely spatial. Both the known magnification of the experiment and the location of a fiducial allow us to put space scales on the data.

This experiment makes use of the spectral dispersion in PPS to measure absorption features which determine the mix region. Figure 6 schematically illustrates the two-dimensional image data we obtain, reduced to the bare essentials. The direction of motion (shock acceleration) is from the S region to the Mo region. Within the sulfur impregnated plastic, absorption features consisting of lines and the K-edge (5.0185 Å) can be distinguished. These features persist throughout the mixed region, then dwindle as the S density component becomes small. As the concentration of payload material

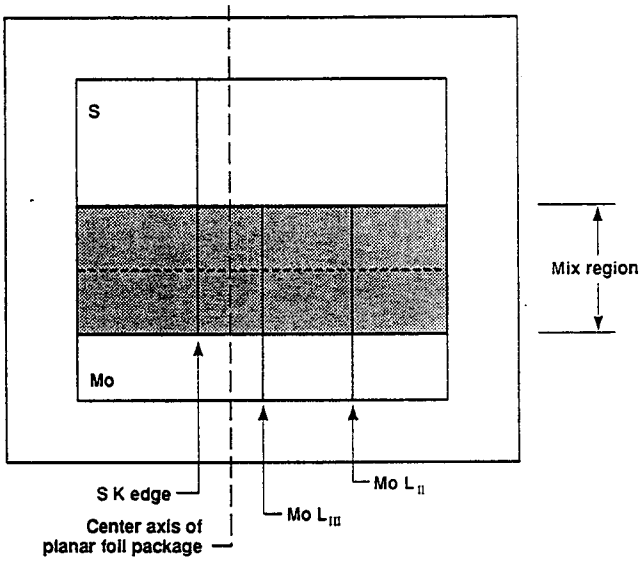

Fig.6. Schematic of point projection spectroscopy image data showing how absorption features are used to quantify the mix width. Here the spectral features are used to quantify the mix region. The location of the package axis of symmetry is indicated for a well aligned experiment.

increases, absorption features from the Mo L_{III} (4.913 Å) and L_{II} (4.719 Å) edges along with lines due to open outer shells become apparent. The interplay of these features is used to quantify the extent of the mix region as shown in Figure 6.

The raw film data are digitized and manipulated on the computer. We subtract background due to chemical fog in developing the film, then use a Henke model to transform film density to intensity over the observable energy range of the data. If necessary, background due to spatial fog is subtracted and the spectral features in the data are straightened. We then obtain a backlighter reference spectrum which is divided into the image converting it to transmission. Finally, space scales are put on the axis and the mix data can be determined from this reduced image. To first order, the width of the mix region can be read directly off the reduced data image; however knowing the opacities, one can also generate areal density distributions of the ablator and payload. This data, along with the absorption features, allows a more judicious determination of the mix width.

The experiment must be aligned such that the mix package is directly between the point backlighter source and the spectrometer, and that the center of the mix package is located between the S K-edge and the Mo L_{III} edge in wavelength space (recall that in PPS this axis of the image is both spectral and spatial). The ideal location of the package center is shown in Figure 6. With this alignment for a cylindrically symmetrical mixed plasma, the distance traversed by the two different wavelength rays is nearly the same and any path length correction is minor. All of the low preheat experiments were well aligned, but some of the normal preheat experiments were not and corrections had to made to the data.[11]

A clear and distinct image of the mix package is very important, so care was taken in the package design to negate the effects of other materials sheathing it. The gold washer cups the package to stop ablator material from billowing out the sides and around the heavier Mo payload. The PyN tamper, which coats the surface of the washer, is spectroscopically inert and hence transparent to the backlighter used. Finally, the spatial resolution of the experiment was studied separately[12]. It is related to the source size of the backlighter (which is approximately the backlighter fiber diameter) and image blurring due to the finite time in which the source is emitting and the motion of the mix package. For these experiments the spatial resolution was no greater than 34 μm.

RESULTS

All data was taken before any reflected shocks could recompress the mix region[4,5]. The normally preheated experiment was performed first, so most of the problems were encountered and solved during these shots. Figure 7 shows two typical frames of image data from the normally preheated experiment, with areal density distributions and mix widths derived from the images. These density distributions were obtained assuming cold opacities in the mix region. However, the assumption breaks down toward the hot ablation region.

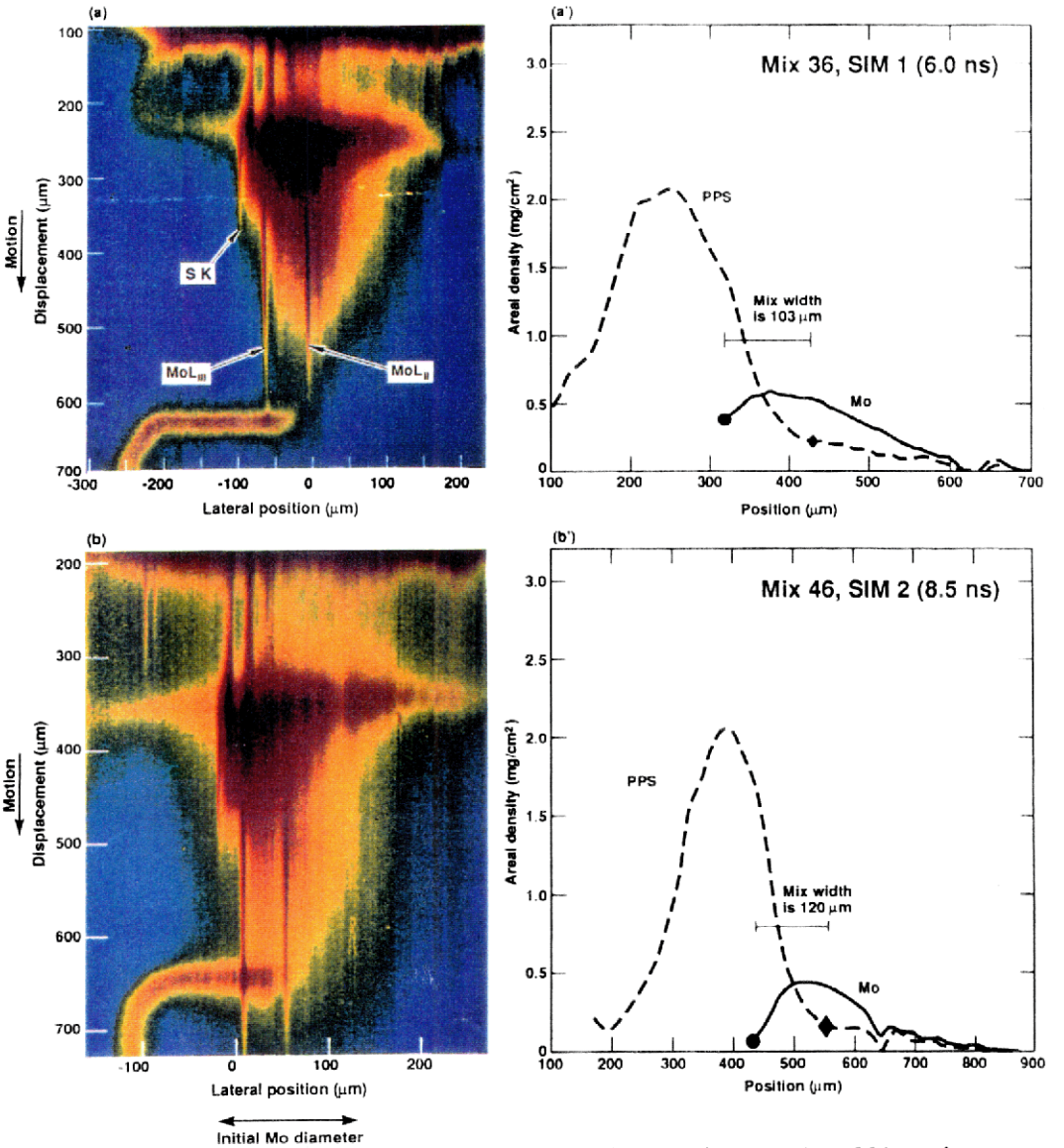

Fig.7. Typical data from the normally preheated mix experiment: a) and b) are image data where a') and b') are areal density distributions indicating mix widths derived from the images. It is not obvious from the images, but the data taken at 6.0 ns was well aligned and only minor corrections were made to the mix width measurement. However, the data taken at 8.5 ns was well off-axis, which led to an overestimate of the mix width prior to corrections.

The low preheat measurements were made on similar targets, but the portion of the drive spectrum which coupled to the interface was severely reduced. For these measurements backlighter delay times were varied from 6.0 to about 9.0 ns after the drive was initiated. Typical low preheat image data is shown in Figure 8. These images are similar to those from the normally preheated experiment, but analysis reveals that the Mo component of the package appears more distinct from the ablator. There is a sharper jump in the backlighter transmission between the ablator and payload for lower preheat which signifies a larger degree of separation than in the the normally preheated experiments. These distinctions are still being quantified.

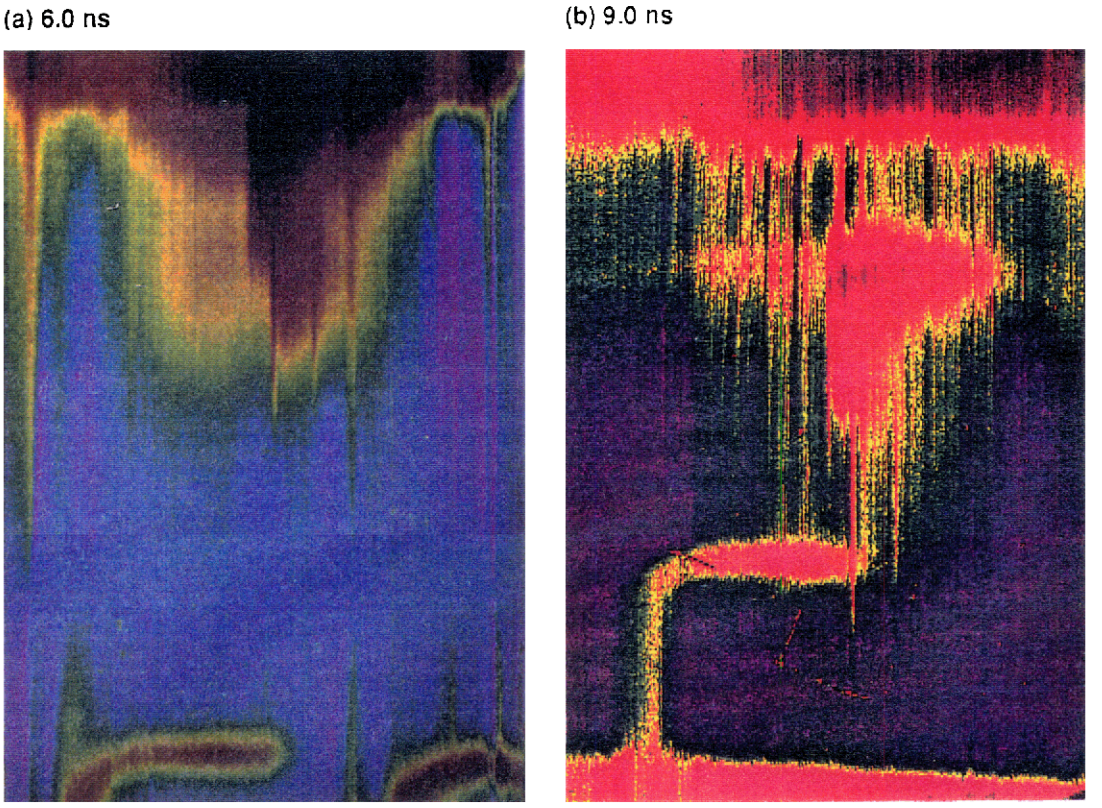

Fig.8. Typical image data from the low preheat experiment for backlighter delay times of 6.0 and 9.0 (8.8) ns.

Again using cold opacities, the areal density distributions were derived for the low preheat data. Figure 9 compares typical areal density distributions from the two different experiments. Note that for the same delay time the normally preheated package is displaced farther and exhibits a greater mix width. In general this is true for all the data. As the Mo payload decompresses less for lower preheat, the basic hydrodynamics are different for the two experiments and the mix region is displaced less.

There are small variations in the mix packages from shot to shot and changes in the drive energy due to laser fluctuations. Rather than correct for these differences, it is useful to plot the mix width against some parameter which accounts for them. The displacement of the mix region serves this purpose quite well. The displacement used here is defined to be that of the center of the mix region. Figure 10 plots all the presently available data versus displacement. Also shown in the figure is the baseline

mix level determined in reference 12. This level is the overall position resolution of our technique as determined in a separate experiment. The difference between the baseline level and the data can be attributed to mix from instability growth.

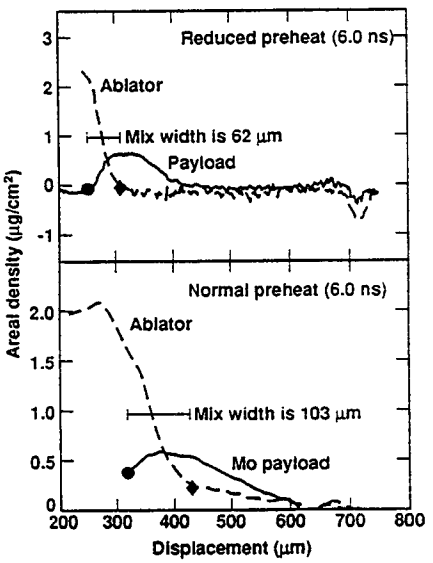

Fig.9. Areal density distributions from the two different experiments taken at the same delay times. Note that the displacements and mix widths are very different due to the change in preheat.

Ignoring the spread in the normally preheated data at larger displacements, they tend to fall on a line. The slope of this line is due mainly to the package decompression. As the displacement also normalizes differences in the hydrodynamics, the low preheat data can be compared here. It is interesting that the data from both experiments follow the same trend within experimental error. We know that the drive is consistent between the two experiments except for the component which couples to the Mo interface. Hence, for consistent drive, the mix width is consistent independent of preheat. However, the hydrodynamics appear very dependent on preheat in these experiments.

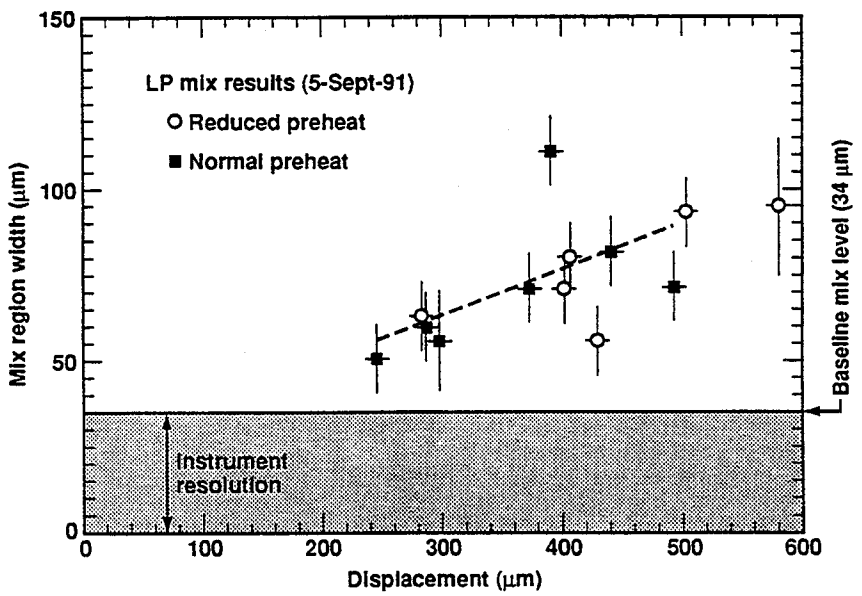

Fig.10. Mix width data from both experiments plotted as a function of the central displacement of the mix region . Baseline mix level due to instrument resolution is also shown (ref 9).

CONCLUSION

We have performed two experiments with different couplings of drive to a material interface in order to determine how x-ray preheat affects mix development in laser accelerated planar foils. These measurements were motivated by significant differences in model predictions, the importance of preheat on inertial confinement fusion, and related issues. The data shows that the reduction of x-ray preheat alters the hydrodynamics as there is less displacement of the package. However, the measured mix width when plotted as a function of displacement is consistent (within the errors) for both experiments. Independent calculations predicted increases in the mix width as a function of time after the drive was initiated. This is in contradiction to the data which show a decrease in mix width for a lower preheat when measured at the same time after drive initiation. Furthermore, both calculations failed to predict any change in the hydrodynamics for reduced preheat. The detailed hydrodynamic differences are significant in these experiments and should be studied thoroughly.

There is much to be learned about instability growth in laser driven mix and only a sound interaction between experiment and modeling/theory can lead to an understanding relevant to the applications. We hope that these data can be used to improve predictive capabilities in environments where preheat is an issue.

ACKNOWLEDGEMENTS

The authors would like to thank Viviane Rupert for many useful discussions and calculations. We also thank Paula Rosen for the modeling which played a role in motivating these experiments and Russell Wallace for all his efforts. Excellent technical assistance was provided by Jan Batteux during the many shots at Nova. Dan Donovan, Marita Spragge and Cathe Adam did a fine job in carefully building the many targets. Finally, we acknowledge Mark Eckart, Rick Stewart and Joe Kilkenny for the encouragement to pursue these studies.

This work was performed under the auspices of the U. S. Department of Energy by the Lawrence Livermore National Laboratory under contract No. W-7405-ENG-48.

---

*Also associated with Department of Mathematics, Massachusetts Institute of Technology, Cambridge, MA 02139

REFERENCES

1. G. I. Taylor, Proc. Roy. Soc. A 201, 191 (1950).
2. Ye. Ye. Meshkov, NASA Tech. Trans. NASA TT F-13, 074 (1970)
3. R. D. Richtmyer, Comm. Pure Appl. Math. 13, 297 (1960)
4. J. C. V. Hansom and P. Rosen, private communication, (1989)
5. V. C. Rupert, private communication, (1990)
6. P. Rosen and J. C. V. Hansom, private communication, (1990)
7. V. C. Rupert, private communication, (1990)
8. T. J. Goldsack, J. D. Molitoris et al., to be published. (1991)
9. The invention and development of point projection spectroscopy is attributed to J. D. Kilkenny (Lawrence Livermore National Laboratory).
10. J. M. Foster, Rev. Sci. Inst. 59 (8), August 1988; J. Foster et al., Proc. of the 7th APS Topical Conf. on High Temperature Plasma Diagnostics.
11. T. J. Goldsack, Proc. 3rd Int'l Work. Phys. Comp. Turb. Mix., (1991), (AIP, N. Y.).
12. J. D. Molitoris, S. Rothman, et al., to be published, (1991)

NON-LINEAR STAGE OF RICHTMYER-MESHKOV INSTABILITY DEVELOPMENT

V.I. Anisimov, A.V. Polionov

All-Union Research Institute of Technical Physics
P.O. Box 245, 454070, Chelyabinsk, USSR

ABSTRACT

A conclusion has been infered that there is an universal function which describes both a linear and non-linear stages of the Richtmayer-Meshkov instability for each absolute value of the Atwood number. It has been drawn from considering gasodynamics equations invariances at the assumption that flows set in nearby a boundary after a shock passing to be isentropic nonviscous ones. The available experimental data [1] have confirmed the inference drawn and allowed to construct the function for the Atwood numbers $A = \pm 0.45$.

Richtmayer-Meshkov instability develops at a perturbed interface existing between two media with different densities and being subjected to an impulsive acceleration as a result of passing a shock wave through it [2,3]. In the work [2] it has been shown that increasing of the sinusoidal perturbation amplitude at the linear stage can be described by the relation:

$$a = a_0 + \frac{2\pi}{\lambda} a_0 A \Delta v t \ , \qquad (1)$$

where a_0 and λ – are initial amplitude and perturbation wave length, respectively, $A = \frac{\rho_1 - \rho_2}{\rho_1 + \rho_2}$ – is the Atwood number, Δv is an interface velocity changing as a result of the shock wave passing through the boundary. (Substances density values ρ_1, ρ_2 and amplitude a_0 are taken just after a shock wave passing).

The simple form of the relation (1), which does not contain such characteristics of substances as a sound velocity allows to hope to obtain some simple dependence for describing a non-linear stage of perturbation development.

Interpenetration of components at a non-linear stage generally speaking does not occur symmetrically. In the following we consider a to be a common mixing zone width although conclusions obtained below extend to both a depth of penetration of a heavy substance into a light one a_1 and of a light substance into a heavy one a_2 ($a = a_1 + a_2$) separately.

At first we make use of the hydrodynamics equations invariance concerning scale transformations of the coordinate and time, which takes place on the assumption of neglecting viscosity, i.e.

large Reynolds numbers. According to the invariance the substitution of variables x_i', t' by $x_i = kx_i'$, $t = kt'$ does not change these equations. We consider the two-dimentional case of a shock wave passing of the specified intensity through the perturbed boundary. Let we have some relationship determining the mixing zone width dependence (the perturbation amplitude) on time $a'(t')$, corresponding to the wave length λ'.
Then, using the above mentioned invariance, we obtain for the dependence of the amplitude a on time t for the wave length $\lambda = \lambda' \frac{a}{a'}$, i. e. for the similar initial perturbations the following relationship:

$$\frac{a(t)}{\lambda} = \frac{a'(t')}{\lambda'}, \quad a(t) = \frac{\lambda}{\lambda'} a'\left[\frac{\lambda'}{\lambda} t\right], \text{ or}$$

$$a(t) = \lambda F\left\{\frac{t}{\lambda}\right\}, \tag{2}$$

where $F\left\{\frac{t}{\lambda}\right\}$ is the certain function which is the common one for all similar perturbations when both the composition of the substances and the shock wave intensity are considered to be the same.

Now we shall deal with the case of passing a shock wave having arbitrary intensity through a perturbed interface. When the shock wave passes through a perturbed interface the latter gains the counstant velocity on which the field of perturbed velocities is superimposed. Further, we shall assume the perturbed flow is an isentropic one. Then the gasodynamics equations admits of implementation of the transformations of time $t = \frac{t'}{k}$ and velocities $u = ku_i'$ [4].
This means that the argument of the function F in the relation (2) must comprise the time multiplied by some velocity characterizing the pulsation field. It is reasonable to assume the perturbation amplitude growth velocity in the linear regime as the characteristic one which in accordence with the formula (1) is equal to:

$$u = \frac{2\pi}{\lambda} a_0 A \Delta v. \tag{3}$$

Thus, for the arbitrary shock wave intensities the relation (2) is generalized as follows:

$$a(t) = \lambda F\left\{\frac{ut}{\lambda}\right\} = \lambda F\left\{\frac{2\pi}{\lambda} a_0 A \Delta v \frac{t}{\lambda}\right\} \tag{4}$$

Now we shall try to drop the condition of initial perturbation

similarity. We note that, while changing the initial amplitude and conserving the perturbation wave length, the following changes take plase in the system: 1) the initial velocity value u is changing in accordence with the formula (3) that has been already taking into account by the relation (4); 2) the spatial distribution of the initial velocities u(x,y,0) is changing, but under the condition $a_0 \ll \lambda$ (linear approximation) its effect can be neglected; 3) the phase of motion is changing that can be taken into account by adding the "initial phase" $\frac{a_0}{\lambda}$ to the argument of the function F.

Scale transformation of a density $\rho = k\rho'$ requires change of a pressure $p = kp'$ but not of u, x, t for conservation of the gasodynamics equation [4]. But validity of (1) implies this corresponding pressure change takesplace at the scale density transformation conserving the Atwood number.

Thus, for the fixed ratio of interacting substances densities in the case of the arbitrary initial perturbations and intensities of shock wave, the perturbation amplitude development (mixing zone width) must be described by the following relation:

$$a(t) = \lambda F\left\{\frac{a_0}{\lambda} + \frac{2\pi}{\lambda^2}\, a_0 A \Delta v t\right\} . \qquad (5)$$

It should be noted that the perturbations development is eventually finished by the stage in which viscosity appears to be substantial. For this final stage our consideration is not valid because the suppositions made while obtaining the expression (2) are not fulfilled.

Our consideration extends to including both directions of crossing an interface by a shock wave. Difference between these two cases must be taken into account by sign A: $A > 0$ for the case of passing a shock wave from a light substance into a heavy one and $A < 0$ for the case of opposite intersecting we suppose $F(-\xi) = F(\xi)$.

Comparing the relation (5) with the expression(1) we can see that the argument of the function F – the phase of motion – represents the mixing zone width which would have been obtained for the given moment if its development had been described by the linear approximation. The function F expresses virtually the deviation from the linear approximation which appears to be the same for the wide class of flows. We have $F(\xi) = \xi$ at small values of argument (at the linear stage), as it follows from the Richtmyer formula (1).

To check permissibility of representation (5) we make use of experimental results, given in the work [1]. In this work, the experimental study of linear, non-linear and transition stages of the Richtmyer–Meshkov instability development has been performed for the Mach number of the falling shock wave $M = 3.5$, for the Atwood number $A = 0.45$ and for some values of a wave length. In the paper the graph of dependence of the mixing zone width a on

time has been presented for five different wave lengths at the same initial amplitude a_0. Using it we plot the experimental points on the graph in coordinates consistent with our proposed dependence ($\frac{a}{\lambda}$ as the function of $\frac{a_0}{\lambda} + \frac{2\pi}{\lambda^2} a_0 A \Delta v t$) – Fig.1.

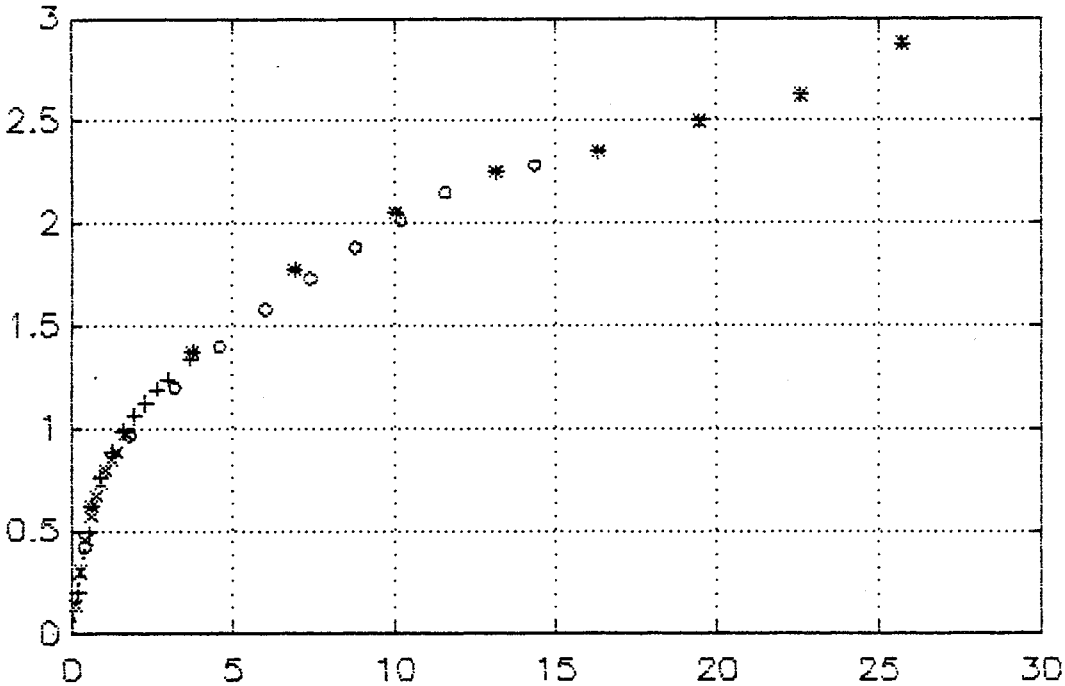

Fig.1. Dependence of the mixing zone width divided by the initial wave length of perturbations $\frac{a}{\lambda}$ on the phase $\frac{a_0}{\lambda} + \frac{2\pi}{\lambda^2} A a_0 \Delta v t$.

* – initial wave length of perturbation λ = 8 MM
o – initial wave length of perturbation λ = 12 MM
\+ – initial wave length of perturbation λ = 24 MM
x – initial wave length of perturbation λ = 36 MM
· – initial wave length of perturbation λ = 72 MM.

It is seen from this figure that five different dependencies, concerned with different wave length are good falling to one curve. Thus the proposed representation (5) is uniformly describing the perturbation development at the linear and non-linear stages for different wave lengths of the initial perturbations. By approximating the obtained dependence of the smooth curve it is possible to build dynamics of perturbation development in time for any wave lengths analogous to the work [1] – Fig.2.

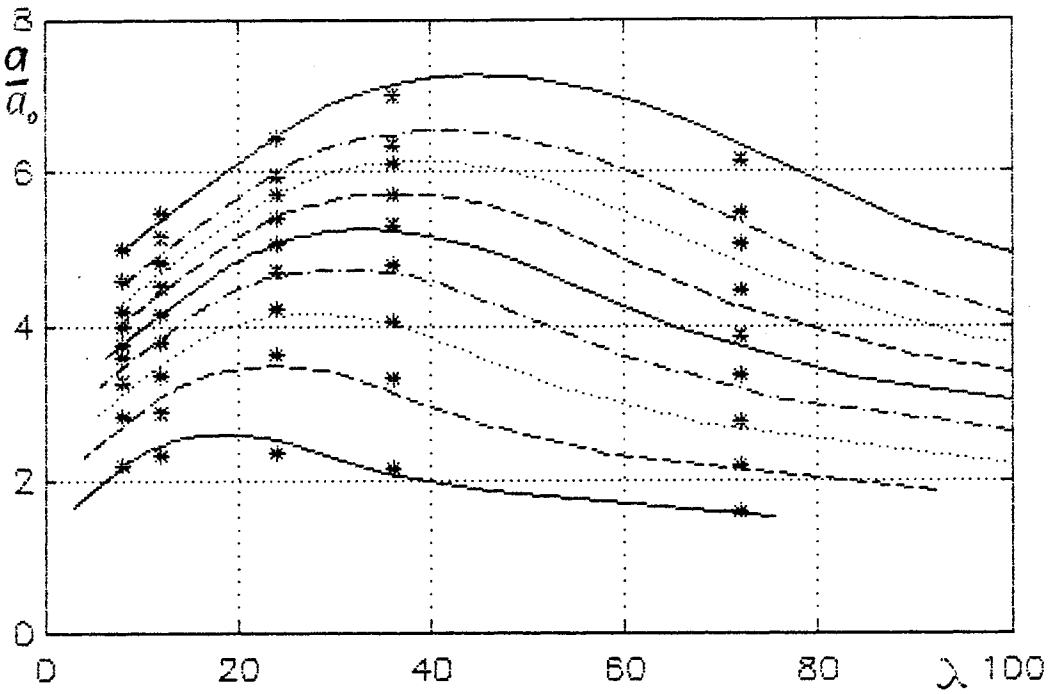

Fig.2. Dynamics of perturbations development in time for different wave lengths.

*** – experimental data from the work [1],**
—— – dependencies (5) for t = 250, 200, 175, 150, 125, 100, 75, 50, 25 mks. from top to bottom, respectively.

The obtained curves are seen to describe rather well the represented experimental results for five wave lengths.

Thus in the work the universal dependence which allows to describe the non-linear stage of the Richtmyer-Meshkov instability development for the wide class of flows has been derived. The obtained dependence for the Atwood numbers A = ± 0.45 has the form, shown in Fig.1.

REFERENCES

1. Aljeshin A.N., Lazareva E.V., Saitzev S.G. and al. Reports of the Acad. of Sci. USSR, ser. Physics, 1990, vol.310, № 5, p. 1105-1108.
2. Richtmyer R.D. – Communs. Pure and Appl. Math., 1960, vol. 13, № 2, p. 297-319.
3. Meshkov E.E. Collection: Investigation of hydrodynamic stability by means of computer /Edited by K.I. Babenko. Moscow, 1981, p. 163-190.
4. Zeldovich J.B., Raizer U.P. Physics of Shock Waves and High

Development of the Rayleigh-Taylor Instability in Systems with Different Compressibility of Media

N.N. Anuchina, M.G. Anuchin, V.I. Volkov, A.E. Guseva,
N.S. Es'kov, V.N. Ogibina, A.V. Polionov, I.A. Potanina.
All-Union Research Institute of Technical Physics,
P. O. Box 245, Chelyabinsk 454070, USSR

ABSTRACT

Numerical results of the influence of medium compressibility upon a development of the Rayleigh-Taylor instability is considered. It is shown the compressibility leads to increasing the perturbation growth rate and to expanding of the mixing zone.

1. INTRODUCTION.

In this paper the influence of medium compressibility upon a development of the Rayleigh-Taylor instability (RTI) is considered. The numerical simulation using the program complexes MAH and MECH shows the compressibility leads to increasing of the perturbation growth rate and to expanding of the mixing zone.

2. PROBLEM STATMENT. LINEAR STAGE OF THE RTI.

The same approach as in the paper[1] is used. Here the comparison of the RTI development at the linear stage for substances with the same initial density profile but with different compressibility is performed to determine the influence of the compressibility itself. The initial density profile is set as follows

$$\rho_{h(l)} = \rho_{0h(l)} \cdot \exp(-z/h_{h(l)}) , \qquad (1)$$

where h and l relate to the heavy and light fluids respectively, $\rho_{0h(l)}$ is the density at the interface z=0, $h_{h(l)}$ are constants.

Two systems with the same initial density profile (1) are compared. In the first case (problem H) fluids are considered to be incompressible. In the second case (problem C) ideal compressible gases with the isothermal initial state are calculated. The increment of the growth rate of small boundary perturbatios is found.

It is shown for any wave number the compressibility leads to increasing of the increment. When the Atwood number is approaching to 1 the compressibility effect vanishes (see Fig.1, 2).

3. NONLINEAR STAGE OF THE RTI SIMULATION. MECHANISM OF COMPRESSIBILITY EFFECT.

Computation method. A development of the nonlinear stage of the RTI in the system described above is studied by means of the program complex MAH. In the MAH the considered system is divided into computational regions at boundaries of which corresponding conditions are set. In each region its own arbitrary tetragonal mesh is used and computations can be performed in the Lagrangian variables (by explicit or implicit difference schemes) or in the Eulerian variables for considerable relative shifts. The inhomogeneous Eulerian method is used to discribe strong interface deformations and topological changes of the regions. Particles-marcers being placed at the boundaries allow to follow the movement of the interface which is not considered to be a line of the mesh. In the course of computations each method can be changed by other one in any computational region.

Computation details. Two runs are carried out for two Atwood numbers A=1/3, 9/11 in the problems H and C with wave number k=1. The initial geometry is shown in Fig.4. At t=0 the density and pressure distributions correspond to the hydrostatic equilibrium. In the case H the incompressibility is simulated by specifying a large value for Poisson's index $\gamma=\gamma_h=\gamma_l=9$. In the case C the motion of each gas is imposed to be isothermal one in order to reach the maximum compressibility. The interface is unperturbed at t=0. The velocity field is set as follows

$$v_{zh(l)} = a_0 \cdot n \cdot \cos y \cdot \exp(\mu_{h(l)} \cdot z) ,$$
$$v_{yh(l)} = (a_0/n) \cdot b_{h(l)} \cdot \sin y \cdot \exp(\mu_{h(l)} \cdot z) , \qquad (2)$$

where $\mu_{h(l)}$ and $b_{h(l)}$ as well as the increment n are the functions of A and γ. At the linear stage the time dependence of the interface form obeys the law

$$a(y) = a_0 \cdot \cos y \cdot \mathrm{sh}(n \cdot t) . \qquad (3)$$

The initial amplitude $a_0=0.1$.

Main computational results. At the linear stage all computational results are in well agreement with analytic solution (see Fig.3, where $\xi_{\pm} = \ln(a_{\pm}/a_0+\sqrt{(a_{\pm}/a_0)^2+1})$, a_+ and a_- are displacements of the "bubble" and "spike" tops, respectively).

When the total amplitude $a\approx 0.4\cdot\lambda$, a deviation from the exponential law in both computations is observed. In Fig.4 the interface form and the field of velocities are shown for A=1/3 at some moments. The essential difference of perturbations behaviour in cases H and C is seen. Plots of perturbation amplitude versus time are given in Fig.5. In the problem H the amplitude growth is gradually reduced till it stops completely. In the case C the perturbation development proceeds much faster, at $t \geq 5$ the amplitude is growing with constant acceleration.

For A=9/11 in the case H the "bubble" growth proceeds much slower than in the compressible case, but the "spike" development velocities in both cases differ rather less (Fig.6, 7). General picture of flows is the same (Fig.8).

Thus the compressibility effect is the more the higher the pressure gradient in the initial flow. The mechanism of the compressibility effect is similar to the mechanism of the convection instability.

4. COMPUTATIONS OF TURBULENT GRAVITATIONAL MIXING IN SYSTEMS WITH DIFFERENT COMPRESSIBILITY.

Computation method. For the computational study the program complex MECH is used. In the MECH the Eulerian irregular difference method being built on the basis[2,3] is realized, but its accuracy and efficiency are better. For describing of the interface motion the own particles, placing only in the vicinity of boundaries, are used for each substance. The mesh and the number of particles can be changed in the process of calculations.

Computation details. Two layers of ideal gases with constant densities are considered in the constant gravitational feild. The initial hydrodynamic equilibrium is provided by an appropriate distribution of the pressure as well as the internal energy. The perturbation of the interface in the form of the broken line with random values of its break points coordinates is set. Two values of density drop are considered (ρ_h/ρ_l=2, 13.5). The gas

compressibility is varied by changing the internal energy. The sound velocity in the incompressible case H is distinguished from the compressible case C by ≈ 4.5 times.

Main computational results. In the compressible case for the density drop $\rho_h/\rho_l=2$ the flow is more chaotic and the mixing zone is expanded faster. Here the curve slope is ≈ 35% more than in the problem H. For the density drop $\rho_h/\rho_l=13.5$ the distinction between the slopes is weaker and equals to ≈ 5% (see Fig.9, 10).

CONCLUSION.

The compressibility of medium leads to increasing of the RTI development rate. In some cases it can radically change the character of this phenomenon.

The compressibility effect is the more the higher the pressure gradient in the initial flow.

The mechanism of the compressibility effect is similar to the mechanism of the convection instability.

REFFERENCIES.

1. Bernstein J.B., Book D. // Phys. Fluid, 1983, vol. 26, N 2, p. 453.
2. Harlow F.H. // Calculation methods in hydrodynamics, M.: MIR, 1967, pp. 316-342.
3. Anuchina N.N. // Numer. methods of continuum mechanics, 1970, vol. 1, N 4, pp. 3-84.

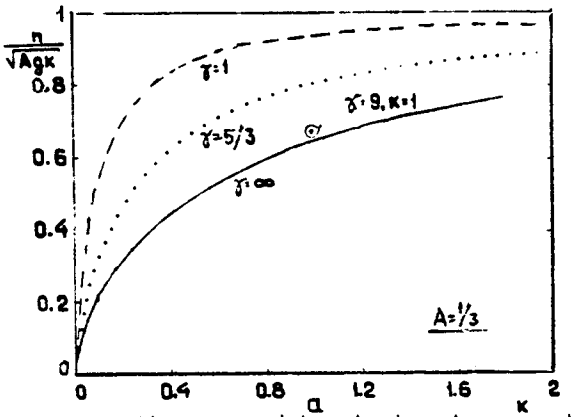

Fig 1. Growth rate, related to it's classic value, versus the wave number k:
A=1/3: — - γ=∞; ··· - γ=5/3;
--- - γ=1; ⊙ - γ=9, k=1.

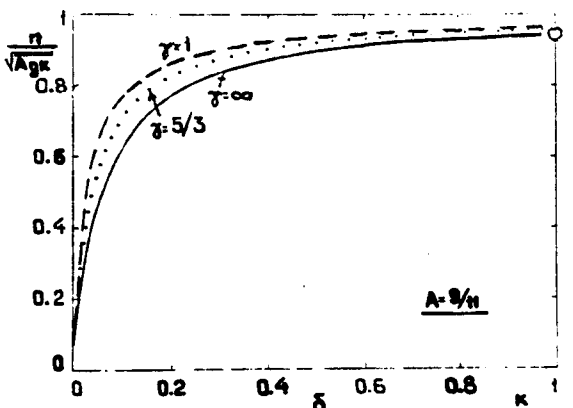

Fig 2. Growth rate, related to it's classic value, versus the wave number k:
A=9/11: — - γ=∞; ··· - γ=5/3;
--- - γ=1; ⊙ - γ=9, k=1.

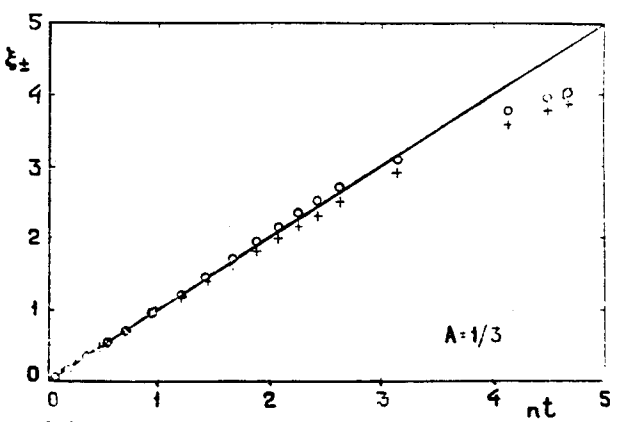

Fig 3. Calculated dependences ξ±(nt). Calculation C.
A=1/3: + - ξ+; o - ξ-; — - analytical solutions for the linear stage.

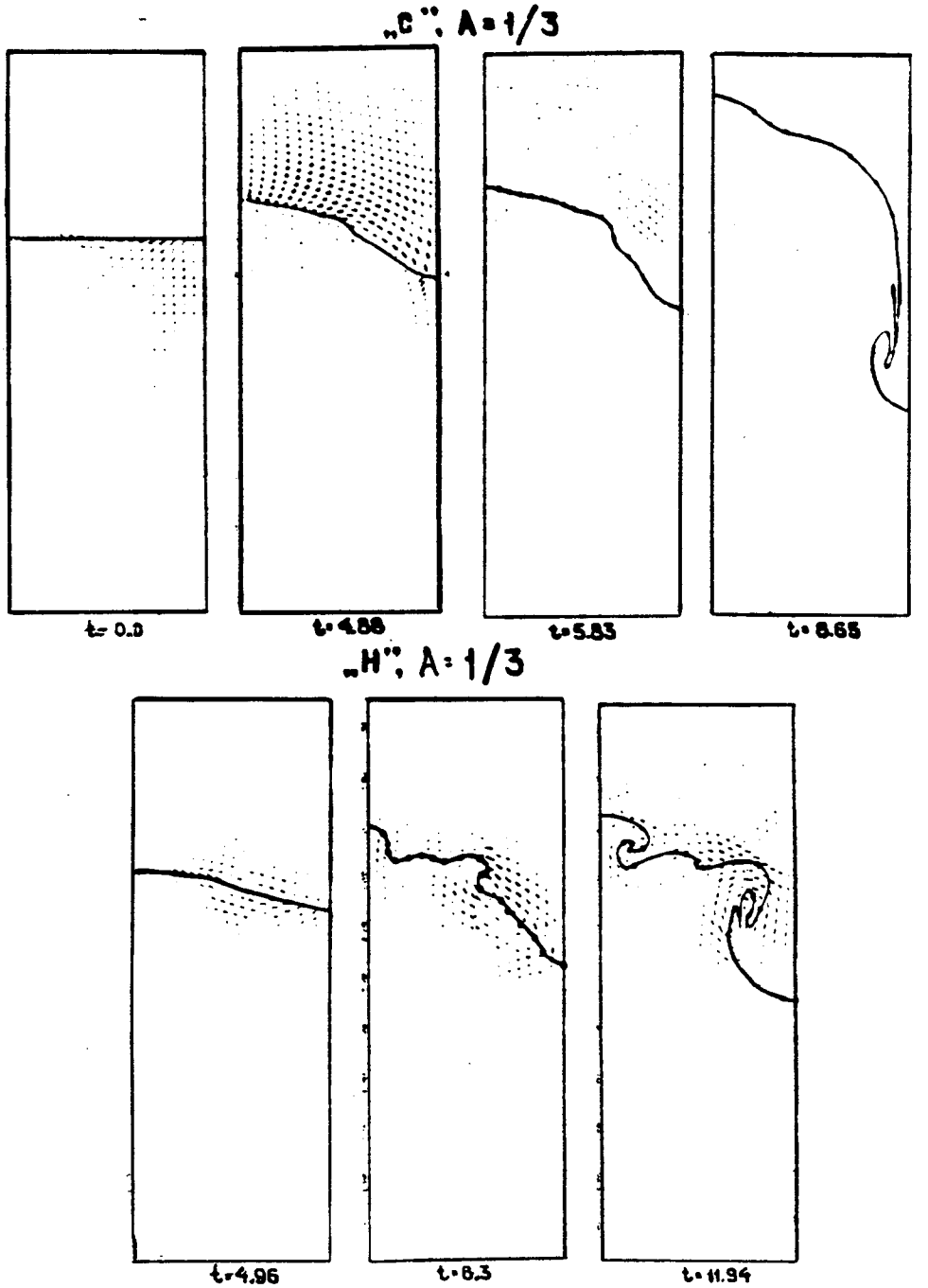

Fig 4. Form of CB and velocity field at different instants of time.

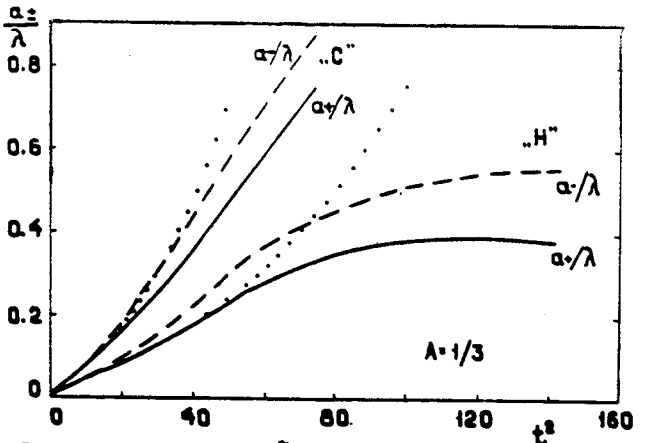

Fig5. Dependence $a_{\pm}/\lambda(t^2)$ in calculations H and C
—·a_+/λ; ----a_-/λ, - exponential law (3), A=1/3

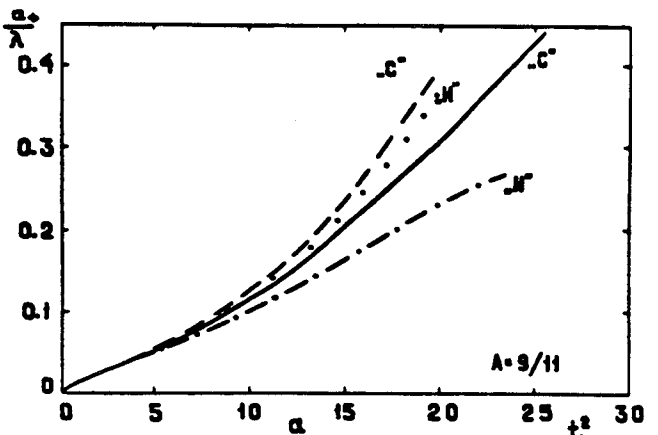

Fig6. Function $a_*/\lambda(t^2)$ in calculations H and C:
----analytical solution for the case C:
···analytical solution for the case H: A=9/11

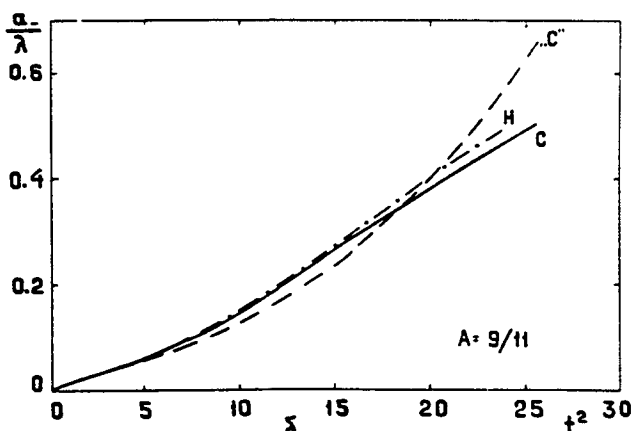

Fig7. Function $a_-/\lambda(t^2)$ in calculations H and C:
A=9/11: ----analitical solution for the case C:

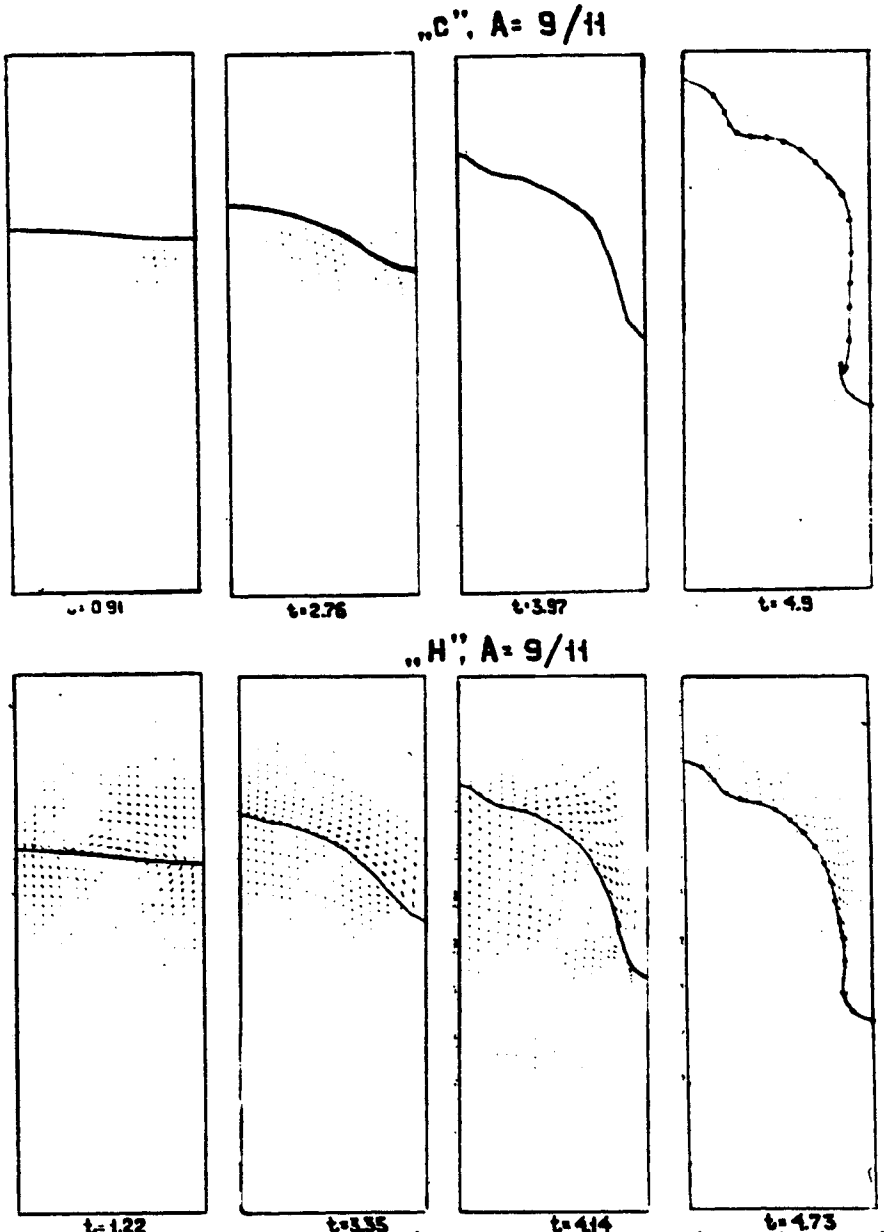

Fig8. Form of CB and velocity field at different instants of time. A= 9/11

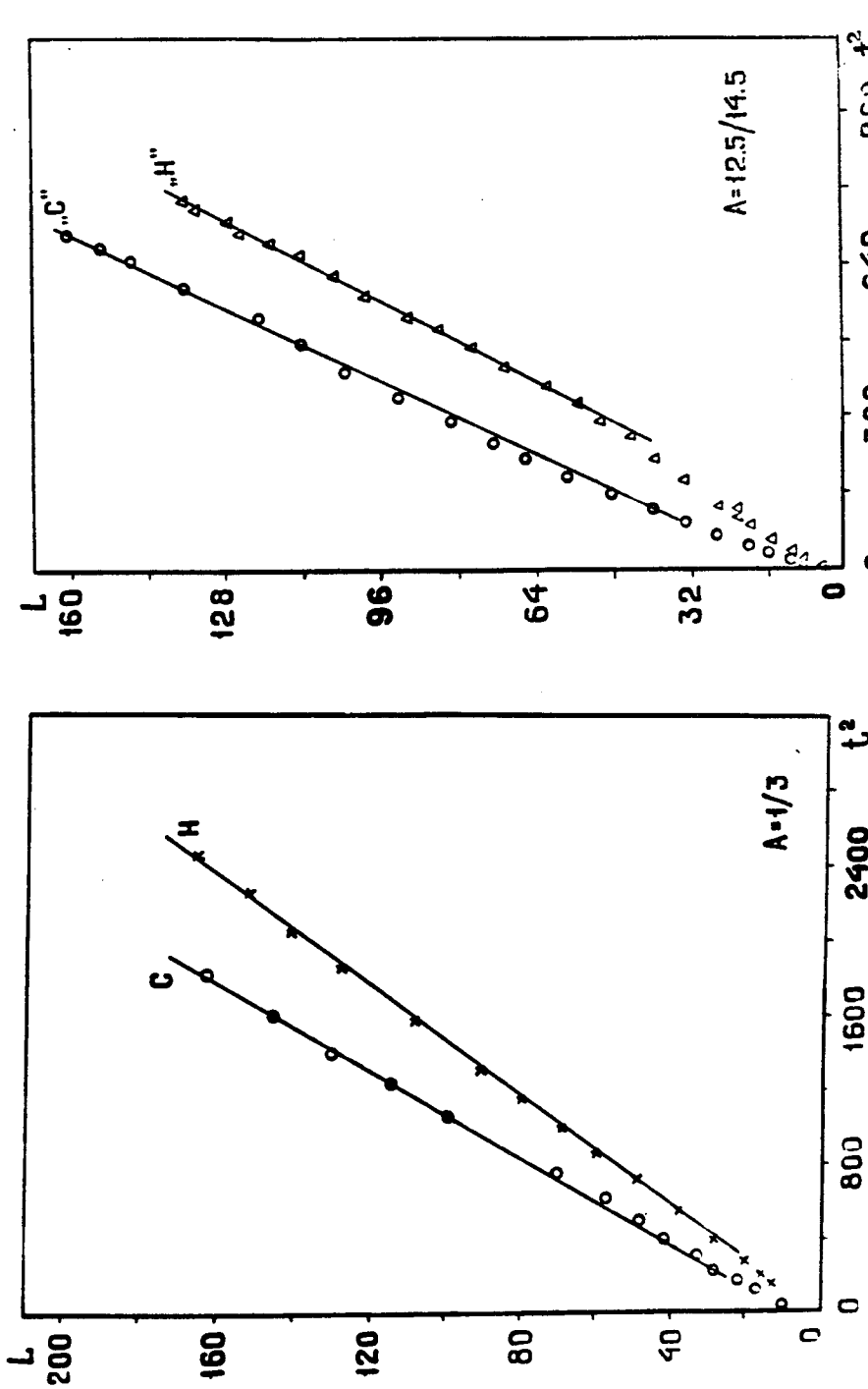

Fig 9. Dependence $L(t^2)$: $\rho_{cr}/\rho_{ok}=2$;
o - calculation C; x - calculation H.

Fig10. Dependence $L(t^2)$: $\rho_{cr}/\rho_{ok}=13.5$;
o - calculation C; Δ - calculation H.

NUMERICAL INVESTIGATION OF RICHTMYER-MESHKOV INSTABILITY

N. N. Anuchina, V. I. Volkov
All-Union Research Institute of Technical Physics,
P. O. Box 245, Chelyabinsk 454070, USSR

ABSTRACT

Numerical results of Richtmyer-Meshkov instability are presented. These results are compared with analytic and experimental investigations.

1. INTRODUCTION

In present work the computational results of the perturbation development at the interface between the gases of different densities under impulse acceleration generated by the stationary shock wave (Richtmyer-Meshkov instability) are described. The transmitting of the shock wave from the heavy gas into light one and vice versa is considered. One-mode initial perturbation of the interface are specified. The features of the linear, non-linear and transition stages are discussed. The numerical results are compared with the R. D. Richtmyer's investigations and the experiments carried out by E. E. Meshkov. The effect of initial perturbation wavelength as well as the mesh size on the flow development is estimated. The computations are performed by the program complex MAH.

2. STATEMENT OF PROBLEMS.

Two plane layers of inviscid non-heatconductive gases (see Fig.1) are considered. The constant pressure $p=p_B$ is spacified at the boundary the position of which is x=0 at the initial moment t=0. Boundaries $x=X_{max}$, y=0, $y=Y_{max}$ are rigid walls. Gases are described by the state equation $p_\alpha=(\gamma_\alpha-1)\cdot e_\alpha\cdot\rho_\alpha$, where $\alpha=1,2,3$ is the region number, ρ_α is the density, e_α is the specific internal energy. At t=0 the stationary shock wave is located in the point $x=X_{sw}$. The one-mode perturbation is specified at the interface as following

Royaumont, France Edited by D. Besnard, J.-F. Hass, P.-A. Holstein & B. Sitt

$$x = X_0 + 0.24 \cdot \cos\left(\frac{2 \cdot \pi}{w} \cdot y\right) , \qquad (1)$$

where X_0 is the initial place of the unpertubed interface.

Computations have been performed for the two systems.

Air-helium system. The shock wave is going from the heavy gas into the light one; X_{sw}=40.3, X_0=41, p_B=1.6482, w=3.75, γ_1=1.67, γ_2=γ_3=1.4. In the first region there is helium with p_1=1.013, ρ_1=0.0001694 and velocity components u_1=v_1=0 at t=0. There is air in other regions; p_2=1.013, ρ_2=0.00125 and u_2=v_2=0 at t=0; p_3=1.6482, ρ_3=0.017285, u_3=12.29, v_3=0 at t=0. Mach number is equal to 1.24.

Air-SF6 system. The shock wave is going from the light gas into the heavy one; X_{sw}=97, X_0=100, p_B=1.8993, w=5.65, γ_1=1.67, γ_2=γ_3=1.4. In the first region there is SF6 with p_1=1.013, ρ_1=0.06187 and velocity components u_1=v_1=0 at t=0. There is air in regions 2 and 3; p_2=1.013, ρ_2=0.001253 and u_2=v_2=0 at t=0; p_3=1.8993, ρ_3=0.019, u_3=15.95, v_3=0 at t=0. Mach number is equal to 1.32.

Pressure, length and density are measured in bar, cm and g/cm^2, respectively.

3. BASIC COMPUTATIONAL RESULTS.

Computations have been performed on the Eulerian movable mesh by the program complex MAH[1]. At first the interface is the mesh line, but the marker-particles for its describing and mix calculating are used under strong deformations.

The computations show that the interface between gases of different dencities is unstable under the stationary shock wave reaching the one from the light gas as well as from the heavy gas. These results are well in agreement with experiments carried out by E. Meshkov[2].

The analysis of the interface form and the amplitude growth obtained in computations shows that accordingly[3] one can divide the development of the initial perturbation into linear, non-linear and transition stages. Consider the principal features of each stage.

The linear stage. Richtmyer[4] studied the perturbation development at the iterface under stationary shock wave travelling from the light gas into the heavy one. He assumed that the amplitude $a \ll \lambda$ and the processes were described by the linearized gas dynamics equations. According to[4], at first the decreasing of the amplitude takes place, then it increases with some acceleration and

with the constant rate later,

$$\frac{da}{dt} = \frac{2\cdot\pi}{\lambda}\cdot u'\cdot a'\cdot A' \ , \qquad (2)$$

where u', a', A' are the interface velocity, the amplitude and the Atwood number, respectively, just after the shock wave passed and λ is the wavelength of the initial perturbation.

$$a' = 2\cdot a_0\cdot(1 - \frac{u'}{D}) \ , \qquad (3)$$

where D and $2\cdot a_0$ are the initial velocity of stationary shock wave and the initial amplitude, respectively. The computational results are qualitatively and quantitatively in agreement with Richtmyer's studies, Fig.6. The minimum value of the computed amplitude is a'=0.37 and a'=0.366 according to (3). For the rate of the amplitude growth we have numerical value da/dt=2.96 and da/dt=3.13 by (2)-(3).

When the shock wave moves from the heavy gas into the light one, the perturbation phase changes, Fig.9. Applying the formulae (2)-(3) we obtain the velocity da/dt=6.295 and the numerical value da/dt=6.35.

In case of the RTI the interface form and the symmetric motion of the light and the heavy substances are conserved at the linear stage. Here, as it can be seen in Fig.2, 3a), the interface form after the passing of the shock wave is disturbed. In Fig.4, 8 the time dependences of the maximum value x_{max} and the minimum value x_{min} of interface points are given. They show the motion of the light gas into the heavy one and vice versa. It is seen that the assymetric flow of the heavy gas and the light one ralative to interface, being initially unperturbed, is observed after the passing of the shock wave. The harmonic analysis of the interface form in the air-SF6 case has been performed. After the passing of the shock wave the interface will just have the form

$$a_1\cdot\cos(\frac{2\cdot\pi}{w}\cdot y) - a_2\cdot\cos(\frac{2\cdot\pi}{w}\cdot 2\cdot y) \ ,$$

i. e. the second harmonic with the negative factor is added to the initial one. The second harmonic decreases the velocity of the light gas and increases the one of heavy gas, i.e. leads to assymetric development of the

perturbation (see Fig.4). Values a_1, a_2 versus time are shown in Fig.7. The harmonics develop independently at first, their amplitudes grow linearly in course of time. Note that the second harmonic leading to the assymetry has no effect (see Fig.7) on the amplitude growth rate, which is equal to the one of the first harmonic as well as (2). Then the gradual transition to the non-linear stage is observed. The harmonics interact and redistribution of the energy over the spectrum begins. The growth rate of the first harmonic falls, but the one of the second harmonic increases. The third harmonic is occured visible. The amplitude growth of the overall interface perturbation decreases; the departing from the law (2) is observed (see Fig.6). One can apparently consider value $a \approx (0.3 \div 0.4) \cdot \lambda$ to be the transition moment to the non-linear stage.

Non-linear and transition stages. The decreasing of the "bubble" velocity continues (see Fig.5). The heavy gas penetrates into the light one with the constant rate. The perturbation amplitude growth of the interface reaches the linear time dependence, but the growth rate is less than observed one at the linear stage. When $a \approx (0.4 \div 0.5) \cdot \lambda$, in fact the penetration of the light gas into the heavy one due to the third harmonic stops. The heavy gas keeps moving with the constant velocity. The amplitude growth rate of the interface perturbation decreases and it is nearly constant up to the moment $a \approx (0.6 \div 0.7) \cdot \lambda$. By degrees the Kelvin-Helmholtz instability makes an appearance. The mushroom-like vortical structure occures at the tops of the "spikes", Fig.3b). The "spike" velocity falls. The rate of the amplitude growth decreases. The transition stage starts with $a \approx 0.7 \cdot \lambda$. The mushroom-like structures grow on the "spikes" of the heavy gas.

The numerical picture of the single-mode perturbation development and motion of "bubbles" and "spikes" agree with the experimental results[3]. The interpenetratation of gases in contrast with[3] is occured unsymmetrically, i. e. "bubbles" and "spikes" have different velocities at the linear stage. These velocities are various from ones in[4], although the development rate of the whole perturbation is rather well in agreement with the Richtmyer estimation.

4. EFFECT OF THE WAVELENGTH.

The effect of the wavelength upon the perturbation development is considered in the air-SF6 case. The initial perturbation is specified of the same form and of the same amplitude as well as (1) only that the wavelengths $\lambda_1 = w/2$

and $\lambda_2=w/4$. The perturbation development rate being proportional to $1/\lambda$ is obtained at the linear stage. In Fig.10 numerical dependences of the perturbation amplitude a(t) on the wavelength λ are given. The maximum amplitude value is seen to displace to the side of long waves in course of time. This is explained by that short-wave perturbations develop more quickly to the later stages and (see above) the amplitude growth rate decreases with the transition from one stage to the next one. Note that the computations were performed with the same number of points per the wavelength.

In Fig.11 the numerical dependences of the ratio a/λ on a_ℓ/λ, where $a_\ell=a'+u_R \cdot t$ and u_R is the amplitude growth rate at the linear stage, are presented. It is seen that the results are well described by one curve through the three stages of the interface perturbation development.

5. EFFECT OF THE MESH SIZE.

To evaluate the effect of the mesh size upon the numerical results the computations of the air-SF6 problem have been carried out with $\lambda=w$ and N meshpoints per the wavelength, where N=10, 20, 50, 100. The number of points in the second direction is also changed simultaneously. In Fig.12 the perturbation amplitudes versus time are given.

REFERENCES.

1. N. N. Anuchina, M. G. Anuchin, V. I. Volkov, N. S. Es'kov et al., USSR Ac. of Sci., Math. Simulation, v. 2, № 4, 3 (1990).
2. E. E. Meshkov, in Coll. Investigation of Hydrodynamic Instability by means of Computer (M.:1981, edited by K. J. Babenko), p. 163.
3. A. N. Aleshin, E. V. Lazareva, S. G. Saitzev, V. B. Rosanov et al., Rep. of USSR Ac. of Sci., v. 310, № 5, 1105 (1990).
4. R. D. Richtmyer, Communs. Pure and Appl. Math., v. 12, № 2, 297 (1960).
5. C. J. Taylor, Proc. Roy. Soc. Ser. A, v. 201, № 1065, 192 (1950).

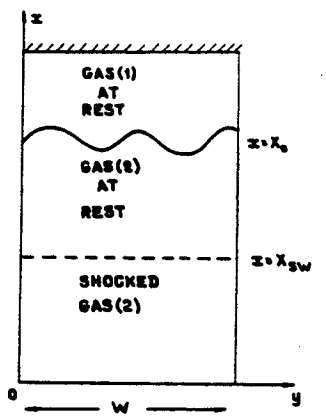

Fig.1 The problem statement.

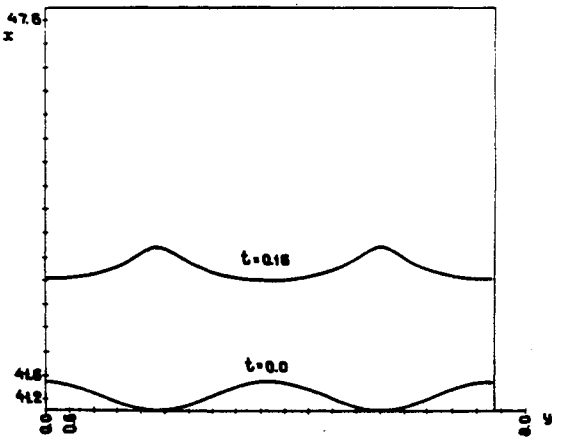

Fig.2 Air-He. The interface form.

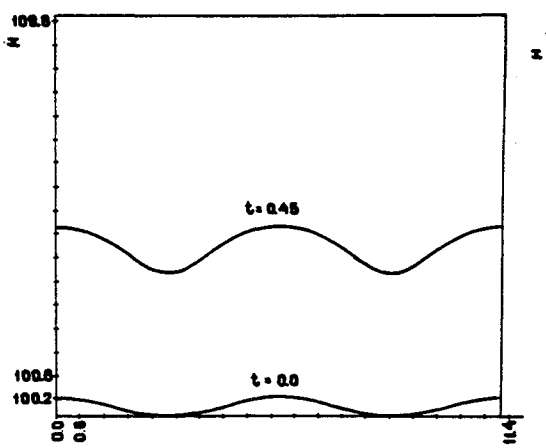

a)

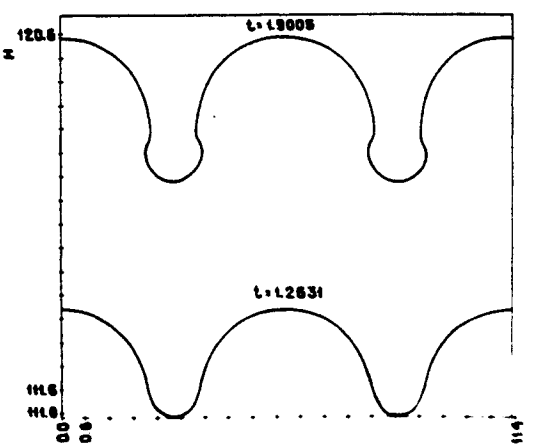

b)

Fig.3 a)-b) Air-SF6. The interface form at some moments.

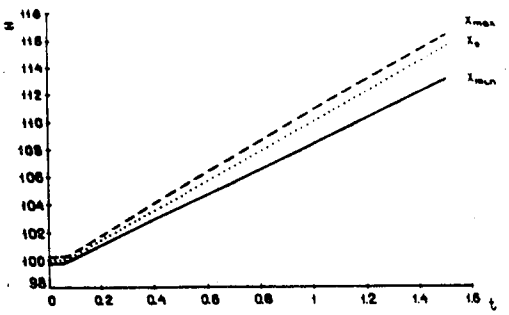

Fig.4 Air-SF6.
Time dependences $x_0(t)$, $x_{min}(t)$ and $x_{max}(t)$.

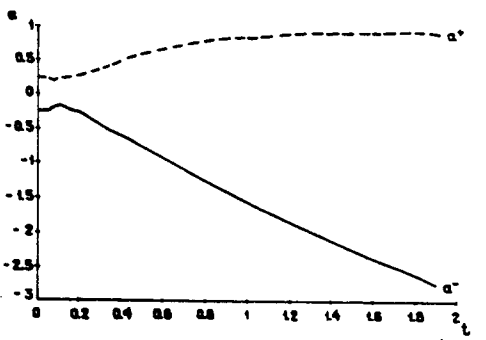

Fig.5 Air-SF6.
Time dependences
$a^+(t) = x_{max}(t) - x_0(t)$,
$a^-(t) = x_{min}(t) - x_0(t)$.

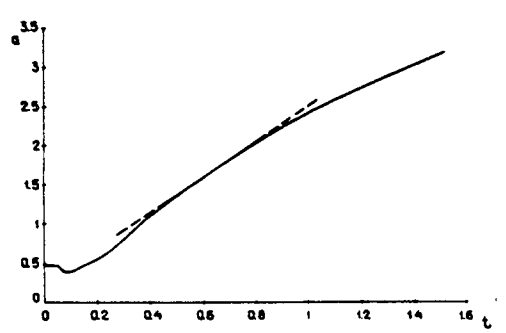

Fig.6 Air-SF6.
Time dependence
$a(t) = x_{max}(t) - x_{min}(t)$.

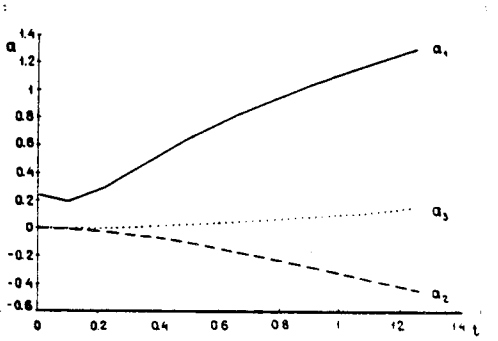

Fig.7 Air-SF6.
Time dependence $a_i(t)$, $a_i(t)$ is the amplitude of the ith mode, i = 1, 2, 3.

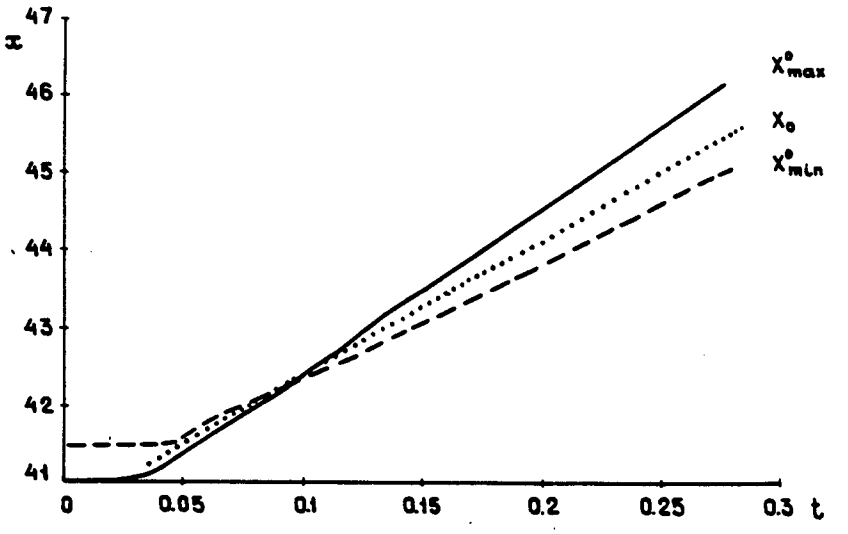

Fig.8 Air-He. Time dependences $x_o(t)$, $x^o_{min}(t)$ and $x^o_{max}(t)$: $x^o_{min}(0) = x^o_{min}(0)$, $x^o_{max}(0) = x^o_{max}(0)$.

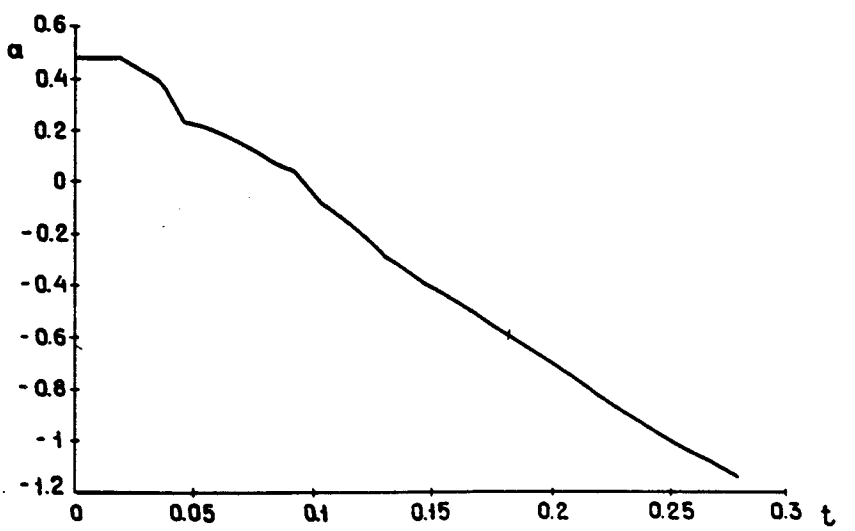

Fig.9 Air-He. Time dependence $a(t) = x^o_{max}(t) - x^o_{min}(t)$.

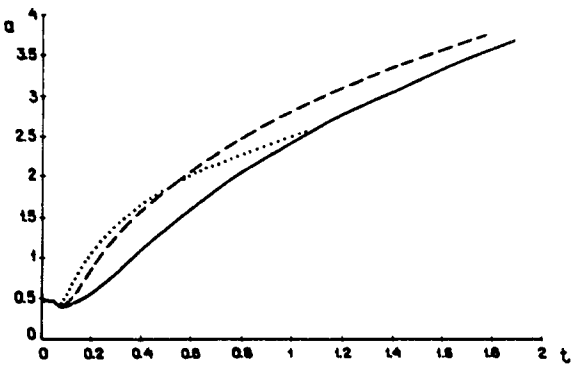

Fig.10 Air-SF6. Time dependences a(t) for some various wavelengths.

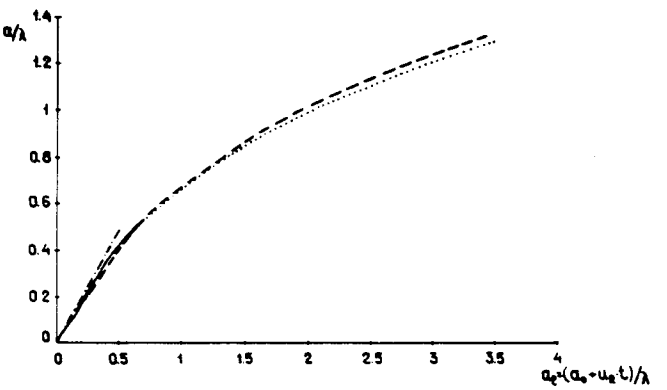

Fig.11 Air-SF6. Time dependences a/λ on a_ℓ/λ, $a_\ell = a' + u_R * t$.

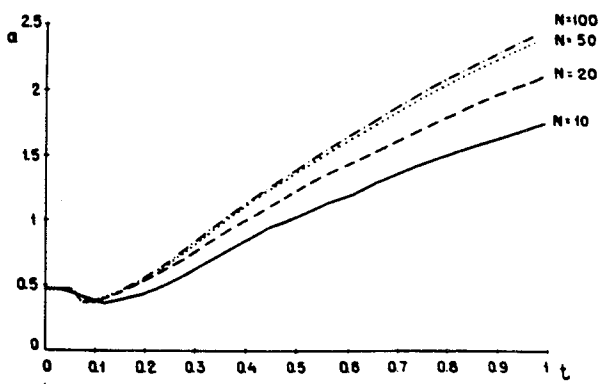

Fig.12 Air-SF6. Time dependences a(t) for some various initial mesh sizes.

SHOCK AND RESHOCK OF AN UNSTABLE FLUID INTERFACE*

Robert F. Benjamin
Los Alamos National Laboratory, Los Alamos, NM 87545 USA

ABSTRACT

Difficulties with experimental studies of the Richtmyer-Meshkov instability are examined. We consider optical systems for explosively driven experiments with liquids, and the problems of the interfacial membrane and diffusion in experiments with gases. We show how the membrane induces deviation from impulsive loading of the unstable interface. Also, we summarize recent analyses of our experiments with a perturbed interface between gases, and show how accelerative instabilities can affect an equation-of-state experiment.

INTRODUCTION AND SUMMARY

We examine the effects of the Richtmyer-Meshkov instability (RMI)[1,2] at shocked liquid/liquid[3,4] and gas/gas interfaces.[5] The RMI is the impulsive analog of the Rayleigh-Taylor instability, an interfacial instability between fluids of different densities. These accelerative instabilities are potential problems in inertial confinement fusion targets, and other applications involving highly accelerated interfaces. An equation-of-state experiment is such an application, as discussed below.

RMI experiments performed with an explosively driven shock tube (X-ST) have advantages over experiments using a compressed-gas shock tube (G-ST) because a liquid/liquid or liquid/gas interface in an X-ST can be formed without a membrane. By constrast, the the gas/gas interface in G-ST experiments either has a diffusive initial mixing-zone width about 1 cm,[6,7] or a membrane initially separating the test gases.[2] However, X-ST experiments are more expensive because much of the apparatus is destroyed each experiment, and they can be fielded only at the few laboratories with explosives capabilities. Also, optical methods are more difficult to use for the X-ST, as we describe below.

We have compared experimental air/He and air/SF_6 results with 2D simulations[5] and found excellent qualitative agreement. The simulation produced a flow pattern quite similar to the experimental shadowgraph[8] of the reshock event in which the air/SF_6 interface is severely distorted during the reshock in a manner that enhances vorticity production.

---

* This work was supported by the US Department of Energy.

The interfacial membrane used in G-ST experiments is believed to influence interfluid mixing, but its effects have not been previously measured or calculated precisely. In the "Membrane" section we show results of a 1D calculation of membrane inertial effects that shows the incident shock wave to be transmitted as a series of compression waves, which produces non-impulsive loading of the interface. Two-dimensional or 3D simulations can use this membrane-induced pressure loading to calculate more accurately the growth rate of the mixing zone. This deviation from impulsive loading may contribute to the lower growth rates observed experimentally, as compared with linear theory.

Another membrane problem is diffusion. We have problems with helium diffusing into the air chamber during air/He experiments. Using measured shock speeds, we estimate the consequent contamination and its effect on growth rates.

APPLICATION

Interfacial instability is a potential problem in equation-of-state (EOS) experiments where high explosive (HE) is used to launch a driver plate toward impact on an EOS sample,[9] as shown in Fig. 1. The hot,

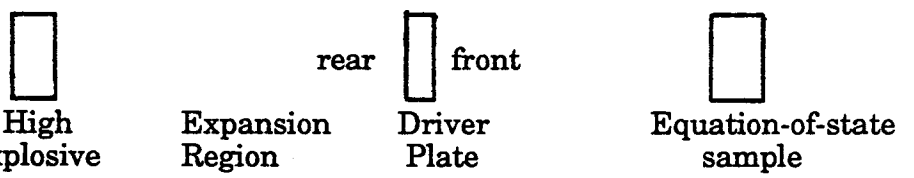

Fig. 1. Schematic layout of an EOS experiment having a flyer plate, where the rear surface may be eroded by accelerative instabilies.

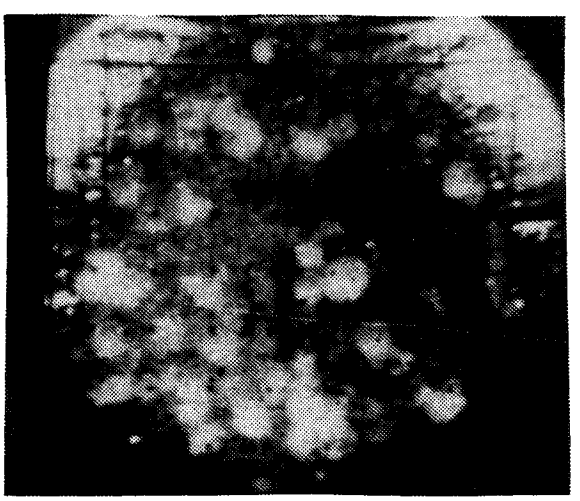

Fig. 2. Time-resolved photograph of the front surface of a flyer plate, showing the penetration of hot gases caused by interfacial instability.

gaseous HE products stagnate against the rear surface of the driver plate, causing acceleration and heating. Because pressure and density gradients are opposed at this interface, accelerative instabilities may erode the surface, to the extent that it is fluid-like. Erosion is enhanced for high- temperature conditions by ablation of the surface. Bubbles of the hot HE gases may penetrate the driver plate, destroying its usefulness as a planar impactor on the EOS sample. An example of this problem is shown in the photograph in Fig. 2. Here the imaged front surface of the driver plate contains patches of light emitted from the hot, penetrating HE gases. Thus, accelerative instabilities limit the minimum thickness of a driver plate.

EXPLOSIVELY-DRIVEN SHOCK TUBE

We consider the possibility of improving the backlighting of our X-ST experiments by using collimated, rather than diffusive illumination. Our conclusion based on the ray-trace calculation discussed below is that collimated lighting would produce caustics[10] and thereby not improve the imaging.

Design of the test chamber is constrained by the interaction between shock wave and windows. We used[3] a large-volume chamber to avoid the interaction of the shock wave with windows. Thus, the lateral dimensions of the test section were larger than the shock front supported by the high explosive. This condition causes a "shock dome," which refracts light. We model the shock dome in optical ray-trace calculations as a spherical lens (viewed perpendicular to its axis) of refractive index, n = 1.51, corresponding to a 50-kbar shock in water. Values for the refractive index of shock-compressed water[11] are given as a function of density ρ (g/cm^3):

$$n = 1 + 0.334\,\rho \qquad (1)$$

The shock dome is immersed in a medium of uncompressed water with n = 1.33. An optical ray-trace calculation was performed for collimated light to determine whether better spatial resolution is attainable, but caustics were found. We conclude that backlighting with a diffusive source is better for measuring the time-resolved profile. Future comparisons of experimental data with 3D simulations having excellent graphics[12] may encourage the use of other imaging and illumination systems, possibly with front lighting.

GAS SHOCK TUBE RESULTS

Our observation of a reshocked air/SF_6 interface showed the difficulty of measuring the amplitude growth rate of reshocked interfaces using shadowgraphy. As shown in Fig. 3, shadowgraphic

images are greatly obscured by the boundary layer flow. Strong optical refraction and small-angle light scattering cause severe broadening of the interfacial profile. This broadening of the instability profile blocks clear observation of the mean flow, and measurement of the amplitude growth rate within the mean flow. Thus, these data show the need for better diagnostics of the mean or core flow.

As we reported at the 1989 Pleasanton Workshop, our feasibility study using imaged light scattering with illumination by a planar sheet of laser light overcomes this problem. We seeded the SF_6 gas with aerosol particles small enough to trace the SF_6 flow. The particles produced strong Mie scattering that we photographed. We observed a well-defined interfacial profile without the severe broadening seen in Fig. 3. Unfortunately we have not yet exploited this method to perform a systematic study of reshocked interfaces.

Fig. 3. This shadowgraph of a discontinuous, single wavelength air/SF_6 interface that has been reshocked shows the broadening of the interfacial profile that obscures measurement of the amplitude growth rate. Air is above the interface and SF_6 below. The initial wavelength was 37.5 mm, and incident shock Mach 1.24.

MEMBRANE EFFECTS

The inertial effect of the membrane is estimated with a 1D code that calculates the fluid dynamical response of the membrane. In addition to this effect, the membrane also possesses strength, which initially inhibits interfluid mixing. Also, membrane fragments may agitate interfacial mixing at later times. Neither strength nor fragmentation effects are modeled here. We find that the inertial effect causes the incident shock wave transmitted through the membrane to become a series of compression waves, which eventually coalesce into a

shock front. Thus, the interface acceleration is not actually impulsive. Also, the shock impedance mismatch between air and membrane causes a slight attenuation of the incident shock strength. We find that the compression waves persist for a distance of about 1,000 times the membrane thickness (corresponding to the ratio of densities between membrane material and gas), which is about 20% of the zero-to-peak amplitude in our experiments. In earlier experiments deploying thicker membranes, the non-impulsive acceleration persisted for a larger fraction of initial amplitude. This deviation from impulsive acceleration may be a cause of the differences between experimental measurements of amplitude growth rate and linear theory.

The 1D code used for this analysis is MACRAME, developed by Joseph Fritz at LANL for the design and analysis of EOS experiments.[13] Macrame is like a characteristics code, except that increments of pressure and velocity (rather than values of Reimann invariants) are transmitted along the characteristic trajectories. The membrane is modeled as a fluid having the EOS of polymethylmethacrylate (PMMA) and the air on both sides of the membrane is modeled as an ideal gas of $\gamma = 1.40$. Figures 4, 5, and 6 show the calculational results for Mach 1.20 incident shock wave, including the clear evidence for non-impulsive acceleration. These pressure histories provide guidance for improved simulations that can include the fluid dynamical effect of the membrane.

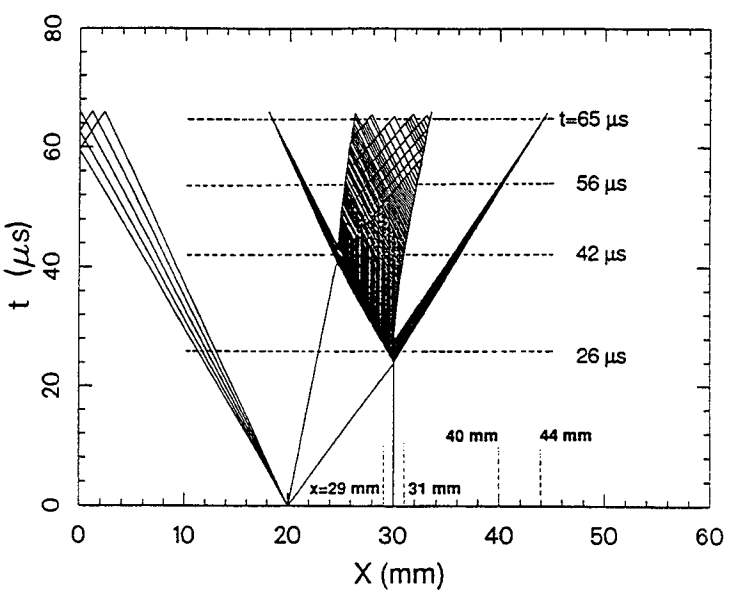

Fig. 4. In this x-t diagram, the incident shock wave in air impacts the membrane at t = 23.9 μs, causing a series of compression waves to be transmitted into the downstream air.

"Shock and Reshock of an Unstable Fluid Interface" by Robert F. Benjamin (Los Alamos)

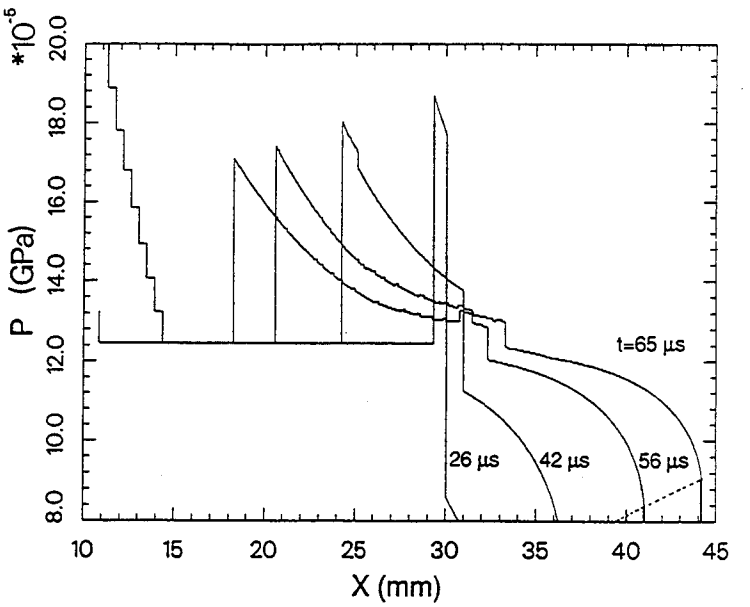

Fig. 5. These pressure profiles for times t = 26, 42, 56, and 65 μs show clearly the transmitted compression waves. A shock wave is formed at about X = 39.5 mm, a distance of 9.5 mm from the 10-μm-thick membrane.

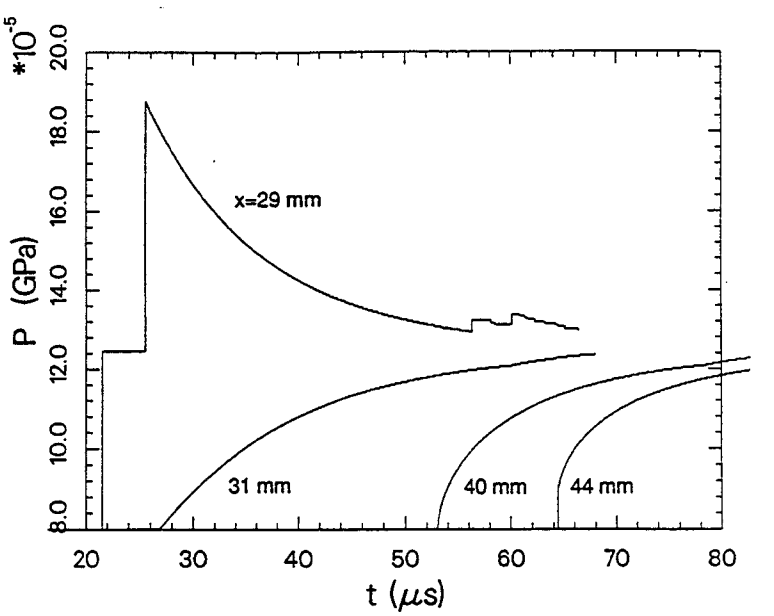

Fig. 6. These pressure histories at four locations show that the interface is not impulsively accelerated.

DIFFUSION

Air/He experiments with extremely thin membranes, $\leq$ 0.5-μm thick, have a problem with helium diffusion through the interfacial membrane. This problem is manifested by an increase in the incident shock wave speed U_S, which we use to estimate the contamination of helium, c = relative molar concentration of helium in the air chamber. For experiments with incident Mach 1.22 shock, we find that c is typically ~10%, corresponding to a decrease in pure-air mass density of 8.6%, and a decrease in the pre-shocked Atwood number of only 2.6%. The speed U_S is not measured within a few mm of the interface, so it is possible that the helium contamination in the vicinity of the interface is even greater than our estimate, which would additionally reduce the Atwood number.

We estimate the contamination by applying the ideal-gas shock-tube equation[14] as a guide, adjusted for attenuation of the shock wave traversing the shock tube.[15] Our calculations show that the helium contamination in the air chamber does not signficantly change the incident Mach number, M_S = 1.22, but it does increase the sound speed A_1, and thereby increase $U_S = M_S A_1$. For example, the 10% helium contamination decreases M_S by only 0.5%, but increases U_S by 5%, which we observe. The increase in A_1 is caused both by an increase in the ideal-gas γ and decrease in density.

Our estimate based on U_S measurements made several cm from the interface suggests that the magnitude of the contamination effect on the amplitude growth rate is small, much smaller than the difference between experimental results and linear theory.

CONCLUSION

Our analyses of difficulties in RMI experiments, including inertia and diffusion of the membrane, show effects that may explain some of the observed differences between experiments and calculations.

ACKNOWLEDGEMENTS

We are grateful for calculations by Joseph Fritz (1D MACRAME), William Swanter (ray-trace), Robert Fuehrer (diffusion), and for experimental assistance from Clint Findley, Vivian Gurule, and Dan Bannerman. We greatly appreciate suggestions and encouragement from Frank Harlow, John Shaner, Harold Rogers, and Robert Reinovsky.

REFERENCES

1 Robert D. Richtmyer, *Commun. Pure Appl. Math.* **13**, 297 (1960).

2 E. E. Meshkov, *Izv. Acad. Sci. USSR Fluid Dynamics* **4**, 151 (1969).

3 R. F. Benjamin and J. N. Fritz, *Phys. Fluids* **30**, 331 (1987).

4 R. F. Benjamin, H. E. Trease and J. W. Shaner, *Phys. Fluids* **27**, 2390 (1984).

5 R. F. Benjamin, D. C. Besnard, and J.-F. Haas, "Shock and reshock of an unstable interface," manuscript in progress, to be submitted to *Phys. Fluids.*

6 M. Brouillette and B. Sturtevant, *Proceedings of the 17th Inter- national Symposium on Shock Waves & Shock Tubes,* Y. W. Kim, ed. (AIP Conference Proceedings #208, New York, 1990), p. 284.

7 C. Cavailler, P. Mercier, G. Rodriguez, and J. F. Haas, *Proceedings of the 2nd International Workshop in the Physics of Turbulent Compressible Mixing* (Pleasanton, 1989), unpublished.

8 R. F. Benjamin, *Proceedings of the First International Workshop on the Physics of Turbulent, Compressible Mixing* (Princeton, 1988, to be published by Springer-Verlag, 1991).

9 R. G. McQueen, S. P. Marsh, J. W. Taylor, J. N. Fritz, and W. J. Carter, "The equation of state of solids from shock wave studies," chap. 7 in *High-Velocity Impact Phenomena,* Ray Kinslow, ed. (Academic Press, New York, 1970).

10 Wolfgang Merzkirch, *Flow Visualization* (Academic Press, New York, 1974).

11 Ya. B. Zel'dovich and Yu. P. Raizer, *Physics of Shock Waves and High-Temperature Hydrodynamic Phenomena,* vol. 2 (Academic Press, New York, 1967).

12 Private communication with Jeff Saltzman (Los Alamos).

13 Joseph N. Fritz (Los Alamos), manuscript in preparation.

14 H. W. Liepmann and A. Roshko, *Elements of Gasdynamics* (John Wiley & Sons, New York, 1957), Chapter 2.

15 Calculation of this estimate by Robert Fuehrer involved solving the shock-tube performance equation implicitly using the Newton-Raphson iteration procedure; to be published as a Los Alamos Report.

TURBULENCE TRANSPORT MODELING OF UNSTEADY MULTIMATERIAL FLOWS : CALIBRATION OF MODEL CONSTANTS.

D.C. **Besnard**, M. **Bonnefille**, P. B. **Spitz**,
Centre d'Etudes de Limeil-Valenton
94195 Villeneuve-St-Georges CEDEX FRANCE
and
F.H. **Harlow**, R.M. **Rauenzahn**,
Los Alamos National Laboratory,
Los Alamos, N.M. 87545 USA

ABSTRACT

A family of turbulence transport models for unsteady multimaterial flows is presented as well as the calibration of some model constants versus incompressible turbulent flows.

I INTRODUCTION

Turbulence transport modeling has a long history of successful engineering applications and recurrent theoretical problems. The latter are due to the procedure itself that is used to derive such models. The underlying assumption in such models is that one can describe a class of turbulent flows with a very small of number a variables, which, in turn, implies that there is a kind of spectral equilibrium in the fluid such that low order moments are enough to describe, on the average, the behavior of this class of flows. However, introducing other complexities such as buoyancy /1-2/, and/or compressibility involves other turbulent correlations for which one does have to derive evolution equations, because of the additional physical processes one has to take into account. This in turn means a few more of the so-called "universal" coefficients in the models, which take care of the physics not described explicitly by the models; hopefully, in the applications that are considered, this part of the physics is not important and allows to consider these coefficients as constant.

We are interested here in describing multimaterial compressible turbulent flows; the different materials are not necessarily mixed initially, which brings in the additional complexity of the modeling of the mixing process itself. We have come to realize it is necessary to keep evolution equation for a number of second order correlations, namely the Reynolds stress tensor components (or its contraction), the fluctuating mass flux, and the density self-correlation. Regarding dissipation variables, it is useful to consider the corresponding ones /2/, but we probably can get away by just keeping an ε equation; this is due to the lack of support for dissipation equations in general.

In Section II, we will therefore present such a second order model, that keeps evolution equations for the Reynolds tensor, the turbulent mass flux, and the density self-correlation, as well as the corresponding dissipation variables. The choice of a mixture equation of state (EOS) is also briefly recalled, as well as the basic ideas to model correlations. Section III is devoted to obtaining plausible values for the coefficients that appear in the model, using some data available in the literature, ranging from single material incompressible flows to incompressible mixtures.

II EQUATIONS OF A SECOND ORDER MODEL

II-1 Mean flow equations

We use here Favre-averaged variables (denoted by the variables without bar) to obtain, from the original conservation laws:

$$\frac{\partial}{\partial t}\overline{\rho} + \nabla.(\overline{\rho}\,u) = 0 \quad , \tag{1}$$

$$\frac{\partial}{\partial t}(\overline{\rho}\,\tilde{u}) + \nabla.(\overline{\rho}\,\widetilde{uu}) = -\nabla\overline{P} + \nabla.\overline{\rho\nu\nabla u} - \nabla.(\overline{\rho uu} - \overline{\rho}\,\widetilde{uu}), \qquad (2)$$

$$\frac{\partial}{\partial t}(\overline{\rho}\,\tilde{I}) + \nabla.(\overline{\rho}\,\widetilde{uI}) = -\overline{P\nabla.u} + \nabla.\overline{\rho\chi\nabla T} - \nabla.(\overline{\rho uI} - \overline{\rho}\,\widetilde{uI}). \qquad (3)$$

where I denotes internal energy. In Eq.(2), appears the divergence of a generalized Reynolds tensor, that will be denoted by **R** such as $\mathbf{R} = \overline{\rho uu} - \overline{\rho}\,\tilde{u}\,\tilde{u}$. Similarly, in Eq.(3), we obtain a turbulent heat flux, denoted here by $\mathbf{S} = \overline{\rho uI} - \overline{\rho}\,\tilde{u}\,\tilde{I}$. In addition, we rewrite the pressure velocity correlation in Eq.(3) as $-\overline{P}\,\nabla.u + PV$, where PV is the term that cannot be expressed in terms of the mean flow variables.

II-2 Mixture equation-of-state

For most materials and equations-of-state, the stiffened gas EOS is a very good local approximation, as long as the coefficients in that equation are adjusted. Let us consider this approximate EOS, involving the two coefficients γ and P_0 : $I = \frac{P+\gamma P_0}{(\gamma-1)\rho}$. From it, it is easy to obtain a mixture EOS. Combining two such equations (for materials 1 and 2), and using a pressure equilibrium assumption, we obtain for the mixture an equation of the same type, and its two coefficients γ and P_0 are :

$\frac{1}{\gamma-1} = \frac{\alpha_1}{\gamma_1-1} + \frac{\alpha_2}{\gamma_2-1}$, and $\frac{\gamma P_0}{\gamma - 1} = \frac{\alpha_1 \gamma_1 P_{01}}{\gamma_1 - 1} + \frac{\alpha_2 \gamma_2 P_{02}}{\gamma_2 - 1}$, where α_1 and α_2 are the volume fractions of materials 1 and 2.

II-3 Physical assumptions

We therefore have three quantities, R, S, PV, that we have either to model or derive evolution equations for. To simplify our task, we restrict ourselves to the following set of circumstances:

- our goal is to study instability induced mixing, and, as a first step, we consider that part of the spectrum of scales for which microscopic diffusion is small compared to the macroscopic perturbations created during the development of the instabilities inducing this mixing,

- we also assume that the Mach number of the velocity fluctuations ($M'=\sqrt{k}/c$, where c is the sound speed in the mixture) is small. This is equivalent to assume (for example through an expansion in M') that the divergence of the velocity is negligible (this excludes supersonic slip in a flow); therefore, there is local equilibrium of the pressures in the different materials. However, nothing is implied in terms of temperatures. Their equilibrium depends upon the turbulent and molecular Prandtl numbers. Notice here that the two length scales -turbulence length scale and mixture length scale- are strongly linked, because the very process of the mixture formation is due to instability development and the subsequent turbulence. In terms of a transport model where one considers only one mean scale for the turbulence, this means that the turbulence length scale cannot be much smaller than the mixture length scale. This is exemplified by the choice of certain models /3/ of a constant ratio between those two quantities.

This assumption breaks down in the vicinity of shocks. Consider for example a shock interacting with a perturbed interface separating two fluids. An early pressure map shows that there is no pressure equilibrium on the interface perturbation length scale, as expected. Also, due to our ensemble averaging procedure, we cannot describe the detailed distortions of the shock passing through a macroscopic mixture. All we can hope for is to obtain a good estimate of the density, energy, and fluctuating energy jumps

across the shock. As a simplifying assumption, we neglect the self consistent interaction of the shock and the fluctuating field.

Our hypothesis of negligible microscopic interfacial exchanges and of local pressure equilibrium implies that fluctuations in density, pressure and internal energy occur only through intermittence. In fact, we obtain this result because only mean scales for the mixture and the velocity fluctuations (respectively L_m and L_t) were considered. We have $L_m/c_s << L_t/\sqrt{k}$, where c_s is the mixture sound speed, and k is the local fluctuating energy. However, the mixing of the two fields induces the generation of an entire spectrum of sizes for eddies and droplets of different materials; for a given size, the absence of pressure fluctuations within each field is true, only if $L_m\delta/c_s << L_t\delta/\sqrt{k\delta}$, where δ denotes a specific range of entity sizes. We therefore recognize the possibility of large scale fluctuations (compared to the mean two-field length scale), and that is why we model the term PV, that takes these fluctuations into account. However, we fully use our above assumption to obtain a simple mixture EOS that depends only upon intermittence, and not explicitly upon turbulence energy.

II-4 Correlation evolution equations

From Eqs.(1-3), we can easily obtain evolution equations for **R** and S. They write :

$$\frac{\partial R_{ij}}{\partial t} = -\frac{\partial}{\partial x_k}\left(\overline{m_i m_j m_k/\rho^2} - \overline{m_i}\,\overline{m_j}\,\overline{m_k}/\overline{\rho}^2\right) + \frac{\overline{m_j}}{\overline{\rho}}\frac{\partial R_{ik}}{\partial x_k} + \frac{\overline{m_i}}{\overline{\rho}}\frac{\partial R_{jk}}{\partial x_k}$$
$$+ \frac{\overline{m_j}}{\overline{\rho}}\frac{\partial \overline{P}}{\partial x_i} + \frac{\overline{m_i}}{\overline{\rho}}\frac{\partial \overline{P}}{\partial x_j} - \overline{\frac{1}{\rho}\left(m_j\frac{\partial P}{\partial x_i} + m_i\frac{\partial P}{\partial x_j}\right)} - \varepsilon_{ij}, \qquad (4)$$

$$\frac{\partial S_i}{\partial t} = -\frac{\partial}{\partial x_k}\left(\overline{m_i m_k I/\rho^2} - \overline{m_i}\,\overline{m_k}\,\overline{I}/\overline{\rho}^2\right) + \frac{\overline{I}}{\overline{\rho}}\frac{\partial R_{ik}}{\partial x_k} + \frac{\overline{m_i}}{\overline{\rho}}\frac{\partial S_k}{\partial x_k}$$
$$+ \frac{\overline{I}}{\overline{\rho}}\frac{\partial \overline{P}}{\partial x_j} - \overline{\frac{I}{\rho}\frac{\partial P}{\partial x_i}} + \frac{\overline{m_i}}{\overline{\rho}}\overline{P\frac{\partial(m_k/\rho)}{\partial x_k}} - \overline{\frac{m_i}{\rho}P\frac{\partial(m_k/\rho)}{\partial x_k}} - \varepsilon_i^S. \qquad (5)$$

where m_i is the mixture momentum. In Eq.(4), ε_{ij} denotes the dissipation of large scale fluctuations into small scale fluctuations. Similarly, ε_i^S denotes dissipation of S. The three last terms in Eq.(5) are the pressure-velocity correlations and denoted by Π_{ij}, which can be rewritten as follows :

$$\Pi_{ij} = \overline{P'\left(\frac{\partial u'_j}{\partial x_i} + \frac{\partial u'_i}{\partial x_j}\right)} - \left(\frac{\partial \overline{P'u'_j}}{\partial x_i} + \frac{\partial \overline{P'u'_i}}{\partial x_j}\right) + \frac{1}{\overline{\rho}}\left(A_j\frac{\partial \overline{P}}{\partial x_i} + A_i\frac{\partial \overline{P}}{\partial x_j}\right) \qquad (6)$$

where $A_i = \overline{\rho' u'_i}$ is the fluctuating mass flux. Its evolution equation can write:

$$\frac{\partial A_i}{\partial t} = -\frac{\partial}{\partial x_k}\left(A_i\overline{u_k}\right) - A_k\frac{\partial \overline{u_i}}{\partial x_k} - T_{ik}\frac{\partial \overline{\rho}}{\partial x_k} - \frac{\partial X_{ik}}{\partial x_k} - \overline{\frac{\rho'}{\rho}\frac{\partial P'}{\partial x_i}} + \frac{\overline{\rho'^2}}{\overline{\rho}^2}\frac{\partial \overline{P}}{\partial x_i}. \qquad (7)$$

$$\frac{\partial A_i}{\partial t} = -\frac{\partial}{\partial x_k}\left(A_i \overline{u_k}\right) - A_k \frac{\partial \overline{u_i}}{\partial x_k} - T_{ik}\frac{\partial \overline{\rho}}{\partial x_k} - \frac{\partial X_{ik}}{\partial x_k} - \overline{\frac{\rho'}{\rho}\frac{\partial P'}{\partial x_i}} + \overline{\frac{\rho'^2}{\rho^2}}\frac{\partial \overline{P}}{\partial x_i}. \quad (7)$$

The correlation $\overline{\rho'^2}$ (that will be denoted by B in what follows) describes density inhomogeneities effects on the turbulence. We again look for an evolution equation and get Eq.(8) :

$$\frac{1}{2}\frac{\partial B}{\partial t} = -\frac{1}{2}\overline{u_k}\frac{\partial B}{\partial x_k} - B\frac{\partial \overline{u_k}}{\partial x_k} - A_k\frac{\partial \overline{\rho}}{\partial x_k} - \overline{\rho}\,\overline{\rho'\frac{\partial u'_k}{\partial x_k}} - \overline{\rho' u'_k}\frac{\partial \rho'}{\partial x_k} + \overline{\rho'^2}\frac{\partial u'_k}{\partial x_k}.$$

II-5 Closures

To model correlations, we proceed in the following way : we propose, for each term to be modeled, the simplest, dimensionally correct, in a correct tensor formulation, linear or quadratic expression satisfying its intrinsic properties. We also make use of our hypothesis of subsonic fluctuations, and neglect terms involving the divergence of velocity fluctuations; we also neglect correlation of higher order than ρ'^2. This leads to the following resulting model :

$$\rho\left(\frac{dK^{ij}}{dt} + K^{ik}\nabla_k u^j + K^{jk}\nabla_k u^i\right) = C_{K1}\rho\sqrt{D}\left(k\frac{\delta^{ij}}{3} - K^{ij}\right) + A^i\nabla_k P^{jk} + A^j\nabla_k P^{ik}$$
$$+ \nabla_k\left(\alpha_K\rho\frac{k}{\sqrt{D}}\nabla^k K^{ij}\right) - C_K\rho\sqrt{D}K^{ij} - \frac{30C_{K2}-2}{110}\rho k\left(\nabla^j\overline{u}^i + \nabla^i\overline{u}^j - \frac{2}{3}\delta^{ij}\nabla_l\overline{u}^l\right)$$
$$+ \frac{8+C_{K2}}{11}\rho\left(K^{ik}\nabla_k\overline{u}^j + K^{jk}\nabla_k\overline{u}^i - \frac{2}{3}\delta^{ij}K_l{}^k\nabla_k\overline{u}^l\right)$$
$$+ \frac{8C_{K2}-2}{11}\rho\left(K^i{}_k\nabla^j\overline{u}^k + K^j{}_k\nabla^i\overline{u}^k - \frac{2}{3}\delta^{ij}K_l{}^k\nabla_k\overline{u}^l\right) \quad (9)$$

$$\rho\frac{dA^i}{dt} + K^{ik}\nabla_k\rho - \rho\nabla_k(A^iA^k) - \rho A^k\nabla_k A^i + \rho A^k\nabla_k u^i = \nabla_k\left(\alpha_a\rho\frac{k}{\sqrt{D}}\nabla^k A^i\right) + \frac{B}{\rho}\nabla_k P^{ik} - C_a\rho\sqrt{D}A^i \quad (10)$$

$$\rho\frac{dB}{dt} + \rho B\nabla_k u^k + 2\rho A^k\nabla_k\rho - \rho A^k\nabla_k B - BA^k\nabla_k\rho - 2\rho B\nabla_k A^k = \nabla_k\left(\alpha_B\rho\frac{k}{\sqrt{D}}\nabla^k B\right) - C_B\rho\sqrt{D}B \quad (11)$$

$$\rho\left(\frac{dD^{ij}}{dt} + D^{ik}\nabla_k u^j + D^{jk}\nabla_k u^i\right) = C_{D1}\rho\sqrt{D}\left(D\frac{\delta^{ij}}{3} - D^{ij}\right) + Da^i\nabla_k P^{jk} + Da^j\nabla_k P^{ik}$$
$$+ \nabla_k\left(\alpha_D\rho\frac{k}{\sqrt{D}}\nabla^k D^{ij}\right) - C_D\rho\sqrt{D}D^{ij} \quad (12)$$

$$\rho\frac{dDa^i}{dt} + C_{Da1}D^{ik}\nabla_k\rho = \nabla_k\left(\alpha_{Da}\rho\frac{k}{\sqrt{D}}\nabla^k Da^i\right) - \rho Da^k\nabla_k u^i + C_{Da2}\frac{D_B}{\rho}\nabla_k P^{ik}$$

$$= \nabla_k\left(\alpha_{DB}\rho\frac{k}{\sqrt{D}}\nabla^k D_B\right) - C_{DB}\rho\sqrt{D}D_B \qquad (14)$$

III - MODEL CONSTANTS

III-1 Methodology

As any other, this model contains unknown coefficients due to closure occuring in its formulation (here 18). These coefficients are considered as "universal" (i.e. valid for a certain class of flows having the same thermodynamical properties), and are supposed to contain the physics not included in the model. In order to obtain these constants, we simplify this model for simple circumstances, and make comparisons with experimental data.

III-2 Determination of model constants

III-2-1 Isotropic homogeneous turbulence

In the case of isotropic homogeneous turbulence, Eqs. (9-14) reduce simply to :

$$U_0\frac{dk}{dx} = -c_k\sqrt{D}\,k \quad , \quad U_0\frac{dD}{dx} = -c_D\sqrt{D}\,D \quad .$$

where U_0 is the constant grid velocity. Experimental results show that turbulence decays as x^{-p}, which leads to the following relationship, by solving the previous system :

$$C_k = \frac{P}{2}\,C_D .$$

III-2-2 Turbulent diffusion

Experiments /4/ show that the turbulence intensity drops off exponentially away from an effective source plane. We therefore assume that :

$k(x) = A_k\,x^{-n}$ and $D(x) = A_p\,x^{-m}$ where A_k and A_D are constant.

This leads to: $c_D\,\alpha_k = 0.103\,\frac{1}{p}$ and $c_D\,\alpha_D = 0.086\,\frac{1}{p^2}$.

III-2-3 Boundary layer flow

The classic modeling of boundary layer flow assumes a constant turbulent shear

$Kxy = -\frac{\tau}{\rho}$ and a universal velocity law (law of the wall) $\frac{\partial u_x}{\partial y} = \sqrt{\frac{\tau}{\rho}}\,\frac{1}{\chi\,y}$

where $\chi = 0.41$ stands for the von Karman constant. By inserting these relations in Eqs. (9-14), we get 8 equations with 7 unknowns. Therefore, we obtain a compatibility relation which writes:

$$0 = 2\sqrt{2}\,\alpha_D\,(c_D + c_{D1})\,(3\,c_D + c_{D1})\,\frac{c_k + c_{k1}}{c_k}\,M^{3/2}$$

$$-8\,\alpha_D{}^2\,\chi^2\,(3\,c_D + 2\,c_{D1})\,\frac{c_k + c_{k1}}{c_k{}^2} + 16\sqrt{2}\,\alpha_D{}^3\,\chi^4\,\frac{c_k + c_{k1}}{c_k{}^3}\,M^{-3/2}$$

$$-c_D\left(\frac{c_D + c_{D1}}{c_k + c_{k1}}\right)^2\frac{1}{\chi^2}\,M^3 + \frac{c_{D1}}{3}\,\frac{1}{\chi^2}\,M^2 \quad ,$$

with $\lambda = \frac{2}{(c_k + c_{k1})^2} M$, and $M = \frac{2}{15}\frac{c_{k1}}{c_k} + \frac{-5 c_{k2}^2 - 10 c_{k2} + 9}{55}$.

Moreover, the experiment leads to $k = \frac{2}{0.3}\frac{\tau}{\rho}$, which can also be written as

$1 + \frac{c_{k1}}{c_k} = \frac{\sqrt{2}}{0.3} M^{1/2}$.

III-2-4 Transversal velocity gradient flow

In this case, we assume a velocity field such that $\frac{\partial U}{\partial y} = \alpha$ (constant) . Balancing production and dissipation, Eqs. (9-14) finally provide expressions for $\frac{K_{ii} - \frac{1}{3}k}{k}$, i = 1, 2, 3 (denoted Ω_i), and $\frac{K_{xy}}{k}$ (denoted Ω_4), functions of c_{k2} and $\frac{c_{k1}}{c_k}$. The experimental values of Ω_i can be found in Rose /5/ and Champagne /6/. For each experiment, we have 4 relations between c_{k2} and c_{k1}/c_k, in which only 3 are independent. The solution to this system is obtained graphically (Fig. 1 and 2). An averaged one is :

EXPERIMENT	c_{k2}	c_{k1}/c_k
ROSE	0.341	0.948
CHAMPAGNE	0.344	0.565

This leads to:

$c_k = -2\,\Omega_4\,(c_{D1} + c_D)\sqrt{\frac{3\,c_D}{2\,c_{D1}}}$,

with $\Omega_4 = -0.163$ (Rose /5/)

-0.171 (Champagne /6/)

III-2-5 Homogeneous turbulence uniform distortion

The velocity field is given by : $U_k = G_{ki}\,x_i + B_k$. The experimental case studied by Townsend /7/ corresponds to the following matrix :

$$G_{ki} = \begin{pmatrix} 0 & 0 & 0 \\ 0 & -\alpha & 0 \\ 0 & 0 & \alpha \end{pmatrix} \quad \text{with } \alpha \text{ constant} ,$$

and $U = B_k$, $V = -\alpha y + By$ and $W = \alpha z + B_z$. As in the previous case, we find 3 relationships between c_{k2} and c_{k1}/c_k. Due to experimental errors, the 3 relationships $c_{k2} = f(c_{k1}/c_k)$ form a triangle in the plane $(c_{k1}/c_k, c_{k2})$. We choose a plausible solution as being the triangle center of gravity. We obtain $C_{k2} = 0.66$, $\frac{C_{k1}}{C_k} = 0.76$. This leads to (with $\omega_2 - \omega_3 = 0.35$) :

$$c_k = (\omega_2 - \omega_3)(c_{D1} + c_D)\sqrt{\frac{1}{1 + \frac{2\,c_{D1}}{3\,c_D}}} ,$$

III-2-6 Coefficient values

We sum up here the above results: $C_{k2} = 0.45$ and $\frac{C_{k1}}{C_k} = 0.76$

EXPERIMENT	c_D/c_k	c_{D1}/c_k	p	$c_k \alpha_D$	$c_k \alpha_k$
ROSE	1.04	3.63	1.92	0.022	0.052
CHAMPAGNE	0.89	4.44	2.25	0.019	0.052

with $\omega_2 = 0.52$ and $\omega_3 = 0.13$ from /8/. We put an additional constraint on our model. It has to reduce to a simpler model /9/, at least partially. This translates into:

$$\varepsilon = c_k\, k \sqrt{D} = 2\, \nu_t\, D \quad \text{with} \quad \nu_t = \alpha_k\, c_k \frac{k^2}{\varepsilon} \ ,$$

which implies: $c_k = 2\, \alpha_k$. This leads to : $c_k = 0.32$ and then, by considering only average values:

c_k	c_{k1}	c_{k2}	c_D	c_{D1}	α_k	α_D
0.32	0.25	0.45	0.31	1.30	0.16	0.06

III-3 Grid turbulence in a stably stratified fluid

We consider the experiment by Itsweire *et al* /10/ on a grid turbulence decaying in a stably stratified fluid. This model is simplified in this case on the basis of the following hypothesis:

- homogeneous stationary turbulence,
- incompressible fluid,
- constant pressure and density gradients in the direction perpendicular to the main flow,
- isotropic dissipation tensor.

In addition, we assume: $K_{zz} = \frac{k}{\alpha}$ and α constant. The original system reduces then to six equations. We denote the Brunt-Vaïsälä frequency by N:

$$N^2 = -\frac{g}{\rho}\frac{\partial \rho}{\partial z} = \text{constant} \quad \text{with} \quad \frac{\partial P}{\partial z} = -\rho g \ .$$

Assuming that N is constant and production balances dissipation in B and D_B equations, it appears that we must assume that: $3\, c_{Da2} + c_{Da1} = 0$, $c_{DB} = c_D$. In that particular case, we can exhibit theoretical expressions for k, D, Da_z and D_B, a_z and B depending on these four quantities. These two relations can be written as:

$$\frac{N^2 k^2}{g\, a_z\, \varepsilon} = A_1 \frac{g\, B\, k}{\rho\, a_z\, \varepsilon} + B_1 \ ,$$

and

$$\frac{2\, N^2 k^2}{\varepsilon^2} = A_2 \frac{N^2 k^2}{g\, a_z\, \varepsilon} + B_2 \ .$$

with : $A_1 = \alpha$, $B_1 = \alpha \frac{c_a}{c_k}$, $A_2 = \frac{c_B - c_k}{(1+\alpha)\, c_k}$, $B_2 = \frac{\alpha\, c_a\, (c_D - c_B)}{(1+\alpha)\, c_k^2}$.

Experiments were carried out considering two Reynolds numbers. For each case, we estimate the values of model constants from a least squares approximation based on experimental measurements. We obtain:

M	α	c_D/c_k	c_a/c_k	c_B/c_k
3.81	3.279	0.971	3.179	2.813
1.905	3.895	1.115	4.352	1.981

For the higher Reynolds number (M = 3.81, Re = 10^4), we find: $c_D/c_k = 0.97$,which is compatible with the previous values found for c_D and c_k ($c_D/c_k = 0.968$). We finally get the following set of constants:

c_k	c_D	c_B	c_a	c_{k1}	c_{k2}	c_{DB}	c_{D1}	α_k	α_D
0.32	0.31	0.90	1.02	0.25	0.45	0.31	1.30	0.16	0.06

together with the relationship: $3\, c_{Da2} + c_{Da1} = 0$. Going back to the solutions k(x) and D(x), using the above values in our model, and comparing with the experimental profiles, we find a fairly good agreement between the experiment and the analytic solution, as it can be seen on Figure 3.

IV CONCLUSION.

This exercise shows the difficulties associated with the determination of the so called universal constants in turbulence transport models. We note, in effect, that not even experiments agree together, which casts some doubts on the proposed set of constants. However, the procedure in itself is very promising and useful. This paper shows, once again, the necessity of well-instrumented and precise experiments. We also note the well-known drawback associated with such a model.

There are 18 unknown constants and only 10 (1 relationship between two other ones) are determined here. More work is necessary and we plan to use additional experiments, among them the Read and Youngs rocket-rig experiments /3/, as well as rapid distortion theory. The remaining constants will have to be determined using shock tube experiment data. Even so, we do not expect this model to give essentially better results for a given family of flow than a simpler one geared toward this particular type of flow, but more to cover a wide range of flow.

REFERENCES.

/1 / W.P. Jones, in "Predictions Methods for Turbulent Flows", W. Kollmann Editor, Hemisphere Publishing Corporation, New York, 379 - 421, (1980).

/2 / J.L. Lumley, O. Zeman, and J. Siess, J. Fluid Mech., 84, 581-597, (1978).

/3 / D.L. Youngs, Physica D 37, 270, (1988).

/4 / A. Sonin, Phys. Fluid, 26, 10, (1983).

/5 / W.G. Rose, J. Fluid Mech., 25, 97, (1966).

/6 / F.H. Champagne, V.G. Harris, and S. Corrsin, J. Fluid Mech, 41, 1- 81, (1970).

/7 / A.A. Townsend, in "The structure of turbulent shear flow", Cambridge University Press, (1956).

/8 / H.J. Tucker, A.J. Reynolds, J. Fluid Mech., 32, 4, 657, (1968).

/9 / B.E. Launder, D.B. Spalding, Comp. Meth. in Appl. Mech. and Eng., 3, 269, (1974).

/10/ E.C. Itsweire, K.N. Helland, and C.W. Van Atta, J. Fluid Mech., 162, 299, (1986).

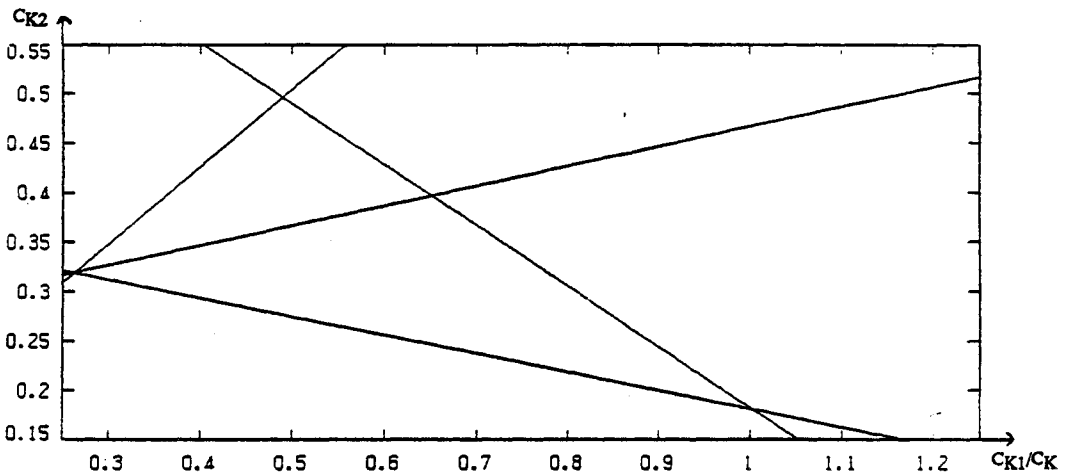

Figure 1 (CHAMPAGNE)

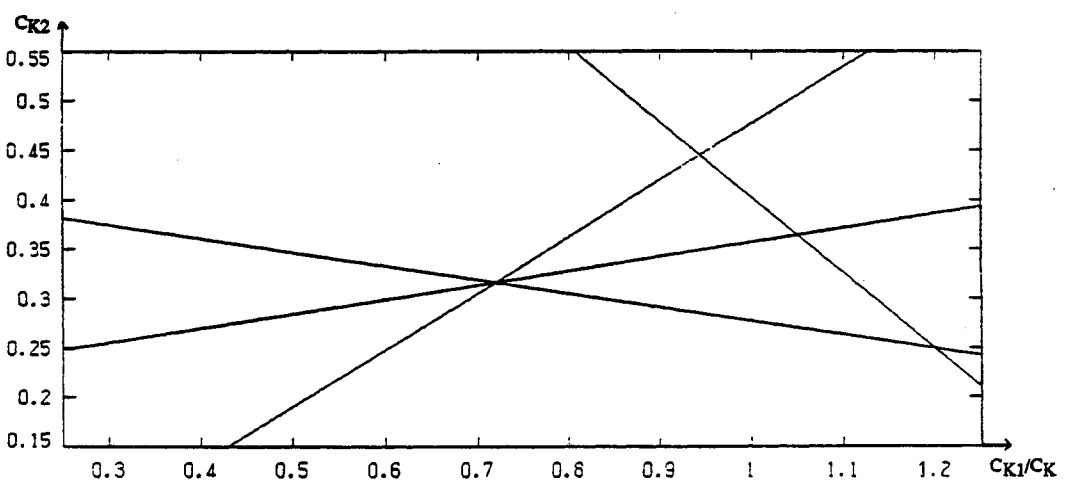

Figure 2 (ROSE)

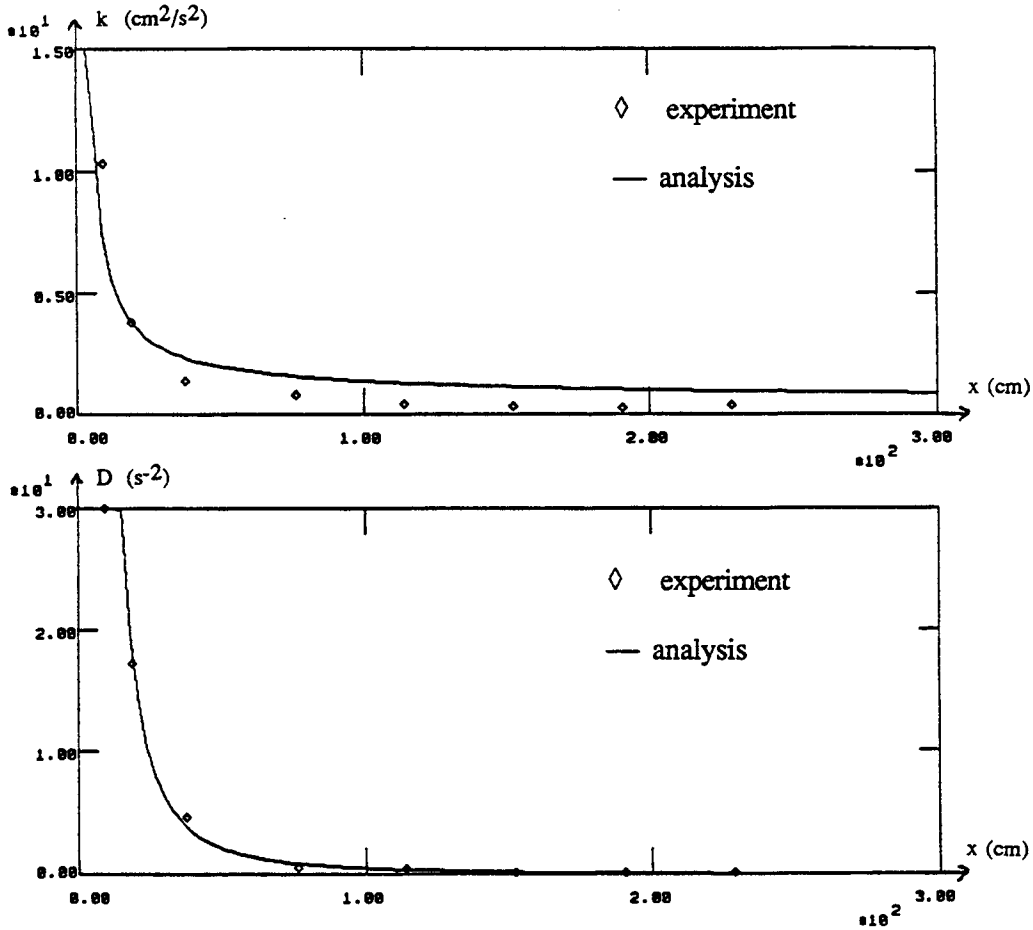
k (cm2/s2)
1.50
1.00
0.50
0.00
◊ experiment
— analysis
x (cm)
0.00
1.00
2.00
3.00
D (s-2)
3.00
2.00
1.00
0.00
◊ experiment
— analysis
x (cm)
0.00
1.00
2.00
3.00

Figure 3

SIMULATION OF SINGLE MODE RICHTMYER-MESHKOV INSTABILITY USING THE ADAPTIVE FREE LAGRANGE METHOD

Donald E. Burton and Alan K. Harrison
Lawrence Livermore National Laboratory
Livermore, California

ABSTRACT

Because of extreme deformation, instability problems have been traditionally modeled using *Eulerian* techniques or *Arbitrary Lagrange Euler* (ALE) techniques. The *free-Lagrange* (FL) method first introduced by Crowley[1] offers a third basic alternative. The specific FL method described in this paper consists of: (1) a 2D staggered-grid hydrodynamics[2] (SGH) differencing scheme appropriate to an unstructured mesh consisting of triangular and quadrilateral zones; (2) a set of primitive mesh optimization algorithms; and (3) a set of rules for *adaptive mesh refinement* which we refer to as the *adaptive free Lagrange* (AFL) method.

In a previous study, Burton[3] showed that the spurious vorticity commonly associated with SGH differencing results from a failure to explicity conserve angular momentum in the difference equations. This led to a significantly improved technique for removing the spurious vorticity, called *spurious vorticity damping* (SVD). SVD was shown to produce superior results in a test problem which had no intrinsic vorticity. In the present study, SVD is shown to also produce superior results in a problem with intrinsic vorticity.

The AFL and SVD methods are applied to a low Mach number shock tube problem and compared with other methods. AFL seems to perform as well as Eulerian methods and is somewhat better at resolving fine structures in the calculation. The SVD method produced results far superior to other methods tried.

INTRODUCTION

Because of extreme mesh distortions, instability problems have been traditionally modeled using Eulerian techniques[4,5] or by Arbitrary Lagrange Euler (ALE) techniques[6]. The free-Lagrange (FL) method, first introduced by Crowley[1], offers a third alternative. In FL, space is discretized into zones formed by lines drawn between nodes and is also discretized into nodal control volumes surrounding nodes, forming a median mesh. Two basic forms of FL have evolved. The first uses a staggered-grid hydrodynamics[2] (SGH) differencing scheme in which velocity is centered at the mesh points, but density, pressure, and energy within the zones. The second uses a Godunov[7] differencing scheme and centers all variables at the mesh points[8,9]. The specific FL method described in this paper consists of: (1) a 2D SGH differencing scheme appropriate to an unstructured mesh consisting of triangular and quadrilateral zones; (2) a set of primitive mesh optimization algorithms[10] which includes an ALE scheme suitable for unstructured meshes (FLALE)[11]; and (3) a set of rules for adaptive mesh refinement[12] which we refer to as an adaptive free Lagrange (AFL) scheme.

Because it is well known that SGH suffers from spurious vorticity on the scale of the mesh size, we begin with a discussion of conservation issues in SGH from which follows a method for removing spurious vorticity. Next, the AFL mesh optimization strategy is described. Finally, we apply the FL method to a low Mach number shock tube problem[13] which produces a Richtmyer-Meshkov (RM) instability. The calculation shows that the AFL method is capable of tracking large deformations as well as Eulerian methods do. We also found that the fine details of the calculation, but not the gross features, were sensitive to the numerical method used to remove the spurious vorticity.

CONSERVATION LAWS

Numerical hydrodynamics involves solving numerical analogs of the conservation laws of physics. Traditionally, however, SGH is formulated to exactly conserve only linear momentum. The conservation of energy is only approximate, and the conservation of angular momentum has been largely ignored in published discussions of SGH differencing. Burton[3,14] showed that SGH can be made to simultaneously conserve numerical analogs of momentum, energy, and angular momentum exactly.

It is well known that SGH suffers from spurious vorticity on the scale of the mesh size because some degrees of freedom are unconstrained by the difference equations and are perturbed by discretization approximations. The study[3] showed that *the nodal motion does not conserve angular momentum, while the motion of the zone centers does.* In practical terms, this means that the angular momentum actually conserved by the differencing scheme is decoupled from the motion of the node points, thereby permitting the observed spurious nodal vorticity to occur. These results were found to apply not only to SGH but to any method using a lumped mass approximation in the acceleration equation, such as many Eulerian and Godunov methods.

In the past, several schemes have been reported which are successful in reducing "hourglass" distortion of quadrilateral zones without affecting physical "shear" modes[15,16]. These schemes are not effective against spurious "chevron" distortion because they consider only deformation of single zones. Further, these schemes have been formulated only for quadrilateral zones and are consequently inadequate for FL applications which may involve not only triangles and quadrilaterals, but arbitrary polygonal zones. Burton[17] devised a more general method, termed *angular viscosity* (AV), which can be applied to arbitrary polygons and which is effective against both hourglass and chevron modes without simultaneously damping physical "bending" modes. This method made use of the then empirical observation that the motion of the zone centers is free from the spurious vorticity seen in the nodes.

The recent observation that the motion of zone centers conserves angular momentum led to a significantly improved method for removing the spurious vorticity called the *spurious vorticity damping* method (SVD, but denoted DEV in Reference 3). SVD uses the zonal information to reduce the error in the nodal velocities. In Reference 3, the method was shown to produce superior results in a test problem which had no intrinsic vorticity. In the following, SVD is shown to also produce superior results in a problem having intrinsic vorticity.

ADAPTIVE FREE LAGRANGE METHOD

The primitive mesh operations[10] which are used for triangular and quadrilateral zones are shown in Figure 1. The ability to add and remove mesh objects (zones, nodes, or faces) is inherent in these operations. MERGE and ZAZ remove objects; CREAP and ZONEBUST add objects; FLIP, SPLIT/UNSPLIT reconnect objects; and FLALE relaxes the mesh. The primitive "slide" operations which allow FL to accommodate large shear distortion are the FLIP, SPLIT, and UNSPLIT operations. An earlier mesh optimization philosophy was to remain as Lagrange as possible by optimizing the mesh only when the timestep became unacceptably small or pathological zones such as boomerangs or bowties occur.

While successful for a broad range of problems, this strategy must be extended for others, such as the RM test problem. As a first step in evolving an improved mesh refinement strategy, an algorithm was implemented which (a) added or removed points in order to preserve the original minimum and maximum mesh sizes (stored locally as original zonal areas and aspect ratios) and (b) reconnected as required to link the best nearest neighbor points. Adaptive free Lagrange (AFL) mesh refinement is obtained by extending this notion so that the mesh size is coupled to the physics of the problem, *e.g.*, vorticity. Specifically, *refined mesh sizes* are calculated by multiplying the *original mesh sizes* by a

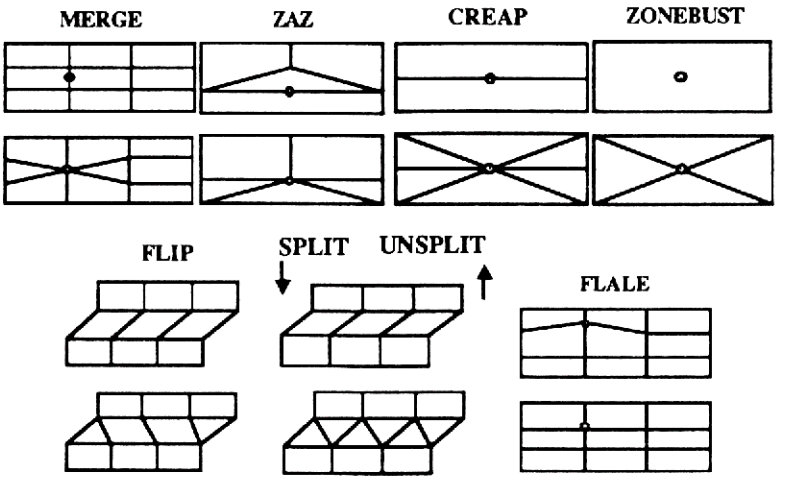

Figure 1. Primitive FL mesh refinement operations for triangular and quadrilateral zones.

refinement factor, which varies from unity to a specified maximum as the magnitude of the vorticity increases. A planned future extension involves the use of an error estimate rather than the vorticity itself.

In the case of the RM test problem, the mesh size was refined by up to a factor of three as the vorticity, which is large near the instability, approached 2×10^4 s^{-1}. Figure 2 illustrates the mesh refinement by overlaying a plot of vorticity on the refined mesh. Nodes were added on edges (CREAP) when the edge stretched by a factor of 1.1 times the refined maximum mesh size; however, the operation was restricted to edges which had rotated by at least 10 degrees with respect to the initial orientation; and no edges shorter than 0.02 cm were created. MERGEs occurred on edges when they had been reduced to 0.8 times the refined minimum mesh size and rotated by at least 10 degrees; and edges longer than 0.02 cm were not merged. The use of factors greater than unity for CREAP and less than unity for

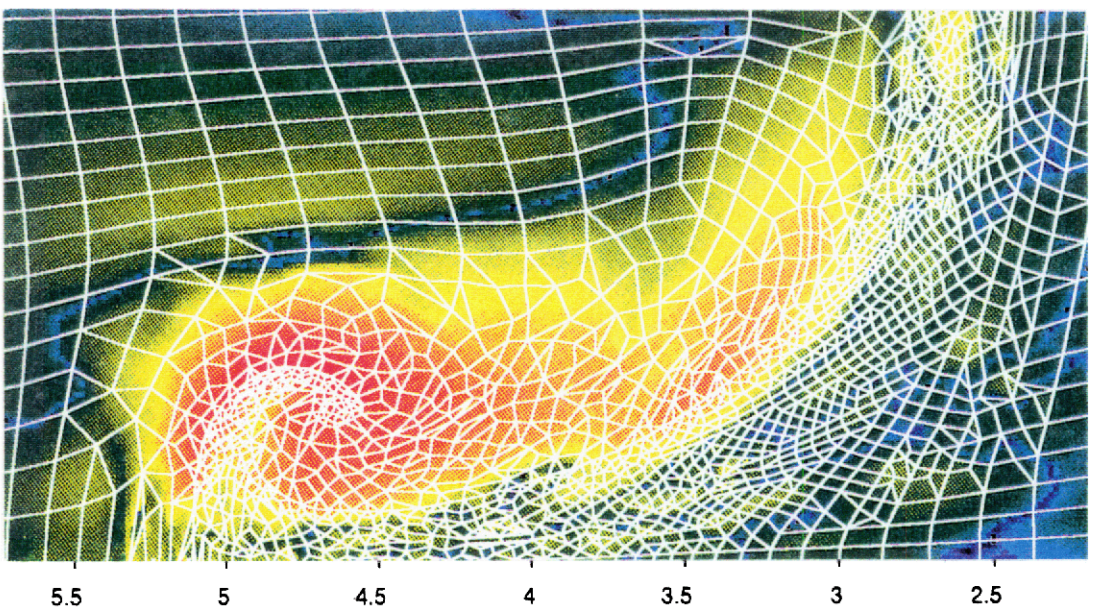

Figure 2. Vorticity Determines Mesh Refinement. Warmer colors denote higher vorticity.

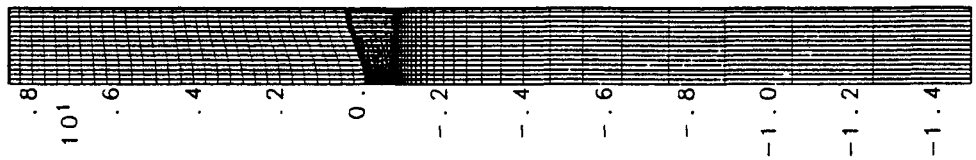

Figure 3. Initial mesh configuration

MERGE introduces hysteresis which is necessary to prevent mesh changes due to minor perturbations. MERGE and ZAZ operations were applied only when the Courant timestep became less than 5×10^{-8} s. A FLALE operation, which involves mesh relaxation and flux-corrected transport (FCT)[18], was applied when the timestep became less than 2×10^{-8} s. The SPLIT/UNSPLIT primitives were used to select nearest neighbors using angle criteria which produces results similar to those of the Voronoi method[19]. Like CREAP/MERGE, the criteria for SPLIT/UNSPLIT is hysteretic. FLIP and ZONEBUST were not used.

TEST PROBLEM

We applied the AFL method to a low Mach number shock tube problem in which an air-Helium interface is perturbed by a single-wavelength displacement, giving rise to a Richtmyer-Meshkov instability. The test problem was denoted TP3 in this conference[13].

The problem consisted of three regions as shown in Figure 3 which were respectively {Helium, air, shocked air}. The corresponding initial conditions were: velocity {0, 0, 12.29=Mach 1.24} cm/ms; density {0.0001694, 0.001225, 0.0017285} g/cm^3; pressure {1.013, 1.013, 1.6482} dyn/cm^2; ratio of specific heats γ {1.67, 1.4, 1.4}. As specified in Reference 13, the shock tube had width W = 7.5 cm

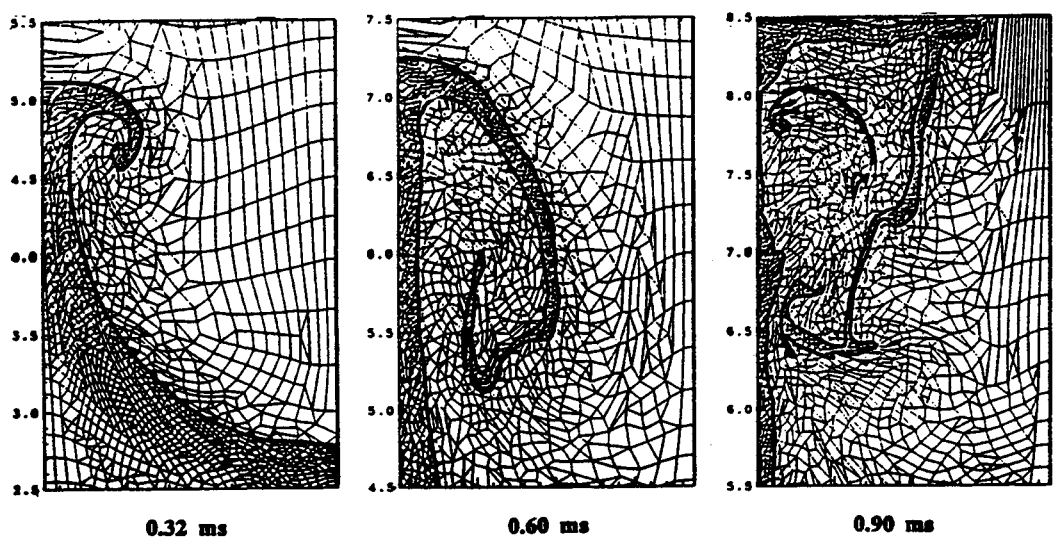

Figure 4. : Zoning in vicinity of the instability at: 0.32, 0.60, 0.90 ms. Rotated 90°.

with reflecting boundaries on the top and bottom. Because of the symmetry of the problem, we reduced the width by a factor of 4. The left boundary was located at x = 8.5 cm and was reflecting. The mean position of the region 1-2 interface was at x=0 and initially had a single wavelength perturbation x= 0.24 *cos* $2\pi(2y/W)$. The region 2-3 interface was located at x = -1.0 cm. The right boundary condition was a constant pressure of 1.6482 dyn/cm^2. The initial time was chosen so that the incident shock crossed x = 0 at t = 0. Specified edit times were 0.12, 0.22, and 0.32 ms. The suggested mesh size (for Eulerian codes) was 0.025 cm. Although our initial zoning was much coarser than this, as shown in Figure 3, the AFL scheme refined down to a size of 0.02 cm.

The right boundary location was not specified in Reference 13 but was taken to be at x = -15 cm, guaranteeing that the shock reflected from it did not reach the material interface by the last requested edit time of 0.32 ms. *Unfortunately, this choice meant that only qualitative comparisons with the results of other calculators could be made after about 0.5 ms.*

Figure 4 shows snapshots of the mesh configuration in the vicinity of the instability at various times throughout the problem. The effects of the adaptive refinement algorithm are clearly visible. Zoning is much finer in areas of high vorticity. The relatively finer zoning in the air spike occurs because the refinement is done relative to the initial zone sizes (Figure 3) which were smaller in the air (about 0.05 cm) than the Helium (0.3 cm) near the interface. Figure 5 shows the density, pressure, and vorticity at 0.32 ms.

Figure 6 shows the number of zones, nodes, and computational cycles plotted versus problem

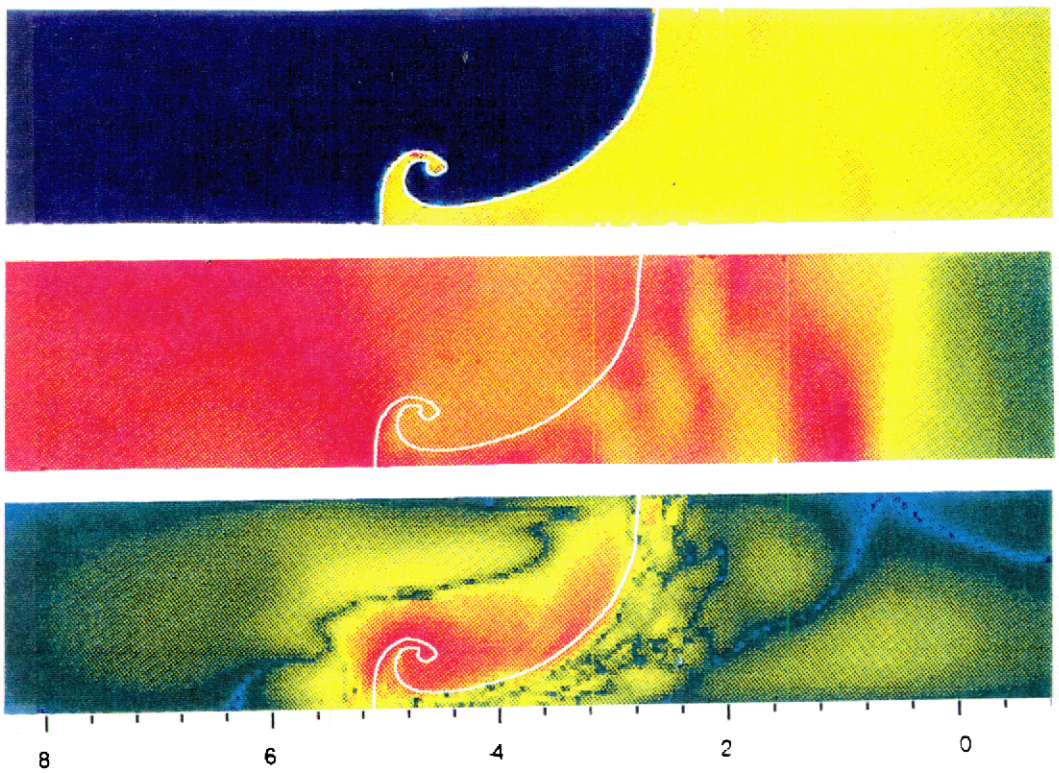

Figure 5. Density, pressure, and absolute value of vorticity at 0.32 ms. Warmer colors denote higher values.

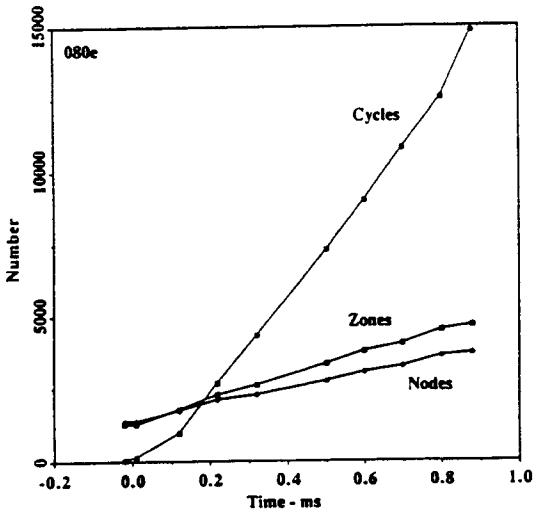

Figure 6. Number of zones, nodes, and cycles vs. problem time. Comparable square Eulerian zoning requires about 110000 zones.

time in the AFL calculation. A comparable Eulerian calculation with 0.02 cm square zoning would have required 110000 zones. However, the great advantage in number of zones is partially offset by the somewhat larger computational overhead required to maintain the FL mesh.

The positions of the bubble and spike are compared in Figure 7, along with the mix width. Also shown are results from an Eulerian calculation due to Wehner[20] and an AMR calculation by Rupert[4]. *Because of the aforementioned differences in problem set up, the calculations cannot be quantitatively compared after about 0.5 ms.* Slight differences in the spike and bubble positions appear at this time because of a reflection off the right-hand boundary of the AFL calculation which was initially at -15 cm. The boundary was located at x = -100 in the Eulerian calculation. Presumably this boundary condition also influenced the large difference in bubble growth which begins at about 0.8 ms. For reasons not currently understood, all of the numerical results show a mixing width which is about twice that observed experimentally[21].

The complete evolution of the material interfaces is shown in Figure 8. The 0.02 cm minimum size specification causes thin features to pinch off (in a mass conserving way) as the problem evolves. Nevertheless, these thin features evolve smoothly and remain clearly identifiable from frame to frame. The AFL results can be compared with the Eulerian Wehner[20] calculation shown in Figure 9. Although differing in some fine details, the results are remarkably similar. The AFL calculation does a somewhat better job of maintaining the integrity of thin features.

Comparative calculations also showed that the SVD method for removing spurious vorticity (described above) produced far superior results to other methods. Figure 10 compares calculations at 0.4 ms using SVD, AV, and a quadrilateral method AHG[16]. In the SVD calculation, the material interface is smooth, and the structure of the "roll up" is well defined. By contrast, in both the AV and AHG calculations, the material interface is relatively rough and tends to break up, presumably because the nodal motion has more structure than is consistent with angular momentum conservation. Although the comparison with AHG is somewhat inappropriate, it was included to make the point that triangles also experience spurious vorticity. Because AHG was developed for quadrilateral codes and had not been intended to be applied to triangles, our implementation of it applied no special damping to triangles in the calculation.

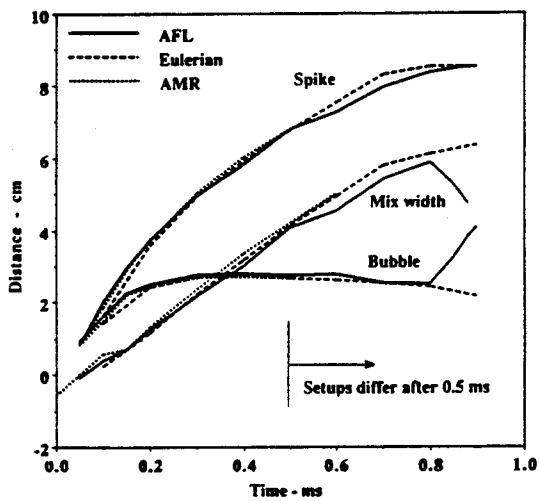

Figure 7. Bubble and spike positions, and mix width for AFL, Eulerian, and AMR calculations.

SUMMARY

We have shown that the AFL method is capable of tracking large deformations which could not otherwise have been done using a Lagrangian method. AFL seems to perform as well as Eulerian methods and is somewhat better at resolving fine structures in the calculation. In particular, AFL seems better at maintaining the smoothness of interfaces, following the folding and bending of filaments, and preserving their continuity.

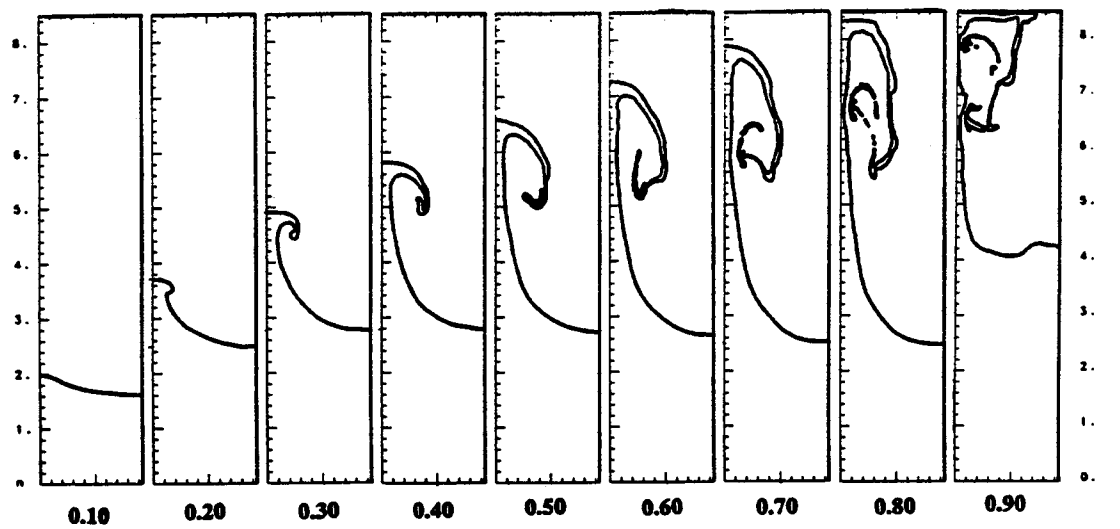

Figure 8. Material interfaces in AFL calculation at various times. Rotated 90°. Problem set up gave rise to differences from Eulerian calculation after 0.5 ms.

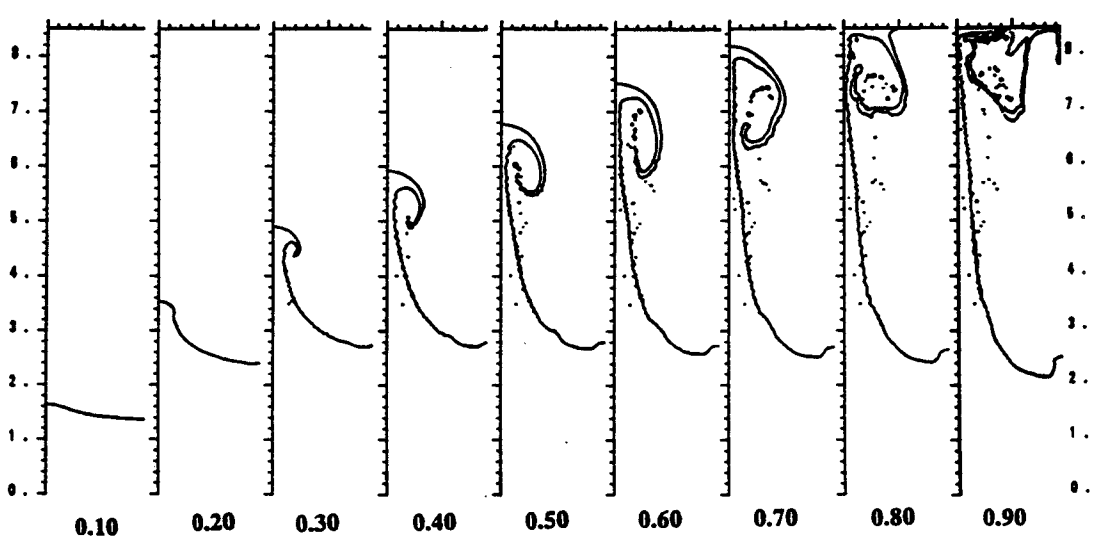

Figure 9. Material interfaces in Eulerian calculation[21] at various times. Rotated 90°.

AFL uses far fewer zones than a comparably resolved Eulerian calculation. Starting with a very coarse mesh compared with the test problem specification, the mesh was refined to the specified resolution only where the physics of the problem dictated. However, the great advantage in number of zones is partially offset by the somewhat larger computational overhead required to maintain the FL mesh.

Both Eulerian and Lagrange SGH differencing methods experience spurious vorticity. We found that the fine details of the test calculation, but not the gross features, were sensitive to the numerical method used to remove the spurious vorticity. We have shown that a new method SVD produced results far superior to other methods tried.

ACKNOWLEDGMENTS

The authors acknowledge Mike Wehner for permission to quote his preliminary results. We also thank Dale Nielsen and Mike Wehner for their helpful comments, and Mike Uyemura and David Hardin for their computer science assistance. The work was performed under the auspices of the U.S. Department of Energy by the Lawrence Livermore National Laboratory under Contract No. W-7405-ENG-48.

REFERENCES

1. W.P. Crowley, "FLAG: A Free-Lagrange Method for Numerically Simulating Hydrodynamic Flows in Two Dimensions," Proceedings of the *Second International Conference on Numerical Methods in Fluid Dynamics*, (Springer-Verlag, New York, 1970), pp. 37-43.
2. J. von Neumann and R. Richtmyer, "A Method for the Numerical Calculation of Hydrodynamic Shocks," *J. Appl. Phys.* **21**, 232 (1950).
3. D.E. Burton, "Conservation of Energy, Momentum, and Angular Momentum in Lagrangian Staggered-Grid Hydrodynamics," Lawrence Livermore National Laboratory Report UCRL JC-105926, November 16, 1990.

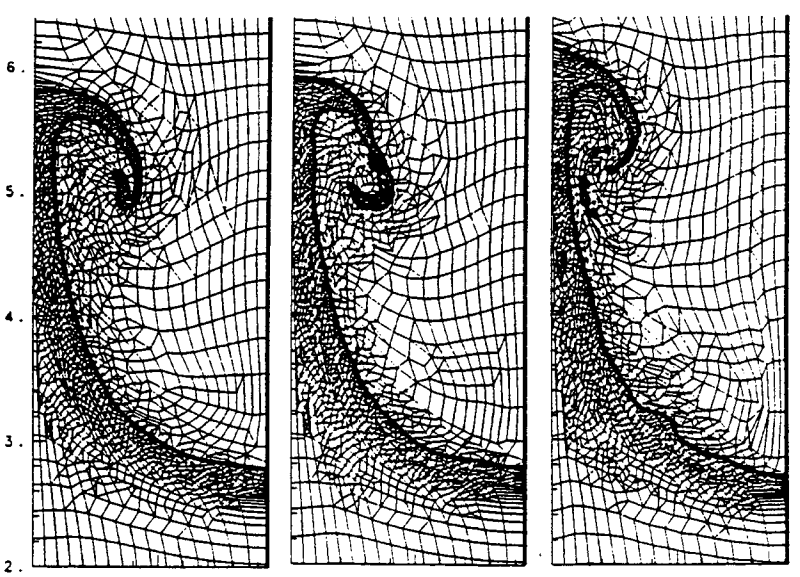

Figure 10. Comparison at 0.4 ms using (a) SVD, (b) AV, and (c) AHG.

4. V. Rupert, "Reference Problems," *Second International Workshop on the Physics of Compressible Turbulent Mixing*, Pleasanton, CA, Nov 1989.
5. M. Wehner, "Pure Eulerian Hydrodynamics Calculations of the Two Standard Test Problems," *Second International Workshop on the Physics of Compressible Turbulent Mixing*, Pleasanton, CA, Nov 1989.
6. K. Mikaelian, "Numerical Simulations of Richtmyer-Meshkov Instabilities in Shock Tubes," *Second International Workshop on the Physics of Compressible Turbulent Mixing*, Pleasanton, CA, Nov 1989.
7. S.K. Godunov, *Mat. Sb.* **47**, 271 (1959).
8. H. Trease, "Three-Dimensional Free Lagrange Hydrodynamics," in *The Free Lagrange Method,* (Springer-Verlag, New York, 1985).
9. R.A. Clark, "The Evolution of HOBO," in Particle Methods in Fluid Dynamics, edited by J.U. Brackbill and J.J. Monaghan, (North-Holland, Amsterdam, 1988).
10. W.P. Crowley, "Free Lagrange Methods for Compressible Hydrodynamics in Two Space Dimensions, " in *The Free Lagrange Method* (Springer-Verlag, New York, 1985).
11. D.E. Burton, "Free Lagrange Advection Slide Lines," Proc. of the *Next Free Lagrange Conference*, Jackson Lake Lodge, Wyoming, June 3-7, 1990. Lawrence Livermore National Laboratory Report UCRL-JC-104257, June 1990.
12. M.J. Berger and J. Oliger , "Adaptive Mesh Refinement for Hyperbolic Partial Differential Equations," *J. Comp. Phys.* **53**, 484 (1984).
13. D. Besnard, "Test Problems for Numerical Roundtable," letter to V. Rupert, March 6, 1991.
14. D.E. Burton, "Exact Conservation of Energy and Momentum in Staggered-Grid Hydrodynamics with Arbitrary Connectivity," Proc. of the *Next Free Lagrange Conference*, Jackson Lake Lodge, Wyoming, June 3-7, 1990. Lawrence Livermore National Laboratory Report UCRL-JC-104258, June 1990.
15. G. Maenchen, and S. Sack, "The TENSOR Code," in *Methods of Computational Physics*, Vol. 3, (Academic Press, New York, 1964).
16. L.G. Margolin and J.J. Pyun, "A Method for Treating Hourglass Patterns," Proc. *Fifth International Conference on Numerical Methods in Laminar and Turbulent Flow*, Montreal, Canada (1987)
17. D.E. Burton, unpublished notes on the Angular Viscosity Method, February 1986.
18. S.T. Zalesak, "Fully Multidimensional Flux-Corrected Transport Algorithms for Fluids," *J. Comp. Phys.* **31**, 335 (1979).
19. G. Voronoi, *Z. Reine Angew. Math.* **134**, 198 (1908).
20. M. Wehner, "2D and 3D numerical instability calculations," *Third International Workshop on the Physics of Compressible Turbulent Mixing*, Abbey de Royaumont, France, June 1991.
21. Robert F. Benjamin, "Experimental results corresponding to standard problem 1," *Second International Workshop on the Physics of Compressible Turbulent Mixing*, Pleasanton, CA, Nov 1989. Los Alamos Rept. LA-UR 89-3832 (revised 12/14/89).

LATE-TIME TURBULENT MIXING OF A HIGH DENSITY GAS BUBBLE IN A SHOCK GAS FLOW (M = 1.14)

Cowperthwaite N, Youngs D, AWE, Aldermaston
Philpott M, Smith A, AWE, Foulness

INTRODUCTION

A series of shock-tube experiments performed at AWE (Foulness) are described and the results compared with the theoretical predictions of Cowperthwaite and Youngs AWE (Aldermaston) using the 2-D code PETRA.

The type of experiment is indicated in Figure 1. A plane shock wave with a flat-top pressure pulse of about 7ms duration propagates along the shock-tube and intercepts a spherical dense gas bubble falling under gravity. By means of shadowgraphs, the development and growth of the bubble is recorded as it is swept downstream.

The shock-tube initially contained air at atmospheric pressure. The bubble gas was freon-12, with density 4.2x greater than air. The shock overpressure was 0.33 bar (5 psi nominal) with flow velocity $76ms^{-1}$.

PREDICTIONS

Figure 2 shows sample predictions of the bubble response which provide a useful basis for interpretation of the experimental observations. The predictions were derived from the PETRA code modelling the problem in 2-D axi-symmetric geometry.

Starting with an initial bubble 3cm in diameter, and shock contact with the front face at time zero (t = o), the time - distance plot shows development of the bubble as it is swept downstream. The time intervals shown are 0.5ms covering the time span 0-5ms, during which the bubble has moved about 20cm.

Observation of the velocities shows that at later times, the front face (upstream end) of the bubble is moving at $47ms^{-1}$, while the downstream end is moving at $67ms^{-1}$. In effect, the bubble extremities are growing apart at $\sim 20ms^{-1}$. Noting that the velocity of the downstream region is essentially that of the flow velocity (less than 0.5ms difference), it is evident that in this region, there is no slippage between bubble and air flow, nor the existence of turbulent mixing.

The active region of the bubble is at the front (upstream end), with the bubble extending in length by virtue of the vortex action induced by the shock passage over it. The distortions and differential motions so induced give rise to a vorticity of sense as to cause movement of the bubble head upstream against the flow. The vorticity initiates a continuous circulation of the freon gas which draws in air which becomes trapped within the interior. The freon gas thereby becomes inhomogeneously diluted and thrown off, moving downstream in a structured formation of connected 'rings' surrounding a central jet. This process tends to repeat at intervals of 1-2ms, thereby maintaining the longitudinal growth of

the bubble.

Although not discernible in Figure 2, each prediction profile is generated as a set of contours representing zones of freon gas concentration. Careful examination of the boundaries shows sharp concentration gradients, limited possibly only by the computational mesh size, indicating the preservation of distinct gas boundaries, consistent with experimental observations. A possible exception is the furthermost downstream region: here there is shadowgraphic evidence of diffuse boundaries, possibly an optical interpretation complicated by low gas concentrations combined with an irregular non-axisymmetric structure.

COMPARISON BETWEEN PREDICTED AND EXPERIMENTAL RESULTS

Figure 3 shows sample experimental (shadowgraph) results, superimposed at the correct scale, and positioned correctly along the time axis. If the comparison with prediction is regarded as qualitative, then the shadowgraphs, more particularly at early times, show generally good agreement. Two of the shadowgraphs are repeated enlarged in Figure 4, showing distinctive features such as the mushroom-shaped head, an axial jet and an optically thin outer shell. Such observations well support the predictions.

If quantitative comparison is considered, then differences are more noticeable, with the observed bubble sizes being larger than predicted. However, several factors underly this observation. Whereas the predictions modelled an initial bubble diameter of 3cm, most of the experimental results shown relate to a larger initial bubble of 3-4cm diameter. Further, the theoretical calculations considered a shock of 0.31 bar (4.5 psi), while the experimental shock pressures were higher at 0.34 bar (5.0 psi). Other differences were that the predictions relate to a cross-section through the bubble whereas the shadowgraphs represent a silhouette outline: also, the predictions do not correctly model the experimental situation because of the axi-symmetric representation of a rectangular cross-section.

COMPUTATIONAL TECHNIQUE

Figure 5 provides details of the PETRA code used for the predicted results with information relevant to the bubble problem.

EXPERIMENTAL ARRANGEMENT

Details of the shock-tube and the test arrangement are provided in Figure 6. The shock-tube featured a rectangular cross-section of 20 x 10cm (8 x 4 inch). The gas bubbles were blown from the end of a pipe projecting from the roof: by careful control of the flow of freon-12 gas and the liquid feed, bubbles were formed at a rate of one every 3 to 4 seconds and fell under gravity to the floor of the shock-tube. Instead of bursting on contact, they instantaneously converted to hemi-spherical shape centred on a small-bore outlet, through which the freon gas was sucked out by a weak vacuum, thereby

avoiding any gas contamination problem due to a layer of freon forming on the floor of the shock-tube.

An electrode arrangement was used which detected the departure of each bubble as it dropped away from the end of the pipe. When suitably dry bubbles (ie of minimum water content, pre-determined by sample weighing as 5% - 10% of the bubble mass) were being formed, the signal from the detector was used to burst the shock-tube diaphragm at a time such that the shock arrival coincided with the bubble having fallen halfway to the floor. As the shock passed the trigger gauge just ahead of the test-section, its signal initiated the sequence of spark sources for the shadowgraph recording system.

NB. An alternative detector system based on deflection of a low power laser beam by the falling bubble has recently been found to offer improved reliability.

Of note in this figure is the reference to the change in cross-section from 20 x 5cm to 20 x 10cm (8 x 2 inch to 8 x 4 inch), (see below).

The plan view of the shock-tube is shown in Figure 7. A divergent section was used to expand the minimum dimension of an existing shock-tube to a size significantly larger than the initial bubble dimension (3-4cm diameter), in order to minimise the influence of bubble confinement. The expansion half-angle was 5° over a length of 30cm; suitability of the design was proved by checking for a vertical plane shock front within the test-section.

The compression chamber was pressurised to 1.59 bar (23 psi), yielding a shock wave duration of approximately 7ms. The end-plate was sufficiently far downstream to avoid the reflected shock from disturbing the shock-wave during the recording period (0 to 6ms).

The bubble was formed at the point shown beween a pair of splash guards to avoid any bursting bubbles from spraying droplets onto the observation windows; the guards were removed before firing the shock-tube.

The shadowgraph system was standard except that it was off-set because of limited working space. The multi-spark source produced four sparks, increased to five on later tests. Four images were recorded on a 5 x 4 inch plate camera plate, the fifth on a separate camera.

SHADOWGRAPH ANALYSIS

Following the visual comparison between prediction and experiment described earlier, the results of the shadowgraph analysis are presented with measurement of bubble (volume) expansion and downstream movement, determined as follows:

Starting with the initial bubble, falling under gravity, the mean radius R_o was measured (mean diameters ranging from 2.4 to 3.9cm), with the observation on sphericity that most of the bubbles showed a variation of no more than 2% between the mean and the largest and smallest diameters. Using the mean radius, the initial bubble volume V_o was then calculated. Considering in turn each of the successive shadowgraphs of the shocked expanding bubble, the volume V(t) was calculated as indicated in Figure 8, treating the volume as a summation of discs of circular cross-section, with

dimensions obtained by reference to grid scales on the optical surfaces of the test-section. This treatment allowed discs to be off-axis without complication. However, visualisation of bubble dissection as circular discs relies on the assumption, as yet without the opportunity for photographic confirmation, that bubble diameters along the line of sight equal those in the vertical direction.

It is noted that this technique determines the volume enclosed by the shadowgraph profile, even where interpretation, aided by prediction, suggests the existence of enclosed voids.

Expansions, defined as $V(t)/V_o$, of up to 20 were recorded during the first 6ms after shock impact.

The other measurement was the displacement X(t) of the front face of the bubble as a function of time.

MEASUREMENT OF BUBBLE EXPANSION

Figure 9 presents the experimental data from 16 tests, showing volume expansion as a function of dimensionless time. A best-fit curve is included.

Volume expansions of up to 20 are evident, while the limit of the dimensionless time axis scale represents typically 5ms.

Each curve consists of three or four data points, and represents one test: each point is the result of the volume measurement of one shadowgraph.

The following observations can be noted:

1. One of the curves included in the lower central group represents a preliminary test before the expansion of the test-section to a 20 x 10cm cross-section. The limitation of only a 5cm (2 inch) width therefore apparently had little effect on bubble growth rate at earlier times. However, the possibility remains that with the shock-tube width only marginally greater than the expanding bubble, growth may have been restricted in the transverse direction, so invalidating the assumption of a circular cross-section as explained under 'shadowgraph analysis'. With shadowgraphs recording only the side-on view, confirmation was not possible.
2. The best-fit curve commences with a slight volume reduction to indicate shock compression.
3. Difficulties in volume measurements were sometimes experienced due to imprecise boundaries on the shadowgraphs at the downstream end. The consequent uncertainty in overall volume measurement was considered as generally $<<10\%$.
4. Extrapolation of these curves back to their origin might indicate a more appropriate origin, - with time zero (t = 0) starting after the shock had passed the bubble centre.

NB. No predictions are shown, as calculations are not yet complete.

MEASUREMENT OF BUBBLE VELOCITY

Figure 10 shows the downstream displacement (measured in bubble

radii) of the front face of the bubble as a function of dimensionless time. In effect, it is a distance - time plot showing the slippage of the bubble within the shocked air-flow.

The full-line represents the movement of the air-flow, and in dimensionless units, has gradient = 1. Without slip, the bubble face would also travel at the air-flow velocity.

Experimentally, the bubble is found to start its travel at a much reduced velocity, eventually reaching about 87% of the flow velocity after about 4-5ms.

The theoretical result is similar, although only about 67% of the flow velocity is attained.

CONCLUSIONS

1. The shock-tube experiments have successfully provided late-time data.

2. Qualitative features of bubble development are in general agreement with the calculational model.

3. Uncertainty remains over possible influence of the shock-tube cross-section on bubble growth and local flow velocity.

4. Further computational studies are required to model the detailed features of bubble development.

5. Further experiments are under consideration to extend the range of parameter investigations, particularly gas density ratios.

FIGURE 1.

OBJECTIVE:-

i) to conduct shock-tube experiments to investigate the behaviour of dense gas bubbles when accelerated by a lighter gas,

ii) to compare results with computational predictions

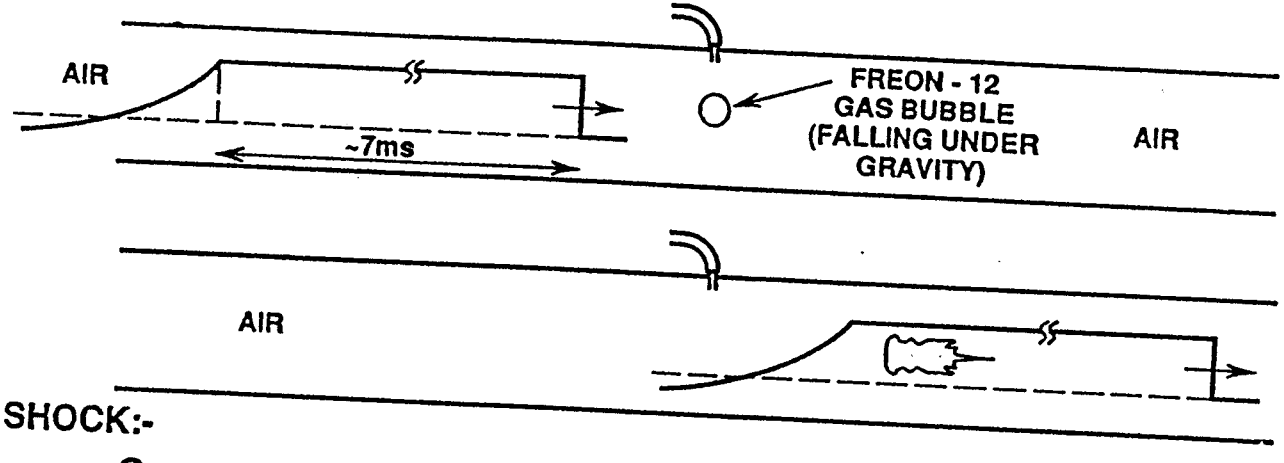

SHOCK:-

Overpressure	5psi (0.34bar)
Mach No.	M = 1.14
Flow velocity	v = 76ms^{-1}

FIG. 2. BUBBLE GROWTH

(Qualitative Comparison Theory vs. Experiment)

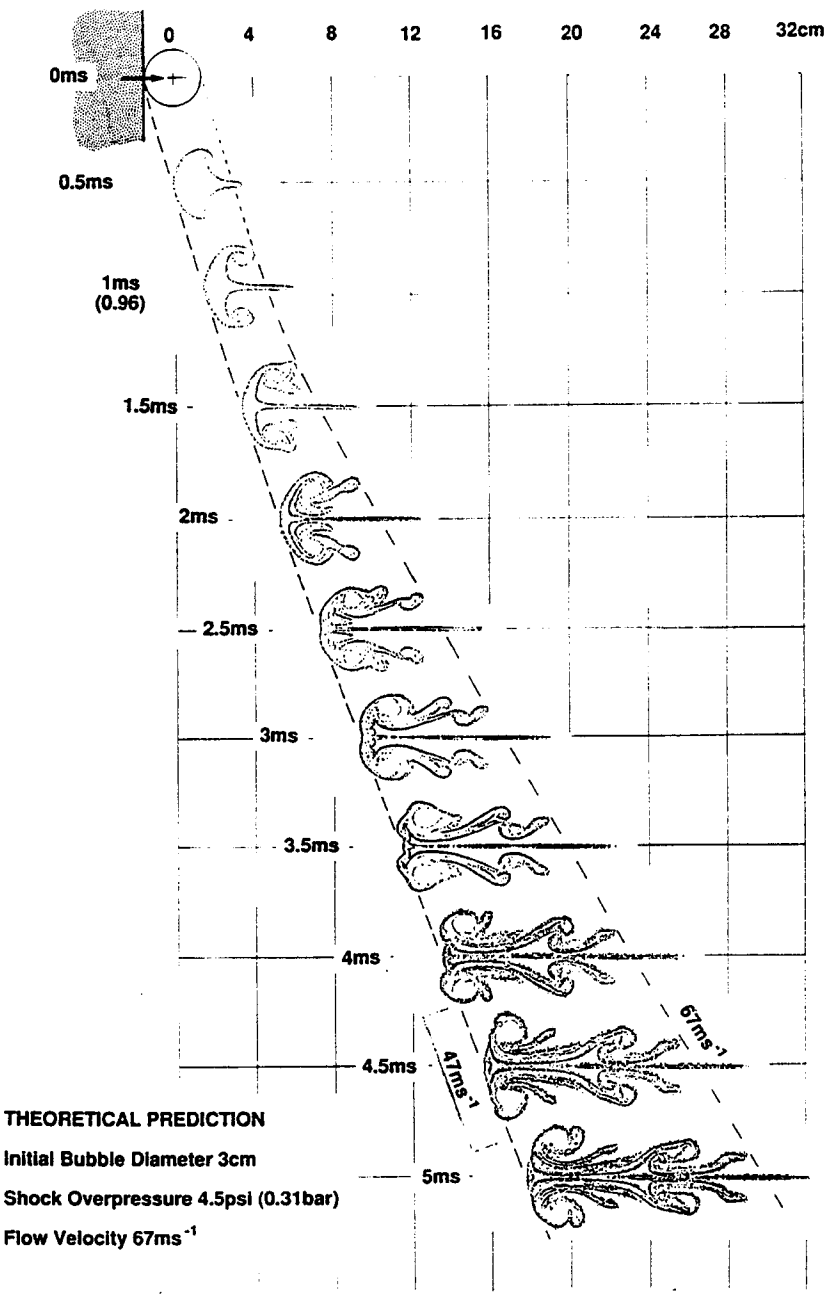

FIG. 3. BUBBLE GROWTH

(Qualitative Comparison Theory vs. Experiment)

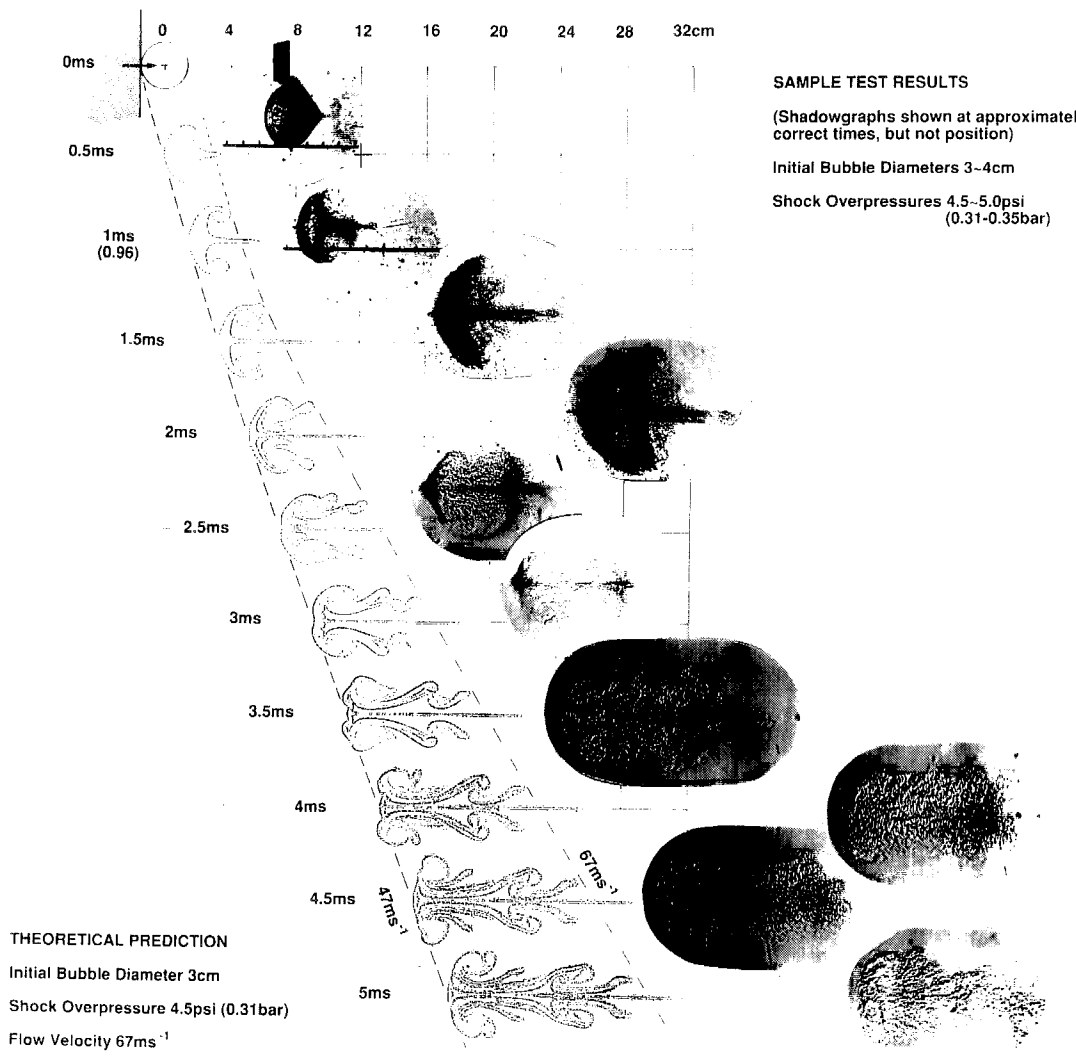

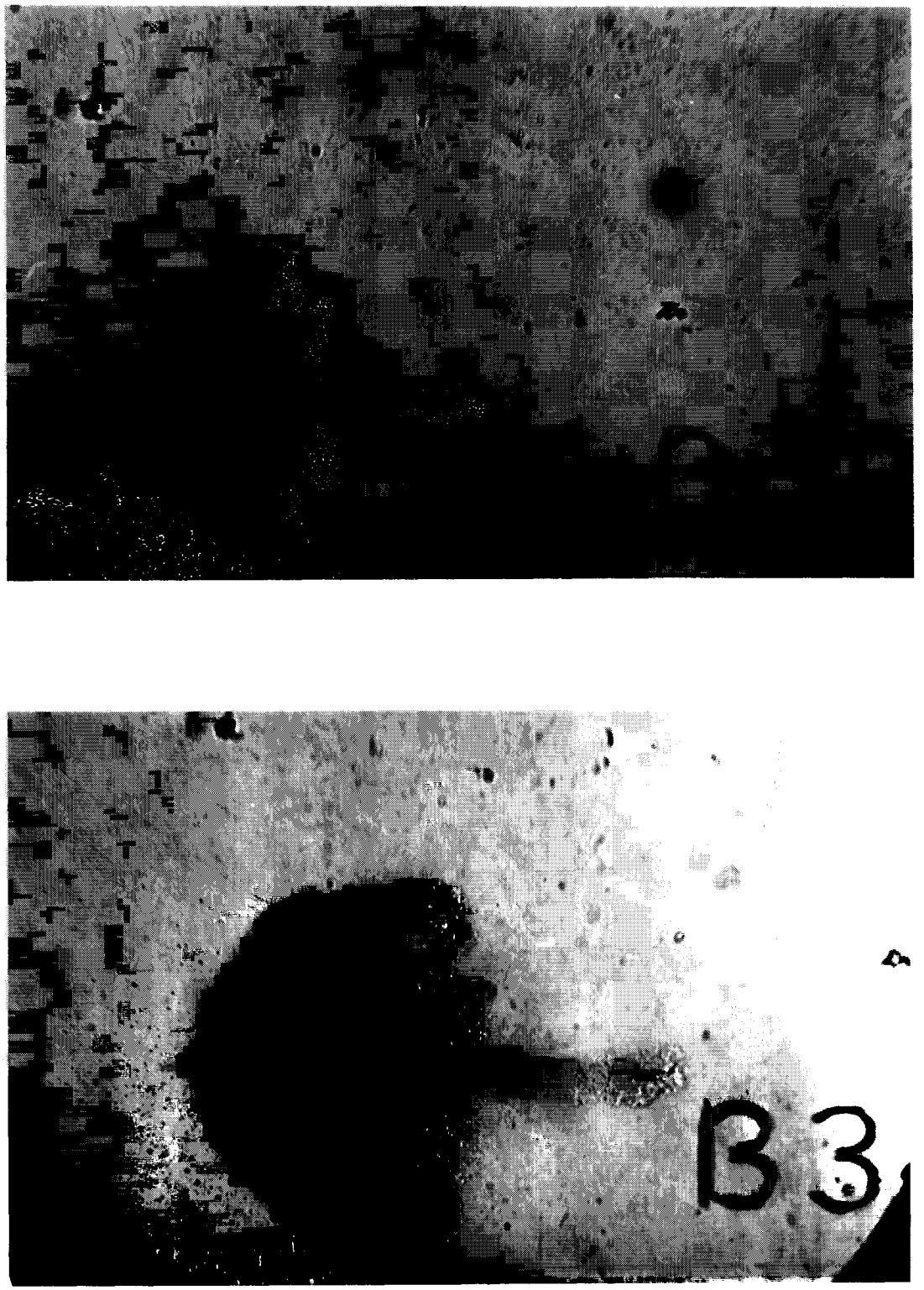

FIGURE 4

FIG. 5. COMPUTATIONAL TECHNIQUE

Calculations have been performed in axisymmetric geometry using the two dimensional Eulerian hydrocode PETRA [1]. Earlier results for the interaction of a shock with a dense spherical inhomogeneity are described in [2].

The main features of PETRA:

- **Explicit finite difference method**
- **Staggered grid**

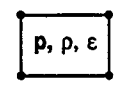

u, v: velocity components at mesh corners
p, ρ, ε: pressure, density, internal energy

Each time step is divided into two phases:

***Lagrangian phase** $\rho \frac{\partial \underline{u}}{\partial t} = -\nabla p$

$\rho \frac{\partial \varepsilon}{\partial t} = -p \, \mathrm{div} \, \underline{u}$

Uses artificial viscosity for shocks.

***Advection phase**

Calculates transport across cell boundaries.
Uses monotonic advection method of van Leer.

Calculates XY advection, YX advection for alternate time steps.
Can use an interface tracking method.

- **Several Lagrangian steps may be used per advection step - greatly speeds up low Mach No. calculations.**

The calculation shown here used:

2000 zones in the axial direction
200 zones in the radial direction

Geometrically expanding zones away from the bubble region.

Bubble diameter = 100 zones

Run time: 100 hours on a Cray-YMP

Interface tracking was not used as a fine scale mixing of the two fluid occurs. Instead, the van Leer method was used to transport volume fractions.

References:

1. **D.L. Youngs, "Time-dependent multi-material flow with large fluid distortion." Numerical Methods for Fluid Dynamics, K.W. Morton and M.J. Baines (Academic Press, New York, 1982).**
2. **N.W. Cowperthwaite, "The interaction of a plane shock and a dense spherical inhomogeneity". Physica D37 (1989) p.264.**

A937

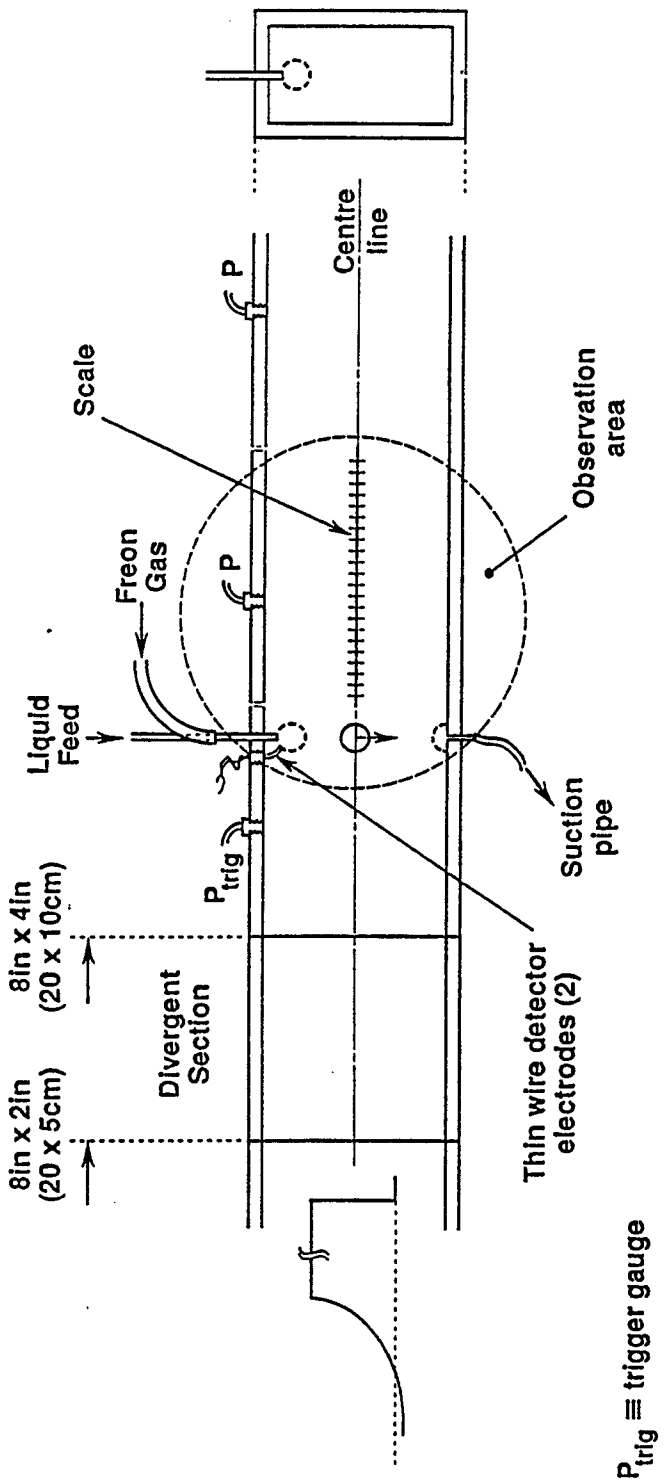

FIG. 6. SHOCK - TUBE TEST ARRANGEMENT

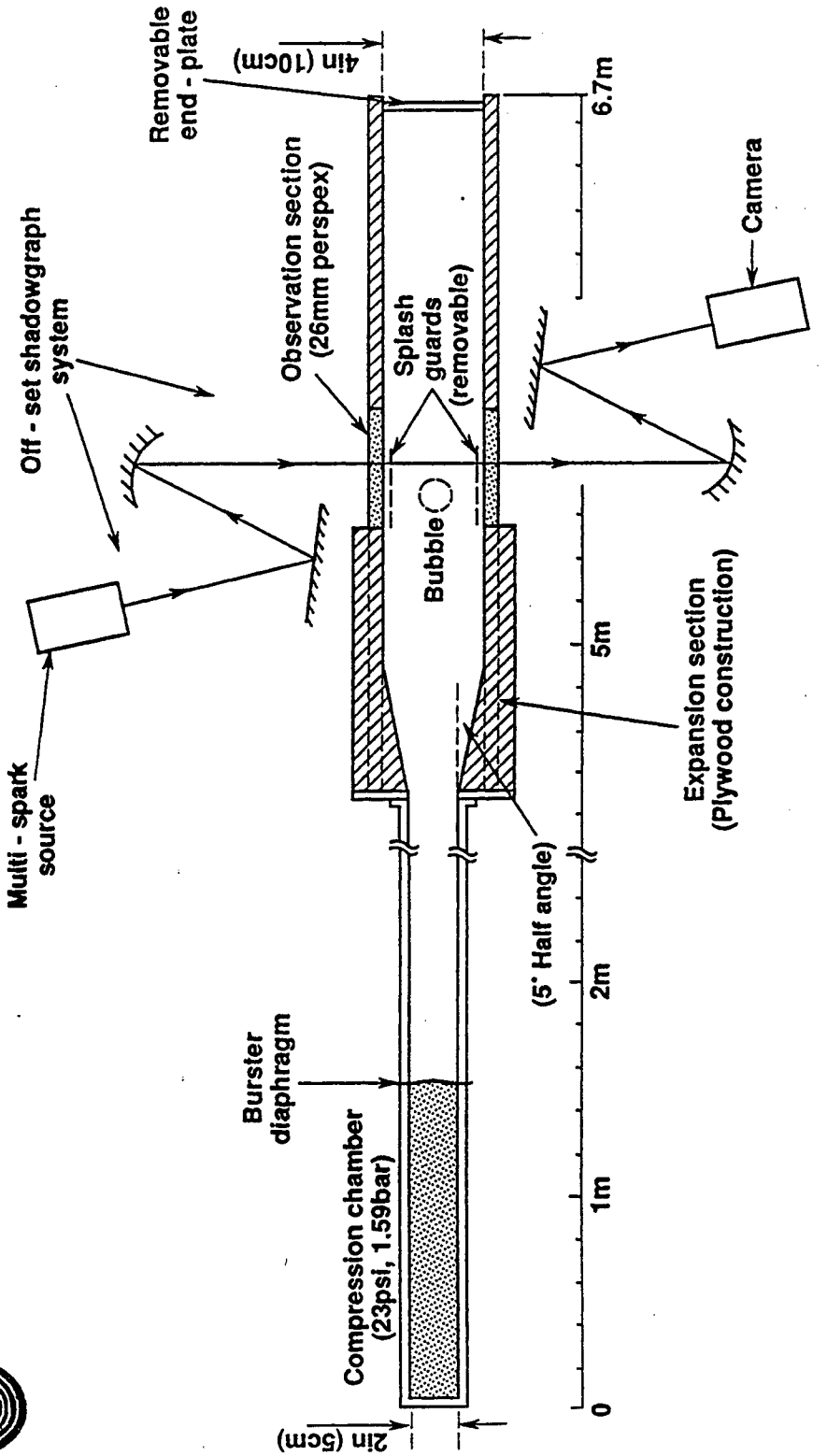

FIG. 7. SHOCK - TUBE (PLAN VIEW)

FIG. 8. BUBBLE MEASUREMENTS (& DEFINITIONS)

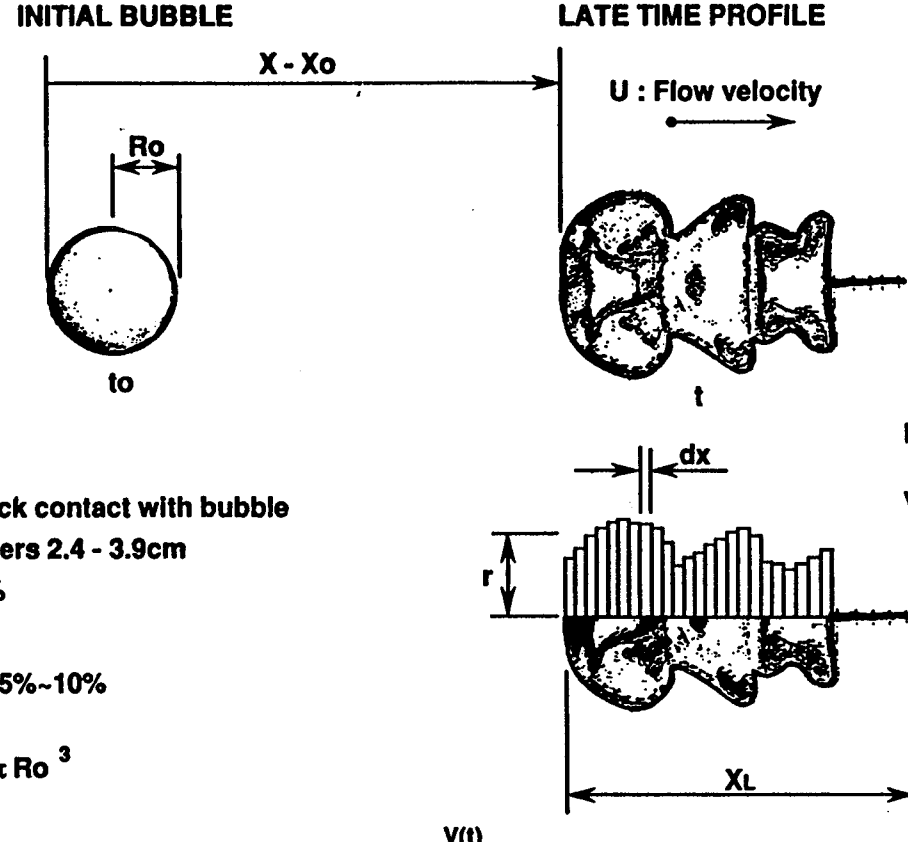

to = Time of shock contact with bubble

Range of diameters 2.4 - 3.9cm

Sphericity ~± 2%

$\frac{\text{Mass of water}}{\text{Mass of gas}}$ 5%~10%

Volume $Vo = \frac{4}{3}\pi Ro^3$

Displacement = X - Xo

Volume $V(t) = \pi \int_o^{X_L} r^2 dx$

Bubble expansion = $\frac{V(t)}{Vo}$ (range studied 1 - 20)

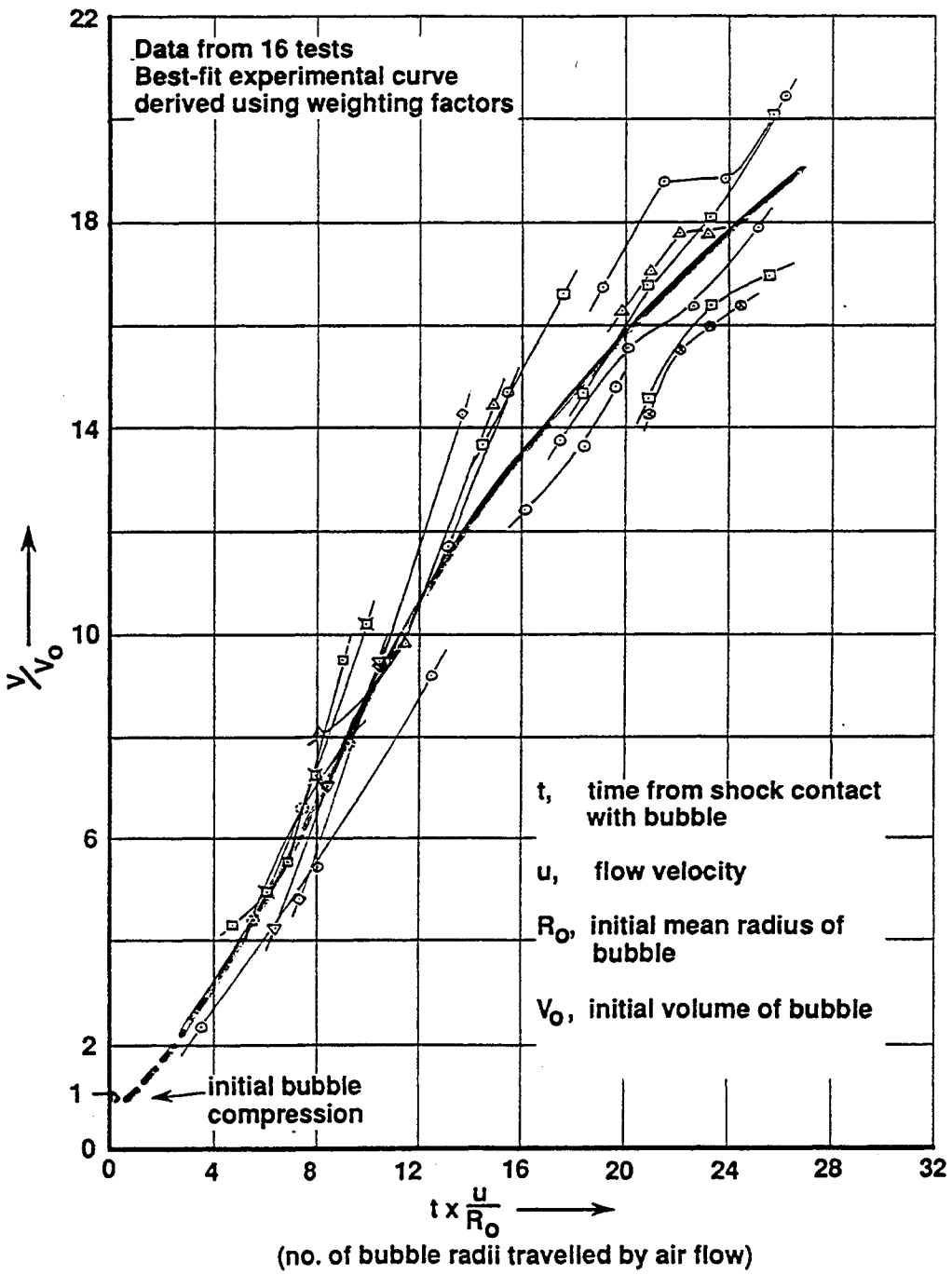
FIG. 9. BUBBLE GROWTH
VOLUME EXPANSION vs. (DIMENSIONLESS) TIME
Data from 16 tests
Best-fit experimental curve
derived using weighting factors
V/Vo
t, time from shock contact with bubble
u, flow velocity
Ro, initial mean radius of bubble
Vo, initial volume of bubble
initial bubble compression
t x u/Ro
(no. of bubble radii travelled by air flow)

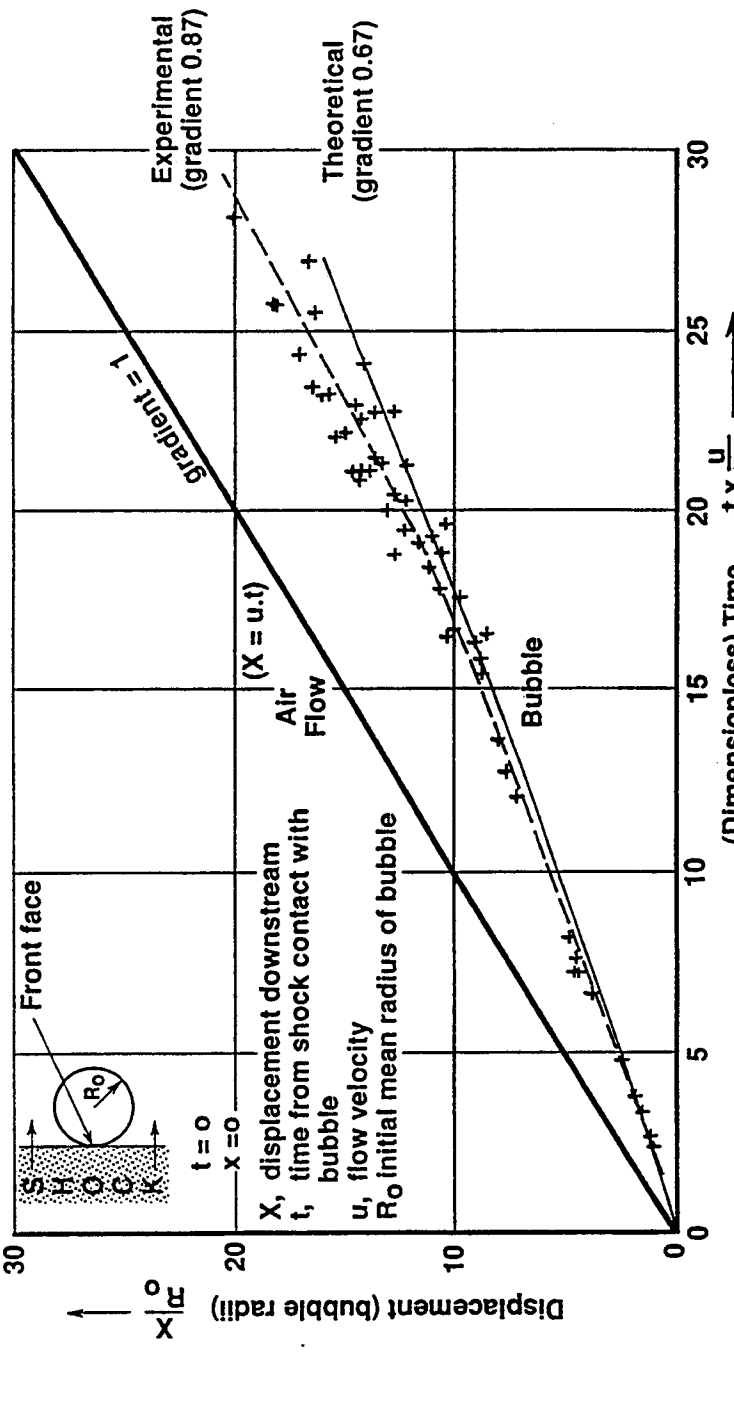

FIG. 10. DOWNSTREAM DISPLACEMENT OF BUBBLE (FRONT FACE)

AS 41

CONCLUSIONS

1. The shock-tube experiments have successfully provided late time data.

2. Qualitative features of bubble development are in general agreement with the calculational model.

3. Uncertainty remains over possible influence of the shock-tube cross-section on bubble growth and local flow velocity.

4. Further computational studies are required to model the detailed features of bubble development.

5. Further experiments are under consideration to extend the range of parameters investigated, particularly gas density ratios.

FIGURE 11.

ENERGY GENERATION BY A SHOCK CROSSING A PERTURBED INTERFACE

WP Crowley
E Burke
Lawrence Livermore National Laboratory

INTRODUCTION

This investigation is directed toward determining, computationally, the amount of "perturbed" kinetic energy that is generated by a shock passing over a perturbed interface.

The traditional experimental approach is to make measurements on a perturbed flow, obtain mean values from these data and to define the difference between the mean and the instantaneous as the perturbed energy. This approach is amenable to numerical simulations as well and the fluctuating kinetic energy (FKE) obtained from it was described by Besnard[1].

Another approach is to obtain two computational results, one perturbed and the other unperturbed and to define the perturbed energy as the difference between these two. This approach is not amenable to physical experiments; from it we derive perturbed kinetic energy (PKE) defined below.

We will compare results from the two methods.

The results presented here were obtained from a new Adaptive Eulerian hydro code, LAM, that modifies the mesh locally to obtain increased accuracy.

We consider only one problem, namely TP6A, which is an air/helium shock tube at Mach 1.24. The initial mesh is 0.23 cm on a side at the interface--initially there are 32 zones transverse to the shock. Initial conditions are as described by Rupert[2]. A density perturbation is applied to the two zones straddling the air/helium interface to form a square wave with a fixed wavelength and a variable amplitude; i.e., the perturbed density is constant for a half wavelength and then it changes according to a random number. There are nlzper zones per half-wavelength; the wavelength is thus 2(0.23)(nlzper) cm. Units are centimeters, grams and microseconds.

Figure 1 shows the two components of PKE (defined below) vs time for three different initial perturbations when the mesh remains fixed in time (levlim=1). This shows us that the perturbed energy is definitely not isotropic and it sets the time scale for different events.

ILLUSTRATION OF NUMERICAL METHOD

The LAM code uses a vanLeer limiter, artificial viscosity and a volume fraction scheme to determine the EOS. In LAM the resolution is controlled by *levlim*. Each zone originates at level-1. Each level-1 zone may be split into 4 level-2 zones. Each level-2 zone may be split into 4 level-3 zones, etc. *Levlim*=3 means resolution to level-3 and no level-4 zones may appear. In these problems the code adapts so as to resolve density gradients.

Figure 2 shows the original mesh and contour lines of density at 300 micsec when the mesh is held constant in time (levlim=1) and the initial perturbation is characterized by nlzper=3. The initial shock moves from left to right.

Figures 3 and 4 shows the mesh and density contours at 300 micsec for a problem with the same initial conditions with the mesh limited by levlim=2 and 3.

DEFINE PROCEDURE AND AVERAGE ENERGIES

To obtain PKE we run two problems. The unperturbed problem produces a velocity field $u_u(x,y,t)$. The perturbed problem produces $u_p(x,y,t)$. A postprocessor code combines the two results to form the averages defined below.

With the y dimension transverse to the shock, we define the strip average

$$\langle f(\bar{x},t)\rangle \equiv \frac{1}{Y2\delta}\int_{x-\delta}^{x+\delta} dx \int_0^Y f(x,y,t)dy$$

and two measures of kinetic energy: Fluctuating kinetic energy FKE(x) = rxx(x)+ryy(x) where

$$rxx(x,t) = \langle u_p u_p \rho_p\rangle - \frac{\langle u_p \rho_p\rangle^2}{\langle \rho_p\rangle}$$

and Perturbed kinetic energy, PKE(x) = uke(x)+vke(x) where

$$2uke = <\rho_p(u_p-u_u)(u_p-u_u)>$$

Similar definitions hold for the transverse components, ryy and 2vke.

If we expand 2uke, write it in terms of rxx and note that, in our case,

$$u_u = \langle u_u \rangle$$
$$\langle \rho_p u_p u_u \rangle = \langle \rho_p u_p \rangle u_u$$
$$\langle \rho_p u_u u_u \rangle = \langle \rho_p \rangle u_u u_u$$

we have

$$2uke = rxx + \frac{[\langle \rho_p u_p \rangle - \langle \rho_p \rangle u_u]^2}{\langle \rho_p \rangle}$$

Thus 2uke ≥ rxx and similarly 2vke ≥ ryy. They will be equal if we choose the mean velocity to be

$$u_u = \frac{\langle \rho_p u_p \rangle}{\langle \rho_p \rangle}$$

For notational convenience, PKE(x) is a function of x and time. PKE is the x-integral of PKE(x)--it is a function of time alone.

RESULTS

Figure 5A shows PKE vs time for different initial perturbations. The initial perturbation for curve G is a square wave with wavelength 8x0.23 cm and amplitude 0.23 cm (this problem is the only exception to the initial perturbation described in the introduction). It takes the shock about 5 micsec to cross an original air zone and at some time between 5 and 10 micsec the shock has crossed the original perturbation. Between 5 and 10 micsec the energy ranges from 6.4e-9 to 5.0e-9. The Leith[3] estimate for PKE for a single wavelength perturbation is

$$E = \int (uke+vke)dx = \frac{\pi}{2\lambda} a^2 U^2 A(\rho_+ - \rho_-)$$

which gives 5.4e-9 when a is taken to be 0.23 cm. Curves H and I have an amplitude that is based on a random number (as described in the introduction) and a half-wavelength of 4nlzper and 1nlzper respectively. After the first shock, PKE depends on the details of the perturbation. Note that PKE continues to grow for about 50 micsec (Fig 1) which is several times the transit time of the shock over the perturbation.

Figure 5B shows PKE and its components vs time (for the same initial perturbation) as the mesh is refined by changing levlim from 3 to 5 for a perturbation described by nlzper=4. The solution converges to the same PKE as the mesh is refined. The solution is not isotropic.

Figure 6 shows uke(x) and vke(x) at 5 micsec as the mesh is refined. We see that uke > vke and that at at least another level of refinement is needed to resolve vke at early times.

Figure 7 compares 2PKE with FKE at 5 micsec with levlim=5. We see that the transverse components agree and that 2uke > rxx.

Figures 8 through 11 compare 2PKE with FKE at times of 5, 10, 20 and 40 for levlim=4. This mesh gives results that are not quite converged, but that imply differences that are important. We see that for times up to 20 micsec 2vke and ryy agree and then they start to disagree. From 5 micsec onward 2uke and rxx disagree. By 20 micsec a trend is established with 2uke >> rxx. There is a hint that FKE is becoming isotropic but this may be only part of an oscillation. By 40 micsec it seems to be well established that PKE >> FKE and that this is due mainly to energy outside the mix layer.

Earlier we noted that PKE grows until about 50 micsec and we see now that this energy is not in the mix layer. The transmitted shock and rarefaction are both warped by the perturbed interface. As the shock moves away from the (small) initial mix region it changes from a warped to a straight configuration but this takes time. While it is healing itself it is generating more PKE. The amount of PKE generated by this mechanism presumably depends on the amplitude of the initial perturbation. The initial shock is thus leaving behind a legacy of perturbed flow for the reflected shock to interact with. This potentially large source of PKE in the wake of the shock, outside the mix layer, may be of interest to model builders.

CONCLUSIONS

- The energy generated at early times is close to theoretical estimates for a single wavelength perturbation.
- After the first shock, the evolution of PKE depends on the details of the initial perturbation.
- The perturbed energy field is not isotropic.
- The energy in the wake of the shock, between the shock and the mixed region, may be large and is considerably underestimated by the FKE approximation.

Reference

1. D. Besnard, J. Gambart and JF Haas, "2-Dimensional simulation of shock-interface interaction", 1989 Workshop on RM and RT Mixing, Pleasanton, Calif.
2. V. Rupert, "Reference Problems", 1989 Workshop on RM and RT Mixing, Pleasanton, Calif.
3. C. Leith, "Working Paper", 1985

FIGURE 1

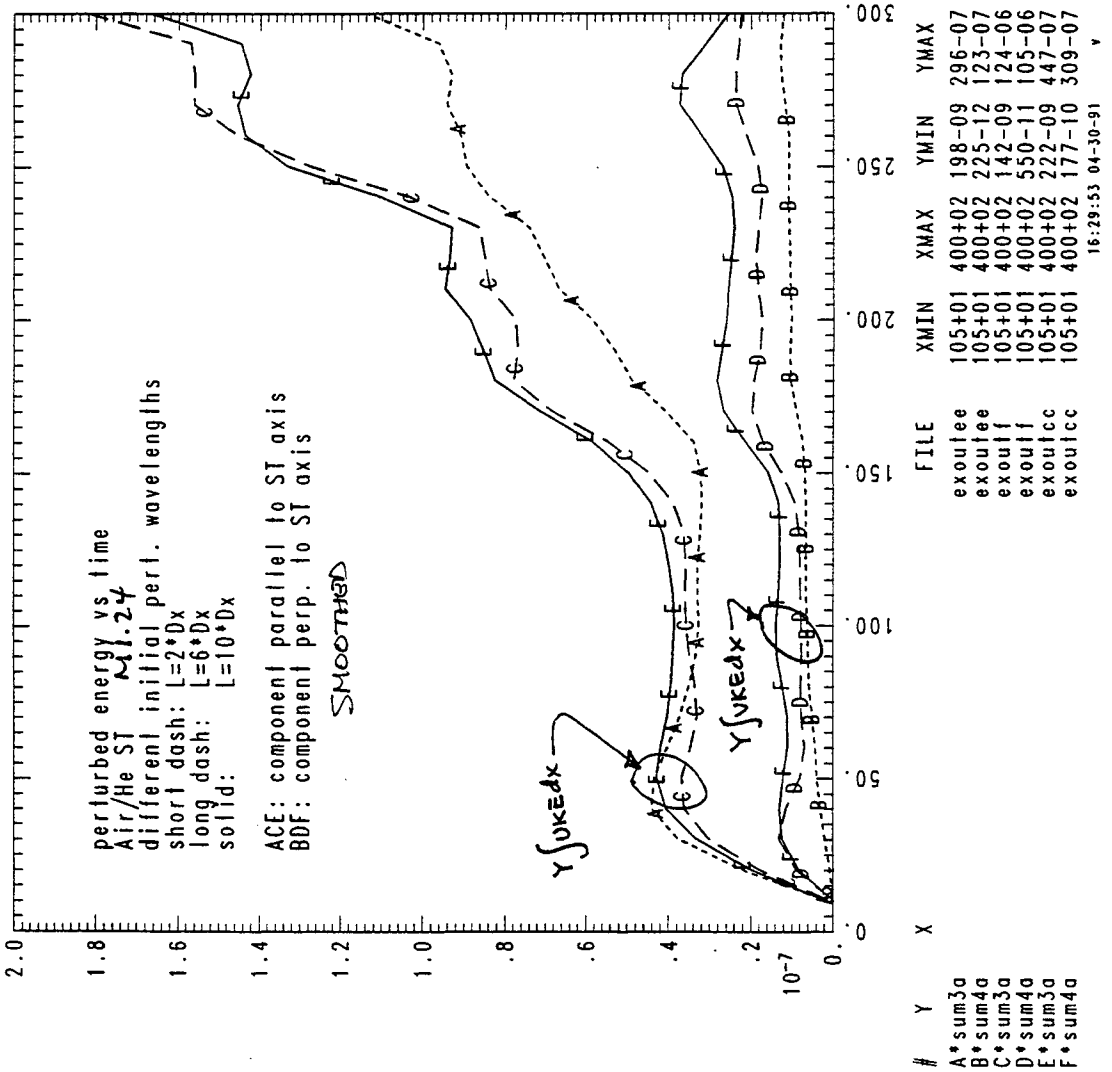
perturbed energy vs time
Air/He ST
M1.24
different initial pert. wavelengths
short dash: L=2*Dx
long dash: L=6*Dx
solid: L=10*Dx
ACE: component parallel to ST axis
BDF: component perp. to ST axis
SMOOTHED
YJUKEDX
YJUKEDX
Y X
A*sum3a
B*sum4a
C*sum3a
D*sum4a
E*sum3a
F*sum4a
FILE XMIN XMAX YMIN YMAX
exoutee 105+01 400+02 198-09 296-07
exoutee 105+01 400+02 225-12 123-07
exoutf 105+01 400+02 142-09 124-06
exoutf 105+01 400+02 550-11 105-06
exoutcc 105+01 400+02 222-09 447-07
exoutcc 105+01 400+02 177-10 309-07
16:29:53 04-30-91

FIGURE 2

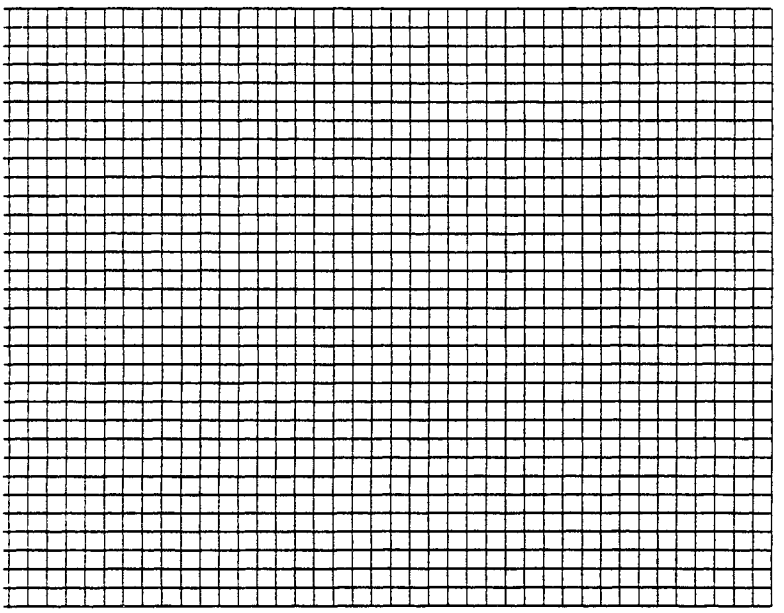

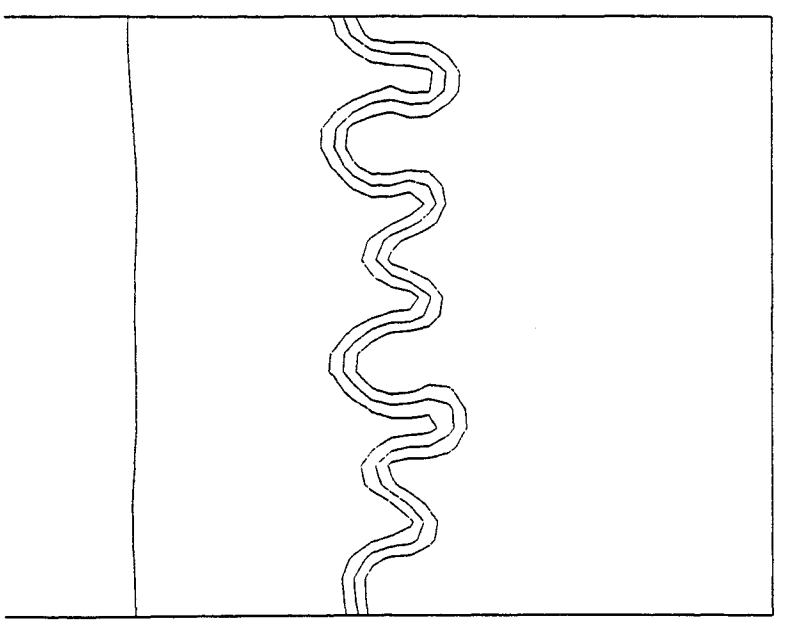

FIGURE 3

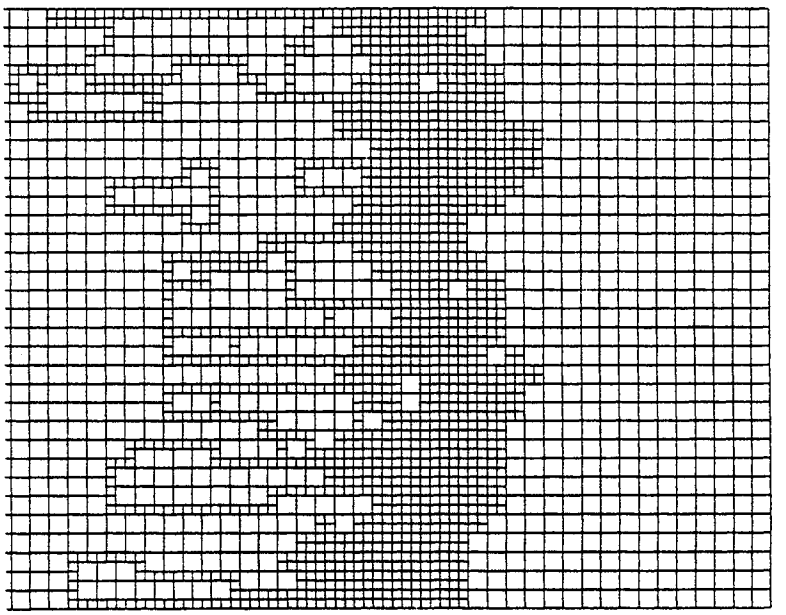

mesh at time = 3.0009e+02, nzones= 3900anem135x

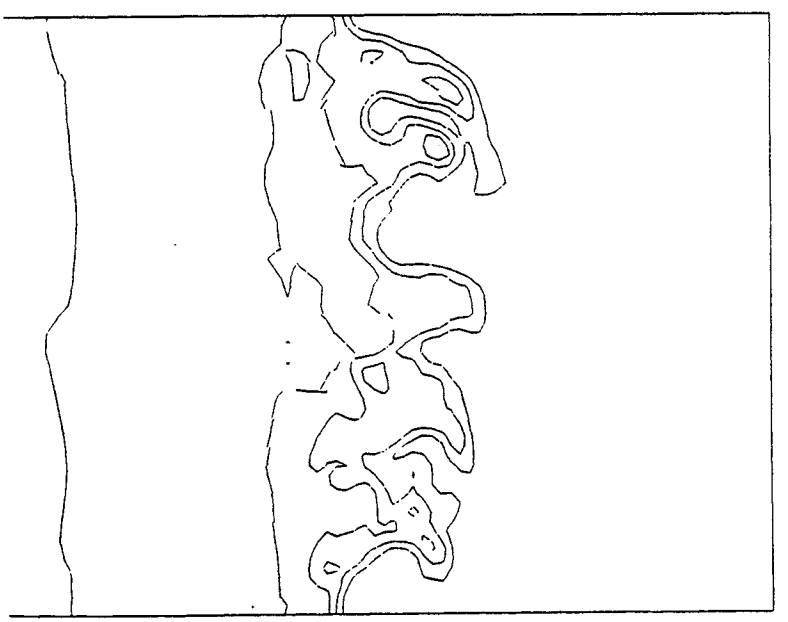

density at time = 3.0009e+02
levels = 2.15e-04 9.85e-04 1.75e-03 2.52e-03 3.29e-03

FIGURE 4

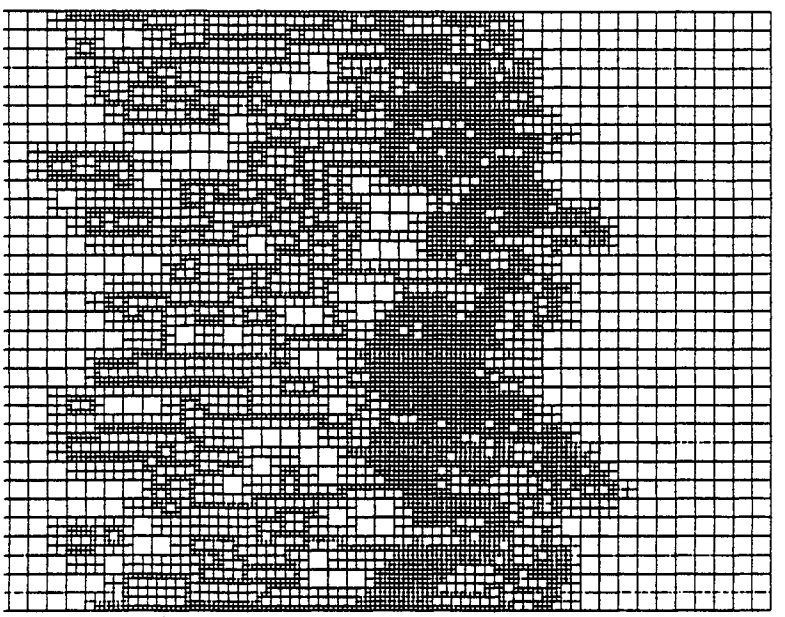

LAM mesh at time = 3.0009e+02, nzones= 9045 ahem135y

LAM density at time = 3.0009e+02
levels = 1.68e-04 8.17e-04 1.47e-03 2.11e-03 2.76e-03

FIGURE 5A

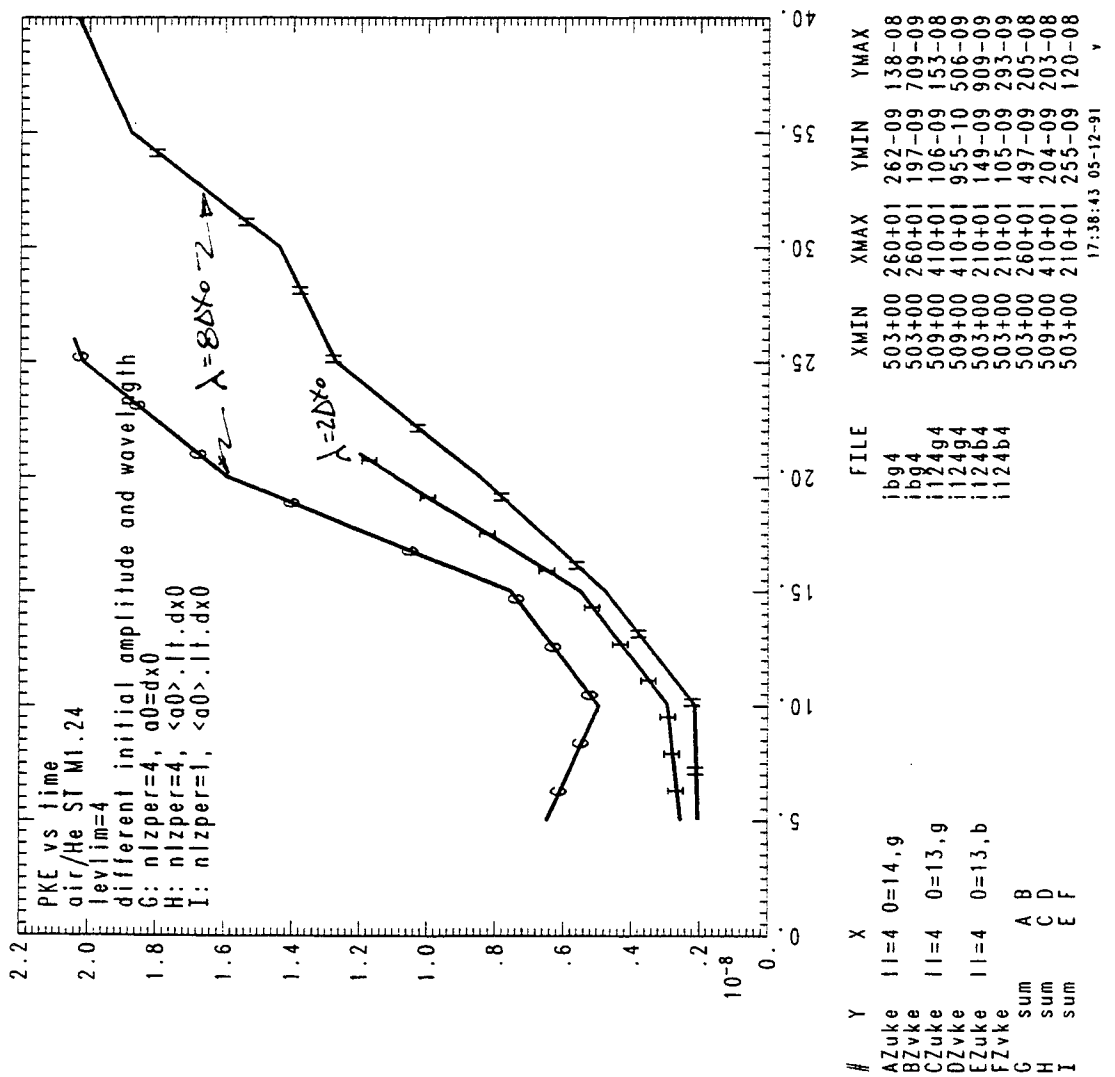
PKE vs time
air/He ST M1.24
levlim=4
different initial amplitude and wavelength
G: nlzper=4, a0=dx0
H: nlzper=4, <a0>.11.dx0
I: nlzper=1, <a0>.11.dx0
λ=8Δx0
λ=2Δx0
10⁻⁸
0. .2 .4 .6 .8 1.0 1.2 1.4 1.6 1.8 2.0 2.2
0. 5. 10. 15. 20. 25. 30. 35. 40.
Y X FILE XMIN XMAX YMIN YMAX
AZuke ll=4 0=14,g ibg4 503+00 260+01 262-09 138-08
BZvke ibg4 503+00 260+01 197-09 709-09
CZuke ll=4 0=13,g i124g4 509+00 410+01 106-09 153-08
DZvke i124g4 509+00 410+01 955-10 506-09
EZuke ll=4 0=13,b i124b4 503+00 210+01 149-09 909-09
FZvke i124b4 503+00 210+01 105-09 293-09
G sum A B 503+00 260+01 497-09 205-08
H sum C D 509+00 410+01 204-09 203-08
I sum E F 503+00 210+01 255-09 120-08
17:38:43 05-12-91

FIGURE 5B

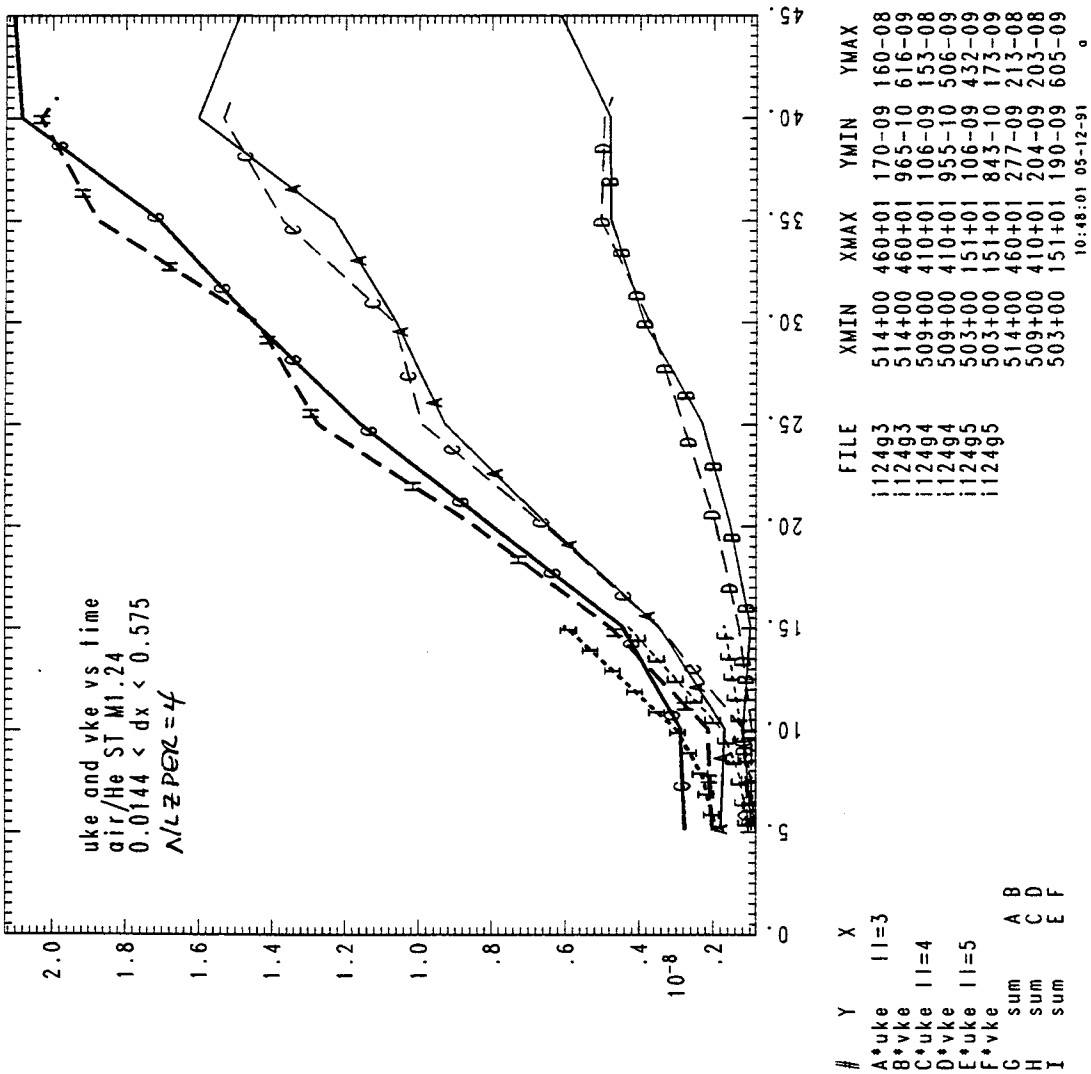
uke and vke vs time
air/He ST M1.24
0.0144 < dx < 0.575
λ/L zone = 4
2.0
1.8
1.6
1.4
1.2
1.0
.8
.6
.4
10^{-8}
.2
0
5.
10.
15.
20.
25.
30.
35.
40.
45.
Y X
A*uke II=3
B*vke
C*uke II=4
D*vke
E*uke II=5
F*vke
G sum A B
H sum C D
I sum E F
FILE XMIN XMAX YMIN YMAX
i12493 514+00 460+01 170-09 160-08
i12493 514+00 460+01 965-10 616-09
i12494 509+00 410+01 106-09 153-08
i12494 509+00 410+01 955-10 506-09
i12495 503+00 151+01 106-09 432-09
i12495 503+00 151+01 843-10 173-09
514+00 460+01 277-09 213-08
509+00 410+01 204-09 203-08
503+00 151+01 190-09 605-09
10:48:01 05-12-91

FIGURE 6

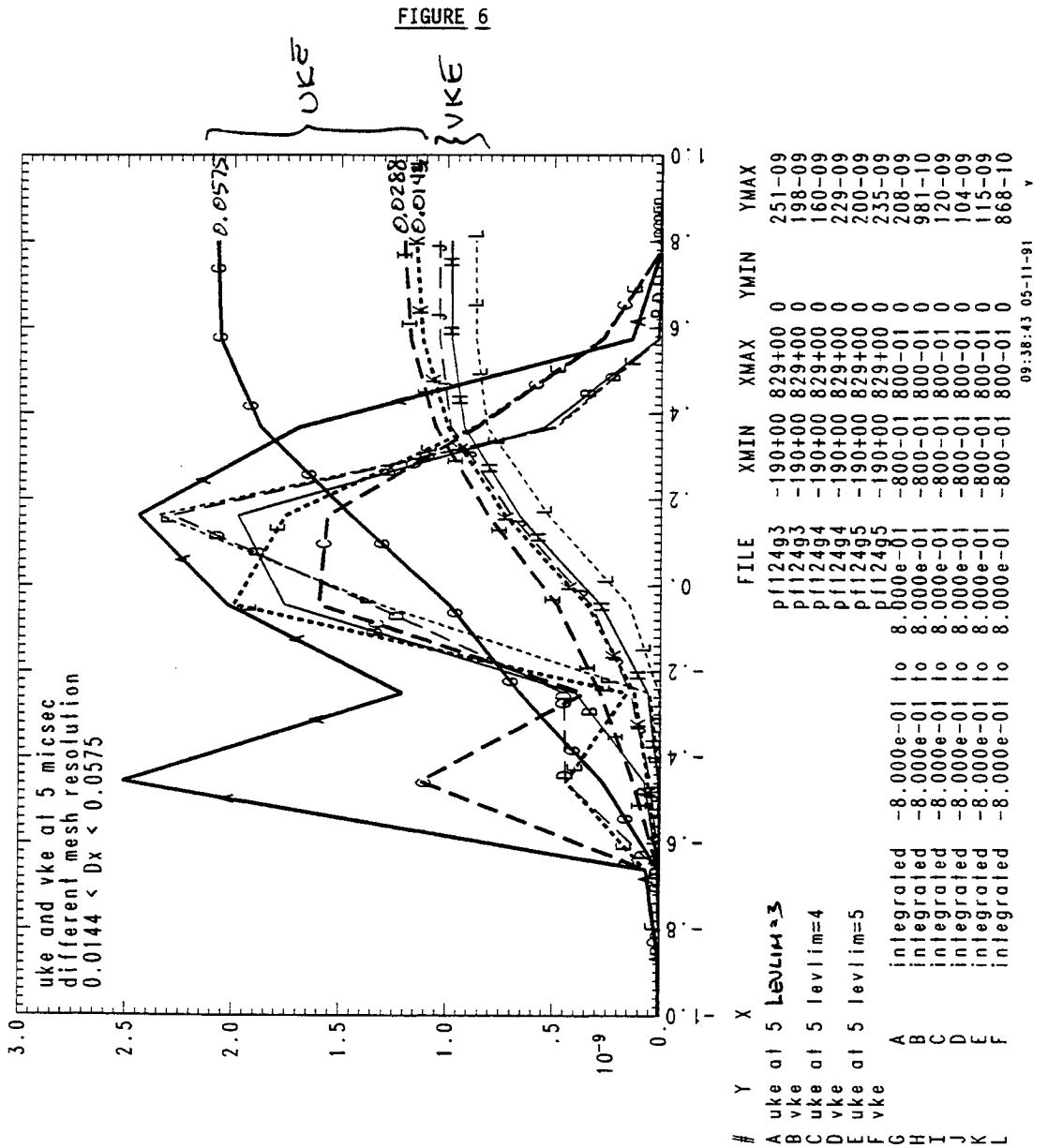

#	Y	X	FILE	XMIN	XMAX	YMIN	YMAX
A	uke at 5 levlim=3		p1124g3	-190+00	829+00	0	251-09
B	vke		p1124g3	-190+00	829+00	0	198-09
C	uke at 5 levlim=4		p1124g4	-190+00	829+00	0	160-09
D	vke		p1124g4	-190+00	829+00	0	229-09
E	uke at 5 levlim=5		p1124g5	-190+00	829+00	0	200-09
F	vke		p1124g5	-190+00	829+00	0	235-09
G		integrated	8.000e-01	-800-01	800-01	0	208-09
H		integrated	8.000e-01	-800-01	800-01	0	981-10
I		integrated	8.000e-01	-800-01	800-01	0	120-09
J		integrated	8.000e-01	-800-01	800-01	0	104-09
K		integrated	8.000e-01	-800-01	800-01	0	115-09
L		integrated	8.000e-01	-800-01	800-01	0	868-10

-8.000e-01 to 8.000e-01

09:38:43 05-11-91

FIGURE 7

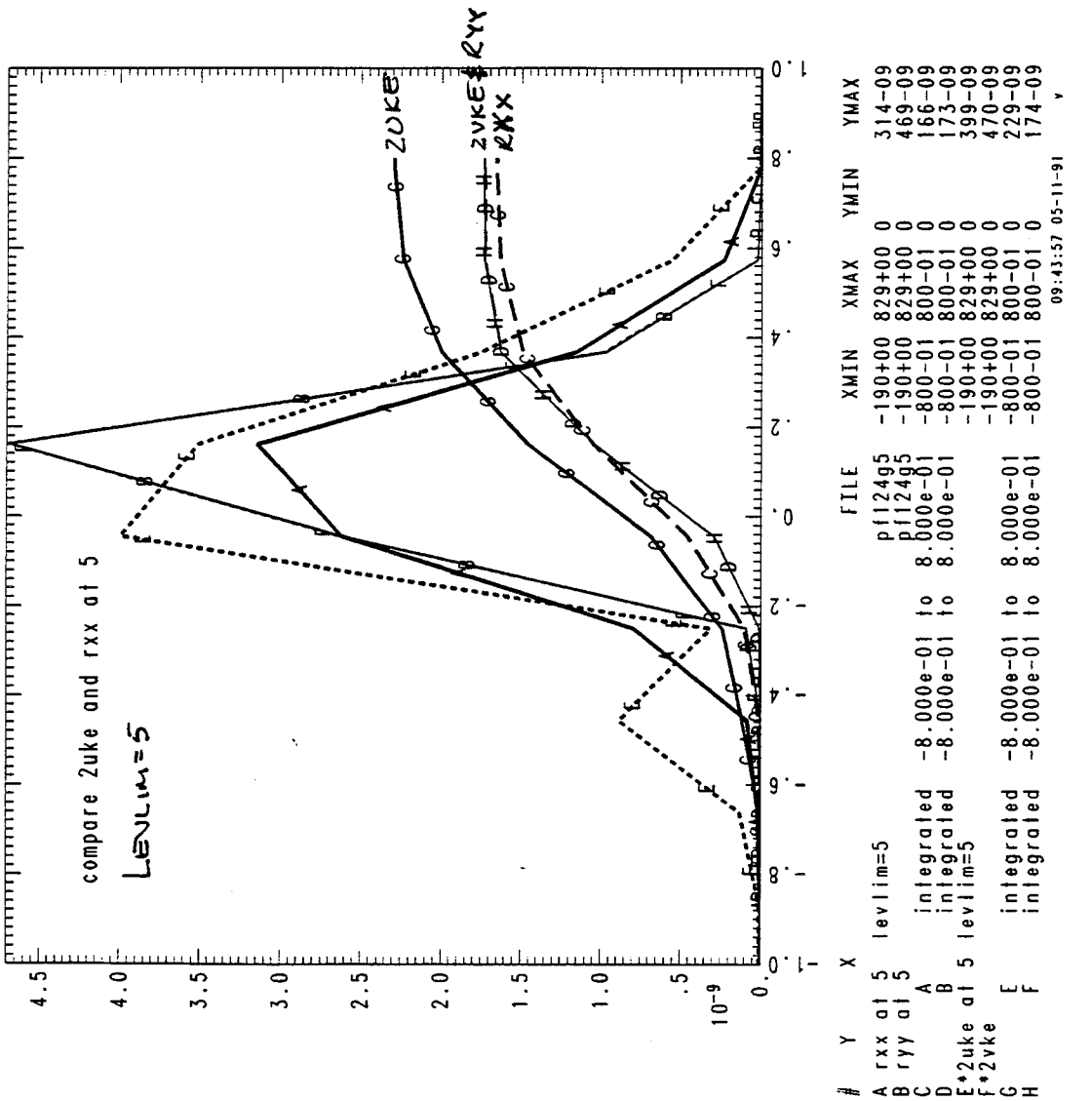
compare 2uke and rxx at 5
Levlim=5
2UKE
2VKE*RYY
2RXX
4.5
4.0
3.5
3.0
2.5
2.0
1.5
1.0
.5
0.
10⁻⁹
1.0
.8
.6
.4
.2
0.
-.2
-.4
-.6
-.8
-1.
Y X FILE XMIN XMAX YMIN YMAX
A rxx at 5 levlim=5 pf124g5 -190+00 829+00 0 314-09
B ryy at 5 pf124g5 -190+00 829+00 0 469-09
C A integraled -8.000e-01 to 8.000e-01 -800-01 800-01 0 166-09
D B integraled -8.000e-01 to 8.000e-01 -800-01 800-01 0 173-09
E*2uke at 5 levlim=5 -190+00 829+00 0 399-09
F*2vke -190+00 829+00 0 470-09
C E integraled -8.000e-01 to 8.000e-01 -800-01 800-01 0 229-09
H F integraled -8.000e-01 to 8.000e-01 -800-01 800-01 0 174-09
09:43:57 05-11-91

FIGURE 8

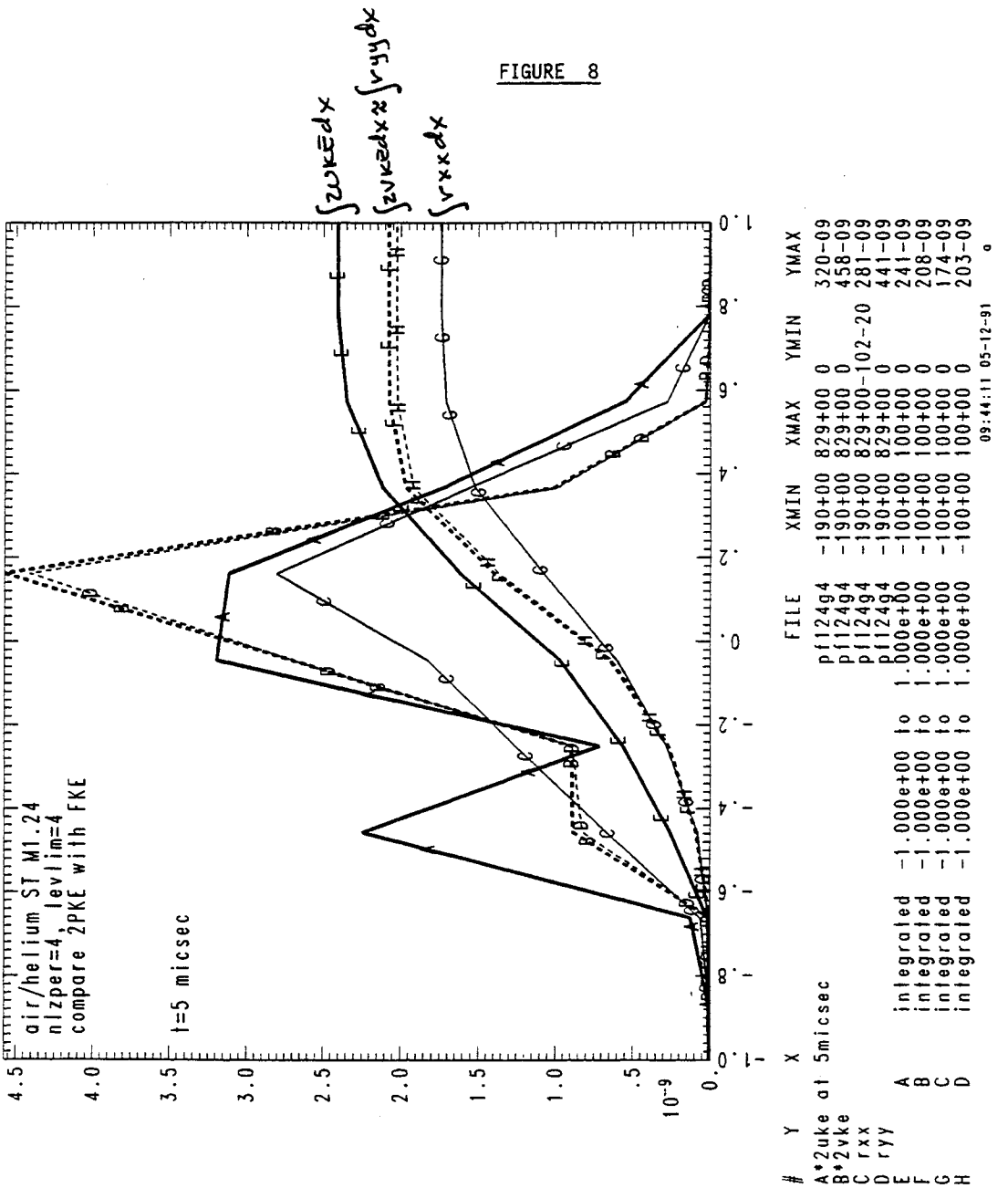
air/helium ST M1.24
nlzper=4, levlim=4
compare 2PKE with FKE
t=5 micsec
4.5
4.0
3.5
3.0
2.5
2.0
1.5
1.0
.5
0.
10^{-9}
1.0
.8
.6
.4
.2
0.
-.2
-.4
-.6
-.8
-1.0
Y X FILE XMIN XMAX YMIN YMAX
A *2uke at 5micsec
B *2vke
C rxx
D ryy
E A integrated -1.000e+00 to 1.000e+00 pf124g4 -190+00 829+00 0 320-09
F B integrated -1.000e+00 to 1.000e+00 pf124g4 -190+00 829+00 0 458-09
G C integrated -1.000e+00 to 1.000e+00 pf124g4 -190+00 829+00 -102-20 281-09
H D integrated -1.000e+00 to 1.000e+00 pf124g4 -190+00 829+00 0 441-09
-100+00 100+00 0 241-09
-100+00 100+00 0 208-09
-100+00 100+00 0 174-09
-100+00 100+00 0 203-09
09:44:11 05-12-91

FIGURE 9

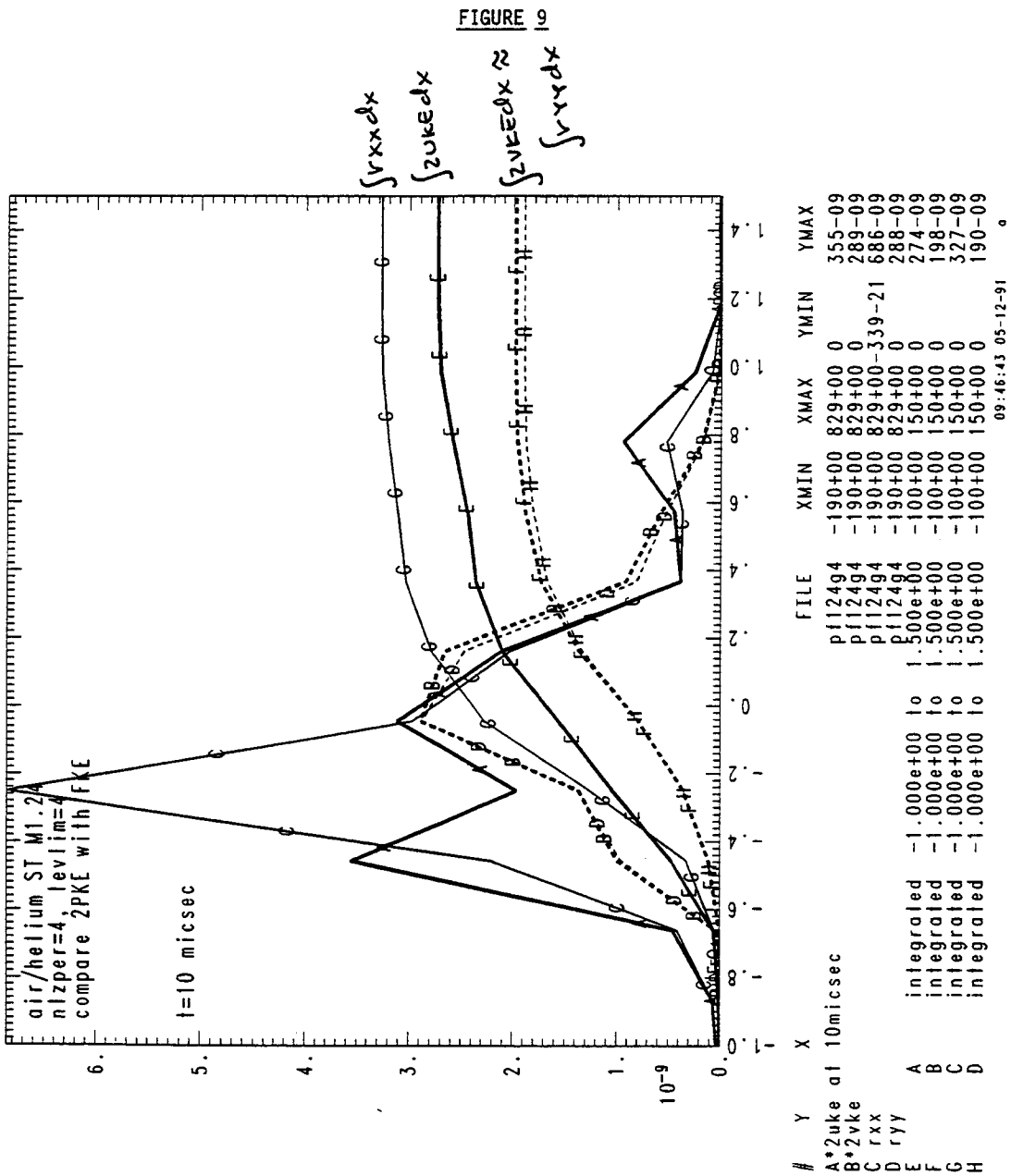
air/helium ST M1.2
nlzper=4, levlim=4
compare 2PKE with FKE
t=10 micsec
$\int rxxdx$
$\int 2ukedx$
$\int 2vkedx \approx \int ryydx$
10^{-9}
Y X FILE XMIN XMAX YMIN YMAX
A *2uke at 10micsec pf12494 -190+00 829+00 0 355-09
B *2vke pf12494 -190+00 829+00 0 289-09
C rxx pf12494 -190+00 829+00 -339-21 686-09
D ryy pf12494 -190+00 829+00 0 288-09
E A integrated -1.000e+00 to 1.500e+00 -100+00 150+00 0 274-09
F B integrated -1.000e+00 to 1.500e+00 -100+00 150+00 0 198-09
G C integrated -1.000e+00 to 1.500e+00 -100+00 150+00 0 327-09
H D integrated -1.000e+00 to 1.500e+00 -100+00 150+00 0 190-09
09:46:43 05-12-91

FIGURE 10

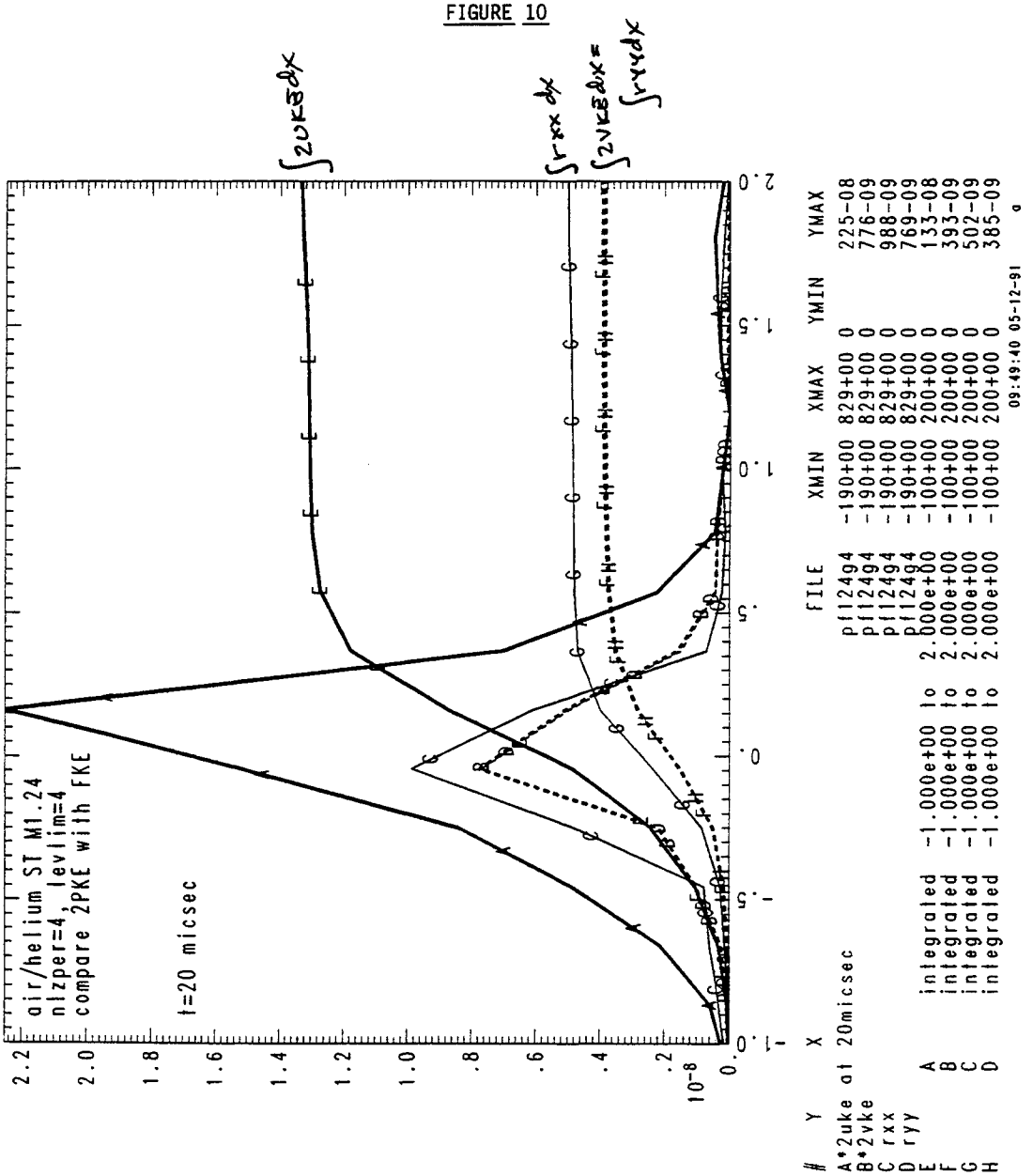
air/helium ST M1.24
nlzper=4, levlim=4
compare 2PKE with FKE
t=20 micsec
∫2vkεdx
∫rxx dx
∫2vkεdx=∫ryydx
Y X FILE XMIN XMAX YMIN YMAX
A*2uke at 20micsec pf124g4 -190+00 829+00 0 225-08
B*2vke pf124g4 -190+00 829+00 0 776-09
C rxx pf124g4 -190+00 829+00 0 988-09
D ryy pf124g4 -190+00 829+00 0 769-09
E A integrated -1.000e+00 to 2.000e+00 -100+00 200+00 0 133-08
F B integrated -1.000e+00 to 2.000e+00 -100+00 200+00 0 393-09
G C integrated -1.000e+00 to 2.000e+00 -100+00 200+00 0 502-09
H D integrated -1.000e+00 to 2.000e+00 -100+00 200+00 0 385-09
09:49:40 05-12-91

FIGURE 11

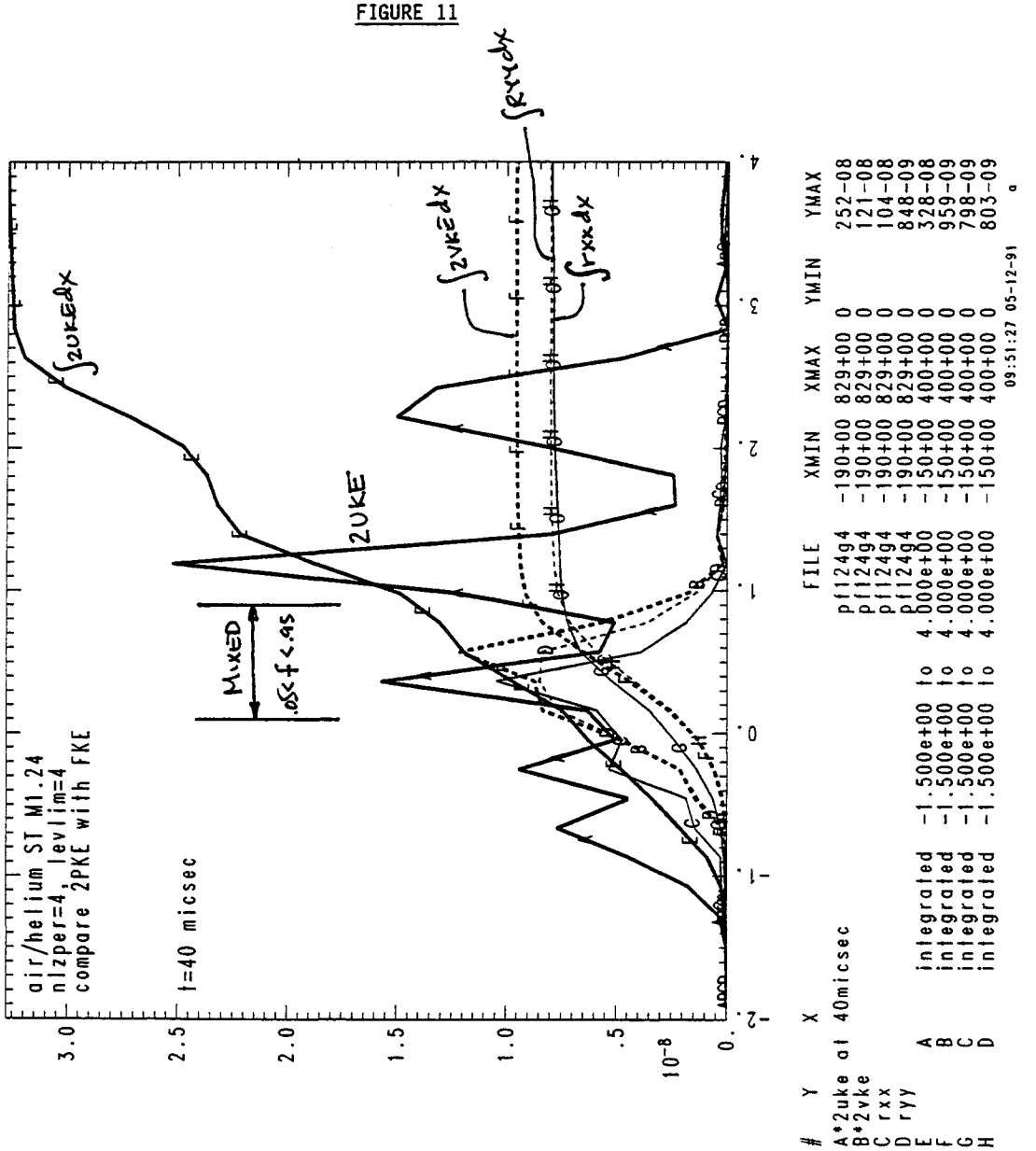

#	Y	X	FILE	XMIN	XMAX	YMIN	YMAX
A	A*2uke at 40micsec		pf124g4	-190+00	829+00	0	252-08
B	B*2vke		pf124g4	-190+00	829+00	0	121-08
C	C rxx		pf124g4	-190+00	829+00	0	104-08
D	D ryy		pf124g4	-190+00	829+00	0	848-09
E	integraled	-1.500e+00 to 4.000e+00		-150+00	400+00	0	328-08
F	integraled	-1.500e+00 to 4.000e+00		-150+00	400+00	0	959-09
G	integraled	-1.500e+00 to 4.000e+00		-150+00	400+00	0	798-09
H	integraled	-1.500e+00 to 4.000e+00		-150+00	400+00	0	803-09

09:51:27 05-12-91

INSTABILITY DEVELOPMENT AT THE INTERFACES OF EXPLOSIVE-SHOCKED METALLIC PLATES

P. Elias - R. Courchinoux - M. Legrand - N. Toque
Centre d'Etudes de Vaujours-Moronvilliers, CEA - FRANCE

ABSTRACT

This experimental work studies the development of a sinusoidal defect initially present at an interface of a metallic plate strongly shocked by high explosive. Results concerning the defect period, its localization and the nature of sample are discussed. A 2-D calculation corresponding to one experimental configuration is also presented.

INTRODUCTION

A lot of theoretical and experimental studies have been devoted to the physical understanding of instability growing up [1,2,3,4]. Nevertheless only a few number of works regarding metallic samples shocked using explosive generators have been published [5,6,7]. Such experiments are generally difficult to interprete because of the numerous parameters which are involved in this kind of instability (Richtmyer-Meshkov, Rayleigh-Taylor, ...).

In this paper, we present some experimental results obtained with different metallic plates on which a periodic defect has been previously machined at the free surface or at the explosive/metal interface. After a short description of the experimental set-up, we study the respective influences of the defect period, its initial localization and the nature of metal.

In the last part, a 2-D numerical calculation shows the capability of our code to correctly restitute such experimental configurations.

EXPERIMENTAL SET-UP AND DIAGNOSTIC

Samples are shocked by cylindrical explosive generators which deliver plane shock waves with an incident pressure of about 50 GPa in tin.

Three parameters have been taken into account in this study :

1. The initial localization of defect.

The defects are machined on the free surface or at the explosive/metal interface. The two corresponding configurations are shown figure 1.

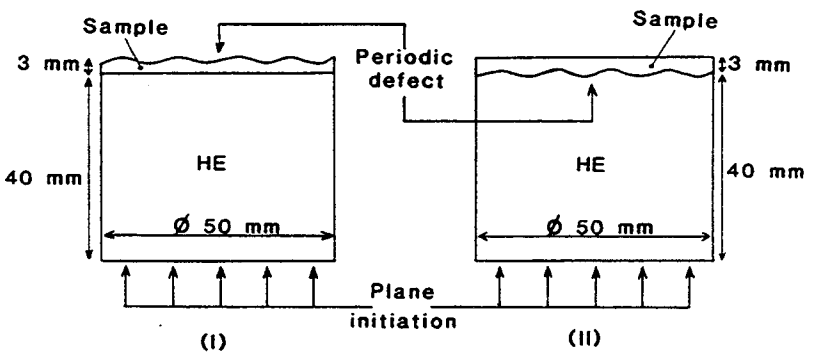

Figure 1 : (I) : Defect on the free surface-(II) : Defect at the explosive/metal interface.

In the second case (II), we may notice that the gap was suppressed between explosive and metal by machining the explosive cylinder with a profile opposed to the metallic sample shape.

2. The period of defect.

The considered values for this study are 3, 6 or 12 mm. The total amplitude of defect is fixed at 0.8 mm in all the cases.

An example of sample is shown figure 2.

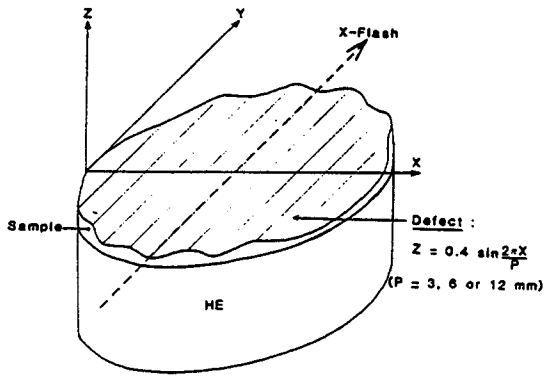

Figure 2 : Schema of samples.

3. The nature of metal.

The different studied materials are tin, steel, copper and magnesium.

A radiographic investigation is made to show up and to measure amplitude of perturbations due to these defects. The used X-Ray generator is a Scandiflash 600 kV which delivers a dose of 20 mrad at 1 meter, during 20 ns (FWHM) with a focalspot size of 1.2 mm.

The radiograph is taken a few microseconds after shock wave transmission in metal (see figure 3). The X-Ray picture allows us to obtain the contours of the shocked metallic plate by avoiding any disturbance due to matter ejection coming from the free surface[8] or due to detonation products. Radiograph processing is made using a profile projector WERTH.

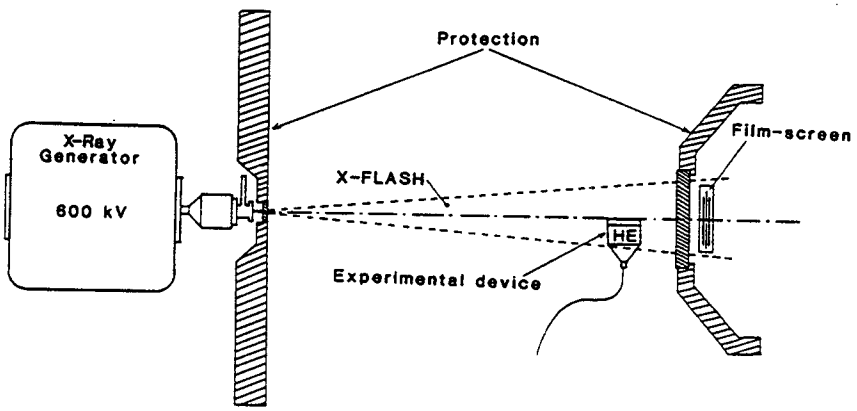

Figure 3 : Experimental arrangement in the firing chamber.

EXPERIMENTS

20 experiments have been made in different configurations summarized Table 1. Concerning the X-Flash instant, the time reference corresponds to the shock arrival at the explosive/metal interface.

For the cases with the defect on the free surface, its initial amplitude is negative because it undergoes an inversion after shock loading.

Defect localization	Material	Atwood number (at the defect interface)	Defect period (mm)	X-Flash instant T (µs)	Defect amplitude	
					Initially (mm)	At T µs (mm)
On the free surface	Tin	1	3	2.70	- 0.8	6.0
				4.84	- 0.8	10.6
			6	4.89	- 0.8	7.6
				7.71	- 0.8	11.0
			12	4.83	- 0.8	5.5
				7.67	- 0.8	7.1
	Steel	1	3	2.83	- 0.8	3.5
				4.80	- 0.8	4.9
			6	4.79	- 0.8	1.5
				7.92	- 0.8	1.6
			12	4.84	- 0.8	0.8
				7.76	- 0.8	0.9
	Copper	1	6	4.67	- 0.8	2.3
				6.83	- 0.8	2.5
	Magnesium	1	6	2.84	- 0.8	3.9
				5.06	- 0.8	5.4
At the Explosive/metal interface	Tin	0.6	6	4.87	0.8	5.0
	Steel	0.63	6	9.16	0.8	5.4
	Copper	0.66	6	9.26	0.8	7.8
	Magnesium	0.02	6	4.92	0.8	2.4

TABLE 1

An example of X-Ray radiograph is shown figure 4.

Static Dynamic T = 9.26 µs

Figure 4 : Obtained X-Ray radiographs (explosive/defect/copper configuration).

Radiograph processing gives the contours of the dynamic plate as shown figure 5.

Obtained experimental contours (magnification : 1.124)

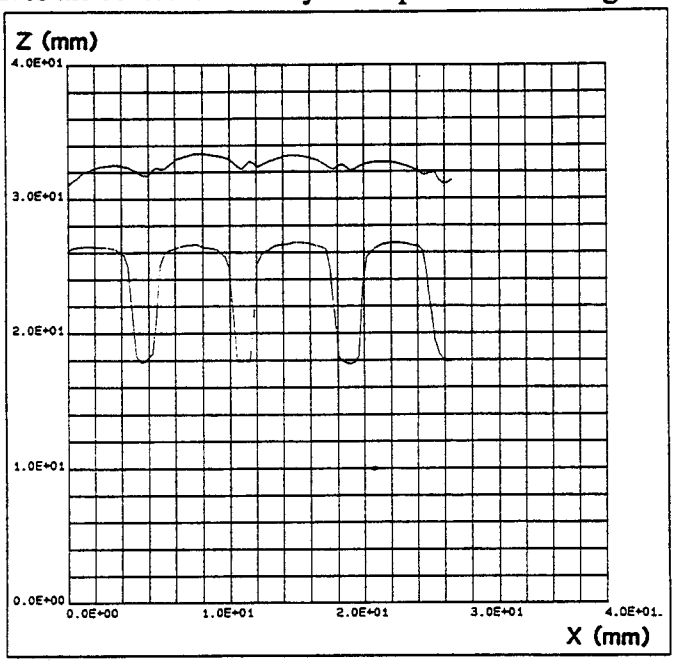

Figure 5 : Contours of the dynamic plate (explosive/defect/copper configuration).

RESULTS

For the 3 considered parameters, we may represent the growing up time histories (A(T)) of defects in a time-amplitude diagram (see figures 6, 7 and 8).

LEGEND :

* TIN

\+ STEEL

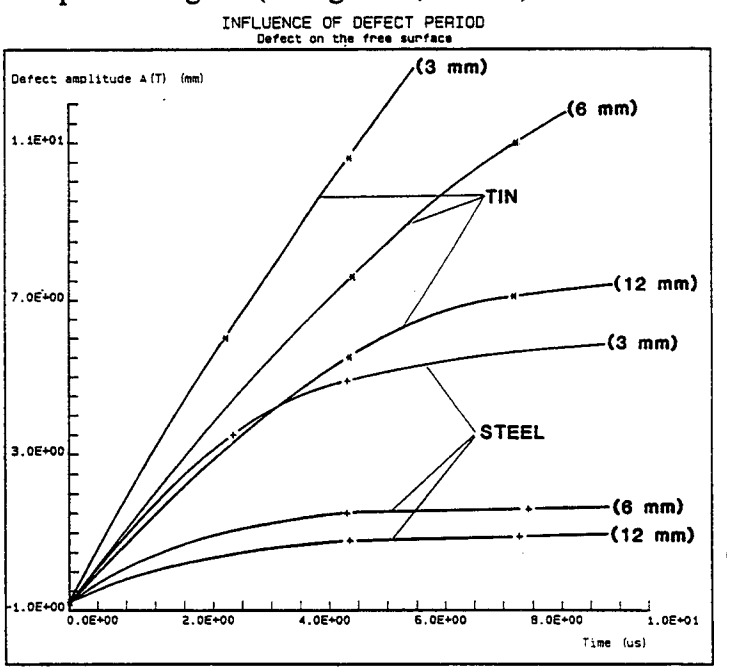

Figure 6 : Influence of the defect period (explosive/tin or steel/defect configurations).

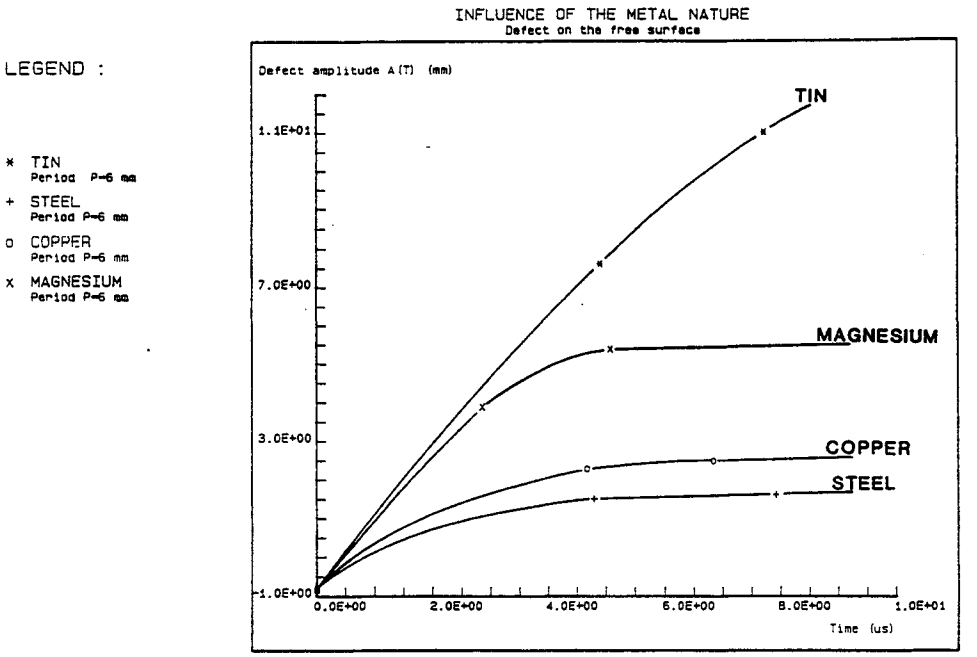

Figure 7 : Influence of the metal nature (explosive/metal/defect configurations).

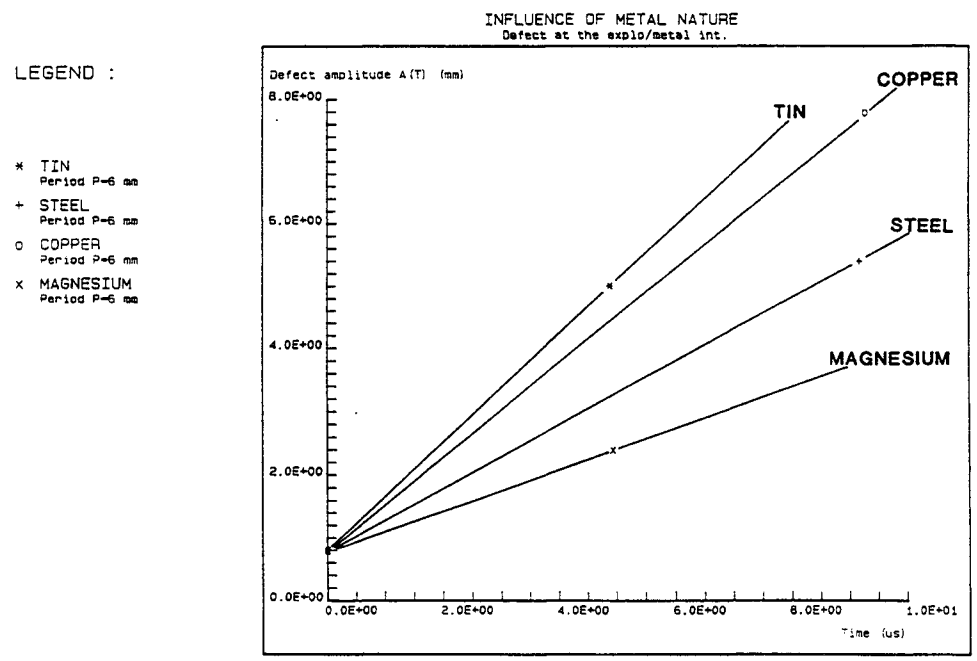

Figure 8 : Influence of the metal nature (explosive/defect/metal configurations).

2-D COMPUTATIONS

The experimental device (without sinusoidal defect) is axisymmetric. This symmetry is lost when a defect is present. Therefore our two dimensional computations (EAD code[9]) doesn't perfectly simulate the system.

The flow is considered to be one dimensional in the perfect case and two dimensional when a defect is added. The lateral boundary conditions are periodic.

The meshes used in these computations must be small enough to allow a precise evaluation of the growth of the defect but the computation time must be reasonable. These difficulties have been solved in the following way :

- the small meshes (30 meshes in a wavelength of the defect) have been used in the perturbed interface zone only,
- the complete treatment of the explosive is limited to the interface region. The remainder of the explosive is simulated by a pressure law which comes from a one dimensional computation.

The computed configuration is shown on figure 9.

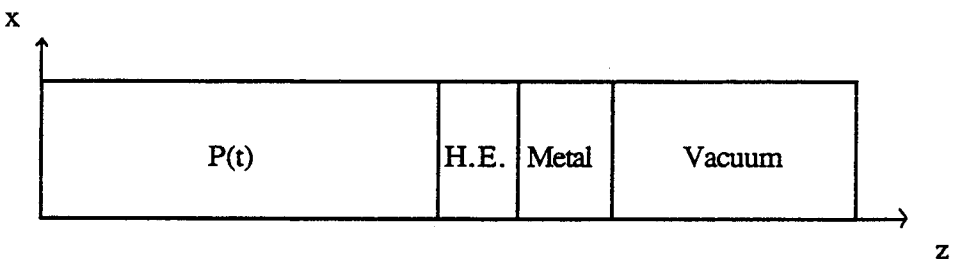

Figure 9 : Initial conditions of EAD calculation.

The width of the eulerian meshes is 0.2 mm in the interface region (1 mm elsewhere).

Numerical results obtained in the explosive/defect/copper case are shown on figure 10.

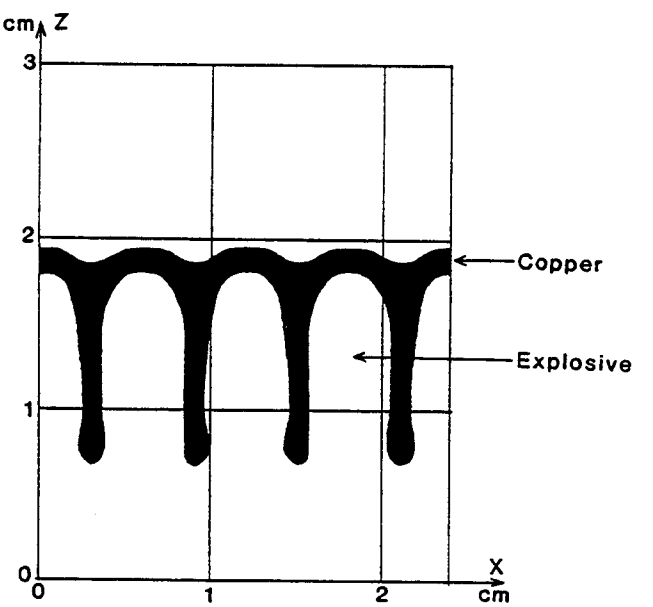

Figure 10 : Numerical results (explosive/defect/copper configuration).

CONCLUSION

In this paper, experiments achieved on tin, steel, copper and magnesium with a flash X-Ray radiography diagnostic, have shown up the respective influences of the defect period, of its localization and of the nature of the explosive-shocked samples.

In the future, experiments are planned in order to study the development of a periodic defect and its transmission at the other interfaces of a multi-layer sample.

Interpretation of the experimental results using 2-D numerical simulations has shown the capability of the EAD code to correctly restitute the considered experimental configuration. The comparison between experiment and calculation seems to be a good test for computed equations of state of the considered materials and for their numerical treatments.

ACKNOWLEDGEMENTS

The authors wish to thank P. CHAPRON for diagnostic development and M. AUTRET, C. FROPO for experimental technical support.

REFERENCES

1. *S. Chandrasekhar - Hydrodynamic and hydromagnetic stability, Oxford Univ. Press (1961), chap. X.*
2. *E. Fermi, J. Von Neumann - Complete Works, Report AECU-2979 (1953).*
3. *R.D. Richtmyer - Comm. on Pure and Appl. Math., Vol XIII (1960), p. 297-319.*
4. *D.L. Youngs - Physica 12D, North-Holland, Amsterdam (1984), p. 32-44.*
5. *V.N. Mineev, E.V. Savinov - Sov. Phy. JETP, Vol. 25, Nber 3 (1967).*
6. *J.F. Barnes et al. - Journ. of Appl. Phy., Vol. 45, Nber 2 (1974).*
7. *J.W. Shaner - Physica 12D, North-Holland, Amsterdam (1984), p. 154-162.*
8. *P. Elias, P. Chapron - Proc. of Shock Waves in Condensed Matter'85, Plenum Press (1986), p. 645-650.*
9. *C. Coste et al. - Computing Methods in Appl. Sci. and Engineering, Glowinsky and Lyons, North-Holland (1982).*

THE LINEAR KELVIN-HELMHOLTZ PROBLEM FOR VISCOUS COMPRESSIBLE FLOWS

L. Hallo and S. Gauthier
CEA, Centre d'Etudes de Limeil-Valenton, 94195 Cedex, FRANCE

ABSTRACT

The linear Kelvin-Helmholtz stability problem for viscous compressible flows is solve by means of a Galerkin method based on a spectral approximation. In this communication, we restrict ourselves to the one-fluid case and we validate the code against some published results. We give both the growth rate and the eigenfunctions in sub- and supersonic configurations.

INTRODUCTION

The linear stability of a viscous compressible mixing layer is the object of a continuous interest for years. Since the pioneering work of Lessen, Fox and Zien[1,2], both inviscid and viscous flows have been investigated by several authors. Blumen[3] studied the instability of an inviscid compressible fluid of a shear layer and gave the growth rate of the most unstable mode. Later, Blumen et al.[4] discovered a second unstable mode which is supersonic and decays weakly with distance from the shear layer. More recently, Macaraeg, Street and Hussaini[5] developed a spectral multi-domain technique in order to solve the highly oscillatory structures and studied high-speed boundary layers and free shear flows.

In this paper, we are reporting a work in progress on the stability of mixing layer for two superposed viscous compressible fluids. In a first step, we solve the linear problem of a temporally growing shear flow in a one-fluid configuration. The numerical code is based on a Galerkin method whose test functions are a non-orthogonal set of polynomials built from the Chebyshev polynomials which satisfied the boundary conditions.

BASIC EQUATIONS FOR THE MIXING LAYER

The evolution equations for a compressible, viscous, thermally conducting gas are the Navier-Stokes equations which write :

$$\frac{\partial \rho}{\partial t} + \nabla_i \rho\, u_i = 0,$$

$$\frac{\partial \rho\, u_i}{\partial t} + \nabla_j \rho\, u_i\, u_j = -\frac{1}{\gamma M^2} \nabla_i P - \frac{1}{Re} \nabla_j \sigma_{ij},$$

where the stress tensor is defined by $\sigma_{ij} = \left(\nabla_i u_j + \nabla_j u_i - \frac{2}{3} \delta_{ij} \nabla_l u_l\right)$

$$\frac{\partial \rho\, T}{\partial t} + \nabla_i \rho\, u_i\, T = P\, \nabla_i u_i + \frac{\gamma}{Re\, Pr} \nabla_i \nabla_i T + \sigma_{ij} \nabla_i u_j$$

where i,j,l = 1,3. This set of equations is closed by the equation of state for the monatomic perfect gas,

$$P = \rho\, T$$

P, ρ and T are respectively are the pressure, the density and the temperature; the u_i are the components of the velocity. The Reynolds, Mach and Prandtl numbers are defined by

$$Re = \frac{U_\infty \rho_\infty \delta}{\mu}, \quad M = \frac{U_\infty}{\sqrt{\gamma R^* T_\infty}}, \quad Pr = \frac{\mu C_p}{k}$$

where U_∞ and T_∞ are taken at the infinity and δ is the mixing layer thickness. The thermal conductivity k and the dynamic viscosity coefficient μ are taken as constants. R^* is the gas constant and C_p the specific heat at constant volume. In these equations we have used dimensionless variables by rescaling length, time, density and temperature as δ, $\delta^2 \rho_\infty / \mu$, ρ_∞ and T_∞ respectively.

We assume that the basic flow is of the form

$$U_0(z) = \tanh z, \; T_0(z) = 1, \; \rho_0(z) = 1$$

where U_0 is the velocity along the x-axis.

In the normal modes analysis, all disturbances are of the form

$$q(x,y,z,t) = Q_0(z) + \hat{q}(z)\, e^{i(hx + ky - \omega t)}$$

where Q_0 and q represent respectively the quantities of mainstream and freestream, while ^ denotes complex disturbance amplitudes; h and k are the disturbance wave numbers and ω is the complex growth rate. The linearized compressible Navier-Stokes equations for the disturbances reads

$$i\omega\rho = -ih\rho_0 u - ik\rho_0 w - v D\rho_0 - \rho_0 Dv - ihU_0\rho$$

$$-i\omega u = -ih\frac{1}{\gamma M^2}\left(\frac{T_0}{\rho_0}\rho + T\right) - \frac{1}{Re}\frac{1}{\rho_0}\left(\frac{4}{3}h^2 + k^2 - D^2\right)u - ihU_0 u - \frac{hk}{3}\frac{1}{Re}\frac{1}{\rho_0}w + \frac{ih}{3}\frac{1}{Re}\frac{1}{\rho_0}Dv + \rho_0 Dv - DU_0 v$$

$$-i\omega w = -ik\frac{1}{\gamma M^2}\left(\frac{T_0}{\rho_0}\rho + T\right) - \frac{1}{Re}\frac{1}{\rho_0}\left(h^2 + \frac{4}{3}k^2 - D^2\right)w - ihU_0 w + \frac{ik}{3}\frac{1}{Re}\frac{1}{\rho_0}Dv - \frac{hk}{3}\frac{1}{Re}\frac{1}{\rho_0}u$$

$$-i\omega v = -\frac{1}{\gamma M^2}\left(\frac{D\rho_0}{\rho_0}\rho + \frac{T_0}{\rho_0}D\rho + \frac{D\rho_0}{\rho_0}T + DT\right) - \frac{1}{Re}\frac{1}{\rho_0}\left(h^2 + k^2 - \frac{4}{3}D^2\right)v - \frac{1}{3}\frac{1}{Re}\frac{1}{\rho_0}iD(hu + kw) - ihU_0 v$$

$$-i\omega T = -\frac{\gamma}{Re\,Pr}\frac{1}{\rho_0}\left(h^2 + k^2 - D^2\right)T - ihU_0 T - (\gamma - 1)T_0 Dv - (\gamma - 1)iT_0(hu + kw) + \frac{2\gamma(\gamma - 1)M^2}{Re}\frac{1}{\rho_0}\left(DU_0 Du + ih\frac{1}{\rho_0}DU_0 v\right)$$

SOLUTION TECHNIQUE

The numerical code is solved by means of a Galerkin method based on a Chebyshev spectral approximation. From the Chebyshev polynomials we built a set of polynomials, R_n which includes the boundary conditions, but do not form an orthogonal system[6]. Expansion on the R_n leads to a finite-dimensional linear operator A. In order to resolve strong gradients, an algebraic mapping[7,8] brings most of the discretization points in the vicinity of the inflectional point. It reads

$$Z_{ps} = \frac{L\, Z_{cs}}{\sqrt{1-Z_{cs}^2}}$$

Subscript ps denotes physical space and cs denotes computational space. L is a parameter.

Characteristics of the freestream are spectrally interpolated onto the new coordinate system, and derivatives of the quantities are obtained using the differentiation operator associated to the stretching. The linear problem is then written under the following form

$$A\,\vec{V} = \omega\, B\,\vec{V} \qquad \text{where} \qquad \vec{v} = (\hat{\rho},\hat{u},\hat{v},\hat{w},\hat{T}).$$

where the operator B is due to the non-orthogonality of the R_n. This eigenvalue problem gives the growth rate and the complex disturbances for different values of the parameters h and k. At last step, we find the eigenvalues and eigenvectors by input into IMSL routine for solution.

The parameter L is calculated by minimizing the following functional with j=2 [9,10].

$$|U|_{2,j} = \frac{1}{N^2}\left(\sum_{k=0}^{N-1} \frac{\pi}{2} c_k\, k^{2j}\, a_k^2\right)^{1/2}$$

Where a_k are the Chebyshev coefficients and c_k has the usual meaning $c_0=2$ et $c_k=1$ for $k>1$. This functional allows us to obtain results in good agreement with references 4 and 5, for a small number of polynomials. It provides a rigorous bound of the projection error in the L^2 norm.

RESULTS

In order to validate the numerical code we have recomputed some cases given in References 1 and 2. Results, summarized in the Table I, show a very good agreement even with 30 Chebyshev polynomials.

Table I. Comparison of temporal eigenvalues for different values of the Mach number with $\gamma = 1.4$, $Pr = 0.7$, $Re = 10^4$

Table I

Mach	Alpha	Blumen's results[3]	Macaraeg's results[5]	ω_i calculated 30 polynom.	ω_i calculated 71 polynom.	L
0.0	0.445	0.190	0.18954	0.18954	0.18954	1.13
0.2	0.426	0.181	0.18112	0.18112	0.18112	1.60
0.5	0.397	0.141	0.14101	0.14101	0.14101	2.10
0.7	0.326	0.101	0.10012	0.10065	0.10012	2.33
0.9	0.208	0.055	0.05450	0.05440	0.05450	2.7

We give two examples of such computations. The first one for a Mach number equal to 0.9. The eigenmode is symmetric with respect to the middle of the layer.

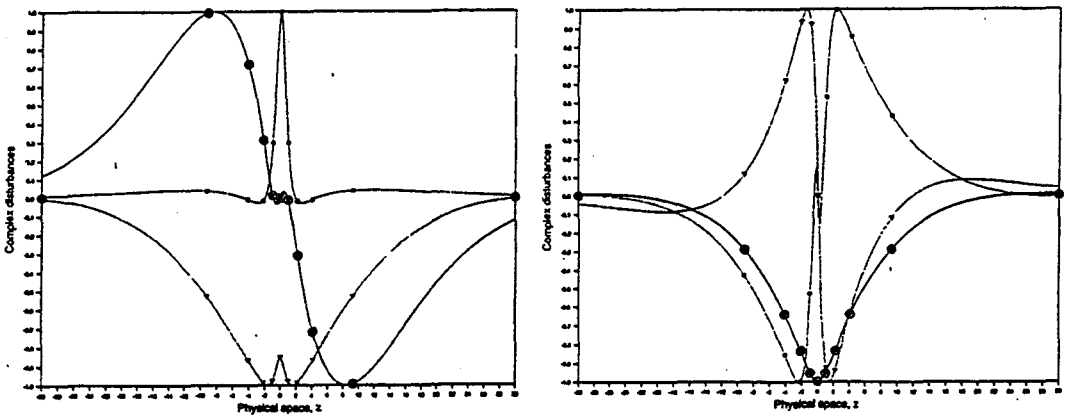

Figure 1. Complex disturbances versus z. The Mach number is 0.9, the Reynolds number is 10^4, $\gamma = 1.4$ and $\sigma = 0.7$. The circles stands for the density and temperrature eigenmode while the squares and the triangles stand for the vertical and the horizontal velocity components respectively.

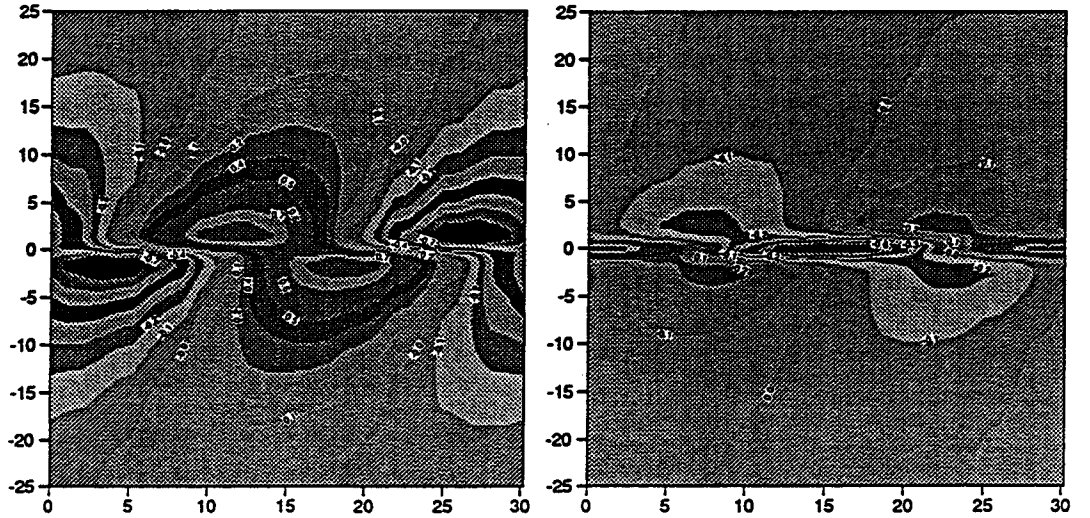

Figure 2. Velocity component contours for the subsonic case M = 0.9.

We have also computed a supersonic case with a Mach number equal to 1.05. In this case the most unstable mode is characterized by a complex eigenvalue with $\omega_i = 0.6072\ 10^{-2}$ and $\omega_r = 0.4669\ 10^{-1}$. The phase velocity is then $v_\phi = 0.207$. Both real and imaginary parts of the first unstable mode have been represented in Figure 3. Note the dissymmetry with respect to the middle of the mixing layer as opposed to the subsonic case[4].

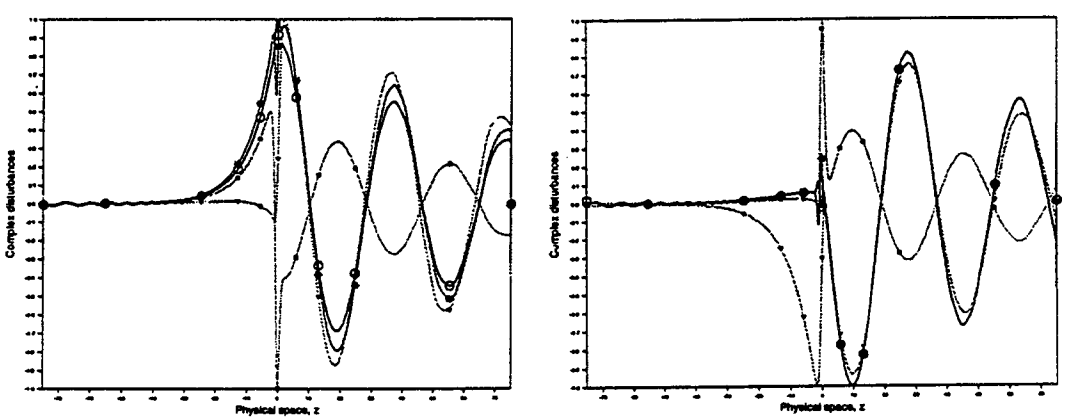

Figure 3. Complex disturbances versus z. The Mach number is 1.05, the Reynolds number is 10^2, $\gamma = 1.4$ and $\sigma = 0.7$.

ACKNOWLEDGMENTS

We would like to thank H. Guillard for helpful discussions.

REFERENCES

1 - M. Lessen, J. A. Fox and H. M. Zien, J. Fluid Mech. **23**, 355 (1965).

2 - M. Lessen, J. A. Fox and H. M. Zien, J. Fluid Mech. **26**, 737 (1966).

3 - W. Blumen, J. Fluid Mech. **40**, 769 (1970).

4 - W. Blumen, P. G. Drazin, and D. F. Billings, J. Fluid Mech. **71**, 305 (1975).

5 - M. G. Macaraeg, C. L. Street and M. Y. Hussaini. A spectral collocation solution to the compressible stability eigenvalue problem. NASA Technical paper 2858, December 1988.

6 - S. Gauthier, T. Desmarais et G. Iooss, Europhys. Lett. **10**, (6), 543 (1989).

7 - C. Canuto, M. Y. Hussaini, A. Quarteroni, and T. A. Zang. Spectral Methods in Fluid Dynamic. Springer Series in computational Physics, Springer-Verlag 1988.

8 - R. W. Metcalfe, S. A. Orszag, M. E. Brachet, S. Menon, and J. J. Riley. J. Fluid Mech. **184**, 207 (1987).

9 - A.Bayliss, A.Gottlieb, B.J.Matkowsky, and M.Minkoff, J. Comp. Phys. **81**, 421 (1989).

10 - H.Guillard, J.M.Malé, R.Peyret, Adaptative spectral methods with application to mixing layer computations. Preprint INRIA 1990, submitted to J. Comp. Phys.

ANALYTICAL AND NUMERICAL STUDIES OF RAYLEIGH-TAYLOR INSTABILITY

N.A. Inogamov,
Institute for Scientific Interchange, 10133, Torino, Italy*)
A.V. Chekhlov, Al.Yu. Dem'yanov
Moscow Institute of Physics and Technology, 141700,
Dolgoprudny, Moscow REgion, USSR
S.I. Anisimov
Ecole Polytechnique, Centre de Physique Théorique,
91128 Palaiseau, France*)
O.M. Belotserkovskii
Institute for Automatic Design, 141700, Dolgoprudny,
Moscow Region, USSR.

INTRODUCTION

In the present paper the flow driven by the Rayleigh-Taylor insability (RTI) is considered. The basic concept of this consideration is a stationary solution. The flow is considered as a sequence of quasi-stationary solutions with transitions between them due to their instability.Stationary solutions are represented by points in a phase space. Linear analysis of the functional neighbourhood of these points shows that these are saddle points and there are separatrices going from and coming to the points. This can be symbolyzed in the following manner

A separatrix is the integral curve passing from one stationary point to the another. The symbolic picture looks like

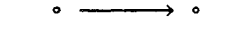

The separatrix represents a transient solution which starts from a stationary solution at $t=-\infty$ and arrives at another one at $t=+\infty$. We consider these transitions along the separatrices and describe the dynamics of our system in terms of the separatrices.

STATIONARY SOLUTION

The problem of stationary solution is rather complicated. It is studied in the paper [1],presented at this Workshop. The result of this study can be summarized as follows:although there is no rigorous theorem of existence and uniquiness of the stationary solution, in practice,the stationary flow with bubble rise velocity approximately equal to $0.23(g\lambda)^{1/2}$ and bubble radius of curvature about $2.5/k$ is realized. This result agrees well with the experiment

INSTABILITY

Let λ be the period of a stationary solution. Consider the disturbance of the stationary solution, which has a space period $m\lambda$, where $m>1$ is an integer. It can be shown that the stationary solution is unstable with respect to such disturbances. Nonlinear growth of the perturbations leads,asymptotically,to the formation of a different stationary solution with the space period $m\lambda$. This process

*) On leave from LD Landau Institute for Theoretical Physics, 117940, Moscow, USSR.

can be symbolized as

$$(\lambda) \cdot \longrightarrow \cdot (m\lambda),$$

where periods of stationary solutions are given in brackets.We studied the instability of stationary solutions numerically.First, let us consider the perturbation with m=2. Two cases are possible: merging of bubbles and competition of bubbles. The principle of merging is shown in Fig.1. Here (a) is the unperturbed chain of tops of the bubbles,(b) is the chain perturbed: the coupling of bubbles into pairs is seen. In Fig.1 (c) the time evolution of the contact boundary is sketched ($t_1<t_2<t_3$) showing the weakening of the central jet in the couple of bubbles and and the strengthening of the side jet which separates the couples.

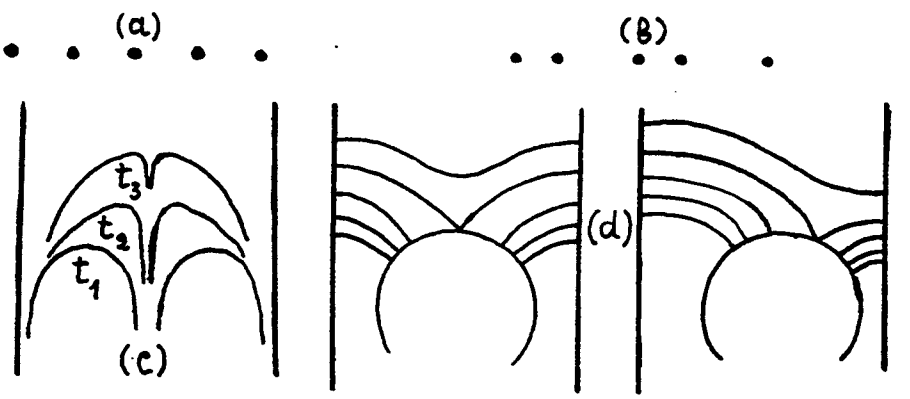

Figure 1

Qualitative explanatiion of this behaviour can be obtained from the electrostatic analogy (see Fig.1 (d)). In this Figure the electric field lines in a plane condenser containing an ideally conducting noncharged cylinder are shown. A displacement of the cylinder closer to one of the plates leads to a change in its polarization.Due to this,the equipotential lines (corresponding to stream lines of the flow around the cylinder) concentrate in the narrow gap between the plate and the cylinder. This leads to the growth of electric stress due to the charge concentration in this narrow region. In hydrodynamic analogy, this means the growth of velocity and according to Bernoully' theorem, to the decrease of pressure. Thus, the attractive force appears between the bubbles.

The results of numerical calculations are shown in Fig.2, where g=2, μ=0.1, λ=10. One can see the weakening of the left jet (separating bubbles in a couple) and the amplification of the right jet (separating the bubbles of two different couples). This is in the agreement with the above qualitative consideration.

The numerical simulation is based on the artificial compressibility method for incompressible Navier-Stokes equations. The mesh used was 40x120.

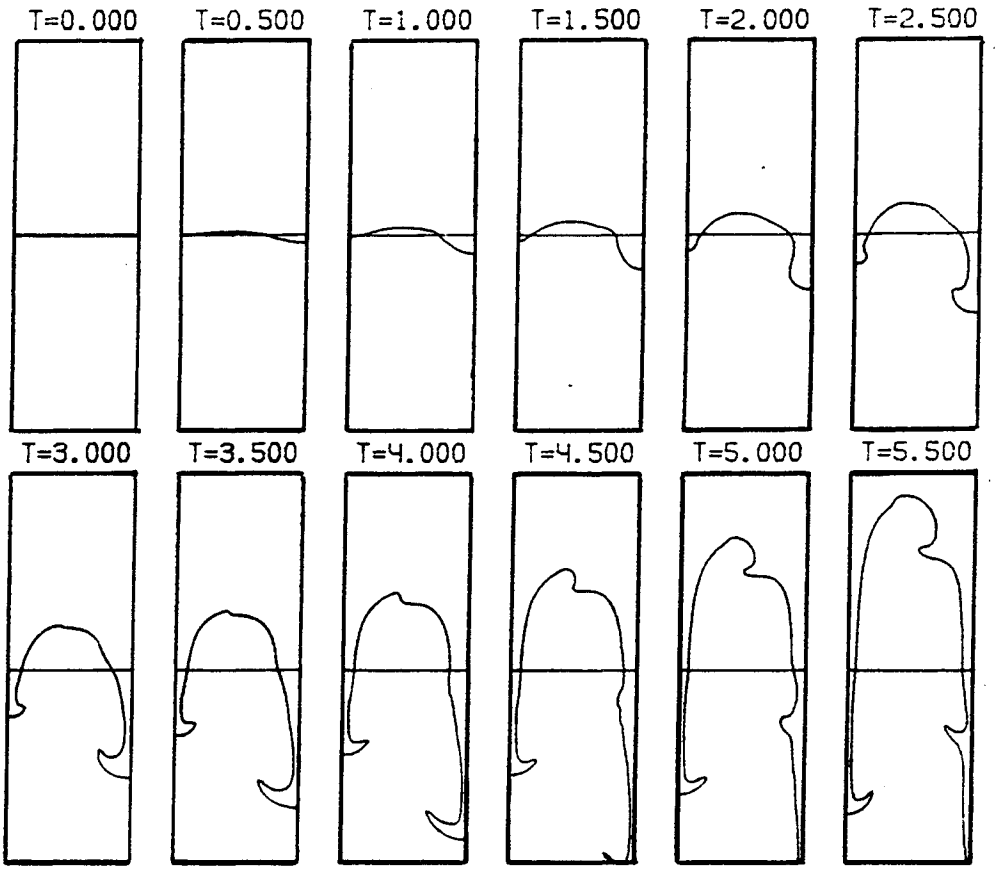

Figure 2

The second case of mode interaction is the competition of bubbles. The principle of the competition is seen in Fig.3 where the non-perturbed (a) and perturbed (b) chains of bubble's tops are represented by points. The results of numerical calculations are presented in Fig.3 (c),(d). In Fig.3 (c) the interaction of two rising bubbles of different size ($\lambda_1/\lambda_2=2$) is shown. The interaction results in slowing down of the lower (left) bubble. In Fig.3 (d) the dependences of non-dimensional amplitudes of the two bubbles,

$$F_1(t) = \ln((A_1-A_0)/\lambda), \quad F_2(t) = \ln((A_o-A_2)/\lambda)$$

on the dimensionless time γt are shown.Here A_o is the unperturbed bubble amplitude; A_1 and A_2 are the amplitudes of the higher and lower bubbles,respectively; γ is the instability growth rate for a plane boundary

$$\gamma=(kgAt)^{1/2} \quad k=2\pi/\lambda$$

λ is the space period of unperturbed flow; $At=(\rho_1-\rho_2)/(\rho_1+\rho_2)$ is the Atwood number.

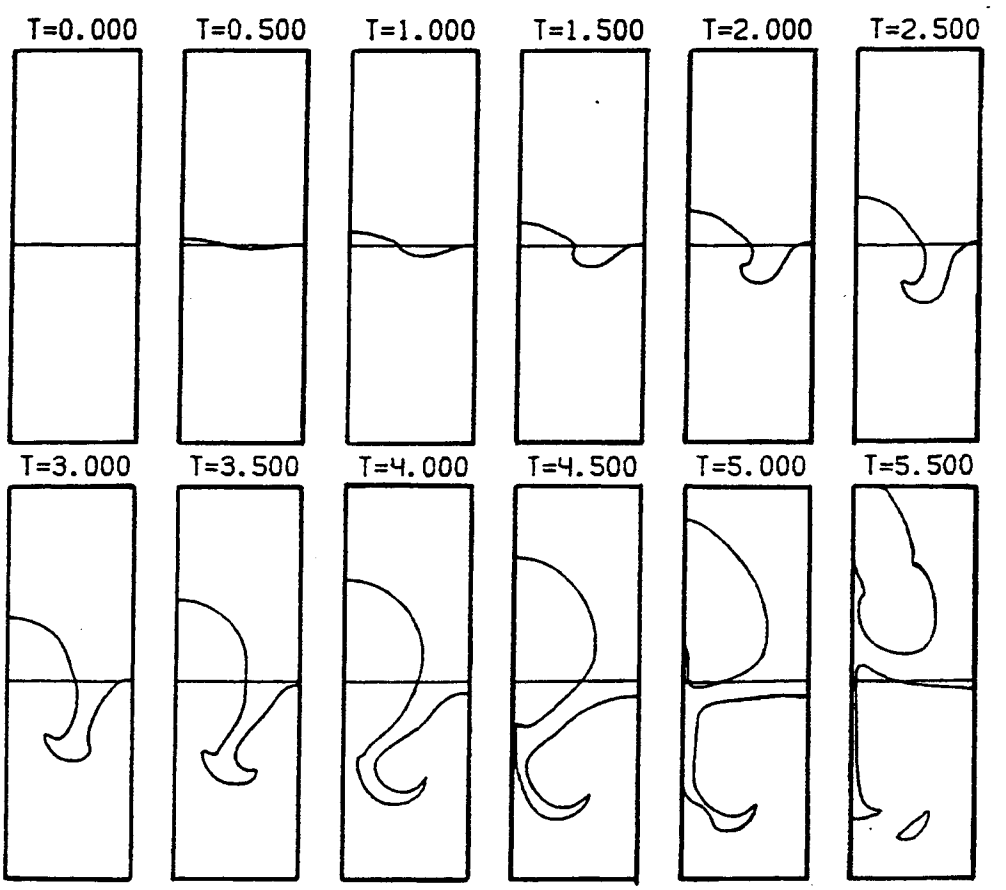

Figure 3 (a),(b),(c)

HOMOGENEOUS SPECTRUM

In this section we discuss the effect of initial disturbance on the development of RTI. We consider first the small amplitude disturbances. In this case the problem is linear and the principle of superposition is valid.

A monochromatic initial disturbance is characterized by three parameters: the wavelength λ, the amplitude of boundary displacement η and the amplitude of velocity pertupbation v. For our analysis,the initial disturbance with homogeneous spectrum is of particular interest. In the case of RTI this spectrum has the following form: $\eta(\lambda)=\varepsilon(\lambda)\cdot\lambda$, $v(\lambda)=\varepsilon(\lambda)\cdot(g\lambda)^{1/2}$, where $\varepsilon(\lambda)$ is a small amplitude its average value being constant. Note that in RMI and KHI homogeneous spectra have the form: η/λ=const and v/λ=const,respectively.

Thus,homogeneous spectra can be characterized by a single parameter which is the relative amplitude,ε . An example of homogeneous spectrum is shown in Fig.4.

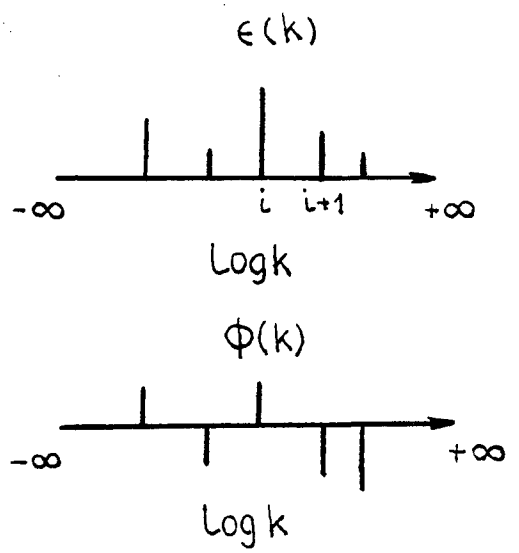

Figure 4

Here $\Phi_i=2\pi(-1)^{[2\chi_i]}\cdot\varphi_i$ is the phase, [...] denotes an integer part, $\Delta_i=C\zeta_i$ is the distance (in log(k) scale) between the successive harmonics with numbers i+1 and i; C is an arbitrary number; $\varepsilon_i=\varepsilon\xi_i$ and $\zeta_i,\xi_i,\chi_i,\varphi_i$ for every i are independent random numbers from the interval (0,1).

STIMULATED TURBULENCE

We consider here two kinds of RT-turbulence which we shall call stimulated and spontaneous turbulence.To study the first one, choose a homogeneous spectrum as the initial condition and consider

its evolution. The analysis shows that the system passes through a number of scale multiplications and demonstrates a cascade-like behavior. Performing the summation of the contact boundary displacements over successive time intervals and taking $\xi_i = 1$ we obtain the result [3]

$$Y_+=(C/|\ln(\varepsilon)|)\cdot gt^2$$

where Y_+ is the distance between the upper boundary of turbulent layer and its initial position, C=const. Note that the above considered turbulent motion is stimulated by certain initial conditions and takes place in a non-limited spatial region (in contrast to the case of RTI in a vertical tube). This is the reason for calling this motion free stimulated RT-turbulence (RTT).

INCOMMENSURABILITY AND SPONTANEOUS RTT

Consider the evolution of RTI in case of bimodal initial perturbation consisting of two monochromatic modes with wavalengths λ_1 and λ_2. Let us assume, first, that the wavelengths satisfy the condition $\lambda_2/\lambda_1=m/n$, where m,n are the integers not having common multipliers. The evolution of the system leads, in this case,to the formation of a stationary solution with spatial period $mn\lambda^*$ where $\lambda^*=\lambda_2/m=\lambda_1/n$. The evolution is quite different if the initial condition contains the modes with irrational ratio of spatial periods. In this case,the system passes, in functional space,close to stationary solutions which have the periods $m_1 n_1 \lambda_1^*$, $m_2 n_2 \lambda_2^*$,where the integers m_i, n_i satisfy the condition that their ratio provides a close rational approximation to the wavelength ratio λ_2/λ_1. This can be shown symbolically in the graph:

Figure 5

The above mentioned motion occurs to be turbulent. We call it spontaneous RTT. In case of incommensurable periods of initial disturbances,the multiplication of spatial scale of the motion takes place. Approximate selfsimilarity is valid for average flow characteristics

COMPETITION BETWEEN STIMULATED AND SPONTANEOUS TURBULENCE

The relation between stimulated and spontaneous RTT is shown in Fig.6.

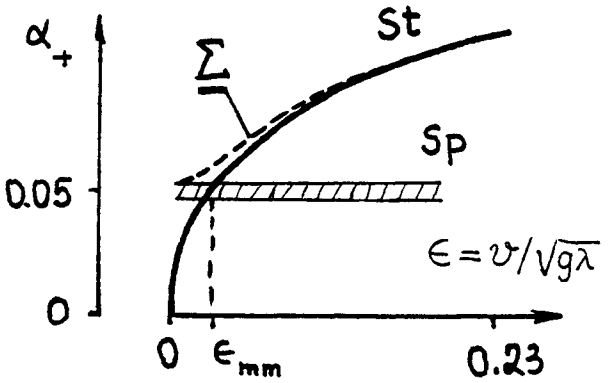

Figure 6

Here $\alpha_+ = Y_+/(gt^2)$, and St, Sp refer to stimulated and spontaneous RTT, respectively, Σ is the summary turbulent mixing coefficient. We consider here the velocity perturbation as the initial condition; the contact line is not perturbed. The turbulent mixing coefficient is considered as a function of non-dimensional velocity perturbation $\varepsilon = v/(g\lambda)^{1/2}$. It is well known that if the condition $\varepsilon << 0.23$ is satisfied, the linear analysis can be applied.

If the equation $\alpha_+ = C/|\ln(\varepsilon)|$ is valid only one point in the (α, ε) plane should be found to calculate the constant C. Let us assume that the initial disturbance has homogeneous spectrum with ε being the characteristic amplitude of the initial disturbance. If ε is not very small the dynamics of the turbulence has stimulated character. Transition to the spontaneous regime occurs when ε reaches some critical value ε_{mm} (see Fig.6). It should be noted that for the spontaneous turbulence regime, the turbulent layer growth rate is higher than that for the stimulated turbulence regime if the condition $\varepsilon < \varepsilon_{mm}$ is satisfied. The critical value of the initial noise ε_{mm}, is very important for applications. It determines the minimum level of contact boundary perturbations for which further "cleaning" of the boundary leads to decrease in the velocity of turbulent layer growth.

To check the above theory numerical calculations were performed. The first calculation was carried out using the mesh 60·360 with square cells. Zero normal velocity at upper and lower boundaries and symmetry conditions at the right and left boundaries were chosen as the boundary conditions. The horizontal scale of the computational region was $\lambda/2$. Initial perturbations with wavelengths $\lambda_1 = \lambda/17$, $\lambda_2 = \lambda/23$, $\lambda_3 = \lambda/31$ and amplitudes $\varepsilon_1 = \varepsilon_2 = \varepsilon_3 = 0.23$ were used. All calculations were performed using only velocity initial disturbances as it was done in the papers [4,5]. From the results of calculations, x-averaged density profiles $\bar{\rho}(y)$ were obtained. They

were used for the calculation of the coefficient of turbulent mixing $\alpha_+ = Y_+/(gt^2)$ assuming "ξ=0.05-criterion". This means that

$$\bar{\rho}(Y) = \rho_1 - \xi\,(\rho_1 - \rho_2)$$

where ρ_1, ρ_2 are the densities of the heavy and light fluids, respectively. Results of this procedure are shown in Fig.7 (a,b).

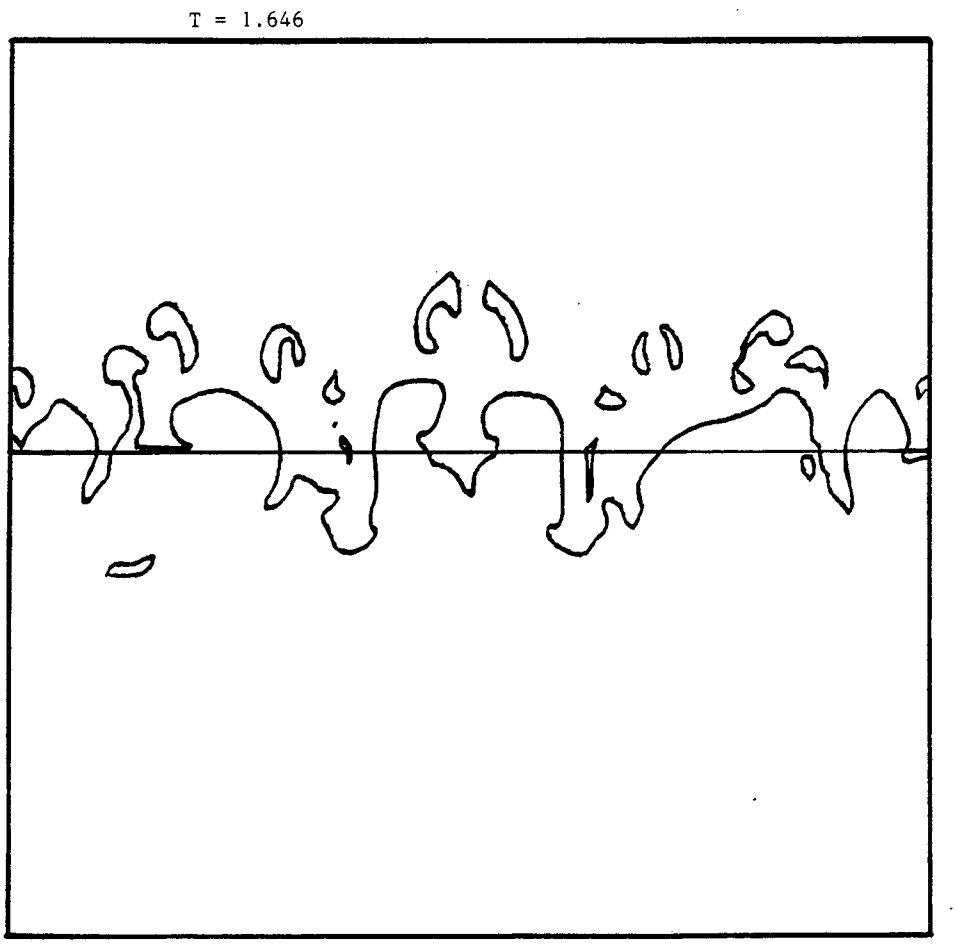

Figure 7 (a)

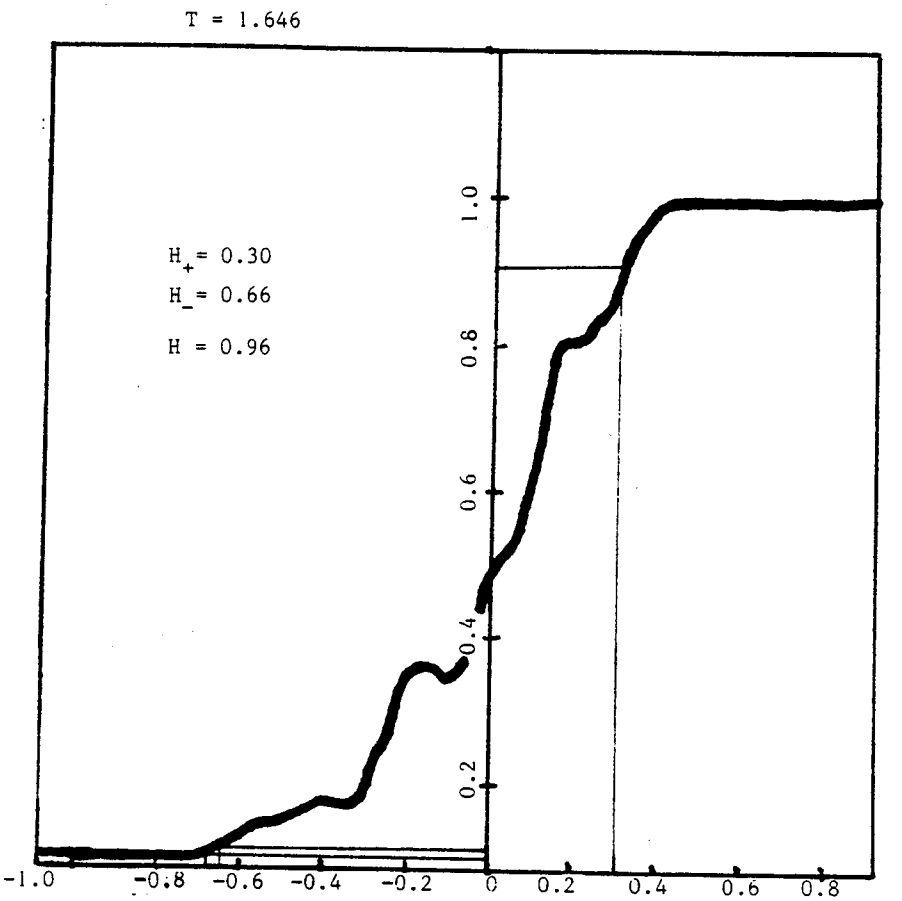

Figure 7 (b)

We obtained the value of turbulent mixing coefficient $\alpha_+=0.07\pm0.01$, which is slightly greater than the value 0.04-0.05 obtained in papers [5,6].

In the second calculation the mesh size was 120x120. All other parameters were not changed. This thickening of the mesh did not change considerably the value of turbulent mixing coefficient.

In the third calculation, using the mesh size was 60·360. The initial conditions were chosen as follows. To the above hree modes with the wavelengths ratio $\lambda_1:\lambda_2:\lambda_3=31:23:17$ and the amplitudes $\varepsilon_1=\varepsilon_2=\varepsilon_3=0.23$ the homogeneous spectrum with wavelengths $\lambda_m=\lambda/2^m$ and amplitudes $\varepsilon_m/0.23=0.15 \ll 1$ was added. Due to the symmetry of boundary conditions at the right and left boundaries the phase must

be equal to $i\pi$, where i is an integer. In this calculation we take φ_m=0. The results of the calculation are shown in Fig.8. The turbulent mixing coefficient is larger in this case.

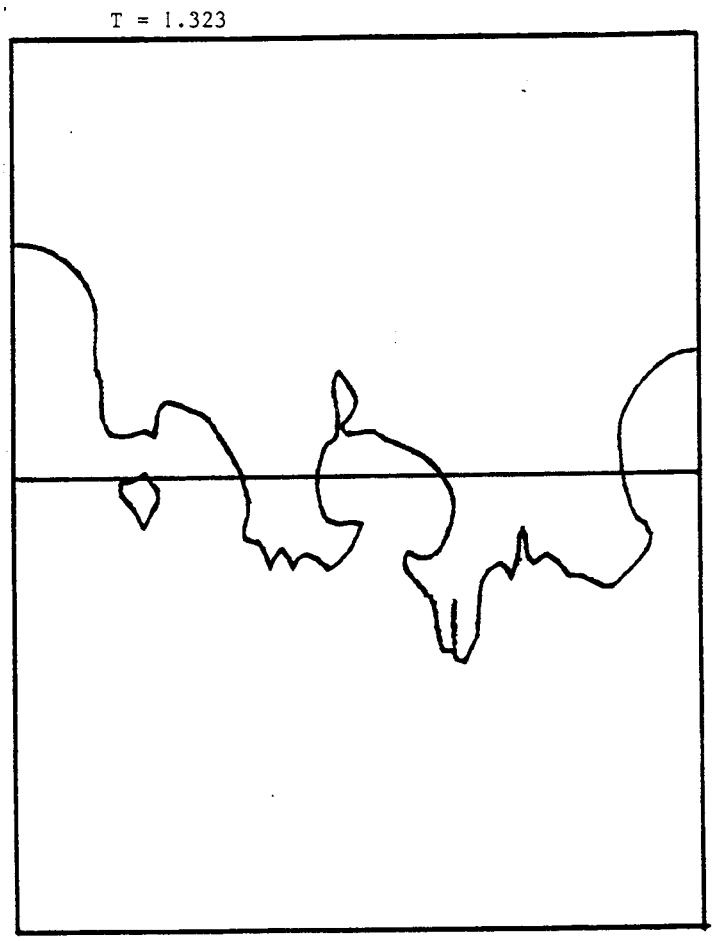

Figure 8

Note that more detailed analysis of the results of numerical calculations is beyond of the limited volume of this paper.

CONFINED TURBULENCE.LINEAR ANALYSIS

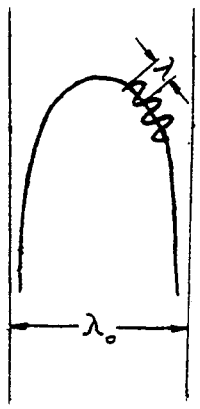

Figure 9

Consider the stability of periodic stationary solution with a period λ_o with respect to short wavelength disturbances. The disturbance under consideration is a wave packet created at the moment $t=t_o$ which moves with the fluid velocity along the boundary streamline. The disturbance wavelength λ increases with time due to fluid acceleration along the streamline. One can show $\lambda(t)=\lambda(t_o)v(t)/v(t_o)$ where $v(t)$ is the local velocity of stationary flow in the point which is passed by the disturbance at the moment t. Taking into account this relation, the amplitude of the disturbance can be written as

$$\eta(t)=A(t)\cdot\exp(\int\gamma\cdot dt),\quad \gamma=(g_{eff}\cdot k)\quad,\quad A(t)=\eta(t_o)v(t_o)/v(t),$$
$$g_{eff}=g_{eff}(t)=g_{ff}(1+Y_x^2)^{-1/2}-v^2/R.$$

Here g_{eff} is the difference between normal projection of the free fall acceleration, g_{ff}, and a centrifugal acceleration, R is the radius of curvature, $y=Y(x)$ is the free boundary equation, $k=2\pi/\lambda(t)$. The estimation of the factor A(t) can be made using the idea of contraction of normal to the boundary amplitudes due to the strain of boundary streamline and the conservation of area in an incompressible fluid flow. With a good accuracy stationary solution near the free boundary can be approximated by the flow in a strip around a cylinder with the radius $R = 2.5/k_o$ and velocity at the infinity $v = 0.23(g\lambda_o)^{1/2}$. It can be shown, that in this case $g_{eff}(y_*)=0$ and the gain is saturated. The gain is equal to

$$\eta(t_*)/\eta(t_o)=[v(t_o)/v(t_*)]\cdot\exp(\int\gamma\cdot dt)=$$
$$=(y(t_o)/y(t_*))^{1/2}\cdot\exp(\int\gamma\cdot dt),$$

$$y(t_o)\ll\lambda\ ,\quad y(t_o)\approx -x(t_o)^2/(2R)$$

where $x(t)$, $y(t)$ define the position of the disturbance at the moment t. In all this cases we use the integration from t_o to t_*. We put also $x(t_o)=\lambda(t_o)/2$.

The results of calculations can be summarized in the following way:

1)The gain about 100 and higher is possible only if the initial scale of the disturbance is sufficiently small, so that $m > 10$ where $m = \lambda_o/\lambda(t_o)$. This means that only short wavelength perturbations with $m > 10$ might be important at the nonlinear stage.

2)The growth of the short wavelength perturbations does not

affect significantly the stationary flow in the bubble neighbourhood,but it can lead to the dispersion of jet.

NUMERICL SIMULATION

We studied in detail numerically the problem of confined stimulated turbulence. Here we restrict ourselves to the case of single disturbing mode. It means that only one mode of disturbance is added to the unperturbed long scale flow. The value of $m=\lambda_0/\lambda(t_0)$ was equal to 20 where $\lambda(t_0)$ is the initial wavelength of the disturbance.It should be noted that this value of m is rather large; the preliminary calculations in [4] were performed only for $m \leq 5$. The present calculations were carried out on the mesh 120·120 using rectangular cells. The dimensions of the computational field L_x, L_y were chosen as: $L_x:L_y=3:1$.Because of the symmetry of right and left boundary conditions the total number of cells in the wavelength λ was 240. The density ratio was taken $\mu=0.1$. The results of numerical calculations are shown in Fig.10. They are in agreement with the above conclusions 1) and 2).

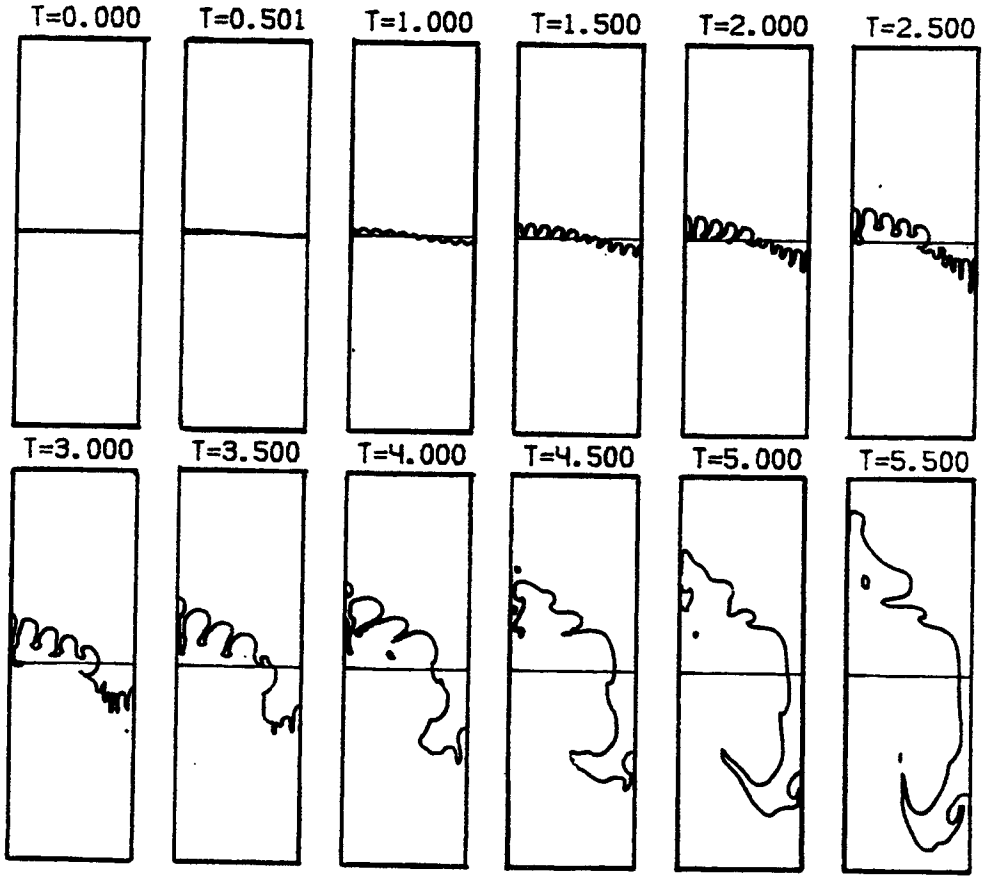

Figure 10

CONCLUSION

Main results of the present paper can be summarized as follows.

1.The existence of stimulated RTT is shown.This turbulence is governed by the usual self-similarity law: the average scale of the coherent structures grows as gt^2, the thickness of turbulent mixing zone is given by $Y_+ = \alpha_+ gt^2$, where the factor α_+ increases when the amplitude of stimulating disturbances increases.

2)Spontaneous RTT was studied. It was shown that the presence of two modes in initial spectrum with incommensurable wavelengths is sufficient to generate this type of turbulence. Important role of incommensurability was also emphasized.

3)Relative role and interaction between spontaneous and stimulated types of RTT is investigated. It was shown that if an initial perturbation amplitude is smaller than some critical value its further lowering does not lead to the decrease of turbulent layer growth rate.

4)We propose the following classification of turbulent mixing regimes: free and confined regimes. The analysis was performed of the confined turbulence in the case $\mu=0$.

5)Stability of the stationary solution to the short wavelength perturbations was studied. We showed that the stationary solution is unstable and the arising flow slightly differs from the initial stationary flow. It follows from our analysis that for the flow in a vertical strip with initially plane contact boundary and $\mu=0$ the regime is reached asymptotically which we call confined RTT if the condition $t(g/\lambda_0)^{1/2} \gg 1$ is satisfied where λ_0 is the width of the strip.

ACKNOWLEDGEMENTS

The authors are grateful to Prof.E.Son for stimulating discussions und useful criticisms.

REFERENCES

[1] N.A.Inogamov, A.V.Chekhlov, Al.Yu.Dem'yanov. Report in this Workshop.
[2] C. Gardner. Phys. Fluids 31 (1988) 447-465.
[3] N.A.Inogamov. Pis'ma v J. Techn. Phys. 4 (1978) 743-747.
[4] O.M.Belotserkovskii, Yu.M.Davydov, Al.Yu.Dem'yanov. Doklady Acad. Nauk SSSR 288 (1986) 1071-1074.
[5] D.L.Youngs. Physica 12D (1984) 45-58.
[6] K.I.Read. Physica 12D (1984) 32-44.

STEADY-STATE FLOW PRODUCED BY RAYLEIGH-TAYLOR INSTABILITY

N.A. Inogamov
Institute for Scientific Interchange, 10133, Torino, Italy*
A.V. Chekhlov and Al.Yu. Dem'yanov
Moscow Institute of Physics and Technology, 141700,
Dolgoprudny, Moscow Region, USSR.

INTRODUCTION

Stationary periodic solution plays an important role in the theory of Rayleigh-Taylor (RT) instability and RT turbulence. In this work we constructed a new formal method which allows to relatively easily solve a very complicated set of non-linear algebraic equations F_m (A) = 0, m = 1, 2, 3,..., N (N is a truncation number) for the amplitudes A = (A_1, A_2,..., A_N) in the expansion of the potential of stationary flow in Fourier series. We calculate the equations up to N =5 and solve them for N ≤ 4.

We examined carefully the obtained equations and their solutions using the following tests :

Test n°1. Our method is based on the re-expansion of explicit function f (x, y) = 0 expanded in zero in an implicit power series y = y (x). We check rightness of coefficient recalculation rules using some known test function f.

Test n°2. Let us examine the correctness of calculation of the equations and the roots. Our method is based on the expansion of kinematic and dynamic boundary conditions in the stagnation point in even power series in horizontal coordinate x. Boundary conditions are satisfied in the corresponding orders in x. Solution with N = 1 satisfies the conditions with x^2 accuracy. The Nth-order solution satisfies the conditions with x^{2N} accuracy. This opens a way to an independent test. Let $\vec{A}$ be the solution of order N. Let φ (x,y) and ψ (x,y) be the potential and stream function corresponding to this $\vec{A}$. Let us find a stream line ψ (x,y) = 0 outgoing from the stagnation point. This point is a saddle point. Zero stream line is a separatrix of this point. This line can be found by two methods. First, we integrate ordinary differential equation $dy/dx = -\psi_x/\psi_y$ from the vicinity of the saddle point. Second, we iteratively solve equation ψ (x,y) = 0 at several fixed x_i for unknown corresponding values of y_i. After that we calculate the difference $D(x) = [-v / (2y) - |g|] / x^{2N}$ in the vicinity of x = 0. If $D(x) \to$ const when $x \to 0$ then the equations and their roots are correct.

The phenomenon of splitting of solution at N= 4 together with the wide spread of solutions at different N can be considered as an indication to the absence of convergence to a single solution.

The points in (w_∞, R) plane are concentrated along a curve which must (in the limit $N \to \infty$) correspond to a single-parameter family of solutions (here w_∞ is the velocity of

* On leave from L.D. Landau Institute for Theoretical Physics, 117940, Moscow, USSR.

bubble rise, R is the radius of curvature at the stagnation point).

The end point on this curve corresponds to the solution with maximum value of w_∞. Three points, corresponding to N = 1,3 and 4F are all located near the end point. They all have values of w_∞, R and velocity distribution very close to those found numerically. But it is interesting to note that values of $\vec{A}$ for N=1 and N = 3 are far from N=4F values.

Note also that in case N= 4 the solution corresponding to N=4F has about 100 times larger radius of convergence of 3D Newton iteration procedure than N=4S solution.

This could be related to the problem of transition from hydrostatic equilibrium with periodic stimulation to asymptotic motion and to the answer to the question: why doesn't anyone see in the experiments solutions different from the asymptotic ones, in spite of the existence of a whole family of solutions?

The above consideration is, to our opinion, the first quantitative argument which supports the hypothesis of the existence of single parameter family of solutions.

In what follows, the theory of asymptotic stage of periodic waves is developed. The asymptotic regime has not been studied completely in earlier works. There are two analytical works in which the periodic flow was expanded into the Fourier series. For a long time, in the only known work [1] the case N=1 was studied where N is the number of harmonics in the series. Recently, the work [2] appeared in which N=3 is considered. We considered higher harmonics.

BASIC EQUATIONS

Let us consider the asymptotic solution. Let us write the periodic potential $\varphi=\varphi(x,y)$, $\Delta\varphi=0$, $\varphi=\nabla\varphi$, $v=\varphi_x$, $u=\varphi_y$ in the form of series of harmonics. The corresponding complex potential $f=f(\xi)=\varphi+i\psi$, $\xi=x+iy$ has the following form:

$$f=-\sum_{n=1}^{N} A_n(\log\phi - \phi^n/n) \ , \ \phi=\exp(i\xi) \qquad (1)$$

The solution is stationary in the coordinate frame connected with the stagnation point.

Let us consider boundary condition on free stream line. Free boundary coincides with zero stream line. Kinematic boundary condition has the following form:

$$\psi = -\sum_{n=1}^{N} A_n \ ((X)^{1/2} - S_n e_n/n) = 0 \qquad (2)$$

where $X=x^2$, $S_n=\sin(n(X)^{1/2})$, $e_n=\exp(-nY)$, $Y=Y_\psi(X)$ correspond to $\psi=0$ stream line. The dynamic boundary condition has the following form:

$$\varepsilon=v^2+u^2+2|g|Y=\sum_{n=1}^{N}\sum_{m=1}^{N} A_n A_m(C_{n-m}\ \eta_{n+m} \ C_n\eta_n - C_m\eta_m +1)+2|g|Y=0 \qquad (3)$$

where v and u are the velocity components calculated using the complex potential (1) , $C_n=\cos(n(X)^{1/2})$ and the trigonometric formula $S_nS_m + C_nC_m = C_{n-m}$ was used. The function $Y=Y_\varepsilon(X)$ corresponds to zero isobar.

Let us expand the functions $\psi(X,Y)$ in (2) and $\varepsilon(X,Y)$ in (3) into theseries at x=y=0:

$$\psi(X,Y)=\sum_{s=1}^{\infty}\sum_{p=1}^{\infty}\psi_{sp}X^sY^p \qquad (4)$$

$$\varepsilon(X,Y)=\sum_{s=1}^{\infty}\sum_{p=1}^{\infty}\varepsilon_{sp}\,X^s\,Y^p \qquad (5)$$

$$\psi_{sp}=\sum_{n=1}^{\infty}A_n\,(-1)^{s+p}\,n^{2s+p}/(2s+p)!/p! \qquad (4')$$

$$\varepsilon_{sp}=\sum_{n=1}^{\infty}\sum_{m=1}^{\infty}A_nA_m(-1)^{s+p}[(n-m)^{2s}(n+m)^p-n^{2s+p}\,m^{2s+p}]/(2s)!/p! \qquad (5')$$

Formula (4′) gives ψ_{sp} at all s,p except s=p=0: $\psi_{oo}=0$. Formula (5′) gives all ε_{sp} except ε_∞ and ε_{o1} , $\varepsilon_\infty=0$, $\varepsilon_{o1}=2$.

Now let us derive equations for unknown amplitudes A_n.These equations are derived from the conditions of coincidence $\psi(X,Y)=0$ and zero isobar $\varepsilon(X,Y)=0$. The main method which allows to formalize the procedure of consequent reductions of equations is based on the transition from the implicit equations $\omega(X,Y)=0$ and $\varepsilon(X,Y)=0$ to the explicit ones $Y=Y_\psi(X)$ and $Y=Y_\varepsilon(X)$ .The set of nonlinear algebraic equations including the A_n have the following form:

$$\beta_n=\bar\beta_n\ ;\ B_n(\psi_{sp},\beta_{n-1},\beta_{n-2},\cdots)/\psi_o=B_n(\varepsilon_{sp},\bar\beta_{n-1},\ldots)/\varepsilon_{o1} \qquad (6)$$

$$n=1,2,\quad ,N$$

Let us exclude all $\bar\beta_{n-1}$, $\bar\beta_{n-2},\ldots,\bar\beta_1$ in the right hand side of (6) from the formula $\beta_m=\bar\beta_m$. We obtain the equation:

$$B_n(\psi_{sp},\beta_{n-1},\ldots)/\psi_o = B_n(\varepsilon_{sp},\beta_{n-1},\ldots)/\varepsilon_{o1} \qquad (7)$$

RESULTS

Set of equations (7) was solved numerically by Newton method. The root of fourth order in the amplitude A_n is far from the root

of third order. Thus,the existence of two solutions at N=4 is demonstrated.Fourier coefficients are presented in the Table.

N	A1	A2	A3	A4
1	-0.577350269	0	0	0
2	-0.552810868	0.111100023	0	0
3	-0.597125695	0.025638482	-0.026125378	0
4S	-0.452597178	0.183772673	-0.040580629	0.003856743
4F	-0.863263138	0.827667316	-0.811676518	0.270526932

We check the agreement of our analytical results and the numerical results obtained by the method of artificial compressibility. and find that the agreement is good.

If single parameter exists it must begin from the point $w_{\infty}=0, R=\infty$ on $(w_{\infty}, 1/R)$-plane. This means that Rayleigh-Taylor problem has a stationary solution with solitary jet (see picture).

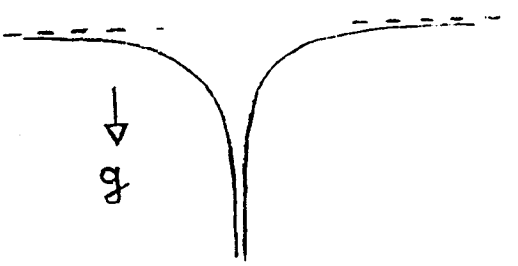

REFERENCES

1. Layzer D. Astroph. J. v. 122, No.1, pp.1-12,1955.
2. Kull H.J. Phys. Rev. Lett. v. 51, No. 16, pp.1434-1437,1983.

EXPERIMENTAL STUDY OF THE GRAVITATIONAL TURBULENT MIXING SELF-SIMILAR MODE

Yu.A.Kucherenko, L.I.Shibarshov, V.I.Chitaikin,
S.I.Balabin, A.P.Pylaev.

PHYSICAL DIVISION
ALL-UNION RESEARCH INSTITUTE OF TECHNICAL PHYSICS
454070, CHELYABINSK-70, P.O.245, USSR

Experimental and theoretical data, being accumulated until now, allow to state that the hydrodynamic flow of fluids in high intensive shock or explosive processes is almost always unstable. Such instability is particularly displayed when the light substance accelerates the heavy one or, alternatively, when the heavy substance is decelerated on the light one. In this case the contact boundary between media having different densities is subjected to the so-called gravitational instability or the Raleigh-Taylor instability. On such boundaries, conditions for generating and developing the turbulent mixing arise. In the common case the turbulent mixing effects upon the flow dynamics and must be taken into account under its computation.

At present taking mixing into consideration is possible, for example, within the limits of semi empirical theories [1,2]. Experiments, in which the mixing is directly measured and conditions for its development are well known, are the good verification and calibration of such theories.

At our Institute the gravitational turbulent mixing study is conducted at the installations EKAP, SOM (see Fig.1,2) with using of fluid media. Fluids having different densities ρ_1 and ρ_2 ($\rho_2 > \rho_1$) are placed into the vessel, a sample container. In the gravity field $\vec{g}$ the light fluid is floating on the heavy one (this is the stable condition). At the interface between the fluids the random initial perturbations of the solid surface roughness type are artificially generated.

At a certain instant of time the sample container starts to be accelerated in the direction $\vec{g}$. In the process of acceleration the unstable system is realized in the artificial gravity field $\vec{g}_1$. The artificial field $\vec{g}_1$ is directed from the heavy fluid to the light one. Development of instability and mixing process are studied by means of X-ray and light techniques. The space-time distribution of turbulent flow characteristics is determined on the basis of the obtained half-tone X-ray pictures as well as photographic images.

The self-similar turbulence is of special interest for the theory. This type of turbulence is determined by minimum of dimensional parameters and is the first class of flows on which the calibration is carried out.

The self-similar turbulence is developing in the region of the plane interface between the infinite incompressible ideal fluids under the action of acceleration $\vec{g}_1$, constant in space and time and directed from the heavy fluid to the light one (see Fig.3). Then all the averaged characteristics of the developing mixing process are dependent on the shown dimensional parameters. By using the theory of dimensionality it is possible to find the general form of the functional dependence for the turbulent mixing zone having the average size $L(\rho_1, \rho_2, g, t)$, such as:

$$L = A^*(n)\, S,$$

where $S=at^2/2$ and for the presented installations this is the way, passed by the sample container by the moment of registration, $A^*(n)=A^*(\rho_2/\rho_1)$ - the arbitrary function of the densities relation.

Thus, the indication of the mixing self-similarity is constancy of the non-dimensional mixing rate, i.e. dL/dS = const, which is dependent only on the densities relation.

At the installations EKAP and SOM studying of the turbulent mixing self-similar modes has been primarily conducted. Conditions, under which the experiments must be carried out to minimize the possible deviations from the self-similar mode of mixing are very important. This is connected with the fact that the mixing can be developed against a background of large-scale flows, arising from any local initial perturbations on the contact boundary (see Fig.4). So that the similar

large-scale perturbations would not distort the picture of mixing, the reasons of their arising were firstly removed and, secondly, the small-scale initial perturbations were generated especially on the whole surface of the contact boundary before applying the acceleration. The obtained X-ray pictures and photographs of the mixing zone are given in Fig.5,6.

The main requirements for carring out the experiment to study the self-similar turbulence are the following [3,4]:

1. The condition of incompressibility - $v_t/C \ll 1$. The turbulent velocity v_t must be less than the sound velocity C in the fluid.

2. Conditions of the fluid ideality - $g_1 \gg \delta^2/L^3$; $g_1 \gg \frac{\sigma}{\rho L^2}$.

Inertial forces must be more than viscous ones (δ - kinematic viscosity) and the surface tension force (σ - coefficient ofP the tension).

3. The condition of the acceleration constancy $\gamma\sqrt{2Sg_1} < C_0$, $S \ll 1$, where l is the reduced acceleration length, C_0 is the sound velocity in gas which accelerates the sample container, γ is the adiabatic index.

4. The requirement of the system infinity - $l_{x,y} \ll \{x_0, y_0\}$. Dimensions of the $l_{x,y}$ pulsations in the mixing zone must be less than the characteristic sizes $\{x_0, y_0\}$ of the sample container.

5. Observations must be carried out at the stage of neglecting the initial perturbations, when $L_0 \ll L$. Dimensions of the mixing zone L must exceed the average

dimension L_0 of the initial perturbations zone, and the spectrum of initial perturbations must be characterized by the wave length values $\lambda \leq L_0$.

While carring out the experiments the parameters of the unstable systems could be varied within the limits [3,4,5]:

1. Artificial gravity field $10^2 g \leq g_1 \leq 2 \cdot 10^4 g$.
2. Relation of densities $1.5 \leq \rho_2/\rho_1 \leq 2 \cdot 10^3$.
3. Sizes of sample container $\{x_0, y_0\} \leq 50$ *mm*.
4. Initial perturbations $L_0 \leq 1$ *mm*.
5. Viscosity of fluids $5 \cdot 10^{-2} \leq \nu \leq 10^2$ cm^2/s.
6. Surface tension $0 \leq \sigma \leq 350$ *dyne/cm*.

The first experiments to determine the mixing development velocity have been conducted using the fluids: mercury-water (n = 13.5). The above-mentioned inequalities for the self-similar mixing process begin to be satisfied with L > 1 mm and $g_1 > 10^2 g$. While using the X-ray technique the penetration of the heavy fluid into the light one was well observed. Dimensions $L_{21}(t)$ of the turbulent mixing zone in the light fluid have been obtained for different instants of time t (see Fig.7). On the basis of the experimental dependences $L_{21}(S)$ or $L(S)$ it is possible to distinguish two regions. During the first stages interpenetration of the fluids takes place in the region I with the higher velocity than in the subsequent instants of time. The mixing velocity dL/dS under this condition is variable. In the region II the mixing proceeds with the constant velocity dL/dS.

The obtained results could not be interpreted

unambiguously because the fluids were not ideal, they were limited in space, and acceleration g_1, under observed displacements S, was not constant. Therefore, the large cycle of research has been conducted, under which the values of acceleration g_1, decreasing of acceleration, the system dimensions, values of viscosity and surface tension were varied and different fluids were used (see Fig.7). As a result of these investigations, it was shown that availability of these two regions is not connected with the above-mentioned reasons. The first region, in which dL/dS was variable, and the second region with the constant value of dL/dS were always observed.

The non-dimensional velocity of mixing dL/dS was dependent only on the densities relation n in the second region, however, in the first region the value of dL/dS was as well dependent on the character of the initial perturbations on the contact boundary (in particular on the dimension of L_0).

The answer was found while conducting the special experiments in which the initial stage of the fluid interpenetration process development was studied. For this purpose the two-dimensional periodic perturbations of the contact boundary (y=0) with the fixed wave length (see Fig.8) were generated. By such experiments it was shown that the velocity of interpenetration (of mixing) is decreased as the turbulization of the flow is increased.

Thus, the two regions, early observed, can be

interpreted as the change of the flow modes. In the initial instants of time the potential energy of the heavy fluid transfers only into one degree of freedom, but then excitation of other degrees of freedom takes place. As the turbulization of the flow proceeds, the self-similar mode of mixing takes place.

As the experiment shows, such transfer completes up to the beginning of the second region. In this region the set of the experimental points $\{L_{21}, S\}$ can be described by the linear relationship $L_{21}(S) = A^*_{21}(n) \cdot S + L^*_0$ with good accuracy. For large displacement of S the observed deviation of the experimental points from the linear relationship is explained by the sample container size effect upon the mixing velocity (the large-scale pulsation growth is restrained).

Investigations at the stage of the mixing constant velocity dL/dS have been conducted in the whole scope during experiments with using of petrol - zinc chloride solution (n=3) and water-xenon under pressure (n=20). These experiments allowed to obtain the half-tone X-ray images of the mixing zone as well as the photographic images of the mixing fronts both in the light medium and in the heavy one. By means of the obtained images we determined the spatial-time distribution of the substance average density $\rho(y,t)$ in the mixing zone (see Fig.9) and the coordinates of the mixing fronts in the light medium $L_{21}(t)$ and in the heavy one $L_{12}(t)$ (see Fig.10). Transfer to the self-similar mode was dependent on the character of initial perturbations, as it was previously mentioned.

The value of the non-dimensional mixing velocity in the self-similar mode at the constant value of n was dependent on the substance average density under which measuring of the mixing front coordinates L_{21} and L_{12} was performed. It was shown that all distributions of density $\rho(y)$ in different instants of time (at different values of the parameter S) can be described by a single non-dimensional dependence:

$$\delta(\varkappa) = \frac{\rho(y)-\rho_1}{\rho_2-\rho_1}; \qquad \varkappa = \frac{y-y_{0.1}}{y_{0.9}-y_{0.1}},$$

where $y_{0.1}$ and $y_{0.9}$ are the fixed coordinates y, at which the value δ may take the values $\delta = 0.1$ and $\delta = 0.9$ (see Fig.11). The non-dimensional velocity of mixing dL_{12}/dS for n=3 as well as for n=20 can be written with rather good accuracy in the form (for the self-similar mode of mixing):

$$\frac{dL_{12}}{dS} = (0.14\pm0.005)\cdot\frac{\rho_2-\rho_1}{\rho_1+\rho_2},$$

where the values of L_{12} were determined on the basis of the density level δ=1 and

$$\frac{dL_{12}}{dS} = (0.11\pm0.01)\cdot\frac{\rho_2-\rho_1}{\rho_2+\rho_1}$$

for $\delta = 0.98$.

It has been shown that the mixing has the asymmetrical character (the heavy fluid penetrates into the light one more quickly), meanwhile, the degree of asymmetry depends on time. As for n=3 the coefficient of asymmetry $k(S)=L_{21}(S)/L_{12}(S)$ reaches readily the maximum value and then it slowly tends to the constant value (see Fig.12).

At the self-similar stage the relation of non-dimensional mixing velocities $\hat{k} = \frac{dL_{21}}{dS} : \frac{dL_{12}}{dS} = \frac{dL_{21}}{dL_{12}}$ is dependent only on densities relation n. The value of $\hat{k}$ is growing with increasing n.

Thus, $\hat{k}$=1.03 for n=1.5, $\hat{k}$=1.14 for n=3, $\hat{k}$=1.8 for n=20, if the position of the mixing fronts was determined according to the densities δ=0.01 and δ=0.98.

The given experimental results, being taken at the self-similar stage of mixing, are in agreement with the results, obtained in works [7,8] by the English investigators on the Rocket-Rig installation.

Experiments, in which the delay in the turbulent mixing development has been found and investigated, are of a special interest. It was noted, while implementing the experiments with mutually soluble fluids, that the turbulent mixing did not develop for a long time, i.e. the delay in the mixing development was observed. This delay in the units of the contact boundary development can be characterized by the value $\hat{S}$. It was shown that this phenomenon of the delay was connected with availability of the transition layer between the fluids with densities $\rho_n(y)$ [6], changing continuously.

To reveal the role of transition layer in the mixing delay two series of experiments have been conducted. In the first series the transition layer was between fluids, ($h^* \neq 0$), but in the second series the transition layer was absent ($h^*=0$). In both series of experiments the same sample container was used, the identical acceleration $\vec{g}_1$,

and the same decreasing of densities $n=\rho_2/\rho_1$ were provided. Density of substances $\rho_n(y)$ in the transition layer was continuously and monotonically changed from ρ_2 up to ρ_1. The distance h^* between points with densities $1.1\rho_1$ and $0.9\rho_2$ (see Fig.13) was taken as an characteristic of the layer thickness. In the center of the transition layer (y=0) the small-scale random initial perturbations were generated. The average dimension of the region, involved in perturbations, was characterized by the size L_0 (the set of wave lengths in the initial perturbations $x \le L_0$ and amplitudes $a \le L_0$).

In Fig. 13 the characteristic X-ray pictures of the mixing development were presented for the systems without the transition layer (h^*= 0) and for ones with the transition layer (h^*= 3 mm). Images have been given for just the same instant of time (S=100mm). It is seen, that the turbulent mixing was not developed by this moment for the system with the transition layer.

In experiments the delay S in the mixing development was determined for different values of the initial perturbation zone L_0 and the transition layer thickness h^*, the relation of densities n was fixed in such experiments. The delay $\hat{S}$ was defined as the distance which the sample container passed by the moment when the mixing front was beyond the dimensions of the transition layer ($L_{21} \ge h^*/2$).

The results of defining the delay in the development of mixing in systems with n=4 are given in Fig.14 where along the vertical line the non-dimensional delay was

plotted and along the horizontal line the non-dimensional value of the initial perturbation zone was plotted. Transition to non-dimensional parameters was carried out over the parameter h^*. The obtained dependences $\hat{S}/h^*=f(L_0/h^*)$ have the non-linear character. The less the relation L_0/h^* is the more the delay in the mixing development will become. According to results of the experiments with the transition layer, carried out with $L_0= 0$, it is possible to state that the delay in the mixing can be however large if the level of the initial perturbations is decreased, i.e.

$$\hat{S}/h^* \to \infty \quad \text{at } L_0/h^* \to 0.$$

So $\hat{S}/h^* > 400$ for the system with $n=2$ at $L_0/h^* \simeq 0$.

Possibility to achieve the necessary delay in the gravitational turbulent mixing development was demonstrated by similar experiments with the transition layer.

At present, investigations of the non-self-similar mixing modes are being carried out at the installations EKAP and SOM.

References

1. V.E. Neuvazhaev, V.G. Yakovlev
"Model and Method for Numerical Calculation of Turbulent Mixing Interfaces Moving with Acceleration" Problems of Atom. Science & Engineering
Series: Methods & Programs for Numerical solution of Math. Physics Problems, Issue 2, p.17, M. 1984.

2. V.A. Andronov, S.M. Bahrah, E.E. Meshkov, V.V. Nikiforov, A.V. Pevnitzky, A.I. Tolshmakov.
"Experimental Study and Numerical Simulation of

Turbulent Mixing in One-Dimensional Flows"
Reports of the USSR Ac. of Si., Vol. 264, N1, p.76, 1982.

3. N.N. Anuchina, Yu.A. Kucherenko, V.E. Neuvazhaev, V.N. Ogibina, L.I. Shibarshov, V.G. Yakovlev "Turbulent Mixing at the Accelerating Interface between Fluids", Mechanics of Fluids, N6, p.157, 1978.
4. Yu.A. Kucherenko, G.G. Tomashev, L.I. Shibarshov "Experimental Study of Gravitational Mixing in the Self-Similar Mode" Problems of Atomic Science & Engineering Series: Theoretical & Applied Physics, Issue 1, p.13, Moscow, 1988.
5. Yu.A. Kucherenko, L.I. Shibarshov "T u rbulent Mixing at the Plane Interface between Media with Different Densities and Being Subjected to the Series of Delta-Shaped Accelerations". Problems of Atomic Science & Engineering Series: Theor. & Appl. Physics, Issue 2, p.3, Moscow, 1986.
6. R.I. Ardashova, S.I. Balabin, N.P. Voloshin, Yu.A. Kucherenko, N.V. Ptizyna, V.I. Chitaikin "Experimental Study of Perturbation Development in the Gravitational Unstable System with Continuous Distribution of Density" Problems of Atom. Sci. & Engineering Series: Theor. & Appl. Physics, Issue I, p.20, Moscow, 1988.
7. K.I. Read "Experimental investigation of turbulent mixing by Rayleigh-Taylor instability", Part 1, Atomic Weapons Research Establishment, Foulness, England, 1984.
8. V.S. Smeeton, D.L. Youngs "Experimental investigation of turbulent mixing by Rayleigh-Taylor instability", Part 3, Atomic Weapons Research Establishment, Aldermaston, England, 1988.

ALL-UNION RESEARCH INSTITUTE OF TECHNICAL PHYSICS ★ U S S R

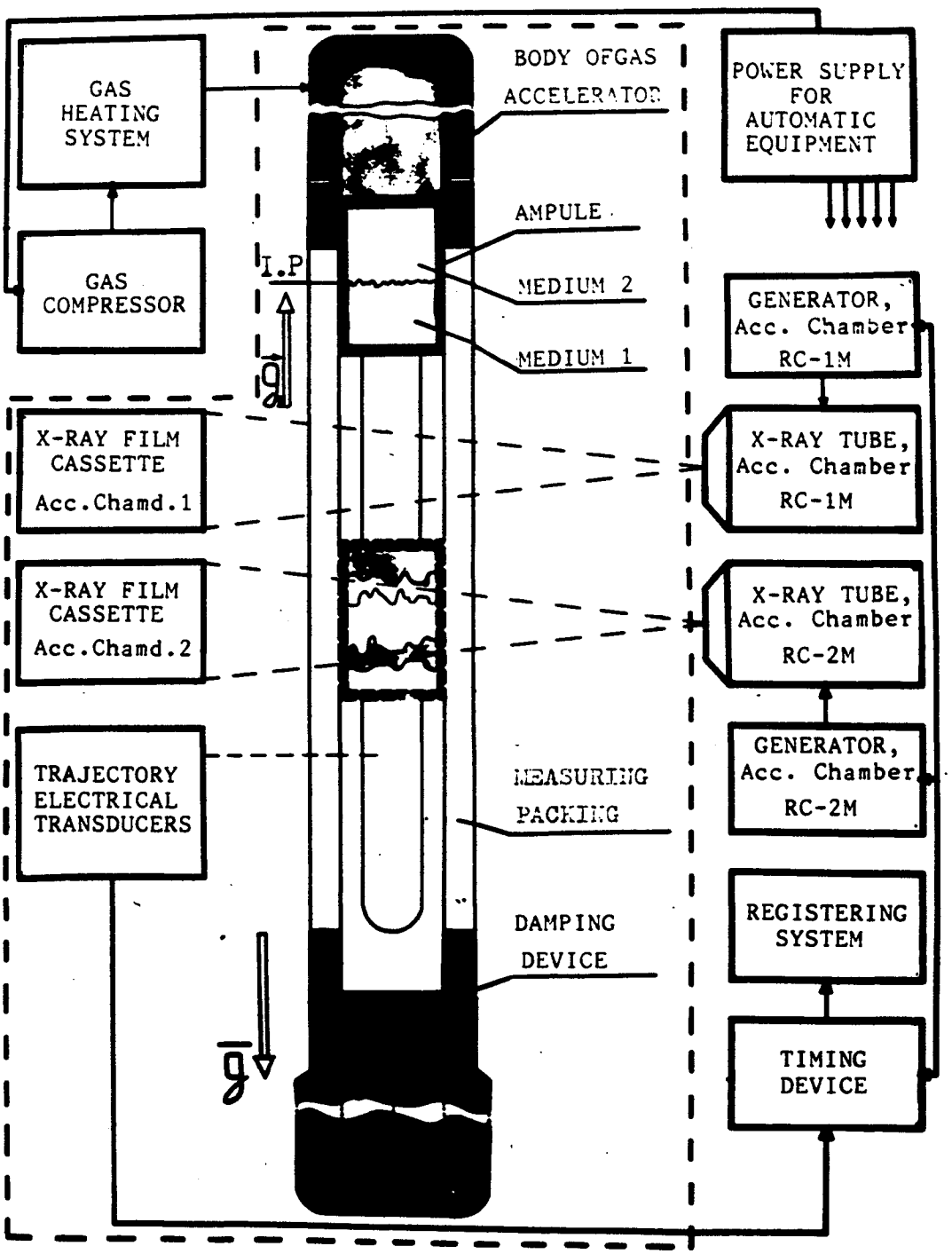

Fig. 1(a) E K A P - COMPLEX INSTALATION TO STUDY TURBULENT MIXING WITH APPLICATION OF PULSE X-RAY METHODS

ALL-UNION RESEARCH INSTITUTE OF TECHNICAL PHYSICS x U S S R

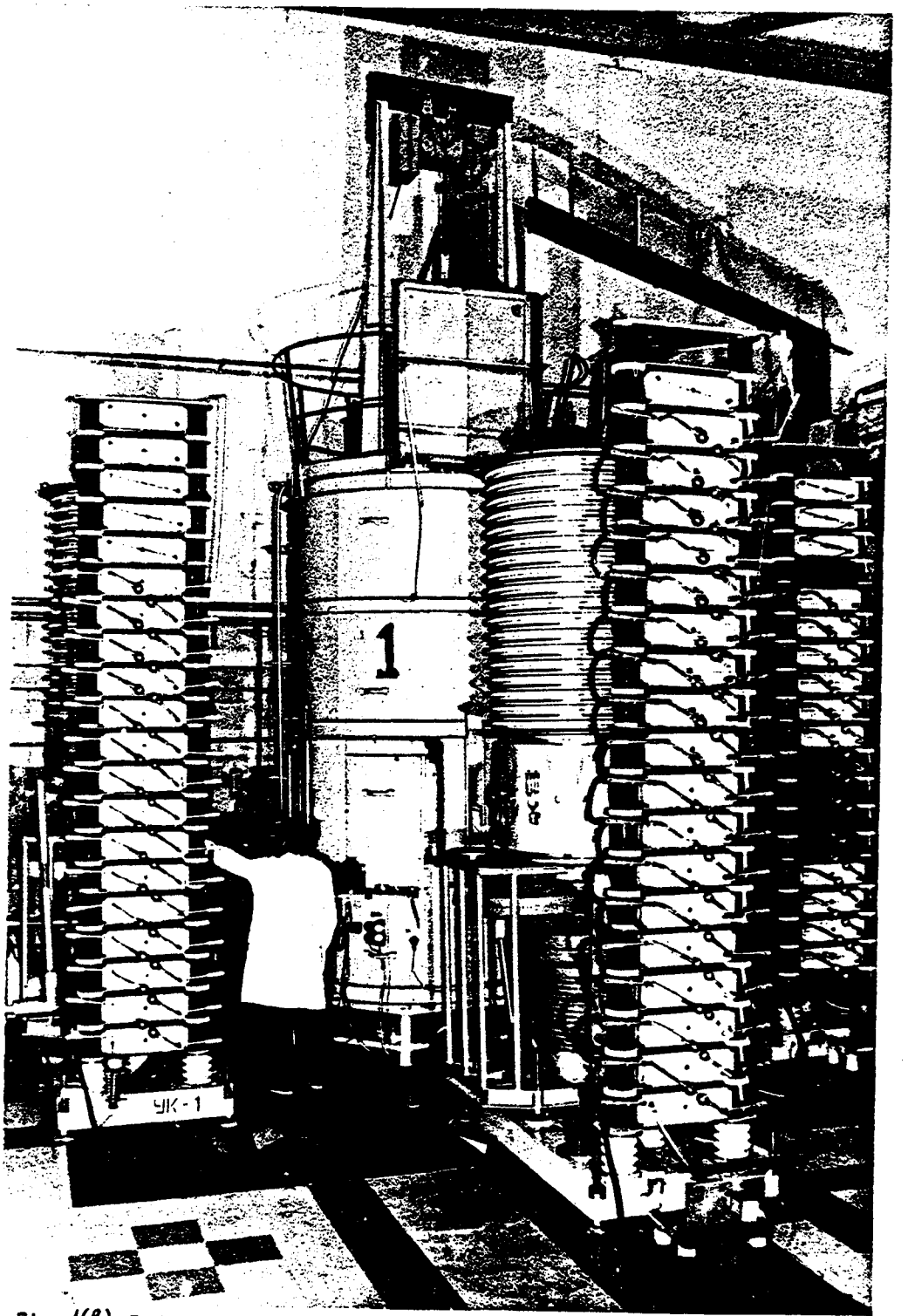

Fig. 1(6) E K A P - COMPLEX INSTALATION TO STUDY TURBULENT MIXING WITH APPLICATION OF PULSE X-RAY METHODS

ALL-UNION RESEARCH INSTITUTE OF TECHNICAL PHYSICS * U S S R

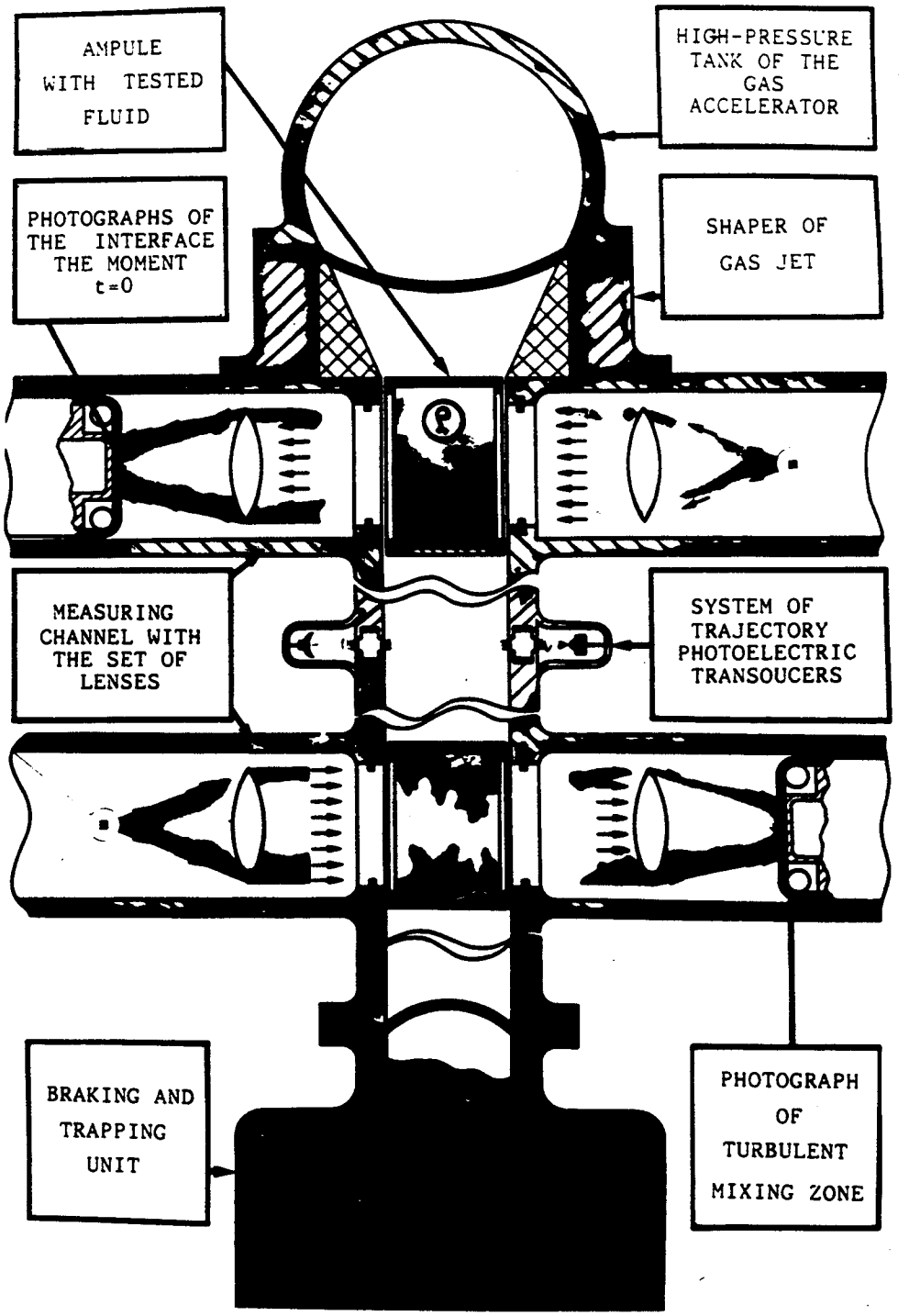

Fig.2(a) S O M - TEST BENCH TO STUDY TURBULENT MIXING WITH APPLICATION OF PULSE LIGHT METHODS

ALL-UNION RESEARCH INSTITUTE OF TECHNICAL PHYSICS ✖ U S S R

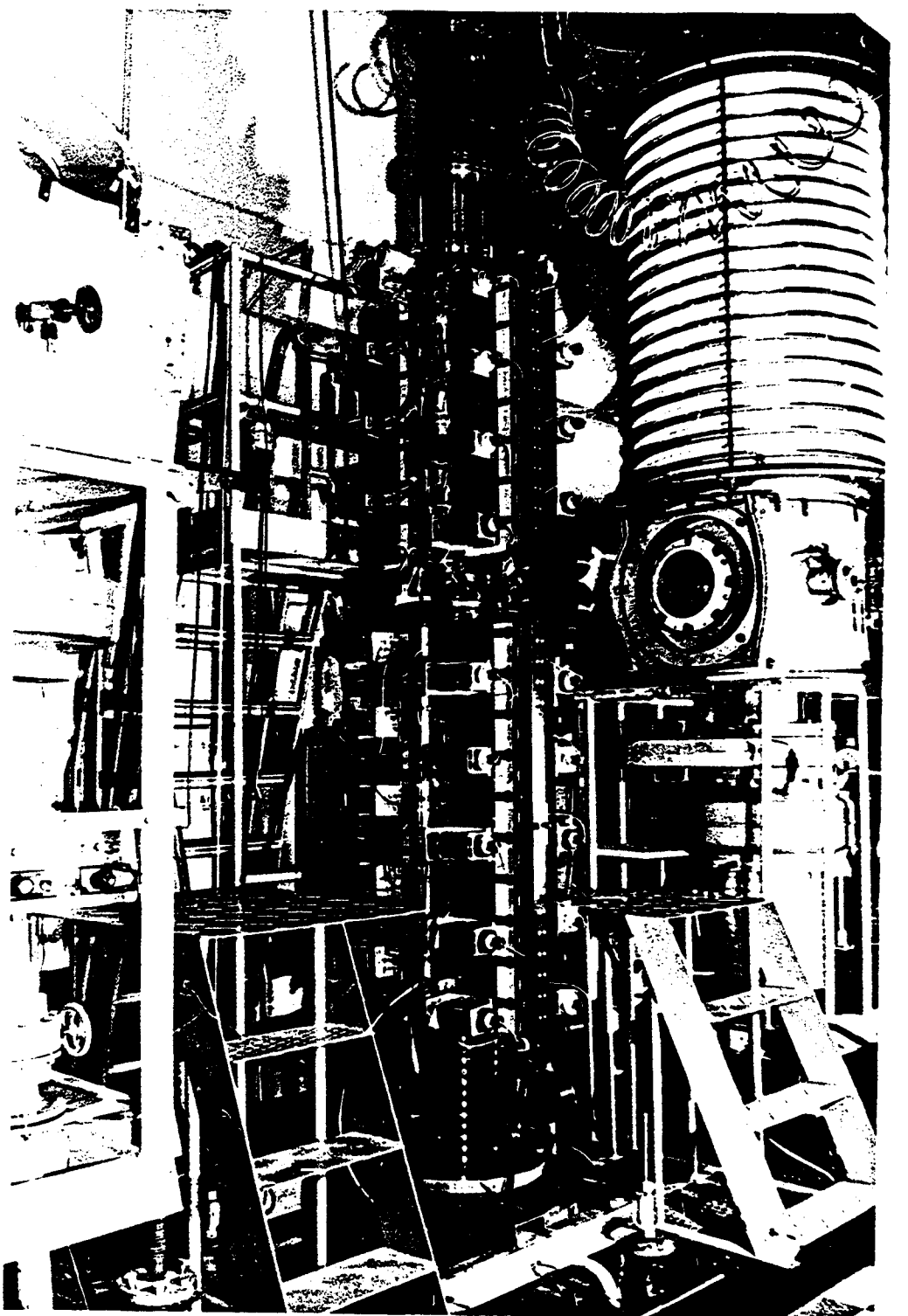

Fig. 2(B) S O M - TEST BENCH TO STUDY TURBULENT MIXING WITH APPLICATION OF PULSE LIGHT METHODS

ALL-UNION RESEARCH INSTITUTE OF TECHNICAL PHYSICS * U S S R

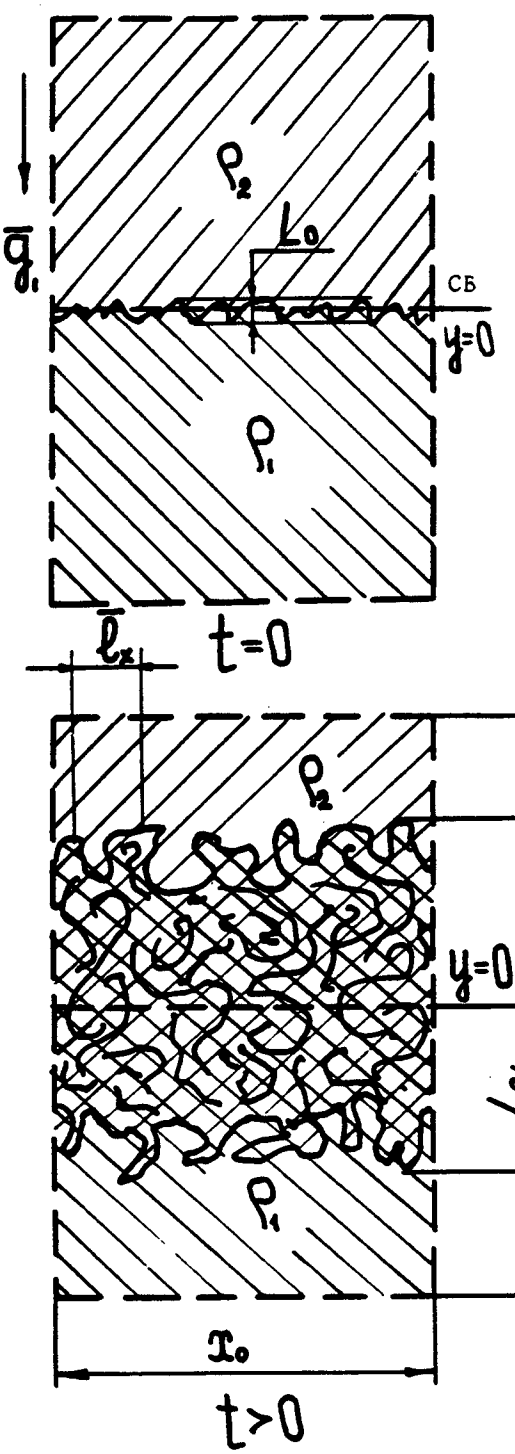

$$L = F(\rho_1, \rho_2, g_1, t);\ L_0 = 0$$

$$\frac{L}{g_1 t^2} = F\left(1, \frac{\rho_2}{\rho_1}, 1, 1\right)$$

$$L = A^*(n) \cdot S$$

$$S = \frac{g_1 t^2}{2}$$

RELATION OF DENSITIES $n = \rho_2/\rho_1$

NON - DIMENSIONAL RATE OF MIXING $\frac{dL}{dS} = A^*(n)$

$$L(t) = L_{21}(t) + L_{12}(t)$$

$$K = \frac{L_{21}}{L_{12}}$$

$$\hat{K} = \frac{dL_{21}}{dL_{12}}$$

FIG.3 DIAGRAM OF TURBULENT MIXING DEVELOPMENT.

ALL-UNION RESEARCH INSTITUTE OF TECHNICAL PHYSICS * U S S R

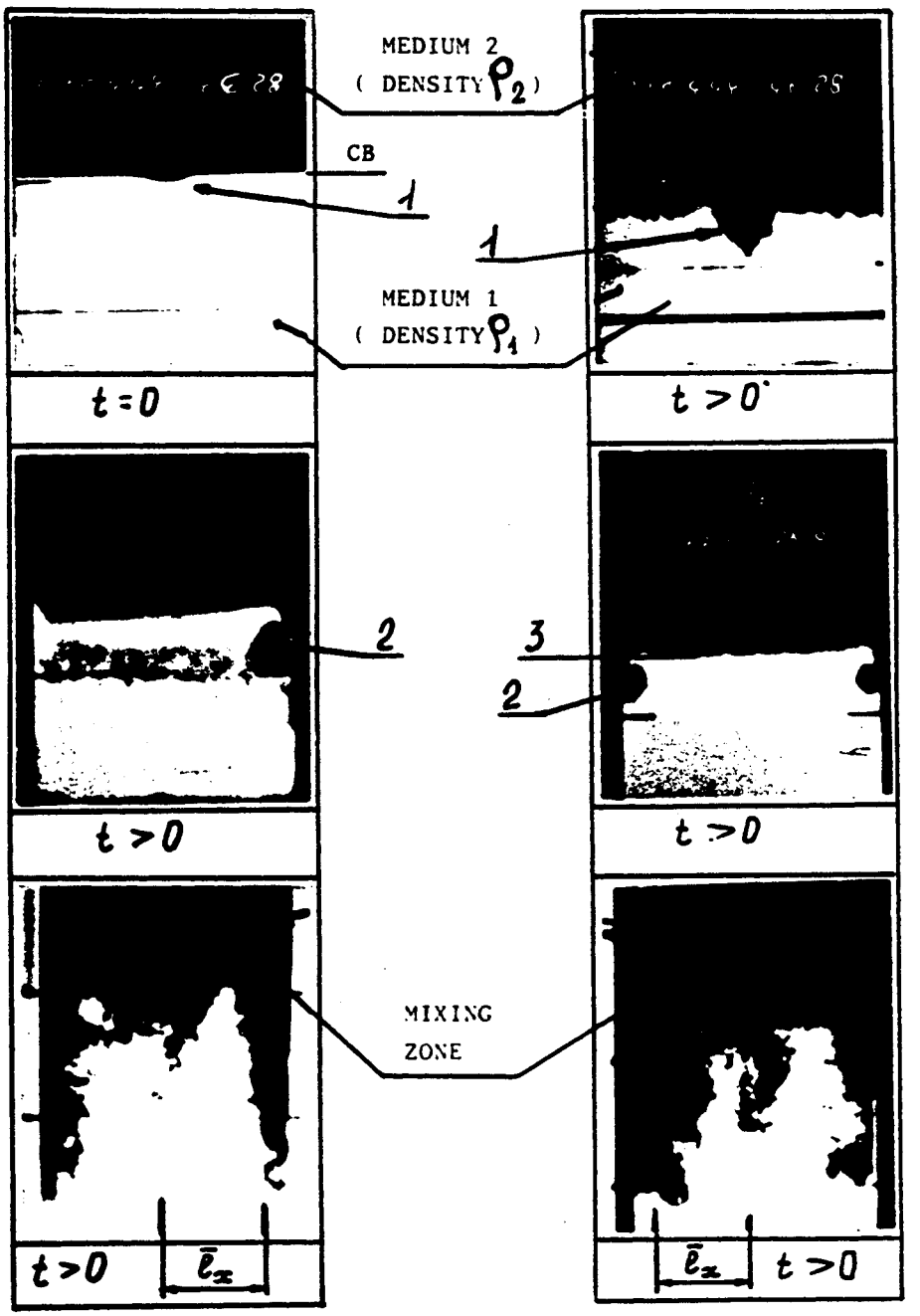

1. LARGE - SCALE PERTURBATIONS IN THE AMPOULE CENTRE
2. LOCAL PERTURBATIONS DUETO THE AMPOULE WALLS
3. POSITION OF THE MIXING FRONT,
   INDUCED BY THE SMALL - SCALE INITIAL PERTURBATIONS

FIG.4 CHARACTERISTIC PROPERTIES OF MIXING DEVELOPMENT.

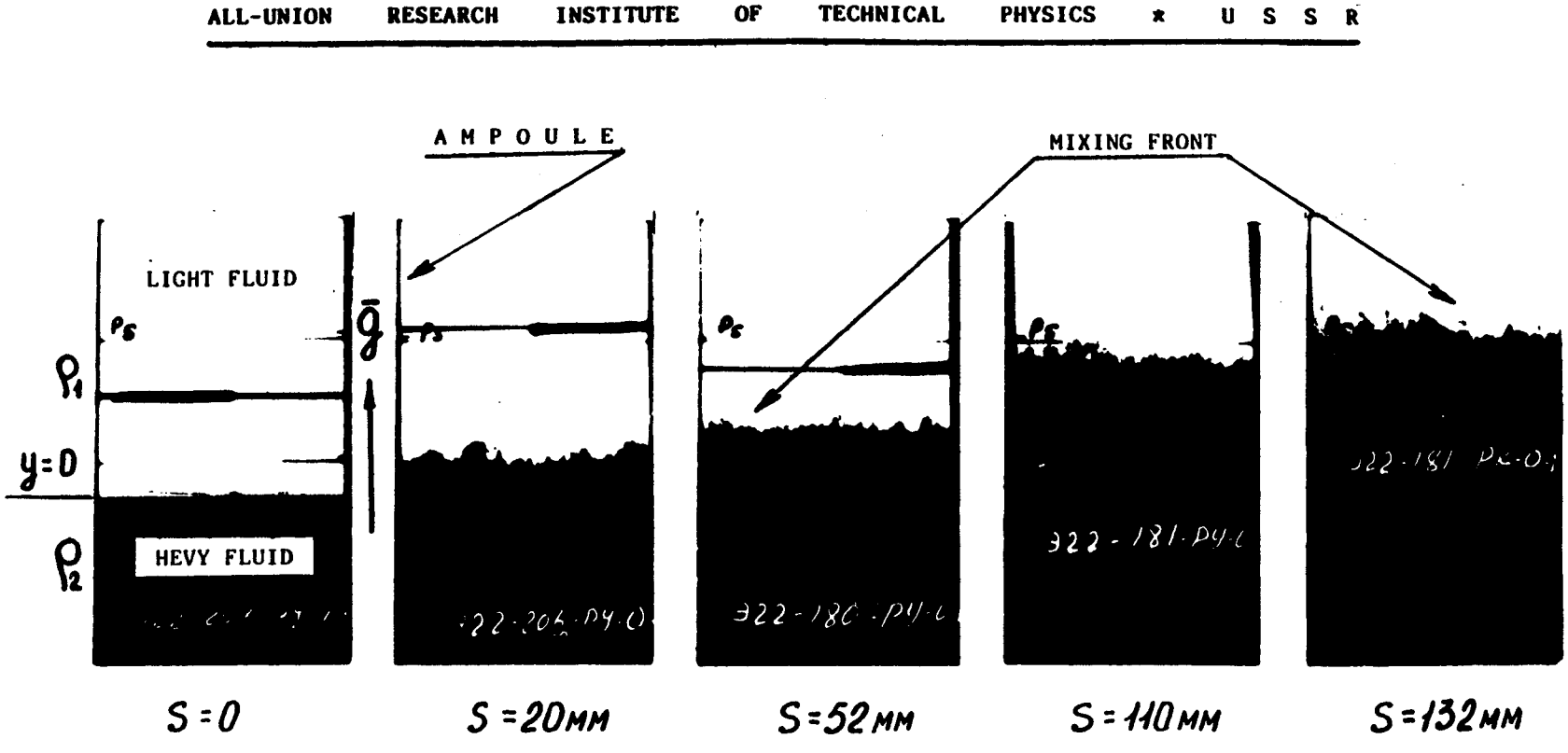

FIG. 5 DIFFERENT STAGES OF MIXING DEVELOPMENT WITH RANDOM SMALL - SCALE INITIAL PERTURBATIONS (EXPERIMENTS WITH MERCURY - MATER , X - RAY TECHNIGUE).

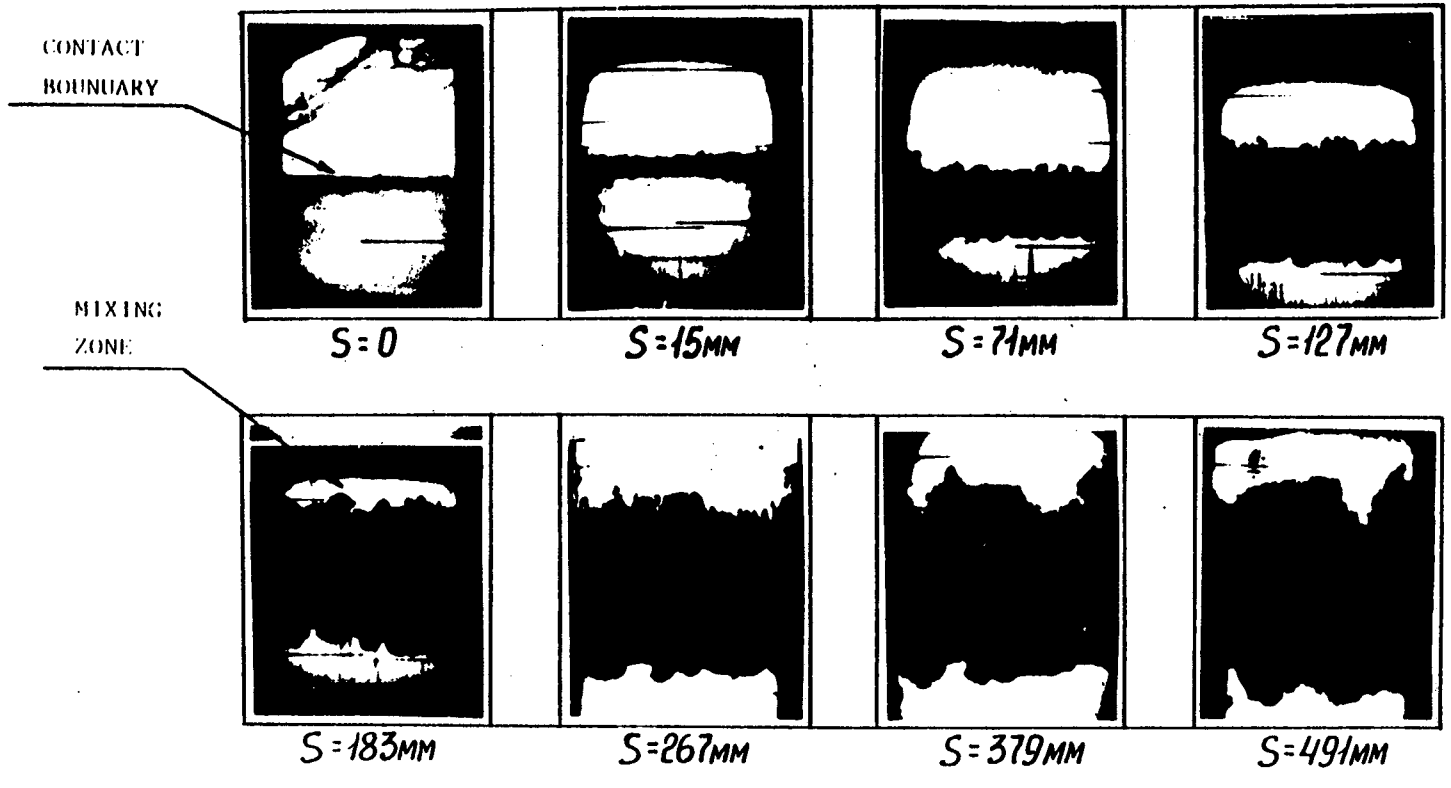

FIG. 6 CHARACTERISTIC PHOTOGRAPHS OF MIXING WITH SMALL - SCALE INITIAL PERTURBATIONS (EXPERIMENTS WITH PETROL - CHLORIDE ZINC).

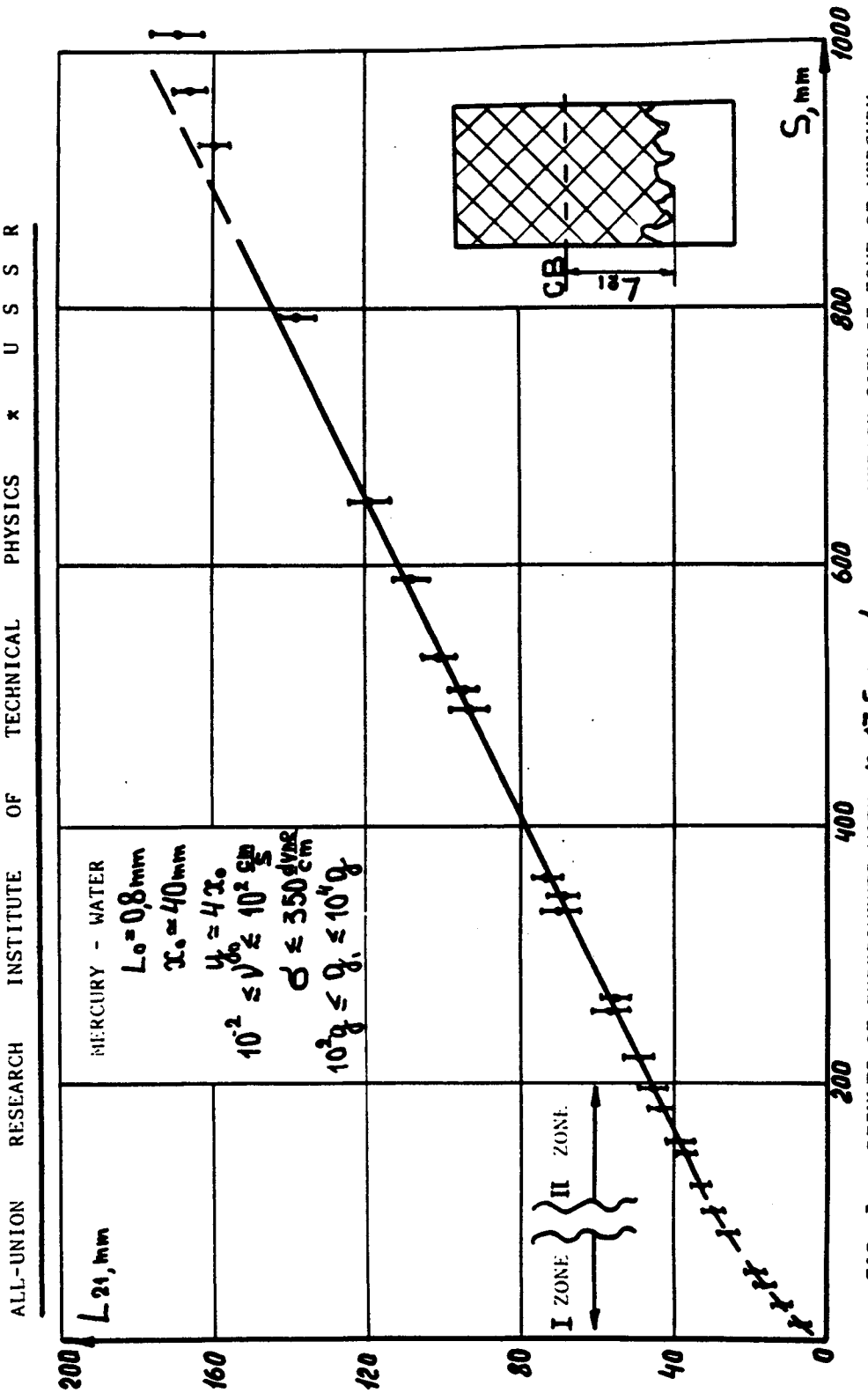

FIG. 7 RESULTS OF EXPEPIMENTS WITH $n=13{,}5$ (L_{21} - AVERAGE SIZE OF ZONE OF MERCURY

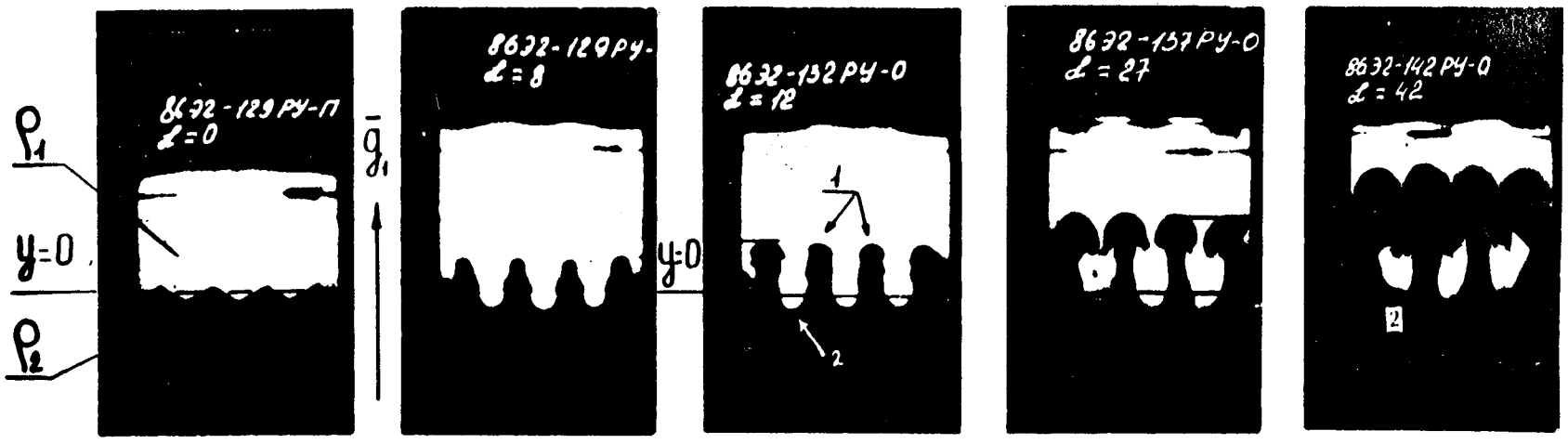

y=0 - INITIAL STATE OF THE CONTACT BOUNDARY;

1 - HEAVY FLUID SPIKES
2 - LIGHT FLUID BUBLES

FIG. 8 DIFFERENT STAGE OF TWO - DIMENSIONAL INITIAL PERTURBATION DEVELOPMENT (X- RAY TECHNIQUE, SYSTEM WITH $n = 13{,}5$).

Proceedings of the 3rd International Workshop on the Physics of Compressible Turbulent Mixing June 1991
Royaumont, France
Edited by D. Besnard, J.-F. Hass, P.-A. Holstein & B. Sitt

ALL-UNION RESEARCH INSTITUTE OF TECHNICAL PHYSICS * U S S R

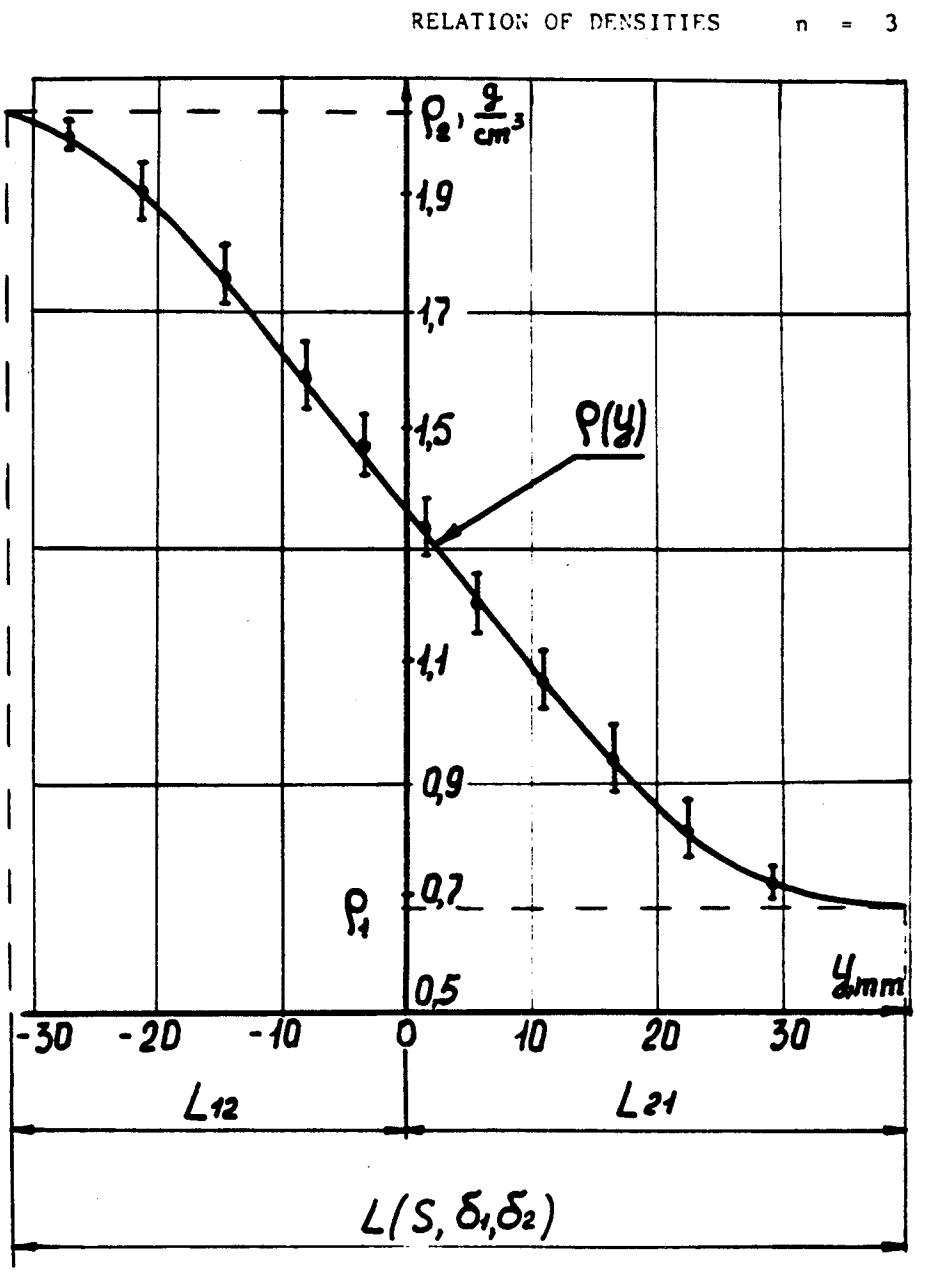

FIG.9 DISTRIBUTION OF THE SUPSTANCE AVERAGE DENSITY IN THE MIXING ZONE UNDER DISPLACEMENT OF THE CONTACT BOUNDARY S · 645 mm (X-RAY TECHNIQUE).

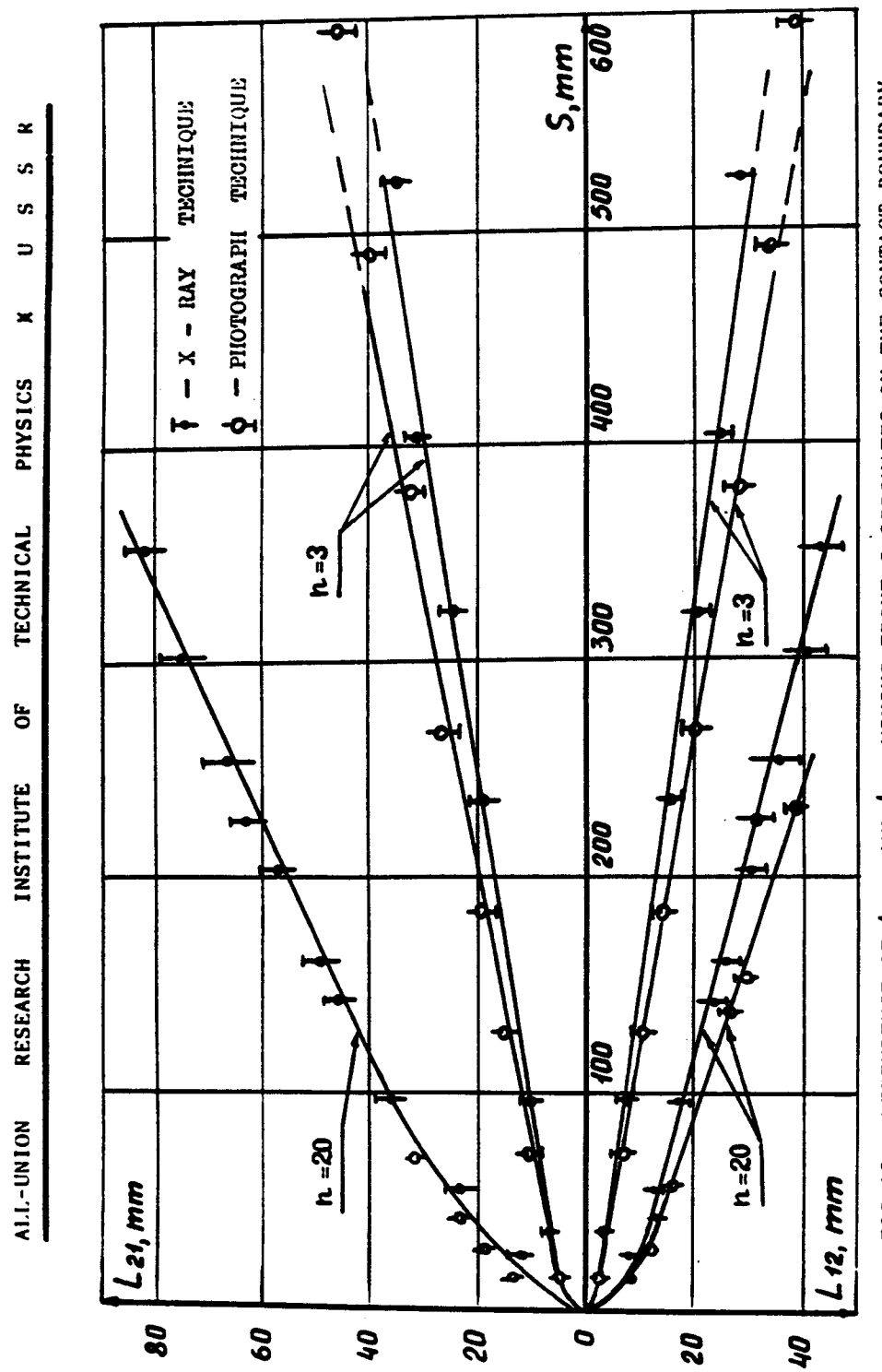

FIG.10 DEPENDENCE OF L_{21} AND L_{12} MIXING FRONT COORDINATES ON THE CONTACT BOUNDARY DISPLACEMENT S (X- RAY TECHNIQUE AT THE DENSITY LEVEL δ =0,01 AND δ =0,98 PHOTOGRAPH TECHNIQUE AT δ =0 AND δ =1).

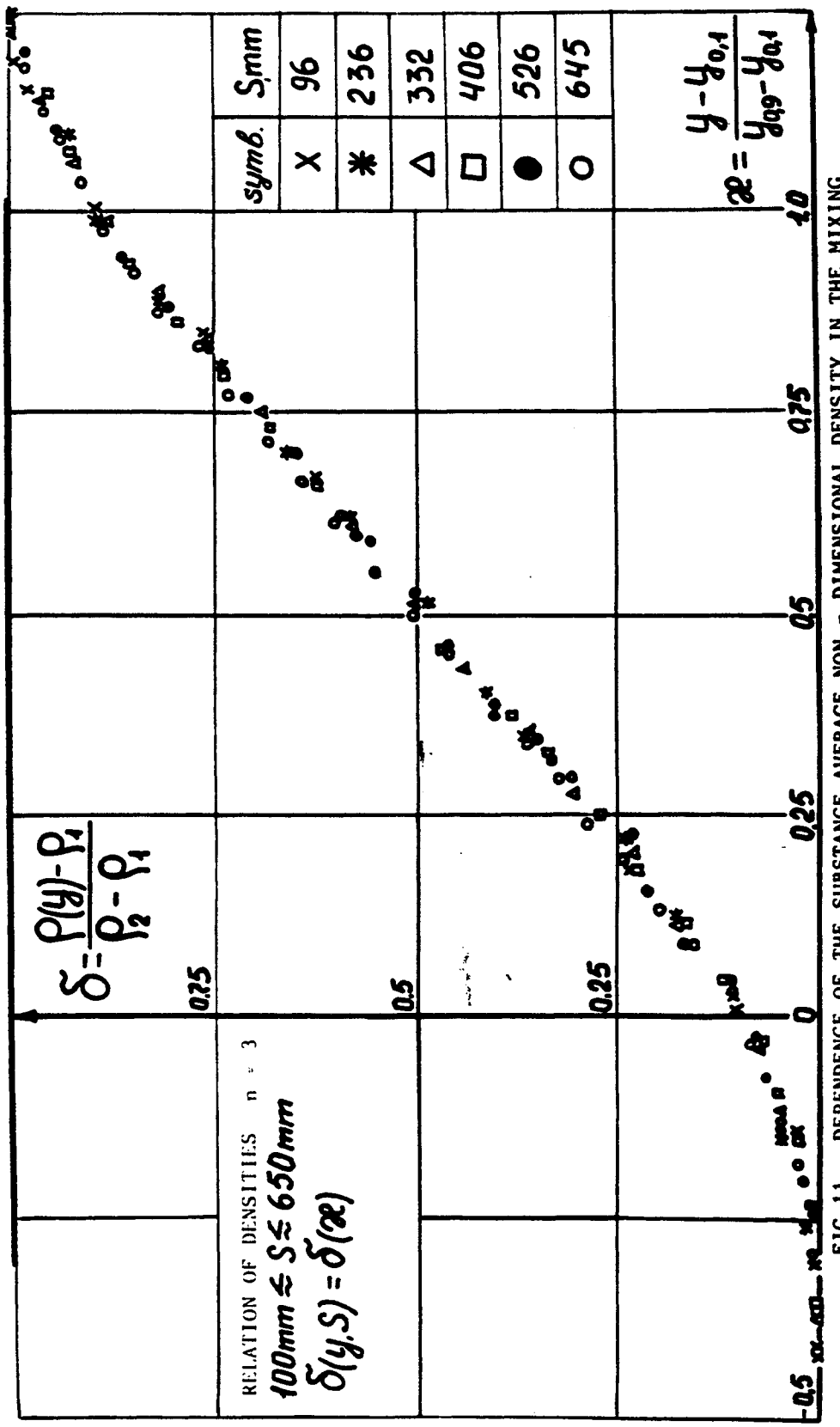

FIG.11 DEPENDENCE OF THE SUBSTANCE AVERAGE NON - DIMENSIONAL DENSITY IN THE MIXING ZONE ON THE NON - DIMENSIONAL COORDINATE (X- RAY TECHNIQUE) - $\delta(\mathcal{R})$.

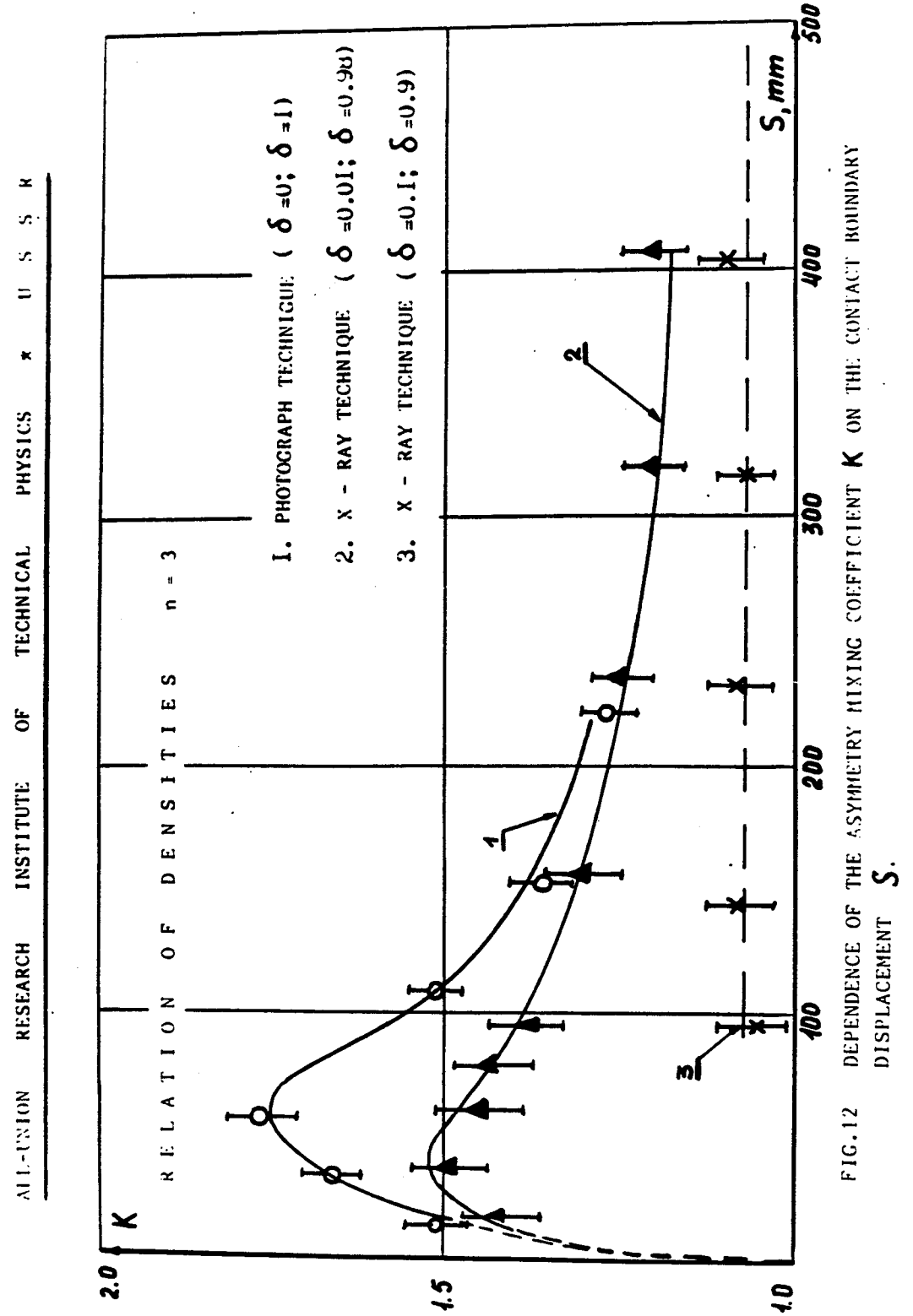

FIG. 12 DEPENDENCE OF THE ASYMMETRY MIXING COEFFICIENT **K** ON THE CONTACT BOUNDARY DISPLACEMENT **S**.

ALL-UNION RESEARCH INSTITUTE OF TECHNICAL PHYSICS * U S S R

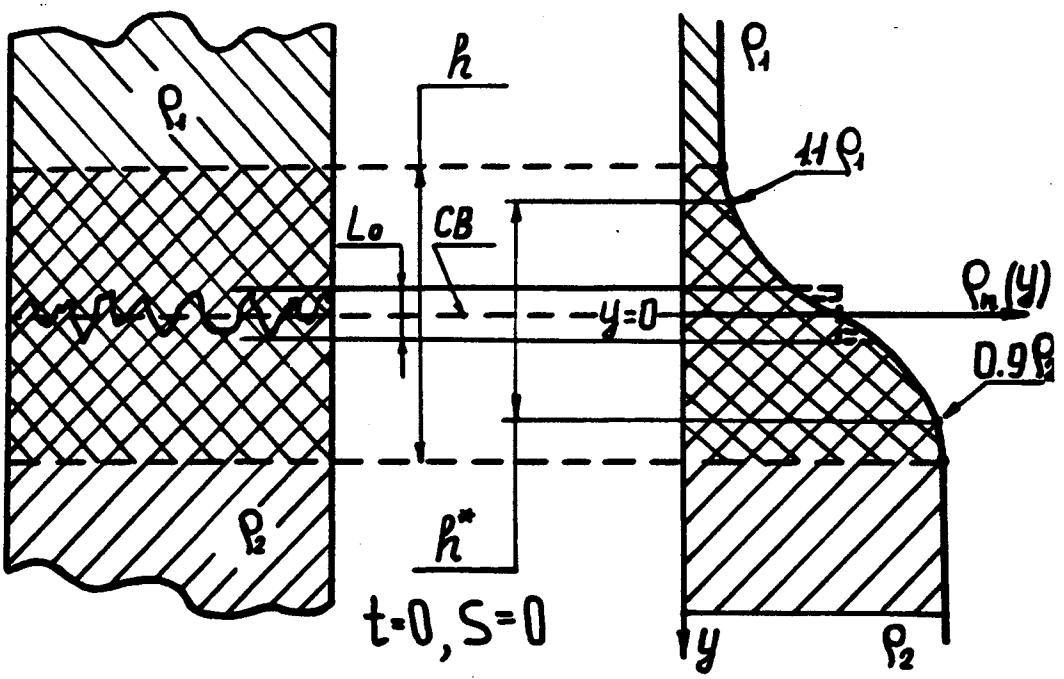

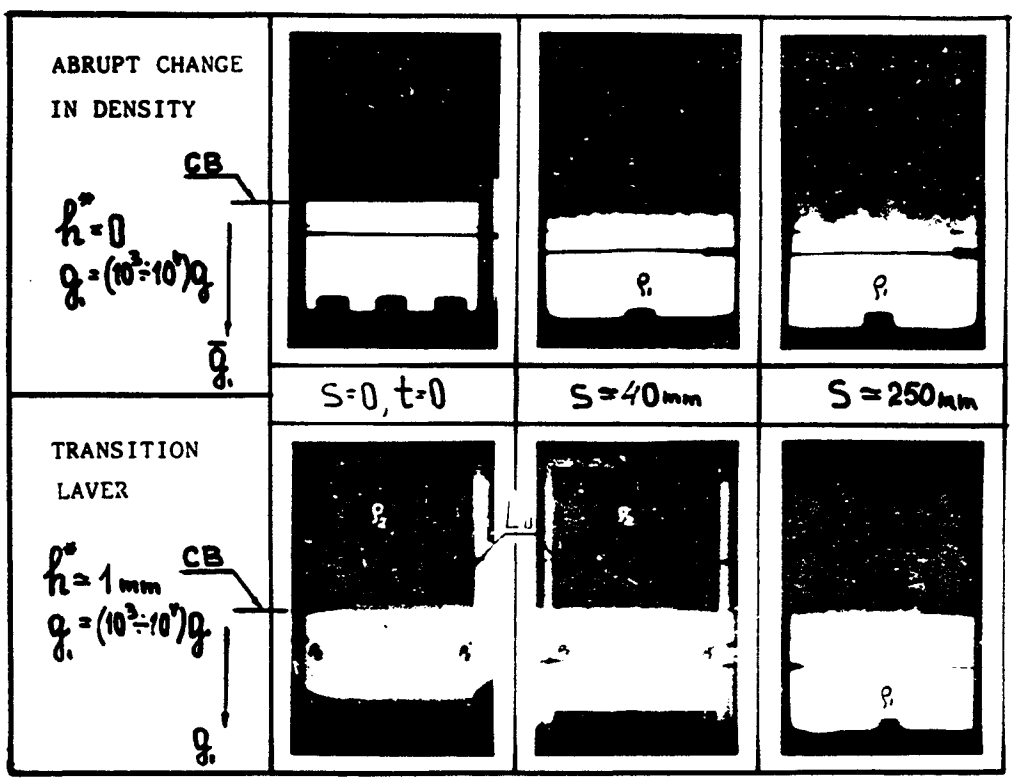

FIG.13 EXPERIMENTS WITH ABRUPT CHANGE IN DENSITY ($h^* = 0$)
AT THE CONTACT BOUNDARY AND WITH TRANSITION LAYER ($h^* > 0$)
(X-RAY TECHNIQUE).

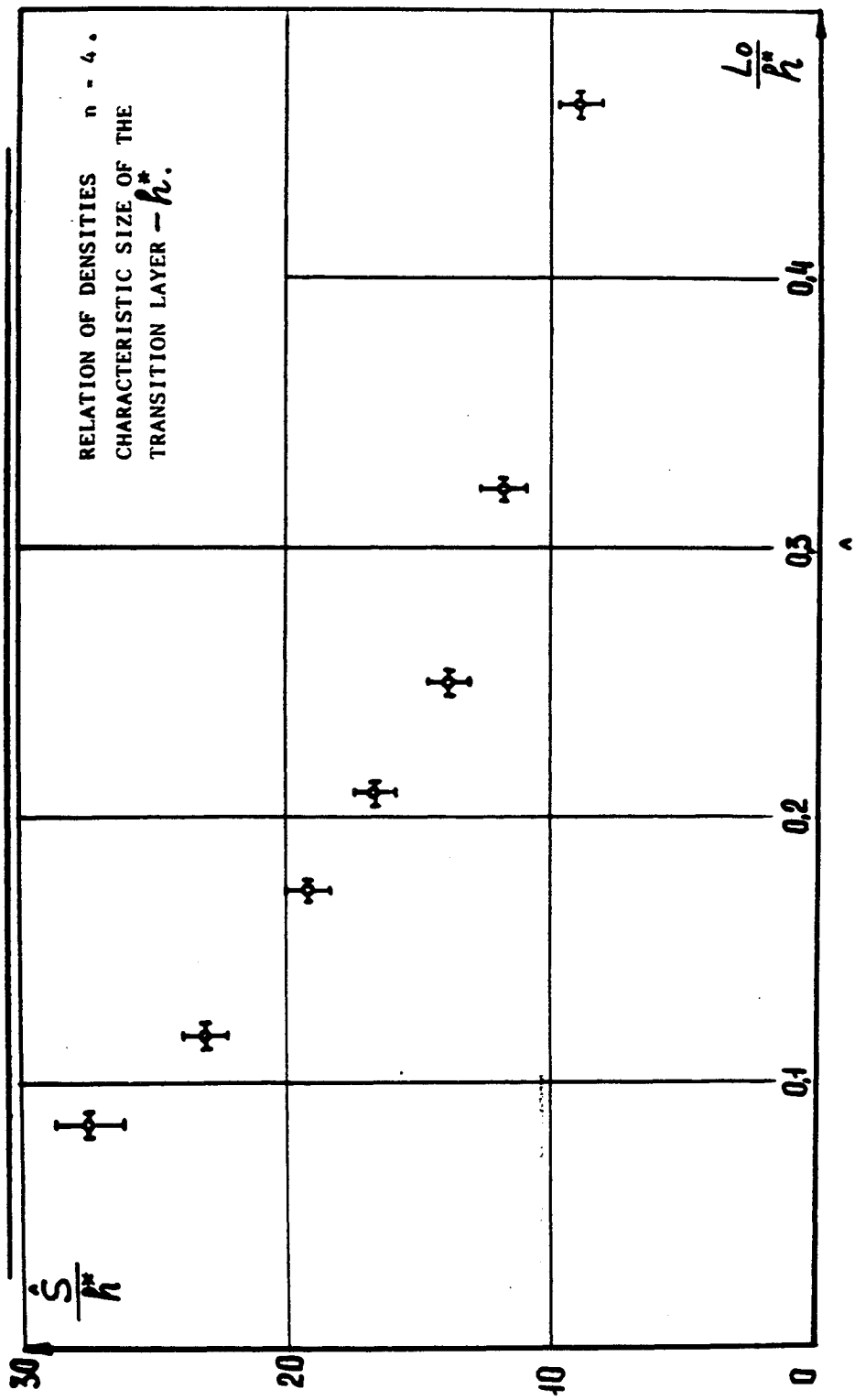

FIG. 14 DEPENDENCE OF MIXING DEVELOPMENT DELAY $\hat{S}$ ON THE SIZES OF THE INITIAL PERTURBATION ZONE L_0.

URA CNRS 230 L.M.F.N.

STRUCTURES and TURBULENCE

in

COMPRESSIBLE SHEAR FLOWS

Yann Lebret - Dany Vandromme

CORIA, U.R.A. CNRS 230, INSA de Rouen, BP8, M^t S^t Aignan

PHYSICAL ASPECTS

- Existence of COHERENT STRUCTURES in Compressible Flows

  (Papamoschou, Roshko experiments)

- Mixing process is in part governed by COHERENT STRUCTURES

  These phenomena are important in :

  → Supersonic Combustion

  → Mixing behind aircraft jets

  → Jet Noise Production

- Unsteady Flows

TURBULENCE MODELLING APPROACH

- Why a Turbulence Modelling Approach ?

  → High Reynolds Flows

  → Limitation of Direct Simulation and Large Eddy Simulation to calculate that flows

  → Transport equation for turbulence quantities are also TIME dependent

⇒ One possible way is : Turbulence modelling approach

Question :

→ Validity of Classical Turbulence Model for large scale time dependent turbulence

TURBULENCE MODELLING APPROACH

- Semi Deterministic Modelling (S.D.M.)

Utilisation of two components splitting

$$f(\vec{x},t) = f_c(\vec{x},t) + f_r(\vec{x},t)$$

f_c is the coherent part of f
f_r is the random part of f

If the random part is weak ⇒ All the scales are solved ⇒ S.D.M.≡ L.E.S.

If the coherent part is weak ⇒ S.D.M.≡Classical Reynolds Averaging

Originality: Randomness exists at all scales

Interest: Classical Turbulence Models can be used to solve unsteady flows

TURBULENCE MODELLING

- Averaged Navier - Stokes equations with FAVRE formalism

$$\overline{\rho}_{,t} + (\overline{\rho}\tilde{U}_j)_{,j} = 0$$

$$(\overline{\rho}\tilde{U}_i)_{,t} + (\overline{\rho}\tilde{U}_i\tilde{U}_j)_{,j} = \overline{\sigma}_{ij,j} - (\overline{\rho}\widetilde{u'_i u'_j})_{,j}$$

$$(\overline{\rho}\tilde{E})_{,t} + (\overline{\rho}\tilde{E}\tilde{U}_j)_{,j} = \overline{(\sigma_{ij}U_i)_{,j}} - \overline{(\lambda_c T_{,i})_{,i}} - (\overline{\rho}\widetilde{u_i' E'})_{,i}$$

→ additive unknown quantities : $\overline{\rho}\ \widetilde{u'_i u'_j}$ etc ⇒ CLOSURE PROBLEM

System is closed with the help of **TURBULENT VISCOSITY HYPOTHESIS**

$$-\overline{\rho}\ \widetilde{u'_i u'_j} = \mu_T\left(\frac{\partial\tilde{U}_i}{\partial x_j} + \frac{\partial\tilde{U}_j}{\partial x_i} - \frac{2}{3}\frac{\partial\tilde{U}_k}{\partial x_k}\delta_{ij}\right) - \frac{2}{3}\overline{\rho}\ k\delta_{ij}$$

TURBULENCE MODELLING (continued)

- **SELECTIONS**

→ zero equation model

$$\mu_T = \bar{\rho}\tilde{U}\ell$$

ℓ is defined with the local width of the shear layer

→ two equations model

$$\mu_T = \frac{C_\mu \rho k^2}{\epsilon}$$

k is the kinetic turbulent energy

ϵ is the dissipation level

In this case, two transport equations have to be solved to find k and ϵ

TURBULENCE MODELLING (continued)

- EQUATIONS USED with k - ϵ turbulence model

$$\frac{\partial}{\partial t}(\bar{\rho}k) + \frac{\partial}{\partial x_i}(\bar{\rho}\, k\widetilde{v_i} - \mu_k \frac{\partial k}{\partial x_i}) = P_k - \bar{\rho}\epsilon + \text{Compressibility}$$

$$\frac{\partial}{\partial t}(\bar{\rho}\,\epsilon) + \frac{\partial}{\partial x_i}(\bar{\rho}\,\epsilon\widetilde{v_i} - \mu_\epsilon \frac{\partial \epsilon}{\partial x_i}) = C_{\epsilon 1}\frac{\epsilon}{k}\bar{\rho}P_k - C_{\epsilon 2}\bar{\rho}\frac{\epsilon\epsilon}{k}$$
$$+\text{Compressibility}$$

$$P_k = -\bar{\rho}\widetilde{u_i'u_j'}\frac{\partial \tilde{U}_i}{\partial x_j}$$

TURBULENCE MODELLING (continued)

EQUATION SET

- One Continuity Equation
- Two Momentum Equations
- One Energy Equation

With the k-ϵ model :

- One Transport Equation for k
- One Transport Equation for ϵ

TURBULENCE MODELLING (continued)

ENERGY COUPLING "Turbulent pressure" $\frac{2}{3}\bar{\rho}k$ must be include in the inviscid part of the equations

- Thermodynamical Instantaneous form of the total energy equation:

$$\rho E = \rho e + \frac{1}{2}\rho U_i U_i$$

After Favre averaging:

$$\widetilde{E} = \bar{\rho}\left(\widetilde{e_i} + \frac{\widetilde{v_\alpha}^2}{2} + k\right)$$

Physical meaning: Transfert of energy between the mean motion and the fluctuations.

NUMERICAL METHOD

SYSTEM to be SOLVED

The equations are cast into the following form:

$$\frac{\partial U}{\partial t} + \frac{1}{V}\int_V \vec{F}d\vec{S} = W \qquad (I)$$

DISCRETIZED EQUATION

The cquation (I) is dicretized on the volume element V, a flux balance is made on each surfaces:

$$\frac{\partial U}{\partial t} + \frac{1}{V}\sum_V \vec{F}d\vec{S} = W \qquad (II)$$

Special attention has been paid to treat implicitely source terms:

$$W^{n+1} = W^n + C^n \delta U^n \text{ with } C^n = \frac{\partial W^n}{\partial U}$$

NUMERICAL SCHEME

CHARACTERISTICS OF THE METHOD

→ Explicit-Implicit Mac Cormack versus 1981

→ Finite Volume

→ Approximate factorization of the implicit operator

→ Cartesien Mesh

→ Accuracy: Second order in space and time

→ Partially implicit treatment of source terms

RESULTS

Two points will be presented :

- Ability to predict unsteady flows with a classical turbulence model
- Influence of the Mach number

RESULTS

UNSTEADINESS

- Theorical Convective Velocity (Papamoschou formulation) = $297 m/s$
- Numerical Convective Velocity = $300 \pm 30 m/s$

Good Agreement between numerical simulation and Papamoschou formulation

Influence of Mach Number

(Same Reynolds Number)

I- FLOW CONFIGURATION

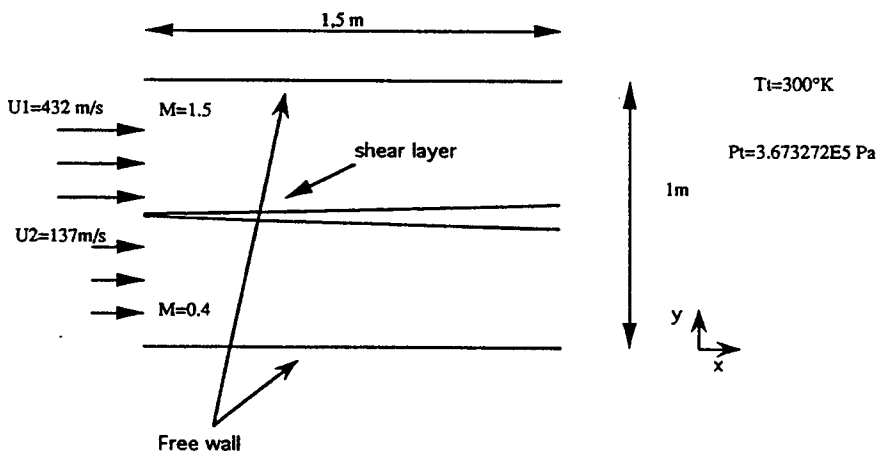

II- FLOW CONFIGURATION

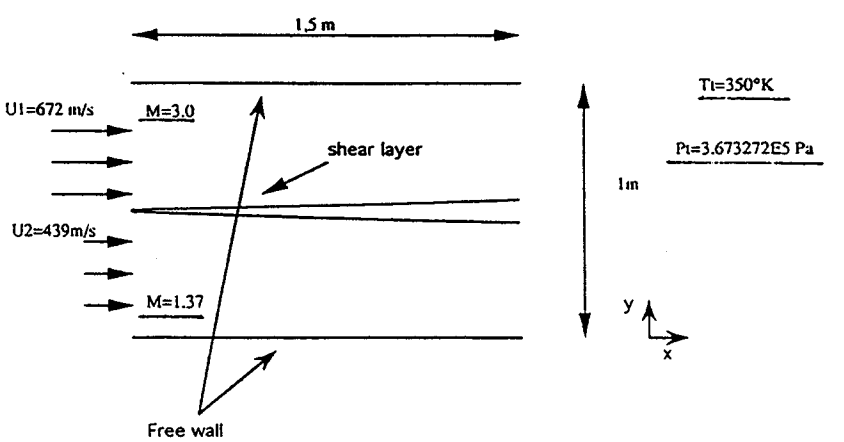

I - VORTICITY FIELD

Time Evolution

$t = 0.150545\ s$

$t = 0.1506209\ s$

$t = 0.1507003\ s$

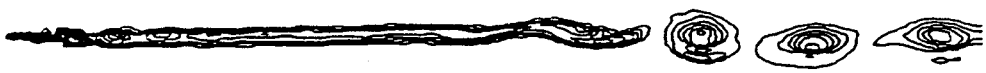

$t = 0.1508591\ s$

$t = 0.1509384\ s$

$t = 0.1510178\ s$

$t = 0.1511766\ s$

$t = 0.152560\ s$

I- ISO ROT LINES

PASSIVE SCALAR

ISODENSITY LINES

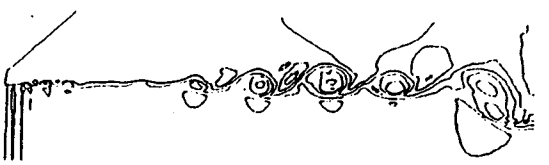

II.

ISO-ROT LINES

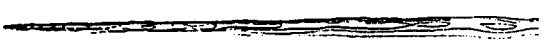

PASSIVE SCALAR

ISODENSITY LINES

CONCLUSION

- Ability to calculate structure coherents without any artificial perturbation

- Correct matching on the determination of the convective Mach number with the Papamoschou formulation with two equations model

- It is reasonable to think that high Reynolds unsteady flows could be solved with the help of turbulence model

- If the Mach number is increasing the structures vanished, but the turbulence modelling needs to be completed in order to have a better description of the growth of the shear layer with the convective Mach number

ABOUT TURBULENT MIXING DYNAMICS AT UNSTABLE BOUNDARY OF LIQUID LAYER, ACCELERATED BY COMPRESSED GAS

E.E.Meshkov, N.V.Nevmerzhitsky
All- Union Sci.- Res. Inst. of Exp. Phys.
607200, Arzamas, Nizhny Novgorod region, USSR

ABSTRACT

The method to investigate the turbulent mixing zone evolution at the liquid layer boundary, accelerated by a compressed gas was developed. The experimental results show that the penetration dynamics of the mixing zone into the layer is described with a function:

$$h_1 = \alpha_1 \cdot A \cdot g \cdot t^2$$

where h_1 - mixing zone penetration depth in the layer, A- Atwood number, g-acceleration, t-time. It was found out that α_1 - value varied from 0.05 to 0.13 depending on the experimental conditions.

INTRODUCTION

If the interface between two different density fluids acceleratively moves, the acceleration being directed from the lighter fluid (with ρ_2 density) to the heavier one (ρ_1) ,then the first becomes unstable (R-T instability [1,2]). R-T instability propagation leads to turbulent mixing of fluids at the unstable interface[3]. The initial stage of R-T instability and turbulent mixing evolution is determined by the initial disturbance nature, but further,as the initial conditions become outworn, the mixing layer width L and the depth of mixing layer front penetration into the heavy fluid h_1, if g = const, must grow with time, as in [4,5]:

$$L = \alpha \cdot A \cdot g \cdot t^2 = h_1 + h_2$$

$$h_1 = \alpha_1 \cdot A \cdot g \cdot t^2 = 2 \cdot \alpha_1 \cdot A \cdot S$$

where $A = \frac{\rho_1 - \rho_2}{\rho_1 + \rho_2}$; S - the path made by the interface; h_2 - penetration depth of the mixing layer into the light fluid, α, α_1 - empirical constants.

The results of the experimental study of turbulent mixing associated with R-T instability evolution [6-11] confirm the above mentioned supposition, though different α_1 values were obtained by different authors. According to the calculated evaluation[12], if $\rho_1 \gg \rho_2$ (and $A \cong 1$, consequently), then $\alpha \cong 0{,}45$ and $\alpha_1 \cong 0{,}2$. In this case asymmetry coefficient of the mixing layer (the ratio of h_2 to h_1) will be 1.24. By performing the experimental study of mixing at the interface of uncompressible fluids and gas-fluid

interface[7,9] we obtained α_1 = 0,06 - 0,07 (for A = 1); in experiments[10] (gas-jelly layer) α_1 = 0,12. In experiments[11] (gas-fluid), where flow nature was close to two-dimensional, we obtained α_1 = 0,04.

At present no exhaustive data on mixing layer structure at gas-fluid interface and on its propagation mechanism are available, however it is known-that the front part of the mixing layer, penetrating the fluid , consists of set of bubbles of different size, expanding in the course of time. Bubble expansion mechanism and the associated mixing layer evolution mechanism are investigated from the different viewpoints[13,14] .

EXPERIMENTAL

We present the experimental study of mixing layer evolution dynamics at the unstable interface of fluid layer, accelerated by compressed gas. The following experimental procedure has been developed. Fluid layer FL was disposed inside 40 x 40 mm^2 square vertical channel PLC made from plexiglas (fig.1(a)). The layer divided the channel in two parts: confined chamber CM (100 - 400 mm long) and outlet channel OC (20 - 80 mm long). Fluid layer in the channel was created as follows: initially a 1-2 mm thick plywood plate was placed inside the channel. Clearance space between the plate and the channel wall was filled with aqueous gelatin solution, which, after being set turns into jelly, holding the plate in the channel and sealing the clearance space between the channel wall and the plate. On the plate top the fluid layer FL (water in the majority of experiments) was poured. On top of the water layer polypropylene particles PP of ≅ 0,3-0,5 mm size were placed (ρ = 0,9 g/cm^3) to create initial perturbations.

At the end of the outlet channel part a hermetically sealed diaphragm was installed. The channel above and under the layer FL, was filled with a compressed gas (air or helium). Pressure equalization in the channel and the chamber was made through the bypass channel (provided in the PLC channel wall) having the diameter of ≅ 1 mm.

The diaphragm was broken through by bursting up a wire pasted on it. The compressed gas escaped from the channel outlet, while the fluid layer started to acceleratively move along the channel, forced by the compressed gas in the chamber .

Flowing process in the channel PLC was illuminated with flash lamp (transmitted light). High-speed recording have been made by frame rotating mirror camera SFR.

RESULTS AND DISCUSSION

Fig. 1(b) comprises frames of recording of experiment N 446 for water layer thickness of 79 mm ; the layer was accelerated with the compressed helium (P_0 = 0,19 MPa).

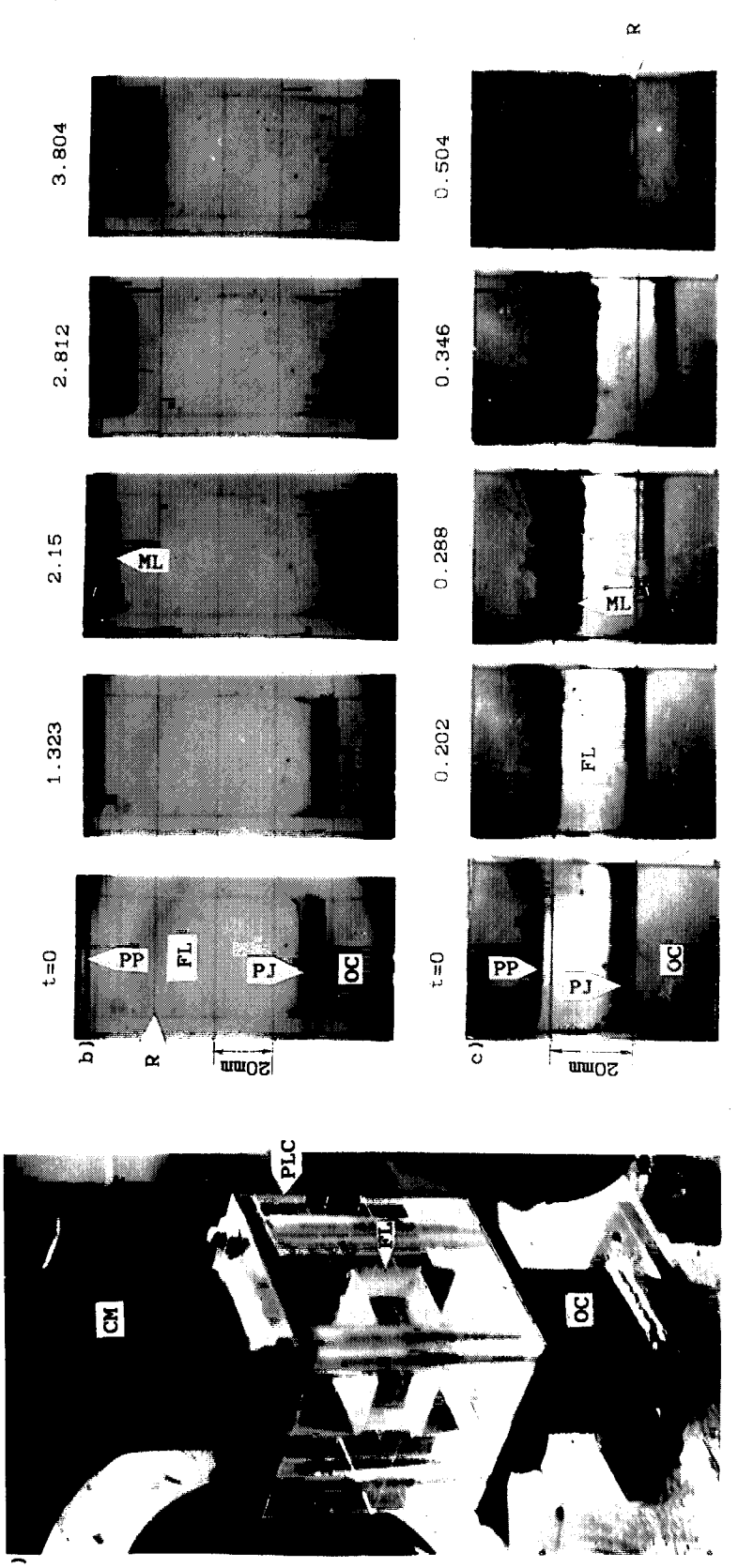

Fig.1. (a) The picture of the experimental apparatus. (b) Frames of the recording of experiment N 446 on accelerating of 79 mm thick water layer under the compressed air (Po = 0,19 MPa). (c) Experiment N 422; 22 mm thick water layer; Po = 4MPa. Designations: PLC - plastic channel with the inner cross-section of 40x40 sq.mm; FL - fluid layer; CM - confined chamber; OC - outlet channel; PJ - plywood plate 1-2 mm thick; LO-polypropylene particles of 0,3-0,5 mm; ML - turbulent mixing layer; R - reference lines at the channel outer surface. Time in milliseconds.

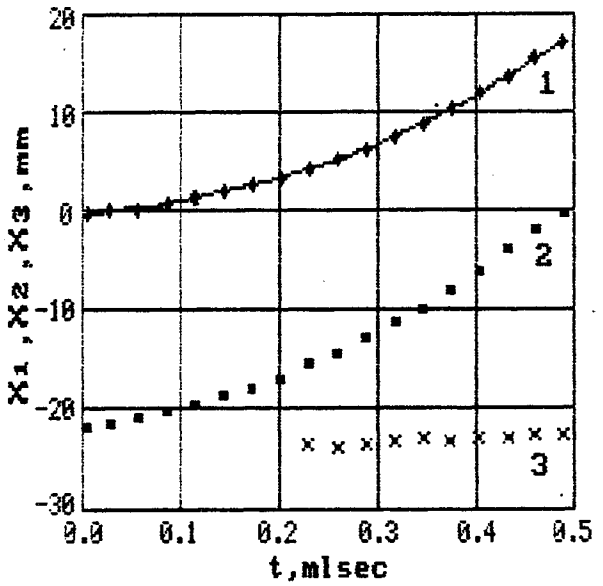

Fig.2.x-t diagram of water layer and turbulent mixing zone fronts motion (exp. N₀.422). Here:(1)-x-t giagram of the stable layer boundary (experiment and the approximating dependence); (2) - x-t diagram of the mixing zone front,penetrating into the water layer; (3)- x-t diagram of the mixing zone front, penetrating into gas.

Fig.1(c) comprises frames of recording of experiment N 422 for water layer thickness of 21,8 mm; the layer was accelerated by the compressed air (P_0 = 4 MPa). Here: FL - fluid layer; PJ - plate with the sealing jelly layer; PP - polypropylene particles; ML - turbulent mixing layer; R - reference lines on PLC channel outer surface; OC - outlet channel.

Photochronogram frames were used to measure the stable layer surface position (x_1), boundary of the mixing layer within the fluid layer (x_2) and boundary of the mixing layer within gas (x_3) as a function of time t. Penetration depths h_1 and h_2 were identified according to the following equations:

$h_1(t) = W - (x_1(t)-x_2(t))$,

$h_2(t) = x_1(t) - x_3(t) - W$,

where W stands for the initial layer FL thickness. The shift (x_1) determines the path (S), made by the layer. It has been evaluated that measurement error value for x_1, x_2 and x_3 is associated with the layer image parallax, occurring when the first is being transferred along the channel < 0,15mm, optical resolution of the recording device being of < 0,5mm.

Experimental dependence $x_1(t)$ was approximated using polynomial of degree 4. The dependence of layer acceleration g on time was obtained by double differentiation of the calculated polynomial. Measurement results of experiment 422 for x_1, x_2, x_3 and approximation results for x_1 are shown on fig.2.

Fig.3(a,b) comprises experimental dependencies $h_1(2S)$ and $h_2(2S)$ and the associated approximating linear dependence as well as g(2S) dependence (a) for experiment N 446, and (b) for

experiment N 422. Experimental dependencies $h_1(2S)$ and $h_2(2S)$ in these and other experiments are practically of linear nature. In this case α_1 was specified as the slope value of the straight line, approximating $h_1(2S)$ dependence at the given part of experimental dependence (several experimental points at the initial dependence part were excluded).

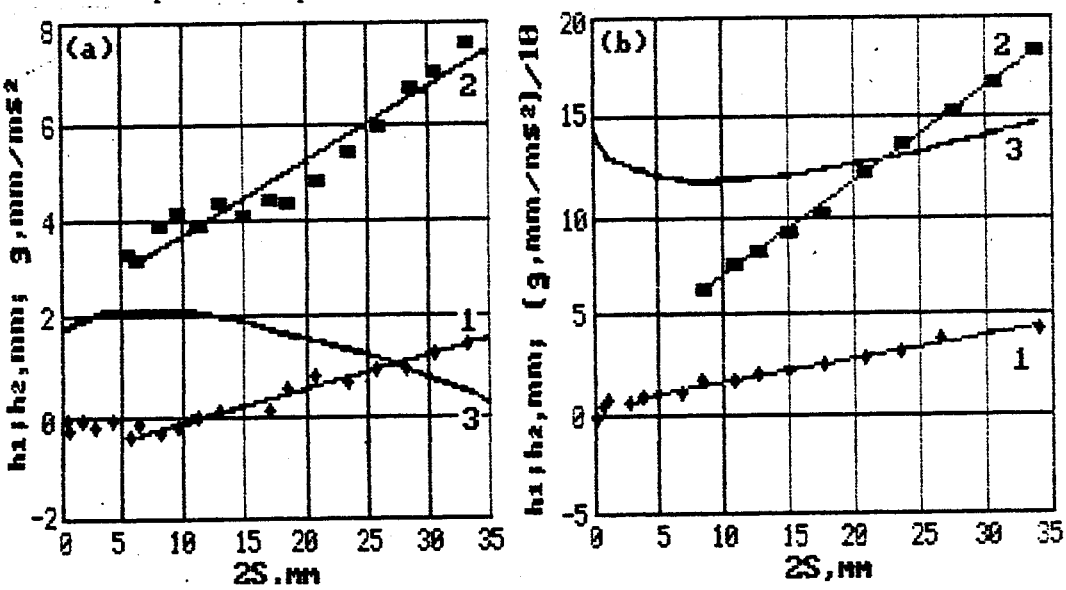

Fig.3. (1) Depth of mixing zone penetration into the fluid layer h_1 (experiment and the approximating linear dependence), (2) depth of mixing zone penetration into gas h_2, (3) layer acceleration vs double value of the path made by the layer. (a) Experiment N₀.446, (b) experiment N₀. 422.

During experimental series not only fluid layer width W (9-80mm) varied, but the pressure of the compressed gas P_0 (0,19 - 4,0 MPa) as well. The mean value g_m (g_m - the mean acceleration at the layer path part, where measurements of α_1 were conducted) varied from $1{,}5\cdot10^3$ to $1{,}3\cdot10^5$ m/sec^2. Experimental results shown in table.

Experimental results shown in table testify to the fact that in accordance with the experimental conditions α_1 value changes from 0.053 to 0.126.

It should be interesting to note, that in this case α_1 value is dependent on acceleration or pressure gradient in the layer (as pressure gradient value is proportional to acceleration). Experimental results are shown on fig.4 as α_1 vs pressure gradient plot. Gradient value in each of the experiment was specified as

$\rho_1 g_m$. Fig.4 shows the results of experiments[7,10] as well. These results satisfactorily coordinate with our measurements results. Experimental results may be approximated using the dependence $\alpha \cong (\text{grad } P)^{0,17}$.

Table. Experimental results.

Exp.No.	P_o MPa	W mm	g_m m/s^2	grad P Pa/m	α_1
411	1,9	51	2.9×10^4	2.9×10^7	0.091
412	1,9	48	3.2×10^4	3.2×10^7	0.095
417	0.5	50	7.9×10^3	7.9×10^6	0.094
422	4.0	22	1.3×10^5	1.3×10^8	0.126
424	1.0	21	3.7×10^4	3.7×10^7	0.101
445	2.5	80	2.9×10^4	2.9×10^7	0.091
446	0.19	79	1.5×10^3	1.5×10^6	0.069
447	0.19	75	2.5×10^3	2.5×10^6	0.053
456	2.5	20	8.8×10^4	8.8×10^7	0.126
460	2.5	30	6.6×10^4	5.3×10^7	0.116

The experimental data available are insufficient to define whether acceleration or pressure gradient serve as a determining factor. At least we can state, that potential energy density ρgh of the accelerated layer increases together with grad $P = \rho g$; as a consequence, when h_1 values are equal, kinetic energy value of turbulent motion of substance in the mixing layer must finally be higher in case of the higher gradient.

Alteration of the pressure gradient may result in the change of the form of bubbles in the front part of the mixing layer, which may affect the rate of their penetration into the fluid. Assuming that the front part of the mixing layer penetrates into the fluid in the form of the "competing" bubbles of different spatial scale, disposed at different levels of the mixing layer (hypothesis[13]), we can state, that density gradient may significantly affect the mechanism of such a "competition".

Supposition on α_1 vs pressure gradient dependence readily coordinates with the viewpoint expressed in [15], judging by which disturbance propagation in RT-instability in nonlinear stage depends rather on pressure gradient than acceleration.

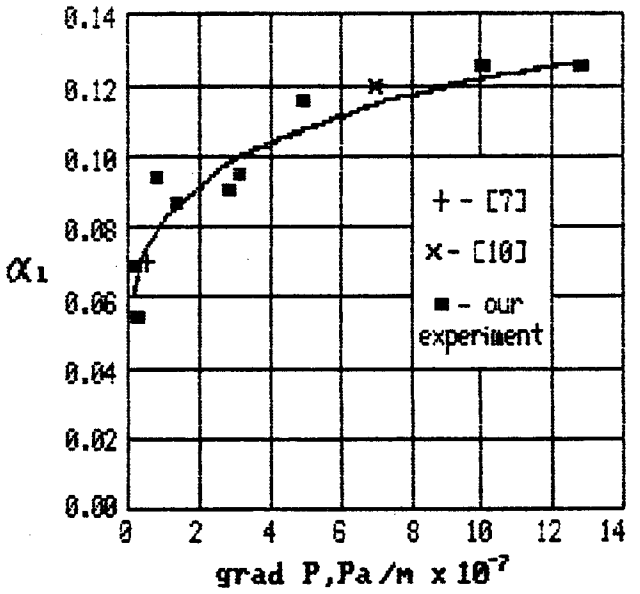

Fig.4. Dependence of α_1 vs pressure gradient in fluid layer.

It should be noted, that dependence of the dimensionless α_1 parameter on the dimensional grad P parameter is automatically associated with the necessity of α_1 dependence on other factors, such as surface tension and/or viscosity.

It should be noted, that in experimental conditions the influence of wave process in accelerated fluid layer on the mixing layer evolution dynamics is possible, as characteristic time values of mixing evolution observations make 500-3500 mcsec, while characteristic time values of sound twofold passing through the accelerating layer make 10-100 mcsec.

Instrumental resolution of the recording optics used was insufficient for obtaining more detailed information on the mixing layer structure; however the characteristic bubble scale for equal s tends to decrease as the density gradient increases. Obviously this happens due to the critical wave number $k_c = ((\rho_1-\rho_2)/\sigma)^{1/2}$ increase[16], which restricts the region of wave numbers k of R-T instability spreading ($k \leq k_c$).

1.Rayleigh,Lord. Scientific papers, vol.II. Cambridge University Press.
2.Taylor J. Proc.Roy.Soc., J.Lond.Ser.A., vol.201, No.1065, p.192, 1950.
3.С.З.Беленький, Е.С.Фрадкин. Теория турбулентного перемешивания. Тр.ФИАН АН СССР, т.29, 1965.
4.В.Е.Неуважаев. ДАН СССР, т.222, No 5, с.1053-1056, 1975.
5.D.L.Youngs. Physica D 12, North-Holland, Amsterdam, 19, 1984.
6. Н.Н.Анучина, Ю.А.Кучеренко, В.Е.Неуважаев, В.Н.Огибина, Л.И.Шибаршов, В.Г.Яковлев. Изв.АН СССР, МЖГ, N 6, с.157-160, 1978.
7. K.I.Read. Physica D 12, North-Holland, Amsterdam,p.45, 1984.
8. Ю.А.Кучеренко, Г.Г.Томашев, Л.И.Шибаршов. ВАНТ, сер. Теор. и прикл.физика, вып.1, с.13, 1988.
9.D.L. Youngs. Physica D37, North-Holland, Amsterdam, pp

270-287, 1989.
10. В.Б. Розанов, И.Г.Лебо, С.Г.Зайцев, Е.В.Лазарева, Е.И.Чеботарёва, А.Н.Алёшин, С.Н.Титов, А.М.Василенко, О.В.Буряков, О.В.Куропатенко, В.И.Ольховская, В.П.Ратников, В.Г.Яковлев, И.Г.Жидов, Е.Е.Мешков, Н.В.Невмержицкий. Экспериментальное исследование гравитационной неустойчивости и турбулентного перемешивания стратифицированных потоков в поле ускорения в связи с задачами инерциального термоядерного синтеза. М., Препринт ФИАН N 56, 1990.
11. M.Andrews, D.Spalding. Phys. Fluids A, , V.2, p. 922-927, 1990.
12. В.В.Никифоров. ВАНТ, сер. Теор. и прикл.физика, вып.1, с.3, 1985.
13. J.Zufiria. Phys. Fluids, V.31, 440-446, 1988.
14. J.Glimm and X.L.Li . Phys. Fluids, V.31, 2077-2085, 1988.
15. G.R.Baker, R.L.McCrory, C.P.Verdon, S.A.Orzag. J.Fluid Mech., V.178, pp. 161-175, 1987.
16. R.Bellman, P.Penington. Quart.J.Appl.Math., v.12, p.151-162, 1954.

COMPARING THE MODELS OF TURBULENT MIXING, INDUCED BY THE RAYLEIGH–TAYLOR– AND THE RICHTMYER–MESHKOV INSTABILITIES

V.E.Neuvazhayev, A.F.Podkorytova, V.G.Yakovlev

All–Union Research Institute of Technical Physics
454070, Chelyabinsk–70, p.o.245, USSR

Abstract

On the suggestion of organizers of "the 3–rd International Workshop on the Physics of Compressible Turbulent Mixing" (June 17–19, 1991, Abbey of Royaumont, France), numerical computations of two problems according to the code TURINB have been performed. Comparison with the results of computations, carried out according to the Youngs model, is given. The obtained disagreements have been explained.

It was suggested to perform comparison of models by using the problems having the self–similar solutions. The results of these problems for different Atwood numbers have been obtained in the nondimensional form. Comparison of all available experiments and computations is suggested to be performed on these problems.

Introduction

At the International Workshop in Pleasanton (November 1989, USA) a number of semiempirical models, designed to predict the turbulent mixing arising at the interface between substances under the action of the Rayleigh–Taylor– and the Richtmyer–Meshkov instabilities. At the next Workshop, planned to be held in June 1991 (Royaumont, France), it is, in particular, suggested to perform comparison between models on the basis of test examples, being taken from D.Youngs work[1]. Statement of these two examples is close to the performed experiments for incompressible fluids with the initial densities relation $\rho_2^\circ/\rho_1^\circ=3$ and under the constant acceleration[1,2]. Results of computing these examples, according to the models[3,4] are presented below and comparison with results, presented in[1], is given.

Moreover, the problems[3,4], based on the precise solutions for the condition of incompressibility under the constant acceleration (the Rayleigh–Taylor instability) as well as the impulsive one[5] (the Richtmyer–Meshkov instability), are suggested, we believe that new tests will allow to perform the more complete comparison of semiempirical models for turbulent mixing.

It is also appropriate to note that while taking into account the compressibility there is a case when the precise solution can be obtained for two unlimited media with different

powers laws of energy release[6]. This solution can be applied for calibrating the two-dimensional codes[7,8] and three-dimensional ones. However, the experimental set-up presents a problem in this case.

1.Mixing of two fluids under constant acceleration

The statement of the problem is taken from the work[1] :

fluid 1: $0<x<100$mm; $\rho_1^0=1$ mg/mm^3

fluid 2: $100<x<200$mm; $\rho_2^0=3$ mg/mm^3

The initial distribution of pressure is determined by the equation

$$-\frac{\partial p}{\rho \partial x} = g = 0.5\text{mm/ms}^2.$$

It was assumed that in the initial moment the pressure p is equal: to 400 kPa along the left boundary, then the equation of state is: $p=\frac{2}{3}\rho E$.

Results of comparison are presented in Fig.1. For the moment t=60ms the profiles of the fraction concentration f_i (3.5) as well as non-dimensional turbulence kinetic energy $\hat{k}=k/k_{max}$ are given. The points, obtained on the basis of the $k\epsilon$-model[4], are connected by a solid line. Formulae and constants of this model are quoted in the following sections: (3.1), spatial grid was selected the same one as in[1] : $\Delta x=5$mm.

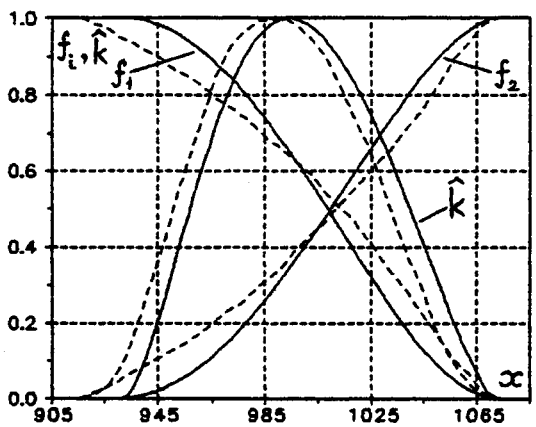

Fig.1

Disagreement between results, obtained according to the code TURINB[3,4], and the Youngs results[1] is, apparently, explained by fact that the spatial grid has influenced upon the computation result in[1]. The computation in[1] corresponds to the case of specifying the non-zero initial roughness which size is equivalent to the initial one of the cell $\Delta x=5$mm, whereas the computations, conducted according to the code TURINB, have been performed under zero roughness. The question on the spatial grid influence upon the solution passing to the self-similarity mode has been discussed in[9].

2.Mixing of three fluids under constant acceleration

The statement of the problem is taken from the work[1] :

fluid 1: $0<x<100$mm; $\rho_1^\circ=1$ mg/mm^3

fluid 2: $100<x<110$mm; $\rho_2^\circ=\sqrt{3}$ mg/mm^3

fluid 3: $110<x<210$mm; $\rho_3^\circ=3$ mg/mm^3

The equation of state, pressure at the left boundary and acceleration are the same as in the problem with two fluids.

The spatial mesh is specified as in[1] : $\Delta x=5$mm in fluids 1 and 3, $\Delta x=2.5$mm in the thin interstitial layer.

Plots of fraction concentrations and the kinetic energy of turbulence are presented in Fig.2.

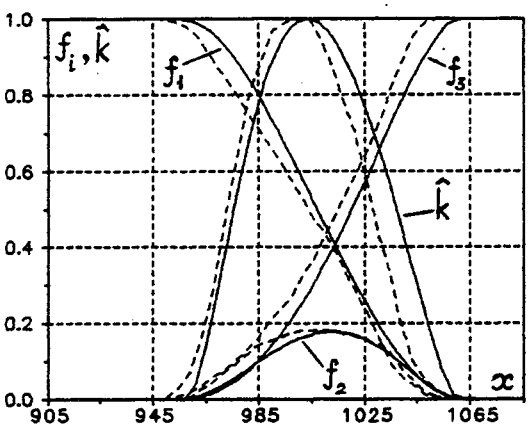

Fig.2

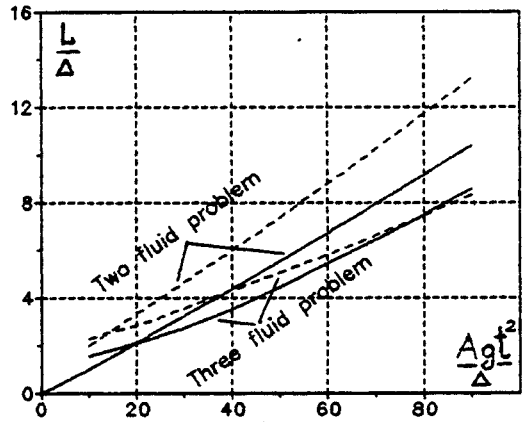

Fig.3

Fig.3 shows the dependence of the mixing zone relative width, determined under the condition that $f_1=f_2=0.05$, upon the value Agt^2/Δ, where A is the initial value of the interstitial layer and the Atwood number A is:

$$A=\frac{|\rho_1^\circ - \rho_2^\circ|}{\rho_1^\circ + \rho_2^\circ}.$$

Note that the computed curve passes through the coordinate origin according to the k-ε-model, whereas in[1] this is not observed. This can be explained by the fact that in the numerical algorithm[4] the resolution of the feature is provided at the beginning of computations when the mixing zone width is less than the cell size.

3.Self-similar solution for two fluids under constant acceleration[3,4]. Dependence of the solution on the Atwood number

Comparison of experiments and semiempirical models are, as rule, performed for problems having stationary or self-similar modes. In our case the self-similar solutions are possible for two media on the assumption of weak compressibility and under the constant acceleration.

In the considered case the equations of k-model have the

form[3]:

$$\frac{\partial\rho}{\partial t}=\frac{\partial}{\partial x}D\frac{\partial\rho}{\partial x} \tag{3.1}$$

$$\frac{\partial\rho v^2}{2\partial t}+\frac{\nu\rho Dv^2}{\alpha^2L^2}=Dg\frac{\partial\rho}{\partial x}+\beta\frac{\partial}{\partial x}\rho D\frac{\partial v^2}{\partial x}+\frac{D}{2}\cdot\frac{\partial\ln\rho}{\partial x}\cdot\frac{\partial\rho v^2}{\partial x}+\frac{5}{6}\rho v^2\left[\frac{\partial\ln\rho}{\partial t}-D\left[\frac{\partial\ln\rho}{\partial x}\right]^2\right] \tag{3.2}$$

$$D=\alpha Lv, \tag{3.3}$$

$$L=2\left[\int_{x_2}^{0} f_2dx/f_2(0)+\int_{0}^{x_1} f_1dx/f_1(0)\right], \tag{3.4}$$

$$f_1=\frac{\rho-\rho_2^0}{\rho_1^0-\rho_2^0}, \qquad f_2=-\frac{\rho-\rho_1^0}{\rho_1^0-\rho_2^0}, \tag{3.5}$$

$$\alpha=0.25; \qquad \nu=1.25; \qquad \beta=0.75. \tag{3.6}$$

Here the mixing zone width is compared on the basis of the fraction concentration and not the mass concentration, as in[3].

In the ke-model, in contrast to the k-model, the dissipative term is considered to be the unknown function of ϵ_t and the following balance equation[4] is derived for it:

$$\rho\frac{dk}{dt}+\rho\epsilon_t=\rho D_\epsilon g\frac{\partial\rho}{\partial x}+\alpha_8\frac{\partial}{\partial x}\rho D_\epsilon\cdot\frac{\partial k}{\partial x}+\frac{2}{3}k\frac{d\rho}{dt} \tag{3.7}$$

$$\rho\frac{d\epsilon_t}{dt}+c_{\epsilon2}\rho\frac{\epsilon^2}{k}=c_\mu c_{\epsilon1}kg\frac{\partial\rho}{\partial x}+\alpha_{\epsilon8}\rho\frac{\partial}{\partial x}\rho D_\epsilon\cdot\frac{\partial\epsilon_t}{\partial x}+\frac{4}{3}\epsilon_t\cdot\frac{d\rho}{dt} \tag{3.8}$$

$$D_\epsilon=c_\mu k^2/\epsilon_t, \tag{3.9}$$

$$\frac{d}{dt}=\frac{\partial}{\partial t}-D_\epsilon\cdot\frac{\partial\ln\rho}{\partial x}\cdot\frac{\partial}{\partial x},$$

$$c_\mu=3.5,\ c_{\epsilon1}=1.43,\ c_{\epsilon2}=1.85,\ \alpha_{\epsilon8}=0.5,\ \alpha_8=0.85.$$

Comparison of models is performed on the self-similar solutions under the different Atwood numbers. Fig.4 show the profiles of fraction concentration and turbulent mixing kinetic energy in dependence on the non-dimensional length η:

$$\eta=\frac{x}{L_1}, \qquad L_1=2\int_0^x f_1dx/f_1(0).$$

Mixing intensity versus the Atwood number is shown in Fig.5, where $s=\frac{gt^2}{2}$, $L_1^{0.95}=L_1(f_1=0.95)$, $L_2^{0.05}=L_2(f_1=0.05)$, solid line – $\frac{dL_1}{2ds}$, $\frac{dL_2}{2ds}$, $\Delta-\frac{dL_1}{2ds}^{0.95}$, $\frac{dL_2}{2ds}^{0.05}$, $x-\frac{dL_1}{2ds}^{0.99}$, $\frac{dL_2}{2ds}^{0.01}$. Mixing is more intensive in the upper part of the figure and less intensive in its lower part.

Some known results, obtained experimentally[2], are also plot-

ted in Fig.5 by sign +. As a matter of fact, the constant models were chosen so as to describe the experiment.

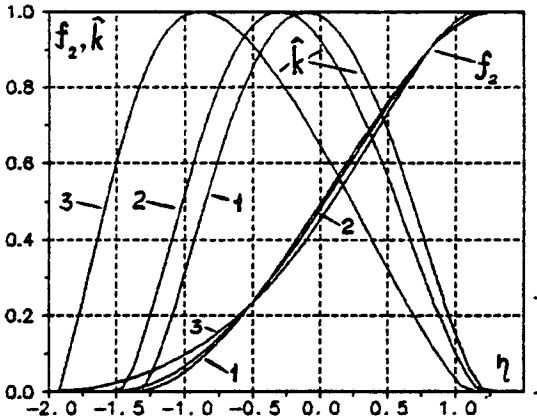

Fig.4

1 – A=0.2, 2 – A=0.5, 3 – A=0.905

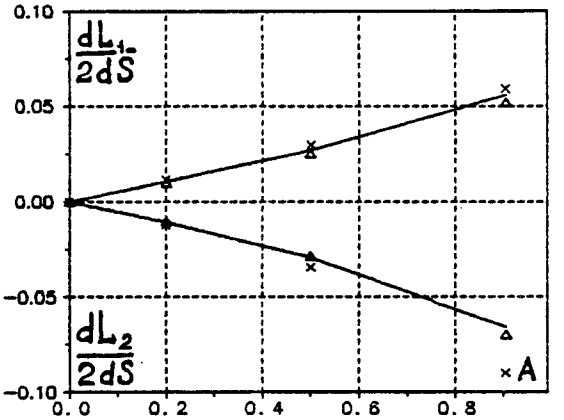

Fig.5

4.Self–similar solution for two fluids under impulsive acceleration. Dependence of solution on the Atwood number

In this section the self–similar solution is given which used for solving the problem on the mixing interface, subjected to the accelerated displacement in the final time interval t_0, so that

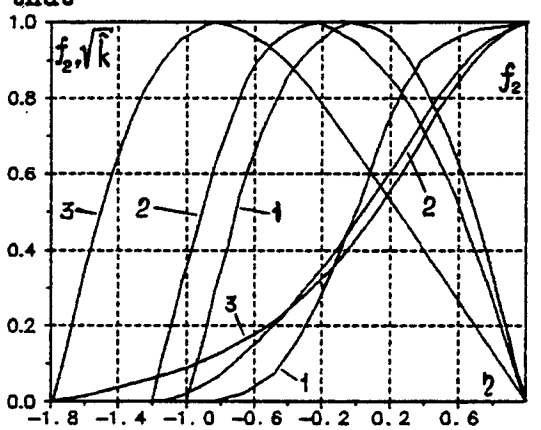

Fig.6

1 – A=0.2, 2 – A=0.5, 3 – A=0.905

$$\int_0^{t_0} g\,dt = U_0 .$$

In Fig.6 the fraction concentration– and the kinetic energy profiles, being built for k–model, are given. The power B determines the law of changing the mixing zone width in time:

$$L \sim (t - t_0)^{1/(1+B)}$$

This power is slightly dependent on the Atwood number.

Conclusion

Comparison of the semiempirical models, based on the code TURINB, with the Youngs model[1] has been performed for two problems, taken from[1]. The obtained disagreements have been explained.

Comparison of models is suggested to be performed by using problems which have the self–similar solutions. Results of these

problems computations have been obtained in the non-dimensional form over a wide range of changing the Atwood numbers. It is suggested to carry out comparison of all available experiments and computations on the basis of these problems.

References

1. Youngs D.L., Physica 37D, (1989), 282-283.
2. Anuchina N.N., Kucherenko Yu.A., Neuvazhayev V.E. et al. Sov. J. Mechanics of Fluids, 6(1978), 157-160.
3. Neuvazhayev V.E., Yakovlev V.G. Coll. Problems of Atom. Sci. & Engineering Ser. Methods & Programs for Num. Sol. of Math. Phys. Problems, 2(1984), 17-25.
4. Neuvazhayev V.E., Yakovlev V.G. Coll. Problems of Atom. Sci. & Engineering Ser. Theor. & Appl. Physics, 1(1988), 28-36.
5. Neuvazhayev V.E. Appl. Mech. & Tech. Physics, 2(1988), 46-51.
6. Neuvazhayev V.E. Appl. Mech. & Tech. Physics, 6(1976), 82-91.
7. Bokov N.N., Kuzmin A.Yu., Neuvazhayev V.E., Frolov V.D. Mathem. Simulation, 9(1989), 1-8.
8. Anuchina N.N., Ogibina V.N. Coll. Numer. Meth. of Contin. Medium Mechanics, 9, 7(1978), 8-11.
9. Neuvazhayev V.E., Yakovlev V.G. Coll. Num. Meth. of Cont. Medium Mechanics, 11, 3(1980), 127-131.

Turbulent Mixing, Induced by the Richtmyer-Meshkov Instability

V.E.Neuvazhayev

All-Union Research Ihstitute of Technical Physics, 454070 Chelyabinsk-70 P.O. 245, USSR

Abstract

Turbulent mixing development, induced by passing of shock waves through the interface, has been studied on the basis of two semiemperical models. The process of transition from random initial perturbations to turbulence is a rather complicated one, but it proceeds in a finite time. Here it is assumed that passing of shock waves through the initial zone of "roughness" leads to the instant development of mixing. The expression for the turbulent kinetic energy, transfered by the arriving shock wave, has been derived. The value of this energy is determined by the value of the non-dimensional parameter which is equivalent to the Richardson number. The analytical solution describing the turbulent kinetic energy decay and the mixing zone width change in time, has been obtained.

The analytical form of constructed solutions allows to perform comparison between the models and to make the choice of constants on the basis of comparison with the known experiments. Comparison of the obtained theoretical results with S.G.Saitzev's experimental data is given for the impulsive acceleration.

Introduction

The problem on the shock wave passing through the interface between two substances is considered. The contact zone is assumed to be "rough" and it is approximately substituted by the mixing zone having the width L_0. Investigation is carried out on the basis of two semiempirical models "k" and "kε", early applied by the author and Yakovlev (1975,1986) to study mixing, induced by the Rayleigh-Teylor instability.

The following idea of the author work (1975) has been used: the kinetic energy "k" in the mixing zone is considered to be independent of the space variable that allows to obtain the analytical solution for acceleration of the arbitrary form. For a single passing through the interface the value of the turbulent kinetic energy is determined by the parameter $\beta_0=U_0 t_0/L_0$, where U_0 is the contact boundary velocity change after the shock wave passing, t_0 is the time of the shock wave passing through the mixing zone with the width L_0.

1. K-model. Statement of the problem

In the case of two incompressible fluids mixing in the gravity field, the equations of model are reduced to the set of two equations: for the mix density ρ and for the turbulent kinetic energy $v^2/2$:

$$\frac{\partial \rho}{\partial t} = \frac{\partial}{\partial x} D \frac{\partial \rho}{\partial x}, \qquad (1.1)$$

$$\frac{\partial \rho v^2}{2\partial t} + \frac{\nu \rho D v^2}{\alpha^2 L^2} = Dg \frac{\partial \rho}{\partial x} + \beta \frac{\partial}{\partial x} \rho D \frac{\partial v^2}{\partial x} + \tag{1.2}$$

$$+ \frac{D}{2} \frac{\partial \ln \rho}{\partial x} \cdot \frac{\partial \rho v^2}{\partial x} + \frac{5}{6} \rho v^2 \left[\frac{\partial \ln \rho}{\partial t} - D \left[\frac{\partial \ln \rho}{\partial x} \right] \right],$$

$$D = \alpha L v. \tag{1.3}$$

Here α, ν, β are the model constans, selected on the basis of comparison with the experiment, L is the width of the zone, involved into mixing, g is the systen acceleration.

Equations (1.1), (1.2) are obtained by averaging from the gasdynamics equations. In the equation (1.1) the mix density ρ appears which is connected with initial densities ρ_1^0, ρ_2^0 and volume fractions f_1 and f_2 by the following formulae:

$$\rho = f_1 \rho_1^0 + f_2 \rho_2^0. \tag{1.4}$$

$$f_2 = \frac{\rho_1^0 - \rho}{\rho_1^0 - \rho_2^0}, \quad f_1 = \frac{\rho - \rho_2^0}{\rho_1^0 - \rho_2^0}. \tag{1.5}$$

We shall consider mixing of two media having the constant initial densities ρ_1^0 and ρ_2^0. Acceleration "g" is considered to be the function dependent only upon the time: g=g(t).

Formulate the boundary conditions. It is reasonable to assume that in the front of mixing into both directions the density is continuously changing up to the initial one but the kinetic energy is zero.

Under constant acceleration such problem will be self-similarity one. Its solutions have been investigated and

given in the author and Yakovlev's work (1984). The mixing front develops asymmetrically into the side of the light substance with the higher velocity. Effect of asymmetry L_2/L_1 depends on the Atwood number

$$A=\frac{\overset{o}{\rho}_1-\overset{o}{\rho}_2}{\overset{o}{\rho}_1+\overset{o}{\rho}_2} \qquad (1.6)$$

and reaches its maximum value equal to 1.1 at A=1, if the mixing front is determined effectively by the volume fraction values $f_1=f_2=0.1$. The kinetic energy of turbulent mixing has the bellwise character. The author (1975) has formerly considered the approximated model, in which the function v was believed to be dependent only on time in the turbulent mixing zone

$$v=\begin{cases} v(t), & |x|\leq L/2, \\ 0, & |x|>L/2. \end{cases} \qquad (1.7)$$

Such approximation allows to build the solution in the analytical form while using the acceleration law arbitrarily in time.

In the present work the early obtained solution is made more precise. This is doing by means of a new determination of the mixing zone width L.

As in the assumption (1.7), the diffusion coefficient D in the equation (1.1) depends only on time, then the solution for the density will have no front, and in the author's work (1975) the front is effectively introduced. This leads to necessity for recalculating the empirical constant α and to some inconvenience in comparison with the experiment.

In the given work the integral way, based on the law of the mixed mass conserving, is proposed. The mixing zone width is

determined by the followind aldorithm:

$$L = 2\left[\int_{x_2}^{0} f_2 dx/f_2(0) + \int_{0}^{x_1} f_1 dx/f_1(0)\right]. \qquad (1.8)$$

where f_1, f_2 are the volume fraction.

Note that this formula can be recommended for processing the experimental results, where the accurate determination of the front is difficult, as well as for the numerical algorithm where difficulties are the same as for processing the experiments. The geometric meaning of the formula (1.8) is demonstrated in Fig.1.

2. Approximate equations of the k-model. The accurate solution.

To obtain the approximate equation instead of (1.2) we integrate both sides of the equation (1.2) for the mixing zone $|x| \leq L/2$. We determine L preliminary from the equation (1.1), solution of which can be presented analytically, if we pass to a new variable:

$$\partial\tau = D\partial t. \qquad (2.1)$$

Then

$$\rho = \frac{\overset{0}{\rho_1} + \overset{0}{\rho_2}}{2} + \frac{\overset{0}{\rho_1} - \overset{0}{\rho_2}}{2}\,\Phi(x/2\sqrt{\tau}). \qquad (2.2)$$

where $\Phi(\eta) = \frac{2}{\sqrt{\pi}}\int_0^{\eta} e^{-z^2} dz$ - integral of probability.

The mixing front x_i is selected in such a way that the area in Fig.1 must be equal to the area of the triangle with the side

Ox_i. It is necessary to note that in the above-formulated approximation the mixing proceeds symmetrically to the left and to the right, that is why $x_1=x_2=L/2$, and on the basis of the areas equality we obtain the following formula:

$$\eta_1 = 2\int_0^\infty (1 - \Phi)d\eta = 2/\sqrt{\pi}.$$

Hence

$$L = 2x_1 = 4\eta_1\sqrt{\tau} = 8\sqrt{\tau/\pi}. \qquad (2.3)$$

The mixing zone width appears in the equation of the kinetic energy balance (1.2). Knowing it from the formula (2.3), we perform averaging of the equation (1.2) over the region $|x|\leq L/2$. By omitting the intermediate calculations we obtain finally:

$$\frac{d\bar{v}^2}{dL} + 4k\frac{\bar{v}^2}{L} = \frac{\Phi(\eta_1)}{2\eta_1^2}gA, \qquad (2.4)$$

$$\frac{dL}{dt} = 8\eta_1^2\alpha\bar{v}, \qquad (2.5)$$

$$k = k_0 + \frac{\Phi(\eta_1)}{24}A^2, \quad k_0 = 0.25 + \frac{\nu}{16\eta_1^2\alpha^2}. \qquad (2.6)$$

Solution of the last equations is presented in the integral form:

$$\bar{v}^2 = \bar{v}_0^2 + \frac{\Phi(\eta_1)}{2\eta_1^2}L^{-4k}\int_{-L_0}^{L} gL^{4k}dL, \qquad (2.7)$$

$$t = \frac{1}{8a\eta_1^2} \int_{L_0}^{L} \frac{dL}{\bar{v}}. \qquad (2.8)$$

3. The Richtmyer-Meshkov instability

This form of instability is obtained while passing through the shock wave interface. In the limits of the above-considered model we shall characterize the arising mixing by the Atwood number, obtained after passing of the shock waves, and by δ-wise shaped acceleration imparting to the interface a certain velocity U_0:

$$U_0 = \int g dt.$$

Obtain the solution for shock waves from the general solution (2.7), (2.8), by building it for the acceleration, specified by the step function

$$g = \begin{cases} g_0, & 0 \le t \le t_0, \\ 0, & t > t_0. \end{cases} \qquad (3.1)$$

For this case we specify the initial data:

$$t = 0: \quad L_0 = \bar{v}_0 = 0. \qquad (3.2)$$

Then, from (2.7) and (2.8) it follows

$$\bar{v}^2 = \begin{cases} \Phi(\eta_1) g_0 AL/(2\eta_1^2(1+4k)), & 0 \le t \le t_0, \\ \bar{v}_1^2 (L_1/L)^{4k}, & t > t_0 \end{cases} \qquad (3.3)$$

$$L = \begin{cases} 8\alpha^2\eta_1\Phi(\eta_1)g_0At^2/(1+4k), & 0\le t\le t_0 \\ L_1[1+2(1+2k)(t-t_0)/t_0]^{1/(1+2k)}, & t>t_0 \end{cases} \qquad (3.4)$$

$$L_1 = \frac{8\alpha^2\eta_1^2\Phi(\eta_1)g_0At_0^2}{1+4k}, \quad \bar{v}_1 = \frac{2\alpha\Phi(\eta_1)g_0At_0}{1+4k}. \qquad (3.5)$$

It is evident that if $\lim_{t_0\to 0} g_0t_0=U_0$, then

$$\lim_{t_0\to 0} \bar{v}_1 = \frac{2\alpha\Phi(\eta_1)AU_0}{1+4k}. \qquad (3.6)$$

If it is supposed that the interface has the initial roughness, effectively characterized by the initial width L_0, then the passing shock wave will lead to arising of the rough zone turbulent velocity equal to

$$\bar{v}_1(L_0) = 2\Phi(\eta_1)\alpha AU_0. \qquad (3.7)$$

Therefore, we have the range of values $\bar{v}_1$ from (3.6) up to (3.7). The definite value of velocity $\bar{v}_1(\beta)$ is obtained in dependence on the parameter $\beta=U_0t_0/L_0$, where t_0 is the time of the shock wave passing through the zone having the width L_0:

$$v_1^2(\beta) = \frac{0.065AL_1}{BL_0}[1-(L_0/L_1)^6]. \qquad (3.8)$$

$$\frac{L_1}{L_0} = \begin{cases} 1+10.2\alpha^2\beta A, & \text{if } \beta A \leq 0.24, \\ (0.924+1.23\alpha\sqrt{\beta A})^2, & \text{if } \beta A > 0.24. \end{cases} \qquad (3.9)$$

After passing the shock waves the mixing will develop according to the solution:

$$\bar{v} = (L_1/L)^{2k}\bar{v}_1(\beta), \qquad (3.10)$$

$$L = L_1[1+8\eta_1^2\alpha(1+2k)\bar{v}_1(\beta)(t-t_0)/L_1]^{1/(1+2k)} \qquad (3.11)$$

Note the important peculiarity of the obtained solution: in the case of the Richtmyer-Meshkov mixing, the mixing zone width is sufficiently dependent upon the initial roughness L_0 as opposed to the Rayleigh-Taylor mixing when at $L_0 \to 0$ the solution tends to the self-similarity law [(3.3), $0 \leq t \leq t_0$], in the considered case at $L_0=0$ the solution can be only a zero one.

For the equations of $k\varepsilon$-model the averaged equations and their accurate solutions at δ-shaped acceleration are similarly obtained.

4. Comparison with experiments, performed by Saitzev et al (1985)

In S.G.Saitzev's experiments the dependence of the non-dimensional value $(dL/dt)/U_0$ upon the Atwood number A was determined. It was found that while the shock waves are passing through the interface the linear dependence of the following type takes place:

$$\left[\frac{dL}{dt}\right]/U_0 = 0.02 + 0.068(0.070)|A|,$$

and after the second wave, when the zone of blurring was of the order of 10 mm, the coefficient for the Atwood number was approximately by an order of magnitude greater. The values of the coefficient while the shock wave moving from the heavy substance into the light one are given in brackets.

Compare these results with the theoretical conclusions of the third section, from which it follows:

$$\left[\frac{dL}{dt}\right]/U_0 = 8\eta_1^2 \alpha \bar{v}_1(\beta).$$

Comparison of the obtained theoretical dependence with S.G.Saitzev's results is given in Fig.2. The experimental results fall within limits, shown by the theory. The comparison is carried out after the second shock wave passing, since the film, appearently, exert a sufficient influence after the first shock wave.

References

Neuvazhayev VE (1975) On the Theory of Turbulent Mixing. Reports of the USSR Ac of Sci 222: 1053-1056

Neuvazhayev VE (1988) Blurring of the Turbulent Mixing Zayer Appl Mech & Tech Physics 2: 46-51.

Neuvazhayev VE, Yakovlev VG (1976) Numerical gasdynamic Computation of the interface Turbulent Mixing, Sov. J. Comp. Math. & Math Physics 16, 2: 440-450.

Neuvazhayev VE, Yakovlev VG (1984) Model and Method for Numerical Computation of Turbulent Mixing for the Interface Moving with Acceleration. Coll. Problems of Atom. Sci. & Engineering Ser. Methods & Programs for Numer. Solution of Math. Phys. problems 2, 16: 17-25

Neuvazhayev VE, Yakovlev VG (1986) Computation of Gravitational Turbulent Mixing according to kε-Model. Coll. Problems of Atom Sci & Engineering, Ser. Theoret. & Appl. Physics 1: 28-36

Saitzev SG, Lasareva EV, Chernukha VV, Belyaev VM (1985) Intensification of Mixing at the Interface between Media with Different Densities while Passing through it a Shock Wave. Reports of the USSR Ac of Sci 283: 94-98.

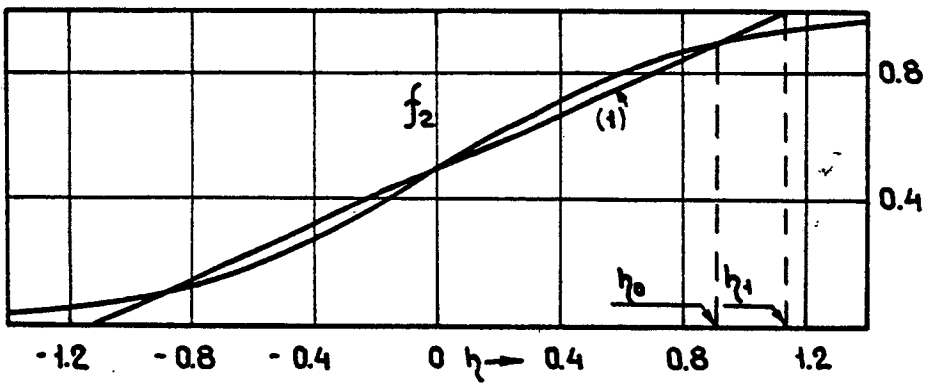

Fig.1 Profile of the volume fraction f_2 from the non-dimensional spacing η: (1)-linear profile, obtained from the conserved mixed mass. $\eta_1=2\sqrt{\pi}$ is the mixing zone, $\eta_0=0,906$ is the half-width, determined via values $f_1=f_2=0.1$.

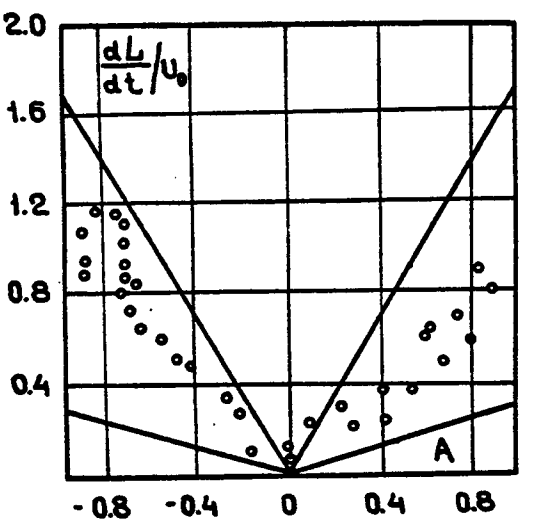

Fig.2 Dependence of turbulent mixing zone expansion velocity on the Atwood number: — theory, ° Saitzev's et al. results (1985).

SHOCK INDUCED MIXING, CONVERGENCE AND HEAT CONDUCTION WITHIN THE FRAMEWORK OF HETEROGENEOUS kε-MODEL

A.V.Polionov.

All-Union Research Institute of Technical Physics
P.O.Box 245, 454070,Chelyabinsk-70, USSR

ABSTRACT

The ways to take into account the effects connected with passing a shock wave through a turbulent mixture, heat exchange in a turbulent mixture and turbulent zone deformation under converging are proposed within the framework of the heterogeneous kε-model (Hkε-model) [1].

1. Turbulent energy increment induced by a shock wave.

Generation terms in the Hkε-model [1] in the k-equation (G_k) and in the ε-equation (G_ϵ) involve the product of an acceleration ($\frac{dv}{dt}$) on a total turbulent mass flow $\overline{\rho u'}$:

$$G_k = \frac{dv}{dt}\cdot(-\overline{\rho u'}) \; ; \tag{1}$$

$$G_\epsilon = \frac{3}{2}\cdot\frac{\epsilon}{k}\cdot\frac{dv}{dt}\cdot(-\overline{\rho u'}) \tag{2}$$

The multiplier $\overline{\rho u'}$ can be written in the form:

$$\overline{\rho u'} = \beta D\frac{c(1-c)(\overset{\circ}{\rho}_1-\overset{\circ}{\rho}_2)^2}{\overset{\circ}{\rho}_1\overset{\circ}{\rho}_2 k}\cdot\nabla p - \frac{\rho^2 D(\overset{\circ}{\rho}_1-\overset{\circ}{\rho}_2)}{\overset{\circ}{\rho}_1\overset{\circ}{\rho}_2}\cdot\nabla c -$$
$$- \frac{D\alpha\rho}{\overset{\circ}{\rho}_1}\left(\nabla\overset{\circ}{\rho}_1 - \left.\frac{\partial\overset{\circ}{\rho}_1}{\partial p}\right|_s\cdot\nabla p\right) - \frac{D(1-\alpha)\rho}{\overset{\circ}{\rho}_2}\left(\nabla\overset{\circ}{\rho}_2 - \left.\frac{\partial\overset{\circ}{\rho}_2}{\partial p}\right|_s\cdot\nabla p\right) . \tag{3}$$

Here ρ; p; v are average values of density, pressure, velocity in the mixture respectively; $\frac{dv}{dt} = \frac{\partial v}{\partial t} + v\frac{\partial v}{\partial x}$; $\overset{\circ}{\rho}_1$, $\overset{\circ}{\rho}_2$ are true values of mixture component densities; c, α are a mass fraction and a volume one of the mixture component "1" ($c\rho=\alpha\overset{\circ}{\rho}_1$, $\rho=\alpha\overset{\circ}{\rho}_1+(1-\alpha)\overset{\circ}{\rho}_2$); k is a turbulent energy related to the mixture mass unit, ε is an intensity of its dissipation; D is a turbulent diffusion coefficient: $D=c_\mu\cdot\frac{k^2}{\epsilon}$; c_μ and β are empirical

coefficients.

The third and the fourth terms of the right side of the equation (3) arise while calculating the correlations $\overline{\overset{\circ}{\rho}_1 u'}$, $\overline{\overset{\circ}{\rho}_2 u'}$ with using the Prandtl's approach. Transfer of density by spikes has been proposed to be adiabatic one. For consideration of $\overline{\overset{\circ}{\rho}_1 u'}$, $\overline{\overset{\circ}{\rho}_2 u'}$ in a shock wave front it is reasonably to assume spikes to be affected by shock loading and to substitute $\left.\frac{\partial \rho}{\partial p}\right|_S$ by $\left.\frac{\partial \rho}{\partial p}\right|_H$ where H means the relationship ρ vs p being realized in the limits of the shock front. Then the contributions of the third and the fourth terms into the generation can be neglected.

The second term in (3) doesn't lead to some singularity in the shock front. Following the equation $\rho\frac{dk}{dt} = G_k$ it is possible to obtain that the turbulent energy increment corresponding to this term depends on the direction of the shock wave propagation: $\Delta[k^{\frac{1}{2}}] \sim (\overset{\circ}{\rho}_1 - \overset{\circ}{\rho}_2)\cdot\Delta v\cdot\nabla c$ (Δv is a velocity change as a result of a shock passing); it is positive while shock passing to the side of increasing density, it is negative while reverse passing and it is zero while passing through the mixture having uniform concentration.

The first term in (3) leads to singularity while decreasing of a shock wave front width hence its contribution is the predominant one. It depends on a shock wave front width and doesn't depend on both a direction of shock wave propagation and a concentration gradient presence.

A shock front while passing through a mixture is spread out to the width equal to an order of magnitude of the characteristic length scale $l = \frac{k^{3/2}}{\epsilon}$. Realization of such spreading during the process of calculation is possible by different ways, for example by introducing a turbulent viscosity as it was proposed in the work [2].

In general a turbulent energy increment under a shock interaction depends on a relation between longitudinal and lateral scales. However taking it into consideration is impossible in the limits of the one component Hke-model. Hence it is necessary to calibrate the model for some average state of the mixture. The calibration demands introduction a new empirical constant which we shall denote as "n" and shall imply that we have realized a shock front spreading over the width "nl" while passing through a mixture having the scale "l". Then the turbulent energy increment corresponding to the first term amounts to: $\Delta[k^{3/2}] \sim \beta\cdot\frac{Д(\Delta v)^2}{n}$, where Д is the shock wave velocity.

The empirical constant β must be calibrated according to the

data of experiment realizing a separation, for example [3] (according to the preliminary estimating [1] $\beta \simeq 0.2 \div 0.3$). The constant "n" must be selected so that it would be possible to describe the experimental change of velocity of the turbulent mixing zone development after passing the shock wave through mixing zone (for example [4]).

2.Taking into account heat conduction in the mixture.

To take into account the effect of heat conduction rather accurately it is necessary to consider the entropy change as a result of heat exchange while performing calculation of correlations by the Prandtl's approach. This concerns such correlations as $\overline{E_1 u'}$, $\overline{E_2 u'}$, $\overline{\rho_1 u'}$, $\overline{\rho_2 u'}$, where E_1, E_2 are specific internal energies of components..However the contributions of the above mentioned correlations are rather small in the most of practical applications. Indeed the shown correlations convey the turbulent transfer of internal energy and density in the limits of each component volume whereas the main turbulent transfer of these characteristics is connected with the component concentration pulsations inducing much more difference in density and internal energy.

This transfer with taking into account the heat conduction has already been presented in the equations of Hke-model [1]. Hence the equations with discarding of the shown correlations are available for the most practical applications.

3.Taking into account the effects induced by convergence.I

While the turbulent zone is converging its deformation arises as a result of extension in the radial direction and compression in the angular one. This leads to decreasing of the turbulent energy portion corresponding to the radial pulsations and intensifying of the angular pulsations. Terms related to the given effects can be obtained by the gasodynamics equations averaging analogous to the one shown in the work [1] but performing for the spherical case. The resultant equation for k will involve the additional terms:

$$\rho \frac{dk}{dt} = \ldots + 4\rho k_r \cdot \frac{v}{r} - 2\rho (k_\theta + k_\varphi) \cdot \frac{v}{r} , \qquad (4)$$

where $k_r = \frac{\overline{\rho [u_r']^2}}{2\bar{\rho}}$; $k_\theta = \frac{\overline{\rho [u_\theta']^2}}{2\bar{\rho}}$; $k_\varphi = \frac{\overline{\rho [u_\varphi']^2}}{2\bar{\rho}}$; u_r', u_θ', u_φ' are the pulsation velocity components. Presence of these terms can be founded after some rather simple transformations in the work [5].

IDr. V.Anisimov took part in obtaining results of this section.

By introducing the parameter characterizing an anisotropy of the turbulent energy, i.e.: $N = \frac{k_r}{k_\theta} = \frac{k_r}{k_\varphi}$, we obtain the following expression for the additional terms:

$$\rho\frac{dk}{dt} = \ldots + \frac{4v}{r}\cdot\rho k\cdot\frac{N-1}{N+2} \ . \qquad (5)$$

In the case of the isotropic turbulence $N=1$ and the additional term is absent.

It is possible to take into account the deformation of the turbulent zone at the small changing of its radius by assuming some value of anisotropy N. However a model with two component is necessary under considerable changing of the radius. Indeed in the case of the sufficient fast deformation $\frac{dk_r}{dt} \sim 4k_r\cdot\frac{v}{r}$; $\frac{dk_\theta}{dt} \sim -2k_\theta\cdot\frac{v}{r}$; whence $k_r \sim r^4$; $k_\theta \sim r^{-2}$; and $N \sim r^6$; that is anisotropy changing is extremely sharp. The similar effects arise at deformation of turbulence in a narrowing canal. It has been described in a few work, for example [6]. The results of this work has been used in the paper [7] for calibrating of the model.

The above mentioned deformation must be taken into account in the ϵ-equation as well. Two equations for ϵ are necessary here for accurate account. They correspond to longitudinal and lateral scales. Approximated account can be realized within the framework of the single-component Hkϵ-model by introducing the effective anisotropy N , as it is proposed above for "k", and by making the plausible assumptions concerning to a length scale behavior. Under rather high intensity of lateral pulsations the characteristic scale will apparently repeat the changes of the lateral scale as the smallest one. Then in the equation for a scale (see [1]) the following terms must be added:

$$\frac{dl}{dt} = \ldots + \frac{2l}{r}\cdot v \ , \qquad (6)$$

that leads to the additional term in the equation for ϵ:

$$\rho\frac{d\epsilon}{dt} = \ldots - 2\rho\epsilon\cdot\frac{v}{r} \ . \qquad (7)$$

In conclusion we write down the resultant equation for ϵ (in comparison with the equation 4-6 [1] some misprints have been corrected):

$$\rho\frac{d\epsilon}{dt} - \frac{\partial}{\partial x}\rho D\frac{\partial \epsilon}{\partial x} + [1.5-c_2]\cdot\frac{\epsilon^2}{k} = \frac{3\epsilon}{2k}\cdot\frac{dv}{dt}\cdot(-\overline{\rho u'}) -$$

$$- c_1\cdot\frac{\epsilon^2\rho}{k^{3/2}}\cdot\sum_i|\alpha_i u_i'| + \frac{3N}{2+N}\cdot\epsilon\cdot\frac{d\rho}{dt} + \rho\epsilon\cdot\frac{v}{r}\cdot\frac{4N-10}{2+N} \quad . \tag{8}$$

here c_1 and c_2 are empirical constants,

$$\sum_i|\alpha_i u_i'| = 2\left|\frac{I\rho}{\overset{o}{\rho}_1\overset{o}{\rho}_2} - \frac{\alpha(1-\alpha)}{\overset{o}{\rho}_1}\cdot\overline{\overset{o}{\rho}_1 u'} - \frac{\alpha(1-\alpha)}{\overset{o}{\rho}_2}\cdot\overline{\overset{o}{\rho}_2 u'}\right| \simeq \frac{2\rho}{\overset{o}{\rho}_1\overset{o}{\rho}_2}\cdot|I|, \tag{9}$$

where I is the Lagrangian mass flow of the first component being determined in [1] by the equation 1-12:

$$I = \rho D\cdot[\ \beta\cdot\frac{\overset{o}{\rho}_1-\overset{o}{\rho}_2}{\rho^2}\cdot\frac{c(1-c)}{k}\cdot\nabla p - \nabla c\ ] \tag{10}$$

with empirical constant β.

REFERENCES

1. A.Polionov. "Heterogeneous kε-Model of Gravitational Mixing." Proceedings of the Plesonton Workshop on R-M and R-T Instabilities. (1989). Editor - V.Rupert.
2. C.E.Leith. "Development of a Two-Equation Turbulent Mix Model". Lawrence Livermore National Laboratory. Rept. UCRL 96036 (1986).
3. David L.Youngs. "Modeling Turbulent Mixing by Rayleigh-Taylor Instability." Physica D, 37, (1989), 270-287, North-Holland, Amsterdam.
4. S.G.Zaitsev, E.V.Lazareva, V.V.Chernukha, V.M.Belyaev. "Intensification of Mixing at the Interface between Two Media with Different Densities while Passing the Shock Wave through It." Reports of the SU Ac. of Sci., 1985, v.283, №1, pp.94-98.
5. V.V.Nikiforov. Turbulent Mixing on the Contact Boundary of Media with Different Densities. Russian J. VANT (Problems of Atomic Science and Technics). Ser. Theoretical and Applied Physics. Issue 1, 1985, pp.3-8.
6. M.S.Uberoi Effect of Wind-Tunnel Contraction on Free-Streem Turbulence. J. Aeronautical Sci. 1956. Vol.23, №8, p.754.
7. V.A.Andronov, V.V.Nikiforov. Calculations of Turbulence Evolution at Axisymmetric Deformation. Russian J. VANT (Problems of Atomic Science and Technics). Ser.Theoretical and Applied Physics. Issue 1, 1990, p.34.

CALCULATION A LENGTH SCALE AND FOURIER COEFFICIENTS AT NUMERICAL SIMULATIONS

A.V.Polionov

All-Union Research Institute of Technical Physics
P.O.Box 245, 454070, Chelyabinsk, USSR.

ABSTRACT

Formulas are presented for finding a turbulent energy, length scales and Fourier coefficients at performing numerical calculations on direct modeling of gravitational turbulence.

Formulas we write below suppose performing 2D-simulations. Their generalization on 3D-simulations won't cause any trouble.

Let's choose coordinate system so that axis "x" coincide with average flow direction; x-component of velocity are denoted by "u", y-component - by "v". The system dimension along y is taken as Δ ($y = 0 \div \Delta$).

Let's define averaging of some value $f(x,y,t)$ as following:

$$\overline{f(x,t)} = \frac{1}{\Delta} \int_0^{\Delta} f(x,y,t)\,dy \ . \qquad (1)$$

Let's define two components of a turbulent energy:

$$k_x = \frac{\overline{\rho(u-\bar{u})^2}}{2\bar{\rho}} \ , \qquad (2)$$

$$k_y = \frac{\overline{\rho(v-\bar{v})^2}}{2\bar{\rho}} \ , \qquad (3)$$

total turbulent energy: $k = k_x + k_y$, (4)

anisotropy degree: $N = \frac{k_x}{k_y}$. (5)

It should be noticed there are other definitions of turbulent energy such as:

$$\overline{\rho u^2} - \frac{\overline{(\rho u)}^2}{\bar{\rho}} = \overline{\rho u'^2} + \frac{\overline{(\rho' u')}^2}{\bar{\rho}} \ , \qquad (6)$$

and

$$\overline{\rho u^2}-\overline{\rho u}^2 = \overline{\rho u'^2} + 2\bar{u}\cdot\overline{\rho' u'}. \qquad (7)$$

Here $u'=u-\bar{u}$; $\rho'=\rho-\bar{\rho}$ .The square of the second order correlations of pulse values are usually small enough so the first above mentioned turbulent energy definition (6) nearly correspond with the one defined in this paper (they differ in the factor $2\bar{\rho}$ as well). But the second mentioned definition (7) contains the member that is big enough ($2\bar{u}\overline{\rho' u'}= 2\bar{u}\overline{\rho u'}$), which depends on average velocity thus it is changing at adding to velocity a constant component.

It should be noticed that the integrated along x turbulent energy defined in this paper and multiplied by $\bar{\rho}$ must remain a constant after being induced by a shock (without viscosity). The mentioned second definition is lacking this quality.

Let's define some correlations which are necessary for length scale calculations:

$$R_{xu}(x,\xi,t) = \frac{\overline{\rho^{\frac{1}{2}}(x-\frac{\xi}{2},y,t)u'(x-\frac{\xi}{2},y,t)\rho^{\frac{1}{2}}(x+\frac{\xi}{2},y,t)u'(x+\frac{\xi}{2},y,t)}}{\overline{\rho(x,y,t)[u'(x,y,t)]^2}}, \qquad (8)$$

$$R_{xv}(x,\xi,t) = \frac{\overline{\rho^{\frac{1}{2}}(x-\frac{\xi}{2},y,t)v'(x-\frac{\xi}{2},y,t)\rho^{\frac{1}{2}}(x+\frac{\xi}{2},y,t)v'(x+\frac{\xi}{2},y,t)}}{\overline{\rho(x,y,t)[v'(x,y,t)]^2}}, \qquad (9)$$

$$R_{yu}(x,\xi,t) = \frac{\overline{\rho^{\frac{1}{2}}(x,y-\frac{\xi}{2},t)u'(x,y-\frac{\xi}{2},t)\rho^{\frac{1}{2}}(x,y+\frac{\xi}{2},t)u'(x,y+\frac{\xi}{2},t)}}{\overline{\rho(x,y,t)[u'(x,y,t)]^2}}, \qquad (10)$$

$$R_{yv}(x,\xi,t) = \frac{\overline{\rho^{\frac{1}{2}}(x,y-\frac{\xi}{2},t)v'(x,y-\frac{\xi}{2},t)\rho^{\frac{1}{2}}(x,y+\frac{\xi}{2},t)v'(x,y+\frac{\xi}{2},t)}}{\overline{\rho(x,y,t)[v'(x,y,t)]^2}}, \qquad (11)$$

$$R_{x\rho}(x,\xi,t) = \frac{\overline{\rho'(x-\frac{\xi}{2},y,t)\rho'(x+\frac{\xi}{2},y,t)}}{\overline{[\rho'(x,y,t)]^2}}, \qquad (12)$$

$$R_{y\rho}(x,\xi,t) = \frac{\overline{\rho'(x,y+\frac{\xi}{2},t)\rho'(x,y+\frac{\xi}{2},t)}}{\overline{[\rho'(x,y,t)]^2}}. \qquad (13)$$

While averaging some difficulties arise since some values of x and y happen to be beyond the system. In this case it is necessary to apply the conditions of periodicity and symmetry.

The length scale is defined usually by the relation:

$$l(x,t) = \int_0^\infty R(x.\xi,t)d\xi \ . \qquad (14)$$

However taking into consideration finite dimensions of the system it is appropriate to determine a length scale in such a way as $l(x,t)=\xi_{\frac{1}{2}}(x,t)$, where $\xi_{\frac{1}{2}}(x,t)$ is the value of ξ that $R(x.\xi,t)$ is equal to $\frac{1}{2}$ at.

Thus we can determine six length scales: l_{xu}, l_{xv}, l_{yu}, l_{yv}, $l_{x\rho}$, $l_{u\rho}$.

It is easy to obtain that R_{yu} and R_{yv} correlations are Fourier's images of the functions k_x and k_y. This result can be obtained if we repeat the reasoning presented in the §1.12 of the book [2]. We must only change t by ξ and $R_E(t)$ by $R_{yv}(\xi)$ or $R_{yv}(\xi)$. As a result we obtain the following relations:

$$R_{yu}(x.\xi,t) = \frac{1}{k_x(x,t)}\cdot\int_0^\infty k_{xn}(x,t)\cdot\cos 2\pi n\xi\cdot dn \ ; \qquad (15)$$

$$k_{xn} = 4k_x(x,t)\cdot\int_0^\infty R_{yu}(x,\xi,t)\cdot\cos 2\pi n\xi\cdot d\xi \ ; \qquad (16)$$

$$k_x(x,t) = \int_0^\infty k_{xn}(x,t)\cdot dn \ ; \qquad (17)$$

and analogous relations for k_y. Here "n" is not a frequency as it is in Hinze's book but it is the reciprocal value of the wave length: $n=\frac{1}{\lambda}$.

It is interesting to get as well a portion of the energy in the long wave spectrum part which produces the main turbulent transfer of mass, internal energy and so on:

$$\frac{k_{x,large}}{k_x} = \frac{1}{k_x}\cdot\int_0^{2/l_{yu}} k_{xn}dn = \frac{2}{\pi}\cdot\int_0^\infty R_{yu}(\xi)\sin 2\pi\frac{\xi}{l_{yu}}\frac{d\xi}{\xi} \ ; \qquad (18)$$

$$\frac{k_{y,large}}{k_y} = \frac{1}{k_y}\cdot\int_0^{2/l_{yv}} k_{yn}\,dn = \frac{2}{\pi}\cdot\int_1^{\infty} R_{yv}(\xi)\sin 2\pi\frac{\xi}{l_{yv}}\,\frac{d\xi}{\xi} \qquad (19)$$

REFERENCES

1. J.O.Hinze. Turbulence. An introduction to its mechanism and theory. McGRAW-HILL COMPANY. INC. New-York Toronto London. 1959.

Oscillations de grande amplitude en mécanique des fluides

Denis SERRE
Ecole Normale Supérieure de Lyon
Unité Mixte de Recherche
ENS Lyon - CNRS n° C 1028
46 allée d'Italie
69364 LYON Cedex 07

Royaumont, France *Edited by D. Besnard, J.-F. Hass, P.-A. Holstein & B. Sitt*

Compressible Visqueux 1-d

Equations de Navier-Stokes

représentation Eulérienne

$$\partial_t \rho + \partial_y (\rho u) = 0$$

$$\partial_t (\rho u) + \partial_y (\rho u^2 + q(\rho)) = \alpha \partial_y^2 u$$

représentation Lagrangienne

$$\partial_t v = \partial_x u$$

$$\partial_t u + \partial_x (p(v)) = \alpha \partial_x (v^{-1} \partial_x u)$$

Donnée initiale

$$v^{\varepsilon}(x,0) = V_0(x, \frac{x}{\varepsilon}) + O(\varepsilon)$$

$$v^{\varepsilon}(x,0) = U_0(x, \frac{x}{\varepsilon}) + O(\varepsilon)$$

Grande amplitude

$$\partial_y V_0 \not\equiv 0$$

Question :

Quel est le comportement de $v^{\varepsilon}(x,t)$ et $u^{\varepsilon}(x,t)$ lorsque $\varepsilon \to 0$?

Compressible visqueux 1-d

Ansatz pour $t >> \varepsilon^2$
$v^{\varepsilon}(x,t) = V(x,t,\frac{x}{\varepsilon}) + O(\varepsilon)$ $u^{\varepsilon}(x,t) = U(x,t) + O(\varepsilon)$

Valeurs initiales
$V(x,0,y) = V_0(x,y)$ $U(x,0) = moy_y\, U_0(x,.) = :$ $\frac{1}{2\pi}\int_0^{2\pi} U_0(x,y)\, dy$

Système d'Evolution
$\partial_t U = \partial_x \Sigma, \quad \Sigma = \frac{\alpha \partial_x U - moy\,(Vp(V))}{moy\,(V)}, \qquad \forall x,t$ $\alpha \partial_t V = V(\Sigma + p(V)), \qquad \forall x,t,y$

Exemple : Solutions homogènes en x.

$U \equiv cste$, $V = V(y)$

$$\alpha\, \partial_t V = V\left(p(V) - \frac{moy\,(V\, p(V))}{moy\,(V)}\right)$$

1- Solutions stationnaires (équilibre)

$p(V) \equiv cste$

2- Solutions stationnaires stables

$p(V) \equiv cste$, et

$V \equiv cste$ *ou bien* $p = p_{Maxwell}$

Nota : Ce résultat ne nécessite pas de terme de capillarité.

Compressible Non Visqueux
1 - d

D. Serre, Ann. IHP (Analyse non linéaire), vol. 8, n° 3-4, 1991, p 351-417.

Equations d'Euler

Formulation Eulérienne

$\partial_t \rho + \partial_y (\rho u) = 0$

$\partial_t (\rho u) + \partial_y (\rho u^2 + p(\rho,e)) = 0$

$\partial_t (\frac{1}{2}\rho u^2 + \rho e) + \partial_y ((\frac{1}{2}\rho u^2 + \rho e + p)\, u) = 0$

Formulation Lagrangienne

$\partial_t v = \partial_x u$

$\partial_t u + \partial_x p(v,e) = 0$

$\partial_t (\frac{1}{2} u^2 + e) + \partial_x (p\, u) = 0$

Cadre abstrait

$\partial_t U + \partial_x f(U) = 0$

$U = (u_1, \ldots, u_m)^t$

Hyperbolicité :

$Sp\ Df = \lambda_1 (U) < \ldots < \lambda_m (U)$

$Ker\ (Df (U) - \lambda_j (U)) = \mathbb{R} r_j(U)$

Champs

Non-linéaire (cf Lax)

$r_j . \nabla \lambda_j \neq 0$

exemple : ondes de pression

$\lambda_E = u \pm c_E$, $\lambda_L = \pm c_L$

Linéairement dégénéré

$r_j . \nabla \lambda_j \equiv 0$

exemple : ondes de vorticité

$\lambda_E = u$, $\lambda_L = 0$

Compressible , Non Visqueux, 1-d

Ansatz

$$U^{\varepsilon}(x,t) = \hat{U}\left(x, t, \frac{\varphi(x,t)}{\varepsilon}\right) + O(\varepsilon)$$

donnée :

$$U^{\varepsilon}(x,0) = U_0\left(x, \frac{x}{\varepsilon}\right) + O(\varepsilon)$$

Critique : Comme dans les modèles k - ε, on suppose que le spectre d'énergie se concentre aux grandes échelles et à celle d'une longueur donnée ε. Cette longueur n'est pas un paramètre des équations, elle vient des conditions initiales.

Changement de variables :

$$U \rightarrow (v_1, v_2, \ldots, v_{m-1}, w) = \phi(U)$$

avec $r_j . \nabla v_n \equiv 0$, où (λ_j, r_j) est le champ linéairement dégénéré.
exemple : $\lambda_E = u$ ou $\lambda_L = 0$, $v_1 = u$, $v_2 = p$.
Nota : λ_j n'est fonction que de v

Termes en ε^{-1}

$$\partial_t \varphi + \lambda_j(v)\, \partial_x \varphi = 0$$

$$v^{\varepsilon}(x,t) = V(x,t) + O(\varepsilon)$$

$$w^{\varepsilon}(x,t) = w\left(x, t, \frac{\varphi}{\varepsilon}\right) + O(\varepsilon)$$

Nota : Les oscillations ne portent que sur w^{ε}.

Compressible, Non Visqueux, 1-d

$$\partial_t U + \partial_x f(U) = 0 \quad \xrightarrow{\phi} \quad \begin{aligned} &\partial_t v + B(v,w)\partial_x v = 0 \\ &\partial_t w + \lambda_j(v)\,\partial_x w + c(v,w)\partial_x v = 0 \end{aligned}$$

Equations Moyennes

$$\partial_t V + \mathfrak{B}(V,W)\,\partial_x V = 0$$
$$\mathfrak{B} = \lambda_j(V) + (\text{moy}\,(B(V,W) - \lambda_j(V))^{-1})^{-1}$$

$$(\partial_t + \lambda_j(V)\,\partial_x)\,\text{moy}\,(h(W)) + \text{moy}\,(h'c)\,\partial_x V +$$
$$+ D\lambda_j(V).\{\text{moy}\,(h(W)) - \text{moy}\,(h(B - \lambda_j)^{-1}(\mathfrak{B} - \lambda_j))\}\partial_x V = 0, \quad \forall h \in C^1$$

Nota : * $\forall (v,w)$, $B(v,w) - \lambda_j(v)$ est inversible.

* Les valeurs propres de $\mathfrak{B}(v,W)$ sont des vitesses de groupe.

Exemple : Euler, formulation Lagrangienne

$v_1 = u$, $v_2 = p$, $w = s$ (entropie)

$$\begin{aligned} &\partial_t u + \partial_x p = 0 \\ &\partial_t p + (c_L)^2\,\partial_x u = 0 \\ &\partial_t S = 0 \end{aligned}$$

Oscillations →

$$\begin{aligned} &u = u(x,t)\,,\ p = p(x,t) \\ &S = S(x,t,\tfrac{x}{\varepsilon}) \\ &\partial_t u + \partial_x p = 0 \\ &\partial_t p + (K_L)^2\,\partial_x u = 0 \\ &\partial_t S = 0 \end{aligned}$$

Exemple : $K_L = (\text{moy}\,((c_L)^{-2}))^{-1/2}$

$K_E = (\text{moy}\,(\rho)\,\text{moy}\,(\rho^{-1}(c_E)^{-2}))^{-1/2}$

NUMERICAL CALIBRATION OF RAYLEIGH-TAYLOR INDUCED TURBULENT FLOWS WITH A k-ε MIX MODEL.

Patrick B. SPITZ and Jean-François HAAS
Centre d'Etudes de Limeil-Valenton
94195 Villeneuve St Georges Cedex FRANCE

ABSTRACT

A k-ε mix model for turbulence induced by Rayleigh-Taylor (RT) or Richtmyer-Meskov (RM) instabilities is described. An analysis of model constants is performed leading to an algebraic relation between the RT production term constants within the Boussinesq limit. With a new initialization procedure extended from Mikaelian's model, calibrations on the Foulness rocket-rig experiments (FRRE) and comparisons with shock tube flows are carried out.

I- INTRODUCTION

Instability-induced turbulent mixing of two materials of different densities has been the subject of a great deal of effort in the scientific community, starting quite a few years ago by the pioneering work of Andronov *et al.* /1/, more recently by Houas *et al.* /2/ in Marseilles, and by Benjamin at LANL /3/, and by Brouillette and Sturtevant at Caltech /4/.

The salient feature of this later work is the two interpretations given to the data obtained from Schlieren photographs. Using the same gas conditions but different geometry (cross section of the shock tube and length between separating membrane and end plate), Brouillette and Sturtevant distinguish the turbulent mixing on the interface from that associated with a wall jet. The latter grows at a rate similar to that reported by Andronov while the former is about five times narrower. However, for both experiments the contact surface between the two gases is materialized by a thin plastic membrane in the shock-tube experiments. The membrane rupture, its history and influence on the turbulent flow are not quite well known and introduce uncertainties on experimental data. In this context of interest, we turn to the FRRE /2/ in which no membrane separates the almost incompressible fluids undergoing a near constant acceleration. This situation looks like being more favorable for model constant calibration purposes.

In Section II, we present the two equation mix model while, in Section III, we analyze the associated model constants and propose a new calibration of RT production term constants based on FRRE thus considered as key experiments. We report in Section IV our initialization procedure which is an extension of Mikaelian's model. In Section V, calibrations and comparisons with shock tube flows are carried out.

II- TWO EQUATION MIX MODEL

II-1 General hypotheses

The two following basic thermodynamical assumptions are being considered as the minimum required for treating the mix of two fluids of different densities. We assume that the two fluids are miscible (which is essentially a matter of observation scale) and the existence of an equilibrium temperature everywhere in the turbulent mixing zone (TMZ). The mixing model is then simply defined by :

$$\rho = \rho_1 + \rho_2 \tag{1}$$

$$p(\rho_1, \rho_2, T) = p_1(\rho_1, T) + p_2(\rho_2, T) \tag{2}$$

$$e(\rho_1, \rho_2, T) = c\, e_1(\rho_1, T) + (1-c)\, e_2(\rho_2, T) \tag{3}$$

where ρ, p, T and e are respectively, the total density, pressure, temperature and internal energy of the TMZ. The indices refer to the partial corresponding quantities of fluids 1 and 2. The concentration of one species (fluid 1) is defined by $c = \rho_1/\rho$.

In this paper, we focus on statistically 1D turbulent flows and we assume that the turbulence field is isotropic and homogeneous in the plane normal to the shock propagation direction. Therefore, the mixing flow can be described by only the mean quantities ρ, c, U, e and p depending only on time t and space coordinate x.

II-2 Reynolds equations

By means of the classic Favre's average, it is straightforward to derive evolution equations for the mean quantities : ρ, c, U and e from Navier-Stokes equations.The complete set of Reynolds equations reads :

continuity
$$\frac{d}{dt}\rho + \rho\frac{\partial}{\partial x}U = 0 \qquad (4)$$

concentration
$$\rho\frac{\partial}{\partial t}c - \frac{1}{\sigma_c}\frac{\partial}{\partial x}\left(\rho D\frac{\partial}{\partial x}c\right) = 0 \qquad (5)$$

momentum
$$\rho\frac{d}{dt}U + \frac{\partial}{\partial x}p + \frac{\partial}{\partial x}\sigma_{11} = 0 \qquad (6)$$

energy
$$\rho\frac{d}{dt}e - \frac{1}{\sigma_h}\frac{\partial}{\partial x}\left(\rho D\frac{\partial}{\partial x}H\right) + p\frac{\partial}{\partial x}U + S - \rho\varepsilon = 0 \qquad (7)$$

where $\frac{d}{dt} = \frac{\partial}{\partial t} + U\frac{\partial}{\partial x}$ is the Lagrangian derivative and $< >$ is the Favre's ensemble average ($<\rho u'^2> = \sigma_{11}$), k and ε will be defined further. In addition, we set :

$D = C_\mu\frac{k^2}{\varepsilon}$: turbulent diffusion coefficient,

$P = \sigma_{11}\frac{\partial}{\partial x}U$: kinetic turbulence production term,

$\sigma_{11} = -\frac{4}{3}\rho D\frac{\partial}{\partial x}U + \frac{2}{3}\rho k$: Reynolds' stress,

$S = -\frac{1}{\sigma_\rho}D\frac{1}{\rho}\frac{\partial}{\partial x}\rho\frac{\partial}{\partial x}p$: R-T turbulence production term,

$H = e + \frac{p}{\rho}$: enthalpy.

II-2 Turbulence mix model

The evolution equation for k can be derived quite easily from the previous equations provided some modelization. Its dissipation rate evolution equation is currently a delicate point. The evolution equation for ε is usually built by comparison to the k-equation. Following the traditional derivation method, we assume that source terms in the ε-equation are equal to those of the k-equation up to a dimensional factor of the form : $C_{\varepsilon i}$. ε/k with i = 0, 1, 2, 3. The equations read /6/ :

- specific turbulent kinetic energy equation

$$\rho\frac{d}{dt}k - \frac{1}{\sigma_k}\frac{\partial}{\partial x}\left(\rho D\frac{\partial}{\partial x}k\right) - S + P + \rho\varepsilon = 0 \qquad (8)$$

- dissipation rate equation

$$\rho \frac{d}{dt}\varepsilon - \frac{1}{\sigma_\varepsilon}\frac{\partial}{\partial x}\left(\rho \; D \; \frac{\partial}{\partial x}\varepsilon \right) - C_{\varepsilon 0}\frac{\varepsilon}{k} S + C_{\varepsilon 1}\frac{\varepsilon}{k} P + C_{\varepsilon 2}\rho \frac{\varepsilon^2}{k} + C_{\varepsilon 3}\rho \varepsilon \frac{\partial}{\partial x} U = 0 \quad (9)$$

Ten model constants are necessary to close this model; their values will be discussed in the next section.

III MODEL CONSTANTS

III-1 Classical model constants

As any other, the k-ε model contains unknown constants due to closure assumptions occuring in the course of its formulation. These constants are to be considered as universal i.e. valid for a certain class of turbulent flows having the same thermodynamical properties and, in addition, are expected to take care of physical effects not included in the model. The classic methodology, currently used to estimate these constants, is to simplify the model for simple turbulent flows and make comparisons with well-established experimental data.

As a matter of fact, some key experiments are very useful in this context. Model constants are evaluated using experimental data which are mostly in the domain of incompressible single material shear flows /6/. For instance, let's mention : homogeneous isotropic turbulence, self induced diffusion of turbulence, nearly homogeneous turbulent shear flow, boundary layer flow, etc... Due mainly to the lack of compressible key experiments (except rapid isotropic compression of homogeneous turbulence), model constants calibrated on incompressible flows are currently used for compressible computations but, as far as we know, without any clear justification.

For all runs reported in this paper, the following conventional choices are made for the classical part of the model constant set :

$C_{\varepsilon 1}$	$C_{\varepsilon 2}$	$C_{\varepsilon 3}$	σ_k	σ_ε	σ_h	C_μ
1.47	1.9	0.35	0.87	1.3	0.9	0.09

III-3 RT production term constants

Two model constants, namely $C_{\varepsilon 0}$ and σ_ρ , are to be estimated now. First, we made an attempt /6/ to estimate the model constants involved in the production terms dealing with RT induced turbulence. They can be obtained by numerical optimization from the measurement of instability and subsequent mix in shock tube flows. Because of all the uncertainties associated with these experiments, we choose to treat the FRRE as key experiments. In this context, the fluids are almost incompressible, and then a simple relation links the mean concentration and density. We can define the density and mass concentration as a function of the volume fraction v :

$$\rho = v\,\rho_1^* + (1 - v)\,\rho_2^* \text{ and } c = \frac{v\,\rho_1^*}{\rho}$$

where both densities ρ_1^* and ρ_2^* are constant for an incompressible flow. Therefore, we get :

$$c = \frac{\rho_1^*}{\rho_2^* - \rho_1^*}\left(-1 + \frac{\rho_2^*}{\rho} \right).$$

This relation has two main consequences. First, if we decompose the mean velocity U into an interface velocity component $V = \Gamma t$ and a diffusion velocity N, this later writes : $N = - \frac{D}{\sigma_c \rho} \frac{\partial}{\partial y} \rho$, by combining equations (4) and (5). Second, by taking into account the following flux definitions :

$$< \rho c' u' > = - \frac{1}{\sigma_c} \rho D \frac{\partial}{\partial y} c \text{ and } < \rho' u' > = - \frac{1}{\sigma_\rho} D \frac{\partial}{\partial y} \rho ,$$

an immediate consequence is the identity of the concentration and mass flux definitions that leads to : $\sigma_c = \sigma_\rho$.

By considering the self similar behavior of mixing in these experiments, we search self similar solutions of the k-ε model within the Boussinesq limit. That approximation /7/ regards the fluid density variation as negligibly small except in terms where it is multiplied by the acceleration. As a result, that hypothesis implies :

$A \rightarrow 0$; $N = 0$; $P = 0$ and ρ = constant, where the Atwood number A is defined as :

$A = \frac{\rho 2 - \rho 1}{\rho 2 + \rho 1}$. Then, the k-ε mix model reduces to :

$$\frac{d}{dt} k - \frac{1}{\sigma_k} \frac{\partial}{\partial x} \left(\rho D \frac{\partial}{\partial x} k \right) - \frac{S}{\rho} + \varepsilon = 0 \qquad (10)$$

$$\frac{d}{dt} \varepsilon - \frac{1}{\sigma_\varepsilon} \frac{\partial}{\partial x} \left(\rho D \frac{\partial}{\partial x} \varepsilon \right) - C_{\varepsilon 0} \frac{\varepsilon}{k} \frac{S}{\rho} + C_{\varepsilon 2} \rho \frac{\varepsilon^2}{k} = 0 \qquad (11)$$

The momentum equation reduces to : $\frac{1}{\rho} \frac{\partial}{\partial x} p = - \Gamma$ which leads to : $S = - \frac{1}{\sigma_\rho} D \Gamma \frac{\partial}{\partial x} \rho$

Assuming a self similar regime, we set for the similarity variable and functions :

$$\eta = \frac{x}{h_1(t)} ; h_1(t) = Y A \Gamma t^2 ; k(x,t) = \Gamma^2 t^2 K(\eta) \text{ and } \varepsilon(x,t) = \Gamma^2 t \, E(\eta) \qquad (12)$$

where $h_1(t)$ is the Youngs' similarity law for RT induced mixing. At this point, we have to make an extra assumption on the RT source term which requires a particular handling. For small Atwood numbers, we assume a linear density profile of the form : $\rho(x,t) = \rho_m \phi(\eta)$ with $\phi(\eta) = (1 + A \eta)$. Performing a series expansion on the RT source term versus A, we finally obtain, retaining only the first term : $\frac{S}{\rho} = - \frac{C_\mu \Gamma^2 K^2}{\sigma_\rho Y E}$. Inserting relations (12) in equations (10) and (11), we end up with self similar equations for K and E :

$$K - \eta \frac{d}{d\eta} K - \frac{C_\mu}{2 \sigma_k \alpha^2 A^2} \frac{d}{d\eta} \left[\frac{K^2}{E} \frac{d}{d\eta} K \right] - \frac{C_\mu}{2 \sigma_\rho \alpha} \frac{K^2}{E} + \frac{E}{2} = 0 \qquad (13)$$

$$E - 2 \eta \frac{d}{d\eta} E - \frac{C_\mu}{2 \sigma_\varepsilon \alpha^2 A^2} \frac{d}{d\eta} \left[\frac{K^2}{E} \frac{d}{d\eta} E \right] - \frac{C_{\varepsilon 0} C_\mu}{\sigma_\rho \alpha} K + C_{\varepsilon 2} \frac{E^2}{K} = 0 \qquad (14)$$

We adopt the simplest resolution method. By noticing that Eqs. (13-14) admit parabolic solutions of the form :

$$K(\eta) = K_0 (1 - \eta^2) \text{ and } E(\eta) = E_0 (1 - \eta^2)$$

where (K_0, E_0) are two constants depending on all the equation parameters, we obtain two consistency relations. The first one writes : $\sigma_k = \sigma_\varepsilon$, in view of model constant calibration, we choose to write the second one as :

$$\sigma_\rho = \frac{C_\mu}{Y\,(4\,C_{\varepsilon 2} - 3)} \frac{(C_{\varepsilon 2} - C_{\varepsilon 0})^2}{4\,C_{\varepsilon 0} - 3}. \tag{15}$$

This later relation will be used as a constraint on σ_ρ along the calibration of $C_{\varepsilon 0}$ against the FRRE. Note that the turbulence time scale is given by : $\frac{k}{\varepsilon} = \frac{C_{\varepsilon 2} - C_{\varepsilon 0}}{4C_{\varepsilon 0} - 3}\,t$.

III-4 Impulsive acceleration case

The above approach can be applied to the case of an impulsive acceleration of the interface which is the RM instability generation of turbulence. We assume that turbulent energy is deposited by some mechanism and study its subsequent spread in space and time according to a reduced set of the k-ε model equations:

$$\frac{d}{dt} k - \frac{1}{\sigma_k} \frac{\partial}{\partial x} \left(\rho\, D \frac{\partial}{\partial x} k \right) + \varepsilon = 0 \tag{16}$$

$$\frac{d}{dt} \varepsilon - \frac{1}{\sigma_\varepsilon} \frac{\partial}{\partial x} \left(\rho\, D \frac{\partial}{\partial x} \varepsilon \right) + C_{\varepsilon 2}\, \rho \frac{\varepsilon^2}{k} = 0 \tag{17}$$

Again, we assume a self similar solution of the form :

$$\eta = \frac{x}{h_1(t)}\,;\; h_1(t) = C_L\, t^\gamma\,;\; k(x,t) = C_k\, t^\alpha K(\eta) \text{ and } \varepsilon(x,t) = C_\varepsilon\, t^\beta\, E(\eta),$$

where C_L, C_k and C_ε are similarity parameters. We substitute into the differential equations and remove the time dependence by coming up with two relations : $\alpha = 2\gamma - 2$ and $\beta = 2\gamma - 3$. Then, the self similar equations write :

$$\alpha K - \gamma \eta \frac{d}{d\eta} K - \left(\frac{C_\mu C_k^2}{\sigma_k C_L^2 C_\varepsilon} \right) \frac{d}{d\eta} \left[\frac{K^2}{E} \frac{d}{d\eta} K \right] + \frac{C_\varepsilon E}{C_k} = 0 \tag{18}$$

$$\beta E - \gamma \eta \frac{d}{d\eta} E - \left(\frac{C_\mu C_k^2}{\sigma_\varepsilon C_L^2 C_\varepsilon} \right) \frac{d}{d\eta} \left[\frac{K^2}{E} \frac{d}{d\eta} E \right] + \frac{C_{\varepsilon 2} C_\varepsilon}{C_k} \frac{E^2}{K} = 0 \tag{19}$$

This differential system has, at least, simple analytic solutions of the form :

$$K(\eta) = K_0 (1 - \eta^2) \text{ and } E(\eta) = E_0 (1 - \eta^2),$$

where (K_0, E_0) are again two constants depending on all the equation parameters. However, consistency requires two compatibility relations to be checked out :

$$\sigma_k = \sigma_\varepsilon \text{ and } \gamma = \frac{2\,C_{\varepsilon 2} - 3}{3\,C_{\varepsilon 2} - 3}.$$

For $C_{\varepsilon 2} = 1.9$, we have : $\gamma = 0.296$; $\alpha = -1.407$ and $\beta = -2.40$. This suggests that for current model constants, the growth following a shock should obey a law close to the fourth root of time. In addition, the time scale of turbulence is then given by : $\frac{k}{\varepsilon} = (C_{\varepsilon 2} - 1)\,t$.

IV MODEL INITIALIZATION PROCEDURE

IV-1 Statistical model initialization

When considering unsteady problems, we do know that closure models do not calculate the initial stages of an hydrodynamics instability development. As a result, when starting a turbulence numerical simulation, a fully turbulent initial state has to be initialized, currently with phenomenological rules on the grounds of the available experimental data. It is clear this situation comes from the splitting of each physical variable into a mean and a fluctuating component. In other words, statistical models of turbulence are unable to describe transition mechanisms to turbulence in one way or the other. In addition, the assumption of a fully turbulent state is definitely necessary for closing all turbulent fluxes by a Fickian gradient-law. On the other hand, we already mentioned /6/ that the final calculated state is slightly sensitive to the initialization state.

IV-2 RT induced flow initialization.

The mixing thickness at the very beginning of the mixing process is estimated from the experiments carried out at Foulness. The self similar behavior of the turbulent mixing is modelized by the following relation :

$$h_1(t) = Y\,A\,\Gamma\,t^2, \qquad (20\text{-a})$$

where h_1 is the penetration of the light fluid into the denser one, $Y = 0.060 \pm 0.006$ is an empirical constant given as practically independent of the Atwood number and evaluated by the experiments, Γ is the acceleration undergone by the separation interface. The penetration of the heavy fluid into the light one is also described by :

$$h_2(t) = \beta\ h_1(t). \qquad (20\text{-b})$$

On the basis of available data /5/, we model the ratio of spike and bubble penetrations by :

$$\beta(A) = \frac{1 - 0.886\,A}{1 - A} \qquad (21)$$

The ratio $\Omega\beta$ of the turbulent kinetic energy contained in the initial TMZ with respect to the directed energy has been estimated by Mikaelian /8/. We extend his simpler model by accounting for the asymmetry of the TMZ and by considering a different density profile which is no longer linear and somewhat more realistic. This extension requires the following conditions :

- $\rho(x1) = \rho 1$ and $\rho(x2) = \rho 2$,

- mass conservation both with or without mix,
- $\frac{d}{dx}\rho = 0$ for $x_1 = h_1(t)$ and $\frac{d}{dx}\rho = 0$ for $x_2 = -\beta\, h_1(t)$.

We therefore take the following ansatz : $\psi(\eta) = a\eta^4 + b\eta^3 + c\eta^2 + d\eta + f$, with $\psi(\eta) = \frac{\rho(x)}{\rho m}$, $\eta = \frac{x}{h_1(t)}$ et $\rho m = \frac{1}{2}(\rho 1 + \rho 2)$. Then, we get :

$$a = \frac{30\,A\,(1-\beta)}{(1+\beta)^5}\ ;\ b = 16\,A\left[\frac{-4+7\beta-4\beta^2}{(\beta+1)^5}\right]$$

$$c = 36\,A\,(1-\beta)\frac{(1-3\beta+\beta^2)}{(1+\beta)^5}\ ;\ d = \frac{24\,A\,\beta\,(3-4\beta+3\beta^2)}{(1+\beta)^5}$$

$$f = \frac{1}{(1+\beta)^5}\left[(1-A)(1+5\beta)+2\beta^2(1-13A)+\beta^4(1+A)(5+\beta)\right].$$

We display, on Fig. 1, the modeled density profile behaviors for Atwood numbers ranging from 0.1 to 0.8 . The dependence of β on A is calculated from relation (21).

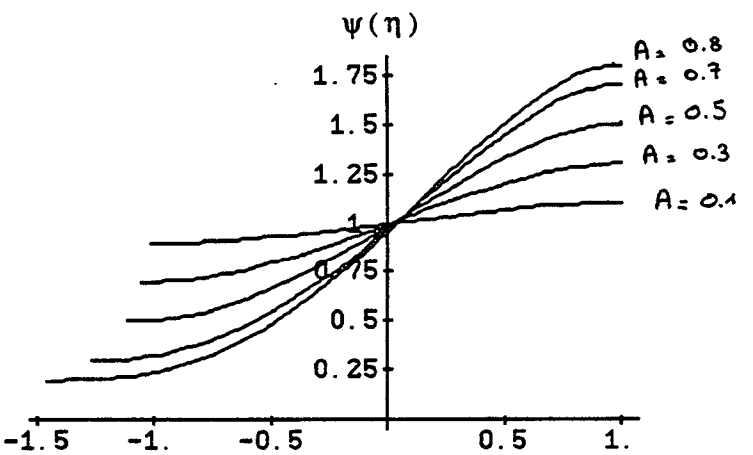

Figure 1

The ratio $\Omega\beta$ is then calculated straightforwardly for the RT and RM cases, we get :

$$\Omega\beta = \frac{2\,\Gamma\,A\,h_1(t)}{5\,U^2}\left[\frac{-\beta^2+3\beta-1}{(1+\beta)+A(1-\beta)}\right]. \qquad (22)$$

In order to eliminate non physical evolution induced by an undesirable minimum located between 1 and $-\beta$, we impose a constraint on β which writes :

$$z^* > 1 \text{ and } z^* > -\beta \text{ ---> } 1 < \beta < \frac{3}{2} \text{ i.e. } 0 < A < 0.814\ ;$$

where $z^* = \frac{3 - 4\beta + 3\beta^2}{5(\beta - 1)}$ is the abscissa of the undesirable minimum. Setting $U = \Gamma t$ and $h_1(t) = Y A \Gamma t^2$, we get for the RT case ratio :

$$\Omega\beta = \frac{2 Y A^2}{5}\left[\frac{-\beta^2 + 3\beta - 1}{(1 + \beta) + A(1 - \beta)}\right].$$

For a symmetric TMZ i.e. $A < 0.5$ roughly , we can set $\beta = 1$ and relation (22) reduces to : $\Omega_1 = \frac{Y A^2}{5}$ which corresponds to the following density profile :

$$\psi(\eta) = -\frac{A\eta^3}{2} + \frac{3A\eta}{2} + 1.$$

For practical applications, the initial shape of $k(x, t = 0)$ is a triangle of height k_{ini} given by Eq. (22) and initial thicknesses given by relations (20-a) and (20-b) . The initial value of the dissipation rate of k is computed from $0.164 \frac{k_{ini}^{3/2}}{(1 + \beta) h_1}$ and also implemented as a triangle (the coefficient value 0.18 comes from a boundary layer flow calibration). Doing so, we do not account for the asymmetry of the k and ε initial profiles. Self similar solutions show that the maximum of k and ε are no longer located on the interface position but rather in the light fluid depending on the Atwood number.

V NUMERICAL SIMULATION RESULTS

V-1 Numerical implementation

The mean flow equations are solved together with Eqs. (8-9) which make up the turbulence mix model. They are imbedded within a 1D Lagrangian compressible hydrodynamics code. As a result, mixing takes place with constant mass per cell as the mesh is moved along with the mean velocity U. The diffusion terms in the k and ε equations are handled in a coupled manner while RT source terms are discretized in an explicit way.

For compressible applications as shock-tube flow simulations, the Richtmyer-Von Neumann artificial viscosity is being used for the shock wave treatment. The numerical treatment of strong discontinuities requires a numerical dissipation in order to smear out shock waves and to smooth gradients, which makes them artificially less efficient in producing turbulent kinetic energy. As a matter of fact, enhancement of turbulent mixing due to shock waves cannot be treated by the simple current numerical schemes.

V-2 Rayleigh-Taylor calibration experiments

The definitions of two simple test problems for a dynamic mix model in a 1D Lagrangian code have been proposed by D.L. Youngs /6/. We use one of them for model constant calibration purposes. The first test problem suggested (TP 2, see numerical round table) considers a two zone geometry characterized by : $L_1 = 10$ cm , $\rho_1 = 1$ g/cm^3 and $L_2 = 10$ cm, $\rho_2 = 3$ g/cm^3. The calculation is carried out in plane geometry and the equation of state for both fluids is : $P = \frac{2}{3}\rho e$. For $t = 0$, the internal energy is set so that the acceleration is uniform i.e. $-\frac{1}{\rho}\frac{\partial}{\partial x}p = 5\ 10^4$ cm/s^2. The initial pressure field is defined by : $p = 400$ kPa at $x = 0$; $p = 350$ kPa at $x = 10$ cm and $p = 200$ kPa at $x = 20$ cm. To maintain a

near constant acceleration, the boundary conditions are therefore : p = 400 kPa at left hand boundary and p = 200 kPa at right hand boundary.

This test problem corresponds approximately to some of the Foulness rocket-rig experiments in which the fluids are being considered almost incompressible. We confirm this hypothesis on Fig. 2 by displaying the density distribution across the TMZ at t = 0.06 ms. Refining the suggested mesh size, we use a computational grid made of 200 zones together with geometric progressions (light fluid 0.973 ; heavy fluid 1.028). This computational grid allows to get the undisturbed region to move with an acceleration close to the prescribed value of Γ (see Fig. 3). As previously stated, we optimize the numerical penetration of the light fluid into the denser one by using $C_{\varepsilon 0}$ as a free calibration parameter with respect to relation (15). The numerical thickness is determined following the prescribed definition of the volume fraction v = 0.05 and by computing the accelerated displacement of the interface with $R_i(t) = 10 + \frac{\Gamma}{2} t^2$.

The turbulence model is turned on at t_B = 5 ms with $h_1(t_B)$ = 0.0418 cm and $h_2(t_B)$ = 0.0375 cm and K_{ini} = 0.0031 . We plot, on Fig. 4, a comparison of theYoungs' similarity law $h_1(t) = Y A \Gamma t^2$ and the computed mixing length. The values which fit best the experimental behavior are σ_ρ = 1.48 and $C_{\varepsilon 0}$ = 0.815 . As a result, we can determine the numerical ratio of bubble and spike penetration β for that simulation. Its time evolution, displayed on Fig. 5, shows an asymptotic value of roughly 1.35 which is different from that obtained by the fitting of experimental data (β = 1.114). We show, on Figs. 6 and 7, the profiles of the specific turbulence kinetic energy k and its dissipation rate ε for different times (t = 10 ; 20 ; 30 ; 40 and 50 ms) in a frame moving with a constant acceleration Γ.

In the FRRE, turbulent mixing is mainly produced by the RT source term by means of a pressure gradient as opposed to shear flows in which turbulence is driven by velocity gradients. We illustrate that statement on Fig.8 which displays, at t = 0.058 ms, the contributions of each turbulence production term. In a different way, the contribution of the pressure effects with respect to the shear effects is usually evaluated by the flux Richardson number R_{if}. We display on Fig. 9, the evolution of R_{if} across the TMZ at the final time of the numerical simulation. We get values of the flux Richardson number quite different from those classically associated with turbulent boyancy flows. The RT source term is clearly predominent.

V-3 Shock tube flow comparisons

We consider here low Mach number shock tube experiments /1, 4/ (close to TP3). An air-helium contact surface is accelerated and decelerated by a shock wave of initial Mach number 1.3 in air. The initial numerical conditions are for each experiment :

Experiment	h_1 (cm)	h_2 (cm)	Kini	t_B (μs)
Andronov air/helium	0.049	0.067	0.0113	25
B. and S. air/helium	0.016	0.022	0.0163	13

The k-ε mix model is operated with the following set of model constants :

$C_{\varepsilon 1}$	$C_{\varepsilon 2}$	$C_{\varepsilon 3}$	σ_k	σ_ε	σ_h	σ_c	C_μ
1.47	1.9	0.35	0.87	1.3	0.9	0.7	0.09

First, we choose to make a comparison of the experimental data and the numerical results obtained while using the previously optimized couple of values : $C_{\varepsilon 0} = 0.815$ and $\sigma_\rho = 1.476$. Second, we look for the best numerical fit using $C_{\varepsilon 0}$ as a free calibration parameter together with relation (15) which determines the σ_ρ value. We display the numerical results for both experiments on Figs. 10-13 . Unfortunately, the calibration carried out on the FRRE does not lead to any numerical optimization of the shock tube experiments. Summing up the numerical optimization of the experimental data, we get the following constant values :

Experiment	$C_{\varepsilon 0}$	σ_ρ
Andronov air/helium	1.0	0.26
B. and S. air/helium	0.78	3.41

VI CONCLUSION

This exercise shows the difficulties associated with the determination of the so-called universal constants in turbulence mix models. In this paper, we have performed an analysis of two crucial problems related with the use of such models : model constants and the initialization procedure for unsteady applications. The chief idea underlying that work was to regard the FRRE as key experiments both for deriving an initialization procedure suitable for asymmetric initial TMZ and for calibrating the model constants involved in the RT turbulence production term.

The analysis carried out within the Boussinesq limit yields an algebraic relation betwen these constants. Of course, this latter is intrinsically limited to small Atwood numbers and certainly badly adapted for Atwood numbers greater than 0.5 . However, it seems, when deriving such models, that model constants do not have to depend upon the Atwood number. As a matter of fact, our wish was to obtain a calibration of $C_{\varepsilon 0}$ and σ_ρ on the FRRE, still valid for shock tube flow experiments; it does not fulfill. In addition, our calibration do not even allow us to discriminate between the two sets of shock tube experiments.

REFERENCES

/1/ V.A. Andronov, S.M. Bakhrakh, E.E. Meshkov, V.N. Mokhov,V.V. Nikiforov, A.V. Pevnitskii and A.I. Tolshmyakhov, Sov. Phys. JETP 44, 424, (1976).

/2/ L. Houas, J. Fortes and R. Brun, in Proceedings of the 17th International Symposium on Shock Waves and Shock Tubes, Bethlehem, PA, 1989, edited by Y.W. Kim, Lehigh University, AIP, (1990).

/3/ R.F. Benjamin; in Proceedings of the International Workshop on the Physics of Compressible Mixing, Princeton, NJ,1988; Lecture Notes in Engineering, (Springer Verlag, Berlin, 1991).

/4/ M. Brouillette and B. Sturtevant, Physica D 37, 248, (1989).

/5/ V.S. Smeeton and D.L. Youngs, AWE report N° 35/87.

/6/ M. Bonnet, S. Gauthier and P.B. Spitz; in Proceedings of the International Workshop on the Physics of Compressible Mixing, Princeton, NJ,1988; Lecture Notes in Engineering (Springer Verlag, Berlin, 1991).

/7/ G.I. Barenblatt,"Self similar turbulence propagation from an instantaneous plane source", in Nonlinear dynamics and turbulence, Eds. D.D. Joseph, Pitman, Marshfield, (1983).

/8/ K.O. Mikaelian, Physica D 36, 343, (1989).

/9/ D.L. Youngs, Physica D 37, 270, (1989).

FIGURE CAPTIONS

Figure 2 : density profile in the TMZ at t = 0.058 s.

Figure 3 : evolution of the interface acceleration in the numerical simulation of the undisturbed case.

Figure 4 : numerical calibration of the penetration of the light fluid into the denser fluid.

Figure 5 : computed ratio of spike and bubble penetrations from the numerical simulation of Foulness rocket rig experiments.

Figure 6: k-profiles in the TMZ for different times within the accelerated frame.

Figure 7 : ε-profiles in the TMZ for different times within the accelerated frame.

Figure 8 : profiles of kinetic production term P and Rayleigh-Taylor source term S at t = 0.058 s .

Figure 9 : flux Richardson (R_{if}) number profile in the TMZturbulent at t = 0.058 s.

Figure 10 : x-t diagram for the Andronov *et al* shock tube experiment.

Figure 11 : calibrations of mixing zone thickness in the Andronov *et al* shock tube experiment.

Figure 12 : x-t diagram for the Brouillette and Sturtevant shock tube experiment.

Figure 13 : calibrations of mixing zone thickness in the Brouillette and Sturtevant shock tube experiment.

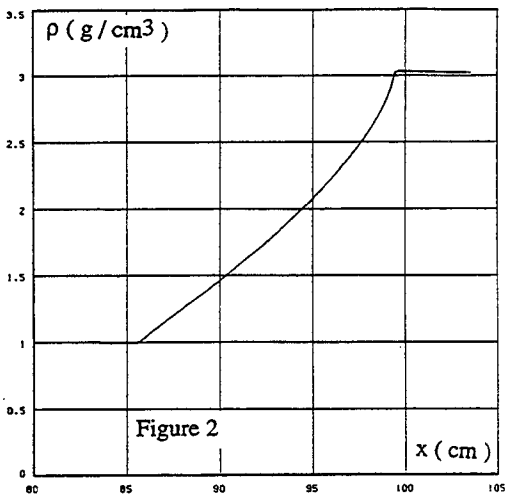

Figure 2

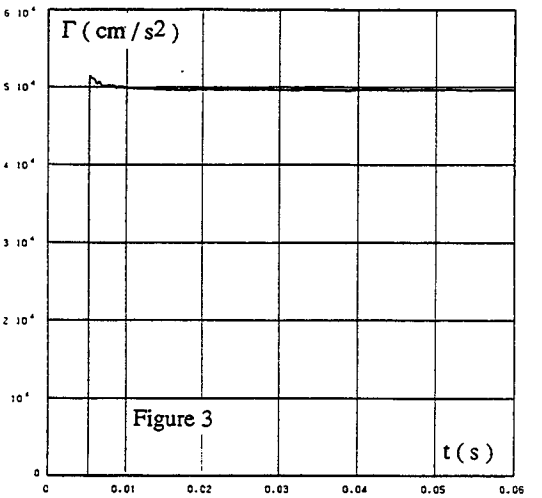

Figure 3

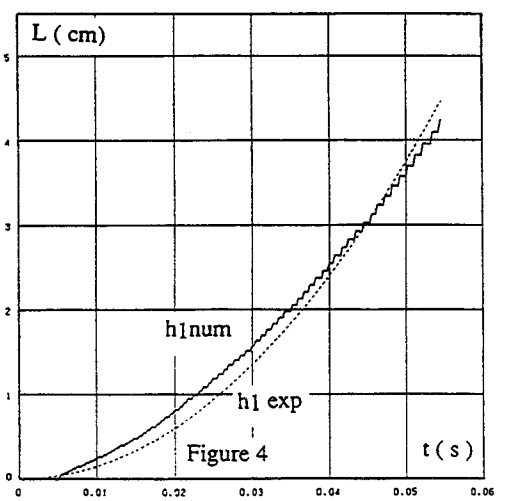

Figure 4

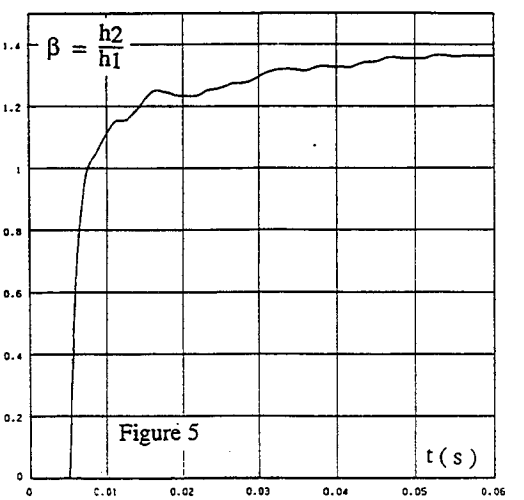

Figure 5

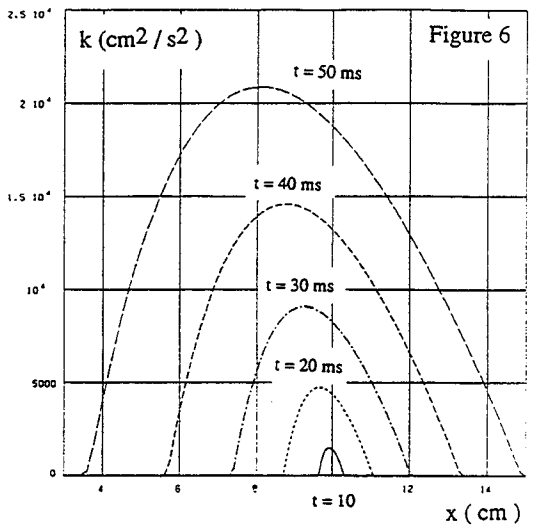
k (cm2 / s2)
Figure 6
t = 50 ms
t = 40 ms
t = 30 ms
t = 20 ms
t = 10
x (cm)

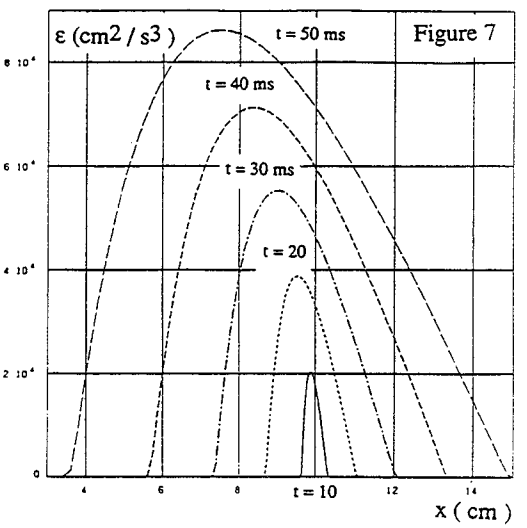
ε (cm2 / s3)
t = 50 ms
Figure 7
t = 40 ms
t = 30 ms
t = 20
t = 10
x (cm)

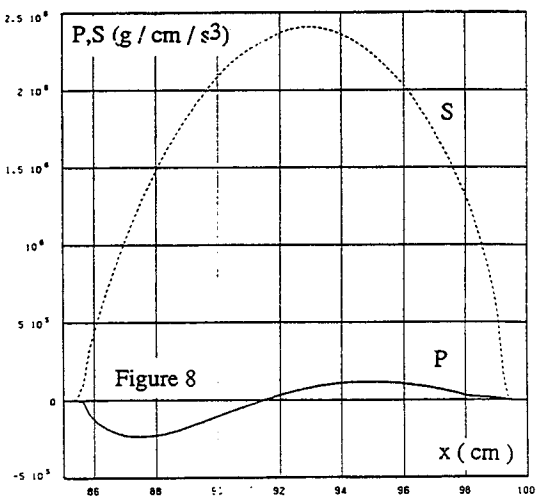
P,S (g / cm / s3)
S
P
Figure 8
x (cm)

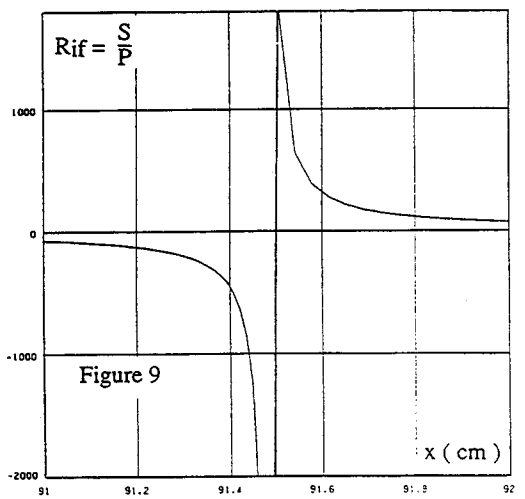
Rif = S/P
Figure 9
x (cm)

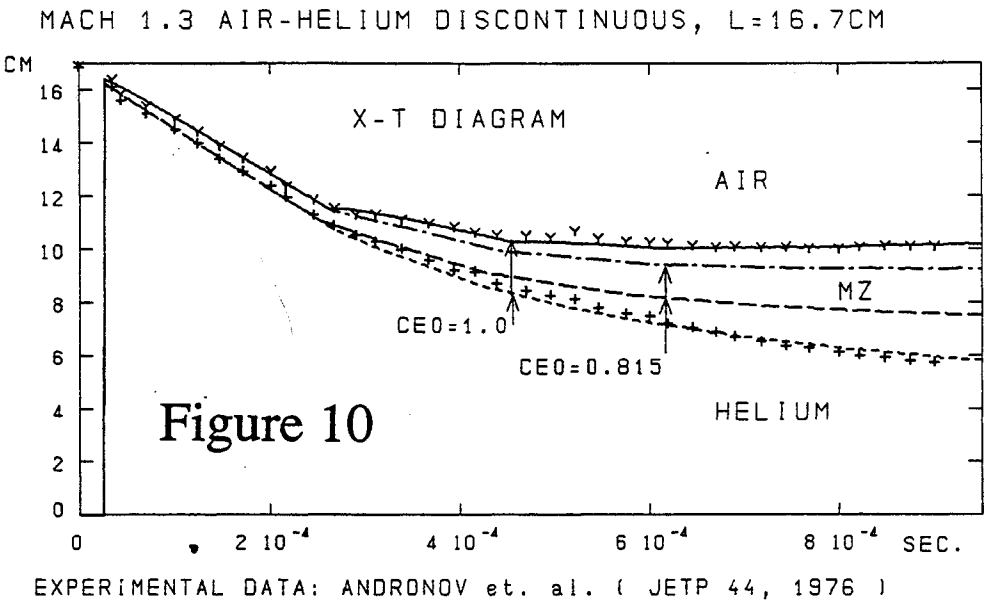

Figure 10

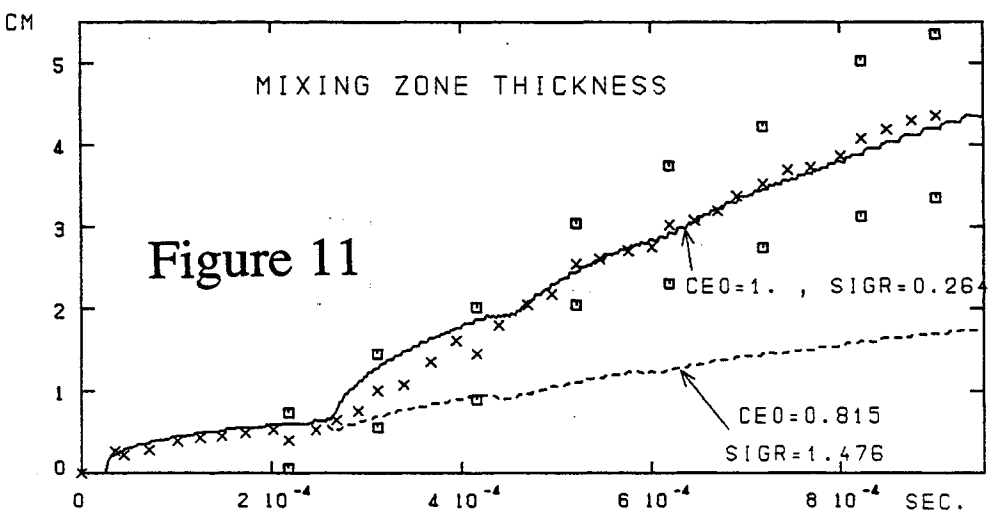

Figure 11

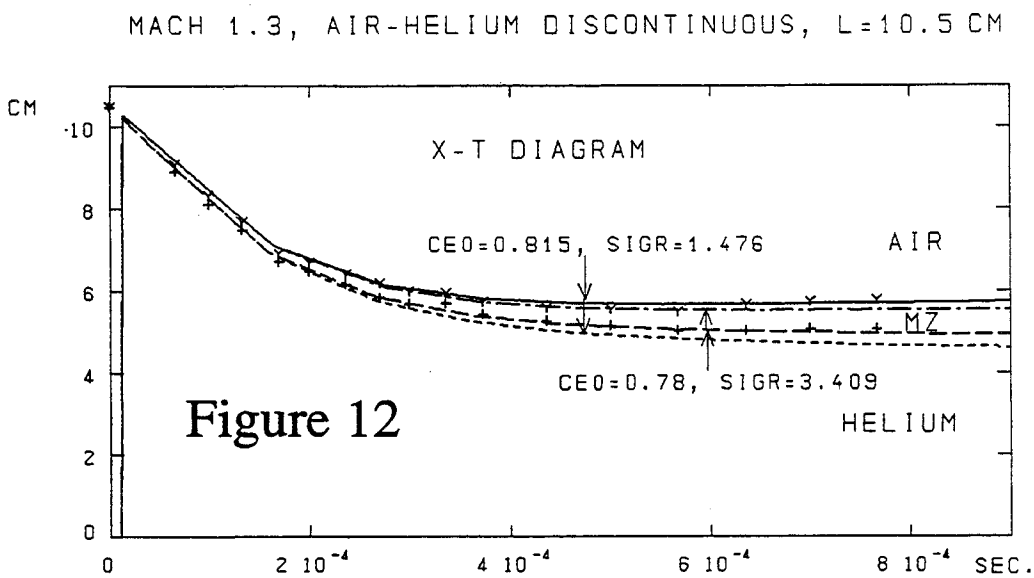

Figure 12

EXPERIMENTAL DATA, BROUILLETTE AND STURTEVANT, PHYSICA 370, (1989)

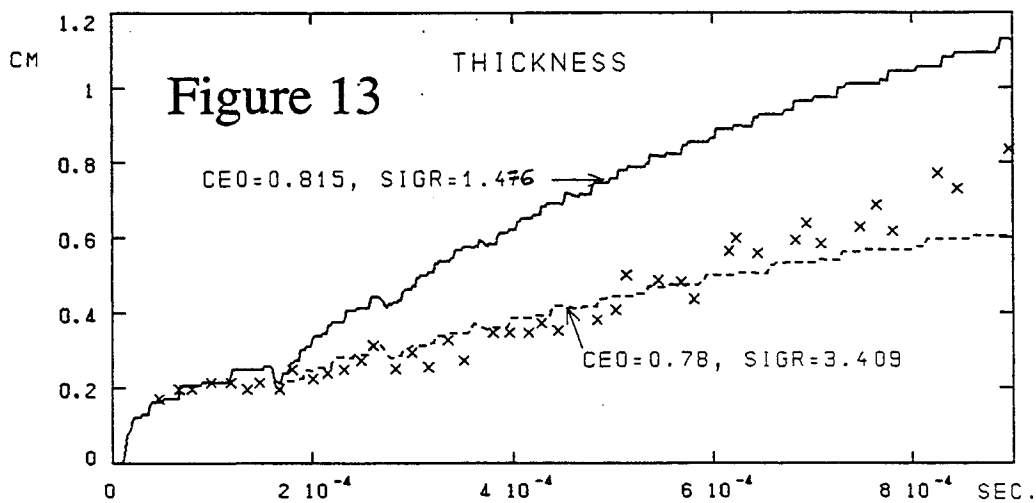

Figure 13

LINES: K-EPSILON MODEL CALCULATIONS (FFRE CONSTANTS AND BEST FIT)

THE THREE DIMENSIONAL NON-LINEAR EVOLUTION OF THE RAYLEIGH-TAYLOR INSTABILITY IN INERTIAL CONFINEMENT FUSION TARGETS

R P J Town and A R Bell
Imperial College of Science, Technology and Medicine, London SW7 2BZ, UK.

ABSTRACT

A spherical three dimensional hydrocode called PLATO has been developed to model the Rayleigh-Taylor instability during the implosion of an Inertial Confinement Fusion target. The code and its geometry are described. Results are presented of the deceleration phase showing greater non-linear growth of the Rayleigh-Taylor instability than is found in two dimensional cylindrical simulations. The three dimensional enhancement of the non-linear growth is much smaller than that found by Sakagami and Nishihara[1].

INTRODUCTION

The Rayleigh-Taylor (RT)[2] instability has been the subject of renewed interest recently because of its potentially deleterious effect on the fusion conditions in an Inertial Confinement Fusion (I.C.F.) target. An I.C.F. target is unstable twice during an implosion: on the outer ablation surface in the acceleration phase and on the inner fuel-shell interface during the deceleration phase.

In the acceleration phase 2D simulations[3,4,5] have shown a reduction in the RT linear growth rate to one half the classical value. This has been confirmed by experimental results[6]. Recent 3D results[7] in planar geometry have shown similar linear growth rates to 2D, but enhanced growth in the non-linear regime. In the deceleration phase the RT instability is expected to behave classically. Simulations have been performed by Sakagami and Nishihara in cylindrical geometry in 2D[8] and recently using a cartesian code in 3D[1]. Sakagami and Nishihara have found no difference in the 3D linear behaviour compared to 2D. They find that the non-linear regime obeys an $\eta g t^2$ law, with an η up to six times the value of comparable 2D cylindrical simulations.

We have written a three dimensional hydrocode in spherical geometry called PLATO to model the deceleration phase. In order to reduce the computational requirements the sphere has been divided up according to the symmetry imposed on the target by the 12 beam Vulcan laser system at the Rutherford-Appleton Laboratory.

THE GEOMETRY OF PLATO

In the 12 beam target chamber of the Vulcan laser system each beam directed at the target forms the centres of the faces of dodecahedra. The point of intersection of the centre of each laser beam with the target surface defines the symmetry of the target. The points form the vertices of 20 equilateral triangles on the surface as shown in figure 1. Consider the triangle defined by the coordinates $\vec{r}_0$, $\vec{r}_1$ and $\vec{r}_2$ which has sides of angle ψ and 'height' χ. The relationship between ψ and χ is:

$$2\chi + \psi = \pi \tag{1}$$

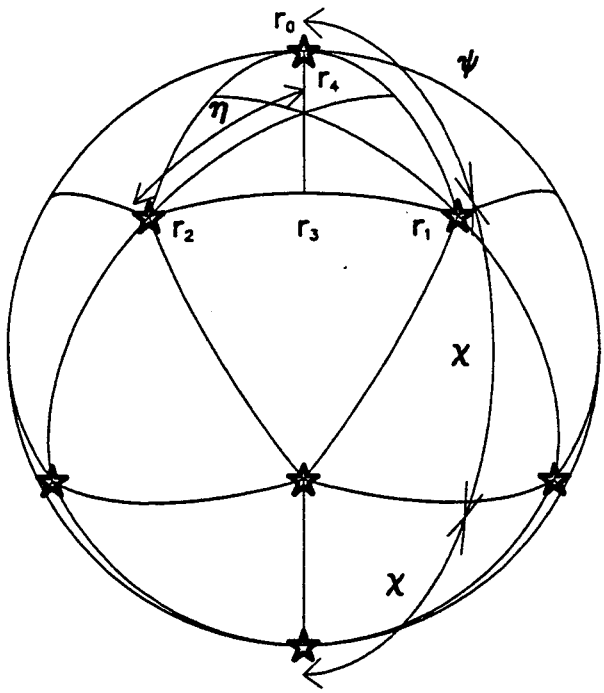

Figure 1: A sphere of unit radius showing the equilateral triangles formed by the centres of the laser beams and the smallest triangles formed by bisecting the equilateral triangles.

The cartesian coordinates of the vertices of the triangle are:

$$\vec{r}_0 = (0, 0, 1) \tag{2}$$

$$\vec{r}_1 = (\cos(\pi/5)\sin(\psi), \sin(\pi/5)\sin(\psi), cos(\psi)) \tag{3}$$

$$\vec{r}_2 = (\cos(\pi/5)\sin(\psi), -\sin(\pi/5)\sin(\psi), cos(\psi)) \tag{4}$$

Now the midpoint ($\vec{r}_3$) of $\vec{r}_1$ and $\vec{r}_2$ lies on the great circle defined by $\vec{r}_1$ and $\vec{r}_2$ and takes the value:

$$\vec{r}_3 = \frac{\sin(\psi/2)}{\sin(\psi)}(\vec{r}_1 + \vec{r}_2) \tag{5}$$

The z component of $\vec{r}_3$ can be obtained from equation (5) and is obviously equal to $\cos(\chi)$:

$$\cos(\chi) = 2\sin(\psi/2)\cot(\psi) \tag{6}$$

Hence by eliminating χ from (6) using equation (1) we obtain the numerical values $\psi = 63.43°$ and $\chi = 58.28°$.

We can now further subdivide the triangle by bisecting the angles between $(\vec{r}_0, \vec{r}_2)$, $(\vec{r}_1, \vec{r}_2)$ and $(\vec{r}_1, \vec{r}_0)$. The computational grid is then defined as the volume contained within $\vec{r}_4$, $\vec{r}_2$ and $\vec{r}_3$. We need to determine the position of $\vec{r}_4$ and the equation of the line connecting $\vec{r}_4$ to $\vec{r}_2$.

We know that $\vec{r}_4.\vec{r}_0 = \cos(\eta)$ (7), where η is the angle between $\vec{r}_0$ and $\vec{r}_4$. Since the triangle defined by $\vec{r}_0$, $\vec{r}_1$ and $\vec{r}_2$ is equilateral it follows that

$\vec{r}_4.\vec{r}_1 = \cos(\eta)$(8) and $\vec{r}_4.\vec{r}_2 = \cos(\eta)$(9). Let $\vec{r}_4 = (A, B, C)$, then by substituting (2) into (7) we get that $C = \cos(\eta)$. Substituting for $\vec{r}_1$ (from (3)) into (8) gives:

$$A\sin(\psi)\cos(\pi/5) + B\sin(\psi)\sin(\pi/5) + \cos(\eta)\cos(\psi) = cos(\eta) \quad (10)$$

and $\vec{r}_2$ (from (4)) into (9) gives:

$$A\sin(\psi)\cos(\pi/5) - B\sin(\psi)\sin(\pi/5) + \cos(\eta)\cos(\psi) = cos(\eta) \quad (11)$$

by subtracting (10) and (11) we see that $B = 0$. The requirement that $\vec{r}_4$ lies on the surface of the sphere gives us that $A = \sin(\eta)$. Hence $\vec{r}_4 = (\sin(\eta), 0, \cos(\eta))$ (12). The value of η is obtained by substituting $A = \sin(\eta)$ into (10):

$$\tan(\eta) = \frac{1 - \cos(\eta)}{\sin(\psi)\sin(\pi/5)} = 37.38° \quad (13)$$

We have found the limits of the computational box. Since the computational volume has a triangular cross-section we find that small triangles run along the line $(\vec{r}_4, \vec{r}_1)$. To maximise the C.F.L. condition[9] on the timestep the largest possible triangles must be employed on the grid. This occurs when the vertices of the triangles fall along the line connecting $\vec{r}_1$ to $\vec{r}_4$.

The cartesian coordinates of the limits of the computational volume are defined as:

$$\vec{r}_4 = (1, 0, 0) \quad (14)$$

$$\vec{r}_1 = (\cos(\psi/2), \sin(\psi/2), 0) \quad (15)$$

$$\vec{r}_3 = (\cos(\chi - \eta), 0, \sin(\chi - \eta)) \quad (16)$$

Consider the vector $\vec{r} = (\cos(\phi)\cos(\theta), \sin(\phi)cos(\theta), \sin(\theta)$ (17) which lies on the line connecting $\vec{r}_1$ to $\vec{r}_4$ which occurs when $\vec{r}.(\vec{r}_1 \times \vec{r}_4) = 0$ (18). Substituting for $\vec{r}$ from (17), $\vec{r}_4$ from (14) and $\vec{r}_1$ from (15) gives:

$$\tan(\theta) = \frac{\sin(\psi/2 - \phi)\tan(\chi - \eta)}{\sin(\psi/2)} \quad (19)$$

Hence we know the coordinates of the grid cells within the computational volume. We can therefore calculate the areas of the grid cell's faces and its volume. These are then used in the hydro-equations which are written in the form of Gentry[10], but with the higher order Van Leer[11] advection phase as interpreted by Youngs[12]. Currently thermal conduction, laser energy deposition and α particle heating are not included.

RESULTS

In a typical I.C.F. implosion a shock wave is launched into the stationary fuel. The deceleration phase starts when the reflected shock wave collides with the incoming shell. To a good approximation we found that the radius of the inner surface ($R1$) obeys $R1 = R1_{mc} + 0.5g(t - t_{mc})^2$ where $R1_{mc}$ is the inner surface radius at the time t_{mc} of maximum compression (20). When the central hot spot region satisfies the conditions for fusion, it ignites and a burn

wave propagates outwards. The deceleration phase ends at this time with the remainder of the shell rapidly expanding. In the absence of α particle heating the shell continues to obey equation (20).

We started the simulations with a one dimensional (1D) $60\mu m$ thick unperturbed shell of density $5.0g/cm^3$ at an initial radius of $130\mu m$ coasting at a velocity of $1.5 \times 10^7 cm/s$ into a stationary fuel of density $0.5g/cm^3$. The region outside the shell had a density of $0.5g/cm^3$ and the same initial inward velocity. A uniform pressure of $2.0 \times 10^{13} dyne/cm^2$ was used in all regions. When the reflected shock wave was almost incident on the inner surface of the shell, at 0.626 nsecs, the simulation was converted to 3D. The radial cells were uniform with a resolution of $0.5\mu m$. There were 10 grid points in each of the θ and ϕ direction giving 20 cells per wavelength. The 1D density profile was perturbed by imposing a variation of amplitude in the position of the inner surface. We assume that each laser beam generates the same angular pattern. The perturbation is thus the sum of the Legendre polynomials from all twelve beams. The lowest order mode which can be imposed on a balanced 12 beam system is the sixth order Legendre polynomial summed over the laser beam poles. The density profile ($\rho(R, \theta, \phi)$) is thus given by equation (21):

$$\rho(R, \theta, \phi) = \rho_{1D}(R + \delta R \sum_{b=1}^{12} P_6(\cos(\xi_b))) \tag{21}$$

where

$$\delta R = \begin{cases} \frac{\delta_0}{2}(\cos(\frac{2\pi(R-R1)}{w}) + 1), & \text{if } R - R1 < \frac{w}{2}, \\ 0.0, & \text{otherwise} \end{cases}$$

and $\cos(\xi_b) = \cos(\theta)\cos(\theta_b) + \sin(\theta)\sin(\theta_b)\cos(\phi - \phi_b)$. The angle ξ_b is the angular distance from the bth laser beam which is sited at the coordinates (θ_b, ϕ_b).

The arrangement of the laser beams implies that the mass distribution ($\sigma(\theta, \phi)$) can be expressed as the sum of all Legendre polynomials summed over the laser beams:

$$\sigma(\theta, \phi) = \sum_{n=0}^{\infty} a_n \sum_{b=1}^{12} P_n(\cos(\xi_b)) \tag{22}$$

where the coefficient a_n is the mass amplitude of the nth mode. In an analogous way to Fourier theory we can obtain the coefficient of the kth mode as follows. At selected times the mass distribution is obtained by integrating from the centre through the shell to the outer boundary the product of the density and radius squared. This is multiplied by the kth Lengendre polynomial and integrated over all angles. This gives us a measure of the RT growth, which we refer to as the mass mode amplitude. The evolution of the mass perturbation is a signature of the RT instability; in secular growth no such movement of mass would be noted. An alternative measure of the RT growth is to calculate the distance ($\Delta R1$) between the tip of the spike ($R1_{min}$) and the head of the bubble ($R1_{max}$).

To assess the non-linear behaviour the initial amplitude of the perturbation was set to $\delta_0 = 0.1R1$ and $w = 0.5R1$ so that the linear regime saturated quickly. We have plotted in figure 2 the inner surface of the shell ($R1$), defined as the surface whose density is 1/e of the maximum density at 1.04 $nsecs$. We see a single

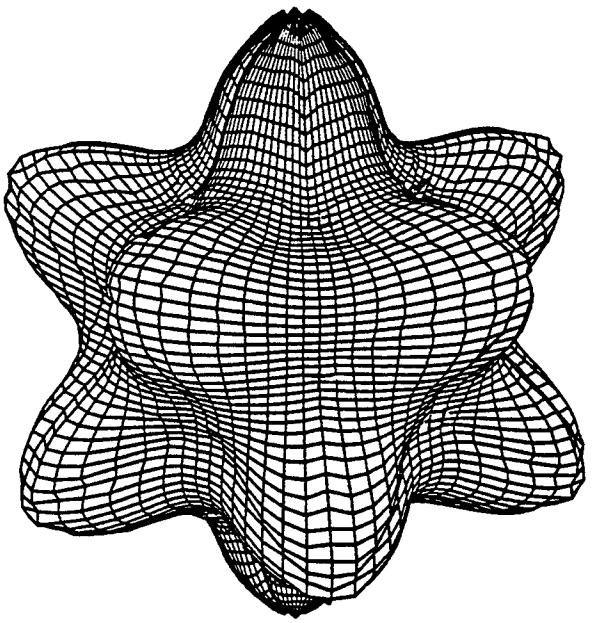

Figure 2: The inner surface of the shell (defined as the surface of constant density equal to 1/e of the maximum density) at 1.04 nsecs. This shows the bubble-ridge arrangement.

well-defined bubble rising up surrounded by a series of interconnecting spikes falling to form ridges. We have termed this the 'bubble-ridge' arrangement.

When we invert ($\delta R \rightarrow -\delta R$) the initial perturbation, which physically means having strongly focussed beams with little beam overlap, the shell distorts quite differently. This is shown in figure 3. Now thin spikes penetrate into the fuel which are surrounded by a valley of interconnecting bubbles. This we have termed the 'valley-spike' arrangement. Although the initial perturbation is a pure inversion the simulation does not remain purely inverted. In particular the bubble in the bubble-ridge arrangement breaks through the back of the shell, which was not observed in the valley-spike arrangement.

In figure 4 we plot the evolution of $\Delta R1$ for both arrangements. There appears to be no difference in the evolution and growth of each arrangement. We achieved a best fit to an $\eta g t^2$ law with a value of $\eta = 0.23$. We have compared this with corresponding simulations in 2D spherical and cylindrical geometries. The 2D spherical case has a slightly larger η of 0.25. However, in cylindrical geometry $\eta = 0.18$.

The mass mode amplitude evolves in quite a different way (figure 5). Now the bubble-ridge arrangement has a higher growth rate than valley-spike. In both cases the mass mode amplitude evolves proportional to gt^2. Mass is redistributed more quickly in the bubble-ridge arrangement resulting in the earlier disruption of the shell. This conclusion is supported by 2D simulations. 2D spherical simulations with the bubble centred on the pole of the coordinate system show growth comparable with the 3D bubble-ridge arrangement. However 2D cylindrical simulations show lower growth.

We can explain the differences between 2D and 3D and between the two 2D geometries by considering the nature of the 'bubble' in the different geometries.

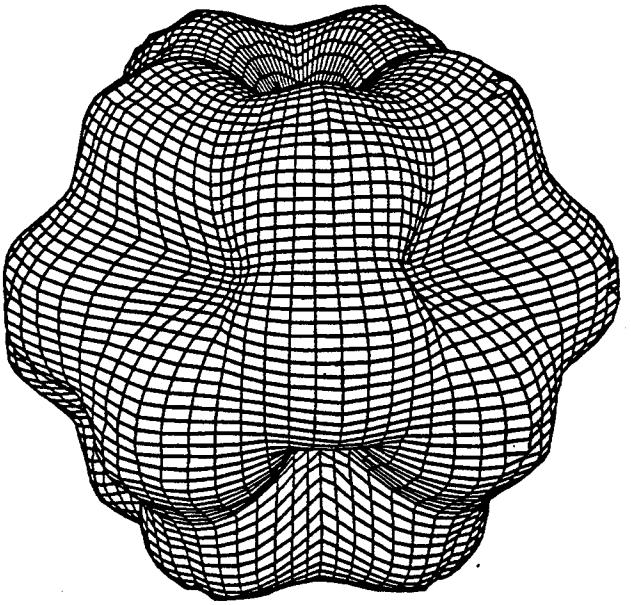

Figure 3: The inner surface of the shell (defined as the surface of constant density equal to 1/e of the maximum density) at 1.04 nsecs. This shows the valley-spike arrangement.

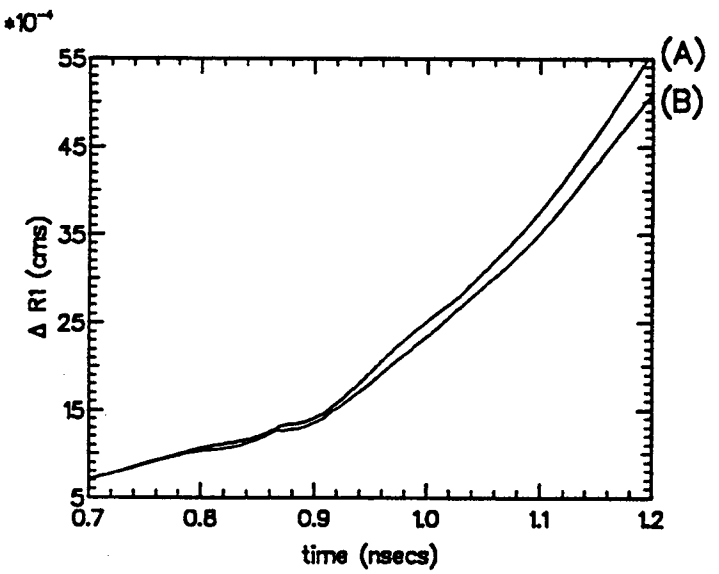

Figure 4: The time evolution of the difference ($\Delta R1$) between the head of the bubble and the tip of the spike for the bubble-ridge (A) and valley-spike (B) arrangements.

In the bubble-ridge arrangement we have a truly 3D bubble surrounded by a

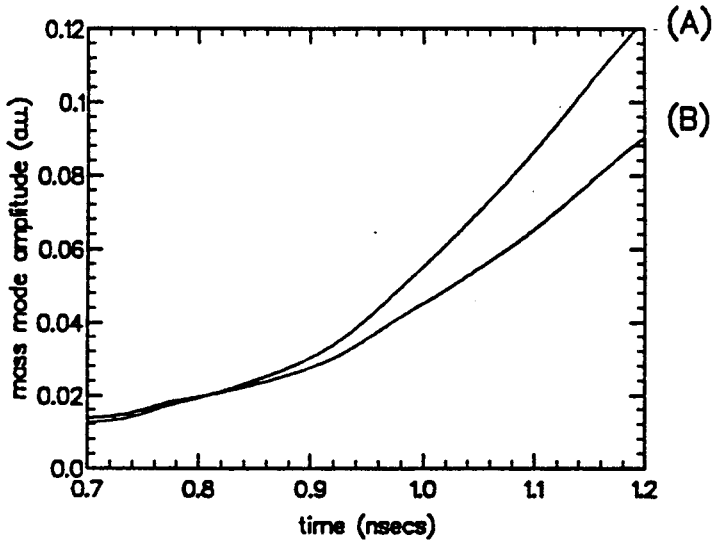

Figure 5: The time evolution of the sixth order mass mode amplitude for the bubble-ridge (A) and the valley-spike (B) arrangements.

ridge of interconnecting spikes. In the 2D spherical case, where the bubble is centred on the pole, the bubble is essentially 3D, surrounded by a ridge around the waist. The 2D cylindrical case, however does not have a bubble; in this case it is like a valley running around the sphere. In the 3D cases and the 2D spherical case the bubble has a larger boundary to feed mass into the spike than in the 2D cylindrical case.

Sakagami and Nishihara find a much larger difference between 2D and 3D. They find 0.2 in 2D, but $\eta = 0.8$—1.1 in 3D. The growth is characterised by them in terms of a mode amplitude calculated by integrating the mass density in the radial direction away from the centre of the target. This can only be related to gt^2 (a distance) by scaling the amplitude by a dimensional quantity. There is considerable uncertainty in the required scaling factor which is further complicated by the change in density and size of the target as it compresses. We suspect that the explanation of their large η lies in the choice of scaling factor.

Let us now examine the differences between the two forms of 3D evolution by looking at the mass distribution $\sigma(\theta, \phi)$. The bubble-ridge arrangement always has less mass in its minimum radial line ($\sigma_{min}(\theta, \phi)$) and the rate at which it thins is always greater than in the valley-spike arrangement. Conversely the valley-spike arrangement always has more mass in its maximum radial line ($\sigma_{max}(\theta, \phi)$) and the rate at which it thickens is always greater than in the bubble-ridge arrangement. The bubble-ridge arrangement is essentially better at bubble development, whereas the valley-spike arrangement is better at spike development. Shell thinning is therefore more rapid in the bubble-ridge arrangement. This shell thinning can cause the shell to breakup, preventing further compression and allowing the fuel to escape. As the bubble increases in size so the mass of the shell at the bubble head is reduced leading to a higher acceleration relative to the rest of the shell. The bubble then sheds mass more quickly.

CONCLUSIONS

We have reported 3D simulations of the RT instability in the deceleration phase of an I.C.F. target. We have found a faster mode evolution in 3D simulations than in 2D cylindrical geometry. This has been attributed to the greater bubble-spike boundary in 3D. We have observed two possible geometries in which the RT instability can grow in 3D: the bubble-ridge and valley-spike arrangements. The mass mode evolution of the bubble-ridge geometry is faster. Shell integrity is maintained for longer if the shell is driven more strongly immediately under the beams rather than at the intersections of the beams. We do not find the much greater non-linear growth in 3D found by Sakagami and Nishihara.

REFERENCES

1. H. Sakagami and K. Nishihara, Phys. Rev. Lett. 65, 432 (1990)
2. Lord Rayleigh, Theory of Sound (Dover, New York, 1945) 2nd Edition G. I. Taylor, Proc. Roy. Soc. London, Ser A 201, 192 (1950)
3. M. Tabak, D. H. Munro and J. D. Lindl, Phys Fluids B2, 1007 (190)
4. J. H. Gardner, S. E. Bodner and J. P. Dahlburg, Phys Fluids B3, 1070 (1991)
5. C. P. Verdon et al, Phys. Fluids 25, 1653 (1982)
6. M. Desselberger, O. Willi, M. Savage and M J Lamb, Phys. Rev. Letts. 65, 2997 (1990)
7. J. P. Dahlburg and J. H. Gardner, Phys. Rev. A 41, 5695 (1990)
8. H. Sakagami and K. Nishihara, Phys. Fluids B 2, 2715 (1990)
9. R. Courant, K Freidrichs an H Lewy 'On the Partial Difference Equations of Mathematical Physics' IBM Journal 215—235 (1967)
10. R. A. Gentry, R. E. Martin and B. J. Daly, J. Comput. Phys. 1, 1 (1966)
11. B. Van Leer, J. Comput. Phys., 276 (1977)
12. D. L. Youngs, Numerical Methods for Fluid Dynamics (Academic Press, 1982)

EXPERIMENTAL INVESTIGATIONS FOR TURBULENT MIXING OF GASES AT THE PLANE INTERFACE UNDER THE INFLUENCE OF THE DECELERATING SHOCK WAVE

A.M. Vasilenko, V.I. Olhovskaya, O.V. Buryakov, V.G.Yakovlev
All-Union Research Institute of Technical Physics,454070
Chelyabinsk 70,P.O. Box 245 USSR.

ABSTRACT

Investigation results for the development of turbulent mixing of gases caused by Rayleigh - Taylor instability are presented in this paper. Instability development was observed after the interface has been passed by the strong decelerating shock wave, generated in the electromagnetic shock tube. The phenomenon was recorded by the Shlieren-system of the ИАБ-451 device. Experiments were analyzed by means of numerical one-dimensional calculations of the flow with assumed stable contact boundaries. Mixing zone width is shown to be in linear relation to the decelerating path covered by the interface. The empirical form of the mixing zone width - as density difference relation at the contact boundary will be determined.

INTRODUCTION

Turbulent mixing arising because of Rayleigh-Taylor instability [1] is of great significance for inertial confinement of thermonuclear plasma in the problem of laser nuclear fusion. A rather detailed review of literature on this point is given in the papers of Y.Birkhoff [2] and D.Sharp [3], where different stages of R-T instability development are systematized. Since theoretical research of the mixing turbulent stage presents a lot of difficulties, then experimental investigations are necessary to understand this phenomenon.

Turbulent mixing of liquid media under quasistationary acceleration was studied by D.Youngs [4], E.Meshkov [5] and B.Sturtevant [6] investigated turbulent mixing of gases under the action of the shock wave front.

The objective of the given work is experimental investigation of the turbulent stage of R-T instability under the combined action of shock and quasi-stationary acceleration.

1. Experimental set-up

1.1. The scheme of performing the experiments.

Experiments were performed in the electromagnetic shock tube, schematically given in Fig.1.1. The shock tube channel with the cross-section of 100x100 mm^2 was partitioned off in the places of compartments joints by two flat nitrocellulose membranes 0.4 mkm thick and was filled with various noble gases, as it is shown in Fig.1.1, and the discharging compartment was

usually filled with helium.

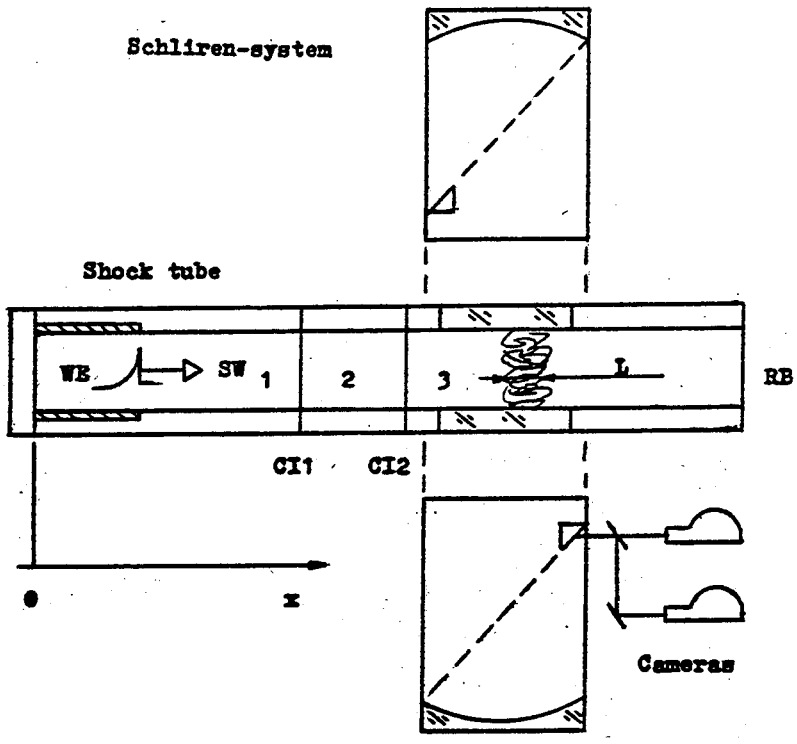

Fig.1.1. Experimental set-up and phenomenon recording.
1-discharge compartment (SW-shock wave; WE- wave expansion; He-working medium);
2,3-left and right sides of the measuring compartment ($\rho_2 > \rho_3$ -the order of gases filling: He, Ar, Kr, Xe);
CI1, CI2 -contact interfaces;
RB - the right boundary separating the shock tube channel from environment air; L - mixing zone width.

Such system of gases layers was affected by the decelerating shock wave, and this caused the second interface to be gravitational unstable in accordance with Taylor criterion [1], since quasi-stationary acceleration generated by the unloading wave is directed from the side of the gas of less density. Application of noble gases made it possible to preserve the relationship of gases densities after the break-down of interface rupture to be constant. The first interface appeared to be stable. Such an arrangement of gases is caused by the necessity to place the most light noble gas, as a pushing one, in the discharge compartment. This allowed to simplify both the procedure of calibrating the mathematical model of flow, and the creation of necessary conditions for the rapid thermal membrane destruction at the cost of shock wave intensity increase when passing across the interface of the gas having greater density.

These conditions were considered to be met if the temperature of even one gas at the interface exceeded the temperature of nitrocelulose flash.

Phenomenon monitoring was performed by means of Schlieren-system of the device ИАБ - 451 optically matched with two cameras СФР - 2М, and by photographing the instability development in the modes of slit sweep and frame photography.

1.2.The description of the flow being generated in the Electromagnetic Shock Tube.

In virtue of the short-term action of discharge current the flow in the electromagnetic shock tube is characterized by the realization of flow modes being close to the automodel flow or to the limit ones under powerful explosion [7] and short-term shock upon the free surface of a gas.

In the given shock tube design, preceding the one with the vacuum compartment [8], the flow is characterized by the presence of the secondary shock wave arising when vacuum cavities collapse after termination of discharge current action.

The moment of reaching the mixing zone by the secondary shock wave terminated, as a rule, the process of phenomenon observation. But in the experiments with dense gases (Xe, Kr, Ar) the secondary shock wave - the interface interaction took place at the initial stage of the instability development. In such cases the analyses of experimental results was made taking into account the flow perturbations of the secondary shock wave.

2. Experimental Results and Discussion

2.1. Interpretation and processing of experimental results.

The mixing zone of gases is determined by the lines of sharp changes in the film blacking, of adjacent to the areas of pure gases. These lines were interpreted as mixing zone boundaries.

Mathematical processing of experimental results was carried out by the procedure given in [8] and by similar procedure [4] in term of the relation

$$\sqrt{L} = \sqrt{L_0} + \sqrt{J2S}, \qquad (1.1)$$

where L - is mixing zone width, L_0 - is the initial mixing zone, S - is the deceleration path ($S = U_0\hat{t} - \hat{x}$), $\hat{t}$ - is time action of deceleration, $\hat{x}$ - is the shift of the interface, J - is intensity of turbulent mixing ($J = dL/d2S$).

When analyzing experimental results the values of J and L_0 where determined for each experiment separately and then averaged taking into account that in every experiment the individual set of initial perturbations is realized.

2.2. Experimental results.

Experiments were performed with following gases: He, Ar, Kr,

Xe. Average atmospheric pressure was 0.976 bar. All the experiments are divided into groups relative to the secondary shock wave.

1. Experiments: He – Ar – He, He – Kr – He, He – Xe – He – experiments with large ratio of gases densities at the interface. The level of initial perturbations was estimated to be 0.6 mm. The secondary shock wave doesn't interact with the mixing zone.

2. Experiments: He – Kr – Ar, He – Xe – Kr, He – Xe – Ar. The secondary shock wave interacts with the mixing zone.

The mixing zone at the initial stage of development is a compact area practically not transmitting light and having weekly expressed protuberances at the boundary (see Fig. 2.1.).

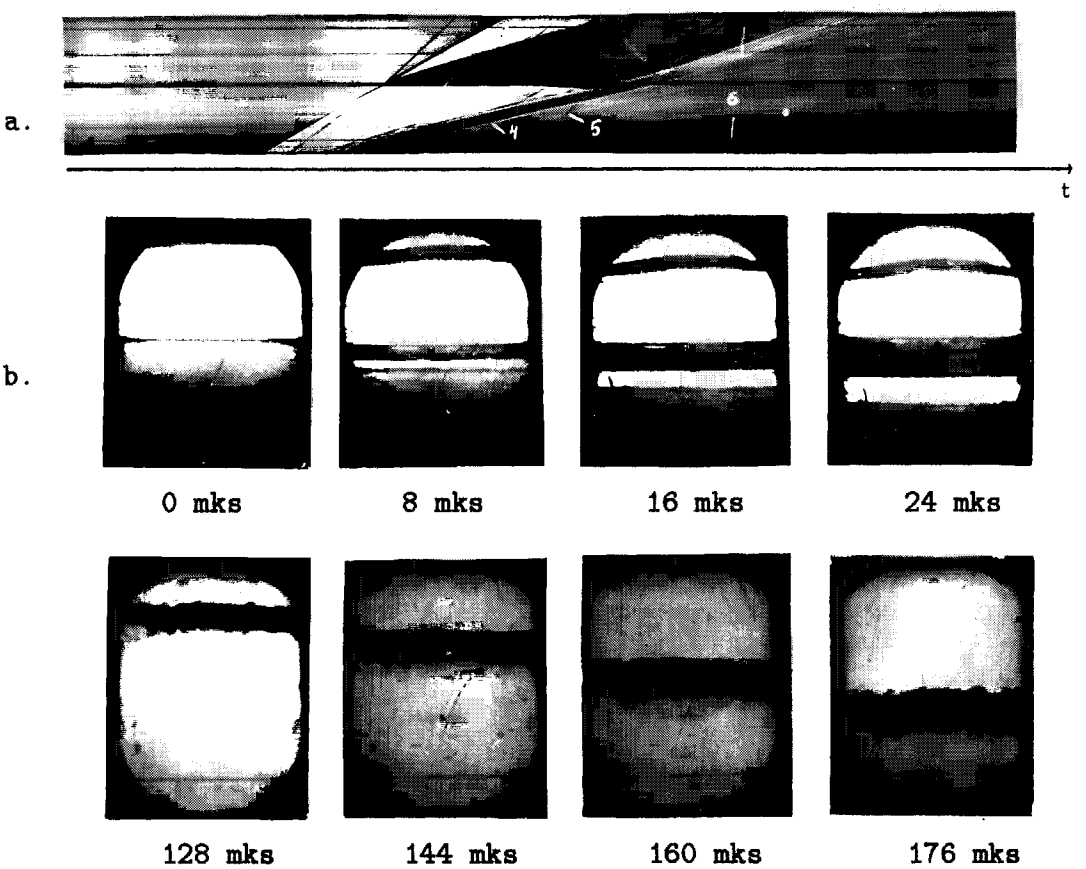

Fig. 2.1. Mixing zone development at the flat interface Ar – He
Flow parameters: incident shock $M_1 = 4.3$, passing shock $M_2 = 2.37$, $G = 3.0 \times 10^6$ m/s^2, gases density ratio $N = 6.35$.
a. Photosweep of the phenomenon. b. Frame photographs.
1 – the front of the shock wave, 2 – the mixing zone,
3 – the unloading wave, 4 – the contact boundary 1,
5 – the front of the shock wave 2, 6 – bench mark lines,
Ar – up, He – down.

The inner structure of the mixing zone can be observed at a

later stage. On frame photographs (see Fig.2.2) it can be clearly seen that more narrow jets of the heavy gas intrude into the light one and there are vortexes on the jets apexes.

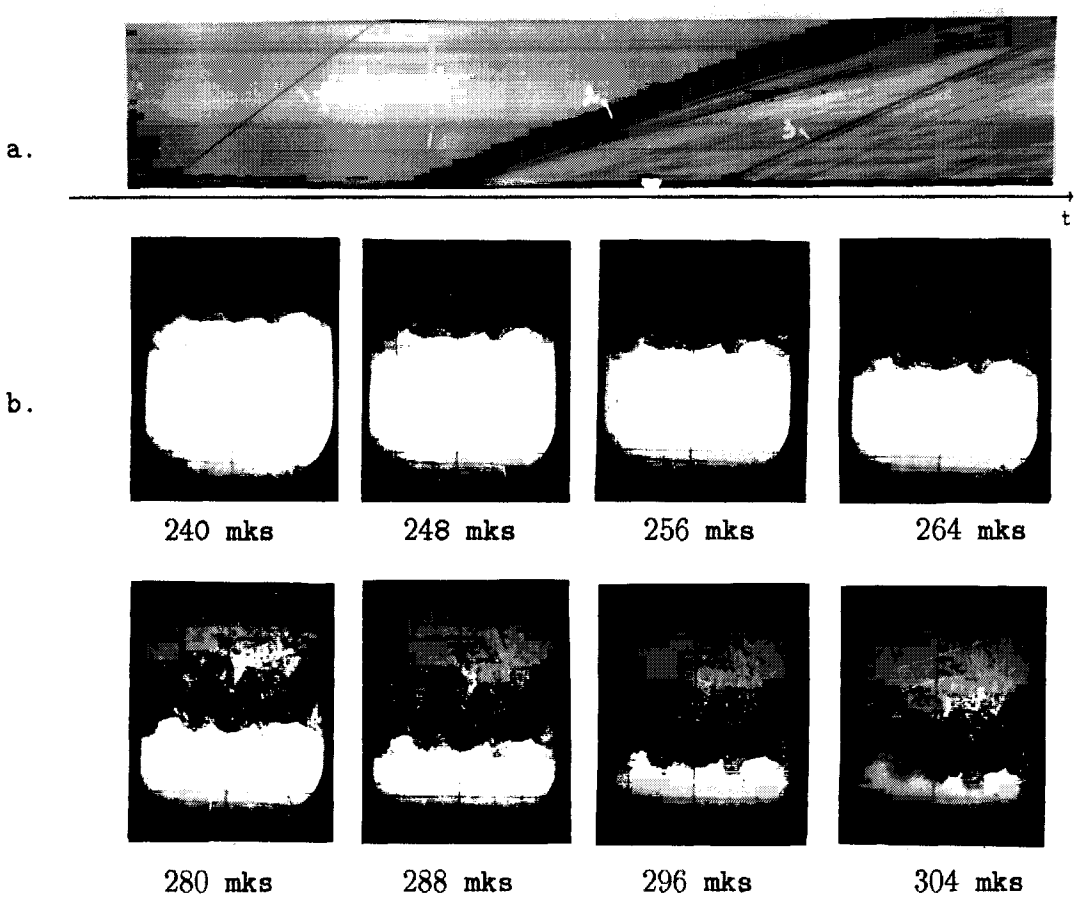

Fig. 2.2. Mixing zone development at the flat interface Kr –He
Flow parameters: M_1 =4.5, M_2 =2.02, G =2.1x10^6 m/s^2, N=11.96.
a. Photosweep of the phenomenon. b. Frame photographes.
1 – the front of the shock wave 1, 2 – the mixing zone,
3 – the front of the shock wave 2, 4 – bench mark lines,
Kr – up, He – down.

Prevalent development of longitudinal dimensions of jets are observed. Jets position in various experiments is different, what is indicative of the random nature of their generation, and this is perhaps specified by the manner of perturbations distribution of the membrane surface density. The jets, in turn, are not quite smooth and have the traces of perturbations of smaller scales up to those of Kolmogorov, where dissipation of turbulent energy takes place.

Comparison of the zone fronts position with calculations shows that mixing goes asymmetrically. A heavy gas intrudes to the greater depth than the light one into the heavy one.

General course of the mixing zone width – time dependence

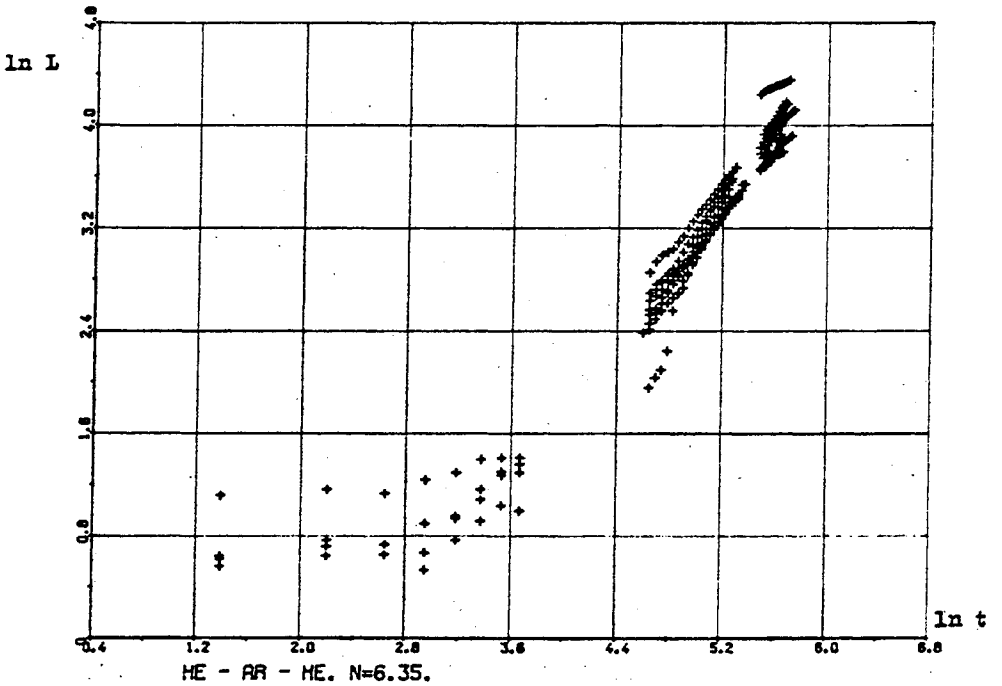

Fig. 2.3. Mixing zone development in time

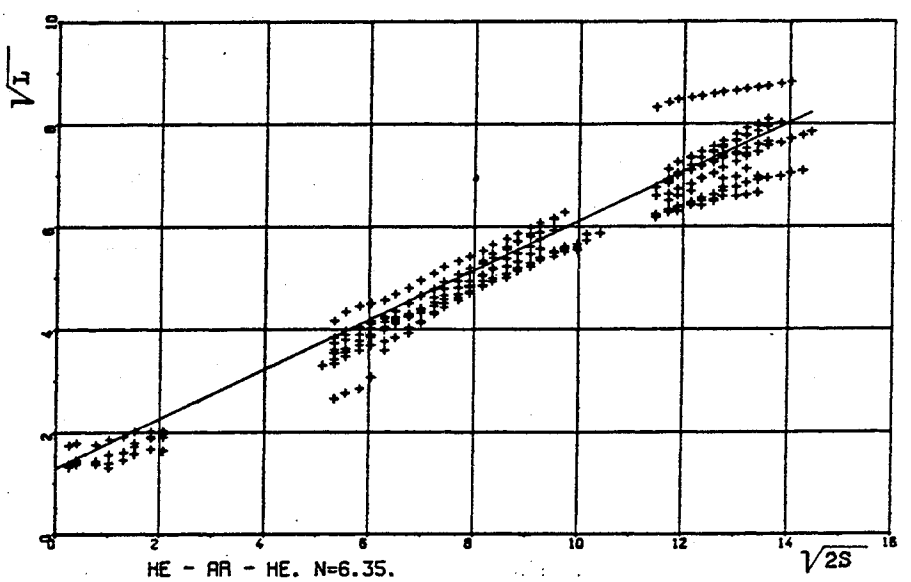

Fig. 2.4. Mixing zone width against the deceleration path

given in Fig. 2.3 in the logarithmic scale demonstrates gradual approach to the quadratic law typical of the limit mixing mode. The approach to the limit mixing mode is quite obvious when processing data in the coordinate plane $\sqrt{L}$, $\sqrt{2S}$ (see Fig.2.4.) in spite of interface acceleration decrease. Correlation coefficient $R(\sqrt{L}, \sqrt{2S})$ is close to 1 and this is indicative of the close linear relation of these parameters. When a certain ratio of these parameters is attained, linear relation between L and S is interpreted as the approaching to the turbulent mixing mode.

Experiments of the second group are experiments with insignificant difference in density. Besides, in these experiments ,we had to take into account additional influence on the interface by the secondary shock wave. When performing the analysis we considered contact boundary motion velocity.

Photos of the mixing development pattern for gases and graphs of data processing are given in Fig.2.5 –2.7.

a.

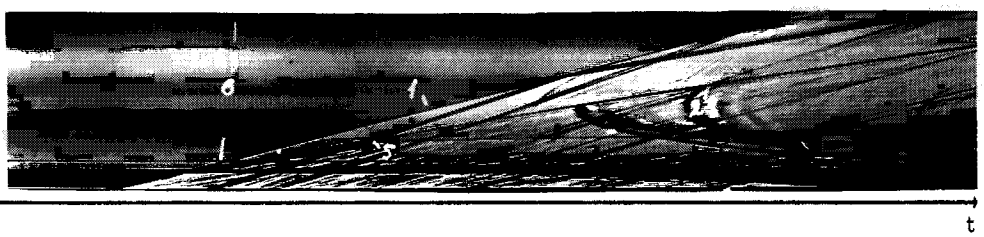

b.

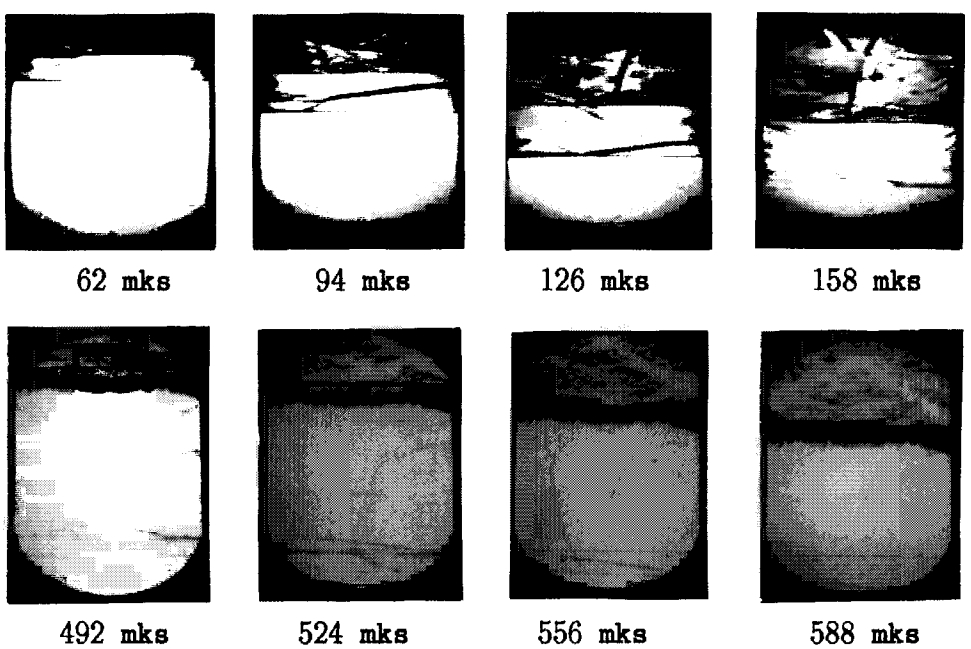

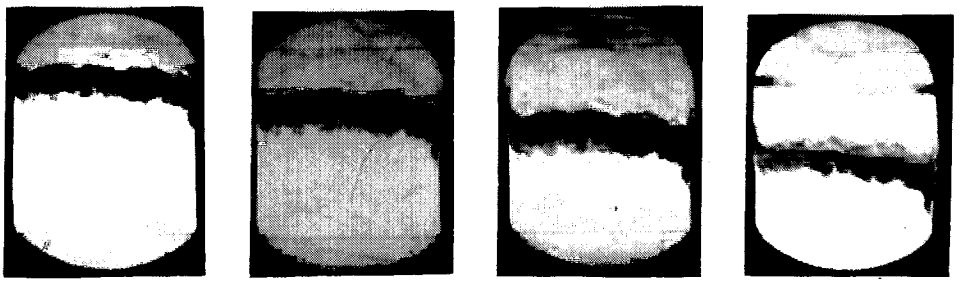

Fig. 2.5. Mixing zone development at the flat interface Xe –Kr
Flow parameters: M1=3.404, M2=2.906, G =0.55x10^{6}m/s^2, N=1.4.
a.Photosweep of the phenomenon. b. Frame photographs.
Xe – up, Kr – down.

To judge by photos (see Fig. 2.5.), the process of instability development in the given series of experiments in principle doesn't differ from the process in the first group of experiments.

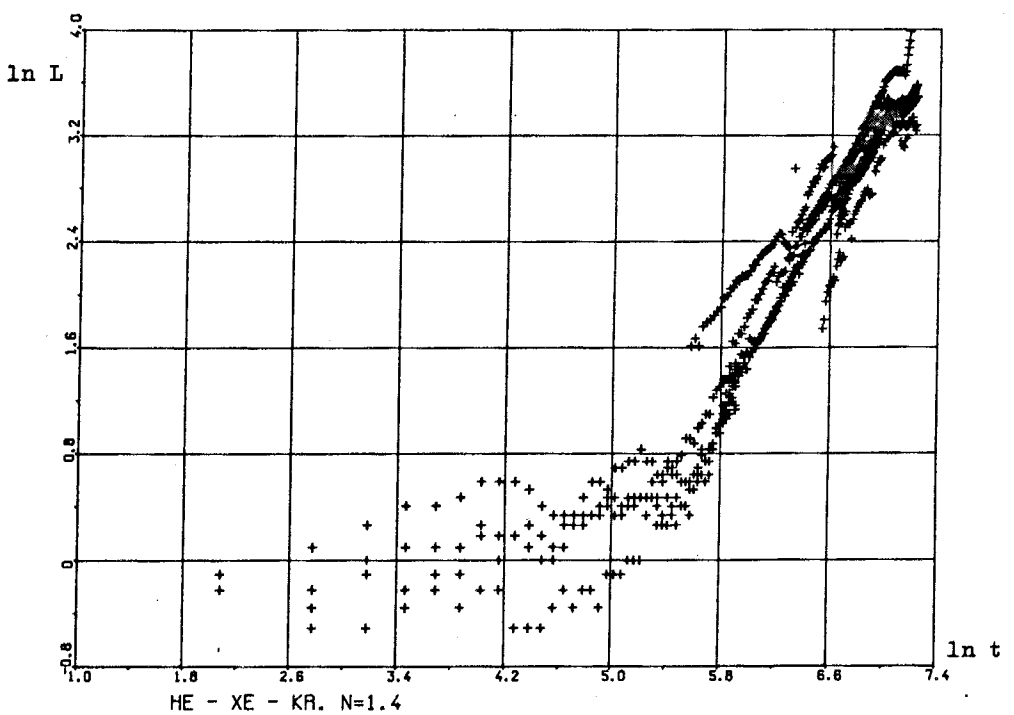

Fig. 2.6. Mixing zone development in time

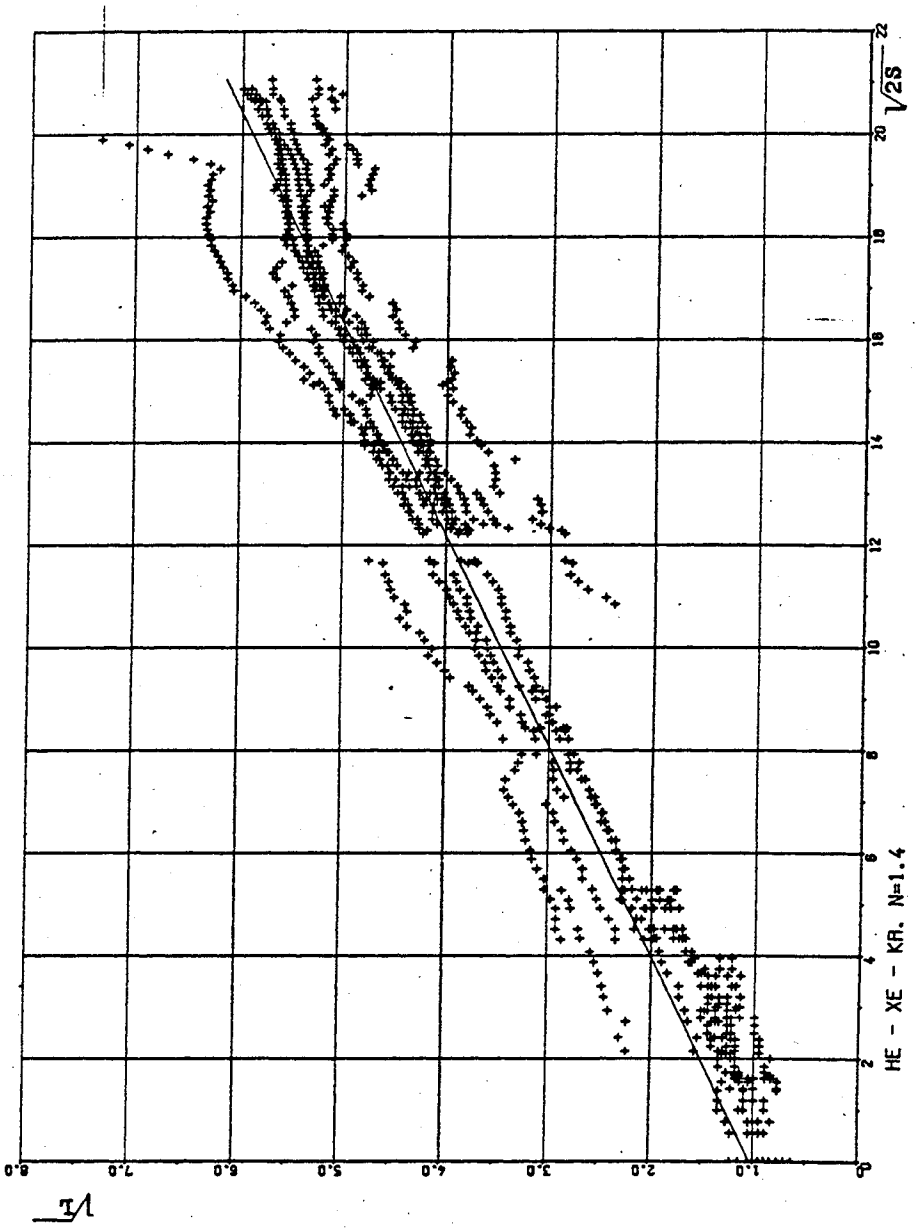

Fig. 2.7. Mixing zone width against the decelerating path

It will be noted that contact area width in the initial stage is far less than in the previous group of experiments. This effect is likely to be related to the lower level of initial perturbations of the contact boundary due to the higher density of gases behind the film. Unfortunately, the level of initial perturbations L_0 eventually didn't decrease because of the second shock wave effect.

2.3. Discussion of Experimental Results

Estimated results of turbulent mixing intensity for gases were compared with Atwood number (see Table.2.1.) being characteristic of the gases density ratio at the contact boundary after the rapture break-down.

Table 2.1. Measuring Results of Mixing Intensity for Various Drops in Gases Densities

Run No	N	A	$J \pm \sigma_J$	L_0, mm	$\hat{L}_0$, mm
1	11.96	0.846	0.246±0.031	0.08	0.6
2	6.35	0.728	0.22 ±0.02	1.0	0.6
3	19.99	0.905	0.315±0.02	0.2	0.6
4	1.88	0.305	0.096±0.011	0.4	0.054
5	1.4	0.167	0.057±0.06	1.1	0.026
6	2.76	0.468	0.139±0.09	0.22	0.054

σ –root mean scattering, $\hat{L}_0$ – estimation of initial roughness.

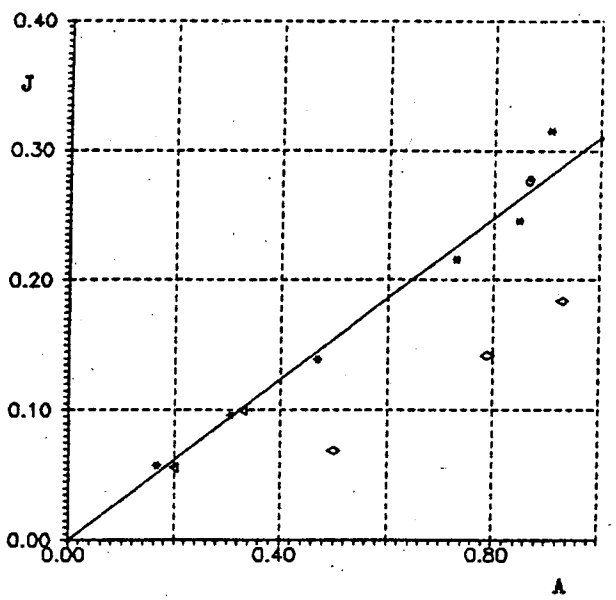

Fig. 2.8. Turbulent mixing intensity against Atwood number ⋆ – experimental results with the flat interface of noble gases, o – results of experiments on the electromagnetic shock tube with the sinusoidal interface of noble gases [8], ◁ – experimental results of Voskoboynikov D.with intersoluble liquids, ◇ – experimental results with nonmiscible liquids and liquids – compressed gas systems [4].

The results of measurements are presented graphically in Fig. 2.8. and have a linear form. The angular coefficient of the straight line was determined according to the method of least squares when the straight line went through the origin. This condition results from a rather obvious assumption that the mixing proper shouldn't be observed in the uniform gas (A=0).

Finally, the relationship for the total width of the mixing zone in the turbulent stage has the form:

$$L = \alpha \frac{N-1}{N+1} \cdot 2S, \qquad (2.1)$$

where α equals 0.31 ± 0.04.

It should be noted that data of mixing intensity measurements in the experiments with the flat interface coincide with the experimental results for sinusoidal interface [8] within error limits. This means that even in case of setting artificial periodical perturbations we can observe the same "mixing zone width - deceleration path" relation as in the experiments with chaotic initial perturbations. Such a stability of mixing intensity indicates that the given jet structure of the mixing zone is typical for the phenomenon of gravitational instability. Having conducted the comparison with the results of experiments performed with liquids one observes the agreement of mixing intensity with known results of D.J. Voskoboynikov and J.J. Kikoin obtained for the mutually soluble media under low accelerations $G=(1.6\div3.3)G_0$ (G_0 - gravitational constant).

At the same time a far less intensity of mixing is observed in the experiments of D. Youngs & Y. Kucherenko [9]. It is possible that the surface tension leading to capillary instability of jets and to additional turbulent energy dissipation affects the process of turbulent mixing.

CONCLUSION

Experimental investigations for turbulent mixing of gases caused by Rayleigh-Taylor instability at the flat interface affected by a strong decelerating shock wave having $M=3.2\div4.5$ under conditions of essential compressibility of gases were performed.

Instability and turbulent mixing development was observed under accelerations of $(5.5\times10^5 \div 3\times10^6)$ m/s^2 for contact boundaries of noble gases having densities relations from 1.4 up to 20 (after the rupture break-down at the interface).

Mixing zone development is estimated to take place proportionally to the decelerating path covered by the interface under the action of the unloading wave.

Turbulent mixing intensity of gases in the investigated interval of the process development obeys the relation

$$J = \alpha \frac{N-1}{N+1},$$

where $\alpha = 0.31 \pm 0.04$ – is the constant of turbulent mixing.

REFERENCES

1. G.I. Taylor, Proc. Roy. Soc. A 201, p. 192 (1950).
2. Y. Birkhoff, "Mir", M., p. 68 – 94 (1964).
3. D.H. Sharp, Physica D 12, p. 3 (1984).
4. D.L. Youngs, Physica D 37, p. 270 – 287 (1989).
5. V. A. Andronov, S. M. Bahrah, E. E. Meshkov et al, Jour. Exp. & Theor. Phys., V.71, 8, p. 806 –811 (1976).
6. M. Brouillette and B. Sturtevant, Physica D 37, p. 248–263, (1989).
7. Ja. B. Zeldovich and Ju. P. Raiser, Physics of Shock Waves and High – Temperature Hydrodynamic Phenomena.,"Nauka", M. (1966).
8. A. M. Vasilenko, O. V. Buryakov, V. F. Kuropatenko et al, Preprint No 56 Phys. Inst. of Acad. of Sciences, p. 32 – 51, M.(1990).
9. Ju. A. Kucherenko, Y. Y. Tomashev, L. I. Shibarshov, Quest. Atom. Scien. and Eng. Issue 1, p. 13 – 19 (1988).

TWO- AND THREE-DIMENSIONAL CALCULATIONS OF SHOCK TUBE RICHTMYER-MESHKOV INSTABILITIES*

Michael F. Wehner
Lawrence Livermore National Laboratory
Livermore CA 94550 USA

Abstract

The geometry of the two-dimensional standard computational test problems is generalized to three dimensions. Results corresponding to one particular test problem are presented in both two and three dimensions for comparison.

Prior to the Second International Workshop on the Physics of Compressible Turbulent Mixing, held in Pleasanton CA in 1989, a set of two-dimensional test problems was distributed to interested parties in order to facilitate the intercomparison of various hydrodynamics codes and algorithms. These problems were intended to test the calculation of explicitly resolvable features believed to be relevant to an understanding of the turbulent mixing of layered fluids. In this context, the test problems were designed to simulate previous experimental shock tube configurations.[1,2] Prior to this meeting at Royaumont, the suite of problems was enlarged to include some substantially different and more difficult shock conditions and geometries.[3] However, all the test problems shared a common feature in their initial interface perturbations. Each experimental configuration was tested with two different interfaces. The first was a single wavelength perturbation given as

$$x = 0.24 \cos(2\pi y/W)$$

while the second was a multiple wavelength perturbation consisting of a superposition of five separate wavelengths given as

$$x = \sum a_n \cos(2\pi n y/W)$$

where $(n,a_n) = (0.5,0.05)$, $(1.5,0.10)$, $(2.0,0.07)$, $(3.5,0.11)$, $(5.5,0.09)$ and W is the width of the shock tube in centimeters.

It should be noted that some of the actual experiments were performed using the single wavelength perturbation while some experiments had diffusive interfaces. No experiments have been performed with this particular multiple-wavelength interface function. Also, the calculational test problems do not include any effect of the membrane.

It is straightforward to generalize the single-wavelength initial perturbation from two to three spatial dimensions by means of a rotation about the center of this function. The resulting function is

$$z = 0.24 \cos\left(\frac{2\pi x}{W}\right) \cos\left(\frac{2\pi y}{W}\right)$$

Just as the two-dimensional single-wavelength function is symmetric about the center of the shock tube, this function also is symmetric but in a three-dimensional sense. This fact can

*Work performed under the auspices of the U.S. Department of Energy by the Lawrence Livermore National Laboratory under Contract No. W-7405-ENG-48.

be utilized to reduce the computational domain of the problem by a factor of four, to significantly aid in obtaining adequate resolution. The same procedure can be performed about each of the individual wavelengths constituting the multiple wavelength perturbation resulting in

$$z = \sum a_n \cos\left(\frac{2\pi n x}{W}\right) \cos\left(\frac{2\pi n y}{W}\right)$$

Note, that the rotation point is the same for each wavelength and, as in the two-dimensional case, there is no symmetry in this function to take advantage of.

TP3 and TP4 of the set of problems distributed by D. Besnard[3] simulate the shock-tube configuration of Benjamin[1]. In this experiment, shocked air was incident on stationary helium at a Mach number of 1.24. The tube width was 7.5 cm across and a rigid reflecting wall was 8.5 cm from the mean interface position. For the test problem, perfect gas gamma law equations of state are presumed for both gases with γ=5/3 for the helium and 1.4 for the air. The density of the helium is 0.0001694 g/cm^3. Behind the shock, the air density is 0.0017285 g/cm^3 and ahead of it the air density is 0.001225 g/cm^3.

In Fig. 1, results for the two-dimensional single-wavelength perturbation version of this problem are shown in the initial configuration and at approximately 200, 300, 400 and 500 microseconds after the shock has arrived at the interface. For these calculations, the air is incident on the helium from right to left. The computational grid is composed of 0.025 cm square zones in the entire region of interest. This resolution is fine enough to reasonably resolve the bubble and spike structures characteristic of these experiments. The interesting features to note are the regions of high vorticity just behind the tip of the penetrating spike of air, resulting in the pronounced roll up or "mushroom" shape. The details of this structure are highly resolution dependent.

In Fig. 2, results for the two-dimensional multiple-wavelength perturbation are shown at the same set of times and at the same spatial resolution. It is interesting to note that the structures, resulting from higher wavelength components of the initial perturbation, begin to form "mushroom" structures at an earlier time. Additionally, these structures have penetrated substantially more into each other leading to increased mixing of the materials.

Unfortunately, spatial resolution to this degree is prohibitively expensive in three-dimensional calculations. Although the single wavelength perturbation case has symmetries to exploit, the multiple wavelength case has none. In this presentation, the zone size chosen was 0.1 cm on a side. Because the bubble and spike structures are so poorly represented at this resolution, we show in Fig. 3 a two-dimensional single wavelength calculation at this mesh size for purposes of comparisons with the three-dimensional calculation. In Fig.4, results for the three-dimensional single wavelength calculation are shown The incident air is shown on top in blue and is traveling downward. The target helium is shown on the bottom in yellow. For reference, the reflecting wall at the end of the tube is at the bottom. Because of the symmetry, only the center fourth of the problem from x = 1.875 to 5.625 cm and y = 1.875 to 5.625 cm is calculated. This domain is chosen to isolate the spike into the middle of the calculation. In Fig.5, the results of the three-dimensional multiple wavelength calculation are shown at the same times and with the same color scheme. In this calculation the entire shock tube is included. Certain comparisons are revealing. In Fig.4, a very noticeable ripple is evident on the side of the helium bubble. This is a zoning effect which may be ascertained by a comparison with the pair of two-dimensional single wavelength calculations. The spike in Fig. 4 also shows a zone imprint at the very tip. However, the degree of "mushrooming" is quite similar to the equivalently resolved two-

dimensional calculation. Figure 5 exhibits similar behavior to the two-dimensional calculation in that some structures are substantially more penetrating than in the single wavelength result. However, these structures are much thinner and tend to break up because they are not resolved. Because of the complexity of the multiple wavelength perturbation flow, it is also difficult to ascertain the degree of "mushrooming" from these two-dimensional pictures of three-dimensional objects. One can be certain that greater resolution is needed.

Conclusions

A three-dimensional generalization of the two-dimensional test problem geometry is presented for both single- and multiple-wavelength perturbations. Much greater resolution in three dimensions is obviously required in order to adequately characterize the bubble and spike structures observed in these type of shock tube experiments. It is hoped that future workshops will generate greater intercomparisons between three-dimensional codes and algorithms.

References

[1] R. Benjamin, "Experimental results corresponding to standard test problem 1", presented at the International Exchange on RM and RT Mixing, Pleasanton CA,USA, November 16 and 17, 1989,.and "Experimental observations of shock stability and shock induced turbulence", in **Proc. of the International Workshop on the Physics of Compressible Turbulent Mixing**, Princeton NJ, USA, 1988, Lecture Notes in Engineering (Springer, Berlin, 1990, in press).

[2] M. Brouillette and B. Sturtevant, "Growth induced by multiple shock waves normally incident on plane gaseous interfaces", **Physica D, 37**, 248 (1989).

[3] D. Besnard, Centre d'Etudes de Limeil-Valenton, private communications, March 1991, (a list of the test problems).

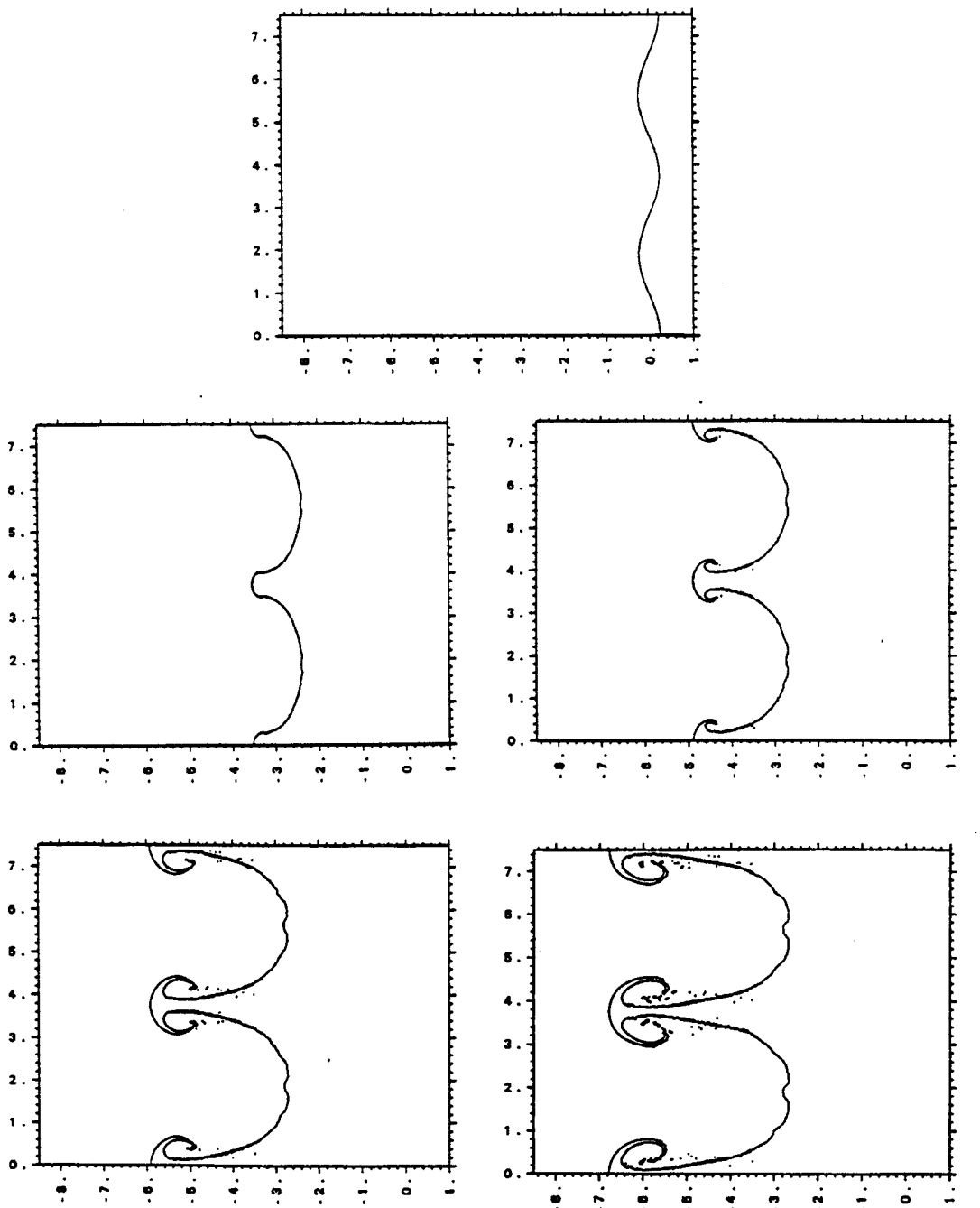

Figure 1. Results for the two-dimensional single-wavelength calculation at fine resolution (see text).

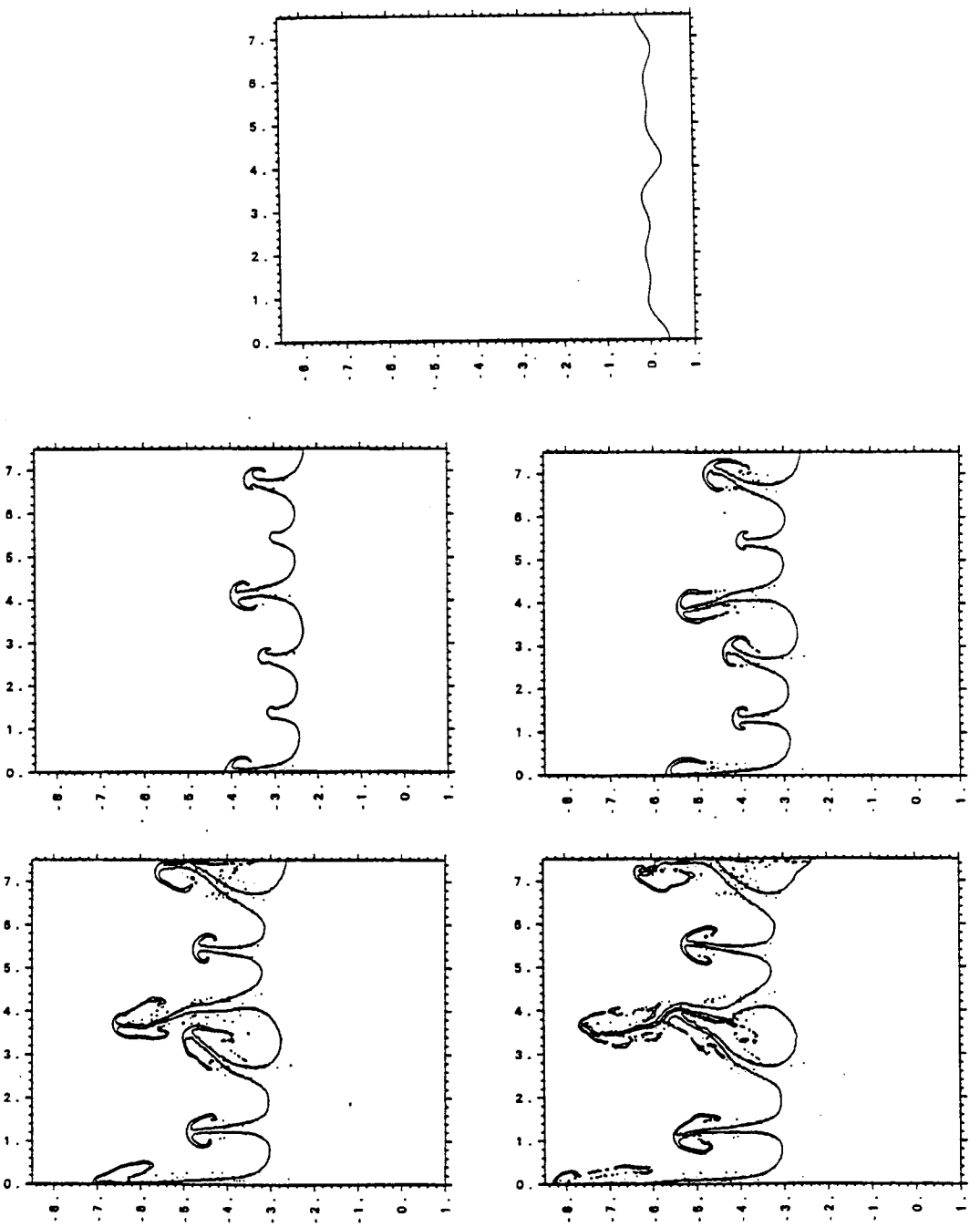

Figure 2. Results for the two-dimensional multiple-wavelength calculation at fine resolution.

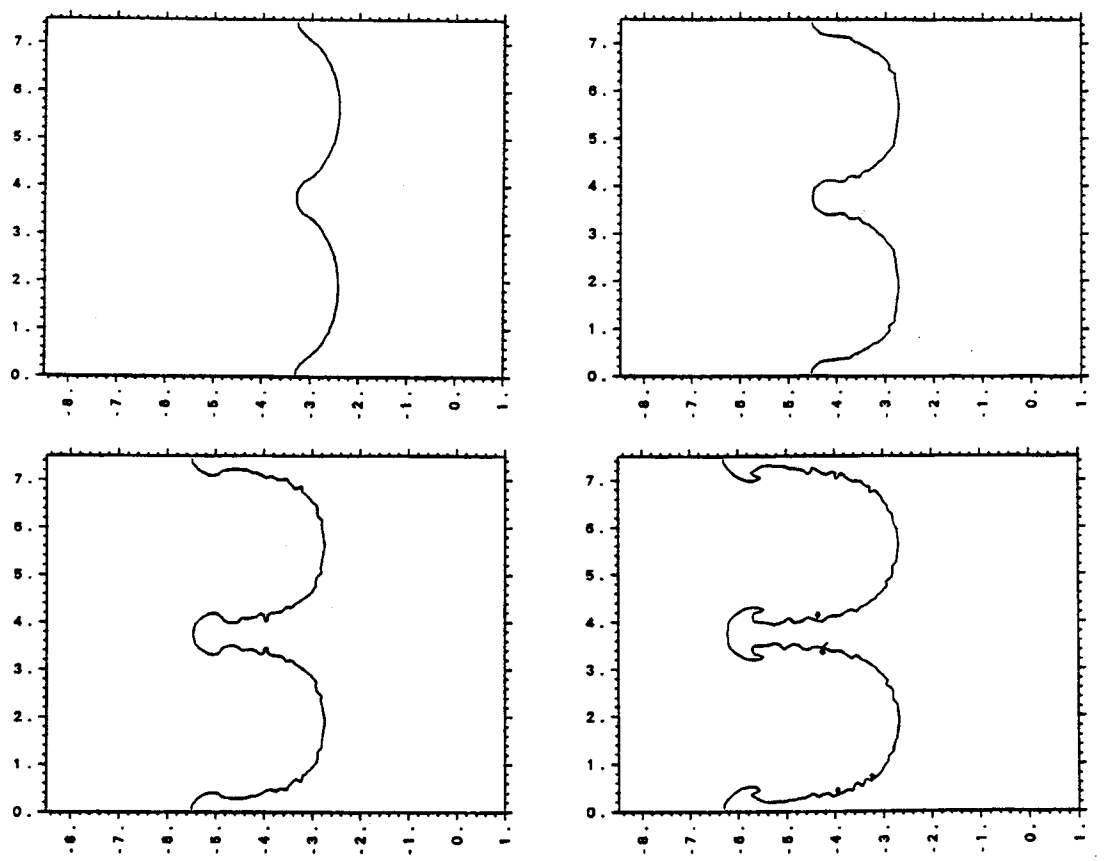

Figure 3. Results for the two-dimensional multiple-wavelength calculation at coarse resolution.

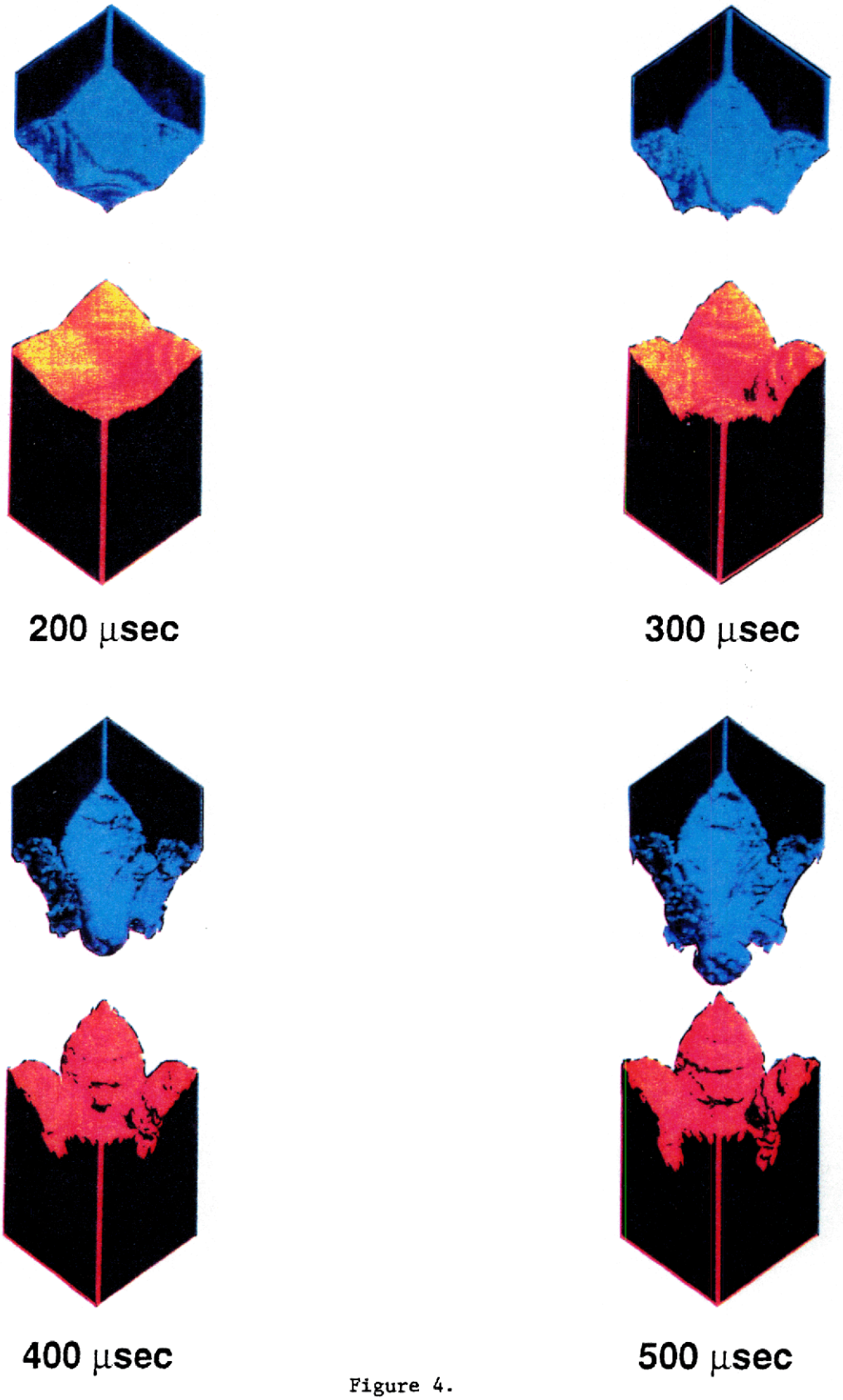

Figure 4.

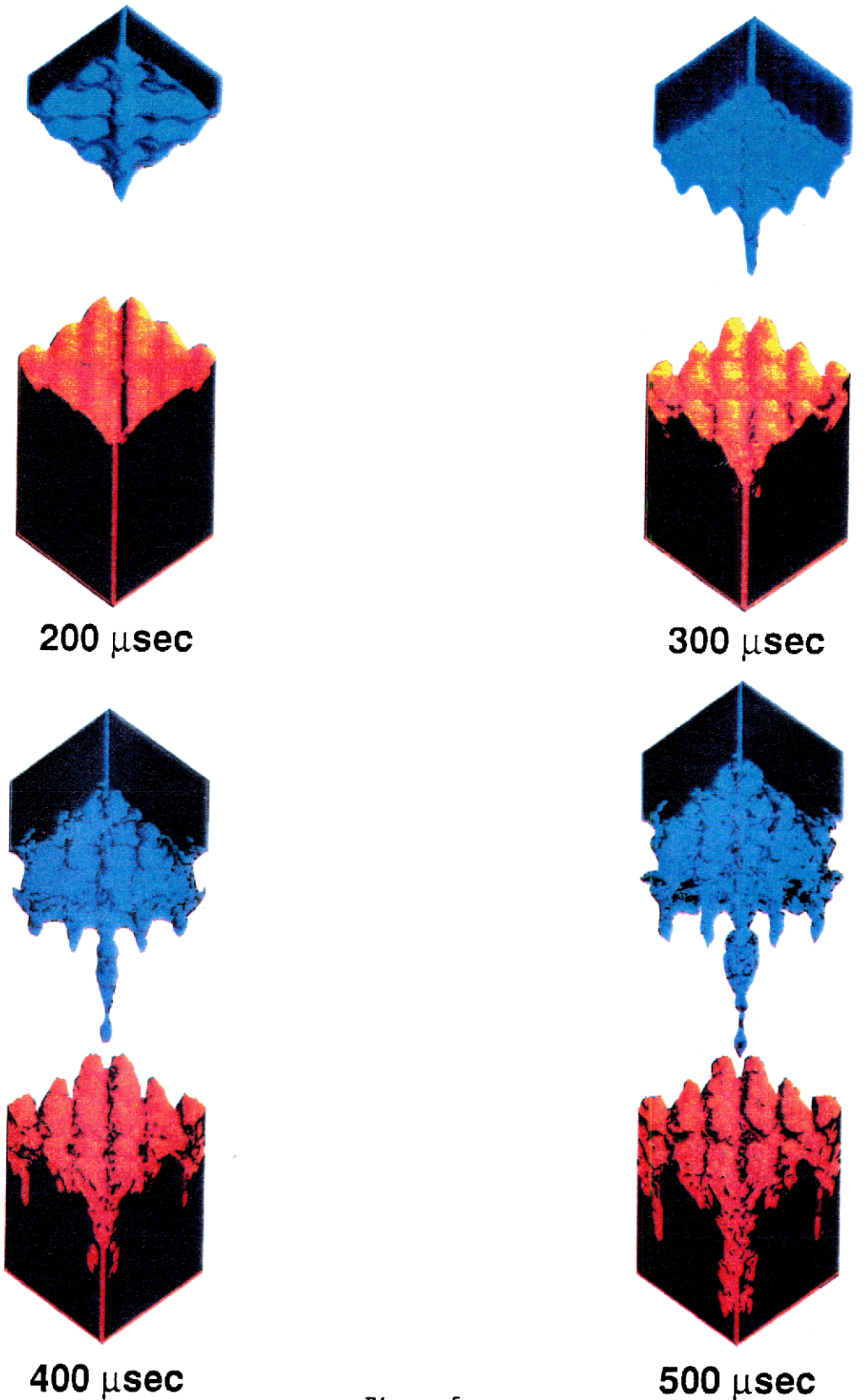

Figure 5.

REMARKS ON THE EXPERIMENTAL ASPECTS

Experimental roundtable discussions: microdensitometry exercise (C. Cavailler)

Flow visualization (schlieren) photographs from shock tube experiments were provided by 4 teams: Caltech, ENIN (Moscow), University of Provence and CEA Vaujours. Unfortunately the data set prepaired by Prof. Zaitsev was lost in the delivery from ENIN to Vaujours via the French embassy in Moscow. From each of the other 3 sets, 4 pictures were chosen to be analysed by a microdensitometer at Vaujours. Each picture (negative or positive transparency) was processed by the microdensitometer along 3 lines perpendicular to the interface. The size of the probing light beam is 25 or 50 μm (in the direction of the traverse) by 250 μm (parallel to the interface). Everyone agreed that, in most cases, the experimenter's eyeballs are as efficient as the microdensitometer for the determination of the position of the edges of mixing zone and for the distinction (when possible) between the turbulence in the boundary layer and that of the interfacial mixing zone. One exception is probably the case of continuous interfaces (for instance the air-helium diffusion zone recorded at Vaujours) from which the microdensitometer provides Gaussian-like shapes suitable to a standard analysis such as defining the diffusion zone thickness as the full width at half maximum. Statistical information on the scales which may be useful to modelers can also better be obtained by microdensitometry than by the eye observation alone.

Comments on the shock tube and Rayleigh Taylor experiments (J-F Haas)

By now several research teams have performed the simple class shock tube experiments: i.e. low Mach number shocks interacting with planar discontinuous interfaces: among the new contributions since Pleasanton:

-Zaitsev et.al. (ENIN) with Mach 1.3 shocks interacting with air-helium or -SF6 interfaces (7.5 cm square tube, 10 cm length for helium or SF6): conditions and results close to Brouillette's experiments.

-Cavailler et. al. (Vaujours) with SF6-air (Mach 1.45) and air-helium (Mach 1.3) (8 cm square tube, 31 cm length downtream of membrane): determining a one dimensional mixing zone thickness soon after the second reflected shock due to shock-boundary layer interactions proved to be difficult.

-Houas et. al. (Marseilles) with air-CO2, -helium and -argon interfaces (8.5 cm square tube, 70 to 140 cm length downstream of membrane) and 1.3 shock waves. The one dimensional mixing zone doesn't survive long after the first reflected shock wave.

For completeness, in the case of the low Mach number benchmark experiments, the test section of Caltech shock-tube used by Brouillette is 11.4 cm square and 10.5 cm or 50-109 cm long downstream of interface; the AWE Foulness shock-tube is 5 by 20 cm in cross section and 14 cm long downstream for the air-helium case, and two interfaces case was also investigated; the

Meshkov air-helium experiments were performed with a tube 4 by 12 cm in cross section and 16.9 cm long between interface and end plate.

Results from high Mach number experiments (M=2.5-3.5, cross section 7.2 by 7.2 cm) with large initial interface perturbation amplitudes were shown by Zaitsev et. al. at Royaumont. Numerical test problems TP8 thru 11 were defined after these experiments. We should also keep in mind the experiments presented by Vassilienko at Princeton (high Mach shock plus deceleration and perturbed interface) and at Pleasanton (low Mach shock plus deceleration and planar interface). For the Royaumont workshop Vassilienko et. al. submitted the results of experiments with high shock Mach number plus deceleration and planar interfaces (cross section 10 by 10 cm).

Because of the three-dimensional character of many shock-tube experiments and the wall effects acting on all of them, traditional flow visualization techniques (shadowgraph-schlieren) give ambiguous results. In Pleasanton we witnessed the emergence of new techniques applicable to shock tube work such as differential holographic interferometry (AWE Foulness and Cranfield Institute of Technology), planar section visualization by light scattering by smoke or aerosol (Meshkov, Benjamin at LANL) and flash X-ray photography (Bonazza and Sturtevant, Caltech). At Royaumont, we saw the maturation of the X-ray method at Caltech (stressing the data reduction procedure) and some preliminary calibration on test cells at Vaujours. The PLIF method (planar laser induced fluorescence) used also at Caltech for the visualization of shocked cylindrical jets (without membrane) and presented by Jacobs appeared to be as promising. One should also keep in mind the spectroscopic methods presented earlier (infra-red emission and absorption of shock-heated CO_2) for mean density, concentration and temperature in mixing zones (University of Provence).

As shown by Benjamin, the membrane transforms the incident shock wave into a series of transmitted compression waves: this may contribute to the discrepancy between experimental and numerical growth rates. On the other hand, according to Meshkov, a different membrane behavior caused the much higher post-reshock mixing zone thickening rate of his air-helium experiments when compared to the corresponding Brouillette experiment.

The structure of mix in incompressible Rayleigh-Taylor experiments is better known now with the continuing progress at Cambridge (Linden et. al.). In the paper by Kucherenko et. al., appeared a review of the extensive work performed at Chelyabinsk on a Rayleigh-Taylor apparatus driven by compressed gas with results for incompressible fluids similar to those from the Foulness rocket rig. Other Rayleigh-Taylor experiments with compressible gases are described by Meshkov and Nevmerzhitsky and by Zaitsev et. al. The experiments by Vassilienko lie in fact in the same category. From all of these RTI experiments one can obtain different asymptotic growth rates depending on compressibility or miscibility. These proceedings also include a paper by Rogatchov et. al. describing 2D experiments on the interaction of a gaseous detonation and a jelly layer.

Comments on high explosive driven experiments (P. Elias)

RTI and RMI experiments using high explosives as shock generator seem to interest most laboratories. Explosively-driven experiments (or gun-driven experiments with a flyer plate) can be performed without membrane in order to study the instability of liquid/liquid or liquid/gas interfaces. Three papers regarding cylindrical (Toque and Legrand) or planar geometries (Elias et. al. and Benjamin et. al., Phys. Fluids 30 (2), 1987) have been presented. During the experimental roundtable discussion, Dr. N. Inogamov presented experiments made in a spherical configuration for simulating a supernova explosion (see Anisimov et. al., Progress in Astronautics and Aeronautics Series, AIAA, 1983, v.87). No direct comparison of RMI and RTI results was made, but participants interested in such investigation may propose a future benchmark experiment.

Comments on laser driven experiments (P.A. Holstein)

In the field of Inertial confinement Fusion two kinds of experiments have been done:
-Ablation front instabilities experiments: usually they are devoted to the study of the exponential growth of a monomode perturbation imposed in a corrugated target.
-Interface instabilities experiments: they are devoted to the study of the turbulent mixing due to instabilities starting from the "natural" rugosity of the interface in a bilayer target.
The first kind of experiments use the face-on radiography of the target as main diagnostic (B.Remington's communication): it has good spatial and temporal resolutions. There is good agreement with Takabe's formula for the growth. Lasnex 2D simulations are in good agreement with the experimental results. The future experiments will be devoted to the study of the mode coupling and the saturation of the growth.
For the second kind of experiments, two diagnostics have been used: point-projection spectroscopy (LLNL and AWE) or emission spectroscopy (CEA-Limeil). The point-projection spectroscopy allows them to to deduce mix thickness. But the diagnostic is difficult to use and gives results with insufficient resolution. Moreover the results are difficult to process. So far, the emission spectroscopy must be improved to give quantitative results about the mix. In both cases the interpration is also difficult and is done with a k-ε model implemented in a hydrocode. However it seems clear now that the Richtmyer-Meshkov instabilities due to the shock passage plays a major role in the developpement of the mixing.
The major part of the physicists came up with the following ideas: first, to separate as much as possible Richtmyer-Meshkov and Rayleigh-Taylor instabilities. Secondly, to use as diagnostic the face-on radiography associated with a corrugated interface because this is the only diagnostic able to give the necessary resolutions for the time being. Two projects have been presented to study the mixing in these new conditions. For Richtmyer-Meshkov instabilities, a laser pulse with a sharp rise must be used (experiment proposed by G.Dimonte and K.Mikaelian from LLNL). A second diagnostic is planned: the side-on radiography with point X-ray source but also with a

source as short as possible: it could give informations on the mix thickness. On the other hand, to favour the Rayleigh-Taylor instabilities, a laser pulse with a gentle rise must be used (experiment designed by B.Remington from LLNL).

Concluding comments (Brad. Sturtevant)

The most notable aspect of experimental studies of R-M instability reported at this workshop was how closely the diagnostics and results from laser and shock tube experiments had come together in the last two years, despite the vastly different spatial, temporal and energy scales that they explore. This also holds true for the high-explosive driven experiments. That all three approaches are now using X-ray techniques to obtain quantitative data on mix will be a stimulus to further development of diagnostic methods and collaboration of scientists in these different fields.

With these developments there is now great potential for designing experiments to discover the important physical processes to be treated in theoretical and numerical models. It is hoped that this will ultimately lead to reduction of the gap between the parameters which are subject to experimental measurement and the parameters which are used in turbulence models.

The shock tube experiments do not seem to have realized all the potential for further development that was promised by results presented at the Pleasanton meeting. There were no reports of further development of planar light scattering and holographic methods. One might say that the "easy" work has been done (or possibly even that it already had been done 20 years ago after the pionneering experiments) and now there remains the more difficult (and expensive?) but rewarding job of carrying out research with new diagnostics and new facilities. Shock tubes used in RM experiments are still of small diameter, so boundary layer effects may obscure the results. This problem is especially serious because it is not known *a priori* in any given experiment whether the apparent layer thickness may be too great (due, say, to lack of instrumental dicrimination of boundary layer mixing) or too small (for example, caused by strain thinning by vortical structures). It is important that new experiments be carried out in larger facilities, of which they are several already in existence throughout the world. Additional benefits deriving from large scale experiments would be increased test time and a larger range of turbulent scales. More attention should be given to other possible large scale, possibly inconventional, experiments, such as the suggestion by E. E. Meshkov during this workshop of a huge water-air experiment at 1 g, to be held at a location where large amounts of water and power for pumping are available.

It is also extremely important that shock tube experiments be carried out at higher Mach number, to cover a larger range of excitation energies more representative of the applications. It is gratifying to see some new high Mach number experiments in progress. They will almost certainly exhibit some new, or at least more vigorous, physics. Increased mixing rates at higher Mach numbers will in

part compensate for limited test time in present experiments. Research at higher Mach number will substantially eliminate problems arising from use of membranes because materials can be used which will pyrolize or vaporize. This will eliminate the effects not only of membrane strength but perhaps also on fine scale roughness on membranes.

A PRELIMINARY REVIEW OF SOME NUMERICAL TEST PROBLEMS

prepared by Didier Besnard and Jean-François Haas
CEA, Centre d'études de Limeil-Valenton
94195 Villeneuve Saint-Georges Cédex

Abstract: We present the definition of the test problems suggested for the numerical round table of the Royaumont workshop and discuss some of the results provided by the participants to the numerical roundtable.

1-INTRODUCTION

The Royaumont Workshop was the third a series of such conferences about the physics of compressible turbulent mixing. What are the goals of such studies? The main one is to acquire a predictive capability about instability-induced mixing of different fluids. More precisely, this means that we need estimates about the mixing zone growth rate, as well as the velocity fluctuations energy that is produced during this interpenetration, as a precursor of turbulence. These diagnostics are related to the hydrodynamics of the flow. In contrast, flow patterns, and scales, are also crucial to understand, in view of coupling to other physical processes (combustion, ...). Therefore, a second important goal is to obtain accurate information about the details of the mixing patterns (fine mix versus coarse mix, two-field scales versus turbulent scales, ...). The question is: are we closer to these goals after this workshop ? To address this question, we present here some results chosen from the large number of diagnostics asked for the numerical roundtable. They exemplify both agreement for large scale patterns between different codes and discrepancies for small scale patterns (as expected, because most codes considered here solve Euler equations only).

2-TEST PROBLEMS

Eleven test problems were proposed. Among them, two addressed the problem of Rayleigh-Taylor instability induced mixing (one 2D simulation and one 1D mixing model calculation), and nine were simulations of Richtmyer-Meshkov instability in shock-tube experiments (low Mach number, high Mach number, 2D simulations and 1D turbulent mixing models calculations). The 2D simulations were to be performed with multimaterial codes treating Euler's equations and without turbulence models. The following reproduces the definition of the test problems sent to the prospective participants.

i/Rayleigh-Taylor induced mixing experiments:

The constant acceleration case was not considered among the test cases of the last worskhop (Pleasanton, CA, November 1989). The test problems TP1 and TP2 are based on 2D calculations described in /1/ and on the results of AWE experiments /2/ for the 1D turbulent model calculations (as originally proposed by D.L. Youngs /3/).

-Test Problem 1

Computational cell: $X_l = 0.$, $X_u = 1.75$ m, $Y_l = 0.$, $Y_u = 3.5$ m;
X-horizontal axis, Y-vertical axis
Suggested printing times: t = 1 10^{-3} s, 2 10^{-3} s, 3 10^{-3} s;
Suggested mesh: 100 x 200;
Equation of state, perfect gases with $\gamma_b = 1.4$ (air), $\gamma_a = 1.67$ (helium);
Gravitational acceleration: g = 0.25 m/msec^2 (about 2.55 10^4 Earth gravities), vertically downwards (1 msec = 10^{-3} s).

Interface definition:

$y = Y_u/2 + \Sigma_{k=5,10} A_k \sin(\nu_k(x-X_l) - \phi_k)$, $X_l \le x \le X_u$,

where $\nu_k = 2\pi k / (X_u - X_l)$, and A and ϕ are given by the following table:

	5	6	7	8	9	10
A(m)	-0.015435	0.00145	-0.021477	0.001488	-0.019203	-0.019989
ϕ(deg)	188.77	-100.4	224.38	233.97	148.9	311.15
ϕ(rad)	3.2947	-1.7521	3.9162	4.0835	2.5988	5.4306

Density and pressure stratification: isothermal about $Y = Y_u/2$, reference density of air $\rho_{b0} = 12.25\ 10^{-4}$ gcm^{-3}, reference density of helium $\rho_{a0} = 1.694\ 10^{-4}$ gcm^{-3}, ambient pressure $P_0 = 1.013$ bar (1 atm);

Spatial pressure and density distribution:

$\rho_a(y) = \rho_{a0} \exp(\beta_a (y-Y))$, $P_a(y) = c_{a0}^2 \rho_a(y) / \gamma_a$, $Y_u/2 \le y \le Y_u$,

$\rho_b(y) = \rho_{b0} \exp(\beta_b (y-Y))$, $P_b(y) = c_{b0}^2 \rho_b(y) / \gamma_b$, $Y_l \le y \le Y_u/2$,

$\beta_a = \gamma_a g / c_{a0}^2$, $c_{a0}^2 = \gamma_a P0 / \rho_{a0}$, $\beta_b = \gamma_b g / c_{b0}^2$, $c_{b0}^2 = \gamma_b P0 / \rho_{b0}$.

Suggested diagnostics:

-a plot of the x-averaged density versus y, for each time;
-same for the volume fraction of air;
-a plot of the mixed layer width versus time, where the layer is defined as the distance over which the x-averaged volume fraction varies from 5% to 95%;
-the value of the fluctuation part of the kinetic energy defined as $\overline{\rho u^2} - \left(\overline{\rho u}\right)^2 / \overline{\rho}$, where the bar indicates an average over x and y, ρ is the density, u is the y-directed velocity, calculated over the mixed region.
-a plot of the fluctuating energy, where the average is taken over x only, as a function of y, for each time (see test problems 3-11 for more details on this diagnostics, valid if one interchanges x and y);
-Interface position for each time;
-2D color and/or contour pressure plot for each time;
-2D color and /or contour density plot for each time;
-2D color and /or contour vorticity plot for each time;
-2D color and /or contour divergence of vorticity plot for each time.

Number of initial bubbles = 9 (information only);
Compressibility ($M^2 = \lambda_g / c_{b0}^2 \cong .42$ per bubble) (information only).

-Test Problem 2

a/ Two fluid problem:
fluid 1: $0 < x < 10$ cm, density ρ=1 g/cm^3;
fluid 2: $10 < x < 20$ cm, density ρ=3 g/cm^3;
Equation of state for both fluids is: $p = \frac{2}{3} \rho e$ where e is the internal energy.

Initial pressure gradient is such that $g = -\frac{1}{\rho}\frac{\delta p}{\delta x} = 5\ 10^4$ cm/s^2, about 51 Earth gravities, close to that obtained in some rocket-rig experiments. The problem has been calculated on a 1D compressible Lagrangian code with boundary conditions $p = 4\ 10^6$ baryes at the left of fluid 1 and $p = 2\ 10^6$ baryes at the right of fluid 2. The fluids are almost incompressible and the undisturbed region moves with acceleration close to g.

b/ Three fluid problem:

fluid 1: $0 < x < 10$ cm, density ρ=1 g/cm^3;

fluid 2: $10 < x < 11$ cm, density $\rho=\sqrt{3}$ g/cm^3;

fluid 3: $11 < x < 21$ cm, density ρ=3 g/cm^3;

same equation of state, boundary conditions (now on fluids 1 and 3) and acceleration.

Suggested diagnostics:

plots of volume fraction, turbulence kinetic energy k, its dissipation ε and length scale l at 0.06 sec., versus x, time evolution of mixing zone thickness, x integrated turbulence kinetic energy up to 0.07 sec.; mesh size suggested in /4/: $\Delta x = 0.5$ cm except for the intermediate layer (three fluid problem) for which $\Delta x = 0.25$ cm.

ii/ Low Mach number shock tube experiments:

In the Pleasanton workshop, some low Mach number shock tube experiments were simulated, and a number of results were discussed. They come from experiments with membrane (air-helium and air/SF6, planar interface /4/, single wave length /5/). A review has been presented at Royaumont and is described separatedly in these proceedings, but people still interested in simulating them were invited to do so. These test problems are denoted by TP3-6. A new test case (TP7) was proposed for Royaumont, corresponding to an experiment without membrane (SF6-air, planar interface /6/).

-Test Problem 3

x=0, mean position of the interface; W shock tube width

region 1: helium at rest (8.5 cm), left of interface, density = 0.0001694 g/cm^3, pressure = 1.013 10^6 baries, $\gamma = 1.67$;

region 2 : air at rest, density = 0.001225 g/cm^3, pressure = 1.013 10^6 baries, $\gamma = 1.4$;

region 3 : shocked air, velocity = 12.29 cm/ms, Mach = 1.24, density = 0.0017285 g/cm^3, pressure = 1.6482, $\gamma = 1.4$.

a/ 2D simulations

Initial interface: single wavelength perturbation $x = 0.24 \cos 2\pi\ 2y/W$, where W =7.5 cm.

For comparison use t=0 when the incident shock reaches x=0; Outputs close to 0.12, 0.22, 0.32 ms; Boundary conditions: at Xmax, applied pressure = 1.6482 bar, at Xmin, Ymin, Ymax rigid wall (zero normal velocity); Suggested initial mesh: square cells, size 0.25 mm in the mixing zone.

b/ 1D models

For comparison use t=0 when the incident shock reaches x=0; Boundary conditions: at Xmax, applied pressure = pressure of shocked fluid, at Xmin rigid wall (zero normal velocity); suggested initial mesh: 2.5 10^{-5} g/cm^2/cell.

-Test Problem 4

same as for TP3, except for initial interface perturbation.

initial interface perturbation at x=0: multiple wavelength perturbation $x = \sum a_n \cos 2\pi ny/W$, (n,a_n) = (0.5,0.05), (1.5,0.10), (2.,0.07), (3.5,0.11), (5.5,0.09).

-Test Problem 5

region 1: SF6 at rest (10 cm), density = 0.006187 g/cm^3, pressure = 1.013 10^6 baries, $\gamma = 1.06$;

region 2 : air at rest, density = 0.001225 g/cm^3, pressure = 1.013 bar, $\gamma = 1.4$;

region 3 : shocked air, velocity = 15.95 cm/ms, Mach = 1.32, density = 0.0019 g/cm^3, pressure = 1.8993 10^6 baries, $\gamma = 1.4$.

a/ 2D simulations

Initial interface perturbation at x=0: single wavelength perturbation $x = 0.24 \cos 2\pi 2y/W$, W=11.3 cm.

For comparison use t=0 when the incident shock reaches x=0; Outputs close to 0.70, 1.10, 1.65 ms; Boundary conditions: at Xmax, applied pressure = 1.8993 bar, at Xmin, Ymin, Ymax rigid wall (zero normal velocity); Suggested initial mesh: square cells, size 0.25 mm in the mixing zone.

b/ 1D models

For comparison use t=0 when the incident shock reaches x=0; Boundary conditions: at Xmax, applied pressure = pressure of shocked fluid, at Xmin rigid wall (zero normal velocity); suggested initial mesh: 2.5 10^{-5} g/cm^2/cell.

-Test Problem 6

same as for TP5, except for initial conditions.

initial interface perturbation at x=0: multiple wavelength perturbation $x = \sum a_n \cos 2\pi ny/W$, (n,a_n) = (0.5,0.05), (1.5,0.10), (2.,0.07), (3.5,0.11), (5.5,0.09).

-Test Problem 7 (1D)

region 1: air at rest (13.2 cm), density = 0.001225 g/cm^3, pressure = 1.013 bar, γ = 1.4;

region 2 : SF6 at rest, density = 0.006187 g/cm^3, pressure = 1.013 bar, $\gamma = 1.06$;

region 3 : shocked SF6, velocity = 9.725 cm/ms, Mach = 1.45, density = 3.427 10^{-3} g/cm^3, pressure = 2.07 10^6 baries, $\gamma = 1.06$.

Initial conditions

Initial width of molecular diffusion zone, based on volume fraction between 5% and 95% = 1.7 cm.

iii/ High Mach number shock-tube experiments:

Numerical diagnostics, for test problems 3-11:

a/ 2D simulations

-a plot of the y averaged density versus x, for each time (indicated in the initial problem definition);
-same for the volume fraction of the gas in region 1;
-a plot of the mixed layer width versus time, where the layer is defined as the distance over which the y averaged volume fraction varies from 5% to 95%;
-the value of the fluctuating part of the kinetic energy (FKE) defined as $\overline{\rho u^2} - \left(\overline{\rho u}\right)^2 / \overline{\rho}$,

where the bar indicates an average over x and y, ρ is the density, and u is the x directed velocity, calculated over the mixed layer.
-a plot of the fluctuating energy, where the average is taken over y only, as a function of x, for each time.

In a second mailing sent to the prospective participants (titled corrections to the numerical diagnostics, yet with some errors), the y only averaged FKE was specified as $R_{uu}+R_{vv}$ where the R's are the components of the fluctuations energy tensor. It should be:

$$R_{uu}+R_{vv} = \overline{\rho(u^2+v^2)} - \frac{\left(\overline{\rho u}\right)^2}{\overline{\rho}} - \frac{\left(\overline{\rho v}\right)^2}{\overline{\rho}} ,$$

where $\overline{\ }$ denotes the y-averaging, i.e.: $\overline{f} = \frac{1}{W}\int_0^W f\, dy$.

Note that $R_{uu}+R_{vv} = 2\,\overline{\rho}\,k$, where k is the fluctuations kinetic energy.

Its *integrated* value over the mixing zone is defined as: $FKE = \int_{MZ} \overline{\rho}\, k\, dx$.

Defining the directed energy in the mixing zone as: $DKE = \frac{1}{2}\int_{MZ} \overline{\rho}\, U^2\, dx$,

where U is the density averaged velocity $\overline{\rho u}\,/\,\overline{\rho}$, an additional variable of interest is the nondimensional ratio FKE/DKE, which is analogous to the ratio used for theoretical estimates of the turbulent energy produced by the interaction of a shock and a random interface.

-a 2D plot of density for each time;
-a 2D plot of pressure for each time;
-a 2D plot of vorticity for each time;
-a 2D plot of the divergence of velocity for each time.

b/ 1D models

-Mixing zone thickness and integrated turbulent kinetic energy versus time.
-profiles of the concentration of the gas in regions 2 and 3, the turbulent kinetic energy k, and its dissipation rate ε, for each output time.

Suggested units are in cgs, i.e. pressure in baryes, densities in gcm^{-3}, k in $(cm/s)^2$, $R_{uu}+R_{vv}$ (y averaged) in baryies, erg/cm^3 or $g\,cm^{-1}s^{-2}$ for the space profiles. For the time

Behind low Mach number shocks, the flow is subsonic and in some cases incompressible. The next step is to look at compressibility effects, due to the higher velocity of the gas flow obtained behind higher Mach number shock waves. The simulations are based on planar interface (argon-helium and helium-argon) experiments /7/, while retaining the same definition of interface geometry as for the low Mach simulations. The test problems are denoted by TP8-11.

-Test problem 8 (see figures 3 a and 3 b)

region 1: helium at rest (37 cm), density = $8.317\ 10^{-5}$ g/cm^3, pressure = $5.065\ 10^5$ baries, $\gamma = 1.67$;

region 2 : argon at rest, density = $8.317\ 10^{-4}$ g/cm3, pressure = $5.065\ 10^5$ baries, $\gamma = 1.67$;

region 3 : shocked argon, velocity = $7.5485\ 10^4$ cm/s, Mach = 3.45, density = $2.6495\ 10^{-3}$ g/cm3, pressure = $7.4143\ 10^6$ baries, $\gamma = 1.67$.

Initial interface: single wavelength perturbation $x = 0.24 \cos 2\pi\ 2y/W$, where W=8 cm.

For comparison use t=0 when the incident shock reaches x=0; Output times 230 microseconds, 300 microseconds, and 400 microseconds; Boundary conditions: at Xmax, applied pressure = $7.4143\ 10^6$ baries, at Xmin, Ymin, Ymax rigid wall (zero normal velocity); suggested initial mesh: square cells, size 0.25 mm in the mixing zone.

For 1D models, no initial perturbation.

-Test problem 9

same as for TP8, except for initial interface perturbation.

initial interface perturbation at x=0: multiple wavelength perturbation $x = \sum a_n \cos 2\pi\ ny/W$, (n,a_n) = (0.5,0.05), (1.5,0.10), (2.,0.07), (3.5,0.11), (5.5,0.09).

-Test problem 10 (see figures 8 a and 8 b)

region 1 : argon at rest (37 cm), density = $8.317\ 10^{-4}$ g/cm3, pressure = $5.065\ 10^5$ baries, $\gamma = 1.67$;

region 2: helium at rest, density = $8.317\ 10^{-5}$ g/cm3, pressure = $5.065\ 10^5$ baries, $\gamma = 1.67$;

region 3 : shocked helium, velocity = $1.8198\ 10^5$ cm/s, Mach = 2.77, density = $2.3861\ 10^{-4}$ g/cm3, pressure = $4.7344\ 10^6$ baries, $\gamma = 1.67$.

Initial interface perturbation at x=0: single wavelength perturbation $x = 0.24 \cos 2\pi\ 2y/W$, W=8 cm.

For comparison use t=0 when the incident shock reaches x=0; Output times 340 microseconds, 380 microseconds, and 500 microseconds ; Boundary conditions: at Xmax, applied pressure = $4.7344\ 10^6$ baries, at Xmin, Ymin, Ymax rigid wall (zero normal velocity); suggested initial mesh: square cells, of size 0.25 mm in the mixing zone.

-Test problem 11

same as for TP10, except for initial conditions.

initial interface perturbation at x=0: multiple wavelength perturbation $x = \sum a_n \cos 2\pi\ ny/W$, (n,a_n) = (0.5,0.05), (1.5,0.10), (2.,0.07), (3.5,0.11), (5.5,0.09).

evolutions, FKE integrated over the width of the mixing zone is in g s^{-2} or erg/cm^2 while FKE averaged over the mixing zone width is in g $cm^{-1}s^{-2}$.

Other recommendations for the round table

Each corresponding simulation could be performed either with a 2D code or a 1D model, or both. To provide a theoretical basis for comparison of the results, a short presentation of each 2D code (10 mn) was asked to each participant, followed by the presentation of the results, in a predetermined format (10 mn). Regarding turbulence models, it was proposed that each participant makes a short presentation of his model, his choice of coefficients, and his initialization procedure.

This set of test problems was too large to be performed by each participant to the round table. Due to the short duration of the round table (3 hours), we proposed to limit the number of test problems for discussion during the round table to TP1, TP2, TP9, and TP11. However, we strongly suggested to use the TP definitions given here for additional calculations, to enhance the quality of the comparison between codes. Participants were of course encouraged to present their results also as posters.

To maximise the effectiveness of these comparisons, it seemed crucial to present numerical diagnostics in a predetermined format. That is why, we suggested that, apart from paper copies of the figures, participants furnish a floppy disk of their data. This would ease the task of processing all the data to extract significant figures. A possible choice of software and microcomputer could be Cricket Graph , and Macintosh.

3- A COMPARISON OF SOME TEST PROBLEMS

As suggested by the organizers, the participants to the numerical round table provided a lot of data: color maps of pressure, density, vorticity and compression, streamwise profiles of spanwise averaged density, pressure, volume or mass fraction and $R_{uu}+R_{vv}$ as well as the time evolution of the mixing zone thickness and its FKE (the kinetic energy of the velocity fluctuations). Some of this data was provided in the form of files, in order to superimpose on the same figure results from different codes, but because of time constraints from our part, we are only able at this time to juxtapose in a much reduced format some of the black and white figures. The comparisons shown here are sketchy: rather straightforward for density, pressure or volume fraction profiles as well as mixing zone width but more difficult for FKE because of different choices of dimension and unit.

-Test problems 1-2

Results from TP1 calculations performed by Bell and Marcus (BM, see paper by Marcus et. al.) and Glimm (G, FTM code, see paper by Glimm et. al.) are given in figures 1 and 2. Figures 1 a, b, c are density contours obtained by BM at time 1, 2 and 3 ms, while figures 1 d, e, f, g are interface plots from G at 0, 1, 2 and 3 ms. Window size for BM and G is 0-1.75 m in the horizontal direction, 0-3.5 m in the vertical dimension for BM. The evolutions of the width of the mixed region versus time appearing on figs. 1 h (BM, scales 0-3.2 ms and 0-0.8 m) and 1 i (G, scales 0-3 ms and 0-1 m) differ slightly: at 3 ms: they are respectively 0.7 and 0.83 m.

Space profiles of spanwise (x)-averaged density (window size 0.95-2.6 m and 0-0.9 kg/m^3), averaged fluctuating kinetic energy (window size 0.95-2.6 m and 0-18 kJ/m^3) and volume fractions (window size 1.2-2.3 m and 0-1) from BM for the three instants are shown on figures 2 c, d and e. The corresponding profiles from G are given on figures 2 f, g, h (averaged density in 10^{-4} g/cm^3), 2 i, j, k (FKE integrated over the span in x and cell size in z, unit kJ/m) and 2 l, m, n (volume fraction). There is an approximate agreement between the shapes of those profiles (but BM is smoother than G). Multiplying the FKE values from BM profiles by 1.75 m

times 0.0175 m (= 0.0306 m^2) brings them closer to the coresponding values from G: for instance at 2 ms, peak FKE from BM, 13.5 kJ/m^3 times 0.0306 m^2 yields 0.413 kJ/m which is close to the peak of the Ef profile from G: 0.4 kJ/m.

The evolutions of fluctuating kinetic energy FKE (averaged over the mixing zone) versus time for BM (fig. 2 a, scales 0-3.2 ms and 0-1.75 10^{-3} kg/m ms^2 or 1.75 kJ/m^3) and (integrated over the mixing zone) for G (fig. 2 b, scales 0-3 ms and 0-0.06 kJ) are similar. To reconciliate the units and compare the two calculations, the BM values should be multiplied by the mixing zone volume: a product of the span (1.75 m), the mixing zone width and the cell size (1.75 cm). For instance, at 3ms: 1.6 kJ/m^3 from BM multiplied by 0.0306 m^2 times 0.7 m (width) becomes 0.0343 kJ to be compared to 0.053 kJ from G.

TP2 calculations (using turbulence models) performed by Spitz and Haas and by Neuvazhaev are described elsewhere in these proceedings. Let us just notice a descrepancy between the mixing zone width for the two fluids problem at 50 ms: from Neuvazhaev's fig. 3, h = 5.5 cm (versus 7.6 cm quoted for Youngs) and from Spitz & Haas figs. 4 and 5, $h = h_1 (1+\beta) = 8.4$ cm.

-Test problems 3-7

TP3-6 will not be described here as they were treated in Pleasanton and partly analysed in the corresponding review enclosed in the present proceedings (by Besnard, Glimm et. al.). Note these calculations were also performed for the Royaumont workshop by other participants: 1D calculations for all test problems by Kramer and Dairiki (Lagrangian hydro calculation with dynamic mix model from W.P. Crowley, not published in these proceedings), 2D simulations by Anuchina and Volkov (see their paper) and Bell and Marcus (TP3, AMR code). There is good agreement between the two-dimensional codes as far as the averaged quantities are concerned. 2-D plots also show the same general features with differences only on the small details.

TP 7 was approximately treated in the paper by Cavailler et. al. in /6/ (initial length of air: 13.2 cm) and in these proceedings (initial length: 31 cm). No comparison was possible since no other calculations were presented of this problem.

-Test problems 8-11

We will discuss in more details the results from the comparison of the high Mach number 2D simulations: TP8-9 on figures 3-7 and TP10-11 on figures 8-12. The results shown here are from Haas and Besnard (EAD code from CEL-V), Macé (GAD code from CEL-V), V. Rupert (VR, AMR code from LLNL), M. Wehner (MW, LLNL) and Bell & Marcus (BM, AMR code, LLNL). TP9 and TP11 were also calculated by Donald Griswold (DG, CALE code, LLNL).

The definition of TP8-9 is recalled on figs. 3 a, b from VR. The interface plots calculated by MW (figs. 4 a, b, c for TP8 and figs. 4 d, e, f for TP9) are representative of most calculations. Some slight differences between the two initially identical waves are noticeable at late time (fig. 4 c, also observed in the EAD results). Some details on the interface vary from code to code and depend on the numerical scheme or the mesh size for a given code (eg. EAD, between cell size 0.5 mm and 0.29 mm) and this influences slightly some of the large scale data such as mixing zone width. For the GAD code, horizontal cell size varies from 0.5 mm at end wall to 0.9 mm at interface, vertical cell size is 0.5 mm.

In spite of some differences in mesh size and in the definition of the mixing zone thickness, there is good agreement between EAD and GAD for TP8 as far as the mixing zone trajectory is concerned (fig. 5 f). Note that for EAD and GAD, one has to substract 37 cm to the space variable x and 27 10^{-6} sec. to the time. The corresponding trajectories obtained by VR

for TP 8 and 9 are shown on figs. 5 g and 5 h. For TP8-9, the effect of the incident shock is to accelerate the interface and change its phase, while the reflected shocks slow down the interface and excite the instability growth rate.

Density profiles (in g/cm^3) for TP8-9 from VR at 0.23, 0.3 and 0.4 ms are shown on figs. 3 c, d, e, on figs. 5 a,b from MW for TP8 and TP9 respectively and on fig. 5c for TP8 from GAD. Fig. 5 d is the averaged pressure profile from GAD (TP8).

FKE or $R_{uu}+R_{vv}$ profiles (in erg/cm^3 or g/cm s^2 or baryes) at 0.23, 0.3 and 0.4 ms are shown on figs. 3 f, g, h from VR (TP8-9), on fig. 5 e from GAD (TP8) and on fig. 6 from EAD (TP8: a 228 μs, b 303 μs, c 403 μs; square cell size 0.29 mm and TP9: d 233 μs, e 303 μs, f 403 μs; square cell size 0.5 mm). A comparison of the shapes of FKE profiles from VR, EAD and GAD shows that the absissa of the maximum are close while the values at maximum obtained by VR are above those from EAD and GAD, presumably because of their coarser cell size. There are significant differences between the details of the profile shapes.

The mixing zone thickness from BM (TP8-9, fig. 7 a), VR (TP8, fig. 7 b and TP9, fig. 7 c), MW (TP8, fig. 7 d) and EAD (TP8-9, fig. 7 f, cell size 0.29 and 0.5 mm respectively) show similar evolutions. In the single mode case (TP8) maximum thickness just before reshock compression are between 3 and 3.1 cm for all codes while in the multimode case (TP9), maximum thickness is 3.6 cm for VR but only 2.6 cm for EAD, 2.7 cm for BM and 2.3 cm for DG.

FKE evolutions are more difficult to compare: the EAD results in erg/cm^2 or g/s^2 units shown in log scale (fig. 7 g) are integrated over the thickness of the mixing zone while the BM results (fig. 7 e) in linear scale expressed in g/cm ms^2 are averaged. To reconciliate the units, the BM results should be multiplied by 10^6 times the mixing zone width in cm. Thus, peak FKE at reshock time (0.24 ms) for TP8 are: from BM 6.45 10^6 g/s^2 (2.15 10^6 g/cm s^2 times 3 cm) versus 2.5 10^6 g/s^2 (EAD, 0.5 mm) and 2.8 10^6 g/s^2 (EAD, 0.29 mm and GAD). For TP9, peak FKE at reshock are 4.725 10^6 g/s^2 (BM, 1.75 10^6 g/cm s^2 times 2.7 cm) and 1.5 10^6 g/s^2 (EAD, 0.5 mm). These significant differences cannot be explained by mesh size alone.

The definition of TP10-11 is given on figs. 8 a, b from VR. The interface plots calculated by MW (figs. 9 a, b, c for TP8 and figs. 9 d, e, f for TP9) are similar to other calculations (except at the last time), with perhaps some more differences for MW between the two initially identical waves at late time (TP10, fig. 9 c).

The mixing zone trajectory in the t-x diagram from VR for TP10 (fig. 10 f) can be compared to the corresponding ones from EAD (lines, 0.5 and 0.29 mm cells) and GAD (points, horizontal cell size decreasing from 0.7 mm at end wall to 0.4 mm at the initial interface position, vertical cell size 0.5 mm) seen on fig. 10 h. Note that the mixing zone was defined by mass concentration thresholds (5-95%) for EAD and volume fraction thresholds (5-95%) for GAD and other codes and that for EAD and GAD, one has to substract 37 cm to the space variable x and 11 10^{-6} sec to the time. Fig. 10 h shows significant differences at late time between the three TP10 calculations whereas the mixing zone trajectories for the TP8 calculations did not differ much (fig. 5 f). In TP10-11, this is probably due to the change of sign of the mean interface velocity at reshock time and the complicated phase inversion which follows.

Averaged density profiles (in g/cm^3) at the three prescribed times (0.34, 0.38 and 0.5 ms) appear on figs. 8 c, d, e (TP10, VR), fig. 10 a (TP11, BM), fig. 10 b (TP10, BM) and fig. 10 c (TP 10, GAD). Fig. 10 d is an averaged pressure profile from GAD (TP10).

FKE profiles (in g/cm s^2) for TP10 from GAD appear on fig. 10 e and on figs. 8 f, g, h from VR. On fig. 11 are FKE profiles from EAD at approximately the three prescribed times

(337 μs, a, d; 381 μs, b, e; 509 μs, c, f) for TP 10 (a, b, c, square cell size 0.29 mm) and TP11 (d, e, f; square cell size 0.5 mm). The comparison of the shapes of FKE profiles for TP10 from VR, EAD and GAD again shows that the absissa of the maximum are close while the values at maximum obtained by VR are significantly higher than those from EAD and GAD, with the least difference at the intermediate time: 0.38ms.

Plots of time evolution of mixing zone thickness shown on figs. 12 a (BM, TP10-11), 12 b (VR TP10), 12 c (MW TP10) and 12 f (EAD, TP10-11) are similar. For TP10, the maximum widths just before the reshock phase are 4.45 cm (VR and BM), 4.85 cm (GAD) and 5 cm (EAD and MW). For TP11, they are again 4.45 cm for BM, 5 cm for EAD and DG (but not corresponding to a maximum).

The late time differences between EAD and GAD mixing zone widths result in differences for FKE (integrated over the mixing zone) shown on fig. 10 g (units: erg/cm^2 or g/s^2 in log scale). This also appears in the dimensionless ratio: FKE/DKE (fig. 12 d, continuous line: 0.29 mm EAD) where DKE is the kinetic energy of the mixing zone in horizontal motion (thus FKE/DKE is analogous to a turbulent intensity). The time evolution of FKE (averaged over the mixing zone width) from BM (units g/cm ms^2 in linear scale, fig.12 e) can be compared with the EAD and GAD results (units erg/cm^2 or g/s^2, log scale, figs. 12 g and 10 g) after multiplying the BM results by 10^6 times the mixing zone width in cm. The peak value of FKE for TP10 at reshock time (0.345 ms) yields: 2.07 10^7 g/s^2 (4.65 10^6 g/cm s^2 times 4.45 cm, BM), 3.2 10^6 g/s^2 (EAD) and 3.8 10^6 g/s^2 (GAD). For TP11, these quantities are: 1.67 10^7 g/s^2 (3.75 10^6 g/cm s^2 times 4.45 cm, BM) and 2.2 10^6 g/s^2 (EAD). These differences may point out to another discrepancy in averaging definition.

4- CONCLUSIONS

From a practical point of view, there is still a need to normalize the averaging techniques and choice of units for the kinetic energy outputs, and to display the results in such a way that they can be plotted together. The high Mach number test problems (TP8-11) have proved to be more trying for the codes than the low Mach number ones (TP3-6), mainly because the conditions (higher flow velocity and longer travel distances) made the instabilities much more violent. The more general goals stated in the introduction will not be discussed here and we refer the reader instead to the conclusion of the Pleasanton numerical roundtable and to the concluding remarks from Alan Spero (all in these proceedings). We thank those who have proposed test problems, who have carried out the calculations for the roundtable and finally Viviane Rupert for her suggestions on this review.

REFERENCES

1- J. Glimm et al, LA-UR-3530.
2- K.I. Read, Physica **12D**, (1984), 45-58.
3- D.L. Youngs, Physica **37D**, (1989) 282-283.
4- M. Brouillette and B. Sturtevant, Physica **37D** (1989) 248-263.
5- R. Benjamin, proceedings of Princeton (Oct. 1988) and Pleasanton (Nov. 1989) meetings.
6- C. Cavailler et al., AIP Conference Proceedings **208**, (1990) 564 and CHOCS **2**, 70-88.
7- S.G. Zaitsev et al., Tep. Vys. Temp., **23**, 3, (1985) 535-541; Sov. Phys. Dokl. **30**, 7, (1985) 579-581; R-M instability of single mode interfaces are also described in these proceedings.

Figure 1 : TP1: two dimensional simulations of the Rayleigh-Taylor Instability.

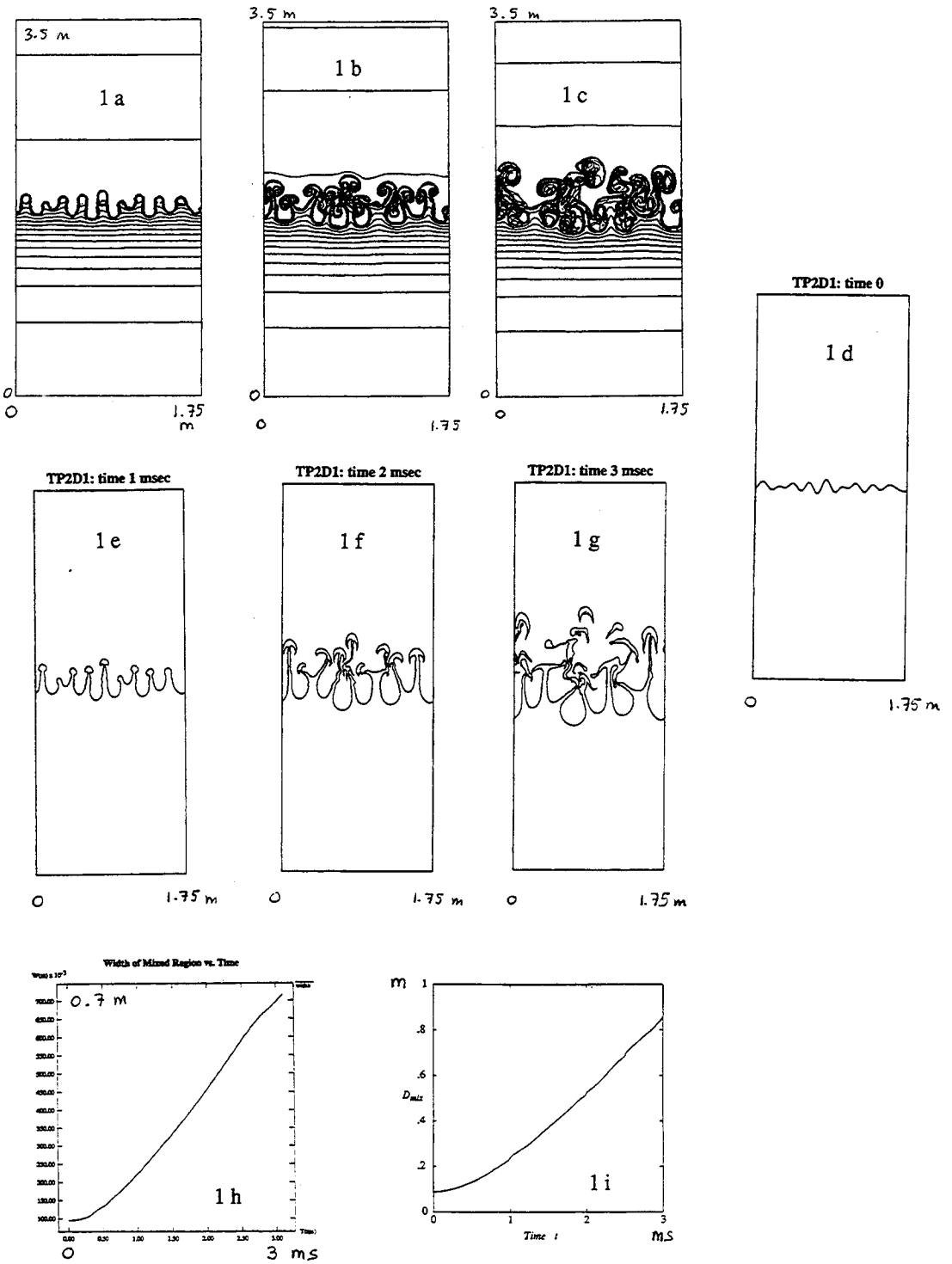

Figure 2 : TP1: two dimensional simulations of the Rayleigh-Taylor Instability.

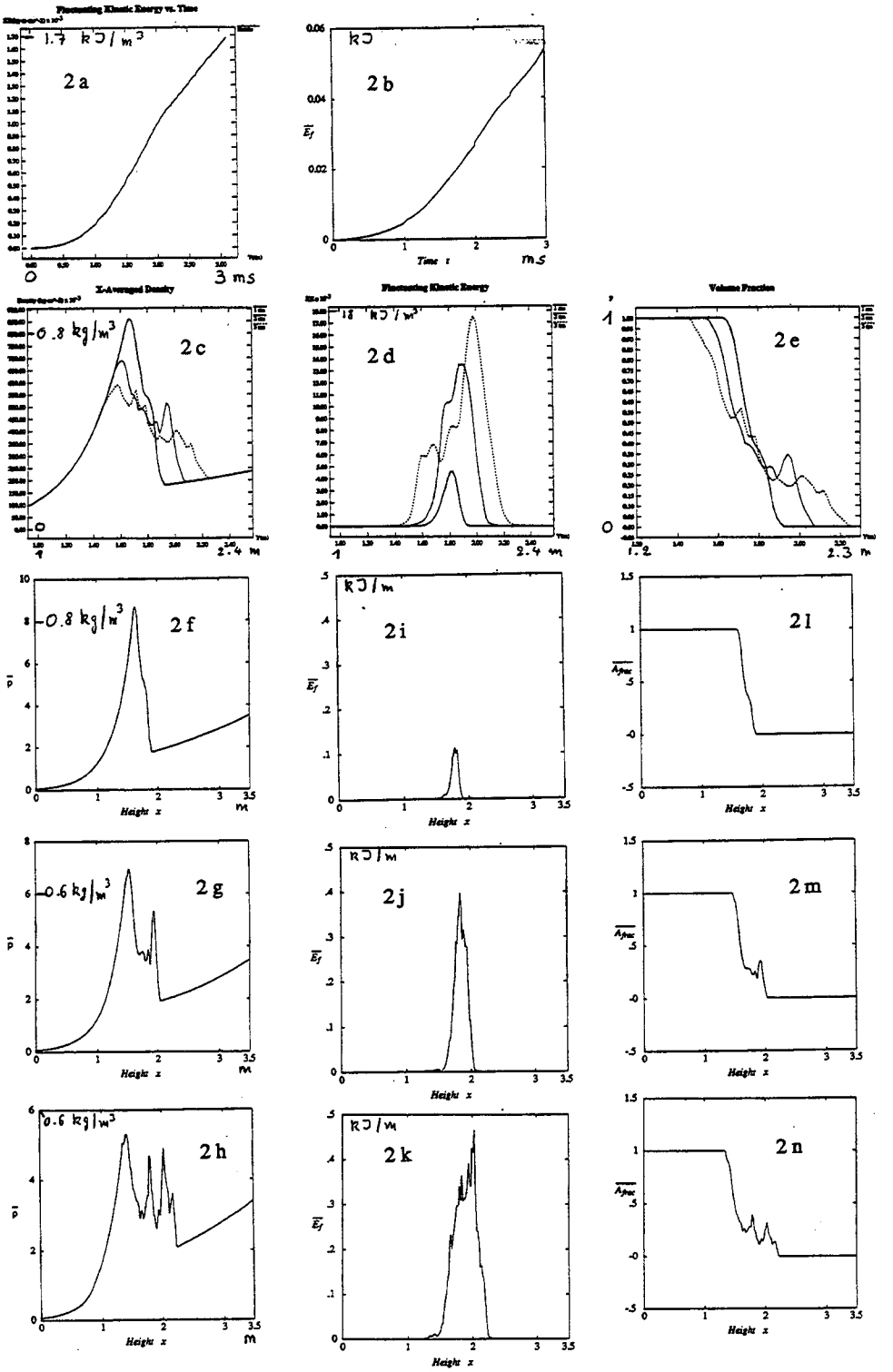

Figure 3 : TP8-9: Richtmyer-Meshkov Instability (from V. Rupert).

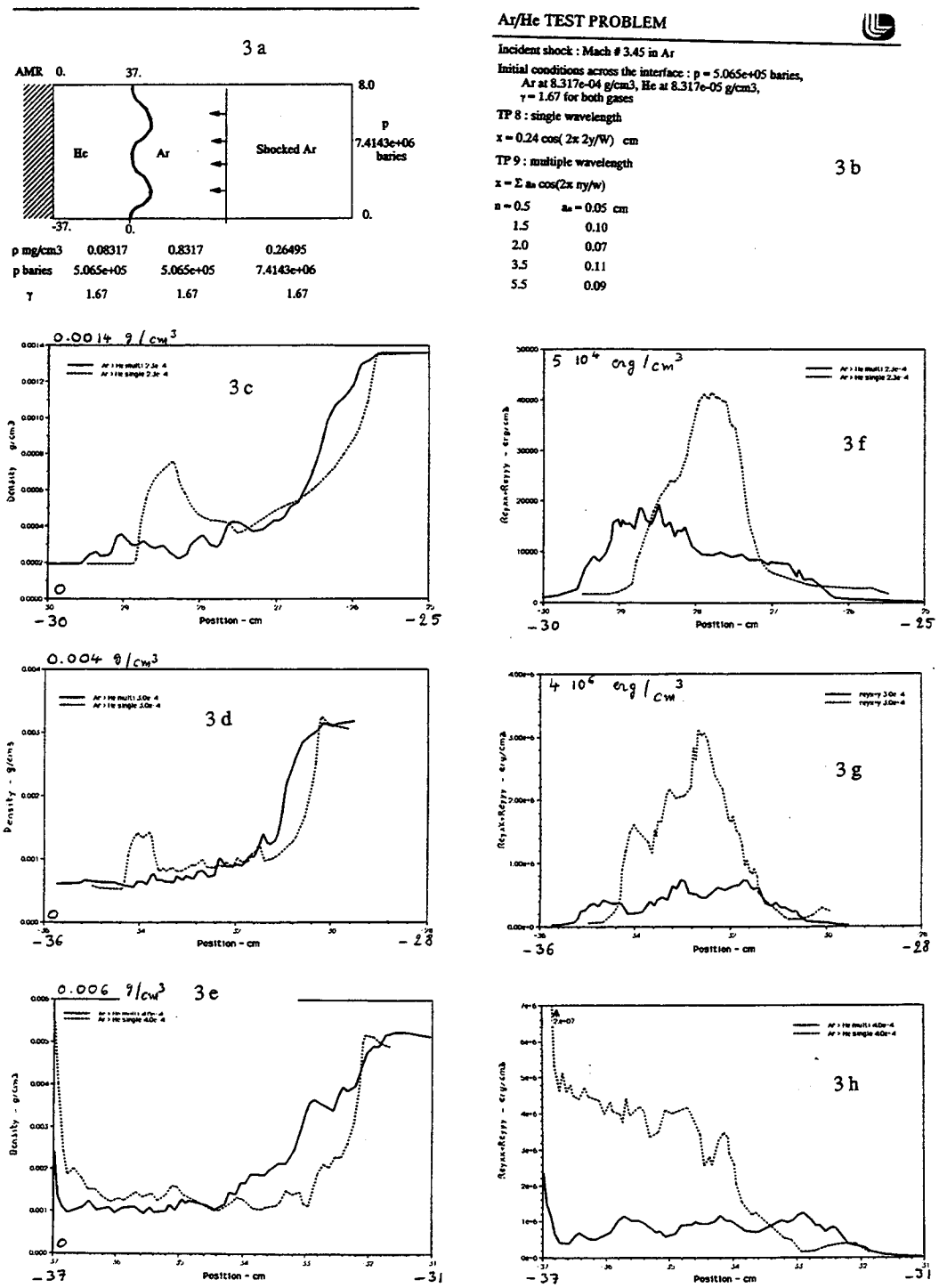

TP8 **Figure 4 : TP8-9: Interface plots (from M. Wehner).** TP9

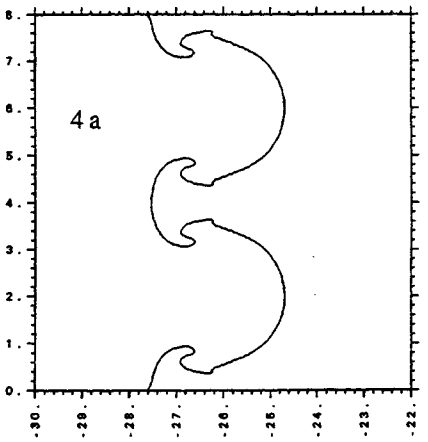

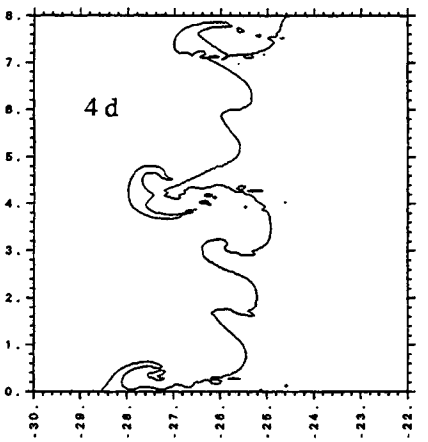

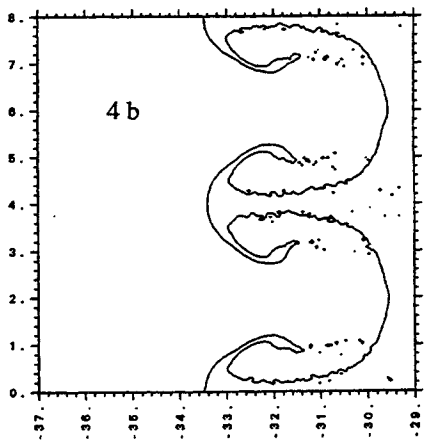

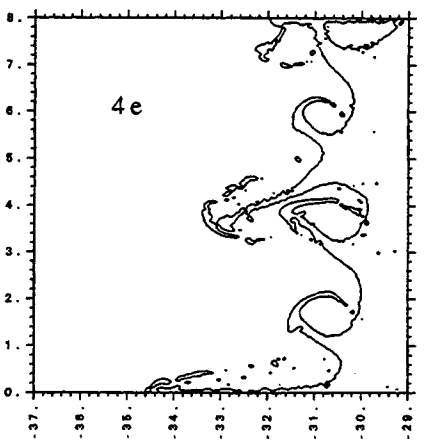

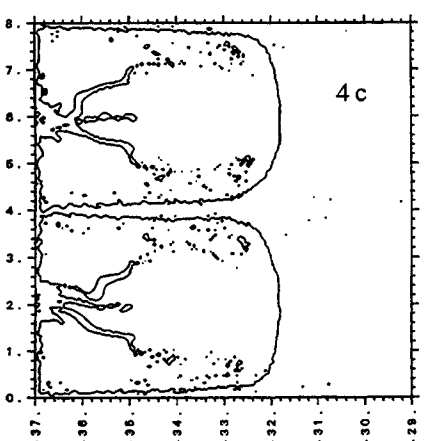

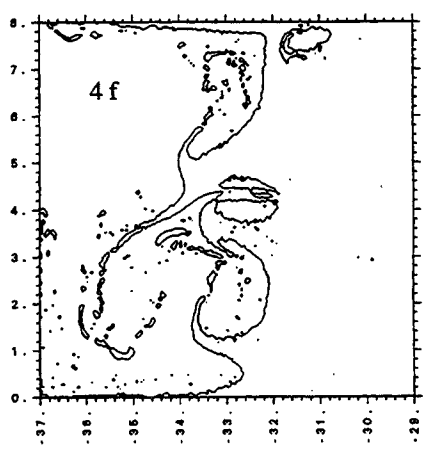

Figure 5 : TP8-9

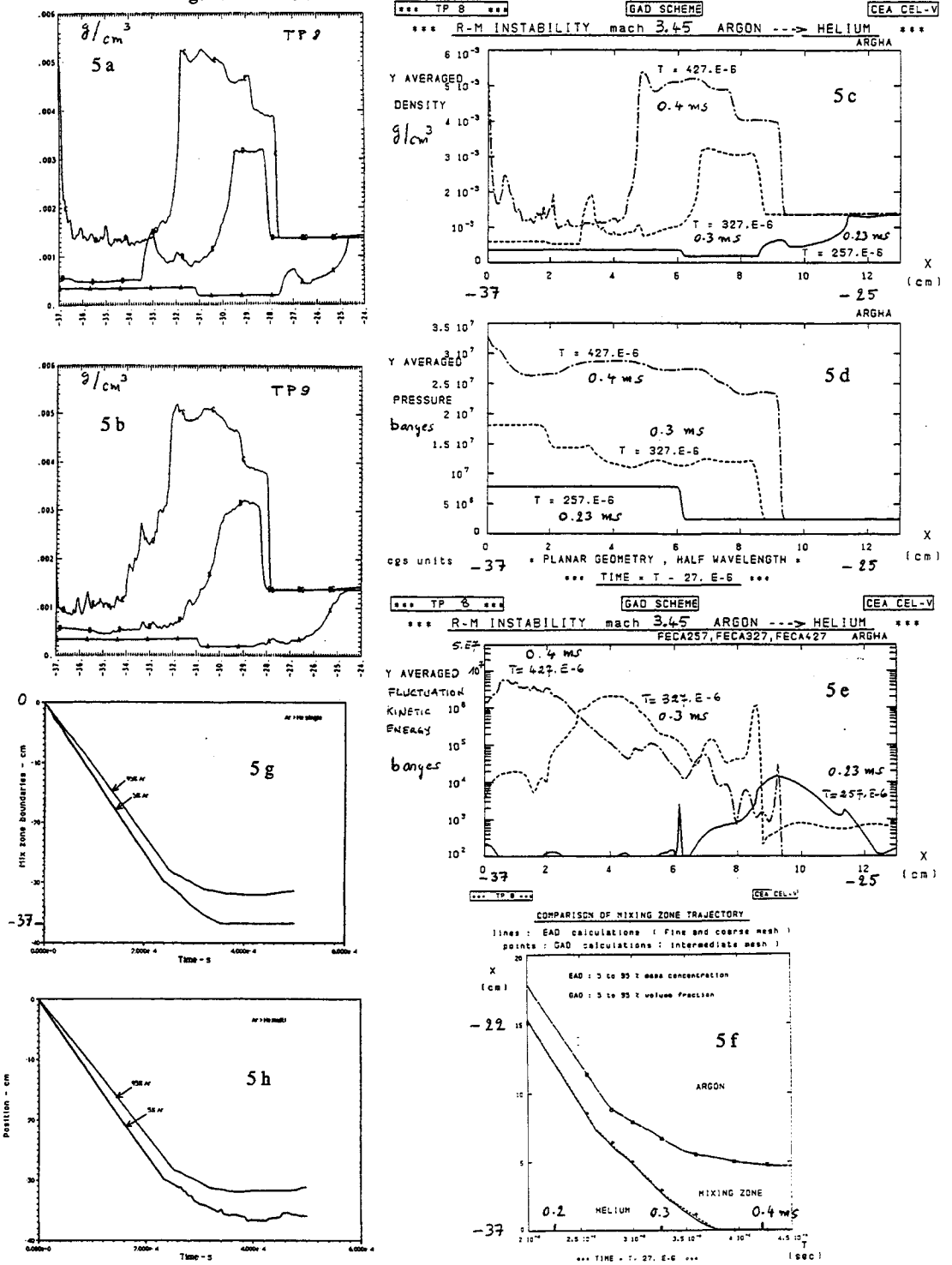

TP8 **Figure 6:** FKE profiles from EAD TP9

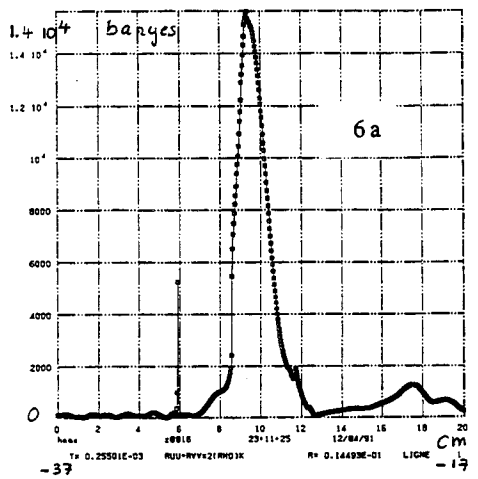

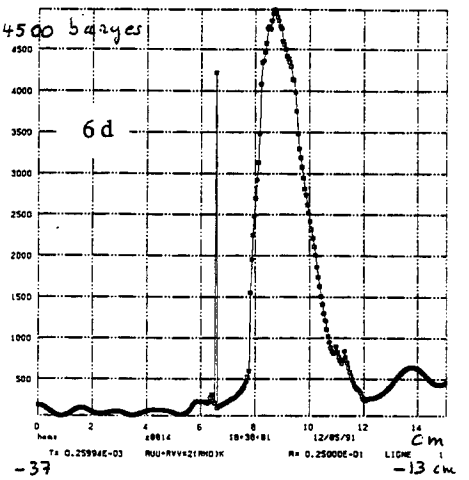

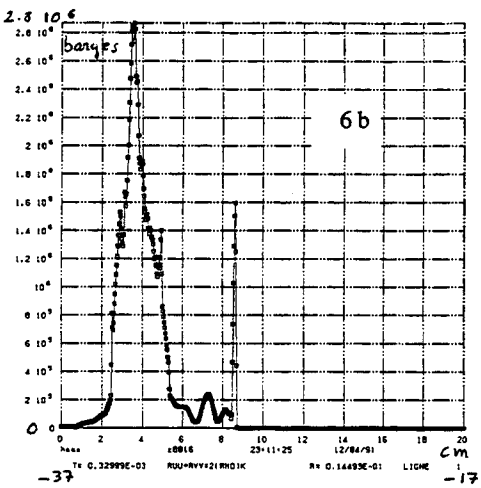

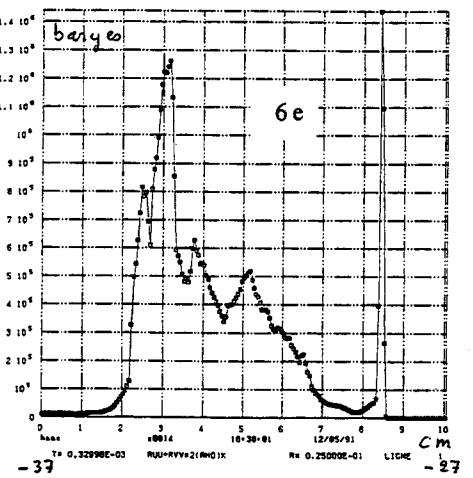

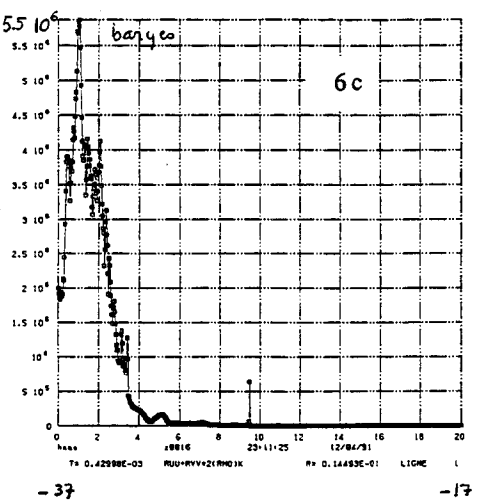

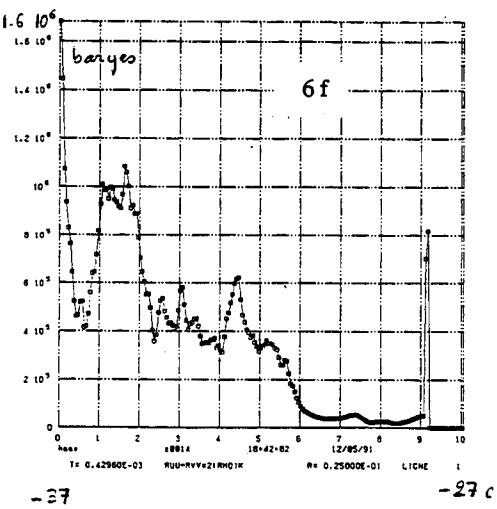

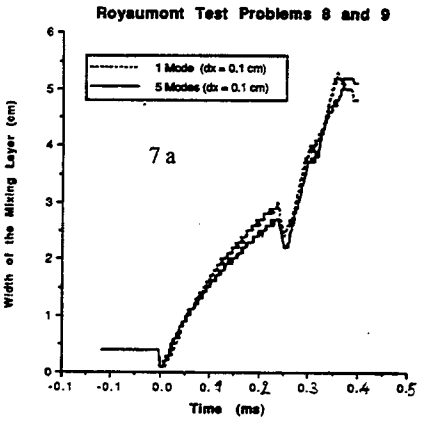

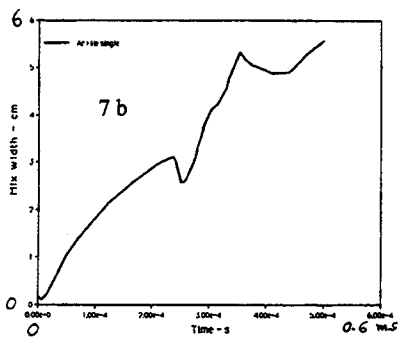

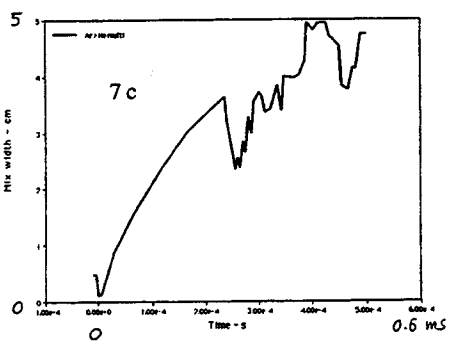

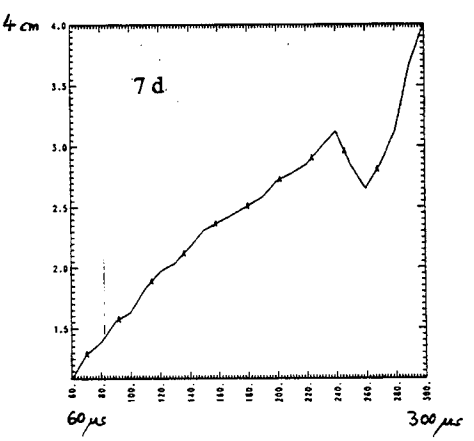

Figure 7: TP8-9 : time evolution of mixing zone width and of FKE

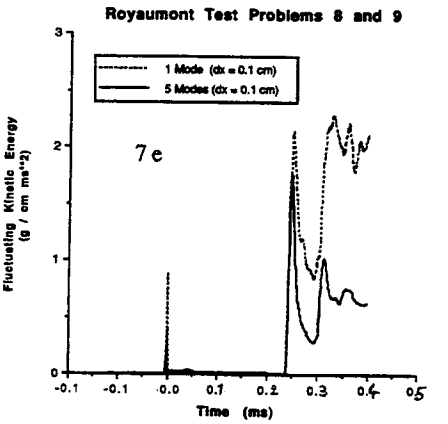

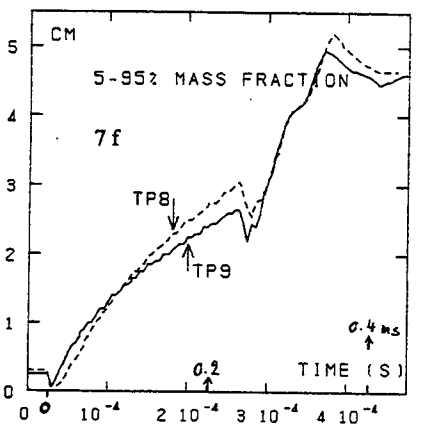

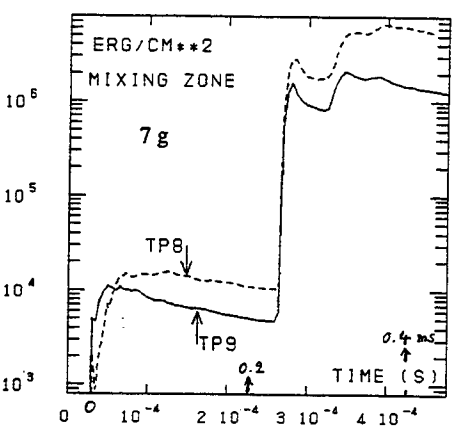

Figure 8 : TP10-11: Richtmyer-Meshkov Instability (from V. Rupert).

PROBLEM DEFINITION : He/Ar

8 a

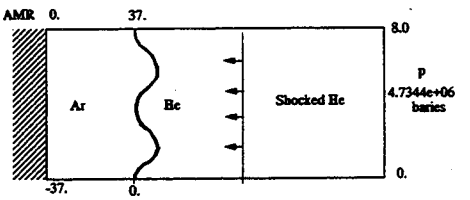

ρ mg/cm3	0.8317	0.08317	0.23861
p baries	5.065e+05	5.065e+05	4.7344e+06
γ	1.67	1.67	1.67

He/Ar TEST PROBLEM

Incident shock : Mach # 2.77 in He

Initial conditions across the interface : p = 5.065e+05 baries, Ar at 8.317e-04 g/cm3, He at 8.317e-05 g/cm3, γ = 1.67 for both gases

TP 10 : single wavelength

x = 0.24 cos(2π 2y/W) cm

8 b

TP 11 : multiple wavelength

x = Σ a_n cos(2π ny/w)

n = 0.5	a_n = 0.05 cm
1.5	0.10
2.0	0.07
3.5	0.11
5.5	0.09

0.003

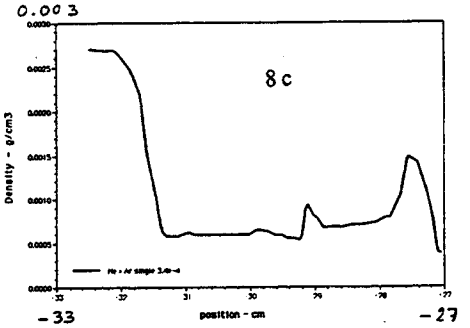

2 10^5

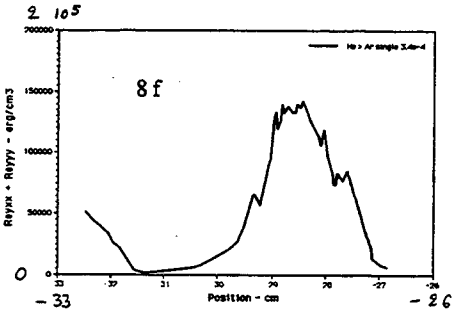

0.005

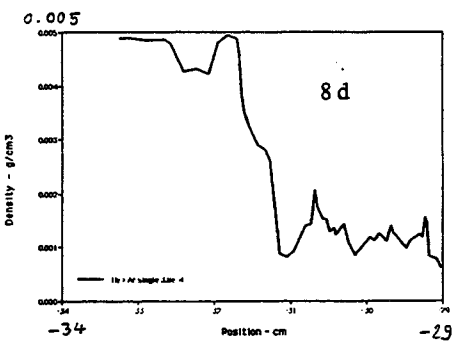

6 10^6

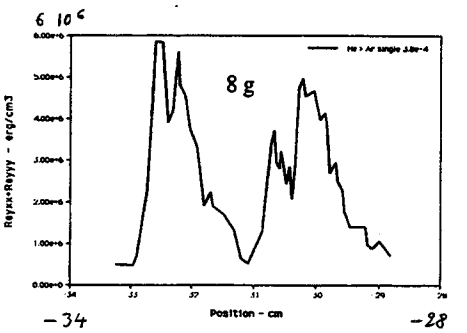

0.004

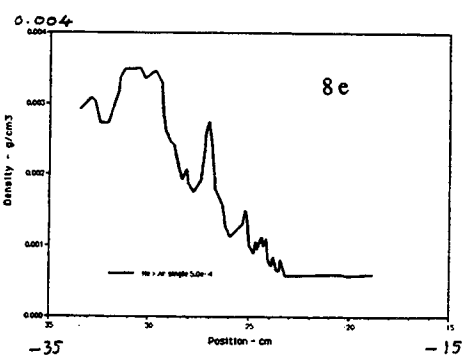

2 10^6

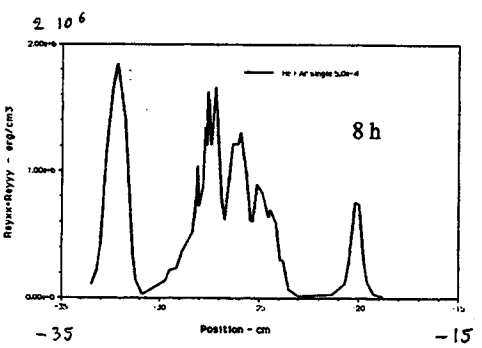

TP10

Figure 9 : TP10-11: Interface plots (from M. Wehner).

TP11

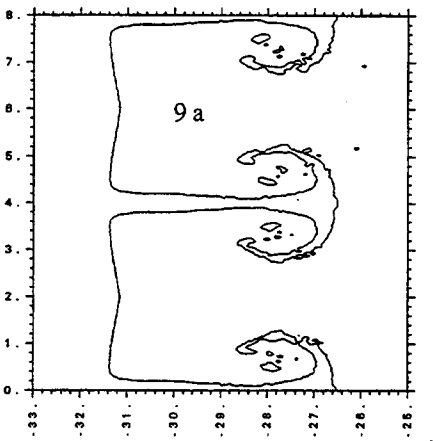

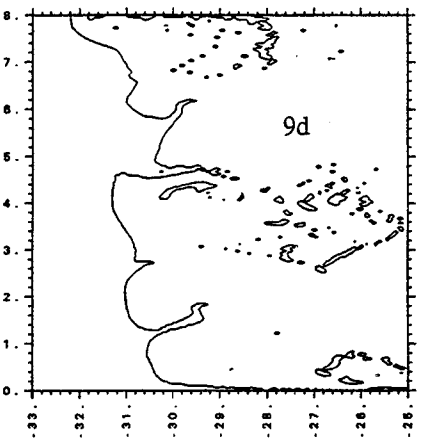

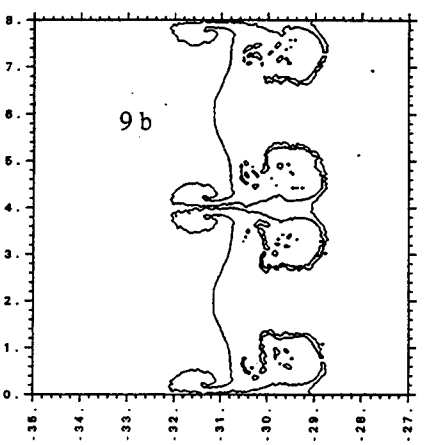

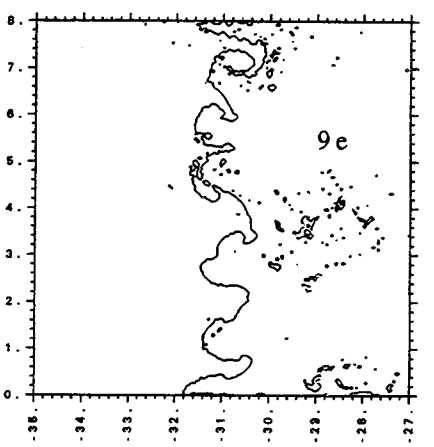

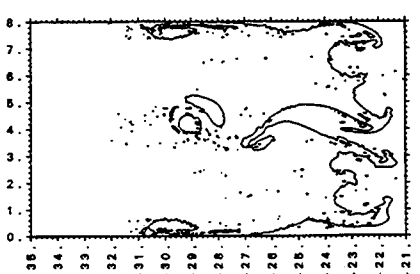

9 c

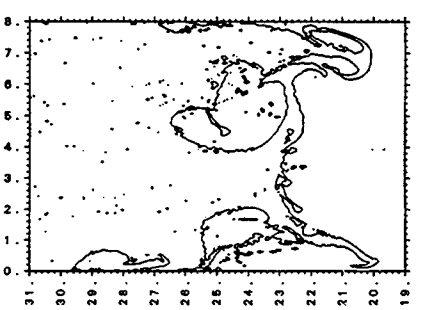

9 f

Figure 10 : TP10-11

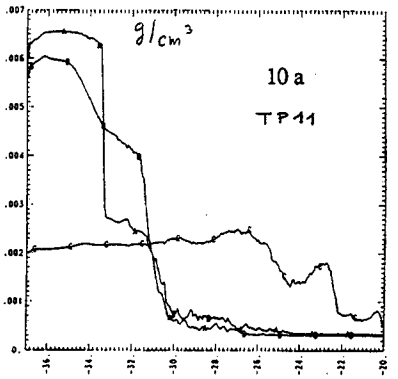

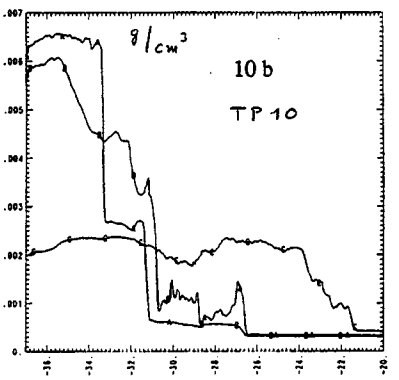

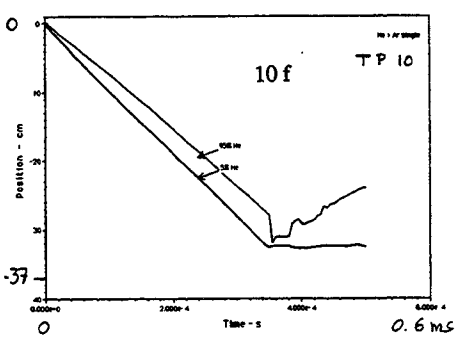

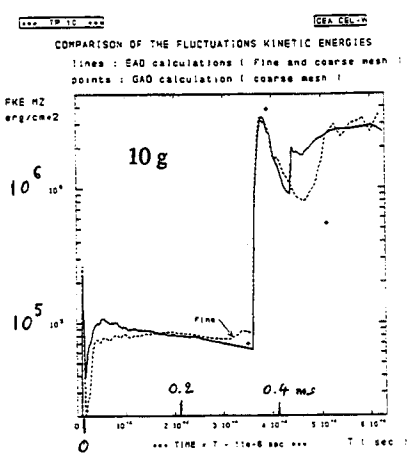

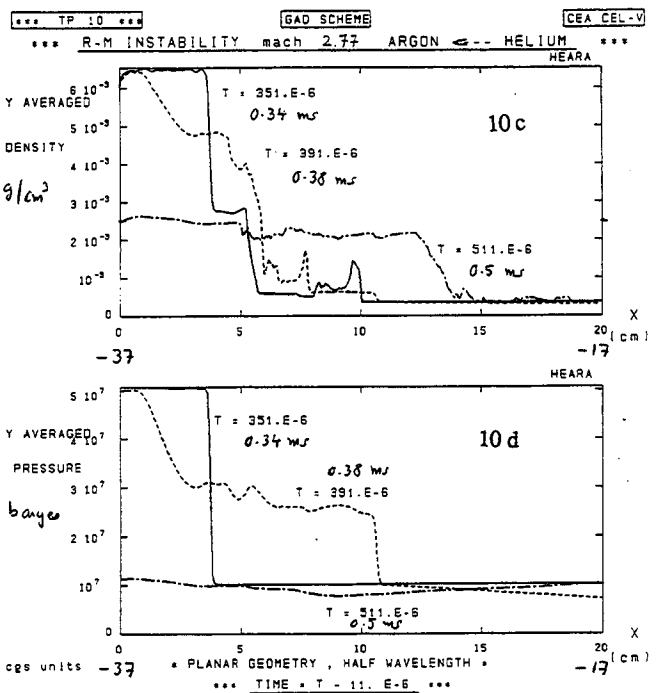

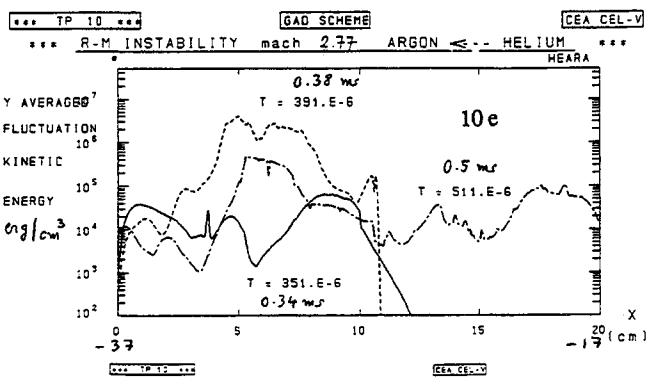

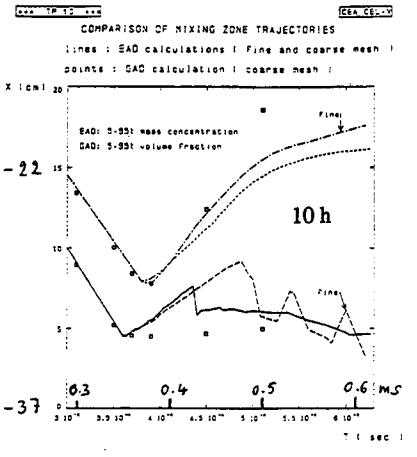

TP10 **Figure 11 : FKE profiles from EAD** TP11

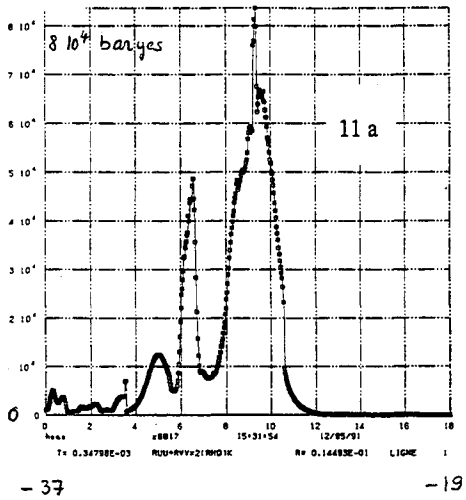

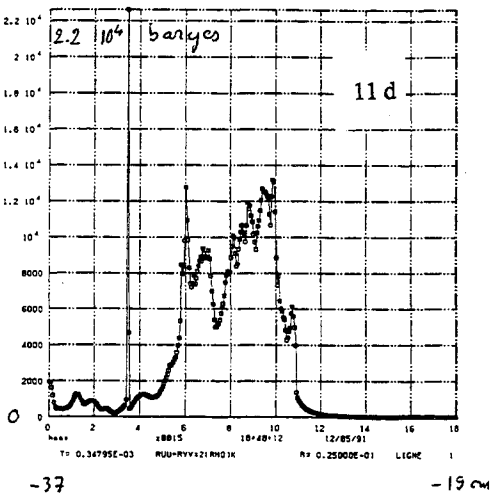

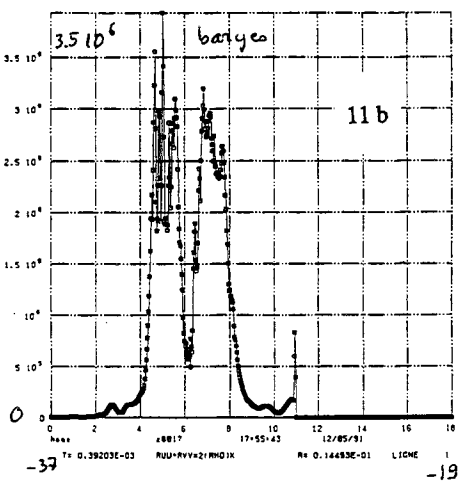

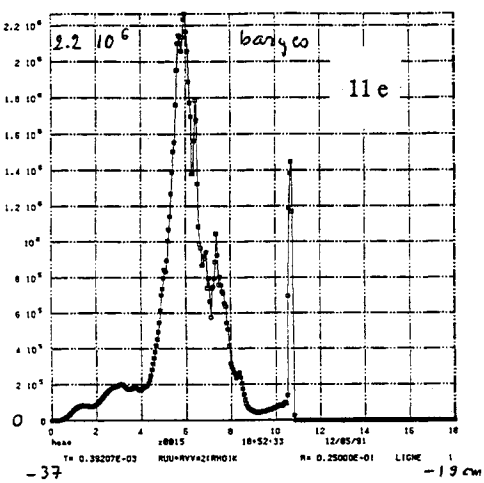

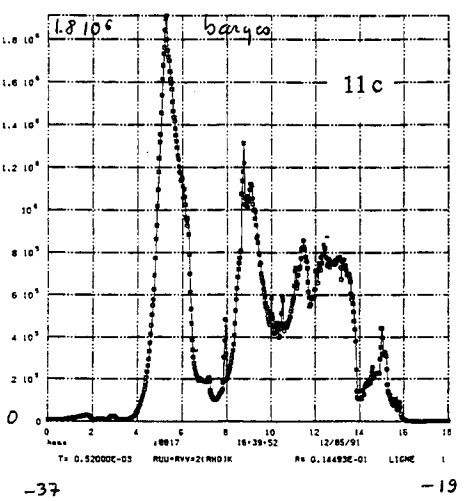

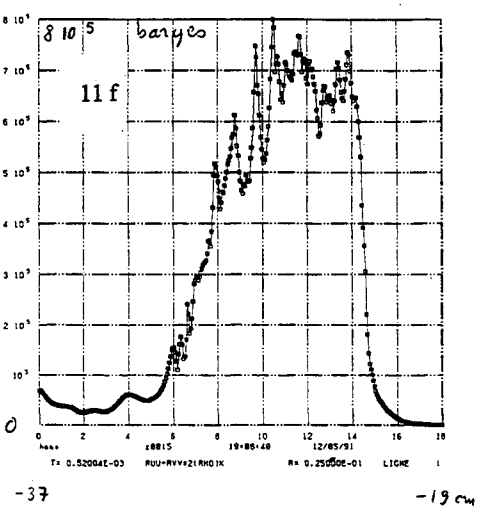

Figure 12 : TP10-11 : time evolution of mixing zone width and FKE

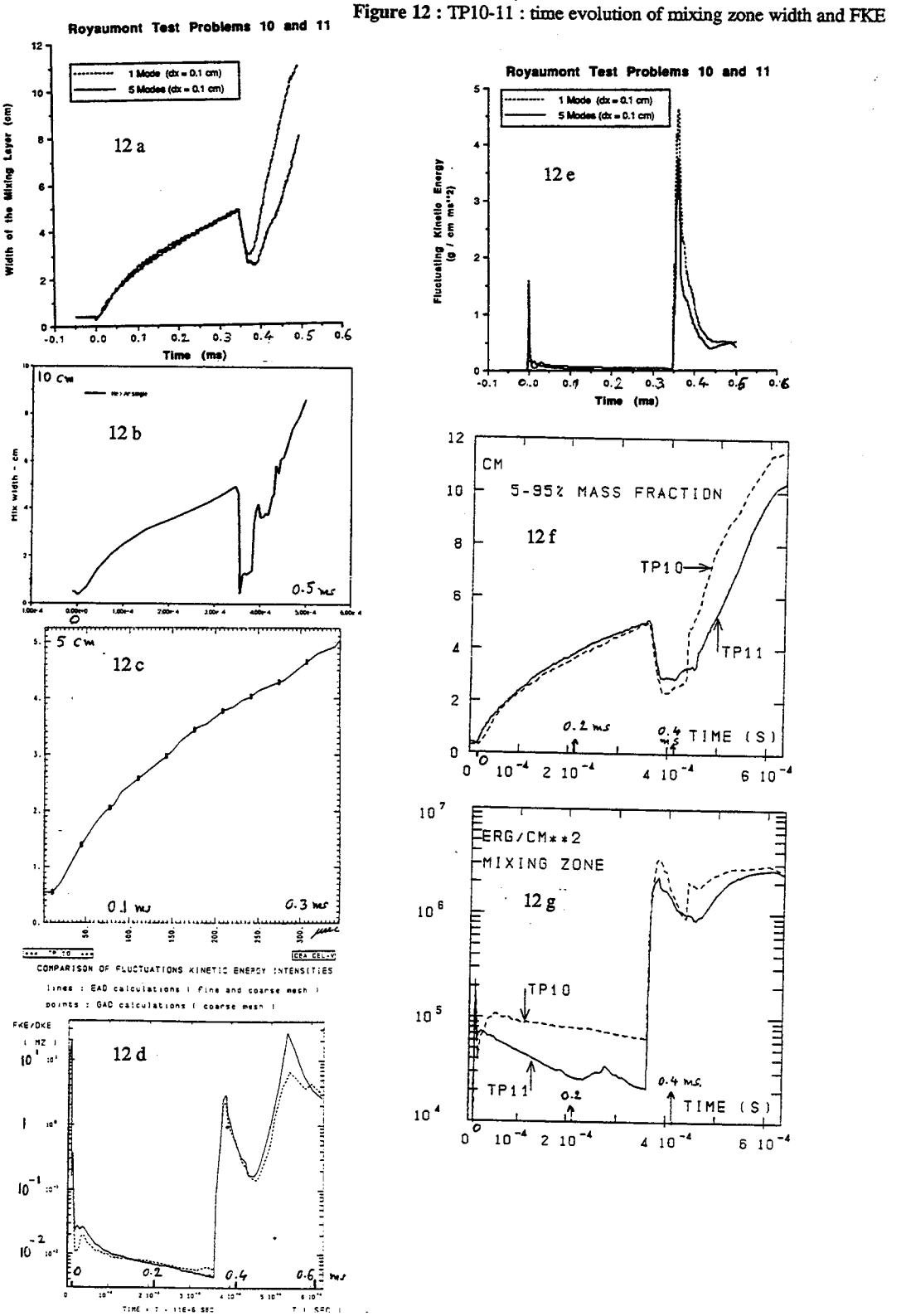

Summary of the Numerical Round Table

by
Alan Spero
Lawrence Livermore National Laboratory

The purpose of the numerical round table was to provide a forum in which the various researchers could make detailed comparisons of the performance of their computer codes on certain standard problems. The problems, which were distributed before hand, included idealized test problems as well as problems meant to represent selected shock tube experiments. The goal was to determine the validity of the numerical results by comparing them with each other and with experimental data. Questions that come to mind in this context are many. What can we accomplish with these codes? What is the most appropriate numerical technique(s)? Should we add more physics to the codes (for example: subgrid scale models, surface tension, material strength, transport modeling)? How can we improve the algorithms?

In my summary I will try to touch upon most of the issues that arose during this round table. The breath and depth of the work presented was very impressive, making the raconteur's job difficult. If I have forgotten to mention someone's work, or if I misrepresent a result, please forgive me.

Let me begin with a few general comments. I was impressed with the wide variety of codes used to simulate fluid motion and with the wide range of numerical techniques. We saw codes that used pure Eulerian techniques, free Lagrangian techniques, adaptive mesh approaches with both Eulerian and/or Lagrangian bases, and the Front Tracking

Method. All spatial dimensionalities from 1-D to 3-D were used. My general impression of the progress with simulation codes was that they are giving very good results.

The simulation codes were evaluated by comparing their performance on test problems proposed at the 2nd Workshop. For modest Mach numbers, in the bubble and spike growth regime, with both single and multi-mode initial conditions and both Rayleigh/Taylor and Richtmyer/Meshkov instabilities the agreement among many of the simulations was impressive. For some of the problems we were able to overlay the interface plots from several different codes (and different numerical methods) and observe remarkable identity. This was even true for the early time development of test problem TP10 which investigated a higher Mach number regime. Other quantities, such as mixing widths were also in good agreement. Some of the test problems showed some sensitivity to mesh size and the interface tracking technique used, but this sensitivity manifested itself only in the details of the interface, particularly when fine filaments developed.

The calculations tended to diverge at late times, after the interfaces had been reshocked. This probably reflects the integrated discrepancies between the calculations, and is therefore perhaps not surprising. We also saw evidence of symmetry breaking at late times in some calculations. This was undoubtedly due to numerical noise. It does raise concerns, makes one circumspect about believing the late time results from any one code calculation, and raises questions about the predictability of the system.

In general, my impression was that the capability to simulate large scale instabilities ("mushroom dynamics") is quite advanced and that at least the gross features of the results in the nonlinear case are independent of the code or algorithm used. Small scale features seemed much more dependant on the zoning chosen, and some of the codes may not be flexible enough to adapt to the fast changing spectrum at later times. I believe it would be

interesting, although it is probably a side issue, to see just how far the intercode agreement extends as one looks at smaller and smaller scales.

Among the various researchers there appears to be a recognition that the turbulent flows resulting from interface instabilities may not be as completely random as we thought. Most of the calculations showed the presence of persistent structures. The role of these structures in the development of the flows and the impact they may have on interpreting experimental diagnostics is yet to be understood.

I was impressed with the capabilities of adaptive mesh schemes used by some of the codes. The clear message these results bring us is that one should "put the zones where the turbulence is!" Others were equally impressed, and there was agreement among the participants that we should concentrate more of our efforts on mesh refinement algorithms.

We also observed that there were large disagreements between the one dimensional kε calculations presented by Dairiki and Kramer and the two dimensional simulations. The 1-D model was calculating a compression ten times greater than that from the simulation. The source of this discrepancy has not yet been elucidated. Since no other 1-D calculation was presented, it is not possible to assess whether the discrepancy was an inherent feature of the model or its particular implementation in the work presented.

It was clear that the age of color videos and animation has arrived. Several of the participants in the plenary sessions presented their calculations on the video monitor. We were all entranced. This proved to be a very effective way of getting a global understanding of the calculated fluid motion, and I think it will become a more and more common technique.

However, I believe that we should not let the beauty of these animations retard efforts to develop better diagnostics. To understand the numerical results, animation is not

enough. Part of the utility of a simulation is that it permits one to extract information about field variables which may or may not be experimentally accessible. Provided the simulation is physically correct, we can then use the simulation in lieu of experiment and get information which allows us to develop more intuition about the important processes. In particular, we could extract from the numerical simulations information about the turbulent fields which are used in 1-D in models such as the kε models discussed below. This will enable us to use the excellent simulation results to understand and validate the models.

We should devote more effort to extracting from the simulations quantities which are measured by the experimentalists. Examples are velocity correlation functions or time-dependent density gradients. It may also be possible to "post-process" the simulations in such a way as to duplicate the experimental diagnostics. Imagine if we had the capability to simulate a shock tube experiment (a 3-D code would probably be required) and the Schlieren photography diagnostic. We could then directly compare the numerical result with the experiment. This might facilitate progress on questions such as the importance/dominance of the boundary layer in the shock tube.

As an aside (and a call to arms for the experimentalists) let me comment that the diagnostic simulation capability mentioned above should not relieve the community of the need to develop "cleaner" experiments. One of the difficulties in comparing shock tube experiments with simulations is that we cannot simulate the effects of the membranes used in the experiments, nor can we exactly reproduce the (unknown) initial conditions of those experiments which do not use membranes. Thus we cannot know whether the discrepancies with experiment are due to problems with the codes or details of the experiments which are not modelled correctly. Relief from this problem would be welcome. The papers by Benjamin, Meshkov, and Toque et al suggest some approaches that may offer a solution.

The experiments are typically three dimensional. To date most of the codes are at most two dimensional, but this is changing. At the round table and in the plenary session there were reports on three dimensional codes. These simulations showed the same persistent structures observed in the two dimensional simulations, but the dissipation of these structures seemed to be greater in three dimensions.

What can we expect to see from simulations at the next Workshop? Clearly the field of three dimensional simulation seems to hold a great deal of promise. I expect a rapid increase in research in this area since it seems to be ripe and to offer the potential for increased understanding of experimental results. I also think that we will see increased attention to persistent structures (in both two and three dimensional simulations) and a greater understanding of their role in turbulent mixing phenomena. The role of dimensionality in dissipative processes will get more attention with a advent of the three dimensional codes. We need to assess this effect if we are to confidently compare our two dimensional simulation results with the inherently three dimensional experiments.

I expect that the people comparing two dimensional simulations will turn more attention to reshocked interfaces, since that is where the calculations seemed to disagree the most. This reshock problem probably demands some of the adaptive mesh algorithms we heard discussed at the Royaumont Workshop. Attempts to include more of the experimental details should also increase. We should look forward to simulation of the membrane (already begun by Benjamin) and boundary layers.

Finally, I hope that we will see more researchers address the key question: to what extent can an experimentally validated simulation code be used to help develop an instability/turbulence model.

Overview of the Roundtable discussion on theoretical problems

The purpose of this roundtable discussion was to review briefly the state of the art and to compare viewpoints on current theoretical issues in the field of compressible turbulent mixing.

The participants were N. AUBRY (B. Levich Institute, City University of New-York), D. BESNARD (CEA, Centre d'Etudes de Limeil-Valenton), A.C. BUCKINGHAM (Lawrence Livermore National Lab.), N.A. INOGAMOV (Landau Institute, Moscow), M. LESIEUR (Institut de Mécanique de Grenoble), K.O. MIKAELIAN (Lawrence Livermore National Lab.), Y. POMEAU (Lab. de Physique Statistique, Ecole Normale Supérieure, Paris), B. SITT (CEA, Centre d'Etudes de Vaujours-Moronvilliers, discussion moderator), D. VANDROMME (Institut National des Sciences Appliquées, Rouen), D.L. YOUNGS (Atomic Weapons Establishment, Aldermaston).

The different problems to be discussed were arranged under four main headings.

1 - <u>One point closure models for compressible turbulence</u>.
(with a view to specific phenomena that must be accounted for : strong gradients, shock fronts, two-phase mixing, turbulence production due to generating instabilities, i.e. Rayleigh - Taylor, Richtmyer - Meshkov, Kelvin - Helmholtz).

2 - <u>Initialization of turbulent state</u>.
(phenomenological models for numerical simulation purposes, empirical and theoretical background, perspectives of improvement)

3 - <u>Transition phase to turbulence</u>.
(the theoretical context : dynamical system approach for chaotic-flow, coherent structures, etc...; the computational context : direct numerical simulation ; a new approach in between : the method of the proper othogonal decomposition).

4 - <u>Other theoretical approches for fully developped turbulence</u>.
(statistical theories, spectral one-point closure models for non-equilibrium situations, large eddy simulation and subgrid-scale modelling).

All the participants contributed actively to the discussions, which were very stimulating. We will not go here into a detailed account, and we will only mention a few particular topics that appear to be of critical importance and interest :

- limited capability of one-point closure models, despite continuing progress and intensive theoretical and practical use, to simulate in a correct way important features (especially three-dimensional structures) of turbulent flow (VANDROMME, BESNARD);

- crudeness of initialization procedures of turbulent state for numerical computations;

- still existing gap between dynamical systems approach applied to a wide variety of specific chaotic flows (POMEAU), and "classical" approaches of transitional or fully developped turbulent flow.

As far as numerical computation is concerned, Direct Numerical Simulation and Large Eddy Simulation are making impressive progress (LESIEUR, YOUNGS), and are becoming effective tools for real flow analysis and modelling studies as well.

A more detailed review of the above-mentionned topics in the context of this roundtable discussion is given below by A. BUCKINGHAM (LLNL), who was one of the organizers of the first International Workshop in this series (Princeton, 1988). M. LESIEUR, who was rapporteur of this roundtable at the final summary session then gives a short presentation of his report.

B. SITT (CEA/CEV-M, Roundtable Organizer)

Theoretical Panel

The following topics discussed are not listed in the order in which they were presented. Instead they are ordered in congruence with notions about their relationship to each other and the current state of progress in theoretical understanding and advances in modeling and numerical simulation procedures. These comments are intended to place sole emphasis on the basic theme subject: the physics of *compressible turbulent* mixing. The discussion is further restricted to notions germaine to high speed (high Mach number) compressible flow situations, where the turbulent acoustical modes can be considered substantially excited and where wave transport of the resulting pressure fluctuations may contribute significantly to the evolution of the turbulence.

K. Mikaelian, LLNL, Livermore, CA: (On initialization).

Mikaelian's discussion of initial condition influences in computations was effectively confined to the sub-transitional linear to non-linear evolution of variable density flow instabilities subjected to shock accelerations. Mikaelian has studied these high acceleration, stratified layer density, instability growth situations extensively. His original theoretical studies have contributed substantially to the understanding of the dynamics of these sub-transitional and transitional processes. They have provided a useful basis for analysis of laser interaction with multi-density layered inertial confinement fusion targets. He has also derived an approximation for estimating the amount of directed shock energy that is converted into transitional random velocity excitation during the interactive passage of a shock wave with a distorted two-fluid interface or distorted single fluid contact discontinuity separating regions of different density.

Unfortunately a similar level of understanding has not been developed for the model initialization process itself in modeled turbulent flow computations. This is by no means a criticism of the thorough and innovative studies on sub-transitional processes of which Mikaelian's work is a notable example. However, there is, at present, insufficient data to provide new theoretical insight on the transition from laminar to turbulent flow. This kind of insight is required for the development and application of consistently effective initialization procedures for modeled, simulated, or experimentally designed studies of the post-transitional (substantially evolved and developed) turbulence process itself.

Initial conditions assigned for computing the evolution of turbulent flows or predictions of the influence of experimental initial conditions on the experimental flow development unfortunately share a common drawback. The influences on the developing statistical structure lack uniqueness. There is also an inadequate experimental/numerical data base and a lack of scientific experience and evidence to enable investigators to reliably test and analyze these conditional influences. Of course, one expects this condition to improve rapidly as more experimental evidence is accumulated in supersonic/hypersonic speed flows. For these flows, of particular interest to this community, compressibility and the associated additional degrees of freedom in the dynamics of the process increase the complexity. For example, compressible flows tend to remain laminar at larger values of critical Reynolds Number than their incompressible counterparts. Moreover, even at much higher Reynolds numbers than that considered sufficient to maintain fully developed turbulent flow, high favorable pressure gradients (accelerations) imposed on compressible flow have been observed to cause the initially turbulent flow to relaminarize.

Examples of this unsatisfactory state of knowledge are particularly evident in the rather dismal record accumulated in predicting transition from compressible laminar to turbulent flow, predicting turbulent flow separation and reattachment, and in predicting the decay of turbulence energy and the variation in turbulent scales of motion at advancingly large distances behind a shockwave through which the turbulence was processed.

Some fairly recent, unexpected experimental observations on other curious behavior in high speed compressible turbulent shear layers have been obtained and reproducibly confirmed. These show the unmistakable imprint of indefinitely persistent initial forced eigenfrequency excitation influences throughout the evolutionary stages of compressible turbulent shear flows. In the fully developed turbulent flow the initial imprint can be readily detected and measured. Moreover, these forcing influences have been successfully tested as a technique for controlling the development of harmonically sympathetic, low frequency, quasi-coherent flow structures in the downstream shear layer. This evidence appears to contradict the traditional view that fully developed turbulence has no persistent initial condition memory and that the fully developed tubulent state is thereby dynamically isolated from its initiation.

What are some common procedures for initializing a simulation or a model computation? Perhaps a short, albeit not comprehensive list might be useful in this review.

A commonly adopted approach in initializing a direct numerical simulation (DNS), for example, is to numerically develop the desired stationary statistical turbulent field for study throughout the grid domain by a computational evolution from a dynamically perturbed unstable laminar flow initial state. The laminar to turbulent transition is numerically simulated starting with an impressed unstable disturbance (for example a two-dimensional Tollmein-Schlichting wave velocity defect profile) on an otherwise steady mean background flow. Under the influence of the explicitly computed nonlinear velocity interactions that result from the initial instability, the flow field evolves, often over many hundreds of computational cycles, until the statistical structure has been established to within some satisfactory closeness to the desired ensemble averages and spectral structure of the pre-selected "stationary" state. This "fully developed" turbulent flow field is then stored and may be used for analysis or even as the initial conditions for a variety of direct numerical simulation experiments. It must be emphasized that these numerical simulation experiments are not a replacement of physical experiments but rather an almost infinitely analyzable supplement to a limited sub range of statistical dynamic flow behavior. This follows, since the numerical results are severely restricted in their statistical dynamic range by the very severe low Reynolds number constraints imposed by memory and computational speed limitations of even the most advanced computers.

Large eddy simulations (LES) and direct numerical simulations (DNS) are also often initiated with a random "seed" of turbulence distributed throughout the computational domain. Care must be taken that the perturbation field is statistically realizeable and that the balance expressed by the mean and variance of all perturbed quantities is physically consistent with an equilibrium (production and dissipation of turbulence kinetic energy are in balance) limit in the physical state being simulated.

Some current examples of such initially "seeded" computations at the LLNL include Leith's LES studies of subgrid scale statistical influences on developing turbulent free shear layers. Leith makes use of a space and time white noise potential function, whose point derivatives provide random fluctuational accelerations to the velocity field. The point accelerations are the initial seeds for his studies on stochastic back scatter influences from the non-resolvable sub-grid scale motions.

Recent LLNL LES computations also include those of Rotman who makes use of random white noise accelerations for seeding either velocity or density initial perturbations applied individually as simulations of existing physical experiments under average value constraints selected to mimic and recreate the shock tube shock wave turbulence interaction experimental results of Hesselink and Sturtevant at Cal Tech (1976). In addition, Buckingham adapts the Leith initial seed procedure together with Monte Carlo shock structure computations for LES studies of shockwave induced viscoelastic turbulent field response.

Initialization and growth of turbulence from unstable flow sources such as RTI and RMI perturbed discontinuous density interfaces have been commonly used in conjunction with κ–ε single point closure model studies of shock tube mixing experiments such as those discussed during the current Royaumont Conference. This procedure has been automated to a large extent through use of a sequence of models from instability growth into the non-linear mixing phase and self-similar turbulent mixing layer evolution in up to three space dimensions by Youngs at the AWE. Crowley at the LLNL initiates his modeled comparisons-with-experiment of the shock enhancement and relaxation of turbulence energy in the compressible turbulent boundary layer by initial value adjustment within the κ–ε model to conditionally match experimental results. The model is adjusted to provide initial turbulence energy and appropriate dissipation balance from these experimentally measured values on selected streamlines, in the Princeton University experiments of Smits and Mouck, (1986).

In a search for a more physically reasonable function to mimic the size scale distribution in evolving compressible turbulence (i.e. the dissipation function, ε, in the κ–ε closure scheme) Wilcox (1988, 1989) has modified and extended the original (Saffman-Wilcox, 1971) κ–ω single point closure notions in a new multiscale formulation. This formulation exploits the more physically satisfactory identification of the second parameter, ω, as the experimentally measurable reciprocal time scale variation of the excited eddy motions being modeled. This identification and model exploitation of ω with measurable reality was probably, in part, due to an original suggestion by Reynolds at Stanford Univesity (1980).

The κ–ω formulation is used as the framework for Wilcox's efforts in developing a more universally applicable multiscale model for compressible high speed turbulent flow calculations. Universally applicable here refers to the lack of need for adjustment of coefficients when when the modeled flows vary from boundary layers to free shear layers or jets or wakes. This model is currently gaining some popularity in NASP (National Aerospace Plane) modeling applications to supersonic and hypersonic boundary layer flows, separated flows, and a few free shear layer mixing computations.

The initiation topic is (if anything is) a ubiquitous obstacle in both modeling and simulation. The variety of prescriptions applied for initiating even the same class of models or simulation tools multiplies almost as the product of the number of modelers with the number of different flow situations. The search for uniform initialization procedures will probably continue. However, it is the writer's view that the growth of specialized procedures for each characteristically different application and, of course for each class of model, will continue to proliferate much more rapidly than the development of any useful initialization uniformity.

Transition: The "Rite of Passage" from laminar to turbulent flow states

Before moving on to some impressions of the other theoretical panel member's interesting contributions, comment is offered on a topic that was only touched on implicitly. The topic is the transition from laminar to turbulent flow. Little formal theoretical progress has been made since the development of the systematic momentum small perturbation theory now more than thirty years in its maturity (Mack ,1960).

Compressible flow carries with it added degrees of freedom over and above incompressible flow with correspondingly richer nonlinear dynamical interactions occuring before the transition process can be considered complete. The momentum criteria based on small perturbation instability analysis carries only slightly into the nonlinear interaction regime. It would appear that further substantial progress in formal development of a transition theory and criteria needs much more than a "kick-start" to advance formal systematic theoretical development. It follows that it is probably overly optimistic to suggest that sufficient understanding and some high confidence predictive capability of the transition process will be obtained in a time frame useful for current and continuing applications and model development. Simple indicators such as momentum thickness Reynolds number criterion, or other computed measures used in conjunction with experimentally determined average mixing layer growth rates, when suitably modified for compressibility influences, will probably have to serve model developers for the immediate future.

It is not a completely negative picture, however. As seen in the course of the Royaumont meeting, the congruence between computed and experimental results for shocked instability growth and interfluid penetration is quite promising. Further emphasis must be given to other, more precise definitions of mixing and transport in the unstable laminar to turbulent flow transition regime. In particular, another scale, that of component concentration in a mixing layer, must be measured and later modeled successfully in shock accelerated flows. The measured and successfully computed variation in both concentration and apparent mixing zone penetration growth and evolution should, automatically, provide new information on the compressible flow transition process from unstable to fully involved turbulent transport regimes. The two following panelelists provided a somewhat more optimistic view.

N. Aubry , Levich Inst. City University of New York

Karhunen-Loeve decomposition, or that variant for modeling and analysis of low wave number structures in turbulent flow termed proper orthogonal decomposition was elegantly presented at the workshop as a potential technique for developing an understanding of the dynamics of turbulent flow. Aubry and her former thesis advisor, Lumley, provide a very effective argument based on their studies of large scale turbulence structure in incompressible boundary layers. The relatively low order of the degrees of freedom for such techniques can be supplemented or expanded, it is claimed, by establishing a larger data base, experimentally or numerically, and then continuing to apply this procedure which yields progressively better approximations to the eigenfunctions characterizing the underlying equations as the data base and the order of the expansions are increased.

Current discussion and questions develop with respect to the potential of application of a technique such as this to studies of compressible turbulence or of the laminar to turbulent transitional states. The conceptual difficulties relate to possible limitations in developing suitable theoretical descriptions of compressible three dimensional flow structure and transition with the a resultingly large number of dynamical interaction scales using essentially a low order system with a practical limit on the degrees of freedom. However, the current success with very complicated wall bounded flows helps to stimulate optimism on application to the possibly even more challenging high speed compressible flow situations from later developments of this promising theoretical procedure.

Y. Pomeau, Lab. de L'ENS, Paris. (Nonlinear Dynamical Systems)

The foreseen difficulties in applying the previously discussed Karhunen-Loeve decomposition procedure to compressible flow situations possessing a substantially enlarged potential dynamic degrees of freedom heirarchy and correspondingly more complexity than that represented by a low order strange attractor system have parallels in considerations about the general applicability of dynamical systems analysis. However, Pomeau provided a spirited defense for the potential development and use of dynamical systems procedures for substantive theoretical analysis and increased understanding of turbulent flow structure and evolution.

Emphasis is often placed on the potential for finding information on the transition process and the existence of an exact finite bound on the degrees of freedom for two dimensional turbulence. This boundedness comment stimulated one of the more spirited discussions on the panel. This was occasioned by the lively discussions between Pomeau and Lesieur. Lesieur pointed to vast number of scales of excitation that must be dealt with in general analysis of even in a simple homogeneous turbulent flow. This number Lesieur suggested may be estimated (with inertial range separation and Obukov-Kolmogorov dimensional analysis arguments) as a number equivalent to the flow Reynolds number raised to the 9/4 power for three space dimensions.

One can be reasonably sure that the spirited arguments between the dynamical systems approach advocates and almost all of the other schools of turbulence theory will continue indefinitely. It also seems equally reasonable to assume that the continuing debate and supporting theoretical and experimental efforts in dynamical systems studies will continue to provide useful information and guidance in further understanding the nature of the transition process.

D. Vandromme, INSA, Rouen

A (somewhat surprisingly) pessimistic view was advanced by Vandromme on the lack of promise of single point closure modeling in compressible flows. His focus appeared to center on several flow features that provide a conceptual challenge for model development in compressible high Reynolds Number flow. These include the unmodeled influence (intrusion?) on the dynamics of compressible turbulence arising from the known anisotropic 3D large scale, almost coherent structures, the apparent persistence of these structures and their influence on scale variations, and the influence of shock waves.

These processes and their influences may be lost or hidden in the conventional time or even mass averaging procedures used to develop the traditional single point closure schemes. Their known presence, however, has been and is an argument for application of both DNS and LES procedures to supplement the sparse experimental data base and to provide needed information for model development.

Another difficulty, emphasized by Vandromme, was three dimensionality which prevails even to a larger extent in high speed compressible boundary layer flows, where wall curvature and shock layer curvature are interrelated. It is useful to recall that in such flows there may exist strongly interacting transverse pressure distribution influences on both the fluctuating velocity field and the energy-density (entropy) field. Another problem area was the prediction or treatment of transition and attendant unsteady phenomena such as shock augmented flow separation and reattachment. These topics have been previously mentioned.

While most of the Workshop participants would probably vote affirmatively to the list of difficulties, a generally pessimistic view seems out of place. This is particularly true since we, by necessity, are required to seek, modify, or even develop more promising modeling approaches to meet current programmatic needs and to provide a data base for future comparison and refinement.

There is grounds for some optimism based on the advances in DNS, LES, spectral methods, and second order moment methods as well as advances in new experimental diagnostics techniques for non-intrusive measurement. Complementary advances have been made on both diagnostic techniques and and numerical-theoretical procedures for 3 dimensional flow reconstruction and data base enlargement from a limited number of experimental observations. These procedures may be and are being applied for refinement and application of single point closure models.

D. Besnard, CEA, Limeil-Valenton, Methods for augmenting model development

A more optimistic view of single point closure development for compressible flow modeling was provided by Besnard. Development and application of a spectral decomposition procedure has been shown to provide rough confirmation of term and coefficient identification in the ubiquitous κ–ε model, as well as more detailed information on fundamental characteristics of evolving turbulence, such as scale variation questions and a fresh interpretation of the dissipation questions.

It is apparent that many of the participants are awaiting later compressible turbulent flow versions of this development that will permit analysis and accurate prediction of the influence of the pressure velocity triple correlation , compressible production, and compressible dissipation of turbulence energy.

In addition, Besnard illustrated the utility of the second order closure procedure (BHR method), in augmenting the development of lower order but easily applied single point closure models. One must note that the BHR framework, simplified by prescription of selected moment interrelations, has been and is the basis of at least one of the more generally successful compressible flow closure models at Los Alamos National Laboratory.

In summary, detailed numerical simulations and more elaborate but time demanding higher order and spectral decomposition procedures and the results they generate for analysis have a demonstrated and important role in practical single point closure model development.

D. Youngs, AWE, Aldermaston. (Model development with experiments)

This topic title is supplied by the writer in response to personal impressions of the special significance of some of D. Youngs group's many contributions to the present state of modeling. The transition and initialization processes are combined by preliminary modeling of the shock driven instability growth into the non-linear and final self-similar stages of behavior.

Emphasis is placed initially on interface tracking as a measure of mixture layer development and penetration. Later efforts include emphasis on the other often neglected but sorely needed measure of the concentration distribution of mixture constituents. This effort was characteristically and thoughtfully planned early on several years ago with the research collaboration of Paul Linden at DAMTP, Cambridge University. It seems to be progressing satisfactorily into higher Mach Number flow investigations.

Special emphasis is placed by Youngs on the necessity of test, simulation and eventually model incorporation of three dimensional influences. Systematic progress, well planned and executed experimental/modeling interactive programs characterize this group's exemplary advances and contributions to the present state of understanding.

M.Lesieur, Inst. de Mecanique, Grenoble. (LES, DNS and Spectral structure)

Lesieur briefly but compellingly explored the present status of LES and DNS procedures for analysis and numerical evaluation and test of fundamental theoretical ideas on the evolution of turbulent structure. He pointed out the access provided for attention to coherent structure influences on the statistical field, isolating new dynamics associated with three dimensional degrees of freedom, vortex dynamics reattachment and splitting processes, the spectral cascade in compressible flows and similar physics that will probably always be difficult to access experimentally. He did not emphasize (obviously because of time limitations) the continued development and exploitation of multi-point closure methods although he has had much to do with their advances and use in theoretical turbulence analysis.

Multi-scale models and other models for compressible flows

The writer was asked to contribute a few comments on the promise or lack of it of multiscale methods applied to single point closure modeling. Time did not permit adequate outlining of this promising approach. Let me briefly summarize some of the themes that might be addressed given sufficient time. The basic idea of multiscale modeling has been summarized in Launder and Schiestel (1980), Schiestel (1987), Wilcox (1988), and in related recent literature from the NASA researchers at both the AMES and Langley Research Centers.

A basic point is that single point, single scalar (e) dissipation cascade turbulence closure modeling is too limited to show the appropriate influence of both large and small scales of excitation on the turbulent field. It is also apparent that under the constraints imposed by the limited classical single point model flexibility, changes in the vector mean strain field cannot be incorporated when rapid changes occur due to contractions or due to shock or expansion interactions. Departure from and return to isotropy is not accounted for, and most of the aspects of strong compressibility can be satisfied for only one part of the spectral range of motions. Anomalies develop when addressing real flow situations and severe model adjustments must be made when moving from strong to weak shearing motions and from shear flows to jets, or wakes, etc.

In contrast, multiscale procedures implement a separate transport equation for each significant range of the dynamic spectrum of excited motions. Initially two spectral ranges and corresponding transport equations have been used to considerably enhance the applicability and universality of the closure to a wider variety of physical situations. Even two schemes eliminate the troublesome and obviously limited dependence on a single Boussinesq (gradient transport) term. Currently under development is a three band model which includes a special (viscoelastic relaxation) phase in the low wave number spectra associated with transient shock interaction effects. (Buckingham, 1991).

Alfred C. BUCKINGHAM (LLNL)

REPORT ON THE THEORETICAL ROUND TABLE

There were three main topics discussed during this round table, namely the classical one-point closure modelling approach, the mathematical problems related to two and three-dimensional turbulence, and the possibilitties of direct and large-eddy simulations.

1) Classical one-point closure modelling approach.

Some pessimism was expressed concerning the ability of this approach to properly take into account coherent structures, shocks, and compressibility effects in general. As a matter of fact, these methods need to be validated with the aid of physical experiments and numerical simulations, either direct-numerical simulations (DNS) or large-eddy simulations (LES). On the contrary, one can be optimistic with new multiscales techniques which are being developed; they are based on two-point closures such as the Direct-Interaction Approximation (DIA) or the Eddy-Damped Quasi-Normal Markovian theory (EDQNM). Of the same family is also the Renormalization-Group approach (RNG). These multiscale techniques may be very useful for the development of a new modelling, intermediate between one-point closures and LES.

2) Mathematical problems in 2 and 3 dimensions.

There are still a lot of questions posed (in 3D) concerning the solutions of Euler or Navier-Stokes equations (existence for arbitrary times, uniqueness, regularity, etc...). Other mathematics arise from the instability theory (linear, secondary, nonlinear). Another important question concerns the dimension of the manifold of Navier-Stokes equations : the standart phenomenology of turbulence, based on classical Kolmogorov analysis, suggests that the dimension is $\sim R_e^{9/4}$ where R_e is the Reynolds number. This is very high. On the other hand, there are conjectures, based on an analogy with Kuramoto-Sivashinsky equation, that the dimension could be low, so that dynamical-system theory could apply. This is suported by a study done for the turbulent boundary layer using the so-called proper-orthogonal expansions.

3) The possibilities of DNS and LES.

They enable to study the nonlinear stages, and give exact access to the fields. Efficient graphics allow to characterize the three-dimensional dynamics of the coherent votices, and how they cascade into small-scale turbulence. They have proven their efficiency in dealing with compressibility. For developed turbulence, the future of these techniques lies in large-eddy simulations, which require efficient subgrid scale models. With the rapidly increasing computing power and speed, these DNS and LES techniques are extremely promising tools to explore the mysteries of the nature of turbulence.

M. LESIEUR (I.M.G.)

INDEX

FRONT COVER

Colorized version of a black and white Schlieren photograph of a mixing zone between air (top, red color) and sulphur hexafluoride (SF6, bottom, blue) induced by the Richtmyer-Meshkov instability in the Vaujours vertical shock tube (horizontal scale 7.5 cm). The incident shock in SF6 (Mach 1.45) has accelerated upward a 1.7 cm wide molecular diffusion zone with a weak embedded perturbation due to the retraction (from right to left) of a separating blade. The picture shows the amplification of these perturbations, 3.15 ms after the initial interaction, and about the time of passage of the second shock reflected from the end plate of the shock tube (located 54.4 cm above the blade). On the original Schlieren picture (printed upside down on page 25 in CHOCS 2, CEA DAM scientific and technical journal) the fine scales visible on the SF6 side are the signature of turbulent mixing in the boundary layers, but the more puzzling smoothness of the edges of the interpenetrating air bubble (center) and SF6 spikes (on its sides) may be due to an optical effect. These details are somewhat erased by the colorization process which was performed by the laser experiments group at Limeil.